METALS. SUPERCONDUCTORS

Electronic structure of Rh, Pt, In, and Sn in the mixed-valence systems $Eu(Rh_{1-x}Pt_x)_2$ and $U(In_{1-x}Sn_x)_3$

Yu. P. Smirnov, A. E. Sovestnov, V. A. Shaburov, and A. V. Tyunis

B. P. Konstantinov St. Petersburg Nuclear Physics Institute, Russian Academy of Sciences, 188350 Gatchina, Leningrad District, Russia

(Submitted December 25, 1999)
Fiz. Tverd. Tela (St. Petersburg) **41**, 1529–1531 (September 1999)

The electronic structure of Rh, Pt, In, and Sn in the mixed-valence systems $Eu(Rh_{1-x}Pt_x)_2$ and $U(In_{1-x}Sn_x)_3$ has been studied by the x-ray K line-shift method. It has been found that the occupation of the Rh $4d$-shell in $Eu(Rh_{1-x}Pt_x)_2$ is higher than that in the metal, and that it grows with decreasing Eu valence (i.e., with increasing $4f$-shell occupation). The electronic structure of Pt, In, and Sn in $Eu(Rh_{1-x}Pt_x)_2$ and $U(In_{1-x}Sn_x)_3$ does not depend on the Eu and U valence and is practically the same as in the metals. These features in the electronic structure of Rh, Pt, In, and Sn in $Eu(Rh_{1-x}Pt_x)_2$ and $U(In_{1-x}Sn_x)_3$ suggest that the electron released in the $f^n \rightarrow f^{n-1}+e$ transitions, rather than transferring to the common conduction band, remains localized at the Eu and U atoms. © *1999 American Institute of Physics.* [S1063-7834(99)00109-4]

The phenomenon of mixed valence (MV) is of widespread occurrence in compounds of the $4f$ and $5f$ elements (the lanthanides and actinides). It originates from the closeness of f levels to the Fermi surface, as a result of which the f shell occupation (the valence of the f element) is sensitive to external conditions, such as the pressure and temperature. Besides the pressure and temperature, the valence can be altered by varying the composition of the compound. For instance, by introducing impurities with a smaller atomic volume into the starting lattice, one can simulate the action of external pressure and initiate a complete or partial transition between f^n and $f^{n-1}+1$ states which are close in energy (a change in the valence state). While systems of this type were extensively studied for both $4f$ and $5f$ elements, major interest was focused on the specific features of the valence transition itself (continuous pattern, presence of jumps, f shell occupation, transition reversibility, etc.). Much less attention was paid to the investigation of the electronic structure of the substituting element, because it was believed that its role reduces primarily to imitation of pressure, and that it is not involved in electronic transformations. Such a model, however, is oversimplified. Indeed, in mixed-valence intermetallics the main and substituting elements form a common conduction band having a common Fermi level, which may involve charge transfer from one element to another, and electron redistribution between subbands with different orbital quantum numbers (s,p,d). This may bring about a change in the electronic structure of both the main and substituting element. There may also change such parameters as the distance of the f level to the Fermi level, as well as the density of states at Fermi level, which affect directly the characteristics of a MV transition. A MV transition ($f^n \rightarrow f^{n-1}+e$) releases an additional free electron, which can transfer to the common conduction band or to the substituting element, or become localized at atoms of the MV elements. This point remains presently unclear. Thus investigation of the electronic structure of the partners of the MV atom, besides being of interest in itself, may shed light on some aspects of the physics of the MV state which still remain unclear.

This paper reports a study of the electronic structure of Rh, Pt, In, and Sn in the mixed-valence systems $Eu(Rh_{1-x}Pt_x)_2$ and $U(In_{1-x}Sn_x)_3$ by the x-ray K line-shift method (see, e.g., Ref. 1). We determined earlier the variation with composition of the f shell occupation, Δn_f (the change in valence), of Eu and U in these systems.[2,3]

The polycrystalline samples used (the same as in Refs. 2 and 3) were prepared by arc melting, were practically single phase, and had lattice parameters agreeing with literature data.[4,5] The scheme of the experiment, the measurement procedure, and the data processing techniques are described in detail elsewhere (see, e.g., Ref. 1).

The experimental K line shifts of Rh and Pt in $Eu(Rh_{1-x}Pt_x)_2$ and of In and Sn in $U(In_{1-x}Sn_x)_3$ are presented in Tables I and II, respectively. All shifts were measured relative to the Rh, Pt, In, Sn metals. Given in the last columns of Tables I and II are our earlier data[2,3] on the variation of the f-shell occupation, Δn_f, of Eu and U in these systems with composition. The values of Δn_f were determined as the difference of the f-shell occupation between states with the lower (f^n) and higher ($f^{n-1}+e$) valence. Obviously, Δn_f is equal to the number of the additional electrons liberated in the $f^n \rightarrow f^{n-1}+e$ transition.

(1) $Eu(Rh_{1-x}Pt_x)_2$. As seen from Table I, all compounds exhibit positive shifts of the Rh $K\alpha_1$ and $K\beta_1$ lines, which increase smoothly with x (with Pt substituted for Rh). The

TABLE I. Experimental shifts (ΔE) of Rh and Pt K lines in $Eu(Rh_{1-x}Pt_x)_2$ vs composition x; $\Delta n_d^{(1)}$ and $\Delta n_d^{(2)}$ is the increase in the Rh $4d$ shell occupation in $Eu(Rh_{1-x}Pt_x)_2$ compared to that in Rh_{met} for two different mechanisms (see text).

	ΔE, meV					
x	$K\alpha_1^{Rh}$	$K\beta_1^{Rh}$	$K\alpha_2^{Pt}$	$\Delta n_d^{(1)}$	$\Delta n_d^{(2)}$	Δn_{4f}^{Eu}
0	+29±4	+50±10	–	0.21±0.02	0.17±0.02	0.77±0.04
0.25	+36±4	+32± 8	+25±18	0.22±0.02	0.18±0.02	0.52±0.04
0.50	+48±4	+60±10	–	0.32±0.02	0.26±0.02	0.20±0.03
0.75	+59±4	+71±16	–	0.39±0.03	0.32±0.03	0
1.0	–	–	+1±12	–	–	0.06±0.04

Note: Given in the last column are the Eu $4f$-shell occupation changes Δn_{4f}^{Eu} from Ref. 2.

shifts of the Pt $K\alpha_2$ line at the two extreme points ($x = 0.25$ and 1.0) were found to be close to zero within experimental error.

The nonzero shifts of the Rh $K\alpha_1$ and $K\beta_1$ lines indicate that the Rh electronic structure (occupation of the outer $5s$ and $4d$ shells) in $Eu(Rh_{1-x}Pt_x)_2$ differs from that of the metal. This difference can be quantified by comparing the experimental shifts with the values obtained in Dirac–Fock-type self-consistent calculations.

As shown by us earlier,[6] the $K\alpha_1$ and $K\beta_1$ line shifts of heavy elements induced by removal from an atom of *s*- and *d*-electrons are opposite in sign (the removal of an *s* electron results in a positive, and that of a *d* electron, in a negative shift) and differ little in absolute magnitude.

The observed positive shifts of the Rh $K\alpha_1$ and $K\beta_1$ lines can be accounted for by two possible mechanisms: (i) charge transfer from Eu to Rh; because the density of states in the Rh $4d$ subband exceeds by about an order of magnitude that in the $5s$ subband, the charge transferring from Eu to Rh fills primarily the $4d$ subband, and the observed shifts are largely due to the change in the Rh $4d$-subband occupation Δn_d, whereas the effect of the $5s$ subband filling on the Rh K line shifts may be neglected; (ii) redistribution of the $5s$ and $4d$ electrons of the Rh itself (a transfer of electrons from the $5s$ to $4d$ subband of Rh will likewise induce a positive shift in the Rh $K\alpha_1$ and $K\beta_1$ line positions). Obviously enough, for such a mechanism $\Delta n_d \equiv -\Delta n_s$.

It would be difficult, based only on our data, to decide between these two mechanisms. It is possible that they coexist.

TABLE II. Experimental shifts (ΔE) of In and Sn $K\alpha_1$ lines in $U(In_{1-x}Sn_x)_3$ vs composition x (against metallic In and Sn as references).

	ΔE, meV		
x	$K\alpha_1^{In}$	$K\alpha_1^{Sn}$	Δn_{5f}^{U}
0	+27±11	–	0.20±0.02
0.2	+25±13	+5±9	0.18±0.02
0.5	+30±13	+1±8	0.14±0.02
0.65	−5±13	–	0.09±0.02
0.8	+45±18	–	0.05±0.02
0.9	0±14	+17±8	0.01±0.02
1.0	–	–	0

Note: Given in the last column is the U $5f$-shell occupation change Δn_{5f}^{U} from Ref. 3.

The mechanism of charge transfer from Eu to Rh appears to be, however, preferable. It is argued for by the large positive difference in electronegativity between Rh and Eu ($\Delta x = 0.9$, see, e.g., Ref. 7). An analysis of magnetic and heat capacity data for intermetallic compounds of rare-earth (RE) elements with $3d$, $4d$, and $5d$ metals made by Buschow[8,9] suggests that the *d*-shell occupation of these elements in intermetallic compounds is larger than that in metals. Finally, Mössbauer measurements made on Ru, Ir, and Os (Rh does not have Mössbauer isotopes) in their intermetallic compounds with RE elements also attest to an increase of charge density at the nuclei of *d* elements in these compounds compared to the corresponding metals.[10]

By comparing the experimental shifts with the shifts obtained from Hartree–Fock atomic calculations one can determine the changes in occupation of the Rh $4d$ subshell, $\Delta n_d^{(1)}$ and $\Delta n_d^{(2)}$, for the above mechanisms. We used in this work the Dirac–Fock (Koopmans), DF(K), model involving a relativistic calculation with complete inclusion of exchange without relaxation, which provides the best agreement with experiment for RE and $4d$ elements.[11,12] We calculated the Rh $K\alpha_1$ and $K\beta_1$ line shifts relative to the accepted electronic configuration of metallic Rh (see below) $\Delta E_{\text{calc }\alpha(\beta)}^{(1)}$ $[\Delta n_d^{(1)}, \Delta n_s \equiv 0]$ for the first mechanism, and $\Delta E_{\text{calc }\alpha(\beta)}^{(2)}$ $[\Delta n_d^{(2)}, \Delta n_d \equiv -\Delta n_s]$ for the second mechanism, within a broad range of Δn_d variation. The calculated shifts were fitted by a second-order polynomial $P_{\alpha(\beta)}^{(1),(2)}$, and the values of Δn_d were found from the equations

$$P_{\alpha(\beta)}^{(1),(2)} = \Delta E_{\exp\,\alpha(\beta)},$$

where $\Delta_{\exp\,\alpha(\beta)}$ are the experimental shifts of the Rh K lines in $Eu(Rh_{1-x}Pt_x)_2$.

The electronic configuration of metallic Rh (with the nine outer $4d$, $5s$ electrons outside the filled [Kr] core distributed as $Rh[Kr]4d^{9-y}5s^y$) is not known well enough and was determined here from a comparison of the experimental shifts $\Delta E_{K\alpha_1}$ $(Rh_2O_3 - Rh_{met}) = 0 \pm 5$ meV and $\Delta E_{K\beta_1}$ $(Rh_2O_3 - Rh_{met}) = -1 \pm 7$ meV with the figures obtained in the HF(K) model with inclusion of the Rh ionicity in Rh_2O_3 according to Pauling[13] ($i = 0.69$). The configuration obtained for metallic Rh is $Rh[Kr]4d^{7.62}5s^{1.38}$.

The variations of the Rh $4d$ orbital occupation $\Delta n_d^{(1)}$ and $\Delta n_d^{(2)}$ obtained by the above method for the two mechanisms under study are presented in Table I. The Rh $4d$ orbital occupation in $Eu(Rh_{1-x}Pt_x)_2$ is seen to be higher than that in

the metal for all the compositions investigated. Note the unexpected dependence of Δn_d on x (the $4d$-orbital occupation of Rh decreases with increasing Eu valence). One could expect that the extra free electron released in the system in the $4f^n \rightarrow 4f^{n-1}+e$ transition (an increase in the valence) would be promoted to the common conduction band and increase in this way the occupation of the Rh $4d$ orbitals as well. This does not happen, however, which suggests that the extra electron liberated in the $4f^n \rightarrow 4f^{n-1}+e$ transition, rather than transferring to the common conduction band, remains instead localized at Eu atoms. The same conclusion of the localization of the extra electron formed in the MV transition at the atoms of the MV element itself was reached in a study[14] of Mössbauer isomer spectra of Eu incorporated in the lattice of the $Sm_{1-x}R_xS$ MV systems (R=Ca, Y, La, Gd, Tm). The Eu isomer shifts measured in these systems do not depend on the number of the additional electrons released in the MV transitions. This assumption is argued for also by our study[15] which revealed suppression of the MV transition (a decrease in valence) in $Sm_{1-x}Gd_xS$ for low Sm concentrations. The phenomenon was accounted for by the fact that the $4f$ electron involved in formation of the MV state hybridizes only with the $6s$ and $5d$ electrons of the neighboring Sm atoms rather than with the conduction-band electrons.

The decrease in the Rh $4d$-shell occupation with increasing Eu valence may be caused by a weakening of the Eu conduction-band screening by the $4f$ electrons induced by a decrease in their number. This should result in a lowering of the Eu $6s$- and $5d$-conduction subband and, hence, in a smaller charge transfer from Eu to Rh.

The close-to-zero shifts of the Pt $K\alpha_2$ line in $EuPt_2$ $Eu(Rh_{0.75}Pt_{0.25})$ may indicate that the electronic structure of Pt in these compounds is the same as in the metal. The independence of the Pt $K\alpha_2$ line shifts on Eu valence provides additional support for the conjecture of the electron released in the MV transition becoming localized at Eu atoms.

(2) $U(In_{1-x}Sn_x)_3$. As seen from Table II, the shifts of the $K\alpha_1$ lines of In and Sn are close to zero within experimental error. The average shifts within the whole compositional range studied are $\overline{\Delta E^{In}_{K\alpha_1}} = +19 \pm 7$ meV and $\overline{\Delta E^{Sn}_{K\alpha\,1}} = +8 \pm 5$ meV (the errors are rms). The conduction bands of In and Sn derive from $5s$ and $5p$ subbands. As shown by us earlier,[6] removal of the outer s and p electrons from an atom results in positive (and about equal in magnitude) shifts of the $K\alpha_1$ lines. Thus both the magnitude and sign of the experimental shifts suggest that there is no charge transfer from U to In and Sn. The independence of the $K\alpha_1$ line shifts of In and Sn on the U valence, i.e., on the number of electrons released in the $5f^n \rightarrow 5f^{n-1}+e$ transition, is not at odds with the above assumption of these electrons being localized at the atoms of the MV element itself. It would be difficult to make a more definite statement, because the change in the U $5f$-shell occupation involved in the MV transition to $U(In_{1-x}Sn_x)_3$ (and, hence, the number of the released extra electrons) is small, $\Delta n^U_{5f} \approx 0.2$ (see Table II). As follows from DF(K) calculations, an increase in the occupation of the $5s(p)$ shells of In or Sn by such an amount (i.e., when all these electrons transfer to these elements) would result in a shift of their $K\alpha_1$ lines by $\simeq -10$ meV (while experiments reveal small positive shifts).

In conclusion, the authors express their gratitude to O. I. Sumbaev for fruitful discussions and criticisms, to E. G. Andreev for assistance in the measurements, and to P. L. Sokolova for preparing the paper for publication.

Support of the Russian Fund for Fundamental Research (Grant 96-02-17811) is gratefully acknowledged.

[1] O. I. Sumbaev, Usp. Fiz. Nauk **124**, 281 (1978) [Sov. Phys. Usp. **21**, 141 (1978)].
[2] M. N. Groshev, V. I. Petrov, Yu. P. Smirnov, A. E. Sovestnov, A. V. Tyunis, V. A. Shaburov, and I. A. Sergeeva, Fiz. Tverd. Tela (Leningrad) **29**, 1035 (1987) [Sov. Phys. Solid State **29**, 592 (1987)].
[3] A. V. Tyunis, V. A. Shaburov, Yu. P. Smirnov, and A. E. Sovestnov, Fiz. Tverd. Tela (St. Petersburg) **37**, 2512 (1995) [Phys. Solid State **37**, 1376 (1995)].
[4] E. R. Bauminger, I. Felner, and S. Ofer, J. Magn. Magn. Mater. **7**, 317 (1978).
[5] L. W. Zhou, C. L. Lin, J. E. Crow, S. Bloom, R. P. Guertin, and S. Foner, Phys. Rev. B **34**, 483 (1986).
[6] E. V. Petrovich, Yu. P. Smirnov, V. S. Zykov, A. I. Grushko, O. I. Sumbaev, I. M. Band, and M. B. Trzhaskovskaya, Zh. Éksp. Teor. Fiz. **61**, 1756 (1971) [Sov. Phys. JETP **34**, 935 (1971)].
[7] S. S. Batsanov, *Electronegativities of Elements and the Chemical Bond* [in Russian] (Sib. Branch, Akad. Nauk USSR, Novosibirsk, 1962).
[8] K. H. J. Buschow, Rep. Prog. Phys. **40**, 1179 (1977).
[9] K. H. J. Buschow, Rep. Prog. Phys. **42**, 1373 (1979).
[10] F. E. Wagner and U. Wagner, in *Mössbauer Isomer Shifts*, edited by G. K. Shenoy and F. E. Wagner (North-Holland, Amsterdam, 1978), p. 431.
[11] V. A. Shaburov, A. E. Sovestnov, Yu. P. Smirnov, A. V. Tyunis, H. Drulis, and M. Drulis, Fiz. Tverd. Tela (St. Petersburg) **40**, 1393 (1998) [Phys. Solid State **40**, 1265 (1998)].
[12] Yu. P. Smirnov, A. E. Sovestnov, A. V. Tyunis, and V. A. Shaburov, Fiz. Tverd. Tela (St. Petersburg) **40**, 1397 (1998) [Phys. Solid State **40**, 1269 (1998)].
[13] L. Pauling, *The Nature of the Chemical Bond and the Structure of Molecules and Crystals* (Cornell University Press, Ithaca, 1940; Goskhimizdat, Moscow, 1947).
[14] J. Nowik, in *Valence Instabilities and Related Narrow-Band Phenomena*, edited by R. D. Parks (Plenum, New York, 1976), p. 261.
[15] A. E. Sovestnov, V. A. Shaburov, Yu. P. Smirnov, A. V. Tyunis, A. V. Golubkov, and I. A. Smirnov, Fiz. Tverd. Tela (St. Petersburg) **39**, 1017 (1997) [Phys. Solid State **39**, 913 (1997)].

Translated by G. Skrebtsov

Cooperative structural effects in relaxing Pd–Er–H and Fe–C systems

V. M. Avdyukhina, A. A. Katsnel'son,* and G. P. Revkevich

M. V. Lomonosov Moscow State University, 119899 Moscow, Russia

L. Dombrovskiĭ and I. Suval'skiĭ

Institute of Atomic Energy, 05-400 Otwock-Swerk, Poland

V. Christov

Institute of Nuclear Studies and Nuclear Energy, 1784 Sofia, Bulgaria
(Submitted January 11, 1999)
Fiz. Tverd. Tela (St. Petersburg) **41**, 1532–1537 (September 1999)

The dynamics of oscillating structural changes in nonequilibrium Fe–C and Pd–Er–H systems is studied. For Fe–C it is established that the Fourier spectrum of the time dependence of its Mössbauer spectra is similar to the Fourier transform of systems in a state of dynamic chaos on which several long-wavelength modes are superposed. The structural–oscillatory effects for Pd–Er–H consist of a combination of oscillatory processes, corresponding to the appearance and partial dissipation of *H–D–M* complexes, vibrational changes in the ratio of the fractions of the erbium-rich and -poor phases, and the difference of the compositions of these phases. The oscillations have a multimode character with periods increasing with time. Thus, cooperative effects associated with collective interactions of the matrix atoms, defects, and ''perturbing'' impurities such as hydrogen and oxygen atoms are clearly seen in the processes studied. It is shown that the synergetic concept in the spirit of the system of nonlinear Lorentz equations is useful for giving a macroscopic description of the observed defects.
 [S1063-7834(99)00209-9]

Data attesting to the fact that oscillatory structural changes occur in nonequilibrium solid-state systems containing hydrogen, carbon, or oxygen under certain conditions have recently been obtained.[1–7] Such oscillations have been observed previously only for strength characteristics. The Portevain–Le Chatelier (PLS) effect, which arises when a solid is stretched and consists in the appearance of a resulting serrated deformation diagram, is well known.[8] This effect is explained by the existence of alternately activated competing processes — rapid multiplication of ''fresh'' dislocations during deformation and blocking of these dislocations as a result of the appearance of segregations and decomposition or ordering of solid solutions. Thermodynamically, the PLS effect is caused by mechanical energy being pumped into the system during continuous stretching, transferring the system to a nonequilibrium state.

As shown in Ref. 9, the nonlinear self-excited oscillations arising in the PLS effect are a characteristic property of thermodynamically open dissipative systems. The oscillations observed in Refs. 1–7 can be explained on the basis of this concept by the fact that the hydrogen, oxygen, or carbon introduced into a solid-state system produce a defect structure in it ''from the inside,'' increasing the energy of the system and putting it into a nonequilibrium state, which subsequently relaxes to a more stable (possibly, metastable) state in a complicated manner. This means that these structural–oscillatory effects do not reduce to the PLS effect, but they do have a conceptual basis in common with the latter — the presence of a nonequilibrium state, the appearance of intermediate defect states (dissipative structures) accompanying relaxation by means of self-organization, and relaxation to equilibrium (metaequilibrium) via such structural states. The fundamental characteristic feature of the phenomena observed in Refs. 1–7 that distinguishes them from the PLS effect is that when hydrogen, oxygen, or carbon is ''pumped'' into the system from the outside, which perturbs the system and creates a strain potential in it, there is no need for continuous application of the ''perturbing'' action.

Microscopic models of the phenomena observed have been proposed in Refs. 1–7. For example, for the system Pd–W–H[1–3] such a model consists in the fact that, when the alloy Pd–W, containing a nonuniform distribution of palladium and tungsten atoms[10] (tungsten-enriched regions having a high degree of short-range atomic order exist in the matrix) is saturated, a nonuniform distribution of hydrogen atoms arises because the hydrogen dissolves well in palladium but does not dissolve in tungsten.[11] Submicroscopic regions of a β phase, where the hydrogen content n_H/n_{Pd} increases to 0.6, as opposed to its much lower concentration outside these regions, appear in the palladium-enriched matrix on saturation. The specific volume of the β-phase regions is larger than the average for the system, and for this reason they consist of clusters which produce internal local stresses in the system. One possible mode of stress relaxation is diffusion of vacancies, produced in the Pd–W system by the specific nature of this system,[12] into these clusters. In consequence, a deficiency of vacancies should arise in the

tungsten-rich regions, and this should stimulate processes leading to the reverse motion of the vacancies. These competing processes generate oscillations in the degree of defectiveness of the system. We note that the change observed in the diffraction effects with time is very large, and this can be due only to the high degree of correlation in the displacement of vacancies in different parts of the experimental sample. In this respect the phenomenon is similar to the Bénard phenomenon[13] and similar phenomena studied on the basis of the synergetic concept. In Ref. 3, a system of nonlinear differential equations for cooperative motion of vacancies in the presence of sources and sinks of vacancies was obtained on the basis of the Lotka–Volterra model, and certain characteristics of the cooperative effect under study were found.

In Refs. 4 and 5 the temporal oscillations observed in the Fe–C system in the characteristics of Mössbauer spectra and the positions of x-ray diffraction peaks were attributed to the fact that the carbon atoms should hop between metastable clusters having a different type of distribution of carbon atoms among octahedral voids should proceed with a high probability via tetrahedral voids. The correlated transitions of carbon atoms from octahedral to tetrahedral voids and back seem to be responsible for the phenomenon observed in Refs. 4–5, since the character of the ordering of carbon atoms is directly related to the characteristics of their arrangement within the interstices.

In Refs. 6–7 a model is also proposed for oscillatory structural changes in systems containing oxygen.

Many questions requiring analysis arise in connection with the phenomena observed in Refs. 1–7 and with the concept, being developed, of the complex and cooperative character of the processes responsible for these phenomena. The following questions are most important: a) Are these oscillations regular? b) Does the observed regularity (irregularity) depend on the type of perturbing impurity? c) Are the factors determining these phenomena the same in the entire range of observation of the phenomena?

The present paper is devoted to an investigation of these questions.

In accordance with the problems posed, systems with hydrogen (Pd–Er–H) and carbon (Fe–C) are studied in the present paper. Some of the data obtained, pertaining to the initial stage of the oscillatory structural changes, have been published in Refs. 4, 5, 14, and 15.

1. EXPERIMENTAL PROCEDURE

The objects of investigation were a hydrogen-saturated alloy Pd–Er and the carbon martensite Fe–C.

After fusion, a sample of the alloy Pd–8 at.% Er prepared from high-purity components was homogenized at 900 °C for 24 h and then quenched. After quenching, the surface of the sample was mechanically ground and polished. The sample was saturated with hydrogen electrolytically at current density 80 mA/cm^2 for 1 h and then stored in air at room temperature. The change in the x-ray diffraction pattern with time (position, shape, and width of the diffraction peaks) was investigated. The measurement procedure is similar to that described in Refs. 14 and 15.

The martensite Fe–C (0.87 wt.% C) samples were prepared from high-purity Armco iron (30 μm thick foil). After gas carbiding treatment and quenching in water and then liquid nitrogen, the samples were etched at room temperature for four months. Then they were immersed for three weeks in liquid nitrogen. Prior to the measurements the samples were thermally shocked by heating to 300 K in 0.5 h and then cooled to 140 K. The Mössbauer spectra were recorded continuously for a long time, the spectral data being recorded every hour. These data were used to find the width of the components of the sextet and the fraction of the sextet, corresponding to the central one, which are associated with the events occurring in the system during each hour of the investigation.

2. EXPERIMENTAL RESULTS

2.1. Pd–Er–H alloy

The positions of the lines for the initial deformed state of the sample indicated that in this state there exist orienting tensile stresses that increase the interplanar distances in a direction along the normal to the surface.[14,16] These stresses were $\sigma = -110$ kg/mm^2, and the lattice period was $a = 3.941$ Å.

Immediately after saturation the diffraction peaks shifted toward smaller angles of diffraction. This indicated that the hydrogen entered the lattice and formed an interstitial solid solution. During storage of the sample, the hydrogen migrated out of the lattice, and the peaks shifted toward large 2θ angles. However, subsequently they passed through positions corresponding to the initial state and moved into the region of even larger angles (Fig. 1). The positions of the diffraction peaks changed only negligibly after storage for 24 h.

For the state corresponding to storage for 48–52 h, the microstresses were $\sigma = 90$ kg/mm^2, and the lattice parameter was $a = 3.946$ Å. Comparing this parameter with the lattice parameter for the initial state showed that, at a minimum, an order of magnitude less hydrogen remained in the lattice ($n_H/n_{Pd} = 0.020 - 0.025$) than present immediately after saturation. The microstresses over this time changed sign and became quite large (σ changes sign no more than 2–3 h after saturation[14]). For a storage period of approximately 6 months, almost all of the hydrogen migrated out of the lattice. The stresses σ decrease over three months to 70 kg/mm^2, after which they remain unchanged.

The shape of the peaks also changes appreciably during storage of the sample. A profile of the (200) diffraction peak for different storage times is presented as an example in Fig. 1. One can see that the shape of this peak (just as the shape of all other peaks) changes nonmonotonically. After storage for 1.5 h the profile is essentially symmetric, while for longer storage times it clearly consists of two bands. After 7 and 48 h the weaker peak is located at a smaller diffraction angle, and after 25 h it is located at a large angle. After 120 h the profile possesses a flat-top shape, and after 4200 h it is once again asymmetric. We note that the shape of the profile of a

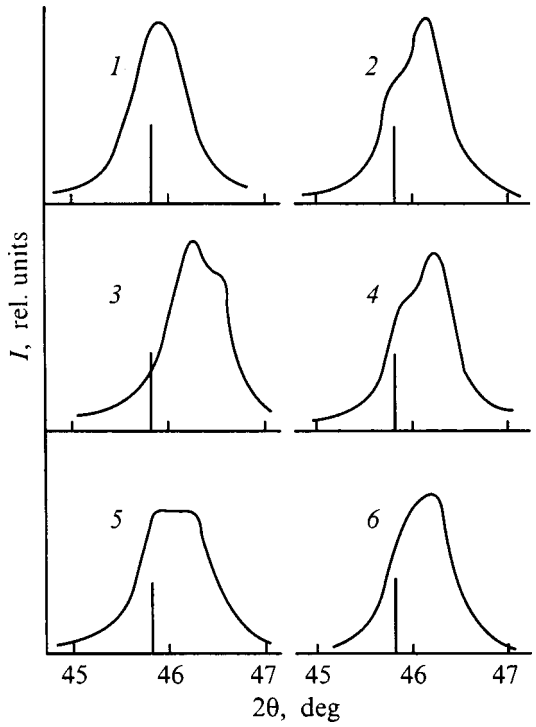

FIG. 1. Profile of the (200) diffraction peak for different sample storage times: *1*—1.5, *2*—7, *3*—25, *4*—48, *5*—120, *6*—4200 h. The vertical line marks the position of the peak of the profile in the initial state.

diffraction peak is determined by the ratio of the areas of the components of the profile and by the distance between them, and for this reason the changes in the asymmetry of the profiles correspond to changes in the ratios of the amounts of Er-rich and Er-poor phases and to the differences in the concentrations of these phases. The observed changes in the profiles of the diffraction peaks could be due only to the change in the ratio of the amounts of phases and their composition, while oscillations in the type of asymmetry of the profiles could be due only to oscillations of the characteristics of the two-phase nature of the system.

The data on the change in the shape of the diffraction peaks show that, after the alloy is saturated with hydrogen, processes leading to redistribution of erbium atoms, which occur during short storage times when the lattice of the sample contains a large quantity of hydrogen, and during quite long times when the amount of hydrogen in the lattice becomes small, commence in it. Erbium-depleted and erbium-enriched phases form as a result of the redistribution of the erbium atoms.

To determine the relative fractions of the erbium-rich and erbium-poor phases as well as the differences in the erbium concentration in these phases, all experimental curves were represented, using a graphics package, in the form of doublets whose components were determined to have a Lorentzian shape.

The data obtained for the erbium-rich fraction C as a function of the sample storage time by analyzing the (200) diffraction line are presented in Fig. 2a (the storage time is given on a logarithmic scale). It is evident that, on the whole, the function $C(t)$ is oscillatory but irregular. The time intervals between the neighboring recorded peaks gradually increase, but the exact nature of their growth could not be established because it was impossible to perform continuous x-ray diffraction measurements over a period of many months.

Oscillatory variations in C are also observed for coherent scattering regions (CSRs) with different orientations relative to the surface. It is interesting to note that the extrema for C in CSRs with different orientations occur at different times.

Figure 2b shows the quantities Δc_{Er} obtained by analyzing the (200) diffraction peak (changes of a similar nature are also observed for regions with other orientations). The fact that the amplitudes of the oscillations in Figs. 2a and b decrease at different rates is interesting. It shows that the redistribution of erbium atoms does not reduce to movement of

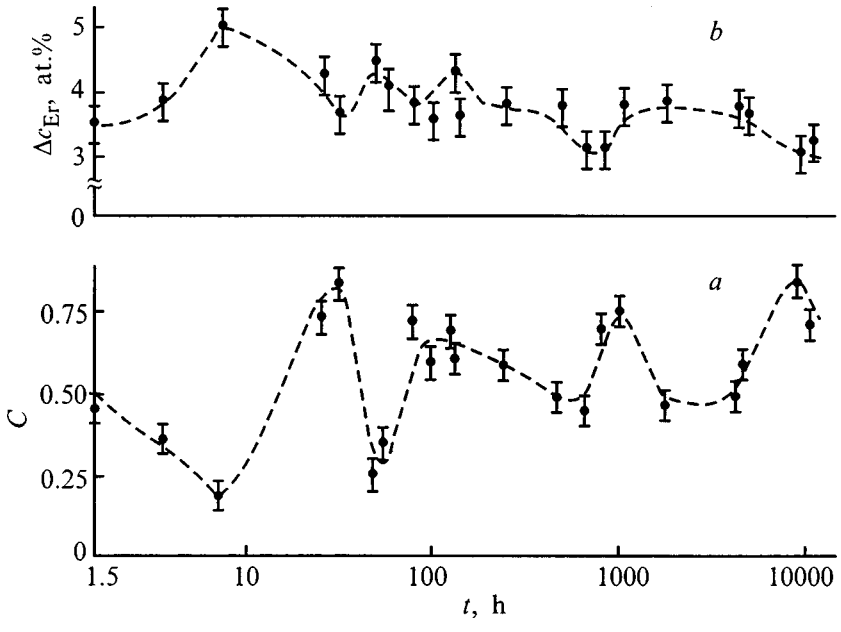

FIG. 2. a—Dependence of the relative fraction of the erbium-enriched phase (C) on the sample storage time. b—Dependence of the difference of the erbium concentrations (Δc_{Er}) in the erbium-enriched and -depleted phases on the sample storage time.

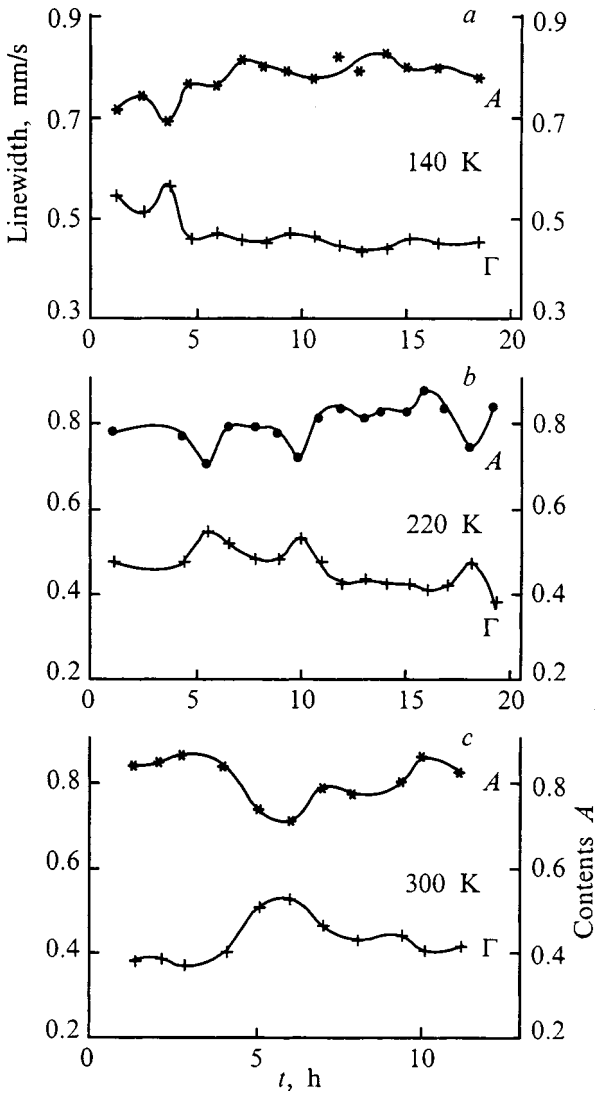

FIG. 3. Time dependence of the width of the Mössbauer lines (Γ) and the relative fraction of the central sextet (*A*) at 140 (a), 220 (b), and 300 (c) K.

the atoms between erbium-rich and erbium-poor regions.

It should be noted that the oscillatory changes in the profile of the diffraction peaks are also observed in blocks with different orientations. However, the positions of the extrema relative to the time axis are different for blocks with different orientations.

2.2. Martensite Fe–C

The time dependences of the widths of the Mössbauer lines and the relative fraction of the central sextet at 140, 220, and 300 K are displayed in Fig. 3. One can see that for all temperatures the linewidths and the fractions of the central sextet change nonmonotonically in time, and their changes become oscillatory.

Sharp regularities are not seen for all temperatures in the observed oscillations of the characteristics of the spectra, though there is no doubt that the oscillations themselves exist. To determine more accurately the nature of the irregular oscillations of the spectra, Fourier spectrometry of the Mössbauer data obtained by continuous measurements for 54 h was performed. The spectra obtained are displayed in Fig. 4. They turned out to be similar in many respects to the Fourier spectra corresponding to a state of dynamic chaos.[17,18] Despite this, certain oscillatory frequencies, which appear most often and correspond to long-wavelength oscillations ($\omega \simeq 0$), as well as 1.7 and $3\,h^{-1}$, can be distinguished. The data obtained confirm that there are no sharp regularities in the time dependence of the oscillatory structural changes. At the same time, they show that the observed oscillations are a superposition not only of many modes, corresponding to oscillations of short-range order in the distribution of carbon atoms in the interstitial space, but also certain long-wavelength modes. The latter could correspond to oscillations of long-range order.

To check this supposition, x-ray investigations were performed of the time dependence of the tetragonality of these systems, since the difference in the lattice periods in the [100] and [001] directions will be proportional to the long-range order parameter η

$$a - c = a_0 n (u_{11} - u_{33})\,\eta,$$

where a_0 is the lattice period in the α-Fe phase, n is the atomic concentration of carbon in the solution, and u_{11} and u_{33} are components of the concentration-induced lattice expansion tensor.

The data obtained are presented in Fig. 5. They show convincingly that the characteristics of long-range order which are due to the difference in the position of the components of the tetragonal doublet (101) and (110) also oscillate. The oscillatory changes in η confirm the cooperative nature of the motion of the carbon atoms in the interstitial space. Therefore, although the oscillations of the measured quantities are irregular, the displacements of the carbon atoms giving rise to them cannot be represented by random walks of these atoms, but rather they have a cooperative nature.

3. DISCUSSION

The results of the x-ray diffraction and Mössbauer investigations on martensite Fe–C and the hydrogen-saturated alloy Pd–Er–H show that the oscillatory structural changes observed in Refs. 1–5 consist of complicated nonequilibrium processes in which cooperative effects are superposed on the irregular motion of atoms and defects. Thus, it has been proved for the Fe–C system that the oscillatory nature of the redistribution of the carbon atoms in time over the interstitial space, though quite irregular, is due to oscillations not only of the short-range order but also of the long-range orders. The latter follows from data obtained by Fourier analysis of the Mössbauer data, which show that the Fourier transform of the time-dependence of the Mössbauer spectra is similar to the Fouier transform of systems in a state of dynamic (deterministic) chaos on which several long-wavelength modes are superposed. The existence of these modes indicates directly the cooperative nature of the structural–oscillatory changes occurring in the carbon martensite, and this is confirmed by the corresponding changes in the tetragonality of this martensite.

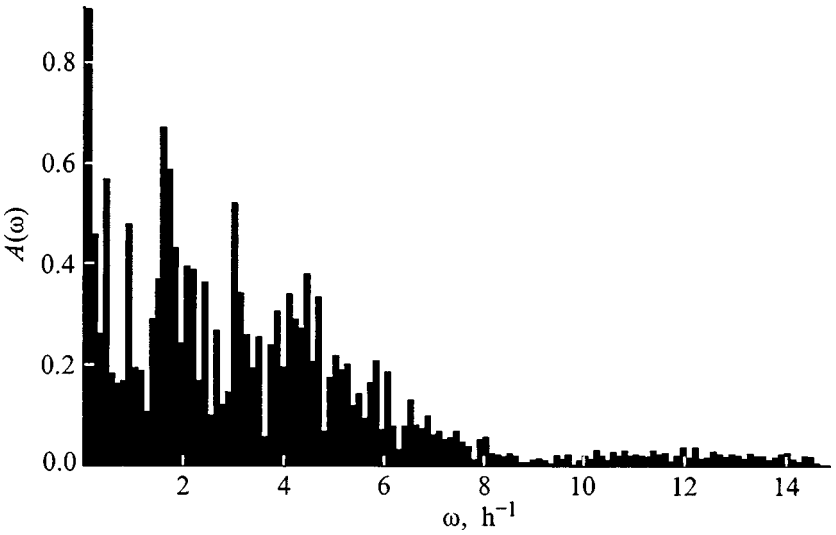

FIG. 4. Fourier transform of the time dependence of the amplitude of the Mössbauer central sextet for Fe–0.87 wt.% C.

Similar data were also obtained for the deformed alloy Pd–Er–H. It was found that the structural oscillatory changes occurring after hydrogen saturation can be presented as consisting of a series of oscillatory processes which continue for at least one year. These changes correspond to a) the appearance and partial dissipation of ''traps'' (*H–D–M* complexes*)*, b) oscillatory changes in the difference of the Er concentration in the Er-rich and Er-poor phases, and c) oscillatory changes in the ratios of the fractions of the indicated phases. The processes enumerated above correspond to cooperative displacements of hydrogen and erbium atoms and defects, whose period grows with increasing lifetime of this alloy after saturation.

The observed differences in the character of the oscillatory time dependence of C and Δc_{Er}, consisting in a slower decrease of the amplitude of oscillations of the former, signify that the indicated redistributions of the erbium atoms cannot be reduced to merely the competition between diffusion against and along a gradient between erbium-rich and erbium-poor regions. In addition, erbium atoms are transported from erbium-poor into erbium-poor and from erbium-rich into erbium-rich regions, which can be activated by the existence of anisotropic *H–D–M* complexes in all existing types of regions. This transport is cooperative, and it cannot reduce to random diffusion walks of erbium atoms in a nonuniform medium.

The complicated processes examined above, leading to cooperative displacement of the atoms, undoubtedly attest to the hydrogen-containing system not being in equilibrium, which is due primarily to the existence of microstresses in this alloy. The fact that these stresses reamin in Pd–Er–H system even after almost all of the free hydrogen has migrated out of the system could be due only to a high stability of the *H–D–M* complexes arising either at saturation or during the first hours of degassing.

The oscillatory character of structural changes, which was established for systems containing hydrogen or carbon and which is due to the nonequilibrium state of these systems, indicates that the synergetic concept is useful for describing their behavior. The irregularity of these changes indicates that simple Lotka–Volterra type synergetic schemes, which could be used to describe the initial stages of relaxation of the system Pd–W–H,[5] cannot be used to describe the oscillatory time dependence of structural characteristics of the system studied. More general approaches, for example, based on a system of nonlinear Lorentz equations,[17,18] must be used to construct a theory of oscillatory structural changes in the complicated systems studied in the present work. However, since the main factors determining these processes are different at different stages of development of the process leading to structural changes, the description of the systems studied here may turn out to be simplified even on this basis. These questions will be examined in a future work. It is important to note that the results obtained in the present and preceding works[1–7] show that structural–oscillatory effects can be encountered under appropriate circumstances in any nonequilibrium systems irrespective of the factors determining the appearance of nonequilibrium.

It is also reasonable to note that the processes associated with structural-oscillatory changes in hydrogen-containing metallic systems and continuing for more than a year without continuous pumping by ''perturbing'' actions could be responsible for the oscillatory changes observed in Ref. 19 in the strength characteristics of thick rolled stock.

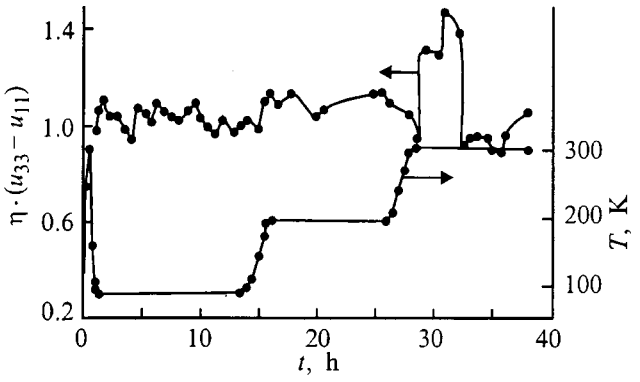

FIG. 5. Time dependence of the long-range order parameter of Fe–0.87 wt.% C for 100, 200, and 300 K.

We thank the Russian Fund for Fundamental Research for support.

*E-mail: albert@solst.phys.msu.su

[1] A. A. Katsnel'son, I. V. Dolya, and G. P. Revkevich, Mosk. Gos. Univer. Ser. 3, Fiz., Astron. **35**(2), 64 (1994).
[2] A. A. Katsnel'son, A. I. Olemskoĭ, I. V. Sukhorukova, and G. P. Revkevich, Vestn. MGU, Ser. 3, Fiz., Astron. **35**(3), 94 (1994).
[3] A. A. Katsnel'son, A. I. Olemskoĭ, I. V. Sukhorukova, and G. P. Revkevich, Usp. Fiz. Nauk **165**(3), 331 (1995).
[4] L. Dabrovski, J. Suwalski, B. Sidzimov, and V. Christov, Acta Metall. Mater. **43**, 2375 (1994).
[5] L. Dabrovski, J. Suwalski, B. Sidzimov, and V. Christov, Nukleonika **39**, 207 (1994).
[6] V. M. Avdjukhina, A. A. Katsnelson, B. N. Kodess, N. S. Kolesova, G. P. Revkevich, and S. M. Zhivotov, Surf. Invest. **12**, 695 (1997).
[7] A. A. Katsnelson, V. M. Avdjukhina, N. S. Kolesova, and G. P. Revkevich, Surf. Invest. **12**, 835 (1997).
[8] M. A. Shtremel', *Strength of Alloys* [in Russian] (MISIS Press, Moscow, 1997), Part 2, p. 526.
[9] L. P. Kubin and Y. Estrin, Acta Metall. **33**, 397 (1985).
[10] Sh. A. Alimov and A. A. Katsnel'son, Fiz. Met. Metalloved. **22**, 468 (1966).
[11] P. V. Gel'd, R. A. Ryabov, and E. S. Kodes, *Hydrogen and Imperfections in the Structure of Metals* [in Russian] (Metallurgiya, Moscow, 1979), p. 221.
[12] A. A. Katsnel'son and A. O. Olemskiĭ, *Microscopic Theory of Inhomogeneous Structures* [in Russian] (Moscow State Univeristy Press, Moscow, 1987), p. 333.
[13] I. Prigogine and G. Nicolis, *Exploring Complexity* (W. H. Freeman, San Francisco, 1989; Mir, Moscow, 1990, p. 342).
[14] V. M. Avdyukhina, A. A. Katsnel'son, N. A. Prokof'ev, and G. P. Revkevich, Vestn. MGU, Ser. 3, Fiz., Astron. **39**(2), 70 (1998).
[15] V. M. Avdyukhina, A. A. Katsnel'son, and G. P. Revkevich, Kristallografiya **44**(1), 49 (1999) [Crystallogr. Rep. **44**, 44 (1999)].
[16] G. P. Revkevich, M. K. Mitkova, A. A. Katsnel'son, and V. M. Christov, Vestn. MGU, Ser. 3., Fiz., Astron. **34**(6), 70 (1993).
[17] H. G. Schuster, *Deterministic Chaos* (Physik-Verlag, Weinheim, 1984; Mir, Moscow, 1988, p. 240).
[18] A. Yu. Loskutov and A. S. Mikhaĭlov, *Introduction to Synergetics* [in Russian] (Nauka, Moscow, 1990), p. 270.
[19] V. M. Piskovets, T. K. Sergeeva, Yu. A. Bashnin, and O. V. Nosochenko, Stal' No. 7, 60 (1994).

Translated by M. E. Alferieff

Athermal luminescence of a tungsten surface irradiated with laser pulses

A. F. Banishev, V. Ya. Panchenko, and A. V. Shishkov

Scientific–Research Center for Technological Lasers, Russian Academy of Sciences, 140700 Shatura, Moscow District, Russia

(Submitted January 29, 1999)
Fiz. Tverd. Tela (St. Petersburg) **41**, 1538–1542 (September 1999)

An investigation of athermal luminescence triggered at a tungsten surface by thermal deformations produced by laser pulses is reported. The spectral composition and time dependence of individual spectral components of the luminescence are investigated. Oscillations of the luminescence intensity are observed, and they are interpreted as a definite sequence of emergence of dislocations at the surface. © *1999 American Institute of Physics.* [S1063-7834(99)00309-3]

Athermal luminescence (mechanoluminescence — ML) of metallic Ag, Au, Pt, and Cu samples irradiated by YAG:Nd laser pulses was investigated in Refs. 1–3. The signal was detected from the backside of the sample, relative to the side exposed to the laser pulses. It was established that ML is due to the emergence of mobile dislocations at the surface, and the ML intensity depends on the initial dislocation density in the sample and on the power density $I_{\text{las.}}$ of the laser pulse. It was found that ML excitation is possible as a result of both thermal stresses and generation of quite powerful acoustic waves (here the laser power density $I_{\text{las.}}$ is above the plasma-formation threshold). The ML intensity increases with $I_{\text{las.}}$. This was attributed to an increase in the flux of dislocations emerging at the surface as a result of an increase in the thermal stresses within the sample. In Ref. 3, calculations and measurements of the temperature of the investigated part of the surface were performed. They showed that the temperature, for example, for copper samples irradiated by $I_{\text{las.}} \approx 10^5$ W/cm^2 laser pulses, did not exceed several tens of degrees and, therefore, the contribution of thermal luminescence to the observed signal can probably be neglected.

It should be noted that photon mechanoemission has also been observed in Refs. 4 and 5, where deformation-induced luminescence of alkali halide crystals was investigated. It was establised that photon mechanoemission in these materials is associated with the motion and intersection of dislocations of a definite type.

The spectral composition and time dependence of the ML intensity are quite complicated. As far as we know, there is no generally accepted model, especially for metals, that can describe the mechanism of photon emission accompanying the generation and motion of defects as well as the dependence of the luminescence on the defect density, temperature, and elastic stresses.

The present paper reports the results of investigating athermal luminescence of tungsten samples irradiated by YAG:Nd laser pulses. Tungsten is distinguished by brittleness and high values of the elastic moduli and, probably for this reason, low dislocation mobility. Therefore, if the ML of metals is due to the emergence of mobile dislocations at the surface, then it should be impeded in tungsten by the low dislocation mobility. The measurements were performed in a vacuum chamber, which made it possible to decrease substantially the contribution of possible oxidative processes to the observed signal. The spectral composition and time dependence of individual spectral components of the luminescence were investigated.

1. EXPERIMENTAL PROCEDURE

The arrangement of the experimental apparatus is shown in Fig. 1. The experimental sample (*3*) was placed in a vacuum chamber (*2*), where the pressure could be varied from 10^{-2} Torr up to 1 atm. The samples were irradiated with YAG:Nd laser (*1*) pulses with $\tau_p = 1.4$ ms and $E_{\max} = 3.5$ J (free-lasing regime). The laser radiation was focused into a 1.2–2 mm spot on the sample surface. Luminescence from the back surface was measured in the experiment (in what follows, to be consistent with preceding works, we shall use the term ML). For this, a photomultiplier (FÉU-79, *4*), onto which the radiation from the surface was directed, was placed approximately 18 cm from the backside of the sample. The temperature of the samples was not measured, but the thermal luminescence of the irradiated section of the surface in the spectral interval 0.5–0.7 μm and the plasma-

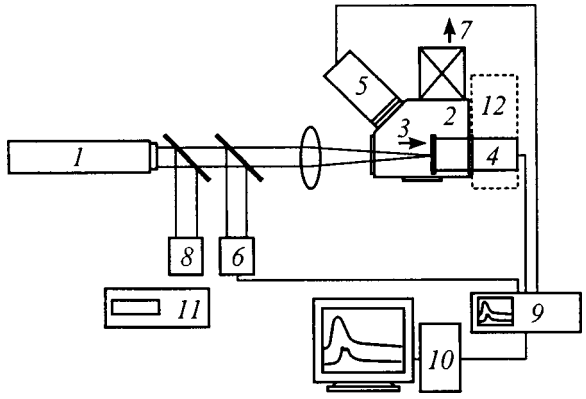

FIG. 1. Experimental arrangement: *1*—YAG:Nd laser ($E_{\max} = 3.5$ J, $\tau_p = 1.4$ ms); *2*—vacuum chamber ($P = 10^{-2}$ Torr); *3*—sample; *4, 5*— FÉU-79 photomultiplier; *6*—photodetector; *7*—to pump; *8*—energy meter; *9*—digital oscillograph; *10*—personal computer; *11*—pulsed voltmeter; *12*—spectrometer.

formation threshold were monitored using a second photomultiplier (FÉU-79, *5*), placed at the front side of the sample at an angle of 45° with respect to its surface and a set of light filters. The signals from both photomultipliers were fed into a digital oscillograph and then into a personal computer. The spectral composition of the luminescence was investigated with a DFS-452 spectrometer (*12*). Tungsten samples ranging in thickness from 100 to 300 μm were used. The surfaces of the samples were cleaned by polishing with diamond powder and then rubbed with ethyl alcohol.

2. EXPERIMENTAL RESULTS AND DISCUSSION

Oscillograms of the signals of the total (in the range 0.4–0.8 μm) luminescence from the back surface (ML) of a tungsten sample irradiated by millisecond laser pulses in vacuum ($P=10^{-2}$ Torr) are shown in Fig. 2a. Figures 2b and 2c illustrate the dependence of the delay in luminescence on $I_{\text{las.}}$. In Fig. 2b the delay Δt_1 was measured relative to the leading edge of the laser pulse, while in Fig. 2c the delay Δt_2 was measured relative to the leading edge of the thermal signal recorded from the front surface of the sample. As follows from Figs. 2b and 2c, the delays Δt_1 and Δt_2 decrease with increasing $I_{\text{las.}}$.

Large changes with increasing $I_{\text{las.}}$ occur in the amplitude and shape of the ML signal. For laser pulses with $I_{\text{las.}} \simeq 4.0\times10^4$ W/cm^2 the signal consists, as a rule, of one spike. As $I_{\text{las.}}$ increases, the amplitude increases rapidly (Fig. 3) and the shape of the signal changes — two, three, and more spikes appear against the background of a generally increasing amplitude (Fig. 2a). This is probably why the spike structure of the signal is virtually unobserved for large signal amplitudes. When a section of the surface is repeatedly irradiated with pulses with $I_{\text{las.}}$, the signal amplitude decreases by approximately 20–25% after irradiation three to five times and then remains constant on the average, though it does fluctuate substantially from pulse to pulse. It should be noted that, as a rule, the largest signal amplitude is observed with the first irradiation.

The appearance of a luminescence signal from the backside of the sample could be due to the following basic reasons: thermal luminescence of the surface, exoemission of particles,[6–8] and ML itself. The ML intensity was measured using a detection scheme in which the photomultiplier operated in the photon-counting mode. The maximum power density of the laser radiation acting on the sample, for which pulses corresponding to individual photons could be reliably resolved in the ML signal, was $I_{\text{las.}} \approx 2.7\times10^4$ W/cm^2.

We shall now estimate the intensity of the ML signal for $I_{\text{las.}} \approx 2.7\times10^4$ W/cm^2. It is evident from Fig. 4 that of the order of 20 photons strike the photomultiplier. Then the intensity of the ML signal is

$$I_{\text{ML}} \approx \frac{2R^2nhc}{r^2St_s\lambda_m}, \tag{1}$$

where $R=18$ cm is the distance between the back surface of the sample and the photomultiplier, $n=2$ is the number of photons striking the photomultiplier, h is Planck's constant, c is the speed of light, $r=0.3$ cm is the radius of the photocathode in the photomultiplier, $S \approx \pi[r_0+(\chi\tau_p)^{1/2}]^2$ is the area of the emitting spot, $r_0 \approx 6\times10^{-2}$ cm is the radius of the spot into which the laser radiation was focused, $\chi=0.54$ cm^2/s is the thermal diffusivity of tungsten, $\tau_p \approx 1.4\times10^{-3}$ s is the duration of the laser pulse, $t_s \approx 0.7\times10^{-3}$ s is the duration of the ML, and $\lambda_m \approx 6\times10^{-5}$ cm is the wavelength of the radiation corresponding to the center of the detected spectral range. The result is $I_{\text{ML}} \approx 2.8\times10^{-9}$ W/cm^2.

We shall now estimate the temperature $T(\tau_p)$, to which the backside of the sample is heated by the end of the laser

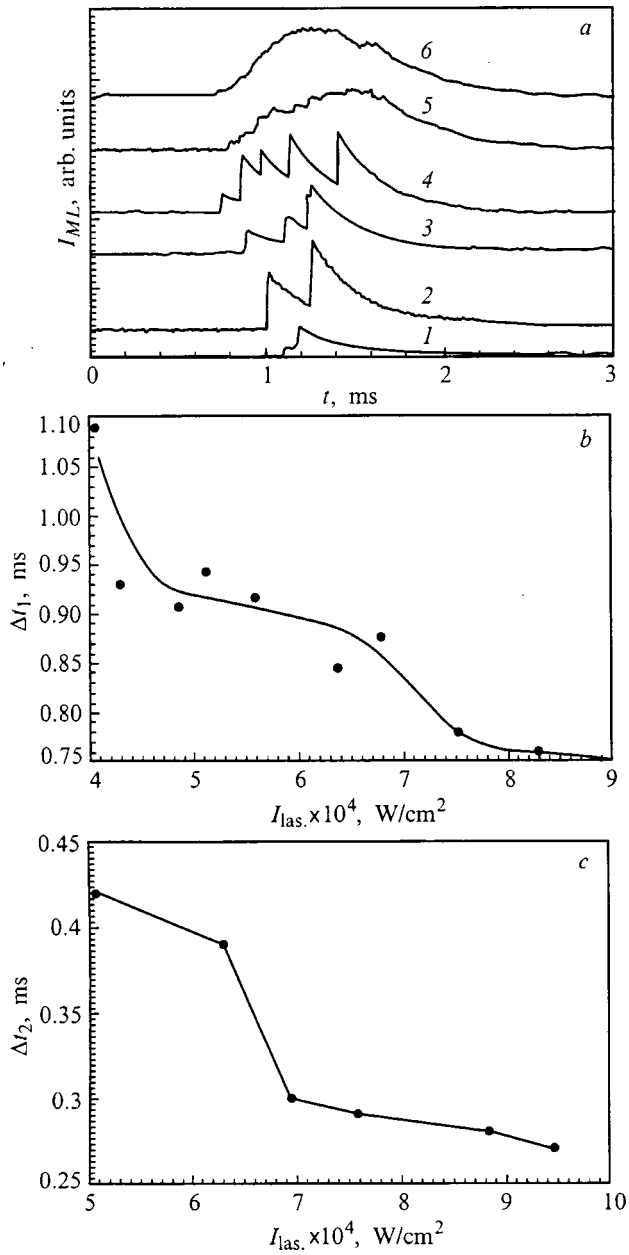

FIG. 2. a—Oscillograms of the ML signal (current regime) with increasing power density of the laser pulse. The sample consists of tungsten. *1*—$I_{\text{las.}}=4.05\times10^4$, *2*—$I_{\text{las.}}=4.32\times10^4$, *3*—$I_{\text{las.}}=4.67\times10^4$, *4*—$I_{\text{las.}}=5.01\times10^4$, *5*—$I_{\text{las.}}=5.63\times10^4$ (signal decreased by a factor of 50), *6*—$I_{\text{las.}}=7.52\times10^4$. b—Dependence of the time delay of the ML signal relative to the leading edge of the laser pulse on $I_{\text{las.}}$. Tungsten sample. c—Dependence of the time delay of the ML signal relative to the leading edge of the thermal wave on $I_{\text{las.}}$. Tungsten sample.

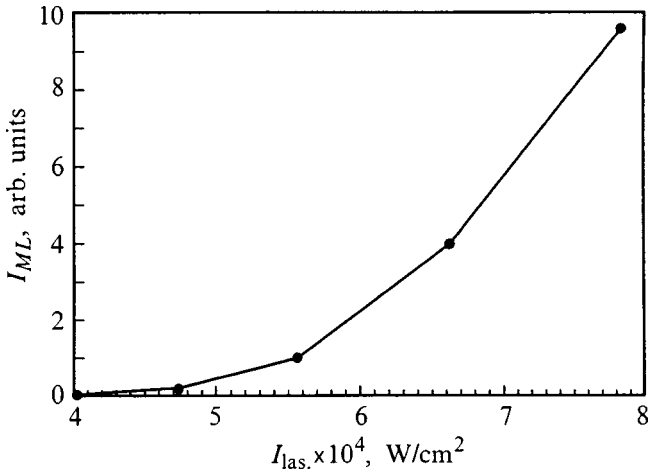

FIG. 3. Amplitude of the ML signal versus $I_{las.}$. Tungsten sample.

pulse, and the intensity I_h of the thermal luminescence for $I_{las.} \approx 2.7 \times 10^4$ W/cm^2. Since in the present experiment $d \leqslant (\chi t)^{1/2} \ll r_0$, where $d \approx 220$ μm is the sample thickness, by the end of the pulse the temperature of the back surface can be expressed by

$$T(\tau_p) \approx T_0 + \frac{AI_{las.}S_0\tau_p}{\pi[r_0 + (\chi\tau_p)^{1/2}]^2 d\rho c_m}. \quad (2)$$

Substituting $T_0 = 293$ K (room temperature), $A = 0.38$ (the absorption coefficient of tungsten), $S_0 = \pi r_0^2$ (the area of the spot into which the laser radiation is focused), $\rho = 18.6$ g/cm^3 (the density of tungsten), and $c_m = 0.13$ J/g·K (the specific heat of tungsten) we obtain $T(\tau_p) \approx 430$ K.

Using the expression for the intensity of thermal luminescence of a heated body we can write

$$I_h \approx 2\pi\varepsilon_\lambda hc^2 \int_{\lambda_1}^{\lambda_2} \frac{1}{\lambda^5} \exp\left(-\frac{hc}{\lambda k T(\tau_p)}\right) d\lambda. \quad (3)$$

Substituting $\lambda_1 = 4 \times 10^{-5}$, $\lambda_2 = 8 \times 10^{-5}$ cm, $\varepsilon_\lambda = 0.4$ (the spectral emissivity of tungsten), $k = 1.38 \times 10^{-23}$ J×K^{-1} (Boltzmann's constant) we obtain $I_h \sim 10^{-16}$ W/cm^2.

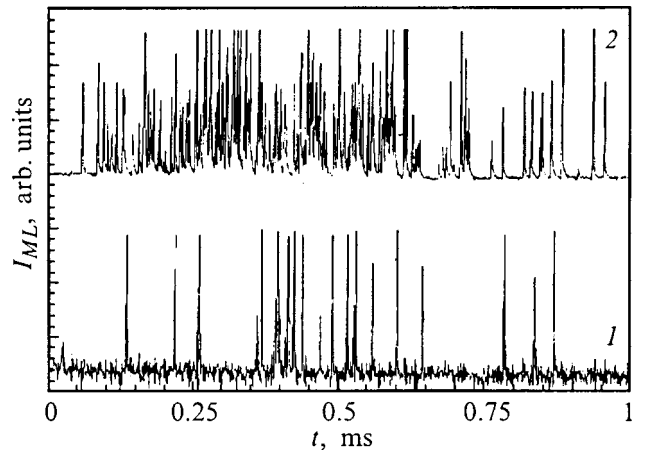

FIG. 4. Oscillograms of ML signal (photon-counting mode) with increasing power density of the laser pulse. *1*—$I_{las.} = 2.7 \times 10^4$, *2*—$I_{las.} = 3.6 \times 10^4$ W/cm^2.

It is evident from these estimates that the contribution of thermal luminescence to the measurements of the ML intensity with $I_{las.} \approx 2.7 \times 10^4$ W/cm^2 can be neglected.

Using the expression (3) we shall estimate the temperature of the backside for which I_h becomes comparable to I_{ML}. Substituting $I_h = I_{ML} \approx 2.8 \times 10^{-9}$ W/cm^2 we find $T(\tau_p) \approx 650$ K. Substituting this value into the expression (2) we find the power density of the laser pulse for which this temperature is attained: $I_{las.} \approx 7 \times 10^4$ W/cm^2.

We shall now estimate the thermal stresses arising in the irradiated region by the end of a laser pulse with $I_{las.} \approx 7 \times 10^4$ W/cm^2 (Ref. 9)

$$\sigma(\tau_p) \sim \alpha G T(\tau_p)/(1-\nu). \quad (4)$$

Substituting $\alpha = 4.45 \times 10^{-6}$ K^{-1} (the thermal expansion coefficient), $G = 1.5 \times 10^{11}$ N/m^2 (the shear modulus), $T(\tau_p) \approx 650$ K, and $\nu = 0.233$ (Poisson's ratio) we obtain $\sigma(\tau_p) \approx 10^9$ N/m^2.

Two important conclusions follow from these estimates. First, the total intensity of the thermal signal in the spectral range 0.4–0.8 μm becomes comparable to the ML intensity already at temperature $T \approx 650$ K (for the experimental materials the real temperature at which $I_h \approx I_{ML}$ is probably even lower). Second, the thermal stresses reach the critical value σ_c for dislocations with size $l \geqslant Gb/\sigma_c \approx 3 < 10^{-6}$ cm, where b is Burgers vector, above which the stresses can become sources of multiplication of Frank–Read dislocations. According to the estimates for $I_{las.} < 7.0 \times 10^4$ W/cm^2, the contribution of the thermal luminescence to the observed signal is negligible. In the opposite case, $I_{las.} \approx 7.0 > 10^4$ W/cm^2, the observed signal is quite complicated and is probably a superposition of the thermal luminescence of ML signals.

According to Refs. 1 and 2, the ML observed from metals irradiated with laser pulses is due to the emergence of mobile dislocations at the surface. The authors attributed the decrease in the signal intensity with each subsequent irradiation of the same section to a decrease in the dislocation density in the sample as a result of the emergence of dislocations at the surface due to the preceding irradiation. However, as noted above, the action of sufficiently large thermoelastic stresses in the crystal ($\sigma > \sigma_c$) can not only give rise to directed motion of existing dislocations but also the generation of new dislocations. Therefore, if the power density of the laser pulse is such that $\sigma > \sigma_c$, then with each subsequent laser pulse a definite fraction of the dislocations can emerge at the surface and new dislocations can be created in the sample. For this reason, if it is assumed that the emergence of dislocations is accompanied by photon emission, as done in Refs. 1, 2, 10, and 11 to explain the nonthermal luminescence of metal samples under mechanical, thermal, and laser-thermal actions, then a flux of dislocations emerging at the surface and ML associated with this flux should be possible after any number of irradiations, if $\sigma > \sigma_c$. This can probably explain the fact that the signal observed in our experiments did not vanish after repeated irradiation, in contrast to Ref. 2 where the signal was observed to decrease and even vanish after several irradiations. Even though the ML signal from tungsten was expected to be low, in the experiment the

ML signal was reliably recorded from $I_{las.}=4\times10^4$ W/cm^2 and above in the current regime and with $I_{las.}=2.5\times10^4$ W/cm^2 in the photon-counting regime.

The shape of the signal and the dependence of its time delay on $I_{las.}$ are interesting. The propagation time of thermal stresses to the backside of the sample and, therefore, the expected delay of the radiative emergence of dislocations as a result of thermal stresses is determined by the propagation time of the temperature front $\Delta t_T \sim d^2/\chi$ from the front to back surfaces (which for a tungsten sample with thickness $d\approx220$ μm is ≈0.9 ms). Therefore, in the experiment, the time delay of ML should probably be measured with respect to the thermal signal detected from the front surface of the sample and not relative to the laser pulse, as done in Refs. 1 and 2. The thermal signal had a definite delay relative to the laser pulse and this delay varied in the range 0.2–0.4 ms as a function of $I_{las.}$. In the present work, for comparison the delay was measured with respect to the laser pulse and the thermal signal. It is evident from Figs. 2b and 2c that as $I_{las.}$ increases, the delays Δt_1 and Δt_2 vary over quite wide limits ($\Delta t_1\approx1.1-0.7$ ms, $\Delta t_2\approx0.45-0.25$ ms), taking on values much less than Δt_T. This provides a basis for assuming that the leading edge of the luminescence signal from the backside is not due to the emergence of dislocations under the action of thermal stresses and of thermal luminescence.

In Ref. 1, where samples were irradiated by laser pulses with power density $I_{las.}$ above the plasma formation threshold $I_{thres.}$, backside luminescence starting before the propagation of thermal stresses was also observed. To explain this fact the authors called attention to the possibility of acoustic waves participating in the radiative emergence of dislocations at the surface. In their opinion, for $I_{las}>I_{thres.}$ a quite powerful acoustic wave is generated, and its propagation time $t_a\sim d/v$ (where v is the propagation velocity of the sound wave) is much shorter than that of the thermal stresses, and for this reason the earlier onset of backside luminescence could be due to a radiative emergence of dislocations under the action of elastic stresses associated with the acoustic wave. However, under our experimental conditions, the power density of the laser pulse was below the melting threshold of the surface, and for this reason the vapor-pressure pulse and therefore the amplitude of the acoustic wave associated with the vapor pressure can be neglected. It is known that dislocation creation and annihilation processes as well as the displacement of intergrain boundaries during deformation could become sources of quite powerful acoustic waves. Therefore, as the thermoelastic stresses propagate from the front surface to the back surface, a moving source of acoustic waves can form. As the thermal deformations approach the back side, the amplitude of the acoustic waves excited in this manner can be sufficient for radiative emergence of dislocations at the surface and, since the propagation velocity of the acoustic waves is much higher than that of the thermal deformations, luminescence should appear before the thermal deformations reach the back surface. It should be noted that the number of acoustic waves and the moments at which they are excited during the time when the thermoelastic stresses are present are most likely random events. This is probably the explanation of why the time delays Δt_1 and Δt_2 in the appearance of backside luminescence of the sample vary arbitrarily by $\Delta t \leqslant 0-0.2$ ms in each irradiation event, while the number of spikes fluctuates.

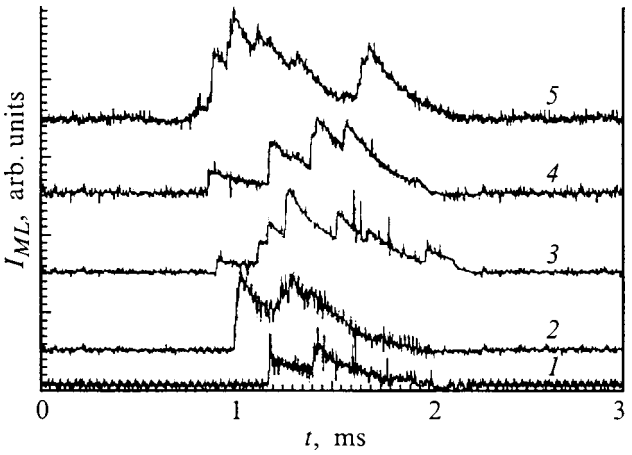

FIG. 5. Oscillograms of ML signal (current mode) with increasing power density of the laser pulse ($\lambda=600$ nm). Tungsten sample. *1*—$I_{las.}=4.02\times10^4$, *2*—$I_{las.}=4.92\times10^4$, *3*—$I_{las.}=5.81\times10^4$, *4*—$I_{las.}=6.71\times10^4$, *5*—$I_{las.}=7.62\times10^4$.

The spike shape of the observed signal is still not completely understood. If the dislocation model of luminescence is retained, as above, then the shape of the signal could be explained by the existence of groups of different kinds of dislocations, characterized by the degree of pinning of the dislocations in the material and by a definite sequence of emergence at the surface. Then, as the thermal stresses approach the backside, the most weakly pinned groups of dislocations will start to move first under the action of the acoustic waves excited in the process and will start to emerge at the surface. Then, the groups of dislocations which are more strongly pinned and are located farther from the surface will emerge next under the action of thermal stresses. However, there are definite doubts concerning such a strict discretization of dislocations with respect to their pinning energy in the material. The multispike shape of the signal could also be due to the combined action on the dislocation emergence process of thermal stresses and elastic stresses caused by acoustic waves. Indeed, the thermal stresses reaching the back side stimulate simultaneously both emergence of dislocations at the surface and excitation of acoustic waves directly at the back surface of the sample. Therefore it can be conjectured that the spike shape of the signal is due to the combined influence of thermal stresses and acoustic waves on dislocation emergence, and the number of spikes is determined by the number of the most intense acoustic waves excited at the back surface.

The spectral composition of ML in the range 0.4–0.6 μm was investigated in this work. It follows from the analysis that luminescence is observed in the entire experimental spectral range and has no sharply expressed local peaks characteristic for atomic or molecular transitions. The time dependence of the spectral intensity of luminescence, just as the time dependence of the total luminescence intensity, has a spiked form. Figure 5 shows oscillograms of the lumines-

cence signals from the back side of the sample for wavelength $\lambda = 0.6$ μm. It is difficult to give an unequivocal interpretation of the origin of the observed luminescence based on the results presented. If it is due to radiative transitions accompanying the rearrangement of the surface electronic states of tungsten atoms at the moment of emergence of a dislocation, then peaks corresponding to these transitions should be observed in the ML spectrum. However, such transitions were not observed in the spectral range 0.4–0.6 μm. It is possible that only the luminescence ''tail'' lies in this range, while the peaks themselves lie outside this range. It is also possible that particle mechanoemission excited by the emergence of dislocations makes a definite contribution to the luminescence. It is known that charged-particle (as a rule electron) emission occurs when a surface is deformed or when a previously deformed surface is heated.[3,7] Then radiative collisions and attachment of electrons to atoms and molecules of the surrounding gas could be responsible for the observed luminescence.

[1] A. M. Kondyrev, I. P. Shcherbakov, K. B. Abramova, and A. E. Chmel', Zh. Tekh. Fiz. **62**(1), 206 (1992) [Sov. Phys. Tech. Phys. **37**, 110 (1992)].
[2] K. B. Abramova, I. P. Shcherbakov, I. Ya. Pukhonto, and A. M. Kondyrev, Zh. Tekh. Fiz. **66**(5), 190 (1996) [Tech. Phys. **41**, 511 (1996)].
[3] K. B. Abramova, A. I. Rusakov, A. A. Semenov, and I. P. Shcherbakov, Fiz. Tverd. Tela (St. Petersburg) **40**(6), 957 (1998) [Phys. Solid State **40**, 877 (1998)].
[4] V. A. Zakrevskiĭ and A. V. Shul'diner, Pis'ma Zh. Tekh. Fiz. **10**(3), 139 (1984) [Sov. Tech. Phys. Lett. **10**, 56 (1984)].
[5] V. A. Zakrevskii and A. V. Shuldiner, Philos. Mag. B **71**, 127 (1995).
[6] V. N. Smirnov, Opt. Mekh. Prom. No. 7, 1 (1986).
[7] J. T. Dickinson, L. B. Brix, and L. C. Jensen, J. Phys. Chem. **88**, 1698 (1984).
[8] R. I. Mints, I. I. Mil'man, and V. I. Kryuk, Usp. Fiz. Nauk **119**(4), 749 (1976) [Sov. Phys. Usp. **19**, 697 (1976)].
[9] J. Christian, *The Theory of Phase Transformations in Metals and Alloys* [Russian translation] (Mir Moscow, 1978), Part 1.
[10] M. I. Molotskiĭ, Fiz. Tverd. Tela (Leningrad) **23**(7), 171 (1981) [Sov. Phys. Solid State **23**, 1269 (1981)].
[11] M. I. Molotskiĭ, Fiz. Met. Metalloved. **55**, 743 (1983).

Translated by M. E. Alferieff

On the nonuniform electron-density distribution in a layer adsorbed on a metal

S. Yu. Davydov

A. F. Ioffe Physicotechnical Institute, Russian Academy of Sciences, 194021 St. Petersburg, Russia
(Submitted February 5, 1999)
Fiz. Tverd. Tela (St. Petersburg) **41**, 1543–1547 (September 1999)

The probability of a transition from a uniform charge distribution (UCD) in the adsorbed layer to a nonuniform one (NCD) caused by the dipole-dipole adatom repulsion is analyzed within the Anderson–Newns Hamiltonian and a simple density-of-states model for the substrate. Two limiting cases are considered, namely, an infinitely wide and a narrow band of allowed substrate states. Criteria for the UCD→NCD transition are obtained. Experimental data on reconstruction of clean metal faces are analyzed. © *1999 American Institute of Physics.* [S1063-7834(99)00409-8]

The distribution of electron density in a monatomic adsorbed layer can be uniform if each atom contains the same number of electrons n (and, hence, the same charge $Z=1-n$), or nonuniform, if n changes in some way in transition from one atom to another. The possibility of nonuniform ordering caused by Coulomb interaction among the atoms adsorbed on a metal surface was first demonstrated in Ref. 1 and analyzed subsequently in detail in Ref. 2. These studies were based on model Hamiltonians which are actually modifications of the Anderson–Newns Hamiltonian[3,4].

The reason for the onset of a nonuniform charge distribution (NCD) can be easily visualized in the following example. Consider two identical ions with charges Z on the surface of a metal substrate at a distance a from one another. Let the atomic radii be r and consider the metal surface as an image plane. Then the interaction energy between these atoms including the image forces can be written as $W=2Z^2e^2[a^{-1}-(a^2+r^2)^{-1/2}]$, where e is the positron charge. Let electrons transfer from one ion to another, making the ionic charges equal to $Z_{\pm}=Z(1\pm c)$, where c is an integer. One readily sees that the interaction energy $W=2Z^2e^2(1-c)^2[a^{-1}-(a^2+r^2)^{-1/2}]$ decreased compared to the case of uniform charge distribution (UCD). It can be shown that the ionic component of the adsorption energy $E_{\text{ion}}=-Z^2e^2/2r$ in the UCD case, whereas in the case of NCD $E_{\text{ion}}=-Z^2e^2(1+c^2)/2r$. Thus as a system transfers to a nonuniform electron-density distribution in the adsorbed layer the ion repulsion energy decreases, and the energy of ionic bonding to the substrate increases. There are, however, two factors interfering with the UCD→NCD transition. These are, first, the intratomic Coulomb repulsion of electrons with opposite spins U, and, second, the increase of the kinetic energy of the electron gas[2]. The latter statement can be understood easily if one recalls the Heisenberg uncertainty relation $\Delta x\cdot\Delta p\sim\hbar$, where $\hbar$ is the reduced Planck's constant. By localizing an electron at a center, one reduces the uncertainty of its coordinate Δx while increasing at the same time that of its momentum Δp, and this is what gives rise to an increase of the kinetic energy. The UCD→NCD transition occurs only if the adatom repulsion energy exceeds some critical value. A quantitative consideration of the related problems can be found in Ref. 2.

A common approach was used[1,2] to consider layers at a metal surface and clean metal faces, since the latter, because of specific features in their geometric arrangement, can also be treated as adsorbed monolayers. A transition to an NCD state may bring about reconstruction of the metal surface, if one takes into account, for instance, electron-phonon interaction.[2,5–7] The same approach was subsequently applied to investigate the reconstruction of semiconductor faces.[8–11]

When describing a system in terms of the Anderson–Newns Hamiltonian, one should discriminate between the cases of the wide and narrow surface bands.[3,4,12,13] While in the case of an infinitely wide band there is only one broadened adatom quasilevel (it is assumed that only one atomic orbital is involved in adsorption) overlapping this band, a narrow continuum band gives rise not only to resonance states but also to local states lying outside the band. Such a difference in the electronic structure of a surface layer should result in a change of the criterion for the onset of the NCD. It is with an investigation of this aspect of the problem that the present work deals.

1. BROAD SURFACE-BAND APPROXIMATION

We shall describe adsorption of a single atom by a Hamiltonian of the form

$$H=\sum_k \varepsilon_k c_k^+ c_k+\varepsilon_a a^+ a+V\sum_k (c_k^+ a+\text{h.c.}). \tag{1}$$

Here ε_k is the energy of the substrate electron in state $|k\rangle$, ε_a is the energy of an atomic electron in state $|a\rangle$, $c_k^+(c_k)$ is the operator of electron creation (annihilation) in state $|k\rangle$, $a^+(a)$ are the corresponding operators for an electron in state $|a\rangle$, and V is the matrix element hybridizing the $|k\rangle$ and $|a\rangle$ states. We prescribe the substrate density of states $\rho_s(\omega)$ in the form

$$\rho_s(\omega)=1/D, \quad |\omega|\leqslant D; \quad \rho_s(\omega)=0, \quad |\omega|>D, \tag{2}$$

where $2D$ is the substrate conduction-band width, and ω is an energy variable (the energy is reckoned from midgap). One can readily show that the adatom Green's function G corresponding to Hamiltonian (1) can be written

$$G^{-1}(\omega)=\omega-\varepsilon_a-\Lambda(\omega)-i\Gamma(\omega), \tag{3}$$

where the functions of the adatom quasilevel hybridization shift Λ and of its halfwidth Γ can be written, taking into account (2), in the following way

$$\Gamma=\pi V^2/D, \quad |\omega|\leqslant D; \quad \Gamma=0,$$

$$|\omega|>D; \quad \Lambda=\frac{V^2}{D}\ln\left|\frac{D+\omega}{D-\omega}\right|. \tag{4}$$

The transition to the infinitely broad-band approximation ($D\to\infty$) results in the vanishing of the shift Λ, whereas the quasilevel halfwidth Γ is considered finite and constant, as before.[3] One can then show easily that the density of states at the adatom ρ and the orbital population n of this adatom are

$$\rho(\omega)=\frac{1}{\pi}\frac{\Gamma}{(\omega-\varepsilon_a)^2+\Gamma^2}, \quad n=\frac{1}{\pi}\arctan\frac{\varepsilon_a-E_F}{\Gamma}, \tag{5}$$

where E_F is the substrate Fermi energy.

Consider now the lattice of adatoms subjected to dipole repulsion. Unlike the procedure used in Ref. 2, we shall not truncate dipole-dipole repulsion at the nearest neighbors and shall take into account long-range interaction by the method developed in Refs. 14 and 15, where it was shown that when in the UCD state, the surface-dipole field shifts the adatom energy level ε_a to ε_a'

$$\varepsilon_a'(\Theta)=\varepsilon_a-\xi\Theta^{3/2}Z(\Theta), \quad Z(\Theta)=[1-n(\Theta)],$$

$$\xi=2e^2\lambda^2N_{ML}^{3/2}A, \tag{6}$$

where Θ is the surface coverage by adatoms, which is defined as the ratio of the number of adatoms in a layer N to that in a monolayer coating N_{ML}, 2λ is the arm of the surface dipole formed by an adsorbed ion and its image in the metal, and A is a dimensionless coefficient depending on the actual adatom lattice geometry. Substituting expressions (6) into Eq. (5) yields a self-consistent equation for determination of the adatom orbital population.

For the sake of simplicity, consider a one-dimensional adatom chain on a metal surface. Such structures are indeed observed in adsorption on groovy faces, e.g. (112).[16,17] We shall assume the chain to consist of identically oriented dipoles with alternating charges $Z_\pm=\tilde{Z}(1\pm c)$ at a distance of a from one another (a ''ferrimagnetic'' chain). It can be shown (see Appendix), that the charges can be found from equations

$$\tilde{Z}(1\pm c)=0.5+(1/\pi)\arctan\{[\varepsilon_a-\xi\Theta^{3/2}\tilde{Z}(1\mp\nu c)]/\Gamma\}. \tag{7}$$

Here and subsequently in this Section, the energy is reckoned from the Fermi level E_F, the coefficient A entering the expression for ξ is 2.40, and $\nu=0.75$ (see Appendix). Note that the charge $\tilde{Z}$, as follows from Eqs. (7), is a function of the order parameter c, and becomes Z in Eq. (6) for $c=0$. As seen from Eqs. (7), the UCD→NCD transition takes place if the condition

$$\Theta^{3/2}\frac{\xi\Gamma}{(\varepsilon_a')^2+\Gamma^2}\geqslant\frac{\pi}{2\nu}, \tag{8}$$

is met, where ε_a' is given by Eq. (6). Using Eqs. (5) and (6), inequality (8) can be recast to the form

$$\Theta^{3/2}\sin^2[\pi Z(\Theta)]\geqslant\pi/2\nu K, \quad K=\xi/\Gamma, \tag{9}$$

where, as before, $Z=\tilde{Z}$ for $c=0$. In deriving the inequalities (8) and (9) we took into account that $(\partial\tilde{Z}/\partial c)_{c=0}=0$, which can be shown using Eq. (7). The threshold coverage Θ_b above which the transition to the NCD state occurs is determined by Eqs. (8) and (9) for $\Theta=\Theta_b$. Figure 1 displays the phase diagram of an adsorption system. (For illustration, we accepted $K=10$, which apparently is close to the lower boundary of possible values of this parameter.) For $\Theta\geqslant\Theta_b$, the NCD state is realized inside the region bounded by the $\Theta_b(Z)$ curve. The characteristic points of the curve are determined from the following expressions

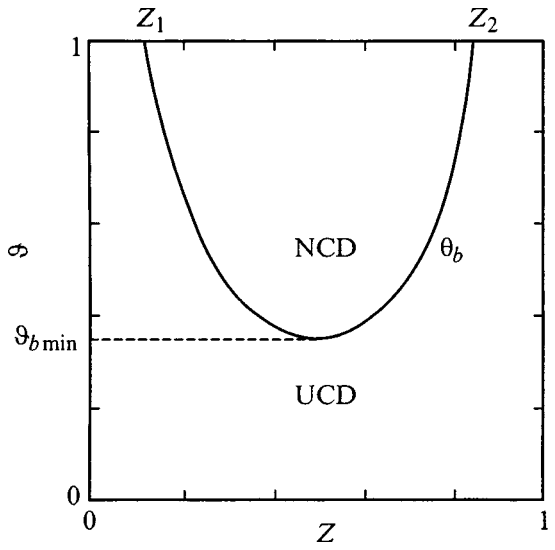

FIG. 1. Phase diagram of an adsorption system in the infinitely wide-band approximation. The threshold coverage Θ_b corresponds to a UCD→NCD transition for $\Theta\geqslant\Theta_b$. Z is the adatom charge in the UCD layer. $K=\xi/\Gamma=10$.

$$Z_1=(1/\pi)\arcsin\sqrt{\pi/2\nu K}, \quad Z_2=1-Z_1,$$

$$\Theta_{\min}=(\pi/2\nu K)^{2/3}. \tag{10}$$

One can show that the UCD→NCD transition is energetically favorable in the same way as this was done in Ref. 2. The change in the ionic energy of the system in such a transition (reduced to one two-atomic surface cell) is $\Delta E_i=-Z^2e^2/2\lambda$. The change in the metal component of the adsorption system ΔE_m energy can be written

$$\Delta E_m \sim -2c\nu\xi\Theta^{3/2}\tilde{Z} + \frac{\Gamma}{\pi}\left[\ln\frac{(\varepsilon_a' + c\nu\xi\Theta^{3/2}\tilde{Z})^2+\Gamma^2}{\varepsilon_a'^2+\Gamma^2} + \ln\frac{(\varepsilon_a' - c\nu\xi\Theta^{3/2}\tilde{Z})^2+\Gamma^2}{\varepsilon_a'^2+\Gamma^2}\right]. \quad (11)$$

The first term in the expression for ΔE_m corresponds to the change in the potential energy of the adatom induced by the shift and change in the population of its quasilevel, while the second term describes the change in the kinetic energy of the adsorption system. Assuming $2c\nu\xi\Theta^{3/2}\tilde{Z}/(\varepsilon_a'^2+\Gamma^2) \ll 1$ and $c^2 \ll c$, one can readily show that all that remains in Eq. (10) for ΔE_m is the first negative term. Hence the UCD→NCD transition is energetically favorable. Therefore this transition takes place as soon as the transition to a nonuniform electron-density distribution becomes possible, i.e. the inequalities (8) and (9) are satisfied. The UCD→NCD transition is clearly a second-order transformation.[2]

2. NARROW-BAND APPROXIMATION

The narrow-band problem appears when a noticeable peak exists in the density of states near the Fermi level, a situation occurring, for instance, on clean (100) faces of tungsten, molybdenum, and chromium.[10] In principle, the surface layer of a metal may be considered as an adatom monolayer, because the electron population of a surface atom differs from that of an atom in the bulk of the metal, where the A and ν parameters entering Eqs. (6) and (7) have different values.

The problem of atom adsorption on a substrate with a finite conduction band is considered in detail in Ref. 13. The energies of the local and resonance adatom levels are determined by the poles of Green's function (3)

$$\omega - \varepsilon_a - \Lambda(\omega) = 0, \quad (12)$$

where the shift function Λ is given by expression (4). When considering a narrow band, it appears logical to assume $2V^2/D^2 > 1$, in which conditions there form in the system two local levels, ω_1 and ω_2, below and above the band, respectively, and one resonance level ω^* (see Fig. 1 in Ref. 13). Moreover, in our subsequent estimates we shall assume $(V/D)^2 \gg 1$, i.e. we are going to consider the case exactly opposite to the approximation of an infinitely wide band.

It was shown[13] that the population n_b of the resonance level ω^* for the case of $2V^2/D^2 > 1$ can be calculated approximately from the expression

$$n_b = \frac{1}{\pi}\left[\arctan\frac{D(\omega^*+D)}{\pi V^2} - \arctan\frac{D(\omega^*+D-F)}{\pi V^2}\right], \quad (13)$$

where F is the Fermi energy reckoned from the band bottom. In a first approximation in the small parameter $(D/V)^2$ one obtains

$$n_b \cong DF/(\pi V)^2. \quad (14)$$

In this approximation, n_b does not depend on the energy of the resonance level ω^*. The first nonzero ω^*-dependent correction for n_b can be written as $[1 - O(D^4/V^4)]$, where $O(\ldots)$ is a small quantity, whose order is determined by the argument. For the population of the local state ω_1 we have[13]

$$n_l = \left[1 + \frac{2V^2}{\omega_1^2 - D^2}\right]^{-1}. \quad (15)$$

The upper local state ω_2 is not filled and is disregarded in what follows.

In the presence of dipole-dipole interaction and nonuniform charge distribution in the adatom lattice, the ε_a' state transforms into two split states $\varepsilon_a^{\pm} = \varepsilon_a' \pm c\nu\Theta^{3/2}Z\xi$, where ε_a' has the same form as in Eq. (6). As before, the charge $Z = 1 - n$, where $n = n_b - n_l$. As a result of the adatom level splitting $[\omega_{1,2} \to \omega_{1,2}^{\pm}, \omega^* \to (\omega^*)^{\pm}]$, the populations n_b and n_l split too. We shall assume in what follows for the sake of simplicity that all population numbers split in the same way, i.e. $Z_p^{\pm} = Z_p(1 \pm c)$, where the p index stands for the l and b indices.

A comparison of Eqs. (7) and (13) shows that the condition for the UCD→NCD transition for the ω^* band states, i.e., the $Z_b \to Z_b^{\pm}$ transition, in the narrow-band case does not differ radically from that in the limit of an infinitely wide band. [Recall that the quasilevel halfwidth Γ entering Eq. (7), as seen from (4), is $\pi V^2/D$.] We shall dwell, therefore, on the UCD→NCD transition for the ω_1 state and stress once more that it is the formation of local states that constitutes the main difference of the narrow-band from infinitely wide-band model.

Consider some characteristic limiting cases. Let $\varepsilon_a^{\pm}/D \gg 1$ and $\varepsilon_a^{\pm} D/V^2 \gg 1$. Using the results of Ref. 13, one can write by analogy

$$\omega_1^{\pm} \cong -D[1 + 2\exp(-\varepsilon_a^{\pm} D/V^2)],$$
$$n_l^{\pm} \cong 2(D/V)^2 \exp(-\varepsilon_a^{\pm} D/V^2). \quad (16)$$

An analysis of the population numbers suggests that the condition for the UCD→NCD transition is $\Theta \geqslant \Theta_b$, where

$$\Theta_b \cong [V^4 \exp(\varepsilon_a' D/V^2)/2\nu\xi D^3]^{2/3}. \quad (17)$$

In the case of an infinitely wide band and for a similar condition $(\varepsilon_a^{\pm}/\Gamma)^2 \gg 1$ Eq. (8) yields

$$\Theta_b \cong (\pi\varepsilon_a'^2/2\nu\xi\Gamma)^{2/3}. \quad (18)$$

While Eqs. (17) and (18) look different, they have nevertheless much in common. First, the numerators of the expressions in parentheses are large quantities. Second, the parameters ξ and ν describing the dipole field in the UCD state and its change in the NCD state, respectively, enter both relations in the same way. The parameters of the problem are typically as follows: for a metal, the quasilevel halfwidth Γ is a few tenths to one eV, and we accept here $\Gamma = 0.5$ eV. Setting $\xi = 3$ eV [which is typical of alkali metal adsorption[18] if one reduces ξ from a square adatom lattice with $A = 9$ (Ref. 14) to a chain with $A = 2.4$ (see Appendix)], and assuming for an estimate $\varepsilon_a' = 2$ eV, one comes in both cases to $\Theta_b > 1$, which shows that a transition to the NCD state is impossible.

Thus an adatom with a charge close to one (low occupation of the adatom orbital) cannot apparently be in an NCD state.

Consider now for a narrow band the case where $(\varepsilon_a^{\pm})^2 \ll D^2$, and for an infinitely wide band, $(\varepsilon_a^{\pm})^2 \ll \Gamma^2$, which corresponds roughly to half-filling of the adatom orbitals ($n \cong 0.5$). Turning again to Ref. 13, we find for a narrow band

$$\omega_1^{\pm} \cong \varepsilon_a^{\pm} - \sqrt{2}V, \quad n_l^{\pm} \cong (1 - \varepsilon_a^{\pm}/2\sqrt{2}V)/2. \tag{19}$$

An analysis of Eqs. (19) and (8) yields the thresholds of the UCD→NCD transition for the narrow and wide bands, respectively

$$\Theta_b \cong (2\sqrt{2}V/\nu\xi)^{2/3}, \quad \Theta_b \cong (\pi\Gamma/2\nu\xi)^{2/3}. \tag{20}$$

For a narrow band this yields $\Theta_b = 0.60$, and for a wide one, $\Theta_b = 0.53$.

Consider now the low-lying quasilevels $\varepsilon_a^{\pm} < 0$ satisfying the inequalities $|\varepsilon_a^{\pm}| \gg D, V$ (narrow band) and $(\varepsilon_a^{\pm}/\Gamma)^2 \gg 1$ (wide band). In these conditions, the adatom orbital is nearly filled. Invoking again Ref. 13, we find for a narrow band

$$\omega_1^{\pm} \cong \varepsilon_a^{\pm}, \quad n_l^{\pm} \cong [1 - 2V^2/(\varepsilon_a^{\pm})^2]. \tag{21}$$

For the narrow and wide bands we obtain, respectively

$$\Theta_b \cong (|\varepsilon_a'|^3/4\nu\xi V^2)^{2/3}, \quad \Theta_b \cong (\pi\varepsilon_a'^2/2\nu\xi\Gamma)^{2/3}. \tag{22}$$

Again in both cases we come to $\Theta_b > 1$.

Thus despite the substantial differences between the narrow- and wide-band models, and the presence in the former of localized states and their absence in the latter, the transition of a uniform electron distribution in a surface layer to a nonuniform one occurs under similar conditions.

3. DISCUSSION OF RESULTS

We are not aware of any observations of a nonuniform charge distribution in metal films adsorbed on high-melting metals.[16] This can be understood if we transform Eq. (8) to

$$\Theta \geqslant \Theta_b = [2\nu\xi\rho_F(\varepsilon_a')]^{-2/3}, \quad \rho_F(\varepsilon_a') = \frac{1}{\pi}\frac{\Gamma}{\varepsilon_a'^2 + \Gamma^2}, \tag{23}$$

where $\rho_F(\varepsilon_a')$ is the density of states at Fermi level, from which the energy is reckoned. Let us make some estimates for the W(112) face, whose work function $\phi = 4.80$ eV,[19] and on which alkali, alkaline-earth, and rare-earth metals can form chains[16]. [A similar pattern is observed for Mo(112) and Re($10\bar{1}0$).] Consider the adsorption of lithium and sodium, because large dipole moments do not permit potassium and cesium to form chain structures. For $\Theta \to 0$, the dipole moments $p = eZ\lambda$ of Li and Na are, respectively, 0.67 and 0.75 a.u. Invoking Ref. 18, one can now find the charge, $Z = 0.31$ and 0.29, and the density of states, $\rho_F = 0.10$ and 0.13 $(\text{eV})^{-1}$ for Li and Na, respectively. The dipole interaction parameter $\xi = 3.21$ eV for Li and 2.72 eV for Na (which can be obtained from Ref. 18 if one takes into account that the ratio of the A coefficients for a chain and a square lattice is 0.27), which yields $\Theta_b > 1$. Hence the UCD→NCD transition is impossible for low coverages. As the coverage increases, the charge on the adatom and its dipole moment decrease because of depolarization, which can readily be shown to lead to a growth of ρ_F, increase of Θ_b, and decrease of the UCD→NCD transition probability.

Consider now the reconstruction of clean metal faces[10,16]. It is well known that among all transition and noble metals the face that undergoes reconstruction most frequently is the (100) face of iridium, platinum, and gold, whose structure acquires a close to hexagonal symmetry and becomes slightly corrugated. The groovy (110) faces of Ir, Pt, and Au reconstruct to become $p(1\times 2)$. In tungsten, molybdenum, and chromium, which are bcc metals, the (100) face reconstructs to produce a $c(2\times 2)$ structure at low temperatures, i.e., the lattice period doubles (Mo undergoes an incommensurate reconstruction). In all these structures, the narrow d band crosses the Fermi level.[10,16]

The surface layer of a metal may be considered as an adatom monolayer, because, for instance, the electron population of a surface atom differs from that of an atom in the bulk (see, e.g., Ref. 17). Although we have been considering a chain of adatoms, the results obtained can be used for interpreting UCD→NCD transitions occurring on a clean face as well, if one sets $\Theta = 1$. Now the A and ν parameters entering Eqs. (6) and (7) will have other values. For different two-dimensional lattices, $A \cong 10$,[20] and ξ is of the order of 10 eV (Ref. 15). Because the surface d band in the above metals lies close to the Fermi level,[10,16] we can use the estimate (20) (the second expression), where by Γ one should understand the surface-band halfwidth (of the order of 1–2 eV). Thus Θ_b is of the order of $\Gamma/\xi < 1$, and an NCD state can be realized. The nature of reconstruction can be understood if one assumes, as this was done in Refs. 2,5–7, that an electronic transition is accompanied by a structural transformation. Note the following point. The narrow d band of transition metals possessing a high density of states ρ_d overlaps the wide sp band having a low density of states ρ_{sp}. Therefore the ω_1 state is not local. Its width, which is proportional to ρ_{sp}, is substantially smaller than that of the d band and may be neglected in our estimates.

Support of the Federal Program ''Surface Atomic Structures'' is gratefully acknowledged.

APPENDIX A

To find the fields of the dipole forces acting on point dipoles with charges $Z_{\pm} = Z(1 \pm c)$, one has to calculate the sums $S_{0,1}$ of the form

$$S_0 = \sum_{m=1}^{\infty} m^{-3}, \quad S_1 = \sum_{m=1}^{\infty} (-1)^{m+1} m^{-3}.$$

They are, respectively, $\zeta(3)$ and $3\zeta(3)/4$, where ζ is the Weierstrass zeta function[21]. Hence $S_{0,1} = 1.2, 0.9$. The field acting on a dipole moment $Z_{\pm}$ is proportional to the quantity $A(1 \mp \nu c)$, where $A = 2S_0$, and $\nu = S_1/S_0$, i.e. $A = 2.40$ and $\nu = 0.75$.

[1] L. A. Bol'shov and A. P. Napartovich, Zh. Éksp. Teor. Fiz. **64**, 1404 (1973) [Sov. Phys. JETP **37**, 713 (1973)].

[2] S. Yu. Davydov, Fiz. Tverd. Tela (Leningrad) **21**, 2283 (1979) [Sov. Phys. Solid State **21**, 1314 (1979)].
[3] P. W. Anderson, Phys. Rev. **124**, 41 (1961).
[4] D. M. Newns, Phys. Rev. **178**, 1123 (1969).
[5] V. E. Kravtsov and A. G. Mal'shukov, Zh. Éksp. Teor. Fiz. **75**, 691 (1978) [Sov. Phys. JETP **48**, 348 (1978)].
[6] V. E. Kravtsov and A. G. Mal'shukov, Zh. Éksp. Teor. Fiz. **77**, 180 (1979) [Sov. Phys. JETP **50**, 91 (1979)].
[7] S. Yu. Davydov and A. D. Chesnokov, Fiz. Tverd. Tela (Leningrad) **24**, 305 (1982) [Sov. Phys. Solid State **24**, 175 (1982)].
[8] A. I. Volokitin, Fiz. Tekh. Poluprovodn. **15**, 2136 (1981) [Sov. Phys. Semicond. **15**, 1240 (1981)].
[9] L. A. Bol'shov and M. S. Veshchunov, Zh. Éksp. Teor. Fiz. **90**, 569 (1986) [Sov. Phys. JETP **63**, 331 (1986)].
[10] L. A. Bol'shov and M. S. Veshchunov, Poverkhnost' **7**, 5 (1989).
[11] S. Pick, Surf. Sci. Rep. **12**, 99 (1990).
[12] T. L. Einstein, J. A. Hertz, and J. Schrieffer, in *Theory of Chemisorption*, edited by J. R. Smith (Springer, Berlin, 1980; Mir, Moscow, 1983).
[13] S. Yu. Davydov, Zh. Tekh. Fiz. **68**(4), 15 (1998) [Tech. Phys. **43**, 361 (1998)].
[14] J. P. Muscat and D. M. Newns, J. Phys. C **7**, 2630 (1974).
[15] S. Yu. Davydov, Fiz. Tverd. Tela (Leningrad) **19**, 3376 (1977) [Sov. Phys. Solid State **19**, 1971 (1977)].
[16] O. M. Braun and V. K. Medvedev, Usp. Fiz. Nauk **157**, 631 (1989) [Sov. Phys. Usp. **32**, 328 (1989)].
[17] L. A. Bol'shov, A. P. Napartovich, A. G. Naumovets, and A. G. Fedorus, Usp. Fiz. Nauk **122**, 125 (1977) [Sov. Phys. Usp. **20**, 432 (1977)].
[18] S. Yu. Davydov, Zh. Tekh. Fiz. **69**(5), 116 (1999) [Tech. Phys. **44**, 584 (1999)].
[19] *Physical Quantities: a Handbook* [in Russian], edited by I. S. Grigor'ev and E. Z. Meĭlikhov (Énergoizdat, Moscow, 1991).
[20] C. E. Carol and J. W. May, Surf. Sci. **29**, 60 (1972).
[21] I. S. Gradshteyn and I. M. Ryzhik, *Tables of Integrals, Series, and Products* (Academic Press, New York, 1980; Russian original, Nauka, Moscow, 1971).

Translated by G. Skrebtsov

Thermal conductivity of $YbInCu_4$

I. A. Smirnov and L. S. Parfen'eva

A. F. Ioffe Physicotechnical Institute, Russian Academy of Sciences, 194021 St. Petersburg, Russia

A. Jezowski and H. Misiorek

Institute of Low-Temperature and Structural Research, Polish Academy of Sciences, 53-529 Wrocław, Poland

S. Krempel-Hesse, F. Ritter, and W. Assmus

J. W. Goethe Universität, Frankfurt a.M. 60054, Germany

(Submitted February 8, 1999)
Fiz. Tverd. Tela (St. Petersburg) **41**, 1548–1551 (September 1999)

The electrical and thermal conductivities of an $YbInCu_4$ polycrystalline sample have been measured within the 4.2–300-K range. The behavior of the heat conductivity has been found to change sharply above and below $T_v = 70-75$ K, the temperature corresponding to an isostructural phase transition from a state with an integral valence ($T > T_v$) to a mixed-valence state ($T < T_v$) of Yb ions. A preliminary qualitative analysis of the results is presented.
 [S1063-7834(99)00509-2]

There is presently an increasing interest on the side of both experimenters and theorists of the leading laboratories all over the world in $YbInCu_4$, a compound exhibiting unique physical properties.

$YbInCu_4$ undergoes a first-order isostructural phase transition at $T_v \sim 40-80$ K and atmospheric pressure. Both before and after the phase transition, the $AuBe_5$-type fcc lattice [$C15b$ structure, space group $F\bar{4}3m$ (T_d^2)] is retained. The phase transition is accompanied by a 0.5% increase in the cell volume for $T > T_v$. The magnitude of T_v depends on the excess or deficiency of a component, the technology of preparation, and arrangement of the Yb, In, and Cu atoms in the lattice.[1–3]

The phase transition in $YbInCu_4$ occurs from a Curie–Weiss paramagnet (states with localized magnetic moments) for $T > T_v$ to a Pauli paramagnet (a nonmagnetic state of the Fermi liquid) for $T < T_v$, a compound with a mixed rare-earth ion valence (called the light heavy-fermion system[4]). XPS data, as well as linear-expansion coefficient and magnetic susceptibility measurements show the valence to change at the phase transition by 0.1, from 3 in the high-temperature phase to 2.9 in the low-temperature one.[1)]

The high- and low-temperature phases represent a semimetal and a metallic state with the Yb4f electrons hybridized weakly and strongly with the conduction electrons, respectively.

As follows from EPR data,[5] the low-temperature phase is characterized by a high density of states at the Fermi level, which is typical of heavy-fermion systems and systems with mixed rare-earth ion valence. The γ parameter (the constant in the temperature dependence of the electronic component of heat conductivity) for the low-temperature phase is $50\ \mathrm{mJ/mol \cdot K^2}$ (Refs. 6 and 7), which likewise indicates that this compound has a fairly high carrier effective mass at the Fermi level compared, for instance, with the $YbInCu_4$-related semimetal $LuInCu_4$, for which $\gamma = 0.8\ \mathrm{mJ/mol \cdot K^2}$ (Ref. 8).

Note a few other interesting physical properties of $YbInCu_4$ which have initiated considerable interest by experimenters.

The phase-transition temperature of this compound can be varied by applying an external magnetic field and hydrostatic pressure, or by using ''chemical'' pressure by substituting La or Lu for Yb, and Ag or Ni for Cu (Refs. 9 and 10) (these substitutions also probably cause changes in the band structure as well).

A magnetic-field-induced metamagnetic phase transition was observed to occur in the low-temperature phase.[11–13]

The phase transition entails a strong change of the Kondo temperature, from $T_K \sim 25$ K for the high-temperature phase to $T_K \sim 500$ K in the low-temperature one.[14]

The phase transition in $YbInCu_4$ was observed to have only one analog, the $\alpha \rightarrow \gamma$ transformation in metallic Ce.[15]

Starting with the first paper of Felner and Nowik[16] that reported on the discovery of a phase transition in $YbInCu_4$ until present, numerous publications have appeared dealing with the investigation made over a broad range of temperatures, magnetic fields, and hydrostatic pressures, of the magnetic susceptibility, electrical conductivity, lattice constant, the Seebeck coefficient, the Hall constant, magnetoresistance, magnetostriction, linear-expansion coefficient, the elastic constants, L_{III}, XPS, UPS and Mössbauer spectra, EPR, NMR, low-energy neutron scattering, the Knight shift in ^{63}Cu and ^{115}In, Cu NQR, and surface phase transition. All the parameters studied undergo a jump-like change at T_v. The electronic band structure of $YbInCu_4$ was calculated.[2)]

We have not been able to find in this sea of publications any information on thermal conductivity studies. However data on the heat conductivity are necessary both for thermo-

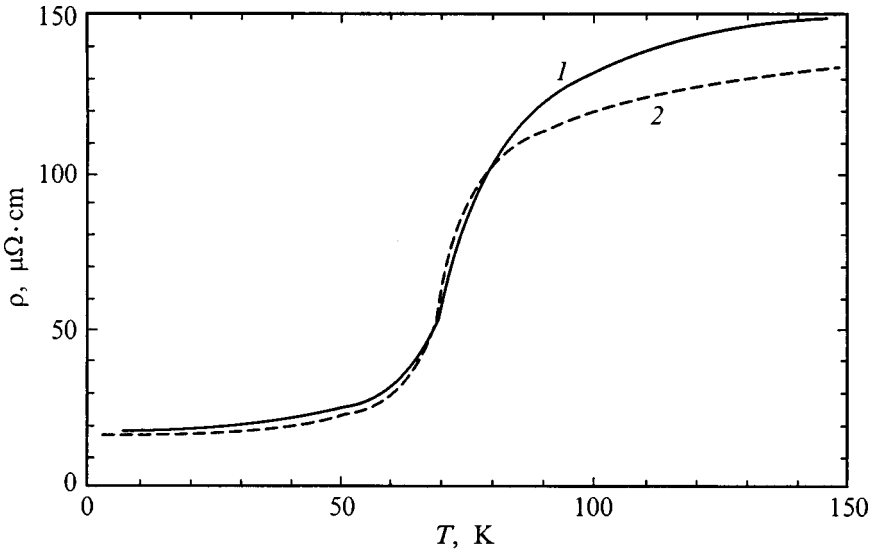

FIG. 1. Temperature dependence of ρ of $YbInCu_4$ polycrystalline samples. *1*—present experiment, *2*—data from Ref. 17.

dynamic calculations and when estimating the thermal regimes for single-crystal growth. From an analysis of the electronic component of the heat conductivity one can derive useful information on the carrier scattering mechanism and the behavior of the Lorentz number both above and below T_v, and from data on the lattice component of the heat conductivity ($\varkappa_{ph}$) one can get an idea of lattice dynamics at the phase transition.

We have carried out measurements of the heat conductivity ($\varkappa_{tot}$) and electrical resistivity (ρ) of a $YbInCu_4$ polycrystalline sample within the 4.2–300-K range. The sample was prepared by the technique described elsewhere.[2,17] The heat conductivity was measured on a setup similar to that used in Ref. 18.

Figure 1 presents our and literature[17] data on $\rho(T)$ of polycrystalline samples. As follows from the figure, for our sample $T_v \sim 70-75$ K. The phase transition is slightly diffuse. Single crystals[17] and polycrystalline samples subjected to a prolonged high-temperature annealing[19] exhibit a sharper transition.

Figure 2 plots $\varkappa_{tot}$ for polycrystalline $YbInCu_4$. The reverse measurement run (from 4.2 to 250 K) reveals a slight hysteresis in the $\varkappa_{tot}(T)$ relation. At $\sim 70-75$ K, one observes a sharp change in the behavior of $\varkappa_{tot}(T)$.

Figure 3 compares the data on $\rho(T)$ and $\varkappa_{tot}(T)$. One readily sees that the change in the nature of the temperature dependence $\varkappa_{tot}(T)$ coincides with the sharp change in the $\rho(T)$ dependence.

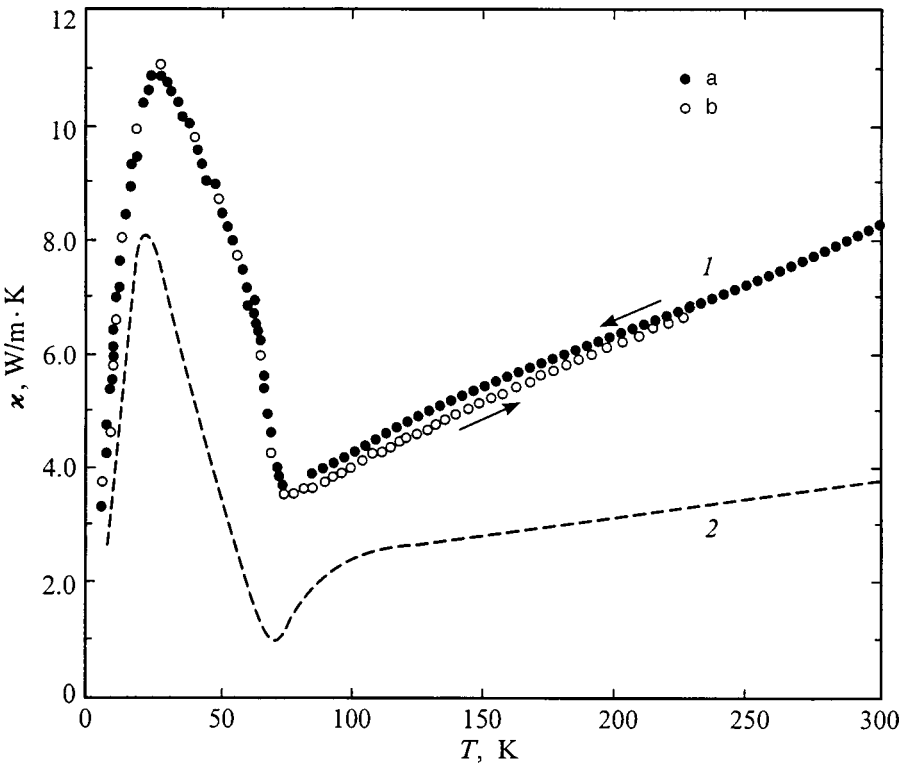

FIG. 2. Temperature dependence of the heat conductivity of an $YbInCu_4$ polycrystalline sample. *1*—$\varkappa_{tot}$, a and b are, respectively, the direct (300→4.2 K) and reverse (4.2→250 K) measurement runs; *2*—$\varkappa_{ph}=\varkappa_{tot}-\varkappa_e$ ($\varkappa_e=L_0T/\rho$).

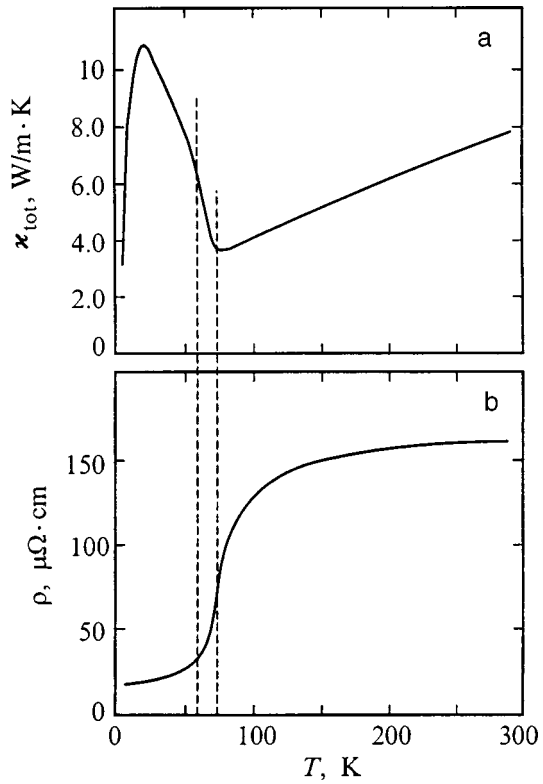

FIG. 3. Comparison of (a) $\varkappa_{tot}(T)$ and (b) $\rho(T)$ for an $YbInCu_4$ polycrystalline sample.

Consider the data obtained for $\varkappa_{tot}(T)$ in more detail. T_v appears to divide the $\varkappa_{tot}(T)$ dependence into two plots relating to two different phases. Indeed, for $T>T_v$ we deal with a magnetic semimetal characterized by stable local moments and a weak hybridization between the Yb4f and conduction electrons. For $T<T_v$, a new phase, namely, a nonmagnetic state of the Fermi liquid with strongly hybridized local Yb4f electrons and the conduction electrons appears. However, as follows from the Hall data,[14,20] one observes in both above phases a fairly high carrier concentration both for $T>T_v$ and for $T<T_v$, which corresponds to semimetals or metals. Thus the experimental $\varkappa_{tot}$ conductivity should include the electronic ($\varkappa_e$) and lattice components of the heat conductivity:

$$\varkappa_{tot}=\varkappa_{ph}+\varkappa_e. \tag{1}$$

In accordance with the Wiedemann–Franz law, classical theory gives the following relation for the heat conductivity $\varkappa_e$ of solids

$$\varkappa_e=L_0T/\rho, \tag{2}$$

where L_0 is the Sommerfeld value of the Lorentz number ($L_0=2.45\times10^{-8}\,W\Omega/K^2$).

We calculated $\varkappa_{ph}(T)$ using Eqs. (1) and (2) and the $\rho(T)$ data presented in Fig. 1. The results of this calculation are shown in Fig. 2 with the dashed curve *2*. The $\varkappa_{ph}(T)$ relation thus obtained is fairly unusual. Within the $T<T_v$ region [to the left of the maximum in $\varkappa_{ph}(T)$], $\varkappa_{ph}\sim T$, while for $T>T_v$, $\varkappa_{ph}\sim T^{0.4}$.

There are at least two possibilities for explaining the above results for $\varkappa_{ph}(T)$.

1. Let us assume that the calculations are correct. Then the temperature dependences obtained for the $\varkappa_{ph}$ can be related only to amorphous or heavily defected materials. $YbInCu_4$ polycrystalline samples were reported[1,3] to be heavily defected both for $T>T_v$ and for $T<T_v$. The high defect concentration is due to In being substituted for Yb or Cu (Refs. 1 and 3, respectively).

2. Now we assume that the above calculations are wrong, because we disregarded a number of factors which affect primarily the electronic part of the heat conductivity.

First, for $T>T_v$ electrons can scatter from disordered Yb spins, which may affect the magnitude and temperature dependence of $\varkappa_e$.[21] For $T<T_v$, there is no electron scattering from disordered spins.

Second, in semimetals the bipolar component of heat conductivity can contribute to $\varkappa_e$.

Third, for $T<T_v$ the $YbInCu_4$ compound may be considered as a light heavy-fermion system. For heavy-fermion systems, $L\neq L_0$ (L can be either smaller or larger than L_0 and depend in a complex manner on temperature).[22]

Finally, L may not be equal to L_0 in materials having a complex band structure (for instance, in the case when intersecting subbands with heavy and light carriers are present[23,24]).

A detailed analysis of $\varkappa_{tot}$ data for $YbInCu_4$, with due account of the above considerations, will be made in a separate publication.

The work was carried out in the framework of bilateral agreements between the Russian Academy of Sciences, Deutsche Forschungsgemeinschaft (Germany), and the Polish Academy of Sciences.

Support of the Russian Fund for Fundamental Research (Grant 99-02-18078) is gratefully acknowledged.

[1)] At the same time x-ray L_{III} absorption spectra[4] yield ~2.9 for the Yb valence for $T>T_v$, and ~2.8 for $T<T_v$.

[2)] References to the main studies of the properties of $YbInCu_4$ can be found in Refs. 11, 17 and the papers specified in the references list of the present paper.

[1] J. M. Lawrence, G. H. Kwei, J. L. Sarrao, Z. Fisk, D. Mandrus, and J. D. Thompson, Phys. Rev. B **54**, 6011 (1996).
[2] E. Fischbach, A. Löffert, F. Ritter, and W. Assmus, Cryst. Res. Technol. **33**, 267 (1998).
[3] A. Löffert, M. L. Aigner, F. Ritter, and W. Assmus, Cryst. Res. Technol. **34**, 267 (1999).
[4] I. Felner, I. Nowik, D. Vaknin, U. Potzel, J. Moser, G. M. Kalvius, G. Wortmann, G. Schmiester, G. Hilscher, E. Gratz, C. Schmitzer, N. Pillmayr, K. G. Prasad, H. de Waard, and H. Pinto, Phys. Rev. B **35**, 6956 (1987).
[5] C. Rettori, S. B. Oseroff, D. Rao, P. G. Pagliuso, G. E. Barberis, J. Sarrao, Z. Fisk, and M. Handley, Phys. Rev. B **55**, 1016 (1997).
[6] J. L. Sarrao, A. P. Ramirez, T. W. Darling, F. Freibert, A. Migliori, C. D. Immer, Z. Fisk, and Y. Uwatoko, Phys. Rev. B **58**, 409 (1998).
[7] N. Pillmayr, E. Bauer, and K. Yoshimura, J. Magn. Magn. Mater. **104–107**, 639 (1992).
[8] K. Takegahara and T. Kasuya, J. Phys. Soc. Jpn. **59**, 3299 (1990).
[9] I. Nowik, I. Felner, J. Voiron, J. Belle, A. Najib, E. du Trembolet de Lacheisserie, and E. Gratz, Phys. Rev. B **37**, 5633 (1988).

[10] C. D. Immer, J. L. Sarrao, Z. Fisk, A. Lacerda, C. Mielke, and J. D. Thompson, Phys. Rev. B **56**, 71 (1997).
[11] T. Shimizu, K. Yoshimura, T. Nitta, T. Sakakibara, T. Goto, and M. Mekata, J. Phys. Soc. Jpn. **57**, 405 (1988).
[12] K. Yoshimura, T. Nitta, M. Mekata, T. Shimizu, T. Sakakibara, T. Goto, and G. Kido, Phys. Rev. Lett. **60**, 851 (1988).
[13] J. M. de Teresa, Z. Arnold, A. del Moral, M. R. Ibarra, J. Kamarad, D. T. Adroja, and B. Rainford, Solid State Commun. **99**, 911 (1996).
[14] A. L. Cornelius, J. M. Lawrence, J. L. Sarrao, Z. Fisk, M. F. Handley, G. H. Kwei, J. D. Thompson, C. H. Booth, and F. Bridges, Phys. Rev. B **56**, 7993 (1997).
[15] D. C. Koskenmaki and K. A. Gschneidner, Jr., in *Handbook on the Physics and Chemistry of Rare Earths*, edited by K. A. Gschneidner, Jr. and L. Eyring (North-Holland, Amsterdam, 1978), p. 337.
[16] I. Felner and I. Nowik, Phys. Rev. B **33**, 617 (1986).
[17] B. Kindler, D. Finsterbusch, R. Graf, F. Ritter, W. Assmus, and B. Lüthi, Phys. Rev. B **50**, 704 (1994).
[18] A. Jezowski, J. Mucha, and G. Pompe, J. Phys. D **20**, 1500 (1987).
[19] K. Kojima, H. Hayashi, A. Minami, Y. Kasamatsu, and T. Hihara, J. Magn. Magn. Mater. **81**, 267 (1989).
[20] Y. Itoh, H. Kadomatsu, J. Sakurai, and H. Fujiwara, Phys. Status Solidi A **118**, 513 (1990).
[21] E. Gratz and M. J. Zuckermann, in *Handbook on the Physics and Chemistry of Rare Earths*, edited by K. A. Gschneidner, Jr. and L. Eyring (North-Holland, Amsterdam, 1978), p. 117.
[22] I. A. Smirnov and V. S. Oskotski, in *Handbook on the Physics and Chemistry of Rare Earths*, edited by K. A. Gschneidner, Jr. and L. Eyring (North-Holland, Amsterdam, 1978), p. 107.
[23] I. A. Smirnov and V. I. Tamarchenko, *Electronic Heat Conductivity in Metals and Semiconductors* [in Russian] (Nauka, Leningrad, 1977), 151 pp.
[24] V. S. Oskotskiĭ and I. A. Smirnov, *Defects in Crystals and the Heat Conductivity* [in Russian] (Nauka, Leningrad, 1972), 160 pp.

Translated by G. Skrebtsov

Magnetic susceptibility and magnetic-field penetration-depth anisotropy in high-temperature oxide superconductors

Yu. M. Gufan,*) I. G. Levchenko, and E. G. Rudashevskiĭ

North Caucasus University Science Center, 344104 Rostov-on-Don, Russia
(Submitted November 3, 1998)
Fiz. Tverd. Tela (St. Petersburg) **41**, 1552–1555 (September 1999)

A phenomenological theory of the magnetic-field penetration-depth ($\lambda_{i\alpha}$) anisotropy in high-temperature superconductors is constructed taking account of the magnetic susceptibility (χ_{ik}) anisotropy of the surface layer. The factor of 1.9 change in the anisotropy λ_c/λ_{ab} with 4% substitution of Co for Cu ions in $YBa_2Cu_3O_7$ is virtually completely due to the increase in the magnetic susceptibility anisotropy. For Cu–Zn substitutions the change in λ_c/λ_{ab} is characterized primarily by a change in the anisotropy of the tensor of the reciprocal effective masses of the charge carriers (pairs). © *1999 American Institute of Physics.* [S1063-7834(99)00609-7]

Magnetic-field penetration-depth anisotropy in high-temperature superconductors is a suitable tool for solving one of the main problems in oxide superconductor physics — the determination of the symmetry and structure of the condensate wave function. Data on the temperature dependence of the penetration depth in superconductors such as $YBa_2Cu_3O_{7-y}$,[1–6] $Tl_2Ba_2CaCu_2O_{8-y}$,[5] $Hg_2Ba_2Cu_3O_{7-y}$,[7] $Bi_2Si_2CaCu_2O_{8+y}$,[8] and $Nd_{1.85}Ce_{0.15}CuO_4$[3,9] and substitutional solid solutions based on them[10,11] are quantitatively different but qualitatively similar. For example, in $YBa_2Cu_3O_7$, which for $0.07<y<0.65$ possesses orthorhombic symmetry,[12] the dependence is linear, which corresponds to the existence of zeros in the excitation spectrum of the Cooper condensate, at low temperatures $T^*\leqslant T_c$ ($T^*/T_c \sim 0.4$,[2,4] $T^*/T_c \sim 0.5$[5]) and strongly nonlinear in the range $T^*<T<T_c$. According to theoretical models a nonlinear dependence is characteristic for ''ordinary'' *S*-type superconductivity in the Landau–Ginzburg approximation or the Casimir–Görter two-fluid model. Similar behavior but with a different transition point between two states of the condensate (with and without zeros in the single-particle excitation spectrum) is also observed in the tetragonal compounds $Tl_2Ba_2CaCu_2O_{8-y}$,[5] $Hg_2Ba_2Cu_3O_{7-y}$,[7] and $Bi_2Sr_2CaCu_2O_{8+y}$. At the same time the dependence in $Nd_{1.85}Ce_{0.15}CuO_4$ corresponds to *S*-wave pairing in the entire temperature range.

An anomalously large (compared with crystal-chemical[16,17]) magnetic-field penetration-depth anisotropy $[\lambda_a/\lambda_b]\geqslant 2$ has been found recently in $YBa_2Cu_3O_{7-y}$ in a plane perpendicular to the Ba–Y–Ba chains.[13–15] This can give additional information about the nature of the superconducting state.

However, the penetration depth in superconductors is, by definition[17,18] and according to the methods for measuring it,[1–11,13–15] an average characteristic of the crystal, assuming definite approximations of the theory for interpreting the experiment. One approximation of the experiment used in all descriptions known to us is that the magnetic susceptibility anisotropy in the surface layer is neglected in the theory. In ordinary (nontransition) metals the magnetic susceptibility is extremely low ($\chi\sim 10^{-5}$) and such an approximation is completely justified. However, as the calculations presented below show, when average characteristics are measured, specifically, the penetration depth in HTSCs in weak fields ($H<H_{c1}$, $H\sim 20-30$ mT), the anisotropy of χ_{ik} can alter substantially to the interpretation of the experimental data.

The fundamental need to take account of the anisotropy of the magnetic-susceptibility tensor $\chi_{ik}=(1-\mu_{ik})/4\pi$, determining the magnetic moment in the surface layer of a semiconductor, is obvious from the following symmetry considerations. For crystals belonging to the orthorhombic and higher-symmetry systems, cut parallel to the basal planes of the unit cell, and for fields oriented along the crystallographic axes, the penetration-depth tensor $\lambda_{i\alpha}$ can be assumed to depend on two indices: the polarization α of the field and the damping direction i. It is obvious that the matrix $\lambda_{i\alpha}$ should not be symmetric with respect to the indices, and for a tetragonal crystal it should be characterized by three components:

$$\lambda_1=\lambda_{c\alpha}=\lambda_{c\beta}, \quad \lambda_2=\lambda_{a\gamma}=\lambda_{b\gamma}, \quad \lambda_3=\lambda_{a\beta}=\lambda_{b\alpha}, \tag{1}$$

where α, β, and γ denote the direction of polarization of the fields along the a, b, and c axes. For an orthorhombic crystal there are six independent components $\lambda_{i\alpha}$. At the same time there are only two phenomenological parameters for tetragonal crystals and three parameters for orthorhombic crystals to describe this anisotropy on the basis of theories neglecting the anisotropy of χ_{ik} (and, correspondingly, of the magnetic permeability tensor μ_{ik}). These parameters are components of the tensor of the reciprocals of the effective masses of the charge carriers (pairs) $k_{ij}=(m_{ef}^{-1})_{ij}$: for tetragonal classes $k_1=k_2=1/m_{aa}=1/m_{bb}$ and $k_3=1/m_{cc}$ and for orthorhombic classes $k_1\neq k_2\neq k_3$.

For an orthorhombic crystal the Landau–Ginzburg potential in the case of a single complex order parameter has the form

$$F = F_0 + \int dV[\mathbf{BH}/8\pi + k_i|D_i\Psi|^2 + a|\Psi|^2 + b|\Psi|^4]$$
$$= F_0 + \int dV[\mu_i^{-1} e_{ik1}\nabla_k A_1 e_{jmn}\nabla_m A_n \delta_{ij}/8\pi + k_i|D_i\Psi|^2 + a|\Psi|^2 + b|\Psi|^4], \quad (2)$$

where $|\Psi|^2$ is the density of superconducting carriers and $D_i = \nabla_i - 4\pi ie/hcA_i$.

Maxwell's equations for superconductors[19–21] are

$$\mathbf{B} = \mathbf{H} + 4\pi\mathbf{M}, \quad \mathbf{B} = \operatorname{curl}\mathbf{A},$$
$$c\operatorname{curl}\mathbf{M} = 4\pi\mathbf{j}^s, \quad c\operatorname{curl}\mathbf{H} = 4\pi\mathbf{j}^e, \quad (3)$$

where $\mathbf{j}^e$ is the current due to external field sources and $\mathbf{j}^s$ is the superconducting current. In accordance with Eqs. (1) and (2), the magnetic moment is determined by the superconducting current $\mathbf{j}^s$ according to the system of equations

$$j_p^s = \delta(F - BH/4\pi)/\delta A_p = 32\pi^2 e^2|\Psi|^2(m^{-1})_{pq}A_q/h^2c, \quad (4)$$

where $A_q = A_q - c/2e\partial\Omega/\partial x_q$ is the gauge-invariant vector-potential of the field and Ω determines the phase of the wave function.

Varying the total nonequilibrium thermodynamic potential with respect to the vector potential gives three equations which make it possible to calculate the damping of the fields. The first equation is

$$\partial\mu_y^{-1}/\partial z(\partial A_x/\partial z - \partial A_z/\partial x) + \partial\mu_z^{-1}/\partial y(\partial A_x/\partial y - \partial A_y/\partial x) + \mu_y^{-1}\partial^2 A_x/\partial z^2 + \mu_z^{-1}\partial^2 A_x/\partial y^2 = 4\pi j_x^s, \quad (5)$$

and the two others are obtained from Eq. (5) by permuting the coordinate axes $x \to y \to z \to x$. Assuming that

$$\partial\mu_y^{-1}/\partial z(\partial A_x/\partial z - \partial A_z/\partial x) + \partial\mu_z^{-1}/\partial y(\partial A_x/\partial y - \partial A_y/\partial x) = 0, \quad (6)$$

we obtain in the London approximation that the tensor characterizing the penetration depth of the field along the distinguished crystallographic axes is determined by six independent components

$$\lambda_{i\alpha} = 32\pi e^2 4\pi^2|\Psi|^2/h^2c^2\mu_{\alpha\alpha}^{-1}m_{ii}. \quad (7)$$

The diagonal components of $\lambda_{i\alpha}$ are zero. A tetragonal crystal ($\mu_{\alpha\alpha} = \mu_{\beta\beta}$, $m_{aa} = m_{bb}$) is characterized by three independent components.

Let us assume that the wave function of the condensate is determined by a superposition of two waves which form a basis for different irreducible representations of D_{4h}. In such a model of the states of a condensate the number of parameters in the theory that determine the anisotropy of $\lambda_{i\alpha}$ formally increases by 2, since the nonuniform part of the Landau potential (for example, in the case of the superposition of $s(z^2 - x^2 - y^2)$ and $d(x^2 - y^2)$ waves) has the form

TABLE I. Measurement of the anisotropy for superconductors (according to the data from Refs. 10 and 11).

Material	λ_c/λ_{ab} (Ref. 10)	λ_c/λ_{ab} (Ref. 11)	μ_c/μ_{ab} (Ref. 10)
$YBa_2Cu_3O_7$	6.62	6.6	1.56
$YBa_2(Cu_{0.95}Zn_{0.05})_3O_7$	4.17	4.4	2.42
$YBa_2(Cu_{0.96}Co_{0.04})_3O_7$	9.13		2.91

$$f_n = k_1(|\nabla_x\eta_s|^2 + |\nabla_y\eta_s|^2) + k_2(|\nabla_x\eta_d|^2 + |\nabla_y\eta_d|^2) + k_3(|\nabla_z\eta_s|^2) + k_4(|\nabla_z\eta_d|^2) + k_5(\nabla_x\eta_s\nabla_x\eta_d^* - \nabla_y\eta_s^*\nabla_y\eta_d + \text{c.c.}). \quad (8)$$

Here η_s and η_d are order parameters in the phenomenological theory that transform according to the irreducible representations A_{1g} and B_{2g} of the group D_{4h}. In Ref. 22 it was established that only three thermodynamically stable states of the condensate which are determined by a superposition of the $s(z^2 - x^2 - y^2)$ and $d(x^2 - y^2)$ waves are possible. This is a superposition with the most general form $\Psi_1 = as(z^2 - x^2 - y^2) + bd(x^2 - y^2)$, where a and b are complex numbers, and two superpositions for particular cases $\Psi_2 = s(z^2 - x^2 - y^2) + id(x^2 - y^2)$ and $\Psi_3 = s(z^2 - x^2 - y^2) + \alpha d(x^2 - y^2)$ (α is real) corresponding to phases of higher symmetry. However, the arguments for the need to take account of the anisotropy of μ_{ik} remain in force even in this case. Indeed, direct calculations show that, if this anisotropy is neglected, the constants $k_1 - k_5$ are grouped in a manner so that the theory predicts two independent components of the tensor $\lambda_{i\alpha}$ in the phase $\Psi_2 = s(z^2 - x^2 - y^2) + id(x^2 - y^2)$, which are related as

$$\lambda_{zx} = \lambda_{xz} = \lambda_{yz} = \lambda_{zy}, \quad \lambda_{xy} = \lambda_{yx}. \quad (9)$$

In the condensate states $\Psi_1 = as(z^2 - x^2 - y^2) + bd(x^2 - y^2)$ and $\Psi_3 = s(z^2 - x^2 - y^2) + \alpha d(x^2 - y^2)$ there arise three independent components $\lambda_{i\alpha}$, but the relations between them

$$\lambda_{yz} = \lambda_{zy}, \quad \lambda_{xy} = \lambda_{yx}, \quad \lambda_{xz} = \lambda_{zx} \quad (10)$$

are different from those required by the symmetry (1).

Let us examine the experiments on the anisotropy of the penetration depth of a field in $YBa_2Cu_3O_7$ from the standpoint of the results obtained. The variance of the data among different works is quite large, due less to the quality of the samples than the measurement procedure. We confined our attention to the results of Refs. 10 and 11, which agree with the data of Refs. 23–26 and pertain to weak fields ($H < H_{c1}$), for which the calculations presented above are valid. The effect of Co and Zn substitutions in $YBa_2(Cu_{1-x}M_x)O_{7-y}$ on the superconducting characteristics, specifically, $\lambda_{i\alpha}$ and χ_{ik}, was studied in Refs. 10 and 11. The values obtained for λ_c/λ_{ab} in Refs. 10 and 11 and the magnetic permeability anisotropy which we computed from the plots presented in Ref. 10 along the corresponding directions of the field at $T = 0$ are presented in Table I.

Using the relations presented above we derived from these data that substitution of Co and Zn for copper affects the change in the masses of the charge carriers (pairs) differently in these solid solutions. The values of the ratio of the

TABLE II. Computed ratios of the anisotropy parameters for two superconducting materials.

Material 1/Material 2	$[\lambda_c/\lambda_{ab}]/[\lambda_c/\lambda_{ab}]$	$[\mu_c/\mu_{ab}]/[\mu_c/\mu_{ab}]$	$[\gamma/\gamma]$
$YBa_2(Cu_{0.95}Co_{0.05})_3O_7$	0.39 (Ref. 10)	1.55	0.5
$YBa_2Cu_3O_7$	0.43 (Ref. 11)	1.55	0.52
$YBa_2(Cu_{0.96}Co_{0.04})_3O_7$	1.9 (Ref. 10)	1.86	1.02
$YBa_2Cu_3O_7$	1.9 (Ref. 10)	1.86	1.02

effective masses of pairs, the magnetic-field penetration-depth anisotropy, and the magnetic-permeability anisotropy are presented in Table II.

It is evident from Table II that the change in the anisotropy λ_c/λ_{ab} of pure $YBa_2Cu_3O_7$ with respect to $YBa_2Cu_3O_7$ with 4% substitution of Co is explained essentially completely by the change in the magnetic permeability ratio. Conversely, the change in the anisotropy λ_c/λ_{ab} with 5% substitution of Zn for Cu ions corresponds mainly to a change in the anisotropy of the effective mass tensor $\gamma=[m_c/m_{ab}]^{1/2}$ in these compounds. In accordance with the data presented above, the values of γ are

$$\gamma(YBa_2Cu_3O_7)\approx 5.3,$$

$$\gamma(YBa_2(Cu_{0.95}Zn_{0.05})_3O_7)\approx 2.7,$$

$$\gamma(YBa_2(Cu_{0.96}Co_{0.04})_3O_7)\approx 5.35. \quad (11)$$

We note that for 5% substitution of zinc for copper ions and for pure $YBa_2Cu_3O_7$ the values of χ_{ab} are known,[10] and therefore the ratio

$$\gamma=[m_{ab}(YBa_2(Cu_{0.95}Zn_{0.05})_3O_7)/m_{ab}(YBa_2Cu_3O_7)]^{1/2} \approx 1.897.$$

can be determined from the relations presented above.

This ratio correlates with the superconducting transition temperatures

$$T_c(YBa_2Cu_3O_7)/T_c(YBa_2(Cu_{0.95}Zn_{0.05})_3O_7)\approx 1.897.$$

The agreement between these values does not correspond to either the predictions of the theory relating the HTSC state with the existence of polarons or with the prediction of the BCS theory.

The problem with the theory is as follows. As long as the pairing mechanism is unknown, the anisotropy of the masses of the charge carriers in the basal plane of orthorhombic crystals must be assumed to be proportional to the orthorhombic distortion $e_0=2(a-b)/(a+b)$, which in $YBa_2Cu_3O_7$ is 0.009[17,18] or 0.008.[16] Then $\lambda_{a\gamma}/\lambda_{b\gamma}=(m_{aa}/\mu_{\gamma\gamma})/(m_{bb}/\mu_{\gamma\gamma})=m_{aa}/m_{bb}\approx 1$. In real crystals $[\lambda_a/\lambda_b]\geqslant 2$ and therefore one of the assumptions used in the phenomenological approach developed above must be rejected — the assumption that the order parameter in the sense of the Landau theory is a single-component parameter, i.e., the assumption of a strong crystal field determining the state of the Cooper D condensate. We underscore that this assertion agrees with the results of measuring fluctuations near T_c[26] and a host of other experimental data.

We thank the Russian Fund for Fundamental Research for financial support.

*)E-mail: gufan@gufan.rnd.runnet.ru

[1] D. A. Bonn, R. Liang, T. M. Riseman, D. G. Baar, D. C. Morgan, K. Shang, P. Dosanjh, T. L. Duty, A. MacFarlane, G. D. Morris, J. H. Brewer, W. H. Hardy, C. Kallin, and A. J. Berlinsky, Phys. Rev. B **47**, 134 (1993).
[2] W. N. Hardy, D. A. Bonn, D. C. Morgan, R. Liang, and K. Shang, Phys. Rev. Lett. **70**, 3999 (1993).
[3] D. E. Oates, P. P. Nguyen, G. Dresselhaus, M. S. Dresselhaus, G. Koren, and E. Polturak, J. Supercond. **8**, 725 (1995).
[4] D. H. Wu, J. Mao, and S. M. Anlage, J. Supercond. **8**, 745 (1995).
[5] A. A. Zhukov, M. R. Trunin, A. T. Sokolov, and N. N. Kolesnikov, Zh. Éksp. Teor. Fiz. **112**, 2210 (1997) [JETP **85**, 1211 (1997)].
[6] A. Fuchs, W. Prusseit, P. Berberich, and H. Kinder, Phys. Rev. B **53**, R14745 (1996).
[7] Y. Y. Xue, Q. Xiong, Y. Cao, and C. W. Chu, J. Supercond. **8**, 465 (1995).
[8] A. Maeda, Y. Iino, T. Hanaguri, N. Motohira, K. Kishio, and T. Fukase, Phys. Rev. Lett. **74**, 1202 (1995).
[9] D. H. Wu, J. Mao, S. N. Mao, J. L. Peng, X. X. Xi, T. Venkatesan, and R. L. Greene, Phys. Rev. Lett. **70**, 85 (1993).
[10] D. N. Sheng, A. M. Campbell, J. D. Johson, J. R. Cooper, F. J. Blunt, A. Porch, and P. A. Freeman, Phys. Rev. B **49**, 1417 (1994).
[11] C. Panagopoulos, J. R. Cooper, and N. Athanassopoulou, Phys. Rev. B **54**, R12721 (1996).
[12] H. Shaked, P. M. Keane, and J. C. Rodriguez, *Crystal Structures of High-T_c Superconducting Cooper Oxides* (Argonne, Illinois, USA, 1994).
[13] A. G. Sun, S. N. Han, A. S. Katz, D. A. Gajewski, M. B. Maple, and R. G. Dynes, Phys. Rev. B **52**, R15731 (1995).
[14] D. N. Basov, R. Liang, D. A. Bonn, W. N. Hardly, B. Dabrowski, M. Quijada, D. B. Tanner, J. P. Rice, D. M. Ginsberg, and T. Timusk, Phys. Rev. Lett. **74**, 508 (1995).
[15] J. L. Tallon, C. Bernhard, U. Binninger, A. Hofer, G. V. M. Williams, E. J. Ansaldo, J. I. Budnick, and C. Niedermayer, Phys. Rev. Lett. **74**, 1008 (1995).
[16] P. M. Horn, D. N. Kean, G. A. Held, J. L. Jordan-Sweet, D. L. Kaiser, F. Holdsberg, and T. M. Rice, Phys. Rev. Lett. **59**, 2772 (1987).
[17] J. Ye and K. Nakamura, Phys. Rev. B **43**, 7554 (1993).
[18] K. Nakamura, J. Ye, and A. Ishii, Physica C *1–13* (1993).
[19] E. M. Lifshitz and L. P. Pitaevskiĭ, *Statistical Physics* [in Russian] (Nauka, Moscow, 1978), Part 2.
[20] L. D. Landau and E. M. Lifshitz, *Electrodynamics of Continuous Media* (Pergamon Press, New York; Russian original, State Technical and Theoretical Literature Press, Moscow, 1957).
[21] D. Shoenberg, *Superconductivity*, 2nd edition (Cambridge University Press, New York, 1952; Inostr. Lit. Press, Moscow, 1955).
[22] A. Ya. Aĭzenberg and Yu. M. Gufan, Fiz. Tverd. Tela (St. Petersburg) **36**, 1636 (1994) [Phys. Solid State **36**, 894 (1994)].
[23] S. M. Anlage, H. Sze, H. J. Snortland, S. Tahara, B. Langley, C. B. Eom, M. R. Beasley, and R. Taber, Appl. Phys. Lett. **54**, 2710 (1998).
[24] S. Mitra, J. H. Cho, W. C. Lee, D. C. Johnsnon, and V. K. Kogan, Phys. Rev. B **40**, 267 (1989).
[25] D. R. Harshan, L. F. Schneemeyr, J. V. Waszcrak, G. Appli, R. G. Cava, B. Batligg, L. W. Rupp, E. J. Ansaldo, and D. L. Williams, Phys. Rev. B **39**, 851 (1989).
[26] S. E. Inderhees, M. S. Salomon, N. Goldengeld, J. P. Rice, B. G. Pazol, and D. M. Ginsberg, Phys. Rev. Lett. **60**(12), 1178 (1988).

Translated by M. E. Alferieff

SEMICONDUCTORS. DIELECTRICS

Acceptor states in cubic semiconductors having a large hole-mass ratio

T. L. Linnik*) and V. I. Sheka†)

Institute of Semiconductor Physics, Ukrainian Academy of Sciences, 252650 Kiev, Ukraine
(Submitted October 30, 1998)
Fiz. Tverd. Tela (St. Petersburg) **41**, 1556–1563 (September 1999)

In cubic semiconductors the hole-mass ratio is small, which makes it possible to use the zero light-hole-mass limit. It was found that variational methods in this popular limit are not necessary to solve the Luttinger equation and not only the entire energy spectrum for the bound states of an acceptor and the eigenfunctions, including in momentum space, but also the behavior of the eigenfunctions at large radii can be determined to a high degree of accuracy. This approach made it possible to suggest comparatively simple relations for the lowest states of each series having different angular momenta, covering the entire range of possible mass ratios for semiconductors. © *1999 American Institute of Physics.* [S1063-7834(99)00709-1]

The first calculations of the energy levels of an acceptor were performed at the beginning of the 1960s. They are directly linked to Luttinger and Kohn, whose successful formulation of the effective-mass method made these works possible,[1–4] though the problem was first formulated in Ref. 5. The next step was taken several years later — Kane's model[6] was used to take account of the finite band gap.[7,8] These works all depend on variational calculations. Evidently, the best known are Refs. 9 and 10, where a somewhat less simplified, compared with Ref. 8, approximation (Luttinger two-band model[2] in the spherical approximation[9] including cubic corrections[10,11]) was used to calculate in detail the acceptor levels using the parameters of real crystals. Interest in this problem has reappeared recently in connection with the desire to calculate the asymptotic behavior of the wave function in real and in momentum space, which is important, for example, for hopping conduction and for hot luminescence. From this standpoint variational methods could be ineffective, since the trial wave function, while generating very accurate values of the energy levels, can describe the asymptotic behavior of the real function much too roughly. An example where variational calculations are not used are Refs. 4 and 12, where the radial Luttinger equations were solved by a series expansion in powers of the radius. In semiconductors with a large ratio of the light and heavy hole masses (m_l and m_h), the acceptor energy is determined essentially only by the mass m_h[8,13–17] and, therefore, the limit $m_l=0$ is admissable in them. This limit merits attention because it admits a nonvariational solution of the problem. A comparison of the calculations has confirmed, specifically, that the variational calculations performed in Ref. 8 are quite reliable. In our opinion this should also be true of Ref. 9.

In the present work we were able to construct using a spherical approximation an expansion in terms of the mass ratio in Luttinger-type radial equations. For infinite hole-mass ratio the new result, as compared to Refs. 13–17, is a calculation not only of the ground state but also the excited states for different angular momenta and for high levels in the same series. The problem was complicated by the fact that the radial functions behave differently at infinity, specifically, one function decays not exponentially but rather as a power of the radius. The behavior of the functions at infinity reflects this specific feature even for an arbitrary mass ratio.

1. VARIATIONAL FUNCTIONAL AND THE EQUATION FOR AN ACCEPTOR

Even though our objective in this work is to examine the limiting cases of the equations for the acceptor states, it is convenient to start with the most general multiband formulation — Kane's scheme.[6] In the spherical approximation, the variables in the corresponding equations were separated in Ref. 8. The wave function with total angular momentum j can be represented as

$$\Psi^{jm}(\mathbf{r})=U_e^{jm}G_e(r)+U_1^{jm}G_1(r)+U_{-1}^{jm}G_{-1}(r)+U_s^{jm}G_s(r). \tag{1}$$

In contrast to Ref. 8, here the radial functions are determined so that matrix elements based on these functions are calculated with a weight of 1.

The spherical four-component valence-band functions ($\nu=1,-1$)

$$U_\nu^{jm}(\mathbf{r}/r)=\sum_\mu \left(\frac{3}{2},l+\nu,\mu,m-\mu\middle|j,m\right)Y_{l+\nu,m-\mu}e_\mu \tag{2}$$

can be expressed, by means of the Clebsch–Gordon coefficients,[18] in terms of the spinors e_μ and the ordinary one-dimensional spherical harmonics Y_{lm} with angular momentum l. Following Ref. 8, the total angular momentum of the system is determined from the angular momentum of the electronic component of the wave function as $j=l+\sigma/2$ ($\sigma=\pm1$).

Since we are interested mainly in the acceptor states, we employed a variational functional[8] written in the hole representation: The hole masses are positive and the valence-band branches are directed upwards, energy is measured from the valence-band bottom, and for bound states the energy is negative. At this stage the most general Kane model made it possible to combine the two limiting cases for the spin-split-off parameter $\Delta=\infty$ and $\Delta=0$. Here it is convenient to introduce the notation

$$\gamma_\sigma=\begin{cases}\sqrt{(L+2)/(2L+1)}, & \Delta=\infty\\ \sqrt{3(L+2)/(2L+1)}, & \Delta=0\end{cases}$$

$$\gamma_{-\sigma}=\sqrt{3L/(2L+1)},$$

where $L=l$ for $\sigma=1$ and $L=-l-1$ for $\sigma=-1$.

At the stage of the transition to a Luttinger-type two-band model for the hole bands we exclude the electronic component G_e of the wave function. We note that for such a transition the band gap E_g is assumed to be large compared with the characteristic acceptor energies. Varying the Kane model functional with respect to G_e and taking account of the preceding remark we obtain

$$\frac{\sqrt{3}E_g}{P}G_e=\gamma_1\left(\frac{d}{dr}+\frac{l+1}{r}\right)G_1+\gamma_{-1}\left(\frac{d}{dr}-\frac{l}{r}\right)G_{-1}. \quad (3)$$

As a result, after substituting for G_e the functional depends only on the hole functions and assumes the form

$$J_h=-\int_0^\infty\left\{\sum_{\nu=1,-1}G_\nu\left(\frac{\hbar^2}{2m_h}\alpha_\nu\Delta_{l+\nu}+\frac{Ze^2}{r}+E\right)G_\nu+\frac{\hbar^2}{m_h}\alpha_0G_1\left(\frac{d}{dr}-\frac{l+1}{r}\right)\left(\frac{d}{dr}-\frac{l}{r}\right)G_{-1}\right\}dr. \quad (4)$$

Here

$$\frac{P^2}{3E_g}=\frac{\hbar^2}{4m_h}\frac{1-\beta}{\beta},\quad \beta=\frac{m_l}{m_h},\quad \Delta_l=\frac{d^2}{dr^2}-\frac{l(l+1)}{r^2}.$$

$$\alpha_{\pm1}=1+\frac{1}{2}\left(\frac{1}{\beta}-1\right)\gamma_{\pm1}^2,$$

$$\alpha_0=\frac{1}{2}\left(\frac{1}{\beta}-1\right)\gamma_{-1}\gamma_1, \quad (5)$$

and for shallow acceptors Z is the reciprocal of the permittivity. Finally, varying with respect to G_1 and G_{-1} we obtain a system of Luttinger-type equations for an acceptor in the spherical approximation that combines the two limiting cases $\Delta=\infty$ and 0,

$$\begin{cases}-\left(\frac{\hbar^2}{2m_h}\alpha_1\Delta_{l+1}+\frac{Ze^2}{r}+E\right)G_1-\frac{\hbar^2}{2m_h}\alpha_0\left(\frac{d}{dr}-\frac{l+1}{r}\right)\left(\frac{d}{dr}-\frac{l}{r}\right)G_{-1}=0,\\ -\frac{\hbar^2}{2m_h}\alpha_0\left(\frac{d}{dr}+\frac{l}{r}\right)\left(\frac{d}{dr}+\frac{l+1}{r}\right)G_1-\left(\frac{\hbar^2}{2m_h}\alpha_{-1}\Delta_{l-1}+\frac{Ze^2}{r}+E\right)G_{-1}=0.\end{cases} \quad (6)$$

For arbitrary L this system was examined in Ref. 3 and can be obtained from the Luttinger Hamiltonian[2] for the case $\Delta=\infty$

$$H_L=\frac{\hbar^2}{4}\left(\frac{1}{m_l}+\frac{1}{m_h}\right)\hat{\mathbf{k}}^2\mathbf{I}-\frac{\hbar^2}{4}\left(\frac{1}{m_l}-\frac{1}{m_h}\right)\times\left[(\mathbf{J}\cdot\hat{\mathbf{k}})^2-\frac{5}{4}\mathbf{k}^2\mathbf{I}\right]-\frac{Ze^2}{r}, \quad (7)$$

where $\mathbf{J}$ is the matrix of 3/2 angular momentum,[2] $\hat{\mathbf{k}}$ is the quasimomentum operator, and $\mathbf{I}$ is a 4×4 unit matrix.

For $\Delta=0$, so that the spin-orbit interaction does not appear in the Hamiltonian, the two variants for L are identical, and $j=l$. The spinors e_μ in the spherical functions (2) become three-dimensional column vectors corresponding to angular momentum 1, and the substitution $3/2\rightarrow1$ must be made in Eq. (2). The corresponding Luttinger Hamiltonian becomes a 3×3 matrix.[2]

A further simplification is possible in semiconductors having a small ratio of the light- and heavy-hole effective masses. As one can see from Kane's equations,[8] for large E_g the electronic part G_e of the radial function is small, and if an attempt is made to exclude it completely from the variational function, then the dependence on the parameter P, i.e., on the light hole, vanishes at the same time. This was first pointed out in Ref. 8 for $\Delta=0$. An acceptor was studied in the same approximation in Ref. 17, and the case $\Delta=\infty$ was studied in Refs. 13–17.

The light-hole effective mass enters in the Luttinger equations as a large quantity, and it can disappear from the functional (4) if Eq. (3) holds with $G_e=0$ (in what follows, when citing the relation (3) we assume that this condition is satisfied). This ratio makes it possible to eliminate one of the functions from the functional J_g, and since an additional relation has been established between the functions, the energy values will be too high. The equation (3) does not impose any restrictions on E_g and m_l, but it does lead naturally to more accurate results as m_l decreases. The corresponding Hamiltonians for the Schrödinger equations for the functions G_ν assume the form

$$H_\nu=-\frac{\hbar^2}{2m_h}\Delta_{l+\nu}-Ze^2\left[\frac{1}{r}+\delta(\nu)D\times\left(-l+\frac{1+\nu}{2}\right)\frac{1}{r^3}D\left(l-\frac{1+\nu}{2}\right)\right]. \quad (8)$$

Here the coefficient $\delta(\nu)=-\nu\gamma_\nu^2(2l+1)/(\gamma_1^2+\gamma_{-1}^2)$ and the inverse operator

$$D(\alpha)=\left(\frac{d}{dr}+\frac{\alpha}{r}\right)^{-1} \tag{9}$$

has been introduced (see Appendix). For the ground state ($j=3/2$, $l=1$) and $\Delta=\infty$ the Schrödinger equation corresponding to the Hamiltonian H_{-1} is identical to the corresponding equation of Ref. 15, written in momentum space.

Although Eq. (8) does not contain the band gap E_g and restrictions on its value can be avoided in the derivation, it was assumed that the problem itself requires a band gap wider than the ionization energy of the acceptor so that the spectrum of the acceptor could be positioned in the band gap (however, resonance levels in gapless semiconductors can also be studied[14]).

2. NONVARIATIONAL SOLUTION OF THE EQUATION FOR AN ACCEPTOR WITH $m_l=0$

As the calculations performed in Sec. 4 show, this limiting case does not give a sufficiently accurate description of real semiconductors. However, it is interesting in that it makes it possible to obtain a nonvariational solution of Eqs. (6) and, therefore, to establish the reliability of approximate variational calculations.

The relation (3) with $G_e=0$ makes it possible to establish a relation between the functions in the form

$$G_1(\gamma)=-\frac{\gamma_{-1}}{\gamma_1}\frac{1}{r^{l+1}}\int_0^r x^{l+1}\left(\frac{d}{dx}-\frac{l}{x}\right)G_{-1}(x)dx, \tag{10}$$

$$G_{-1}(\gamma)=-\frac{\gamma_1}{\gamma_{-1}}r^l\int_\infty^r x^{-l}\left(\frac{d}{dx}+\frac{l+1}{x}\right)G_1(x)dx. \tag{11}$$

For the ground state the relation (3) and Eq. (10) for functions of a different kind were used in Ref. 16. It is evident from these relations that G_1, in contrast to G_{-1}, drops off at infinity according to a power law and, therefore, a search for the solution for G_1 in the form of an expansion in terms of hydrogen-like functions (which most closely corresponds to the spirit of the problem) should be ineffective, while success should be expected if attention is focused on the function G_{-1}.

Writing the Schrödinger equation $(H_{-1}-E)G_{-1}=0$, it is convenient, as always, to switch to dimensionless units, measuring r in terms of the Bohr radius for a heavy hole $a_B=\hbar^2/m_hZe^2$ and energy in Rydbergs $R_y=(Ze^2)^2m_h/2\hbar^2$. Eliminating the reciprocal operators the equation for G_{-1} becomes

$$\left\{\left(\frac{d}{dr}+\frac{l+3}{r}\right)\left(\frac{d}{dr}-\frac{l}{r}\right)\left[\Delta_{l-1}+\frac{2}{r}+E\right]+\delta(-1)\frac{2}{r^3}\right\}G_{-1}(r)=0. \tag{12}$$

A solution was found in the form of the series

$$G_{-1}(r)=\frac{\gamma_1}{N_0}\sqrt{2\lambda}(2\lambda r)^l e^{-\lambda r}\sum_{n=0}^{N}A_nL_n^{2l-1}(2\lambda r),$$

$$N_0^2=2(\gamma_1^2+\gamma_{-1}^2)\sum_n A_n^2(n+l)\frac{(n+2l-1)!}{n!},\quad N\to\infty, \tag{13}$$

Here $L_n^\alpha(x)$ are generalized Laguerre polynomials.[19] It is evident from the relation (3) that the normalizations of the functions G_ν differ only by the factor γ_1/γ_{-1}, and the coefficient in the definition of G_{-1} is chosen so that the complete wave function (1) is normalized to 1 (in the Luttinger approximation $G_e=G_s=0$).

It follows from the behavior at infinity for a discrete spectrum that $E=-\lambda^2$, and the equation for the coefficients becomes

$$a_nA_{n-2}+b_nA_n+A_{n+2}=0, \tag{14}$$

where

$$a_n=n(n-1)[1-\lambda(n+l-2)]/d_n,$$

$$b_n=\{4\delta(-1)-2[1-\lambda(n+l)](n^2+2nl+2l^2+5l+2)\}/d_n,$$

$$d_n=(n+2l)(n+2l+1)[1-\lambda(n+l+2)]. \tag{15}$$

We call attention to the fact that the equation for A_n contains only even or odd n, which leads to two different sets of levels. The relation (14) can be written in the form

$$\frac{A_n}{A_{n-2}}=\frac{-a_n}{b_n+\dfrac{A_{n+2}}{A_n}} \tag{16}$$

and developed, for example, for even n, into a continued fraction

$$\frac{A_2}{A_0}=-b_0=-\cfrac{a_2}{b_2-\cfrac{a_4}{b_4-\ldots}}. \tag{17}$$

This is now an equation for λ and, therefore, for the energy. This is essentially the condition for the determinant of the system (14) to be zero and hence for the system to be solvable. For odd n, the n in Eq. (16) must be increased by 1.

The determined solution and normalization N_0 converge only at the roots of Eq. (17). It can also be shown that the second solution of Eq. (12) is also regular at the origin and that at infinity it does not satisfy the initial equation (8) (it starts with r^{l+2}).

Starting from relation (10), it was found that it is convenient to represent the function $G_1(r)$ in the form

TABLE I. The energies of the ground and several excited states of an acceptor in the limit of zero effective-mass ratio.

l	$\Delta=\infty,\ j=l+1/2$			$\Delta=0,\ j=l$		
	$-E_0$	$-E_1$	E_2	$-E_0$	$-E_1$	E_2
$l=1$	0.4360	0.1349	0.0703	0.5976	0.1687	0.0826
$l=2$	0.1213	0.0629	0.0395	0.1589	0.0772	0.0465
$l=3$	0.0610	0.0382	0.0264	0.0760	0.0455	0.0306
	$\Delta=\infty,\ j=l-1/2$					
$l=2$	0.2252	0.1019	0.0582			
$l=3$	0.0986	0.0565	0.0367			

$$G_1(r)=\frac{\gamma_{-1}}{N_0}\sqrt{2\lambda}\Bigg\{(2\lambda r)^{l+2}e^{-\lambda r}\times\sum_{n=\mu,\mu+2,\ldots}^{N-2}B_n L_n^{2l+3}(2\lambda r)+\tilde{\gamma}\,\frac{\lambda}{(2\lambda r)^{l+1}}\int_0^r(2\lambda x)^{2l+1}e^{-\lambda x}L_\mu^{2l+1}(2\lambda x)dx\Bigg\},\quad(18)$$

separating explicitly the singularity at infinity; $\mu=0$ refers to solutions from the set with even n and $\mu=1$ with odd n (a sum of the same type should appear in Eq. (13)).

The coefficients B_n and $\tilde{\gamma}$ are obtained from the recurrence relations

$$B_n=\frac{1}{(n+2l+2)(n+2l+3)}\{(A_n-A_{n+2})+n(n-1)B_{n-2}-\tilde{\gamma}\delta_{n,\mu}\}.\quad(19)$$

The coefficient $\tilde{\gamma}$ is of special interest, since it stands next to a term exhibiting nonstandard behavior at infinity

$$\tilde{\gamma}=\frac{2}{(2l+2)^\mu}\sum_{n=\mu,\mu+2,\ldots}^{N}\frac{(n+2l-1)!}{(2l)!n!}(n+l)A_n.\quad(20)$$

For the ground state ($j=3/2$, $L=1$, $\mu=0$) $\tilde{\gamma}=0.703$.

The computational results for the absolute values of the energy for the first excited states with different values of the total angular momentum j are presented in Table I.

For $\Delta=\infty$, $j=l-1/2$ and $l=1$ the relation (3) becomes meaningless, since γ_1 vanishes, but the system of equations (6) degenerates into two uncoupled hydrogen-like equations with light and heavy hole masses. For $\Delta=0$ there is no dependence on the dropoff and therefore $j=1$.

3. SIMPLE VARIATIONAL METHOD FOR $m_l=0$

Nnumerical calculations showed that for the lowest energy levels of each series in l the coefficient A_0 is the largest coefficient in the expansion (13), so that $G_{-1}(r)$ can be described by a simple variational function of the form

$$G_{-1}(r)=N_{-1}r^l e^{-\tilde{\lambda}r},\quad N_{-1}=\frac{\gamma_1}{N_p}(2\tilde{\lambda})^{l+1/2},$$

$$N_p^2=(\gamma_1^2+\gamma_{-1}^2)(2l)!.\quad(21)$$

Indeed, it turned out that compared with the preceding section the normalizations N_p and N_0 are close, and the parameters λ and therefore the eigenvalues and the eigenfunctions themselves differ very little.

After minimizing with respect to λ the average energy for the Hamiltonian H_{-1} from the relation (8) is

$$E=-\tilde{\lambda}^2,\quad \tilde{\lambda}=\frac{1}{l}+\frac{\delta(-1)}{(l+1)(2l+1)}\left[w-\frac{l+1}{l}\right],$$

$$w=(2l+1)2^{2l+1}\left[\ln 2-\sum_{n=1}^{2l+1}\frac{1}{2^n n}\right].\quad(22)$$

The approximation (21) turned out to be successful (for the ground state it is identical to the approximation in Ref. 15). Indeed, the lowest energy levels in each series with fixed j and l with three signs are identical to those presented in Table I. The ground state ($j=3/2$, $l=1$), where the energy $E=-0.434$ Ry for $\Delta=\infty$, is calculated less accurately.[15] For $\Delta=0$ the value $E=-0.598$ Ry was obtained in Ref. 8.

As we have already mentioned, an important feature of the behavior of the function $G_1(r)$ is that the drop-off at infinity is not exponential but a power-law, and for the simple variational function (21) for the lowest state of each series it is described similarly to the last term in Eq. (18):

$$G_1(r)=\frac{1}{2}\,\frac{\gamma_{-1}}{N_p}\sqrt{2\tilde{\lambda}}\left(\frac{2\tilde{\lambda}}{r}\right)^{l+1}\int_0^r x^{2l+1}\exp(-\tilde{\lambda}x)dx$$

$$\to\frac{1}{2}\,\frac{\gamma_{-1}}{N_p}\sqrt{2\tilde{\lambda}}\left(\frac{2\tilde{\lambda}}{r}\right)^{l+1}(2l+1)!\ \text{as}\ r\to\infty.\quad(23)$$

This estimate of the asymptotic behavior of the wave function differs from the exact solution obtained according to Eq. (18) only by the coefficient $\tilde{\gamma}$, which is close to 1 for the ground state.

For the series with $l=1$ and $j=3/2$, which includes the ground state, a set of four degenerate wave functions repeats the form of the Luttinger Hamiltonian (7)

$$\Psi(\mathbf{r})=\frac{1}{\sqrt{4\pi}}\left\{G_{-1}\mathbf{I}-\left[(\mathbf{J}\cdot\mathbf{r})^2/r^2-\frac{5}{4}\mathbf{I}\right]G_1\right\}\frac{1}{r},\quad(24)$$

and the functions themselves $\Psi^m(\mathbf{r})$ are the corresponding columns of this matrix. The last factor must be taken into account when switching to the standard definition of the wave functions (see the discussion following Eq. (1)). The angular part in front of G_1 contains only d functions and therefore according to Eq. (23) the ground-state wave functions are strongly anisotropic at large distances.

Both components of the ground-state wave function for the variational and exact solutions are presented in Fig. 1. We note that in the figure the calculations performed using the method of Ref. 8 (see Sec. 6) are identical to the exact calculations from the preceding section: A difference arises in the third decimal place at the maximum.

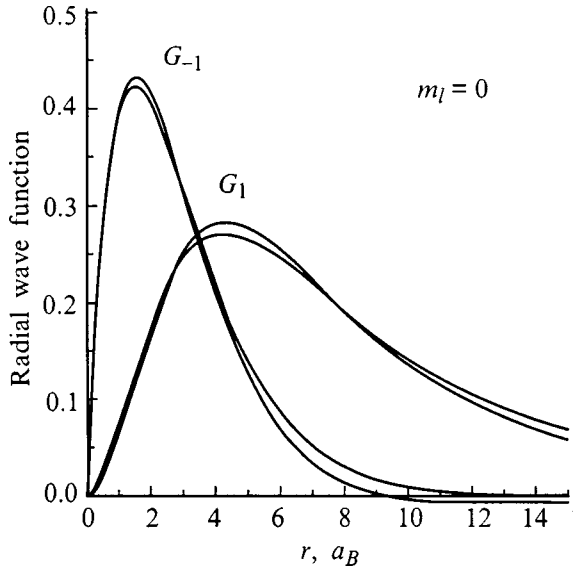

FIG. 1. Radial wave functions for the ground state ($j=3/2$, $l=1$, $\mu=0$) in the limit $m_l=0$. The curves with a larger maximum correspond to the exact solution (Sec. 2), and curves with the smaller maximum correspond to the approximate solution (Sec. 3). The change in sign for the function G_{-1} is admissable, since the theorem on the number of zeros of eigenfunctions is inapplicable to Eq. (12).

4. CORRECTIONS OF ORDER m_l/m_h TO THE ENERGY AND EIGENFUNCTION

Determining from the first equation of the system (6) the function G_1 in dimensionless units

$$G_1=-\frac{\alpha_0}{\alpha_1}\frac{1}{\Delta_{l+1}+\dfrac{2}{\alpha_1 r}+\dfrac{E}{\alpha_1}}\hat{R}(r)\,G_{-1},$$

$$\hat{R}(r)=\left(\frac{d}{dr}+\frac{l+1}{r}\right)\left(\frac{d}{dr}-\frac{l}{r}\right), \tag{25}$$

we transform the variational function J_h (4) to the form

$$J_h'=\int_0^\infty G_{-1}\left\{-\left(\alpha_{-1}\Delta_{l-1}+\frac{2}{r}+E\right)+\frac{\alpha_0^2}{\alpha_1}\hat{R}(r)\right.$$

$$\left.+\frac{1}{\Delta_{l+1}+\dfrac{2}{\alpha_1 r}+\dfrac{E}{\alpha_1}}\hat{R}(r)\right\}G_{-1}dr. \tag{26}$$

In the denominator in Eq. (26) $1/\alpha_1\propto m_l/m_h$, and the average eigenvalue $\Delta_{l+1}\propto\tilde{\lambda}^2$ is large compared with the other terms, so that the denominator can be expanded in powers of $1/\alpha_1$, using the relation

$$\frac{1}{A+B}=\frac{1}{A}-\frac{1}{A}B\frac{1}{A+B}=\frac{1}{A}-\frac{1}{A}B\frac{1}{A}+\frac{1}{A}B\frac{1}{A}B\frac{1}{A}-\ldots \tag{27}$$

where

$$A=\Delta_{l+1},\quad B=\frac{2}{\alpha_1 r}+\frac{E}{\alpha_1}.$$

Then the expansion

$$\hat{R}(r)^+\frac{1}{\Delta_{l+1}+\dfrac{2}{\alpha_1 r}+\dfrac{E}{\alpha_1}}=\Delta_{l-1}-\frac{E}{\alpha_1}-\frac{2}{\alpha_1}I_1+\left(\frac{E}{\alpha_1}\right)^2 I_2$$

$$+\frac{2E}{\alpha_1^2}(I_1I_2+I_2I_1)+\left(\frac{2}{\alpha_1}\right)^2 I_1I_2I_1+\ldots,$$

$$I_1=\frac{1}{r}+\frac{2l+1}{2l+2}\left\{D(-l)\frac{1}{r^2}-\frac{1}{r^2}D(l)\right\},$$

$$I_2=\frac{1}{2l-1}\{D(-l)r-rD(l)\}. \tag{28}$$

will appear in the equation for G_{-1}. The equations from Appendix 1 were used to work with the inverse operators; Eqs. (A.5) make it possible to express products of the type $I_\mu I_{\mu'}$ in terms of the first power of $D(\mu)$. All integrals can be calculated for the variational function (21). As a result, the individual terms in J_h' are proportional to powers of $1/\tilde{\lambda}$, which reflects poorly the behavior of J_h' for small λ. Indeed, as follows from Eq. (26), the functional is bounded in this range of $\tilde{\lambda}$. This is because a power series expansion in powers of $\tilde{\lambda}$ gives a poor description of J_h'. An alternative expansion free of this drawback is a continued fraction, which converges in a wider region than the corresponding series. On this basis

$$J_h'=\left(\alpha_{-1}-\frac{\alpha_0^2}{\alpha_1}\right)\tilde{\lambda}^2-\frac{2\tilde{\lambda}}{l}-\frac{\alpha_0^2}{\alpha_1^2}\frac{C_1}{1-\dfrac{1}{\alpha_1}\dfrac{C_2/C_1}{1+\ldots}}-E, \tag{29}$$

where

$$C_1=E+\frac{2\tilde{\lambda}}{l+1}w,$$

$$C_2=\left(\frac{E}{\tilde{\lambda}}\right)^2\frac{2l+3}{2l-1}+\frac{2E}{\tilde{\lambda}}\left[\frac{l+1}{l}-w\right]+8\frac{1-w}{2l+3}. \tag{30}$$

If the limit $m_l\to 0$ is taken in Eqs. (29) and (30), then the average energy (22) is obtained from J_h'. The initial operator for J_h' with fixed E on the right-hand side of Eq. (26) has a hermitian form and therefore J_h' can be minimized with respect to $\tilde{\lambda}$, and this minimum should be zero. The values found for the energies agree well with the calculations in Ref. 9 for all mass ratios used there. The exact solution with $m_l/m_h=0$ for the function G_{-1} was found in the form of an expansion in terms of hydrogen functions with exponential decay at infinity, while a power-law dropoff was obtained for the function G_1. For a finite hole mass ratio the behavior of G_{-1} can likewise be expected to change, but the corresponding correction should be of the order of the mass ratio m_l/m_h. Choosing the variational functional in the simple form (21), we ignored this fact, but the good result obtained with real mass ratios justifies this choice.

We note that to analyze the asymptotic behavior attention should be focused on the slowly decaying function G_1, for which, as Eq. (25) shows, a large change in behavior at large r should be expected.

We shall use Eq. (25) to find the second component G_1 of the wave function

$$\left[\Delta_{l+1}+\frac{2\eta k}{r}-k^2\right]G_1(r)=-\frac{\alpha_0}{\alpha_1}\hat{R}(r)G_{-1}(r)$$

$$=\frac{\alpha_0}{\alpha_1}\tilde{\lambda}C\left(\frac{d}{dr}-\frac{l+1}{r}\right)r^l e^{-\tilde{\lambda}r},$$

$$\eta=\frac{1}{\alpha_1 k},\quad k^2=-E/\alpha_1. \tag{31}$$

Once again, here G_{-1} is chosen in the form (21), but a new factor C is introduced in place of the normalization factor N_{-1}, since the function G_1 and therefore the overall normalization will change.

A solution for the function $\partial/\partial\tilde{\lambda}(G_1/\tilde{\lambda})$ can be easily obtained by expanding in a series in Laguerre polynomials. This series can be summed, and the result is

$$G_1(r)=\frac{\alpha_0}{\alpha_1}\tilde{\lambda}Cr^{l+2}\int_{\tilde{\lambda}}^{\infty}\frac{\tau d\tau}{(\tau-k)^{l+2-\eta}(\tau+k)^{l+2+\eta}}$$

$$\times\int_k^{\tau}(t-k)^{l+1-\eta}(t+k)^{l+1+\eta}e^{-rt}dt, \tag{32}$$

and at infinity the function behaves as

$$G_1(r)=\frac{\alpha_0}{\alpha_1}\tilde{\lambda}C(2k)^{2l+3}\Gamma(l+2-\eta)r^{l+2}e^{-kr}U'(r)$$

$$\times\int_{\tilde{\lambda}}^{\infty}\frac{\tau d\tau}{(\tau-k)^{l+2-\eta}(\tau+k)^{l+2+\eta}}, \tag{33}$$

where $U'(r)=U(l+2-\eta,\ 2l+4,\ 2kr)$ is a confluent hypergeometric function which decays at infinity.[19] For small m_l, so that η and k cancel, the relation (33) passes into Eq. (23).

The quantity η is not small (for example, $\eta=0.66$ for GaAs), and it should be neglected, even though the series $U'(r)$ can be truncated, switching to Bessel functions. The real wave function is related to G_1 by a factor r and for the ground state, taking account of the leading term in $U'(r)$ at infinity, it decays as $r^{\eta}\exp(-kr)/r$ (compare with Refs. 13 and 14). This behavior changes very little when more accurate calculations are performed (specifically, as a function of the method for calculating G_{-1}). For the parameters of GaAs both components of the ground-state wave function calculated by the method this section and also by the variational method using the equations of Sec. 6 are presented in Fig. 2.

The radial functions G_ν are related to one another via the hypergeometric functions U and M, appearing in the fundamental solutions of the corresponding hydrogen operators of the system (6). They contain terms with $\ln(r)$ for r close to zero.[3] This was also reflected in Ref. 12, where the system of equations (6) was solved by a power series expansion taking account of this fact. This feature vanishes in the limit $m_l\to 0$, which is what enabled us to find a solution in the form of an expansion in the polynomials (13).

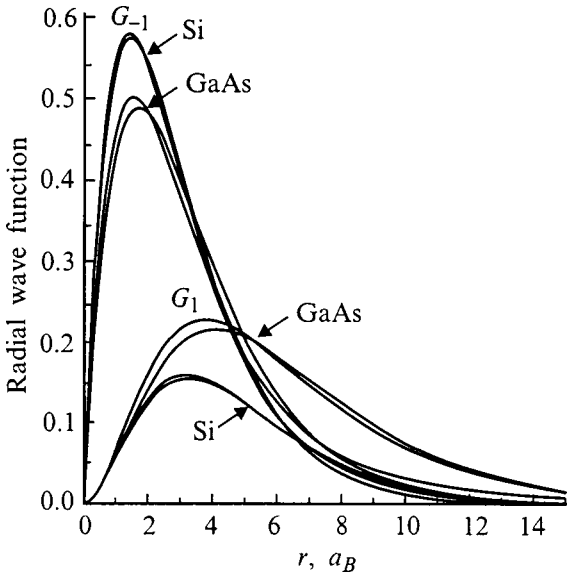

FIG. 2. Radial wave functions for the ground state of an acceptor for two values of the mass ratio $\beta=m_l/m_h$ ($\beta=0.14$ for GaAs and 0.348 for Si[9]). The curves with the larger maximum correspond to the variational solution (Sec. 6) and curves with the smaller maximum correspond to the approximate solution (Sec. 4).

5. MOMENTUM REPRESENTATION

An acceptor with zero light-hole mass was first studied in Ref. 15 in the momentum representation for the ground state. This approach was adopted in most subsequent works where this approximation was used. The calculations performed in the present paper make it possible to write down easily the wave functions in **k** space.

To calculate the integrals containing spherical functions only their dependence on l is important, and at this stage only one term (for example, $Y_{l+\nu,m}$) need be considered in the angular parts U_ν. The wave function (1) can be represented conventionally in the form

$$\Psi(\mathbf{r})=\sum_{\nu=-1,1}Y_{l+\nu,m}(\mathbf{r}/r)G_\nu(r), \tag{34}$$

and its Fourier transform is

$$\Psi(\mathbf{k})=\frac{1}{(2\pi)^{3/2}}\int e^{i\mathbf{k}\cdot\mathbf{r}}\Psi(\mathbf{r})/r\,d\mathbf{r}$$

$$=i^{l+\nu}\frac{1}{\sqrt{k}}\sum_{\nu=-1,1}Y_{l+\nu,m}(\mathbf{k}/k)$$

$$\times\int_0^{\infty}J_{l+\nu+1/2}(kr)G_\nu(r)r^{1/2}dr. \tag{35}$$

Here an expansion of a plane wave in spherical functions[18] was used, and $J_n(r)$ are Bessel functions. Using

the relation (10), the integrals in Eq. (35) are equal to one another to within a constant factor. According to Eq. (13), the radial function G_{-1} can be written as

$$G_{-1}(r)=\frac{\gamma_1}{N_0}\sqrt{2\lambda}\frac{(2\lambda r)^l}{(1-t)^{2l}}\exp\left(-\frac{1+t}{1-t}\lambda r\right), \tag{36}$$

if the substitution $t^n\to A_n$ is made in the expansion of G_{-1} in powers of t (here the generating function for Laguerre functions was used[19]). After the integral is calculated, the generating function for the Gegenbauer polynomials C_n^l is obtained,[20] and as a result

$$\Psi^{jm}(\mathbf{k})=(\gamma_1 U_{-1}^{jm}(\mathbf{k}/k)-\gamma_{-1}U_1^{jm}(\mathbf{k}/k))F(k),$$

$$F(k)=\frac{(4q)^{l-1}(l-1)!}{N_0\lambda\sqrt{\pi\lambda}}\frac{8}{(1+q^2)^{l+1}}$$

$$\times\sum_{n=\mu}(n+1)C_n^l\left(\frac{q^2-1}{q^2+1}\right)A_n, \tag{37}$$

where $q=k/\lambda$.

For the series with the ground state ($J=3/2$, $l=1$, $\Delta=\infty$)

$$\Psi(\mathbf{k})=\frac{1}{\sqrt{4\pi}}\left(\frac{(\mathbf{J}\cdot\mathbf{k})^2}{k^2}-\frac{1}{4}\right)F(k). \tag{38}$$

The angular dependence for this series is identical to that found in Ref. 15.

The work closest to the results of Sec. 2, but in momentum space, is Ref. 21, where the obtained equation is an analog of Eq. (8). In the present work the energy levels and wave functions of the first four states for $j=3/2$ (two each for $l=1$ and $l=2$, $\Delta=\infty$) were found approximately, but the solution method employed did not permit investigating the entire spectrum.

6. COMPARISON WITH THE VARIATIONAL METHOD

The main drawback of variational methods is that the eigenfunctions are computed much less accurately than the eigenvalues. However, for $m_l=0$ we showed that the exact and variational calculations of both components G_1 and G_{-1} performed by the methods of Ref. 8 are essentially identical. The Kane Hamiltonian was calculated in Ref. 8. Similar calculations can be performed in the Luttinger approximation adopted here, if the same expansion as in Ref. 8 in Laguerre polynomials with the additional factor r (as was indicated at the beginning of Sec. 1) is used for $G_i(r)$

$$G_i(r)=\sqrt{2\lambda}\sum_{n=0}^{\infty}a_n^i F_n(2\lambda r),$$

$$F_n(x)=\sqrt{\frac{n!}{(n+2\nu)!}}\,x^\nu\exp(-x/2)L_n^{2\nu}(x),\quad \nu\leqslant l. \tag{39}$$

This set of basis functions with $\nu\neq l$ is convenient for calculating the matrix elements of optical transitions between series with different values of l.[22] The matrix elements of the operators, with respect to the orthonormalized functions $F_n(x)$, appearing in the function (4) are

$$\left\langle n\left|\frac{1}{x}\right|m\right\rangle=\frac{1}{2\nu},$$

$$\left\langle n\left|\frac{1}{x^2}\right|m\right\rangle=\frac{1}{2\nu}\left(\frac{n+1}{2\nu-1}-\frac{m}{2\nu+1}\right),$$

$$\left\langle n\left|\frac{1}{x}\frac{d}{dx}+\frac{d}{dx}\frac{1}{x}\right|m\right\rangle=\frac{n-m}{2\nu},$$

$$\left\langle n\left|\frac{d^2}{dx^2}+\frac{\nu^2}{x^2}\right|m\right\rangle=\frac{1}{2}\left(\frac{1}{2}\delta_{nm}+n-m\right). \tag{40}$$

These formulas are valid for $n\geqslant m$, and their right-hand sides should be multiplied by

$$h_{nm}=\sqrt{\frac{n!(m+2\nu)!}{m!(n+2\nu)!}}. \tag{41}$$

The numerical matrix for the Hamiltonian repeats completely the structure of Eqs. (6) with the operators replaced by the corresponding matrices, according to the previous relations. Diagonalization with respect to the parameters a_n^i is performed in the standard manner, and variation with respect to λ can be performed even for the excited states of a series with total angular momentum j using the lowest state of this series.[8]

As we have already mentioned, for $m_l=0$ the wave functions calculated by this variational method are essentially identical to the exact wave functions. To check the quality of these functions for $m_l\neq 0$ we reconstructed the function $\tilde{G}_1(r)$ from the computed variational function $G_{-1}(r)$, according to the second equation of the system (6), in terms of the fundamental solutions of the hydrogen factor next to $G_1(r)$. The functions $\tilde{G}_1(r)$ and $G_1(r)$ agree well for $r<15$; they differ in the third decimal place. The function $\tilde{G}_{-1}(r)$ calculated similarly in terms of $\tilde{G}_1(r)$ is the same as the variational function $G_{-1}(r)$ to within approximately the same accuracy.

This work was supported by the International Science Fund.

7. APPENDIX

We shall determine the inverse operator $D(\alpha)$ from the solution of the equation

$$\left(\frac{d}{dr}+\frac{\alpha}{r}\right)F(r)=f(r) \tag{A.1}$$

as

$$f(r)=D(\alpha)f(r)\equiv r^{-\alpha}\int_c^r x^\alpha f(x)dx,$$

$$(c=0,\alpha>0\quad\text{and}\quad c=\infty,\alpha\leqslant 0). \tag{A.2}$$

The functions F and f must behave in the required manner at zero and infinity, similarly to the behavior of the eigenfunctions for bound states. The lower integration limit c was chosen on the basis of this condition.

From the commutation relation

$$\left(\frac{d}{dr}+\frac{\beta}{r}\right)\left(\frac{d}{dr}+\frac{\alpha}{r}\right)=\left(\frac{d}{dr}+\frac{\alpha+1}{r}\right)\left(\frac{d}{dr}+\frac{\beta-1}{r}\right) \quad \text{(A.3)}$$

we obtain formally

$$D(\alpha)D(\beta)=D(\beta-1)D(\alpha+1). \quad \text{(A.4)}$$

This equality can be checked by solving an equation similar to Eq. (A.1) but with two operators. All other relations are established similarly:

$$D(\alpha)\frac{1}{r}=\frac{1}{r}D(\alpha-1), \quad D(\alpha)r=rD(\alpha+1),$$

$$\left(\frac{d}{dr}+\frac{\alpha}{r}\right)D(\beta)=D(\beta+1)\left(\frac{d}{dr}+\frac{\alpha+1}{r}\right),$$

$$D(\alpha)D(\beta)=\frac{1}{\beta-\alpha-1}[D(\alpha)r-rD(\beta)]. \quad \text{(A.5)}$$

*)E-mail: lynnyk@class.semicond.kiev.ua
†)E-mail: sheka@class.semicond.kiev.ua

[1] J. M. Luttinger and W. Kohn, Phys. Rev. **97**, 869 (1955).
[2] J. M. Luttinger, Phys. Rev. **102**, 1030 (1956).
[3] D. Shechter, J. Phys. Chem. Solids **23**, 237 (1962).
[4] K. S. Mendelson and H. M. James, J. Phys. Chem. Solids **25**, 729 (1964).
[5] C. Kittel and A. H. Mitchell, Phys. Rev. **96**, 1488 (1954).
[6] E. O. Kane, J. Phys. Chem. Solids **1**, 249 (1957).
[7] L. V. Keldysh, Zh. Éksp. Teor. Fiz. **45**, 364 (1963) [Sov. Phys. JETP **18**, 253 (1964)].
[8] V. I. Sheka and D. I. Sheka, Zh. Éksp. Teor. Fiz. **51**, 1445 (1966) [Sov. Phys. JETP **24**, 975 (1967)].
[9] A. Baldereschi and N. O. Lipari, Phys. Rev. B **8**, 2697 (1973).
[10] A. Baldereschi and N. O. Lipari, Phys. Rev. B **9**, 1525 (1974).
[11] I. A. Merkulov and A. V. Rodina, Fiz. Tekh. Poluprovodn. **28**, 321 (1994) [Sov. Phys. Semicond. **28**, 195 (1994)].
[12] Sh. M. Kogan and A. F. Polupanov, Zh. Éksp. Teor. Fiz. **80**, 394 (1981) [Sov. Phys. JETP **53**, 201 (1981)].
[13] B. L. Gel'mont and M. I. D'yakonov, Fiz. Tekh. Poluprovodn. **5**, 2191 (1971) [Sov. Phys. Semicond. **5**, 1905 (1971)].
[14] B. L. Gel'mont and M. I. D'yakonov, Zh. Éksp. Teor. Fiz. **62**, 713 (1972) [Sov. Phys. JETP **35**, 377 (1972)].
[15] B. L. Gel'mont, V. I. Ivanov-Omskiĭ, and M. I. Tsidil'kovskiĭ, Usp. Fiz. Nauk **120**, 337 (1976) [Sov. Phys. Usp. **19**, 879 (1976)].
[16] Yu. F. Berkovskaya, B. L. Gel'mont, and É. I. Tsidil'kovskiĭ, Fiz. Tekh. Poluprovodn. **22**, 855 (1988) [Sov. Phys. Semicond. **22**, 539 (1988)].
[17] B. L. Gel'mont and A. V. Rodina, Fiz. Tekh. Poluprovodn. **25**, 2189 (1991) [Sov. Phys. Semicond. **25**, 1319 (1991)].
[18] L. D. Landau and E. M. Lifshitz, *Quantum Mechanics* (Pergamon Press, New York, 1974; Russian original, 4th ed., Nauka, Moscow, 1989).
[19] *Handbook of Mathematical Functions*, edited by M. Abramowitz and I. A. Stegun (National Bureau of Standards Applied Mathematics Series, 1964; Nauka, Moscow, 1979).
[20] I. S. Gradshteĭn and I. M. Ryzhik, *Table of Integrals, Series, and Products* (Academic Press, New York, 1980; Russian original, GIFML, Moscow, 1962).
[21] Y. T. Rebane, Phys. Rev. B **48**, 11772 (1993).
[22] V. I. Sheka and D. I. Sheka, Ukr. Fiz. Zh. **14**, 720 (1969).
[23] A. V. Malyshev, I. A. Merkulov, and A. V. Rodina, Fiz. Tverd. Tela (St. Petersburg) **40**, 1002 (1998) [Phys. Solid State **40**, 917 (1998)].

Translated by M. E. Alferieff

Centers of charge nonuniformity and reduction of copper oxide CuO during irradiation with nitrogen ions

N. N. Loshkareva,*) Yu. P. Sukhorukov, S. V. Naumov, B. A. Gizhevskiĭ, and G. N. Tatarinova

Institute of Metal Physics, Ural Branch, Russian Academy of Sciences, 620219 Ekaterinburg, Russia

T. A. Belykh

Ural State Technical University, 620002 Ekaterinburg, Russia

(Submitted December 28, 1998)
Fiz. Tverd. Tela (St. Petersburg) **41**, 1564–1567 (September 1999)

Long-range reduction of CuO to Cu_2O and Cu was observed by irradiating polycrystals and different planes of CuO single crystals ((110) and (020)) with 16-MeV nitrogen ions with fluence 10^{17} cm^{-2}. The infrared absorption spectra show an increase in the number of hole $[CuO_4]^{5-}$ and electronic $[CuO_4]^{7-}$ centers. The highest density of electronic centers and reduction occur near the surfaces of the samples. © *1999 American Institute of Physics.* [S1063-7834(99)00809-6]

Copper oxide CuO is a model for studying the semiconductor phase of copper–oxygen high-temperature superconductors.[1] Mobile charge carriers in CuO are absent, and the low-mobility charge carriers form a phase-nonuniform nanoscopic structure — nuclei of a phase of polar (electronic and hole) centers in the main CuO matrix.[2] Since annealing and doping cannot appreciably influence the inhomogeneous-phase structure because of the narrow homogeneity range, we investigated the characteristic features of the charge structure of CuO by producing additional nucleation centers by irradiation with different high-energy particles — electrons[2] and He^+ ions.[3] An investigation of CuO single crystals irradiated with 4.6-MeV He^+ ions[3,4] revealed a host of unusual phenomena: long-range action and the appearance of new IR absorption lines, including a line associated with the scattering of light by centers of charge inhomogeneity. Our aim in the present work is to determine the nature of the change produced in the charge-inhomogeneous structure of CuO when implanted He^+ ions are replaced by heavier nitrogen ions having a higher energy — 16 MeV.

1. SAMPLES AND EXPERIMENTAL RESULTS

Three CuO single crystals, obtained by the fluxed solution method, as well as CuO polycrystals were investigated. Two of the single crystals possessed natural facetting — the crystal faces were (110) planes, and the third crystal was cut in the form of a wafer, so that the plane of the crystal was the (020) plane. The samples were irradiated with nitrogen ions in the U-120 cyclotron at USTU–UPI. The energy of the nitrogen ions was 16 MeV, the fluence was 10^{17} cm^{-2}, and the vacuum was 10^{-6} Torr. The ion flux was 10^{12} ions/$cm^2 \cdot s$.

The x-ray phase analysis was performed on a DRON-2 diffractometer.

The bulk resistivity of the samples was measured by a standard four-contact method. Current contacts, made of an In–Ga alloy, were deposited on the end faces, and potential contacts were deposited on the irradiated or unirradiated face. The surface resistivity on different faces of the sample was also estimated. The current and potential contacts were deposited in a single row on the faces investigated.

The absorption spectra for natural and linearly polarized light were measured with an improved, automated IKS-21 spectrometer in the photon energy range 0.12–1.5 eV. Grating polarizers based on teflon and polyethylene were used as polarizers. The reflection coefficient given in Ref. 5 for the crystal was used to calculate the absorption coefficient.

1.1. X-ray data

The phase composition of the samples changed immediately after irradiation with nitrogen ions: X-ray analysis showed the presence of Cu_2O and copper on the irradiated face and the opposite unirradiated face of the single crystals, and in larger quantities on the opposite face than on the irradiated face. We have observed such long-range response to irradiation by high-energy particles for irradiation of CuO with H^+ ions.[3] The projected depth calculated using the TRIM program[6] is 6.2 μm in our case. Metallic copper was observed visually only on the faces opposite to the irradiated faces. For CuO-(110) samples it was observed in the form of a continuous copper surface, while for CuO-(020) it had the form of individual impregnations. According to the x-ray data, after the samples were allowed to stand in air for two months, the metallic copper on the irradiated faces vanished, while the amount of copper on the opposite faces decreased only slightly. Electrical and optical measurements were performed on such cured samples.

Figure 1 compares the ratio of the intensities of the x-ray diffraction lines of the Cu_2O and Cu phases that appeared on the surface of a single crystal after irradiation with the ratio of the line intensities for a Cu_2O polycrystal. The high, compared with the normal distribution, intensity of certain reflections seems to be due to the presence of texture of the Cu_2O

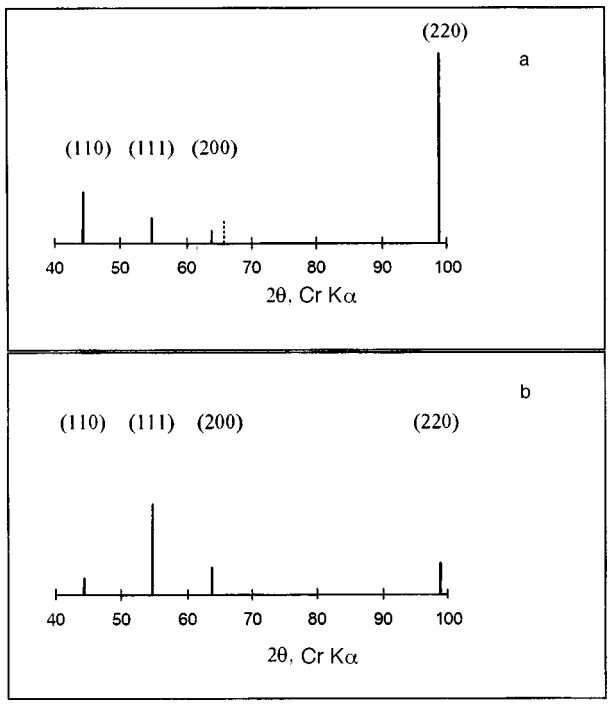

FIG. 1. Ratio of the intensities of x-ray diffraction lines of Cu_2O: a—on the surface of a CuO-(020) single crystal after irradiation; the dotted line is a Cu line; b—polycrystalline Cu_2O, our data and data from Ref. 10; top—indices of Cu_2O.

phase in the [110] direction of CuO-(020). We note that when a $\sim 10-15$ μm layer was ground off the single crystals the character of the texture changed (see Table I, which also gives the sample thicknesses). The ratio of the line intensities could also change because of the effect of irradiation with nitrogen ions on the Cu_2O phase which appears, resulting in a displacement of copper ions into vacant locations in the Cu_2O structure. However, the absence of any changes in the ratio of the line intensities for the polycrystalline CuO sample after irradiation and for the specially irradiated polycrystalline Cu_2O sample makes the first reason (texture) more likely.

A layer-by-layer analysis was performed to study the nature of the changes occurring in the interior volume of the crystals — measurement of the spectra and resistivity with grinding and polishing of the faces of the single crystals and monitoring of the phase composition on the surface of the faces according to x-ray data. Layer-by-layer analysis indicates that the second phases Cu and Cu_2O are predominantly present near the surfaces of the faces. When the copper film is ground off (a ~ 10 μm thick layer is removed), cuprous oxide Cu_2O remains and the amount of Cu_2O decreases with further grinding of both surfaces of the single crystals. The depth of the second phase Cu_2O is different for different single crystals and polycrystals. Thus, for a 1.5 mm thick polycrystal the reduced phase Cu_2O on the irradiated face side was observed right up to depths ~ 50 μm from the surface, while for the unirradiated face it was observed to 20 μm. For single crystal No. 2 the CuO-(110) phase of Cu_2O was absent even at a depth of 10 μm from the irradiated face and 30 μm from the unirradiated face.

TABLE I. The form of the Cu_2O texture on the faces and in the interior volume of CuO single crystals.

Sample	No. 1 CuO-(110)	No. 2 CuO-(110)	No. 3 CuO-(020)
Thickness, μm	1000	270	290
Irradiated face	No	[200]	[220]
Unirradiated face	[200]	No	No
After grinding of irradiated face	[110]	–	[200]
After grinding of unirradiated face	[200]	–	No

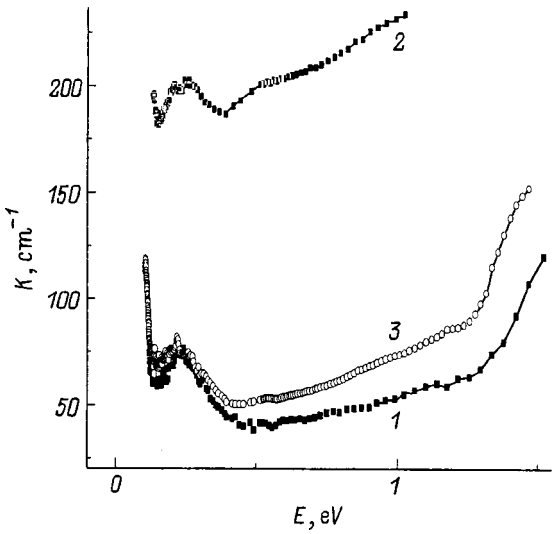

FIG. 2. Absorption spectra of a CuO-(110) single crystal before (*1*) and after (*2*, *3*) irradiation with nitrogen ions (natural light); *2*—unground sample; *3*—10 μm layer ground off the unirradiated face.

1.2. Resistivity

After the copper deposits were ground off, the bulk resistivity ρ of the irradiated CuO single- and polycrystals was close to the initial, preirradiation value of ρ — $(1-3)\times 10^2$ $\Omega\cdot$cm. The surface resistivity of both the irradiated and opposite faces increased approximately by an order of magnitude. After a 20–40 μm thick layer was removed, for the single crystal No. 1 (see Table I) and the polycrystal, the surface resistivity decreased to the initial values. The Cu_2O phase either is not visible or only traces of it are present. The higher surface resistivity is due to the presence of a large quantity of the Cu_2O phase, whose resistivity is higher than that of CuO, in the near-surface layers. The decrease in the surface resistivity correlates with the decrease in the amount of the Cu_2O phase.

1.3. Optical spectra

The absorption spectra of CuO-(110) and CuO-(020) single crystals before and after irradiation (samples Nos. 2 and 3 in Table I) are displayed in Figs. 2 and 3. As one can see from the figures, a large increase in the absorption coefficient of the irradiated samples is observed in the experi-

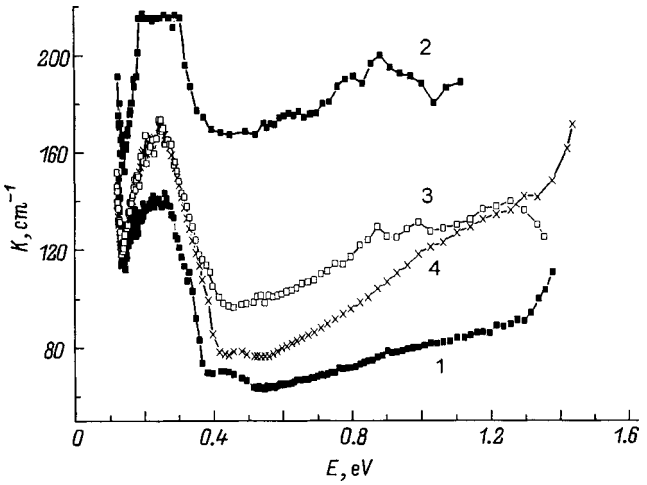

FIG. 3. Absorption spectra of a CuO-(020) single crystal before (*1*) and after (*2–4*) irradiation (polarized light, $\mathbf{E} \| [\bar{1}01]$); *2*—unground sample; *3*—10 μm layer ground off the unirradiated face; *4*—another 20 μm ground off the unirradiated face.

mental range. When the unirradiated face of a CuO-(110) single crystal was polished, a ~10 μm layer was removed and the spectrum of such a sample approached that of the unirradiated crystal (curve *3* in Fig. 2) and a second Cu_2O phase remained on the unirradiated face. The spectrum remained virtually unchanged when an additional 20 μm thick layer was ground off the unirradiated face. Removal of a 10 μm layer from the irradiated face likewise did not change the spectrum. At this stage of grinding (30 μm from the unirradiated side and 10 μm from the irradiated side) only traces of Cu_2O phase were observed on both sides.

The absorption spectra before and after irradiation are presented for a CuO-(020) single crystal for light polarized in the [101] direction — the axis of greatest anisotropy in the (020) plane. The largest increase in absorption is observed at high energies. Just as in the case of a (110) plane, polishing of the unirradiated face (removal of a 10 μm layer) decreased the absorption coefficient (curve *3* in Fig. 3). Grinding another 20 μm from the unirradiated face brought the spectrum closer to the initial one (curve *4*). This trend was also observed with further grinding. However, the absorption remained greater than the initial level even after an 80 μm layer was removed from the unirradiated face and a 100 μm layer was removed from the irradiated face. In addition, the Cu_2O phase was still observed on the irradiated side.

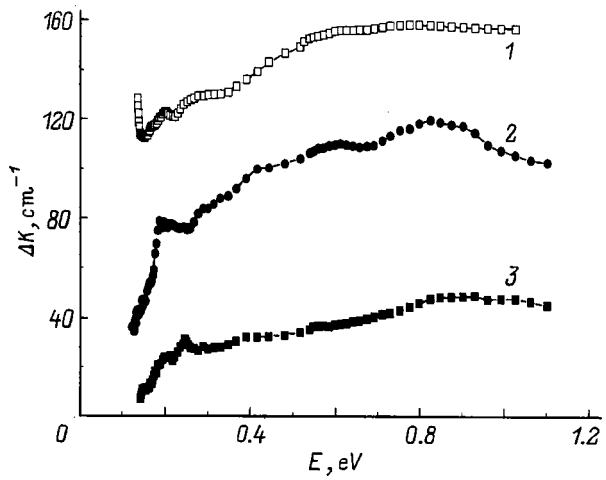

FIG. 4. Difference of absorption spectra before and after irradiation for two single crystals: *1*—CuO-(110); *2*—CuO-(020) unground sample; *3*—CuO-(020) after a 10 μm layer was ground off the unirradiated face.

From the difference of the absorption coefficients before and after irradiation, presented in Fig. 4 for both samples, two regions with the greatest increase in absorption can be seen near energies 0.2 and 0.8 eV.

2. DISCUSSION

The infrared absorption spectra of CuO single crystals irradiated with nitrogen atoms are formed by changes occuring in the charge-inhomogeneous structure and by the presence of additional Cu_2O and metallic copper phases. The copper phase makes the largest contribution to absorption. In the range investigated, the absorption of the copper film is large and virtually wavelength-independent. Our measurements showed that the absorption coefficient of the Cu_2O single crystal is at least two times smaller than that of the CuO single crystal. The strongst Cu_2O line in the experimental range at 0.14 eV is absent in the spectra of the irradiated crystals. Therefore cuprous oxide Cu_2O as a second phase does not introduce any changes in the spectrum of the irradiated samples. The difference of the spectra before and after irradiation for both the (100) and (020) planes is not wavelength-independent, as would be the case if the difference was determined only by inclusions of metallic copper. The fact that the spectra are different shows that the absorption intensity near 0.2 and 0.8 eV is higher after irradiation. These energies correspond to absorption bands associated with transitions in hole and electronic Jahn–Teller centers, respectively.[1] It is known[1] that optical transitions are forbidden in a triplet electronic Jahn–Teller center and in CuO. Therefore, in CuO single crystals irradiated with nitrogen ions optical transitions in an electronic center become allowed in the presence of strong local distortions, similarly to CuO crystals irradiated with H^+ ions.[3] The number of electronic centers changes predominantly with a general increase in the number of hole and electronic centers.

The x-ray data obtained in layer-by-layer analysis and the resistivity measurements show that reduction of CuO to Cu_2O and copper occurs predominantly on crystal faces, i.e., irradiated and unirradiated faces. Precipitation of copper is also noted in cracks and pits in the crystals. The fact that the absorption spectra come closer to the initial spectra when the crystals are ground shows that the number of charge-inhomogeneity centers is also larger in regions next to the crystal boundaries. The formation of a large number of electronic centers is probably the first stage of the reduction process CuO–Cu_2O–Cu, which occurs near boundaries. An electronic Jahn–Teller center is a cluster $[CuO_4]^{7-}$ with a low valence of the cation (formally Cu^+), and therefore it serves as a precursor of the Cu_2O phase. We observed a similar long-range effect with formation of predominantly electronic centers and reduction of CuO to Cu_2O and Cu in

our investigations of CuO crystals irradiated with 4.6-MeV H^+ ions.[3]

The most likely mechanism of long-range action seems to be an elastic-wave mechanism combined with radiation-stimulated diffusion.[7,3] Elastic waves arising at the end of cascades of atomic collisions while a sample is bombarded with high-energy ions give rise to displacement and excitation of the atoms and the formation of additional polar centers. It should be noted that we also observed an increase in the absorption coefficient in a region corresponding to transitions in the electronic Jahn–Teller center for a CuO polycrystal under shock-wave loading.[8] The formation of a Cu_2O phase was not observed. A long-range action mechanism leading to defect formation on the surface opposite to the irradiated surface has been proposed in Ref. 9. The essence of the mechanism is that energy is transferred in the form of potential energy of defects. The transferred energy at the face opposite to the irradiated face can be converted into an elastic wave, which can give rise to the formation of defects at the surface and, in our case, it can even lead to oxygen losses. Strong stresses in the surface layers could be responsible for the texture on the faces and the change in texture in the interior of the sample.

In summary, irradiation of single- and polycrystals of CuO with 16-MeV nitrogen ions at a 10^{17} cm^{-2} fluence leads to the formation of electronic and hole Jahn–Teller centers and reduction of CuO to Cu_2O and Cu with Cu_2O texture. Defect formation and reduction have a long-range character. The appearance of centers and the reduction of CuO occur predominantly near the irradiated and unirradiated surfaces of the samples.

We are grateful to A. S. Moskvin and V. E. Naĭsh for a helpful discussion.

This work was supported by the Russian Fund for Fundamental Research (grant No. 96-16063).

*)E-Mail: magsemi@ifm.e-burg.su

[1] A. S. Moskvin, N. N. Loshkareva, Yu. P. Sukhorukov, M. A. Sidorov, and A. A. Samokhvalov, Zh. Éksp. Teor. Fiz. **105**, 967 (1994) [JETP **78**, 518 (1994)].
[2] Yu. P. Sukhorukov, N. N. Loshkareva, A. S. Moskvin, V. L. Arbuzov, A. S. Ovchinnikov, N. M. Chebotaev, and A. A. Samokhvalov, Fiz. Tverd. Tela (St. Petersburg) **39**, 2141 (1997) [Phys. Solid State **39**, 1916 (1997)].
[3] N. N. Loshkareva, Yu. P. Sukhorukov, B. A. Gizhevskiĭ, A. S. Moskvin, T. A. Belykh, S. V. Naumov, and A. A. Samokhvalov, Fiz. Tverd. Tela (St. Petersburg) **40**, 419 (1998) [Phys. Solid State **40**, 383 (1998)].
[4] B. A. Gizhevskiĭ, T. A. Belykh, S. V. Naumov, N. N. Loshkareva, Yu. P. Sukhorukov, T. M. Pyatkova, N. M. Chebotaev, and A. A. Samokhvalov, Fiz. Khim. Obrab. Mater. **1**, 9 (1998).
[5] A. A. Samokhvalov, N. N. Loshkareva, Yu. P. Sukhorukov, V. A. Gruverman, B. A. Gizhevskiĭ, and N. M. Chebotaev, JETP Lett. **49**, 523 (1989).
[6] J. Brersack and L. Hullmark, Nucl. Instrum. Methods **174**, 257 (1980).
[7] B. A. Gizhevskiĭ, T. A. Belykh, V. A. Teplov, S. V. Naumov, N. N. Loshkareva, Yu. P. Sukhorukov, and N. M. Chebotaev, in *Collection of Works on the Detection of Ionizing Radiation* [in Russian] (Ekaterinburg, 1996), p. 3.
[8] E. A. Kozlov, E. V. Abakshin, V. I. Tarzhanov, B. A. Gizhevskii, M. V. Degtyarev, and S. V. Naumov, L. M. Voronova, and G. N. Tatarinova, in *Abstracts of Vth International Conference Zababakhin Scientific Talks*, Snezhinsk, Chelyabinsk District, Russia (1998), p. 20.
[9] Yu. V. Martynenko and P. G. Moskovkin, Neorg. Mater. **34**, 1142 (1998).
[10] L. I. Mirkin, *Handbook of X-Ray Crystallographic Analysis of Crystals* [in Russian], edited by Ya. S. Umanskiĭ (Physical-Mathematical Literature, Moscow, 1961), 863 pp.

Translated by M. E. Alferieff

Emergence of exciton near-surface localized states in the reflectance spectra of low-Se $CdS_{1-x}Se_x$ crystals

N. R. Grigor'eva, B. A. Kazennov, B. V. Novikov, and O. K. Anbushinova

Institute of Physics, St. Petersburg State University, 198904 St. Petersburg, Russia

A. V. Sel'kin

A. F. Ioffe Physicotechnical Institute, Russian Academy of Sciences, 194021 St. Petersburg, Russia

R. A. Bisengaliev

Kalmyk State University, 358000 Élista, Russia

(Submitted February 1, 1999)
Fiz. Tverd. Tela (St. Petersburg) **41**, 1568–1574 (September 1999)

A study is reported of the effect of exciton localization by solid-solution compositional inhomogeneities near the crystal surface, which gives rise to new unusual features in the optical excitonic spectra. These features, observed in exciton reflectance spectra of $CdS_{1-x}Se_x$ with low Se contents ($x \sim 0.01$), were studied in the 4.2–200-K temperature range. Models of the localizing excitonic potentials providing an adequate description of the experimental reflectance spectra were found. Nonlinear model potentials taking into account the diffusion mechanism at the onset of structural inhomogeneities and the state of the real crystal surface were invoked. The shape of the additional structure in the reflectance spectra was found to be very sensitive to the type and parameters of the near-surface potential well. [S1063-7834(99)00909-0]

Solid solutions based on II–VI compounds are well studied materials enjoying broad application in microelectronics and laser technology. $CdS_{1-x}Se_x$ is one of the most comprehensively investigated compounds of this group. It has been studied already for more than 30 years by various techniques including exciton spectroscopy.[1–5] The cadmium sulfide and selenide form a continuous and unlimited substitutional solid solution. The optical properties of this compound were measured within a broad composition range. The gradual variation of the gap E_g of the $CdS_{1-x}Se_x$ crystal with composition x ($E_g = 2.58$ eV for pure CdS and $E_g = 1.85$ eV for pure CdSe at liquid-helium temperature) could be described with acceptable accuracy in terms of the virtual-crystal model. While this simplest theoretical model did not take into account the disorder in crystal structure, it nevertheless permitted an adequate reproduction of a number of properties of these solid solutions.[6]

The exciton localization processes characteristic of solid solutions were shown[1–4,7,8] to contribute substantially to the optical properties of these compounds even if an individual atom of the substituting impurity does not produce a bound state. Exciton localization occurs in this case in the wells of the potential relief created by random compositional fluctuations. The localized states form a continuous density-of-states tail of the corresponding exciton band and are not separated from free states by an energy gap. The continuum model[9] corresponding to this situation describes adequately the energy spectrum of the crystal for Se concentrations above 2–3%.

At the same time the properties of the above solid solutions at low concentrations of Se, on the one side, and of S, on the other, remain largely unknown. The optical spectra of such crystals exhibit quite frequently new features associated with an inhomogeneous distribution of the composition x in depth of the sample. For instance, studies of semiconductors whose near-surface layers contained the $CdS_{1-x}Se_x$ solid solution with a low concentration of one of the ionic components revealed clearly pronounced anomalies in excitonic reflectance spectra.[10,11] Such ''anomalous'' optical spectra were apparently observed for the first time in Ref. 12. It should be pointed out that such spectra were observed accidentally, and the corresponding experimental data were interpreted in terms of fairly crude models.

This paper reports a systematic investigation of reflectance spectra of the $CdS_{1-x}Se_x$ solid solutions with Se concentration of 0.1–3%. Besides samples characterized by classical exciton-reflectance (ER) profiles, some of the crystals studied exhibited anomalous reflectance spectra. An analysis of these spectra showed that the ER features observed in this case can be well described quantitatively within the model of the exciton-localizing near-surface potential (ESP) in the form of a potential well with a monotonic exponential tail extending into the bulk of the sample and a bottom lying at a certain distance from the surface. This form of the ESP is attributed to the monotonic decrease of the S content toward the surface of the ''anomalous'' samples and can be associated with other real features in the structure of the near-surface region.

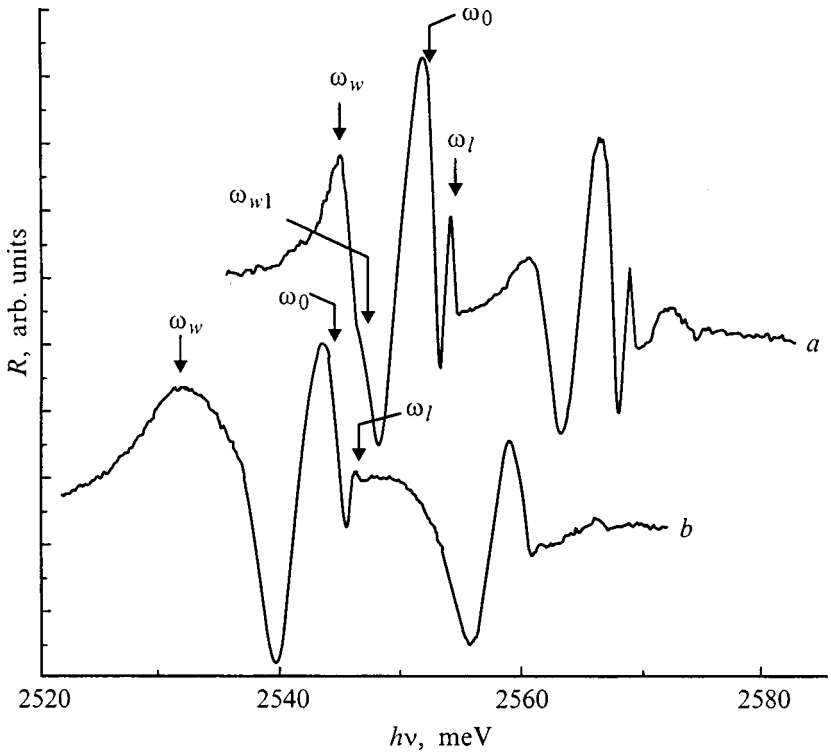

FIG. 1. ER spectra of samples (a) $K1$ and (b) $K2$. The arrows denoted by ω_l, ω_0, ω_w, and ω_{w1} relate to the $A_{n=1}$ excitonic resonance region.

1. EXPERIMENTAL TECHNIQUE

The near-surface exciton-localizing potential may be created both from specific crystal-growth conditions and as a result of external factors acting on the surface.[10–12] In both cases one observes anomalous excitonic reflectance. We studied reflectance spectra of $CdS_{1-x}Se_x$ crystals of two groups grown from a vapor phase. The technology[11] used to grow crystals of the first group produced samples which consisted mostly of pure CdS, with only a layer of the $CdS_{1-x}Se_x$ solid solution present near the surface (the sample series denoted subsequently by $K1$). The Se concentration in the near-surface layer of the $K1$ samples did not exceed 1% and decreased away from the surface into the bulk. The technology employed to grow samples of the second group was characterized by the presence of CdS and CdSe molecules at strongly differing partial pressures in the growth zone of the vapor phase, which provided favorable conditions for the formation of a heterogeneous structure. The near-surface S content in the solid solutions thus prepared decreased toward the surface (the series denoted in what follows by $K2$).

The samples were single-crystal platelets with the hexagonal axis **C** parallel to the surface plane. The excitonic reflectance spectra were measured in p polarization with $\mathbf{E}\perp\mathbf{C}$, within the spectral interval containing the A and B excitonic states. The temperature range covered was 4.2 to 200 K. The reflectance spectra were measured on an automated setup based on a DFS-24 monochromator.

2. RESULTS AND DISCUSSION

The low-Se crystals can be classed according to their ER spectra in two groups. For most samples, these spectra have a classic profile, and they can be interpreted in terms of the simplest light-reflection models. The low-energy shift of the excitonic resonances in the spectra of these crystals is accounted for by the narrowing of the gap with increasing Se content, and the line broadening is associated with the existence of random compositional fluctuations causing an increase of the decay coefficient Γ. At the same time some samples exhibit considerably transformed ER spectra. Anomalous ER spectra differ radically in shape from the classical ones.

Following Ref. 10, the anomalous features in reflectance spectra are attributed to exciton localization in the near-surface region of semiconductor crystals. Clearly pronounced anomalies in ER spectra were observed in a $CdSe_{1-x}S_x$ solid solution with low S content, and their onset was attributed to structural inhomogeneities associated with near-surface compositional variations (a variation of composition x along the surface normal).[10] Our reflectance spectra (Fig. 1) of low-Se ($<1\%$) $CdS_{1-x}Se_x$ mixed crystals can also be associated with the creation of an exciton-localizing near-surface potential. The spectrum in Fig. 1a was taken from the sample ($K1$) whose ER spectrum was discussed in Ref. 11. This spectrum is shown over a broader frequency range and is compared with the spectrum of Fig. 1b obtained from a new sample ($K2$) grown in our laboratory.

As seen from Fig. 1, the two ER spectra, both for the $K1$ and $K2$ crystals, have anomalous profiles and are qualitatively similar. In place of the conventional pattern in the region of the excitonic resonance, there are three maxima and as many minima. Both ER spectra are strongly extended along the frequency scale. For instance, the distance between the extreme ER maxima in the A_{n-1} exciton region is approximately 9 meV for the $K1$ crystal and 14 meV for the $K2$ sample. The ER spectra of the samples of both groups

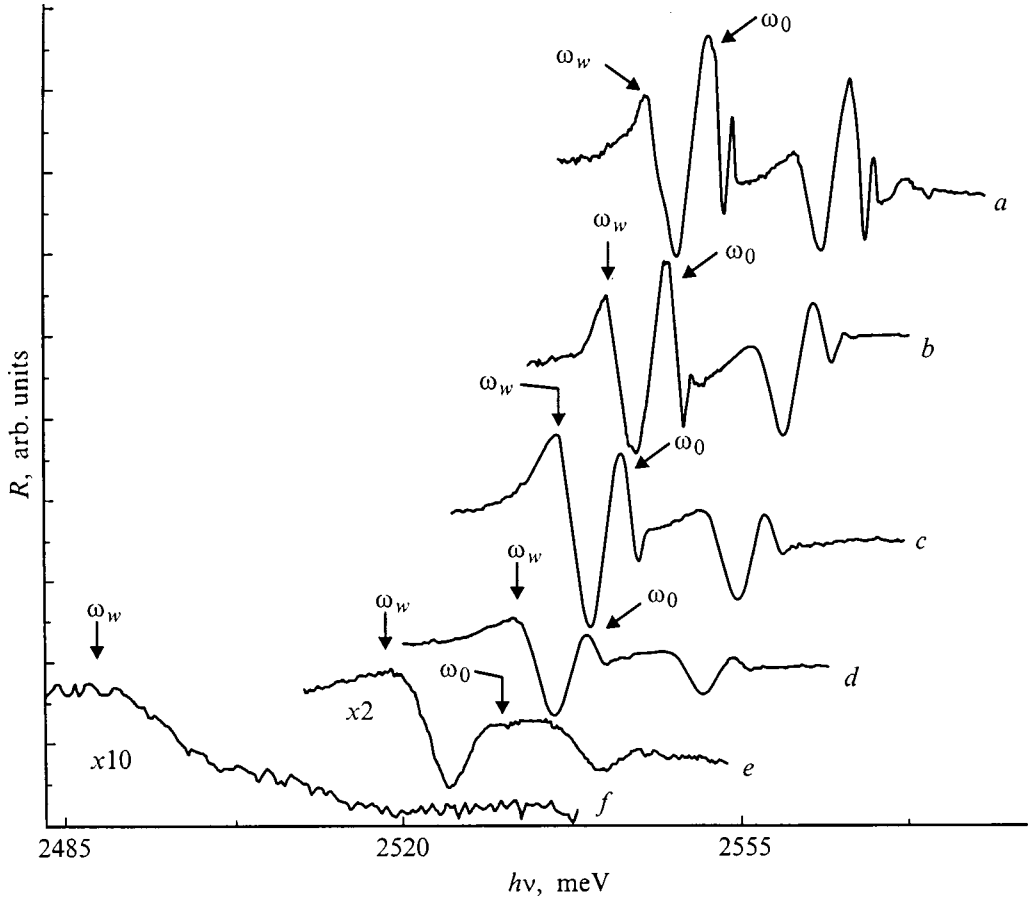

FIG. 2. Variation of the $K1$ ER spectrum with temperature T(K): a—4.2, b—40, c—80, d—100, e—140, f—200. The arrows denoted by ω_0 and ω_w relate to the $A_{n=1}$ excitonic resonance region.

exhibit a spike near the A_{n-1} longitudinal exciton frequency ω_l, the main maximum at the resonance frequency ω_0, and an additional structure peaking at ω_w. This structure adjoins at the low-frequency side the region of the A_{n-1} transverse-exciton resonance frequency ω_0. The short-wavelength structure ($\omega > \omega_l$), due to the contribution of the excitonic resonance B, is largely similar to the A resonance structure ($\omega < \omega_l$).

The ER spectra of the $K1$ samples differ from those of the $K2$ samples primarily in a general shift of the former toward higher energies. Besides, the spike in the $K1$ ER spectrum has a higher intensity, and the features in the additional structure differ in shape and position. The ER additional structure of the $K1$ crystal consists of a deep minimum, of a step (ω_{w1}) adjoining it on the low-frequency side, and a maximum after it. The ER additional structure of the $K2$ crystal also exhibits a deep minimum and several poorly resolved features on the low-frequency side which add up to form a broad maximum, with the distance from ω_0 to this maximum being larger than that from ω_0 to the maximum in the $K1$ ER spectrum.

The localizing ESP was shown[11] to originate from the difference in the gap width between the bulk of the sample and near its surface. ER calculations made with an ESP consisting of a square potential well and a linear tail extending into the bulk revealed that the ER additional structure in the $K1$ sample can be assigned to the presence of a potential well in the ESP. In view of the similarities between the anomalies exhibited by the $K1$ and $K2$ samples, we made a conjecture that the ER additional structure of the $K2$ sample is also due to the presence of a potential well in the near-surface region of the crystal.

Figures 2 and 3 display reflectance spectra of samples $K1$ and $K2$ obtained at different temperatures. It is seen that as the temperature increases, the ER spectrum shifts as a whole toward lower energies, and its features decrease in amplitude to finally disappear. The first to vanish with increasing temperature is the spike; this occurs at 30 K for the $K2$ sample and above 40 K for the $K1$ crystal. The part of the ER spectrum due to free excitons and containing the main maximum at 4.2 K persists up to $T = 100$ and 140 K for the $K2$ and $K1$ samples, respectively.

The additional structure in the ER spectra of both samples is observed at higher temperatures compared to the structure due to the free exciton. Besides, its intensity falls off considerably slower than that of the main maximum. As a result, the additional structure becomes the strongest feature in ER spectra as the temperature increases.

It should be pointed out that the main changes in the ER spectra of the $K1$ sample (Fig. 2) occur at higher temperatures than those of sample $K2$. For instance, at $T = 80$ K the $K1$ ER spectrum exhibits the same features as at 4.2 K, with the exception of the spike at ω_l. As for the $K2$ sample, its 80-K ER spectrum exhibits disappearance not only of the

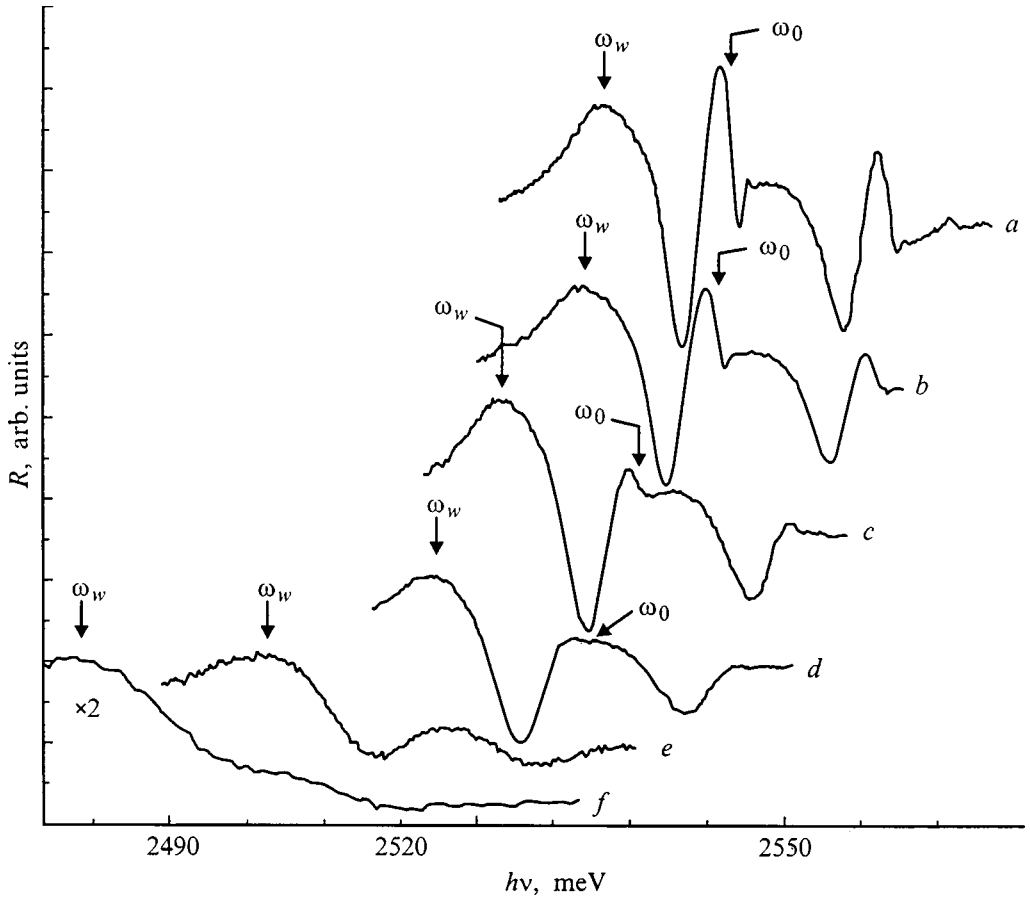

FIG. 3. Variation of the $K2$ ER spectrum with temperature T(K): a—4.2, b—30, c—80, d—100, e—140, f—180. The arrows denoted by ω_0 and ω_w relate to the $A_{n=1}$ excitonic resonance region.

spike at the ω_l frequency but of the minimum on the high-energy side of ω_0 as well, and the intensity ratio of the various ER features changes substantially too.

Note that the additional structure above 80 K in the $K1$ ER spectrum falls off rapidly in intensity and increases considerably in halfwidth. At the same time the intensity and halfwidth of this structure in the ER spectrum of sample $K2$ vary more smoothly within the temperature range studied than those of the $K1$ sample. The $K2$ sample retains the excitonic structure up to $T=180$ K, and the $K1$ sample, up to $T=200$ K.

The variations in the ER spectra of samples $K1$ and $K2$ with increasing temperature are seen to follow the same pattern, which suggests that the mechanisms responsible for the ER anomalies of the samples under study and associated with the localization of the exciton as a whole in the potential well are identical. This conclusion is supported also by the fact that the luminescence spectra of both types of anomalous crystals obtained by us undergo with increasing temperature the same stages of variation, which correlate with the changes in the ER spectra. The correlations between the reflectance and luminescence spectra will be the subject of another paper.

In order to establish the particular kind of the excitonic potential and determine the position of the excitonic resonances for the samples under study, reflectance spectra were numerically simulated for a broad variety of parameters of various model potentials. The simulation was performed by a method[13] based on multilayer approximation of the region of ESP variation (see also Refs. 10 and 14). The calculations were carried out for the $A_{n=1}$ and $B_{n=1}$ excitons. Spatial dispersion was included only for the $A_{n=1}$ excitonic state, because the ESP simulation was based on ER data in the region of the A resonance, where the spatial dispersion contribution due to the B resonance is small. The 7-nm thick native near-surface exciton-free (dead) layer was taken into account in all cases.

The model ESP was constructed under the assumption that the Se concentration decreases monotonically into the bulk through diffusion in the course of crystal growth, to vanish altogether in the $K1$ samples and to reach a certain limiting level in the $K2$ samples. Therefore the model potentials used were based essentially on a continuous ESP decaying exponentially toward the surface, which reflected the variation of gap width in accordance with the Se atom distribution in the near-surface region of the samples.

Figure 4 shows a theoretical ER spectrum, which reproduces closely the features of the $K1$ experimental ER spectrum. The ESP model used in the calculations included a region of exponentially falling-off potential and a region of a constant potential adjoining the surface. The potential represented a well 7.5 meV deep and 16 nm wide with a diffuse $CdS-CdS_{1-x}Se_x$ interface. The transition region from a solid solution to pure CdS extended over 230 nm. The model

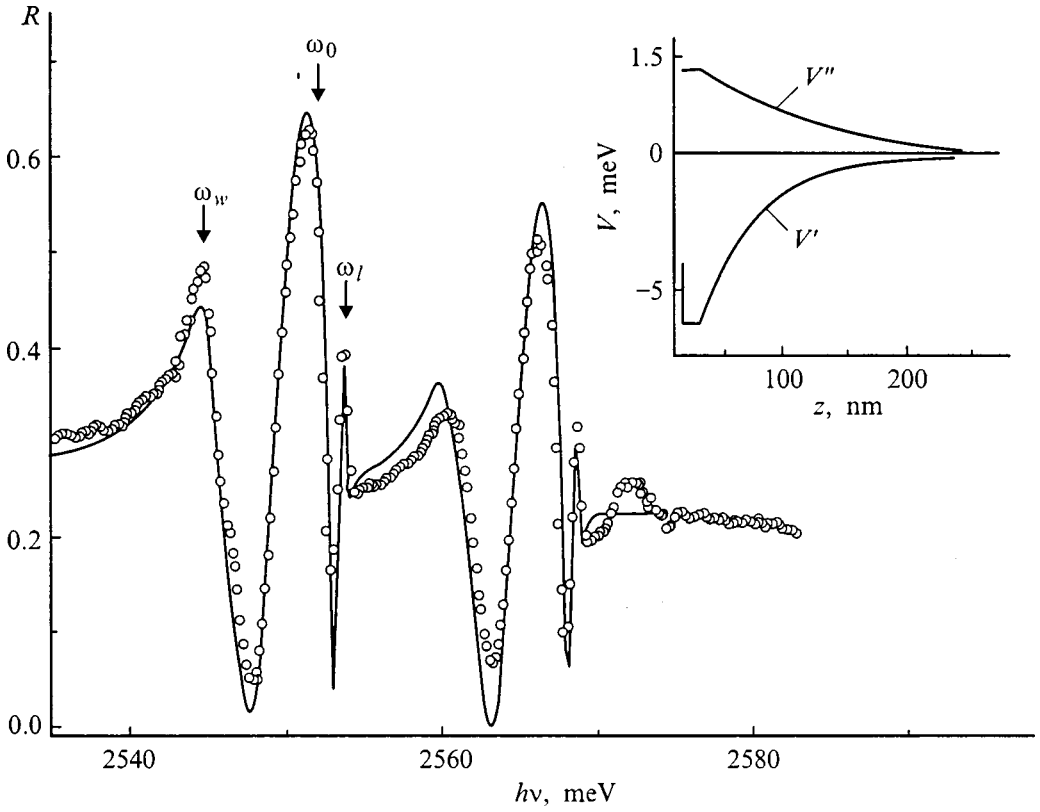

FIG. 4. Comparison of an experimental $K1$ ER spectrum with calculations. The arrows denoted by ω_l, ω_0, and ω_w relate to the $A_{n=1}$ excitonic resonance region. The inset shows coordinate dependences of the real, $V'(z)$, and imaginary, $V''(z)$, parts of the near-surface excitonic potential $V(z)$; $z=0$ is the outer boundary of the crystal.

potential-well depth coincides to a good accuracy with the gap difference between pure CdS and the $CdS_{0.99}Se_{0.01}$ solid solution on the surface of a $K1$ sample. The potential $V(z)$ (see inset in Fig. 4) was constructed using analytic expressions of the kind

$$V(z) = -V' \exp[-a'(z-z_0)] + iV'' \exp[-a''(z-z_0)],$$

$$23 < z < 253 \text{ nm},$$

$$V(z) = -V' + iV'', \quad 7 < z < 23 \text{ nm},$$

with the following parameters: $V'=7.5$ meV, $V''=1.3$ meV, $a'=0.019$, $a''=0.0056$, and $z_0=23$ nm. The potential variation region was 246 nm, and the numbers of elementary layers were $N=360$ for the exponentially decaying region, and $N=7$ for the region of constant potential. The bulk parameters used are: $\omega_0^A=2.5517$ eV, $\omega_0^B=2.56765$ eV, $\hbar\Gamma^A=0.18$ meV, $\hbar\Gamma^B=0.185$ meV, $\omega_{LT}^A=2$ meV, $\omega_{LT}^B=1.58$ meV, and $\varepsilon_0=8.5$.

To obtain an ER spectrum with characteristic features of the experimental reflectance spectrum of the $K2$ sample (Fig. 5), one used the ESP model which not only included the Se concentration variation near the sample surface but took into account the built-in surface charge as well. The surface of CdS crystals bears usually adsorbed oxygen, and its molecules, as acceptors, bind a considerable negative charge on the surface, which increases the excitonic potential because of the band upbending. The presence of a strong nonuniform electric field results in exciton ionization, which requires introduction of a damping parameter increasing rapidly toward the surface. This initiated our consideration of a potential whose region of variation consists of an increasing and a decaying subregion.

The most adequate description of the shape of the additional structure in the $K2$ spectrum and of the intensities of all ER features was provided by a model representing a 15-meV deep asymmetric potential well with a minimum at a distance of 57.7 nm from the crystal surface, whose asymptotes are a rising exponential near the crystal surface and a decaying exponential in the region adjoining the bulk of the sample. The potential $V(z)$ (see inset to Fig. 5) was constructed using an analytic expression of the form

$$V(z) = V_1' \exp[-a'(z-z_0)] + V_2' \exp[-b'(z-z_0)] + iV'' \exp[-a''(z-z_0)]$$

and the following parameters: $V_1'=398$ meV, $V_2'=-87.4$ meV, $V''=8.9$ meV, $a'=0.068$, $b'=0.023$, $a''=0.013$, and $z_0=7$ nm. The potential variation region was 420 nm wide, and the number of elementary layers $N=480$. The bulk parameters used are as follows: $\omega_0^A=2.5439$ eV, $\omega_0^B=2.5571$ eV, $\hbar\Gamma^A=0.2$ meV, $\hbar\Gamma^B=0.215$ meV, $\omega_{LT}^A=2$ meV, $\omega_{LT}^B=1.58$ meV, and $\varepsilon_0=8.5$. Note that exciton reflectance spectra in the ESP model described by a sum of two exponentials (the Morse

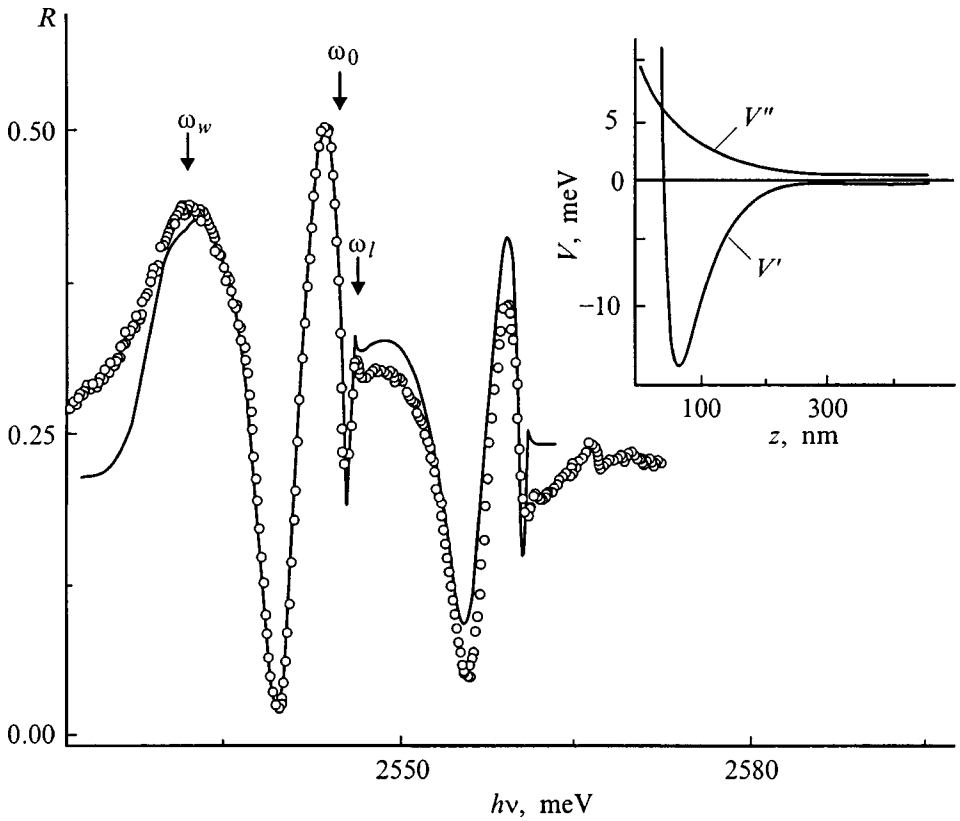

FIG. 5. Comparison of an experimental $K2$ ER spectrum with calculations. The arrows denoted by ω_l, ω_0, and ω_w relate to the $A_{n=1}$ excitonic resonance region. The inset shows coordinate dependences of the real, $V'(z)$, and imaginary, $V''(z)$, parts of the near-surface excitonic potential $V(z)$; $z=0$ is the outer boundary of the crystal.

potential) were calculated[15,16] in terms of a purely analytic representation of the potential, without using multilayer approximation[10,13,14].

As shown by a theoretical analysis of the temperature dependence of ER spectra, the gradual disappearance of the features with increasing temperature observed by us can be simulated by increasing the damping parameter in the bulk of the crystal, and the effect of this parameter turns out to be dominant.

Thus we have observed in $CdS_{1-x}Se_x$ solid solutions ($x<0.01$) anomalies in ER spectra characteristic of samples with varying composition x in the near-surface region, a phenomenon seen earlier[10] only in solid solutions close in composition to CdSe. The transformation of ER spectra with temperature was studied. ESP models have been found which provide the best fit to experimental ER spectra of samples of two types grown in different technological conditions. The ER spectra were calculated with nonlinear model ESPs reflecting the diffusion mechanism of variation of the solid solution composition near the surface of ''anomalous'' samples. The simulation revealed that the shape of the additional structure in the ER spectra of ''anomalous'' samples is very sensitive to the parameters of the near-surface potential well for excitons, and this makes possible determination of the shape and parameters of the ESP with a high accuracy. The ESP models considered in this work permit one to describe the experimentally observed ER spectra more accurately than the square potential-well ESP model proposed in Ref. 11.

The authors express gratitude to A. N. Reznitskiĭ for fruitful discussions and comments.

The work was performed by one of the authors (A. V. S.) within the RFBR Projects 96-02-16933 and 97-02-18138 and joint research with Univ. Aut. De Puebla, Centro de Ivestigaciones en Dispositivos Semiconductores (Puebla, Mexico).

[1] S. Permogorov, A. Reznitsky, V. Travnikov, S. Verbin, G. O. Müller, and M. Nikiforova, J. Lumin. **24/25**, 409 (1981).
[2] S. Permogorov, A. Reznitsky, V. Travnikov, S. Verbin, G. O. Müller, P. Flögel, and M. Nikiforova, Phys. Status Solidi B **105**, K57 (1981).
[3] S. Permogorov, A. Reznitsky, S. Verbin, G. O. Müller, P. Flögel, and M. Nikiforova, Phys. Status Solidi B **113**, 589 (1982).
[4] E. Cohen and M. D. Sturge, Phys. Rev. B **25**, 3828 (1982).
[5] Y. S. Park and D. S. Reynolds, Phys. Rev. **132**, 2450 (1963).
[6] A. N. Pikhtin, Fiz. Tekh. Poluprovodn. **11**, 425 (1977) [Sov. Phys. Semicond. **11**, 245 (1977)].
[7] S. A. Permogorov, A. N. Reznitskiĭ, and S. Yu. Verbin, Izv. Akad. Nauk SSSR, Ser. Fiz. **49**, 2019 (1985).
[8] S. Permogorov and A. Reznitsky, J. Lumin. **52**, 201 (1992).
[9] A. A. Klochikhin, S. A. Permogorov, and A. N. Reznitskiĭ, Fiz. Tverd. Tela (St. Petersburg) **39**, 1170 (1997) [Phys. Solid State **39**, 1035 (1997)].
[10] A. V. Kiselev, B. V. Novikov, and A. E. Cherednichenko, *Exciton Spectroscopy of the Near-Surface Region in Semiconductors* [in Russian] (LGU, Leningrad, 1987).
[11] A. S. Batyrev, N. V. Karasenko, B. V. Novikov, A. V. Sel'kin, and L. N. Tenishev, JETP Lett. **62**, 408 (1995).

[12] N. A. Davydova, É. N. Myasnikov, and M. I. Strashnikova, Fiz. Tverd. Tela (Leningrad) **15**, 3332 (1973) [Sov. Phys. Solid State **15**, 2217 (1973)].
[13] A. V. Sel'kin, Vestnik St. Petersburg State Univ., Geol., No. 2, 87 (1996).
[14] H. A. Coyotécatl and G. H. Cocoletzi, J. Phys.: Condens. Matter **10**, 79 (1998).
[15] F. Pérez-Rodríges and P. Halevi, Phys. Rev. B **45**, 11854 (1992).
[16] F. Pérez-Rodríges and P. Halevi, Phys. Rev. B **53**, 10086 (1995).

Translated by G. Skrebtsov

Thermo- and photostimulated depolarization in self-compensated CdF_2:Ga and CdF_2:In crystals

A. S. Shcheulin, A. K. Kupchikov, and A. I. Ryskin

Russian Research Center ''Vavilov State Optical Institute,'' 199034 St. Petersburg, Russia
(Submitted February 4, 1999)
Fiz. Tverd. Tela (St. Petersburg) **41**, 1575–1581 (September 1999)

A study is reported of the conductivity of CdF_2 semiconductor crystals doped by indium and gallium donor impurities and residing in a semi-isolated state. The latter results from self-compensation of the impurities, in the course of which one half of them creates two-electron *DX* centers, and the second is ionized. Photo- and thermostimulated depolarization of these crystals has been studied. It was shown that the observed polarization/depolarization phenomena have a nonlocal nature and are due to the charges present in these crystals changing their positions. These changes may be formally considered as charge displacement to macroscopic distances considerably in excess of the interatomic ones. The mechanisms responsible for these phenomena are discussed. © *1999 American Institute of Physics.* [S1063-7834(99)01009-6]

The present work discusses the effect and aftereffect of an external electric field on semiconductor crystals with carriers localized at sufficiently deep levels, as a result of which the crystal is in a semi-isolated state; having a low conductivity, it may thus be considered as an insulator. Such a state is characteristic, in particular, of the III–V and II–VI compounds containing *DX* centers. In such crystals, the electrons of donor impurities are localized in pairs at the impurity ions, and this process is accompanied, as a rule, by considerable lattice distortions called ''large lattice relaxation.''[1] This process leaves half of the donor centers without the valence electrons, i.e., ionized (the d^+ state). This charge distribution among the impurities (i.e., self-compensation) transfers the crystal to the semi-isolated state; indeed, because the binding energy of the *DX* center is comparatively high, the conductivity of the crystal with the valence electrons of the impurities localized at these centers turns out to be low. Such crystals become semi-insulating at a fairly low temperature T (in GaAlAs:Si, for example, for $T<50$ K). Photoexcitation of a crystal ionizing the *DX* centers at this temperature does not result in electron trapping back to the ionized (single-electron) center, because *DX*-center formation distorts strongly the lattice, which requires a substantial thermal energy. Thus light transfers the impurity centers to the ''conventional'' donor state, and the crystal acquires a conductivity that persists in the dark for a fairly long time (determined by the crystal temperature); this is the so-called persistent photoconductivity, which is the most characteristic property of crystals with *DX* centers.[2,3]

We have studied the conductivity and effect of electric field on the semi-insulating CdF_2 crystals containing Ga and In impurities. CdF_2 has the fluorite structure (O_h symmetry) and is a wide-gap ($\sim$7.8 eV) dielectric. Its structure can be presented as a sequence of fluorine cubes, in which half of the central positions are occupied by cadmium ions. It can be readily doped by Group III ions to high concentrations (provided their ionic radii differ not very strongly from that of cadmium), and the F^- ions compensating the excess impurity charge are located in interstitials, i.e., the empty central positions of the above-mentioned cubes. Such a crystal also is nonconducting. However its heating in a reducing ambient of hydrogen or metal vapors (additive coloring) results in a part or all of the fluorine ions leaving the bulk of the crystal, with their electrons becoming localized at the impurities to form a hydrogen-like donor state with a binding energy of $\sim$0.1 eV (which is much higher than the donor binding energy in typical semiconductors). As a result, the crystal acquires noticeable conductivity and becomes an *n*-type semiconductor. It is monopolar because of the absence of hole conduction in cadmium fluoride.

Two of the above impurities, namely, Ga and In, form, besides a shallow donor state ($Me^{3+}+e_{hydr}$, M=Ga, In), a deep ground state characterized by large lattice relaxation (Fig. 1). This relaxation gives rise to a potential barrier separating the metastable donor from the ground state. The barrier height for In is less than 0.1 eV, and that for Ga, of the order of 1 eV (Ref. 4) (this is the highest barrier observed in impurity centers of such type). Each of these states is associated with a broad and strong photoionization absorption band, which lies in the UV-visible region for the deep level, and for the shallow one, in the IR region.[5–7] Figure 2 illustrates a fragment of the absorption spectrum of the CdF_2:In crystal.

As shown earlier,[4,8–12] the deep state of these two impurities has a negative correlation energy and contains two electrons, i.e., it may be considered as a singly-charged M^{1+} ion. Thus it is an analog of the *DX* state in typical semiconductors and possesses all its properties. Since most of the centers transfer to the ground (deep) state, the crystal will have at a low enough temperature an equal number of *DX* centers and ionized donors (M^{3+}) for a relatively low shallow-center concentration, i.e., the crystal will become

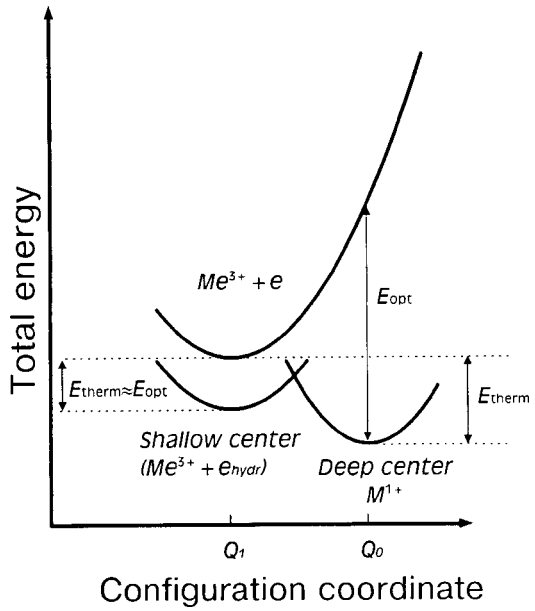

FIG. 1. Configurational diagram of a bistable center in CdF_2. The thermal and optical ionization energies are approximately equal for the shallow, and differ strongly for the deep center state.

self-compensated. Its absorption spectrum exhibits only one UV-visible band. When illuminated within this band, the deep centers will transform into the shallow ones by reaction (1):

$$M^{1+}+M^{3+}+h\nu\rightarrow 2(M^{3+}+e_{\mathrm{hydr}}), \tag{1}$$

$$2(M^{3+}+e_{\mathrm{hydr}})+kT\rightarrow M^{1+}+M^{3+}. \tag{2}$$

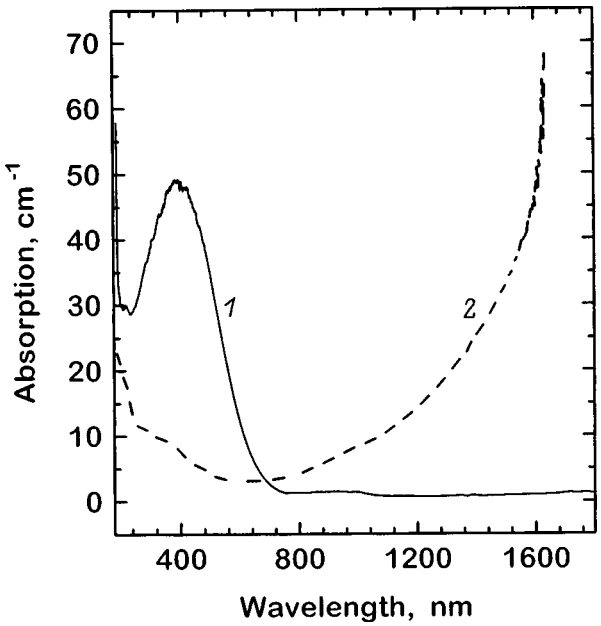

FIG. 2. A fragment of the absorption spectrum of a CdF_2:In crystal ($N_{In}=2.7\times10^{18}$ cm^{-3}) obtained at $T=5$ K (*1*) before and (*2*) after illumination in the UV-visible band. Only the short-wavelength edge of the IR absorption band, whose maximum lies around 6 μm, is shown.

As a result, the UV-visible band disappears, and an IR band appears (Fig. 2). Reactions (1) and (2) underlie the use of CdF_2:M crystals as media for reversible recording of holographic gratings.[13–16]

Being metastable, the shallow state persists indefinitely if the temperature is low enough. According to the height of the potential barriers presented above, the temperature above which rapid decay of the metastable state by reaction (2) sets in is $\sim$40 K for In and $\sim$200 K for Ga. CdF_2:Ga was shown[12] to have one more low-temperature decay channel of the metastable state, which is associated with the presence in this crystal of a second deep Ga center. This channel operates efficiently only in lightly doped CdF_2:Ga crystals. We shall not consider it in what follows, as one can easily demonstrate that its inclusion would not change the conclusions drawn from this study.

Recent calculations[17] show that the deep state of the center for both impurities is strongly distorted with respect to the corresponding fragment of the regular crystal; indeed, the impurity ion shifts in it along a fourfold axis, i.e., in the direction of the interstice, to enter the neighboring (empty) fluorine cube. Hence this state possesses a noticeable dipole moment.

As will be shown below, application of an electric field to a self-compensated CdF_2:M crystal polarizes it, which can be deduced from the generation of an electromotive force (emf) accompanying heat- or light-induced crystal depolarization. An analysis of this effect brings one to a conclusion that the polarization/depolarization of the crystal occurs through displacement of the impurity charges to macroscopic distances. Possible mechanisms of this displacement are discussed.

1. SAMPLES AND EXPERIMENTAL TECHNIQUES

The CdF_2:Ga and CdF_2:In crystals were grown by the Stockbarger–Bridgman method and additively colored in potassium vapor. The concentration N_M of the active (reduced) impurity in the crystals was derived from the absorption in the photoionization-induced absorption band of the shallow centers (see Ref. 18) and varied from 10^{16} to 5×10^{18} cm^{-3}.

The electric measurements were performed in a dc electric field. The field was applied to a parallelepiped-shaped sample measuring typically $6\times6\times2$ mm through indium contacts deposited on the broad planes. The sample was placed in an UTREX-type cryostat whose temperature could be varied from 64 to 300 K. One studied the temperature dependence of the conductivity of the crystals, their I–V curves, and depolarization kinetics. These kinetics were measured in the following way. A field of up to 500 V was applied for a long time, of the order of one hour, to the sample maintained at a fixed temperature within the 64–100-K range, and this field, as will be seen later, polarized the crystal. After this, the sample electrodes were shorted for a few seconds to remove residual static charge, and a VK2-16 voltmeter was connected to the sample to measure the potential difference across the contacts. Voltage measurements on the sample were carried out during a time from a few min to a few hours, depending on the actual relaxation

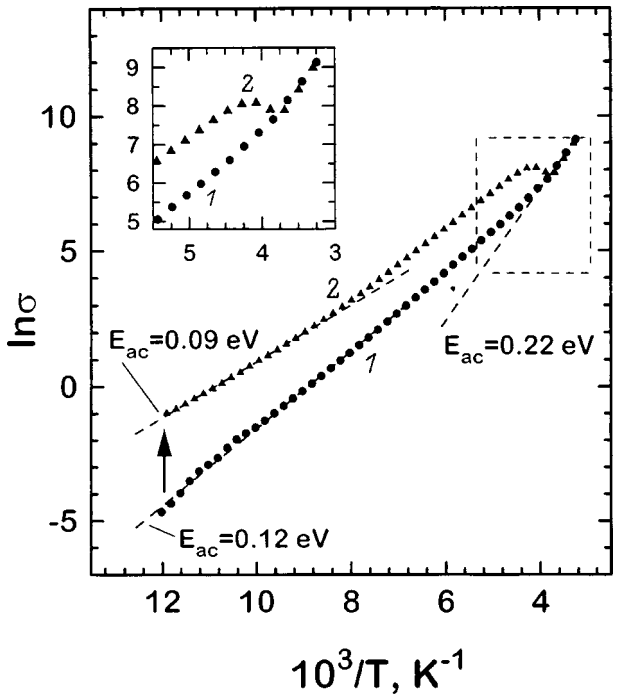

FIG. 3. Arrhenius plot for the conductivity of a CdF_2:Ga crystal ($N_{Ga} \approx 1\times10^{16}$ cm^{-3}) obtained under (*1*) slow cooling and (*2*) slow heating of a cooled crystal subjected to a short illumination. The straight lines indicate the parts of the graphs which can be assigned a certain activation energy (E_{ac}). The arrow shows the change in conductivity after the illumination. The inset presents on an enlarged scale the fragment of the graph in the dashed rectangle.

rate. The capacitance of the measuring circuit was ~280 pF.

One studied also the effect of illumination within the deep-center photoionization absorption band (300–600 nm) on the electric properties of the crystals. The illumination was made through the polished side planes of the sample.

2. EXPERIMENTAL RESULTS AND THEIR DISCUSSION

2.1. Temperature dependence of the conductivity

At room temperature, the crystals have a resistivity of 0.1 to $10^4\ \Omega\cdot$cm, depending on the type and concentration of the active impurity, and are ''good'' *n*-type semiconductors. Their *I–V* characteristics are practically linear, reversal of the applied voltage polarity does not affect their resistivity, and no delay between voltage application and the electric current is observed. Thus the contacts used may be considered ohmic to a reasonable accuracy.

An Arrhenius plot of the temperature dependence of conductivity σ reveals the presence of two activation energies for both impurities, namely, ~0.18 eV within the 300–200-K interval and 0.10 eV from 100 to 64 K for In, and 0.22 eV from 300 to 260 K and 0.12 eV within the 150–64-K region for Ga. For illustration, Fig. 3 presents an Arrhenius plot obtained for one of the CdF_2:Ga samples. Based on the results of our studies[4,11,12] of the optical spectra of these crystals and the available literature data[5–7,19], it may be conjectured that the first energy reflects for both ions the feeding by deep levels of the shallow donor levels equilibrated with the conduction band, and the second, the depth of the latter levels. Accepting this assumption and neglecting the temperature dependence of electron mobility, we obtain the following binding energies (thermal ionization energies) for the deep and shallow levels in CdF_2: 0.29 and 0.10 eV for In, and 0.34 and 0.12 eV for Ga, respectively. These values do not differ much from the ones obtained earlier in optical experiments for In [0.25 eV (Ref. 5) and 0.10 eV (Ref. 19)] and for Ga [0.39 eV (Refs. 11 and 12) and 0.12 eV (Ref. 20)]. In view of the crudeness of our assumption concerning the electron mobility, the binding energies obtained from the electrical and optical experiments may be considered, on the whole, to be in reasonable agreement.

The above analysis illustrates the electronic nature of conduction in the semiconducting cadmium fluoride, which originates from the conduction-band filling as a result of thermal ionization of the shallow donor levels.

Below 100 K, the conductivity of the crystals is low, and application of a voltage initiates in a crystal a temperature-dependent, long-lived (up to an hour) transient process, resulting in a decrease of its resistivity in time. Within this temperature region, the self-compensation of the crystals is nearly complete. Their resistivity indicates a certain population of the donor states, particularly in Ga, but even in this case most of the conduction electrons are localized at deep centers.

Illumination of a crystal in this temperature region gives rise to an enhanced long-lived dark conductivity, i.e., persistent photoconductivity, caused by photoinduced transformation of the ground to metastable state (Fig. 3; it should be stressed for clarity that by persistent photoconductivity one understands the dark conductivity generated in the crystal after its illumination). For $T<200$ K, the metastable state in CdF_2:Ga is stable, i.e., following photoinduced transformation of the deep into shallow centers the reverse thermally induced process practically does not occur.[12] The Arrhenius plot of persistent photoconductivity in this temperature region (Fig. 3) yields a slightly lower activation energy (0.09 eV) than the above value for the dark conductivity of the same crystal (0.12 eV). This is possibly due to a change in the electron mobility which we have neglected; indeed, different conditions for electron scattering in a dark and illuminated sample may produce such an effect. Above 200 K, thermal transformation of the shallow to deep centers takes place, thermal equilibrium sets in between them, and the persistent photoconductivity disappears, as evidenced by the inset in Fig. 3. Similar phenomena are observed to occur in the CdF_2:In crystal as well, but its metastable state is stable for $T<40$ K, and therefore its light-induced persistent conductivity undergoes slow relaxation within the temperature region studied.

2.2. Thermally stimulated crystal depolarization

In all the crystals studied, depolarization follows similar kinetics. After switching off of the electric field which acted on a sample for a long time and removing the static charge, the signal measured by the voltmeter rises by a close-to-exponential law, reaches a maximum, and falls off slowly (Fig. 4). The latter process reflects the voltage discharge, and

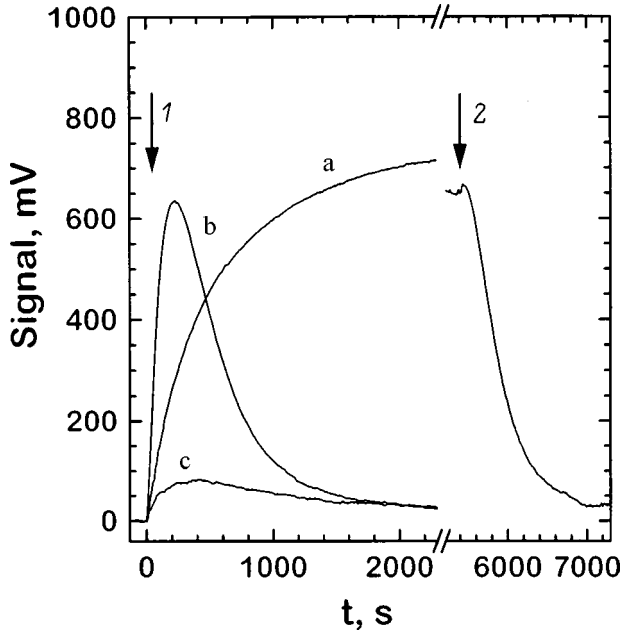

FIG. 4. (a) Thermally stimulated and (b) photostimulated depolarization signal of a CdF_2:Ga crystal ($N_{Ga} \approx 1 \times 10^{16}$ cm^{-3}) polarized in a 450-V/cm field at $T=64$ K. The arrows identify the moments of light switching: (*1*) immediately after turning on the voltmeter and (*2*) after the completion of the thermally stimulated depolarization process. Curve c shows thermally stimulated depolarization of a crystal to which the field was applied after the completion of process (b).

the large time constant of the discharge circuit determines the slow rate of decay. The amplitude and the sign of the signal depend on the magnitude and polarity of the applied field (Fig. 5). This implies that the observed response is associated with relaxation processes in the crystal subjected to the field, i.e., it reflects thermally stimulated depolarization

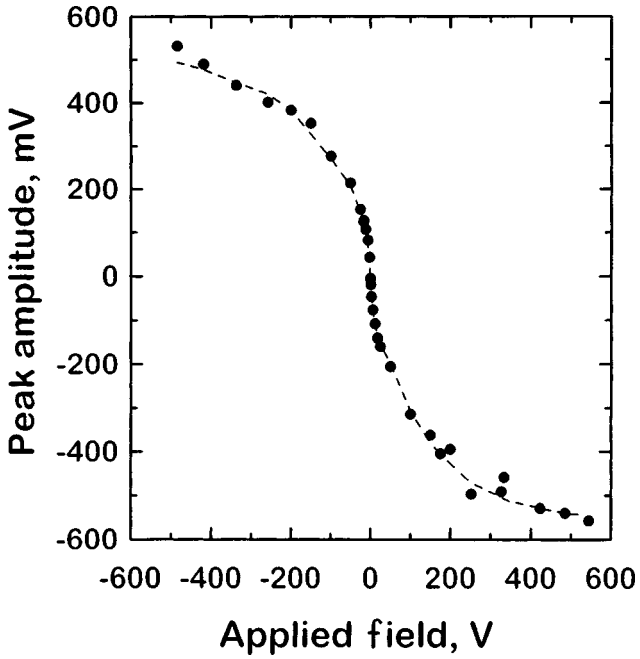

FIG. 5. Thermally stimulated depolarization signal of a CdF_2:Ga crystal ($N_{Ga} \approx 1 \times 10^{16}$ cm^{-3}) plotted against applied voltage for $T=77$ K.

of the crystal. The field polarizes the crystal, which at a low temperature is essentially an insulator. During the relaxation process, an emf acts in the crystal and generates a potential difference across the capacitor plates, and it is this difference that is measured by the voltmeter. The decay of the crystal state produced by the field can be identified with its thermally stimulated depolarization. The lower the resistivity of the sample, the shorter is the time taken by its depolarization.

The polarization of a crystal with *DX* centers may have either local or nonlocal nature. Polarization of the first type may arise as a result of the *DX* center having a dipole moment. In this case the polarization is induced by the realignment of the randomly oriented dipole moments of the deep (*DX*) centers with the field, with the degree of their orientation depending on the moment **p**, field **E**, and temperature. The field dependence of the polarization is described in this case by the Langevin function. The amplitude of the polarization signal can be written

$$U = n_p p = n_p p\left[\coth(a) - \frac{1}{a}\right], \tag{3}$$

where n_p is the total number of dipoles in the volume of the sample, p is the average projection of the dipole moment **p** on the direction of the field, and $a=(\mathbf{pE})/(kT)$.

We call nonlocal the polarization caused by the field-induced displacement (redistribution) of charges in the lattice. Assuming the field dependence of polarization to be described by the Langevin function (3), one can determine the dipole moment from experimental data if the concentration of the active centers in the crystal is known. Because the experimental relationship deviates markedly from (3) (note, in particular, the absence of saturation in the high-field domain), this procedure is unstable and permits only an estimate of the interval of possible values, $p=100-1000$ Debye. Such large values are unrealistic for a local dipole whose moment is due to a displacement of the ions in the *DX* center of the order of interatomic distances (see above) and having $p \sim 1$ Debye.

In principle, CdF_2:M crystals may have local dipoles of one more type. Additive coloring may result in an incomplete reduction of the impurity. In this case a certain amount of the F^- ions and, accordingly, the same amount of the M^{3+} ions will be left in the crystal. They can associate to form $F^- + M^{3+}$ dipole pairs. Such pairs were observed to exist, in particular, in SrF_2 crystals with fluorite structure activated by rare-earth ions.[21–23] The dipole moment of such a pair is also of the order of 1 Debye and, hence, the above qualitative considerations apply fully to such dipoles as well. That they do not contribute to thermally stimulated depolarization of CdF_2:M is supported also by the existence of photostimulated depolarization of these crystals (see below); obviously, the polarization/depolarization produced by such dipoles cannot depend on illumination.

Thus the observed polarization has a nonlocal nature and originates from charge displacement through macroscopic distances substantially in excess of the lattice constant. It appears natural to associate these charges in the CdF_2:M semi-insulating crystal with deep (*DX*) centers and ionized donors (d^+) with the charges of -1 and $+1$, respectively,

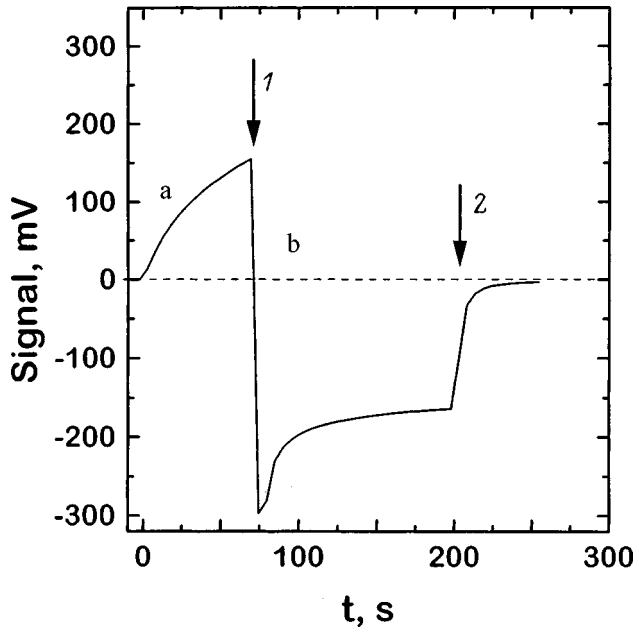

FIG. 6. (a) Thermally stimulated depolarization signal and (b) photoresponse of a CdF_2:Ga crystal ($N_{Ga}=7\times10^{17}$ cm^{-3}) polarized in a field of 210 V/cm at $T=69$ K. The arrows refer to the moments of (*1*) switching on and (*2*) switching off the illumination.

relative to the cation position. The assumption of a nonlocal character of the observed phenomena is buttressed by experimental studies of the effect of illumination on a crystal polarized by an electric field.

2.3. Photostimulated depolarization of crystals

Crystal illumination produces various effects, depending on the crystal conductivity. For high-resistivity samples with a low concentration of the active impurity, turning on the illumination immediately after the field turnoff and removal of the static charge results in a fast (on the scale of thermally stimulated depolarization phenomena) rise and decay of the response. Switching on illumination in the course of thermally stimulated depolarization produces the same effect. The later the time when the illumination is switched on, the smaller is the magnitude of the induced photoresponse, but it is always followed by a fast decay (Fig. 4). The sign of the response depends on that of the applied voltage, and this permits one to identify the response with photostimulated depolarization of the sample.

Illumination of low-resistivity (heavily doped) samples generates a very fast and saturating photoresponse, whose sign, as that of the fast response, does not depend on the polarity of the applied voltage and which thus cannot be considered to be the photostimulated depolarization signal (Fig. 6).

Consider now the effect of illumination on high-resistivity samples. Illumination ionizes deep centers, i.e., transforms them to shallow ones by reaction (1). By initiating motion of the electrons trapped by the donor ions (a hydrogen-like center is the neutral state of a donor), illumination accelerates crystal depolarization. This process develops fairly rapidly because of the considerable concentration of free electrons in a phototransformed sample exhibiting persistent photoconductivity. Thus the assumption of the sample polarization to be due to charge redistribution in an ensemble of remote donors permits one, in accordance with the concepts of photochromic transformations in CdF_2:M crystals,[4,8–12] to explain their photostimulated depolarization as well.

When an electric field is applied to a photodepolarized crystal (without switching off the illumination), one observes a weak response signal identical in shape with the photoresponse (Fig. 4). It can probably be associated with the presence in such a crystal of a residual concentration of deep centers (and, accordingly, of ionized donors).

In low-resistivity samples, the persistent photoconductivity is so high as to cause extremely fast sample depolarization, and after the transient process the sample generates an emf, i.e., it operates as a photodiode (Fig. 6). Application of an external field to a preliminarily illuminated sample initiates a large current flow through it, and switching off the voltage does not produce any response.

2.4. The mechanisms of polarization and depolarization

The above shows that the polarization of CdF_2:M crystals in an external electric field is due to charge redistribution in an ensemble of donors spaced from one another. As a result of field application, the concentration of DX centers in the region adjoining the plus contact exceeds that of the ionized donors, i.e., a space charge restricting charge transport through the contact forms in it.[24] In these conditions, this contact is no longer ohmic. A rough estimate of the thickness of the layer occupied by the space charge, based on the amplitude of the response for the given parameters of the electric circuit, yields figures varying from a few microns in heavily doped samples to fractions of a mm in lightly doped ones. The depolarization consists in a heat- or light-stimulated spreadout of the space charge.

Illumination of the crystal transfers the donors to the metastable state; in Ga it persists at the temperature of the experiment for a very long time, and in In it relaxes in times from an hour to a day, depending on the temperature. After illumination of the crystal, the efficiency of space charge formation decreases substantially (down to zero in low-resistivity samples).

Because at the temperature of the experiment the donors themselves are spatially fixed (ion motion in cadmium fluoride for $T<100$ K is impossible), the mechanisms responsible for the charge transport among them are of fundamental importance. In an illuminated crystal this mechanism is obvious. Illumination in the UV-visible band destroys the deep (DX) centers, and the photoelectrons generated in this way become trapped by ionized donors (d^+); thus charge redistribution is effected in this case by free electrons.

As for the mechanism of polarization/depolarization, it may be that free electrons are responsible for charge redistribution in this case as well, because although their number in the temperature range studied (64–100 K) is small, it is nevertheless finite. Note, however, the following contradictory point. By fitting the signal rise function with an expo-

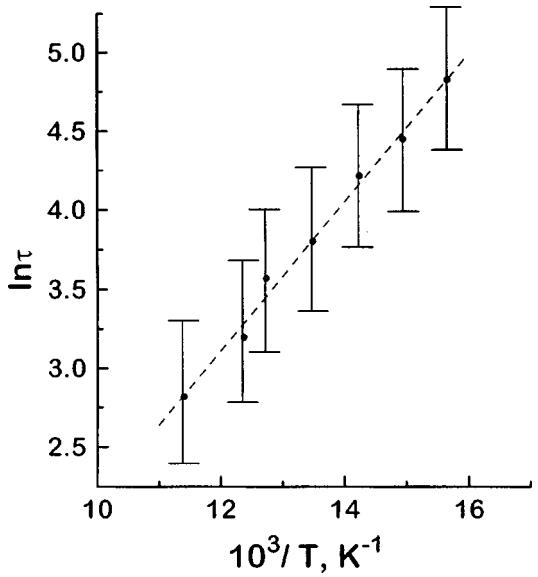

FIG. 7. Arrhenius plot for the time constant τ of the rise in the thermally stimulated depolarization signal in a CdF_2:Ga crystal ($N_{Ga} \approx 1 \times 10^{16}$ cm^{-3}).

nential and finding its time constant τ for various temperatures, one can derive from the Arrhenius plot the activation energy of the thermally stimulated depolarization process [for CdF_2:Ga, it is (0.04 ± 0.02) eV, Fig. 7]. This energy is considerably smaller than the shallow-donor binding energy (~ 0.1 eV). We cannot explain at present this controversy and have to restrict ourselves to pointing it out.

Thus the polarization/depolarization phenomena observed in this work to occur in the CdF_2 semi-isolating crystals doped with Ga or In indicate them to be of a nonlocal nature. They are due to a change in position of the charges present in such crystals, which can formally be considered as their displacements to macroscopic distances beyond the interatomic scale. Such charges in these crystals are the *DX* centers and ionized donors charged to -1 and $+1$ with respect to the cation. In the course of the polarization/depolarization processes, the charges become redistributed over the ensemble of spatially fixed, spaced donors by electronic excitations.

[1] D. J. Chadi and K. J. Chang, Phys. Rev. Lett. **61**, 873 (1988).
[2] P. M. Mooney, J. Appl. Phys. **67**, R1 (1990).
[3] D. V. Lang, in *Deep Centers in Semiconductors*, edited by S. T. Pantellides (Gordon & Breach, New York, 1986), p. 489.
[4] A. S. Shcheulin, A. I. Ryskin, J. M. Langer, and K. Swiatek, Phys. Lett. A **222**, 107 (1996).
[5] U. Piekara, J. M. Langer, and B. Krukowska-Fulde, Solid State Commun. **23**, 583 (1977).
[6] J. E. Dmochowski, W. Jantsch, D. Dobosz, and J. M. Langer, Acta Phys. Pol. A **73**, 247 (1988).
[7] J. M. Langer, Rev. Solid State Sci. **4**, 297 (1990).
[8] S. A. Kazanskii, A. I. Ryskin, and V. V. Romanov, Appl. Phys. Lett. **70**, 1272 (1997).
[9] S. A. Kazanskiĭ, A. I. Ryskin, and V. V. Romanov, Fiz. Tverd. Tela (St. Petersburg) **39**, 1205 (1997) [Phys. Solid State **39**, 1067 (1997)].
[10] A. I. Ryskin and P. P. Fedorov, Fiz. Tverd. Tela (St. Petersburg) **39**, 1050 (1997) [Phys. Solid State **39**, 943 (1997)].
[11] A. S. Shcheulin, D. E. Onopko, and A. I. Ryskin, Fiz. Tverd. Tela (St. Petersburg) **39**, 2130 (1997) [Phys. Solid State **39**, 1906 (1997)].
[12] A. I. Ryskin, A. S. Shcheulin, and D. E. Onopko, Phys. Rev. Lett. **80**, 2949 (1998).
[13] A. I. Ryskin, A. S. Shcheulin, B. Koziarska, J. M. Langer, A. Suchocki, I. I. Buczinskaya, P. P. Fedorov, and B. P. Sobolev, Appl. Phys. Lett. **67**, 31 (1995).
[14] B. Koziarska, J. M. Langer, A. I. Ryskin, A. S. Shcheulin, and A. Suchocki, Mater. Sci. Forum **196–201**, 1103 (1995).
[15] A. Suchocki, B. Koziarska, T. Langer, and J. M. Langer, Appl. Phys. Lett. **70**, 2934 (1997).
[16] A. I. Ryskin, A. S. Shcheulin, E. V. Miloglyadov, R. A. Linke, I. Redmond, I. I. Buchinskaya, P. P. Fedorov, and B. P. Sobolev, J. Appl. Phys. **83**, 2215 (1998).
[17] C. H. Park and D. J. Chadi, Phys. Rev. Lett. **82**, 113 (1999).
[18] F. Mozer, D. Matz, and S. Lyu, Phys. Rev. **182**, 808 (1969).
[19] J. M. Langer, Lect. Notes Phys. **122**, 123 (1980).
[20] J. M. Langer, T. Langer, G. L. Pearson, B. Krukowska-Fulde, and U. Piekara, Phys. Status Solidi B **66**, 537 (1974).
[21] E. L. Kitts, Jr., M. Ikeya, and J. H. Crawford, Jr., Phys. Rev. B **8**, 5840 (1973).
[22] B. P. M. Lenting, J. A. J. Numan, E. J. Bijvank, and H. W. den Hartog, Phys. Rev. B **14**, 1811 (1976).
[23] J. Fontanella, D. L. Jones, and C. Andeen, Phys. Rev. B **18**, 4454 (1978).
[24] M. A. Lampert and P. Mark, *Current Injection in Solids* (Academic, New York, 1970; Mir, Moscow, 1973).

Translated by G. Skrebtsov

The insulating and conducting crystal states. Localization and delocalization of electronic states

E. K. Kudinov

A. F. Ioffe Physicotechnical Institute, Russian Academy of Sciences, 194021 St. Petersburg, Russia
(Submitted November 6, 1998)
Fiz. Tverd. Tela (St. Petersburg) **41**, 1582–1592 (September 1999)

An *ab initio* analysis is made of the localized (in Mott's sense) and delocalized (band) states of an electron in a crystal. The criterion of a difference between these states is the behavior of the off-diagonal elements in the one-particle electronic density matrix $\langle \hat{\psi}^+(\mathbf{r})\hat{\psi}(\mathbf{r}')\rangle$ for $T=0$. Localization can be related to its exponential falloff for $|\mathbf{r}-\mathbf{r}'|\to\infty$, and delocalization, to its power-law decay. This corresponds to the analyticity of the density matrix in $\mathbf{k}$ space of the Brillouin zone in the first case, and to a singularity (Fermi step) in the second. This analyticity gives rise also to a power-law decay of the correlation functions. In a normal system, localization can be identified with the insulating state, and delocalization, with the conducting state. It is shown that the above localization criterion is applicable to disordered systems as well. Electron localization in superconductors is also discussed. It is pointed out that the above criterion of localization is met also in the BCS superconducting state and in the localized-pair model. The reason for the considerable difference between the properties of the insulating and superconducting states lies in that there are no static fluctuations in the number of electrons, $\langle(\Delta N)^2\rangle_0$, in the ground state of an insulator whereas in a superconductor ODLRO results in nonzero fluctuations of N of a quantum nature. © *1999 American Institute of Physics.* [S1063-7834(99)01109-0]

A variety of phenomena in crystals can be understood only under the assumption that, in addition to band states, a crystal can support also localized ones. For instance, it is within the assumption of the electron localization that one considers[1,2] the Mott insulator and the Mott (insulator-conductor) transition.[1)]

A long time ago, Goodenough[5] showed by a semiempirical approach that systematization of the properties of transition-metal compounds leads one inevitably to the assumption of the existence of electronic states in a crystal of two types, namely, band and localized ones.

The idea of the existence of two types of electronic states underlies the concepts of ''mixed valence'' and ''heavy fermions.''

In many cases, localized states are described in a crystal in terms of the zero-bandwidth model. However in a band model (which neglects electron interaction) infinitely narrow bands cannot be realized in principle. Therefore the problem of localized states requires taking interaction into account.

It should be pointed out that a sufficiently general definition of the notion of localization itself is still lacking; therefore, localization is usually discussed based on certain model concepts.

In principle, because of the interaction among electrons, the nature of their localization could be revealed in the course of a detailed consideration of a fairly simple model. The Hubbard model[6] has been claiming this role for a long time. However despite the apparent simplicity its proper application entails formidable mathematical difficulties. Concrete results are obtained at the expense of introducing uncontrollable assumptions, and their interpretation meets with serious obstacles.

It appears worthwhile to attempt an *ab initio* consideration of the problem of electronic localized states, without using any model concepts. It is to this approach that the present paper is dedicated. Its major objective lies in demonstrating that the analytical properties of a one-electron density matrix in $\mathbf{k}$ space are intimately related to the intuitive concept of localization and can serve as a basis for conferring a strict meaning to such notions.

The present paper should be considered a continuation of a previous paper,[7] which studied the problem of a general criterion of a difference between the conductor and insulator. (Its first section plays an auxiliary part. It uses model concepts to illustrate the properties which will subsequently be derived from general considerations.)

1. THE HARTREE APPROXIMATION. LOCALIZED AND BAND STATES

The objective of this Section is to demonstrate, based on simple model concepts, the features of the problems essential for our subsequent consideration. A number of points which would be important only for a comprehensive analysis of the models was dropped without any relevant comments.

Consider the simplest model in which the Mott insulating state can be realized. This is a periodic lattice of N ions with $N_e=N$ electrons. The field operators $\hat{\psi}^+$, $\hat{\psi}$ are chosen in the form

$$\hat{\psi}_\sigma(\mathbf{r})=\sum_{\mathbf{m}} \varphi_{\mathbf{m}}(\mathbf{r})a_{\mathbf{m}\sigma}, \tag{1}$$

where $\mathbf{m}$ is the lattice-site position vector, $\varphi_{\mathbf{m}}=\varphi(\mathbf{r}-\mathbf{m})$ is an orthonormalized set of orbitals localized at lattice sites, and $a^+_{\mathbf{m},\sigma}$, $a_{\mathbf{m},\sigma}$ are Fermi operators of creation and annihilation of an electron with spin σ at site $\mathbf{m}$. The Hamiltonian of the system can be written

$$H=H_0+W, \quad H_0=\sum_{i=1}^{N}\left(\frac{\mathbf{p}_i^2}{2m}+U(\mathbf{r}_i)\right),$$

$$W=\frac{1}{2}\sum_{i\neq j} V(\mathbf{r}_i-\mathbf{r}_j), \tag{2}$$

where $U(\mathbf{r})$ is the periodic ionic potential, and $V(\mathbf{r})$ is the Coulomb repulsion.

The basis set of the $\{\varphi_{\mathbf{m}}\}$ single-electron functions is certain to be incomplete. Therefore even if we find the exact ground state of Hamiltonian (2) in this basis [i.e. in the representation of operators (1)], its wave function Φ_0 and energy E_0 will be functionals of $\{\varphi_{\mathbf{m}}\}$. Therefore complete determination of the ground state includes also minimization of E_0 over the set of $\{\varphi_{\mathbf{m}}\}$ functions.[2)]

We shall look for the ground-state function in the form

$$\Phi_0=\prod_{\mathbf{m}} a^+_{\mathbf{m}\sigma_{\mathbf{m}}}|0\rangle=\varphi_0\{\sigma_{\mathbf{m}}\}, \tag{3}$$

where $\sigma_{\mathbf{m}}$ is the projection of the spin at site $\mathbf{m}$. Restricting ourselves to the Hartree approximation, we drop in the expression for $E_0=\langle\Phi_0|H|\Phi_0\rangle$ the exchange terms depending on the spin configuration $\{\sigma_{\mathbf{m}}\}$ to obtain

$$E_0=\sum_{\mathbf{m}}\int \varphi_{\mathbf{m}}(\mathbf{r})H_0\varphi_{\mathbf{m}}(\mathbf{r})d\mathbf{r} + \frac{1}{2}\sum_{\mathbf{m}\neq m'}\int \varphi^2_{\mathbf{m}}(\mathbf{r})\varphi^2_{\mathbf{m}'}(\mathbf{r}')V(\mathbf{r}-\mathbf{r}')d\mathbf{r}\,d\mathbf{r}'. \tag{4}$$

Minimization of E_0 with respect to $\varphi_{\mathbf{m}}$ under the condition $\int\varphi_{\mathbf{m}}\varphi_{\mathbf{m}'}d\mathbf{r}=\delta_{\mathbf{m}\mathbf{m}'}$ (we may recall that the solutions of the Hartree equations are not automatically orthogonal) yields

$$H_0\varphi_{\mathbf{m}}(\mathbf{r})+\sum_{\mathbf{m}\neq m'}\int \varphi^2_{\mathbf{m}'}(\mathbf{r}')\varphi_{\mathbf{m}}(\mathbf{r})V(\mathbf{r}-\mathbf{r}')\,d\mathbf{r}' = \Lambda_{\mathbf{m}}\varphi_{\mathbf{m}}(\mathbf{r})+\sum_{\mathbf{m}\neq m'}\Lambda_{\mathbf{m}\mathbf{m}'}\varphi_{\mathbf{m}'}(\mathbf{r}), \tag{5}$$

where $\Lambda_{\mathbf{m}}$ and $\Lambda_{\mathbf{m}\mathbf{m}'}$ are Lagrange's multipliers. We shall look for $\varphi_{\mathbf{m}}(\mathbf{r})$ in the form $\varphi(\mathbf{r}-\mathbf{m})$; then $\Lambda_{\mathbf{m}}$ does not depend on $\mathbf{m}$, and $\Lambda_{\mathbf{m}\mathbf{m}'}=\Lambda(\mathbf{m}-\mathbf{m}')$. This reduces the coupled equations (5) to one, integro-difference-differential equation. Note that as a result of the exclusion of the term with $\mathbf{m}=\mathbf{m}'$ from $\Sigma_{\mathbf{m}}$ the effective potential in (5) is not periodic; indeed, the attractive potential of ion $\mathbf{m}$ is not screened by the cloud of the electron localized at it, as is the case with the other ions. (This exemplifies Mott's concept of the electron and hole attraction, i.e. Mott localization). Obviously enough, as the lattice constant a increases, the solution of (5) will tend to the single-atom $\varphi_{0\mathbf{m}}$ function. As the ions approach one another, the above potential becomes weakened due to the screening action of the neighboring electronic clouds (the effective well becomes more shallow and narrow). For large enough a, the state will become insulating (the Mott insulator) because of the formation of a gap in the current excitation spectrum (pair + hole) initiated by the Coulomb repulsion of two electrons present at one site. The state corresponding to a minimum of energy will be 2^N-fold degenerate in spin. Taking into account exchange interaction results in a spin ordering and partial lifting of this degeneracy.

Equation (3) is not the only solution, the other being the band type. The field operators are taken in the form

$$\hat{\psi}_\sigma(\mathbf{r})=\sum_{\mathbf{k}} \psi_{\mathbf{k}}(\mathbf{k})a_{\mathbf{k}\sigma}, \tag{1a}$$

where $\mathbf{k}$ is the quasimomentum, $\psi_{\mathbf{k}}(\mathbf{k})$ are Bloch-type functions, and $\Sigma_{\mathbf{k}}$ denotes summation over the Brillouin zone (BZ). The wave function of the system is searched for in the form

$$\Phi_{0b}=\prod_{\mathbf{k}} a^+_{\mathbf{k}\uparrow}a^+_{\mathbf{k}\downarrow}, \tag{3a}$$

and the values of $\mathbf{k}$ correspond to half-filling of the BZ.

By applying variational procedure, we obtain an equation for the $\psi_{\mathbf{k}}(\mathbf{r})$ functions which, in contrast to Eq. (5), is translationally invariant

$$H_0\psi_{\mathbf{k}}(\mathbf{r})+\sum_{\mathbf{k}'}\int d\mathbf{r}'\,|\psi_{\mathbf{k}'}(\mathbf{r}')|^2V(\mathbf{r}-\mathbf{r}')\psi_{\mathbf{k}}(\mathbf{r}) = \Lambda_{\mathbf{k}}\psi_{\mathbf{k}}(\mathbf{r}). \tag{5a}$$

Thus there exist two types of the ground state for our problem, which correspond to two methods of choosing the trial wave function, namely, the state of type (3) with electrons localized at lattice sites, and that of type (3a), in which the electrons fill the BZ to one half. The solutions of the first type correspond to the Heitler-London model, and those of type two, to the Bloch model. The properties of states of the second type are adequately described by the model of noninteracting electrons, whereas for states of the first type the interaction plays a dominant role.

It is fairly obvious (and can be confirmed by a straightforward estimation) that for $a\to\infty$ state (3) is energetically preferable, and for small a, the band state (3a) is favorable. There are at least two ways in which the system can change its state and which can be interpreted as the insulator-conductor transition.

(1) In the first case, $\varphi_{\mathbf{m}}(\mathbf{r})$ decreases exponentially for $|\mathbf{r}|\to\infty$ within the region of significant values of a. Neglecting exchange effects (i.e., the lifting of spin degeneracy), state (3) can be conveniently described by a density matrix representing a mixture of all 2^N equally weighted spin configurations

$$\rho_0=2^{-N}\sum_{\{\sigma_{\mathbf{m}}\}}\langle 0|\prod_{\mathbf{m}} a^+_{\mathbf{m}\sigma_{\mathbf{m}}}\ldots\prod_{\mathbf{m}} a^+_{\mathbf{m}\sigma_m}|0\rangle \tag{6}$$

(the mean value of the $\hat{A}$ operator is obtained if one substitutes $\hat{A}$ for the dots). In state (6), the only means of the a^+,a products that are nonzero are those which contain, besides $a_{\mathbf{m}\sigma}$, also $a^+_{\mathbf{m}\sigma}$, with

$$\langle n_{\mathbf{m}\sigma}\rangle_0=\frac{1}{2},\quad \langle n_{\mathbf{m}\uparrow}n_{\mathbf{m}\downarrow}\rangle_0=0,\quad (n_i=a_i^+a_i). \tag{7}$$

The insulating state (3) and (6) is realized if it corresponds to a minimum in energy; for instance, in this case the formation of pairs consisting of an electron with quasimomentum $\mathbf{k}$ and a hole with $\overline{\mathbf{k}}$ must be unfavorable. The normalized density matrix of such an (excited) state $\rho_1(\mathbf{k}\overline{\mathbf{k}})$ state is obtained from Eq. (6) through replacements

$$\prod_{\mathbf{m}} a^+_{\mathbf{m}\sigma_{\mathbf{m}}}\to 2a^+_{\mathbf{k}\sigma}a^-_{\overline{\mathbf{k}}\sigma'}\prod_{\mathbf{m}} a^+_{\mathbf{m}\sigma_{\mathbf{m}}}, \tag{8}$$

$$a_{\mathbf{k}\sigma}=N^{-1/2}\sum_{\mathbf{m}} e^{i\mathbf{k}\mathbf{m}}a_{\mathbf{m}\sigma_{\mathbf{m}}}.$$

Using ρ_0, ρ_1 in an explicit form, we find that the ρ_1 energy exceeds E_0 by

$$\Delta E(\mathbf{k},\overline{\mathbf{k}})=\frac{1}{2}[\varepsilon(\mathbf{k})-\varepsilon(\overline{\mathbf{k}})]+\frac{U}{2},$$

$$\varepsilon(\mathbf{k})=\sum_{\mathbf{g}} J(\mathbf{g})e^{i\mathbf{k}\mathbf{g}}, \tag{9}$$

where

$$J(\mathbf{g})=\int \varphi_{\mathbf{m}}H_0\varphi_{\mathbf{m}+\mathbf{g}}d\mathbf{r},$$

$$U=\int \varphi^2_{\mathbf{m}}(\mathbf{r})\varphi^2_{\mathbf{m}}(\mathbf{r}')V(\mathbf{r}-\mathbf{r}')d\mathbf{r}d\mathbf{r}', \tag{10}$$

and U is the Hubbard energy. $\Delta E(\mathbf{k}\overline{\mathbf{k}})$ has a minimum at the value of $\mathbf{k}$ corresponding to min $\varepsilon(\mathbf{k})$ and at $\mathbf{k}$, corresponding to max $\varepsilon(\mathbf{k})$. Because $\Sigma_{\mathbf{k}}\varepsilon(\mathbf{k})=0$, min $\varepsilon(\mathbf{k})=-\varepsilon_0<0$, and max $\varepsilon=\varepsilon_1>0$, which yields the condition for min E_0

$$\min\Delta E=\Delta E_0=-\frac{\varepsilon_0+\varepsilon_1}{2}+\frac{U}{2}>0. \tag{11}$$

This is the well-known condition for a positive gap in the current excitation spectrum of the Mott insulator (within the Hubbard model). Let the quantity ΔE_0 vanish in a compressed crystal at a certain $a=a_c$, to become subsequently $\Delta E_0<0$ for $a<a_c$. This implies an instability of the insulating state for $a<a_c$, which should be reflected in the thermodynamic criterion of stability, namely, for $a<a_c$ the isothermal compressibility $\partial P/\partial V$ (for $T=0$) becomes positive (a change in a gives rise to a change in V, i.e. a_c corresponds to V_c). For $V<V_c$ ($a<a_c$), the system transfers in a jump to a stable phase with a lower energy; this also implies that for a certain $V>V_c$ the phases will have equal energies, thus signaling a conventional first-order transition without an order parameter[3)] (with a possibility of existence of a critical point where the transition is continuous). In these conditions, the final phase may turn out to be either conducting or insulating.

(2) The second case assumes the possibility of a continuously varying pattern of decay of the solution to Eq. (5) with varying a. It may turn out that as a decreases to become $a<a_c$, the exponential character of the decay will be smoothly replaced by a power law, with the condition of stability left unchanged. There are grounds to expect (we shall see it later) that a power-law decline of the wave function $\tilde{\varphi}_{\mathbf{m}}(\mathbf{r})$ of such a state corresponds to a conducting (or an intermediate between the insulating and conducting) state of the crystal. One should then expect the onset of a continuous insulator-conductor transition, with its features being pronounced weaker than those of a second-order transition. This case cannot be described in terms of the standard Hartree method, because the self-consistent potential in Eq. (5) has always a Coulombic tail $\sim|\mathbf{r}|^{-1}$. There are here an infinite number of bound states and, hence, the solution to (5) corresponding to the lowest energy will always decay exponentially. To describe it, one would have to modify the Hartree method so as to include screening. The above reasoning is essentially a modified account of Mott's consideration. Accepting its arguments for the avalanche nature of such a transition, one may conclude that in a general case such a smooth transition is impossible and can be realized only in the form of a critical point.

We shall present now expressions for a single-particle density matrix contracted in spin indices for the cases considered above. For the state described by the density matrix (6)

$$\rho(\mathbf{r}\mathbf{r}')=\sum_{\sigma}\langle\hat{\psi}^+_{\sigma}(\mathbf{r})\hat{\psi}_{\sigma}(\mathbf{r}')\rangle=\sum_{\sigma\mathbf{m}}\langle n_{\mathbf{m}\sigma}\rangle_0\varphi_{\mathbf{m}}(\mathbf{r})\varphi_{\mathbf{m}}(\mathbf{r}')$$

$$=\sum_{\mathbf{m}}\varphi_{\mathbf{m}}(\mathbf{r})\varphi_{\mathbf{m}}(\mathbf{r}'). \tag{12}$$

For state (3a) (case 1):

$$\rho(\mathbf{r}\mathbf{r}')=\sum_{\mathbf{k};k<k_c}\psi^*_{\mathbf{k}}(\mathbf{r})\psi_{\mathbf{k}}(\mathbf{r}'),$$

$$\psi_{\mathbf{k}}(\mathbf{r})=N^{-1/2}\sum_{\mathbf{m}} e^{i\mathbf{k}\mathbf{m}}\varphi_{\mathbf{m}}(\mathbf{r}). \tag{13}$$

For case (2), $V<V_c$

$$\rho(\mathbf{r}\mathbf{r}')=\sum_{\mathbf{m}}\tilde{\varphi}_{\mathbf{m}}(\mathbf{r})\tilde{\varphi}_{\mathbf{m}}(\mathbf{r}'). \tag{14}$$

There is an essential difference in the behavior of $\rho(\mathbf{r}\mathbf{r}')$. In state (6), $\rho(\mathbf{r}\mathbf{r}')$ falls off exponentially for $|\mathbf{r}-\mathbf{r}'|\to\infty$. In state (3a) and in case (2), ρ decreases by a power law [this follows from the nonanaliticity of $n(\mathbf{k})$ in Eq. (13) and a power-law decline of $\tilde{\varphi}_{\mathbf{m}}$ in Eq. (14)].

Thus a model analysis shows that:

(1) In a general case, the insulator-conductor transformation is a first-order transition accompanied by a loss of thermodynamic stability of the electronic system (case 1). A continuous transition (case 2) can take place only in the vicinity of a critical point;

(2) The electronic states in an insulator are localized (exponential decrease of $\varphi_{\mathbf{m}}$), Eqs. (3) and (6), and in a

conductor they are delocalized, Eq. (3a). This difference becomes reflected also in the behavior of the single-electron density matrix for $|\mathbf{r}-\mathbf{r}'|\to\infty$. (One can readily verify that higher-order density matrices

$$\langle \hat{\varphi}^+_{\sigma_1}(\mathbf{r}_1)\hat{\varphi}^+_{\sigma_2}(\mathbf{r}_2)\ldots\hat{\varphi}_{\sigma'_1}(\mathbf{r}'_1)\hat{\varphi}_{\sigma'_2}(\mathbf{r}'_2)\ldots\rangle \tag{15}$$

exhibit a similar difference in the asymptotic behavior for $|\mathbf{r}_i-\mathbf{r}_k|\to\infty$).

2. ELECTRONIC ONE-PARTICLE DENSITY MATRIX OF A CRYSTAL

We shall accept the above-mentioned exponential decay of the one-particle electronic density matrix for $|\mathbf{r}-\mathbf{r}'|\to\infty$, which occurs in Mott's insulator model, to be the main characteristic of the localized state in an electronic system. Accordingly, a power-law falloff of this matrix will be considered as an indicator of delocalization. A trivial illustration of the above is provided by the density matrices of the bound electronic state and of the continuous spectrum in an atom.[4)]

Consider a one-electron density matrix folded with the spin variable[5)]

$$\rho_0(\mathbf{r}\mathbf{r}')=\sum_\sigma \langle \hat{\psi}^+_\sigma(\mathbf{r})\hat{\psi}_\sigma(\mathbf{r}')\rangle. \tag{16}$$

We shall assume ρ_0 to be normalized to the total number of electrons N_e,

$$\int \rho_0(\mathbf{r}\mathbf{r})d\mathbf{r}=N_e. \tag{17}$$

The matrix $\rho_0(\mathbf{r}\mathbf{r}')$, as any particle density matrix, is an Hermitian matrix with nonnegative eigenvalues. The eigenfunctions ψ and eigenvalues n satisfy a homogeneous linear integral equation with a kernel $\rho_0(\mathbf{r}\mathbf{r}')$

$$\int \rho_0(\mathbf{r}\mathbf{r}')\psi(\mathbf{r}')d\mathbf{r}'=n\psi(\mathbf{r}), \quad n\geqslant 0. \tag{18}$$

The ground-state density matrix of a crystal is invariant under crystal symmetry-group transformations. It can be decomposed in eigenfunctions[4]

$$\rho_0(\mathbf{r}\mathbf{r}')=\sum_{\mathbf{k}\alpha} n_\alpha(\mathbf{k})\psi_{\mathbf{k}\alpha}(\mathbf{r})\psi^*_{\mathbf{k}\alpha}(\mathbf{r}'), \tag{19}$$

where

$$\psi_{\mathbf{k}\alpha}(\mathbf{r})=e^{i\mathbf{k}r}u_{\mathbf{k}\alpha}(\mathbf{r}), \quad \sum_{\mathbf{k}\alpha} n_\alpha(\mathbf{k})=N_e,$$

$\psi_{\mathbf{k}\alpha}$ is a Bloch-type function, α is a ''band'' index; generally speaking, the number of terms in Σ_α (the number of ''bands'') is infinite[6)], $\mathbf{k}$ is a quasiwave vector, and $\Sigma_\mathbf{k}$ denotes summation over the BZ. We write the $\hat{\psi}_\sigma(\mathbf{r})$ operator in the basis of the $\psi_{\mathbf{k}\alpha}$ functions, $\hat{\psi}_\sigma(\mathbf{r})=\Sigma_{\mathbf{k}\alpha}\psi_{\mathbf{k}\alpha}a_{\mathbf{k}\alpha\sigma}$. A comparison of ρ_0 in Eqs. (16) and (19) shows that $n_\alpha(\mathbf{k})=\Sigma_\sigma\langle a^+_{\mathbf{k}\alpha\sigma}a_{\mathbf{k}\alpha\sigma}\rangle$, i.e. that $n_\alpha(\mathbf{k})$ has the meaning of the average number of electrons in a state with given $\mathbf{k},\alpha$. Because a^+,a are Fermi operators, $0\leqslant n_\alpha(\mathbf{k})\leqslant 2$, and therefore the strongest nonanalyticity in $n_\alpha(\mathbf{k})$ can be a first-order discontinuity (a Fermi step). Because the kernel in Eq. (18) has the full symmetry of the system, the symmetry properties of $n_\alpha(\mathbf{k})$ are the same as those of the one-electron energy $\varepsilon_\alpha(\mathbf{k})$ in the band theory, and the quantities $n_\alpha(\mathbf{k})$ and $u_{\mathbf{k}\alpha}$ are periodic in $\mathbf{k}$ space with the period of the reciprocal lattice.

Consider first the case of a low-symmetry crystal, where all the ''bands'' are nondegenerate. Let all $n_\alpha(\mathbf{k})$ and $u_{\mathbf{k}\alpha}$ in Eq. (19) be analytic as functions of $\mathbf{k}$ along the real axis. Then one can maintain that $\rho_0(\mathbf{r}\mathbf{r}')$ decreases exponentially for $|\mathbf{r}-\mathbf{r}'|\to\infty$. Indeed, transferring in Eq. (19) to the Wannier functions

$$\varphi_{\mathbf{m}\alpha}=N^{-1/2}\sum_\mathbf{k} e^{i\mathbf{k}\mathbf{m}}\psi_{\mathbf{k}\alpha}(\mathbf{r}), \tag{20}$$

we obtain

$$\rho_0(\mathbf{r}\mathbf{r}')=\sum_{\alpha\mathbf{m}\mathbf{m}'} S_\alpha(\mathbf{m}-\mathbf{m}')\varphi_{\mathbf{m}\alpha}(\mathbf{r})\varphi_{\mathbf{m}'\alpha}(\mathbf{r}'),$$

$$S_\alpha(\mathbf{m})=N^{-1}\sum_\mathbf{k} n_\alpha(\mathbf{k})e^{i\mathbf{k}\mathbf{m}}. \tag{21}$$

If $u_{\mathbf{k}\alpha}$ is analytic in $\mathbf{k}$ (which is always true for a nondegenerate band), then the Wannier function $\varphi_{\mathbf{m}\alpha}$ decreases exponentially for $r\to\infty$ (to be exact, faster than any power of r^{-1}, Ref. 9). The proof of this statement is based essentially on the analyticity of $u_{\mathbf{k}\alpha}$ as a function of $\mathbf{k}$ (see Appendix 1). One can readily verify that $S_\alpha(\mathbf{m})$ likewise falls off exponentially for $|\mathbf{m}|\to\infty$.[7)]

However if for some α the $n_\alpha(\mathbf{k})$ function has a discontinuity at a surface in $\mathbf{k}$ space, the decrease of ρ for $|\mathbf{r}-\mathbf{r}'|\to\infty$ will follow a power-law course (as $|\mathbf{r}-\mathbf{r}'|^{-2}$).

Thus localization of electronic states can be identified with the analyticity of the occupancies $n_\alpha(\mathbf{k})$, and delocalization, with their nonanalyticity.

If the ''bands'' are degenerate (either as a result of crystal symmetry or for some arbitrary reason), the $n_\alpha(\mathbf{k})$ and $u_{\mathbf{k}\alpha}$ quantities, being functions of $\mathbf{k}$, have singularities of the type of branch points at the ''band'' contacts. Therefore the Wannier functions decay in this case not exponentially but rather by a power law, and some terms in Eq. (19) have such singularities.

Nevertheless it can be shown that in the case where the problem has, besides such singularities, no other singularities in $\mathbf{k}$,[8)] their contributions will cancel after the summation over α in Eq. (19). This relates in full measure to the similar sums [for instance, to $\Sigma_\alpha n_\alpha(\mathbf{k})$] where the summation is performed over a group of bands joining at a point $\mathbf{k}_c$ (usually it is the $\mathbf{k}_c=0$ point), which corresponds to maximum symmetry[9)] (see Appendix 2). As a result, the expressions

$$\sum_\alpha n_\alpha(\mathbf{k})\psi_{\mathbf{k}\alpha}(\mathbf{r})\psi^*_{\mathbf{k}\alpha}(\mathbf{r}'),$$

$$\sum_\alpha \psi_{\mathbf{k}\alpha}(\mathbf{r})\psi^*_{\mathbf{k}\alpha}(\mathbf{r}'), \quad \sum_\alpha n_\alpha(\mathbf{k}) \tag{22}$$

turn out to be single-valued analytic functions of **k**. As shown in Appendix 2, $\rho(\mathbf{r}\mathbf{r}')$ decays faster than any power of $|\mathbf{r}-\mathbf{r}'|^{-1}$ for $|\mathbf{r}-\mathbf{r}'|\to\infty$, similar to the nondegenerate case.

We see that all singularities originating only from crystal symmetry do not affect in any way the exponential character of the asymptotic behavior of the single-electron density matrix. Therefore the above-formulated localization criterion is equivalent to the statement that in a localized state the single-particle ground-state density matrix in **k** representation [i.e., the quantity $\rho(\mathbf{k})=\Sigma_\alpha n_\alpha(\mathbf{k})$] is analytic in **k**, and the $n_\alpha(\mathbf{k})$ quantities themselves do not have singularities except those which are due to degeneracy.

The asymptotic decay of $\rho(\mathbf{r}\mathbf{r}')$ will follow a power-law behavior, and the state of an electronic system will be delocalized, if any of the $n_\alpha(\mathbf{k})$ functions has as a function of **k** singularities other than those caused by degeneracy.

All this boils down to the statement that Mott localization means smearing of the Fermi step. (Note that in the ground state of a nonideal gas, $n(\mathbf{k})$ has always a singularity $\sim k^{-\gamma}$, $0<\gamma<2$ for a Bose gas (pp. 228–237 in Ref. 10) and a ''step'' for a Fermi gas.[11]

3. EXAMPLES

3.1. Band model

The ground-state density matrix $\rho_0(\mathbf{r}\mathbf{r}')$ in the band model is a particular case of Eq. (19), where $n_\alpha(\mathbf{k})$ are equal either to 2 (filled band), or to $2\theta[\mu_0-\varepsilon_\alpha(\mathbf{k})]$, which is a Fermi step (partial filling, μ_0 is the chemical potential for $T=0$), or to zero.

If all bands are nondegenerate and all $n_\alpha(\mathbf{k})$ are either 2 or 0, then all $n_\alpha(\mathbf{k})$ are analytic in **k** throughout the BZ, and one can show, as this is done in Appendix 1, that $\rho_0(\mathbf{r}\mathbf{r}')$ falls off exponentially for $|\mathbf{r}-\mathbf{r}'|\to\infty$. In the case of degenerate bands, the decay will be exponential if all joining branches are filled. Therefore in the cases under consideration, which correspond to a band insulator, the localization criterion is met.

If the bands are partly filled (band-theory conductor), the decay assumes a power-law form $\sim|\mathbf{r}-\mathbf{r}'|^{-2}$. If in the degenerate case part of the branches are empty and the other part is filled (this may happen if all states on one branch lie energywise higher than the states of the other, except the contact point), the nonanalyticities do not cancel, and the decay, while following a power law, is faster than that for a band conductor, $\sim|\mathbf{r}-\mathbf{r}'|^{-3}$. It appears only natural, because such a state (it is frequently called a gapless second-order semiconductor) occupies an intermediate position between an insulator and a conductor; indeed, an arbitrarily small strain creates a Fermi step.

3.2. The Hubbard model

Consider the Hubbard model for the case where the number of electrons N_e is equal to that of lattice sites N. Its Hamiltonian can be written

$$H=\sum_{\mathbf{m},\mathbf{g}\sigma} Ja^+_{\mathbf{m}+\mathbf{g}\sigma}a_{\mathbf{m}\sigma}+\frac{K}{2}\sum_{\mathbf{m}\sigma} n_{\mathbf{m}\sigma}n_{\mathbf{m}-\sigma}. \tag{23}$$

The summation over **m** is performed here over lattice sites, and over **g**, over the nearest neighbors; $\sigma=\uparrow,\downarrow$ is the spin index, J is the transfer integral between the nearest neighbors, and $K>0$ characterizes the one-site Coulomb repulsion. Straightforward Hubbard decoupling [Hubbard I (Ref. 6)] yields the following expression for $n(\mathbf{k})$ for $T=0$

$$n(\mathbf{k})=\sum_\sigma \langle a^+_{\mathbf{k}\sigma}a_{\mathbf{k}\sigma}\rangle=1+\frac{\varepsilon(\mathbf{k})}{\sqrt{\varepsilon(\mathbf{k})^2+K^2}}. \tag{24}$$

Here

$$a_{\mathbf{k}\sigma}=\frac{1}{\sqrt{N}}\sum_{\mathbf{m}} e^{i\mathbf{k}\mathbf{m}}a_{\mathbf{m}\sigma},\quad \varepsilon(\mathbf{k})=J\sum_{\mathbf{g}} e^{i\mathbf{k}g}.$$

One can easily verify that the normalization condition $\Sigma_{\mathbf{k}}n(\mathbf{k})=N$ for Eq. (24) holds. The $n(\mathbf{k})$ function is analytic and periodic with a period of the reciprocal lattice for real **k** (although it has branch points in the complex region). Therefore a state is localized (in our sense) for any real parameters J and K.

In the case $N_e\neq N$, a Fermi-step-type singularity appears in $n(\mathbf{k})$, which makes the state delocalized.

4. DISORDERED SYSTEMS

The localization criterion introduced above was based on the asymptotic behavior of the density matrices in coordinate representation (16), is essentially not connected to translational invariance, and has a meaning for disordered systems as well. However a straightforward application of matrix (16) to particular cases is inconvenient. Therefore a transition to expansion (19) was made for translationally invariant systems, which made possible reformulation of the above criterion in terms of the analytic properties of the characteristics of the system in **k** space.

Expansion (19) was based on quasimomentum conservation in a translationally invariant system. In a disordered system, however, there can be no symmetry elements (we assume that one of the fundamental properties of a disordered system of noninteracting particles is nondegeneracy of all orbital states in a simply connected sample of a finite size), and it might seem at first glance that there is in this case no other way except direct use of Eq. (16).

Nevertheless, there is a law of conservation of total current throughout the sample cross section in steady state in a disordered system as well. Because the total current through any cross section in a simply connected system is zero, current states may be realized only in a multiply connected sample. One can introduce a quantum number similar to the momentum by imposing certain boundary conditions and assuming the bulk properties to be independent of these conditions (as an example of this may serve cyclic boundary conditions). (We shall restrict ourselves to an analysis of a three-dimensional case, because low-dimensional cases are fairly specific.)

Consider the Schrödinger equation for an electron in an arbitrary external dc field $U(\mathbf{r})$.

$$\frac{\hat{\mathbf{p}}^2}{2m}\psi(\mathbf{r})+U(\mathbf{r})\psi(\mathbf{r})=\varepsilon\psi(\mathbf{r}). \tag{25}$$

We shall look for complex solutions to this equation in the form

$$\psi(\mathbf{r})=f(\mathbf{r})e^{i\chi(\mathbf{r})}, \tag{26}$$

with real $f(\mathbf{r})$ and $\chi(\mathbf{r})$. Inserting (26) into Eq. (25) yields

$$-\frac{\hbar^2}{2m}(\nabla^2 f-(\nabla\chi)^2 f)+Uf=\varepsilon f, \tag{27}$$

$$f\nabla^2\chi+2\nabla\chi\nabla f\equiv\frac{1}{f}\,\mathrm{div}\,\mathbf{j}=0,\quad \mathbf{j}=f^2\nabla\chi. \tag{28}$$

Here $\mathbf{j}(\mathbf{r})$ has the meaning of the current vector.

Let us choose a parallelepiped-shaped region of volume V with edges L_x, L_y, and L_z, and assume the opposite faces to be identical to make it a three-dimensional thorus. We also impose the following conditions on f and the phase χ:

$$f(x+L_x,y+L_y,z+L_z)=f(x,y,z), \tag{29}$$

$$\chi(x+L_x,y+L_y,z+L_z)=\chi(x,y,z)+2\pi(s_x+s_y+s_z), \tag{30}$$

where s_x, s_y, s_z are three arbitrary integers, i.e. after traveling around the torus, a multiple of 2π is added to the phase χ. [Condition (30) can be interpreted as the existence of vortex lines, which pass through the torus ring holes corresponding to the x, y, z directions, and in traveling around which the χ function is incremented by $2\pi s_x$, $2\pi s_y$, $2\pi s_z$, respectively). Equation (30) can be conveniently recast in the form

$$\chi(\mathbf{r})=\overline{\chi}(\mathbf{r})+\mathbf{kr}, \tag{31}$$

where $\overline{\chi}(\mathbf{r})$ is a single-valued function [i.e., a function obeying boundary conditions of the type (29)], and $\mathbf{k}$ is a vector with components $2\pi(s_x/L_x, s_y/L_y, s_z/L_z)$. Equations (27) and (28) together with boundary conditions (29) and (30) determine, in principle, the eigenvalues and eigenfunctions $\varepsilon(\mathbf{k})$ and $\psi_{\mathbf{k}}(\mathbf{r})$ for all values of $\mathbf{k}$. The latter eigenfunctions can be written[10)]

$$\psi_{\mathbf{k}}(\mathbf{r})=e^{i\mathbf{kr}}u_{\mathbf{k}}(\mathbf{r}), \tag{32}$$

where the modulating factor $u_{\mathbf{k}}(\mathbf{r})\equiv\exp[i\overline{\chi}(\mathbf{r})]f(\mathbf{r})$ is a bounded function of $\mathbf{r}$ in volume V and possesses the property of ''macroscopic homogeneity,'' which means that the integral $\int_{\Delta V}|u|^2 d\mathbf{r}$ taken over a macroscopic volume $\Delta V \ll V$ does not depend on the position of ΔV within V. (Obviously enough, the Bloch multiplier $u_{\mathbf{k}\alpha}$ in band theory possesses the same property.)

Because the eigenfunctions (32) are complex, to each state corresponds a $\mathbf{k}$-dependent current density (28). Note that the total current through the cross section which reduces the connectivity of the region by unity is conserved. [One can envision these functions as obtained from the free-particle $\exp(i\mathbf{kr})$ states as a result of an adiabatic switching-on of the $U(\mathbf{r})$ potential under boundary conditions (29) and (30). In this case to each value of $\mathbf{k}$ corresponds only one solution.] As a result of time reversal invariance, each state with $\mathbf{k}\neq 0$ is doubly degenerate. If $\psi_{\mathbf{k}}(\mathbf{r})$ is the solution to Eq. (25), then $\psi^*_{\mathbf{k}}(\mathbf{r})\equiv\psi_{-\mathbf{k}}(\mathbf{r})$ is also a solution to Eq. (25) with the same energy.

Note that the condition of orthogonality for the pair of functions $\psi_{\mathbf{k}}$, $\psi^*_{\mathbf{k}}$ is not automatically satisfied. The reason for this lies in that the quantum number $\mathbf{k}$ is not an eigenvalue of any conserved operator. Therefore this pair should be orthogonalized, which is always possible. (For the same reason the $\mathbf{k}$ vector is not conserved in elementary processes.)

We finally obtain an orthonormalized system of eigenfunctions of Eq. (25), which can be used in describing the properties of the equilibrium state of the system under consideration.

A disordered system also can support localized solutions $\varphi_\gamma(\mathbf{r})$ (γ is a quantum number characterizing the localization point), which decay exponentially with distance. Obviously enough, the conserved current associated with them is always zero. Such states are nondegenerate.

It is natural to conjecture that localized states occupy the lower part of the energy spectrum, with delocalized states of the type (26) lying higher up. Assuming the solutions to Eq. (25) to be exhausted by these two types, we see that the state of a system of noninteracting electrons will be localized in our sense, if the Fermi level does not reach the energy boundary separating the two types of states (the mobility edge), and delocalized, if the Fermi level lies in the band of delocalized states.

Similar to the way this was done in Sect. 2, one can expand the one-electron ground-state density matrix of the system with interaction in the set of functions of the above two types

$$\rho_0(\mathbf{rr}')=\sum_\gamma n_\gamma\varphi_\gamma(\mathbf{r})\varphi^*_\gamma(\mathbf{r}')+\sum_{\mathbf{k}} n(\mathbf{k})e^{i\mathbf{k}(\mathbf{r}-\mathbf{r}')}u_{\mathbf{k}}(\mathbf{r})u^*_{\mathbf{k}}(\mathbf{r}'). \tag{33}$$

While the first term on the right side always decays exponentially for $|\mathbf{r}-\mathbf{r}'|\to\infty$, the second term, as before, falls off exponentially if $n(\mathbf{k})$ and $u_{\mathbf{k}}$ are analytic functions of $\mathbf{k}$.[11)]

Note that the above consideration did not include configurational averaging (the approach of Edwards[13]), which is usually invoked in such problems. Generally speaking, this averaging is not physically necessary, because it is simply a calculational technique which facilitates obtaining concrete results. At the same time it is capable of distorting substantially the asymptotic behavior of the density matrix.

5. SUPERCONDUCTIVITY

In the BCS model of superconductivity, the expression for the one-particle electronic ground-state density matrix written in the single-band Bloch approximation has the form

$$\langle \psi_\sigma^+(\mathbf{r})\psi_{\sigma'}(\mathbf{r}')\rangle = \frac{1}{2V}\sum_{\mathbf{k}} \langle a_{\mathbf{k}\sigma}^+ a_{\mathbf{k}\sigma'}\rangle e^{i\mathbf{k}(\mathbf{r}-\mathbf{r}')} = \delta_{\sigma\sigma'}\frac{1}{2V} \times \sum_{\mathbf{k}} \frac{\sqrt{(\varepsilon(\mathbf{k})-\mu)^2+\Delta_{\mathbf{k}}^2}-(\varepsilon(\mathbf{k})-\mu)}{\sqrt{(\varepsilon(\mathbf{k})-\mu)^2+\Delta_{\mathbf{k}}^2}} \times e^{i\mathbf{k}(\mathbf{r}-\mathbf{r}')}, \quad (34)$$

where $\Sigma_{\mathbf{k}}$ denotes summation over the first Brillouin zone. We assume that the band energy $\varepsilon(\mathbf{k})$ and the gap $\Delta_{\mathbf{k}}$ are analytic and periodic (with the reciprocal-lattice period) functions of $\mathbf{k}$, and $\Delta_{\mathbf{k}}$ does not vanish on the Fermi surface (for the sake of simplicity, we assume it to be constant). Thus at $T=0$ the onset of ODLRO results in disappearance of the Fermi singularity because of its moving to the complex region, and $n(\mathbf{k})$ is an analytic function on the real axis.[12] Thus one can maintain that the density matrix under consideration decays exponentially as $|\mathbf{r}-\mathbf{r}'|\to\infty$.

We transform the BCS ground-state wave function

$$\Phi_0 = \prod_{\mathbf{k}} (u_{\mathbf{k}} + v_{\mathbf{k}} a_{\mathbf{k}\uparrow}^+ a_{-\mathbf{k}\downarrow}^+)|0\rangle, \quad (35)$$

$$u_{\mathbf{k}}^2 = \frac{1}{2}\frac{\sqrt{(\varepsilon(\mathbf{k})-\mu)^2+\Delta^2}+\varepsilon(\mathbf{k})-\mu}{\sqrt{(\varepsilon(\mathbf{k})-\mu)^2+\Delta^2}},$$

$$v_{\mathbf{k}}^2 = \frac{1}{2}\frac{\sqrt{(\varepsilon(\mathbf{k})-\mu)^2+\Delta^2}-\varepsilon(\mathbf{k})+\mu}{\sqrt{(\varepsilon(\mathbf{k})-\mu)^2+\Delta^2}},$$

in the following way:

$$\Phi_0 = \prod_{\mathbf{k}} u_{\mathbf{k}} \exp\left(\frac{v_{\mathbf{k}}}{u_{\mathbf{k}}} a_{\mathbf{k}\uparrow}^+ a_{-\mathbf{k}\downarrow}^+\right)|0\rangle = \left(\prod_{\mathbf{k}} u_{\mathbf{k}}\right)\exp\left(\sum_{\mathbf{k}} \frac{v_{\mathbf{k}}}{u_{\mathbf{k}}} a_{\mathbf{k}\uparrow}^+ a_{-\mathbf{k}\downarrow}^+\right)|0\rangle. \quad (36)$$

We next transfer in the sum over $\mathbf{k}$ in the exponential to the $a_{\mathbf{m}}^+$ operators in the Wannier representation

$$a_{\mathbf{k}\sigma}^+ = \frac{1}{\sqrt{N}}\sum_{\mathbf{m}} e^{i\mathbf{k}\mathbf{m}} a_{\mathbf{m}\sigma}^+,$$

where $\mathbf{m}$ is the lattice site vector. The argument of the exponential in Eq. (36) can be transformed as

$$\hat{R} \equiv \sum_{\mathbf{k}} \frac{v_{\mathbf{k}}}{u_{\mathbf{k}}} a_{\mathbf{k}\uparrow}^+ a_{-\mathbf{k}\downarrow}^+ = \sum_{\mathbf{m}\mathbf{m}'} S(\mathbf{m}-\mathbf{m}') a_{\mathbf{m}\uparrow}^+ a_{\mathbf{m}'\downarrow}^+,$$

$$S(\mathbf{m}) = \sum_{\mathbf{k}} \frac{v_{\mathbf{k}}}{u_{\mathbf{k}}} e^{i\mathbf{k}\mathbf{m}}. \quad (37)$$

Because $v_{\mathbf{k}}$ and $u_{\mathbf{k}}$ depend on $\mathbf{k}$ only through $\varepsilon(\mathbf{k})$, we have $S(-\mathbf{m})=S(\mathbf{m})$, and therefore $\hat{R}$ can be recast in the form

$$\hat{R} = \sum_{\mathbf{m}} \hat{R}(\mathbf{m}),$$

$$\hat{R}(\mathbf{m}) = \frac{1}{2}\sum_{\mathbf{g}} S(\mathbf{g})(a_{\mathbf{m}\uparrow}^+ a_{\mathbf{m}-\mathbf{g}\downarrow}^+ + a_{\mathbf{m}-\mathbf{g}\uparrow}^+ a_{\mathbf{m}\downarrow}^+), \quad (38)$$

which permits one to rewrite the BCS wave function

$$\Phi_0 = \left(\prod_{\mathbf{k}} u_{\mathbf{k}}\right)\prod_{\mathbf{m}} \exp(\hat{R}_{\mathbf{m}}|0\rangle. \quad (39)$$

Note that the operator form $a_{\mathbf{m}\uparrow}^+ a_{\mathbf{m}-\mathbf{g}\downarrow}^+ + a_{\mathbf{m}-\mathbf{g}\uparrow}^+ a_{\mathbf{m}\downarrow}^+$ is a spin singlet. The quantity $v_{\mathbf{k}}/u_{\mathbf{k}}$ is an analytic function in $\mathbf{k}$ space, and therefore $S(\mathbf{g})$ decays exponentially for $|\mathbf{g}|\to\infty$. Hence the weights of the $a_{\mathbf{m}-\mathbf{g}\sigma}^+$ operators decrease exponentially as one moves away from the central site $\mathbf{m}$. The argument of the exponential is determined by the imaginary part of the coordinate of the branch point in the $u_{\mathbf{k}}$ and $v_{\mathbf{k}}$ quantities, and in the BCS model is equal to the Cooper pair radius $\sim \hbar v_F/\Delta$ (v_F is the velocity on the Fermi surface). We now move (formally) Δ to infinity (from the physical standpoint this means that the coupling constant is large compared to the gap width) under the condition that the equations for the chemical potential and for the gap function Δ are satisfied (we drop here some trivial manipulations). In this limit, only the term with $\mathbf{g}=0$ will be left in the sum over $\mathbf{g}$ in the expression for $\hat{R}(\mathbf{m})$, and the normalized wave function will take on the form

$$\Psi_0 = \prod_{\mathbf{m}} (u + v a_{\mathbf{m}\uparrow}^+ a_{\mathbf{m}\downarrow}^+)|0\rangle, \quad (40)$$

$$u = \frac{1}{2}\sqrt{1-n}, \quad v = \frac{1}{2}\sqrt{n}, \quad n = \frac{N_e}{N}.$$

(Such a state was considered in Ref. 14). The wave function Ψ_0 is constructed of the localized functions $\varphi_{\mathbf{m}}(\mathbf{r})$. For $n=2$, it transforms to

$$\prod_{\mathbf{m}} (a_{\mathbf{m}\uparrow}^+ a_{\mathbf{m}\downarrow}^+)|0\rangle, \quad (41)$$

which is the ground-state wave function of a band insulator (with a completely filled band). The (39), (40), and (41) functions, as well as the Mott insulator wave function (3), have similar structures; namely, they form as a result of action on the vacuum state of the operator product $\Pi_{\mathbf{m}}\hat{A}_{\mathbf{m}}$. The $\hat{A}_{\mathbf{m}}$ operator is a sum of the products of the Fermi creation operators $a_{\mathbf{n}\sigma}^+$ for an electron in a localized orbital state $\varphi_{\mathbf{n}}$ at site $\mathbf{n}$ with a spin σ; the weight of these states is maximum when $\mathbf{n}$ is close to $\mathbf{m}$ and decreases exponentially as $|\mathbf{n}-\mathbf{m}|\to\infty$. The $\hat{A}_{\mathbf{m}+\mathbf{m}'}$ operator is obtained from $\hat{A}_{\mathbf{m}}$ by translation of all site indices by $\mathbf{m}'$.

For the wave function (3), the $\hat{A}_{\mathbf{m}}$ operator reduces to the $a_{\mathbf{m}\sigma_{\mathbf{m}}}^+$ operator, and for (41) it is the product $a_{\mathbf{m}\uparrow}^+ a_{\mathbf{m}\downarrow}^+$, i.e. these operators create a one- and a two-electron state at a site, respectively. In the (40) case, the $\hat{A}_{\mathbf{m}}$ operator creates at a site a state representing a quantummechanical superposition of the vacuum and two-electron states. It can be conceived as a vacuum-''diluted'' state (41). In the case of (39), the operator creates a state which is a superposition of states with any even number of electrons, but the electronic density remains concentrated around the site because of the above-mentioned exponential decay. Thus in all the cases we have considered, the one-particle density matrix decreases exponentially for $|\mathbf{r}-\mathbf{r}'|\to\infty$.

Note that the state (40) can be realized only under the assumption that the kinetic energy in the Hamiltonian of the system may be neglected. For this reason, the charge transfer mechanism does not operate here, i.e., despite the presence of OLDRO, such a system is an insulator. However because it is the onset of OLDRO that determines the temperature of the superconducting transition, in some problems dealing with superconductivity one can sacrifice the possibility of describing current states for simplification of the model.

The above considerations give one grounds to maintain that the onset of superconducting state (at least within the models studied here) is associated with localization of the electronic state of the system.

6. DISCUSSION OF RESULTS

(1) The definition of localization of an electronic state in a crystal proposed above has been formulated as the property of analyticity of the one-particle ground-state density matrix in **k** space.

By prescribing the initial one-particle electronic Green's function[13] $G_0(\mathbf{r}\mathbf{r}',t-t')$ [which is directly connected to the initial one-particle density matrix $\rho_0(\mathbf{r}\mathbf{r}')$] and the interaction Hamiltonian λV, one fully determines the perturbative series in λ. One can maintain that, in the region of convergence of this series in parameter λ, all singularities in the characteristics of the system under consideration will originate from those in the initial function (as well as from those in V, for instance, from the Coulomb singularity), and no other singularities can appear.[14] If the initial functions are analytic in (quasi)momentum, one may expect that space correlators of the type of $\langle A(\mathbf{r})B(\mathbf{r}')\rangle$ will approach for $|\mathbf{r}-\mathbf{r}'|\to\infty$ their limiting values by an exponential law $\exp(-\eta|\mathbf{r}-\mathbf{r}'|)$, $\eta>0$.

(2) In our opinion, the above definition is in accord with the purely intuitive idea of localization and is in full agreement with the criterion of the difference between a conductor and insulator, which was proposed[7] earlier and is based on the absence (insulator) or presence (conductor) of the field effect (i.e., expulsion of the electric field from the volume of the conductor). The latter was associated with the nature of statistical fluctuations $p=V^{-1}\langle d_x^2\rangle$ of the electronic dipole moment **d** in the ground state of the system, which are normal $\lim_{V\to\infty}p<\infty$ (insulator) or anomalous $\lim_{V\to\infty}p=\infty$ (conductor). The above exponential behavior of the space correlators accounts for the normal character of dipole-moment fluctuations in localized state.

Thus electron localization in a normal system results in the onset of the insulating, and delocalization, of the conducting state.

(3) By means of cyclic boundary conditions one can introduce a parameter **k** similar to the wave vector in the case of disordered systems as well. By invoking the particle-current conservation law, it is possible to extend the above considerations to disordered systems.

(4) The localization of the electronic state in a superconductor (Sec. 5) might seem somewhat unexpected. However the formation of a gap in the BCS superconducting state inevitably brings about disappearance of the Fermi singularity and of the analyticity in **k** of all functions of the problem. In our opinion, the disappearance of the Fermi singularity in the superconducting state is a more fundamental aspect of this transition than the gap formation, which is one of possible realizations of the mechanism by which the singularity can be destroyed. For instance, the local-pair model[14] or the bipolaron model[15] do not contain any analog of the BCS gap at all, because they start not with the Fermi gas state but rather with the Paulion gas (the term ''boson'' adopted in the literature does not appear quite adequate).

(5) The above consideration, in our opinion, offers a satisfactory answer to the question that was discussed heatedly in the years following the publication of the BCS paper, namely, what is the difference between the insulating and superconducting gap? As pointed out by us in Ref. 7, the difference consists in that in an insulator (as in any other system in the absence of ODLRO) the rms fluctuation $\langle\Delta N^2\rangle_0$ of the number of electrons N in the ground state is zero, and this provides the above-mentioned ''normality'' of the dipole fluctuations. At the same time in the superconducting state, as a result of a breakdown of the conservation of the total number of electrons (which is a consequence of the OLDRO) fluctuations (of the quantum nature!) in N occur in the ground state as well (indeed, in the BCS model $\langle\Delta N^2\rangle_0=4\Sigma_{\mathbf{k}}u_{\mathbf{k}}^2v_{\mathbf{k}}^2$). Note that the existence of quantum fluctuations in the number of electrons in a ground-state superconductor is essentially equivalent to the statement of realization of ODLRO and, in our opinion, is more revealing.

The possibility of forming charged layers at sample boundaries in a superconductor, which are required for the field effect to appear, is particularly well demonstrated in the local-pair model (40); indeed, the u and v coefficients can vary smoothly in the vicinity of the boundary, as a result of which a vanishingly small electric field inside a sample is screened completely. This is a direct consequence of the ''vacuum dilution'' (i.e., ODLRO) mentioned in Sect. 5. In the Mott insulator (3) this is impossible, because here the charge on a site can change only through creation of pair-hole complexes, a process requiring a finite excitation energy.

(6) We note in conclusion that crystallization from a liquid (or gas) state can be interpreted as localization of a state of an atomic system in the above sense (as disappearance of the Fermi or Bose singularity; in actual fact, crystallization takes place at temperatures substantially above the degeneracy point, except, possibly, in quantum crystals). It can be shown that the presence of a singularity results in an anomalous response to shear stresses (similar to the field effect in conductors), and its absence, in a normal shear response.

APPENDIX A

1. We shall show that, in a nondegenerate case, the Wannier function $\varphi_{\mathbf{m}}(\mathbf{r})$ tends to zero for $|\mathbf{r}-\mathbf{r}'|\to\infty$ faster than any power of $|\mathbf{r}|^{-1}$. One can write the following expressions relating the Bloch factor $u_{\mathbf{k}}(\mathbf{r})$ to the Wannier function

$$\frac{1}{\sqrt{N}}\sum_{\mathbf{m}} e^{-i\mathbf{k}(\mathbf{r}-\mathbf{m})}\varphi_{\mathbf{m}}(\mathbf{r})=u_{\mathbf{k}}(\mathbf{r}). \tag{A1}$$

The $\psi_{\mathbf{k}}(\mathbf{r})$ and $\varphi_{\mathbf{m}}(\mathbf{r})$ functions are normalized to unity, so that

$$\int_{v_0}|u|^2 d\mathbf{r}=\frac{1}{N}$$

(here v_0 is the unit-cell volume; obviously enough, $u_{\mathbf{k}} \sim N^{-1/2}$). Next we integrate both sides of equality (A1) over the volume V of the system (assuming the boundary conditions to be cyclic). After some manipulations we obtain the equality ($\varphi_0 \equiv \varphi_{\mathbf{m}}|_{\mathbf{m}=0}$)

$$\frac{1}{\sqrt{N}}\int_V e^{-i\mathbf{kr}}\varphi_0(\mathbf{r})d\mathbf{r}=\int_{v_0} u_{\mathbf{k}}(\mathbf{r})d\mathbf{r}. \tag{A2}$$

(It is easy to see that the left- and right-hand parts of this equality are of the same order in N.) Integration on the left side of the equality is performed over the whole volume V (with a subsequent transition to the $V\to\infty$ limit), and on the right-hand side, over the unit cell. If the band is nondegenerate, the $u_{\mathbf{k}}(\mathbf{r})$ function is analytic for all real $\mathbf{k}$, and, hence, the right side of (A2) is analytic too.

On the left side, the integrand contains a dependence on $\mathbf{k}$ in the exponential $e^{-i\mathbf{kr}}$ and, because the V volume is finite, the left side is also analytic for real $\mathbf{k}$. Let us fix the $\mathbf{k}$ direction in (A2) by presenting $\mathbf{k}$ in the form $\mathbf{k}=k\mathbf{e}$, $\mathbf{e}^2=1$. Next we continue both parts of Eq. (A2) to the complex region by replacing k with $k+i\delta$. Because the singularities always lie at a finite distance from the manifold on which the function is analytic, one can choose δ so small that the right and, hence, the left parts of (A2) will not leave the analyticity region. Then Eq. (A2) takes on the form

$$\frac{1}{\sqrt{N}}\int_V e^{(-ik+\delta)\mathbf{er}}\varphi_0(\mathbf{r})d\mathbf{r}=\int_{v_0} u_{(k+i\delta)\mathbf{e}}(\mathbf{r})d\mathbf{r}. \tag{A3}$$

For a fixed δ, the left side tends for $V\to\infty$ to a finite value due to Eq. (A3). Because for the integral on the left side of Eq. (A3) there always exists a region $\delta\mathbf{er}>0$ within which the exponential under the integral sign increases, the above implies that $\varphi_0(\mathbf{r})$ must decrease faster than any power of $|\mathbf{r}|^{-1}$ for $\mathbf{r}\to\infty$ in order to cancel this increase. Note that Eq. (A3) implies also the reverse statement, namely, if $\varphi_0(\mathbf{r})$ decreases exponentially, then $u_{k\mathbf{e}}$ is an analytic function of k on the real axis and in its neighborhood.

2. Consider the relation

$$M(\mathbf{k},\mathbf{rr}')=\sum_{\alpha} n_{\mathbf{k}\alpha}u^*_{\mathbf{k}\alpha}(\mathbf{r})u_{\mathbf{k}\alpha}(\mathbf{r}').$$

Using Eq. (A1), express $u_{\mathbf{k}\alpha}(\mathbf{r}')$ through $\varphi_{\mathbf{m}}$:

$$\sum_{\alpha} n_{\mathbf{k}\alpha}u^*_{\mathbf{k}\alpha}(\mathbf{r})u_{\mathbf{k}\alpha}(\mathbf{r}')$$

$$=\sum_{\alpha} n_{\mathbf{k}\alpha}u^*_{\mathbf{k}\alpha}(\mathbf{r})\frac{1}{\sqrt{N}}\sum_{\mathbf{m}} e^{-i\mathbf{k}(\mathbf{r}'-\mathbf{m})}\varphi_{\alpha}(\mathbf{r}'-\mathbf{m}).$$

After integrating both parts of this equality over $\mathbf{r}'$ within the volume V and some manipulations similar to those used to transfer from (A2) to (A3), we come to

$$\sum_{\alpha} n_{\mathbf{k}\alpha}u^*_{\mathbf{k}\alpha}(\mathbf{r})\int_{v_0} u_{\mathbf{k}\alpha}(\mathbf{r}')d\mathbf{r}'$$

$$=\sum_{\alpha} n_{\mathbf{k}\alpha}u^*_{\mathbf{k}\alpha}(\mathbf{r})\frac{1}{\sqrt{N}}\int_V e^{-i\mathbf{kr}'}\varphi_{\alpha}(\mathbf{r}')d\mathbf{r}'.$$

If the $M(\mathbf{k},\mathbf{rr}')$ expression is an analytic function of $\mathbf{k}$ on the real axis, it can be shown, as before, that for a fixed $\mathbf{r}$ the quantity M tends to zero for $|\mathbf{r}-\mathbf{r}'|\to\infty$ faster than any power of $|\mathbf{r}'|$.

APPENDIX B

Consider the problem of diagonalization of an Hermitian matrix B_{ik} of order n

$$\sum_k B_{ik}C_k=\Lambda C_i, \tag{B1}$$

where $\mathbf{C}\equiv\{C_i\}$ is the eigenvector, and Λ is the eigenvalue.

Let all B_{ik} be analytic and single-valued functions of variable x on the whole real axis. The solution of the problem is n eigenvectors $\mathbf{C}_\alpha$ and n eigenvalues Λ_α, and the latter are the solutions of an nth-degree algebraic equation, whose coefficients are analytic functions of x on the real axis. The eigenvalues and eigenvectors will be analytic functions of x at all points of the real axis, except the degeneracy points, where two (or more) eigenvalues coincide; at these points the eigenvalues and eigenvectors have singularities of the type of branch points.

We transfer to the complex plane $z=x+iy$ and make cuts going from points on the real axis to infinity. On making an analytic continuation of $\Lambda(x)$ to the complex plane, we present the $\Lambda(z)$ function as an analytic function which is single valued on an n-sheeted Riemann's surface with the above cuts, with the degeneracy points being now the branch points of the corresponding order. Next we label accordingly the n branches of the $\Lambda(z)$ function and n sheets of the Riemann surface and establish a one-to-one correspondence between them. It will readily be seen that as one travels around a branch point, the n sheets will undergo a certain permutation.

Consider the expression

$$\Phi(x)=\sum_{\alpha=1}^{n} F(\Lambda_\alpha(x)), \tag{B2}$$

where $F(v)$ is an arbitrary analytic function of v. Analytic continuation yields $\Phi(z)=\Sigma_{\alpha=1}^{n}F[\Lambda_\alpha(z)]$, where the summation is performed over all branches of the $\Lambda(z)$ function. The quantity $\Phi(z)$ does not change under permutation of the branches. In view of the above, one may conclude that this function does not change when traveling around any branch point of the $\Lambda(z)$ function, i.e., that when summed over all branches the contributions due to different branch points cancel. Therefore any function of the type $\Phi(x)$ is single

valued and analytic at any point on the real axis and, hence, within a certain band containing the real axis.

Let $k<n$ branches of the $\Lambda(z)$ function assume the same value at point z_0. Then the same reasoning will lead us to the statement that a sum similar to (B2) but in which the summation is performed only along the specified branches is a single-valued function of z within a finite neighborhood of point z_0. As before, we fix the direction of the **k** vector, $\mathbf{k}=k\mathbf{e}$, in Eqs. (22) and consider k in place of x. All these expressions are seen to have the form of (B2), whence it follows that they have no branch points. Because the degeneracy in a crystal can be only two- and threefold (two- and fourfold if spin-orbit interaction is taken into account), only two or three bands can come in contact. One readily sees that as one goes around the branch points, only the bands in contact undergo permutation, and therefore the associated singularities will cancel in the expressions of the type (22) when summed already only over these bands.

Note that in concrete problems one meets usually a ''degenerate'' case, where the band contact point is a point of ''nonsingle-valuedness'' of the type of $\sqrt{z^2}$ rather than that of branching.

[1)]Long before Mott (1936), localized states were used by Shubin and Vonsovskiĭ[3] in their ''polar model of a metal,'' which was subsequently developed also by Bogolyubov.[4]

[2)]In many problems only the type of the basis functions and not their actual form is essential, and therefore such minimization is usually disregarded. This procedure becomes, however, necessary when considering fundamental problems. A lack of proper understanding of the need of such procedure in the BCS era resulted in discussions concerning gauge invariance.

[3)]It was shown[7] that in the conducting state there is an anomalously fluctuating variable, namely, the dipole moment of the electronic system $\mathbf{d}=-e\Sigma\mathbf{r}_i$, where $\mathbf{r}_i$ is the coordinate of the ith electron. Indeed, for $T=0$ the quantity $V^{-1}\langle d_x^2\rangle$ has an order $V^{1/3}$, whereas the onset of an order parameter requires V^1.

[4)]A recent communication[8] proposes a criterion for the insulating nature of a state, which is essentially similar to the one given above. The authors of Ref. 8 limit themselves to an analysis of some particular model without claiming a general *ab initio* treatment. Note that in Ref. 8 the insulating nature of a state is identified with localization, which, as this will be shown below, is not always right.

[5)]Here and in what follows, we neglect spin-orbit interaction. It will become clear later on that its inclusion would not affect the main results of this work. Because we are interested in the properties connected with the charge, which is a spin invariant, one can restrict oneself to the spin-invariant part of the density matrix.

[6)]Finiteness of the number of ''bands'' would mean incompleteness of the set of kernel eigenfunctions $\rho_0(\mathbf{r}\mathbf{r}')$ (kernel degeneracy), whence it would follow that the ground-state wave function is a linear combination of products of an incomplete set of single-electron functions. This is possible only for special model Hamiltonians, among which is the band-model Hamiltonian.

[7)]This follows from the well-known relation of the behavior of the Fourier coefficients for $n\to\infty$ to singularities of the expanded function.

[8)]We should rather have said, no other singularities for real **k**; as for singularities for complex **k** (such a singularity, $\sqrt{[\varepsilon(\mathbf{k})-\mu]^2+\Delta^2}$, appears in the BCS model!), they do not alter in any way the conclusion to be drawn below.

[9)]Because the multiplicity of degeneracy can be only 2 or 3 (2 or 4 if the spin-orbit coupling is taken into account), such groups consist of two or three ''bands.''

[10)]The $\psi_{\mathbf{k}}(\mathbf{r})$ functions actually coi ncide with the functions introduced by Anderson in his pioneering work[12] on ''dirty'' superconductors. However the **k** parameter was not introduced in Ref. 12 in an explicit form.

[11)]This can be readily verified if, on setting a fixed direction $\mathbf{r}-\mathbf{r}'=R\mathbf{e}$ and $\mathbf{e}^2=1$, and directing the z axis along **e**, one performs integration by parts as $\exp(ik_zR)dk_z=(iR)^{-1}d\exp(ik_zR)$. All terms of this expansion in R^{-1} vanish.

[12)]When analyzing the equation for $\Delta_{\mathbf{k}}$, one usually simplifies the calculations by truncating the effective potential in momentum space, i.e. by introducing a singularity which does not exist in the real problem. We naturally ignore such singularities. The only singularity that we take into account is the Fermi step in normal state at $T=0$.

[13)]There can be naturally more than one seed Green's function; for instance, when taking into account electron-phonon interaction, one should add the phonon function.

[14)]All these considerations do not naturally relate to the approach of Edwards.[13]

[1] N. F. Mott, *Metal-Insulator Transition* (Taylor & Francis, 1990).
[2] N. F. Mott, Philos. Mag. **6**, 287 (1961).
[3] S. P. Shubin and S. V. Vonsovskii, Proc. R. Soc. London, Ser. A **445**, 149 (1934).
[4] N. N. Bogolyubov, *Lectures on Quantum Statistics, Selected Works*, Vol. 2 [in Russian] (Naukova Dumka, Kiev, 1971).
[5] J. B. Goodenough, *Magnetism and the Chemical Bond* (Wiley, New York, 1963).
[6] J. C. Hubbard, Proc. R. Soc. London, Ser. A **276**, 238 (1963); *ibid.* **277**, 237 (1964); *ibid.*; **281**, 401 (1964).
[7] E. K. Kudinov, Fiz. Tverd. Tela (Leningrad) **33**, 2306 (1991) [Sov. Phys. Solid State **33**, 1299 (1991)].
[8] R. Resta and S. Sorella, cond-mat/9808151.
[9] E. J. Blount, *Solid State Physics*, Vol. 13 (Academic, New York, 1963).
[10] N. N. Bogolyubov, *Quasi-Means in Statistical Mechanics Problems, Selected Works*, Vol. 2 [in Russian] (Naukova Dumka, Kiev, 1971).
[11] J. M. Luttinger and J. C. Ward, Phys. Rev. **118**, 1417 (1960).
[12] P. W. Anderson, J. Phys. Chem. Solids **11**, 26 (1962).
[13] S. F. Edwards, Philos. Mag. **3**, 1020 (1958).
[14] E. K. Kudinov, Fiz. Tverd. Tela (Leningrad) **31**, No. 6, 14 (1989) [Sov. Phys. Solid State **31**, 922 (1989)].
[15] A. S. Aleksandrov, Zh. Fiz. Khim. **57**, 273 (1983).

Translated by G. Skrebtsov

Thermal defect formation in undoped and Cr- and Mn-doped $Bi_{12}SiO_{20}$ crystals

T. V. Panchenko and L. M. Karpova

Dnepropetrovsk State University, 320625 Dnepropetrovsk, Ukraine
(Submitted November 12, 1998)
Fiz. Tverd. Tela (St. Petersburg) **41**, 1593–1596 (September 1999)

The thermally stimulated depolarization currents and the temperature dependences of optical absorption are investigated. Interaction processes between defects are observed. A model consisting of association–dissociation of quasidipoles in the form of donor–acceptor pairs with a distribution of activation energies and relaxation times is proposed. © *1999 American Institute of Physics.* [S1063-7834(99)01209-5]

Defects of thermal origin strongly influence the properties of photorefractive $Bi_{12}SiO_{20}$ crystals (BMO, where M $=$Si, Ge, Ti).[1–7] Vacuum annealing increases the dark and photoconductivity,[1] it transforms the optical absorption, photoconductivity, and photo- and thermal luminescence spectra,[2–4] and it intensifies the photogalvanic effect.[5] The oxygen vacancies formed are associated with complex BiO_7 ions, since annealing is accompanied by diffusion and reduction of Bi ions.[3,4]

Annealing in oxygen after vacuum annealing restores the initial properties. This reversibility indicates that the processes leading to the formation and vanishing of oxygen vacancies are important (relative to Bi metamorphosis).[1,3,6] Primary annealing in oxygen does not change the properties of BMO, i.e., these materials are saturated oxides.[1,2]

BMO crystals are also sensitive to heating in air, which gives rise to thermal bleaching[3,7–9] and transfers the crystals into an ''initial'' state with reproducible charactersitics.[10,11] Heating in the presence of an electric field gives rise to a sharp increase of the dark electric conductivity and increases the mobility of charge carriers.[12,13]

The diversity of changes produced in the properties of BMO crystals by heat treatment gives rise to the interest shown in the nature of thermally induced processes, which is unknown.

Our objective in the present work is to study thermal defect formation in pure and Cr- and Mn-doped $Bi_{12}SiO_{20}$ crystals (BSO, BSO:Cr, and BSO:Mn, respectively).

1. EXPERIMENTAL PROCEDURE

BSO, BSO:Cr (0.05 mass%), BSO:Mn (0.1 mass%) crystals were grown by the Czochralski method. The doping technology is described in Ref. 14.

The temperature spectra $I(T)$ of thermally stimulated depolarization (TSD) currents and the influence of temperature on the optical absorption spectra $\alpha(E,T)$ in the photon energy range $E=0.5-3.3$ eV in and the temperature range $T=300-700$ K were investigated.

The polarization temperature $T_p=300-525$ K and the holding time $t_b=30-3.6\times10^3$ s at $T=T_p$ before a polarizing voltage $U_p=180$ V was applied were varied in the TSD experiments. The polarization time ($t_p=30$ min) and U_p remained constants (Fig. 1). The samples were prepared in the form of $(\sim0.9)\times2\times10\ \mathrm{mm}^3$ bars. Pt electrodes, forming barrier contacts,[15] were deposited by cathodic sputtering on $2\times10\ \mathrm{mm}^2$ surfaces cut in the (010) plane. The current was measured with the samples heated at the rate $b_1=0.16\ \mathrm{K\cdot s^{-1}}$ in a microcomputer-controlled apparatus, described in Ref. 16.

The samples for the optical measurements were prepared in the form of polished plates with area $8\times8\ \mathrm{mm}^2$ (in the (001) plane) and thickness $d=0.1-5$ mm. The optical transmission spectra $t(E)$ were measured using Specord M40 and Specord NIR61 spectrophotometers. The temperature was varied at the rate $b_2=0.02\ \mathrm{K\cdot s^{-1}}$. The spectra $t(E)$ were scanned through 10 K in the ''heating–cooling'' regime. The absorption spectra $\alpha(E)$ were calculated from known relations taking account of reflection and refraction.[17,18]

2. RESULTS

2.1. TSD current spectra

Two groups, A and B, of peaks in the TSD current can be distinguished in the $I(T)$ spectra in the ranges $T_1=300-600$ K and $T_2=600-800$ K, respectively. For low T_p the group-A peaks are quasidiscrete (BSO:Cr) or weakly structured (BSO, BSO:Mn). The group-B peaks possess an almost smooth envelope, attesting to strong overlap. As T_p increases to 520 K, some group-A peaks vanish (in BSO and BSO:Cr), and all other group-A and -B peaks increase and are better resolved. The group-A peaks in BSO:Cr and BSO:Mn crystals form a characteristic packet with a Π-shaped envelope and protracted low-temperature shoulder (Fig. 1). In Arrhenius coordinates this shoulder bends in a manner so that the slope angle (effective thermal activation energy E_a^{T*}) increases with temperature. This shows that the electrically active defects have a quasicontinuous energy distribution. Assuming the distribution to be Gaussian and following Ref. 19, we estimated its width $\Delta E_a^{T*}=\{[2KT_1T_2/(T_2-T_1)]\times[E_a^T(T_2)-E_a^T(T_1)]\}^{0.5}$ and the most likely value of the thermal activation energy of defects $E_{0a}^T=(\Delta E_a^T)^2/2kT-d(\ln I(T))/d(1/kT)$ (see Table I).

It is interesting to note an analogy between the general form of the spectra $I(T)$ and $\alpha(E)$, where two bands can

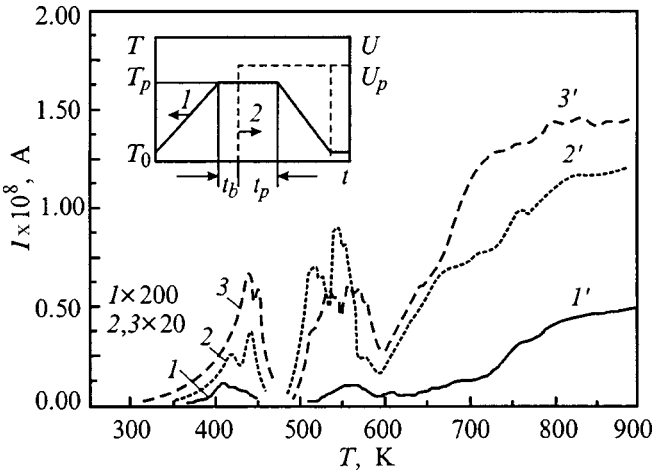

FIG. 1. TSD current spectra $I(T)$ for BSO (*1,1′*), BSO:Mn (*2,2′*), and BSO:CR (*3,3′*) crystals. Polarization conditions: $T_p=373$ (*1,1′*, *2,2′*) and 473 K (*3,3′*), $t_b=300$ s. Inset: Curves of the dependences $U_p(T)$ and $T_p(T)$.

also be distinguished in the energy ranges $E_1=1.2-1.8$ eV (A) and $E_2=1.8-3$ eV (B), the A band having the form of a Π-shaped envelope.[20] In both cases the current I and absorption α are observed to increase from BSO crystals to BSO:Mn and BSO:Cr crystals (Fig. 1 and Ref. 20) and as the Cr and Mn concentrations increase.[21] The same defects are responsible for the A and B bands of the spectra $I(T)$ and $\alpha(E)$, but the values of the thermal activation energy E_a^T and the optical activation energy E_a^O are substantially different (see Table I).

2.2. Dependence of TSD on the polarization conditions

The dependences $I_m(T_p)$ and $Q(T_p)$, where I_m is the depolarization current at the maximum, $Q=\int I(t)dt$ is the freed charge, and t_1 and t_2 are moments in time, were analyzed.

For a short holding time ($0<t_b\leqslant 30$ s) the dependences $I_m(T_p)$ for the A peaks and $Q(T_p)$ for the B peaks in BSO and BSO:Cr crystals pass through a maximum, and their low- and high-temperature shoulders can be described by the expressions I_m, $Q\sim(1/T_p)\exp(-E_a^T/kT)$ and I_m, $Q\sim(1/T_p)$, respectively (Figs. 2a and 2b), i.e., they are close to the model spectra for dipole polarization.[19,22]

As the time t_b increases, $t_b>30$ s, the type of extremality of these dependences is observed to change for BSO:Cr crystals — they pass through a minimum at $T_p\approx 420$ K with exponential low- and high-temperature shoulders (Fig. 2b). For undoped BSO the maximum of the dependence $Q(T_p)$ (B peak) is observed to broaden (Fig. 2a).

The dependences $Q(T_p)$ for the A and B peaks in BSO:Mn crystals possess, as a rule, two extrema at $T_{p1}\approx 370$ and $T_{p2}\approx 420$ K, which for small and large t_b are the temperatures of either the maximum or minimum of the curves $Q(T_p)$. For intermediate values of t_b the dependences $Q(T_p)$ characteristic for dipole polarization are observed (Fig. 2c).

The fact that the holding time t_b strongly affects the dependences $I_m(T_p)$ and $Q(T_p)$ points to an interaction between dipoles. The passage of the curves $I_m(T_p)$ and $Q(T_p)$ through a maximum or minimum with exponential shoulders attests to an association–dissociation type interaction between dipoles in BSO:Cr and BSO:Mn crystals.[19,23] The dissociation energy E_{dis} is different from the association energy E_{ass} (see Table I).

2.3. Temperature dependences of the optical absorption

As temperature increases, the absorption decreases in the A band and increases in the B band (Figs. 2d–2f). The absorption drops off either in a step fashion (for BSO and BSO:Mn in the entire region of the A band, and for BSO:Cr in a narrow range $E=1.6-1.7$ eV) or with a passage through a minimum (for BSO:Cr for $1.6\geqslant E\geqslant 1.7$ eV). In the B band, distinct steps (for BSO at $E\geqslant 2.2$ eV, for BSO:Mn at $E\geqslant 2.5$ eV) or maxima (for BSO:Mn, BSO:Cr for $E=2.2$–2.5 eV) are observed against a general exponential increase in the absorption (Figs. 2d and 2f). The curves $\alpha(T)$

TABLE I. Energy characteristics of electrically and optically active defects and their interaction processes in BSO, BSO:Cr, and BSO:Mn crystals.

Crystal	ΔE_a^{T*}, eV ΔT, K	E_{0a}^T, eV ΔT, K	E_a^T, eV T_m, K	E_a^O, eV	E_{ass}, eV ΔT, K	E_{ass}^*, eV ΔT, K	E_{dis}, eV ΔT, K	E_{dis}^*, eV ΔT, K
BSO : Cr	0.29	0.82 300–450	1.27 531	1.48–1.73	0.2–0.6, 400–500	0.02–0.28 430–500	0.1–0.3, 300–400	0.14–0.2, 300–350
BSO : Mn	0.26	0.6 300–400	1.25–1.54, 640–700	2.23–2.35	0.1–0.3, 300–470	0.32 470–520	0.3–0.5, 470–560	0.53 520–560
BSO	0.28	0.7, 340–390	0.7, 554 0.9, 599 600	1.4–1.65				

Note: The values of E_a^T and E_a^O are presented for the TSD current peaks and optical absorption bands for which the dependences $I_m(T_p)$, $Q(T)$, and $\alpha(T)$ were investigated; the values of E_a^T were calculated by the ''initial slope'' method, and the TSD current peaks were extracted from the $I_m(T)$ spectra by ''thermal cleaning'';[19,22] the values of E_a^O were determined from the position of the maxima in the absorption bands of the spectrum, $\alpha(E)$; E_{ass} and E_{dis} were found from the dependences $I_m(T_p)$, and $Q(T_p)$, and E_{ass}^* and E_{dis}^* were found from the dependences $\alpha(T)$.

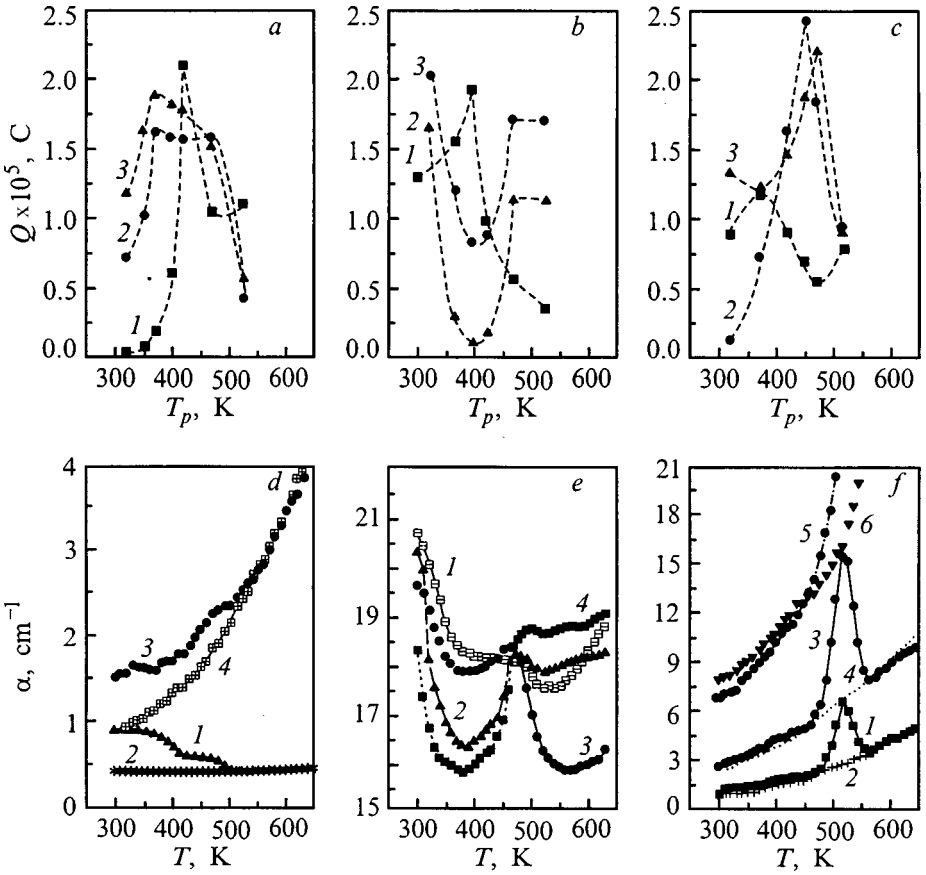

FIG. 2. Effect of the holding time t_b on the dependences of the freed charge in the region of the A (a, b) and B (c) peaks of the TSD current on the polarization temperature $Q(T_p)$ for BSO (a), BSO:Cr (b), BSO:Mn (c) crystals: $t_b=30$ s (a, b, c, curves *1*), 1.8×10^2 s (a, b, c, curves *2*), and 3.6×10^2 s (a, b, c, curves *3*). Temperature dependences obtained for the optical absorption $\alpha(T)$ for BSO (d), BSO:Cr (e), and BSO:Mn (f) crystals during heating (d, *1, 3*; e, *1, 3*; f, *1, 3, 5*) and cooling (d, *2, 4*; e, *2, 4*; f, *2, 4, 6*) for various photon energies: d — $E=1.65$ (*1,2*) and 2.23 eV (*3,4*); e — $E=1.487$ (*3,4*) and $E=1.735$ eV (*1,2*); f — $E=2.23$ (*1,2*), 2.35 (*3,4*), and 2.54 eV (*5,6*).

are characterized by hysteresis (Figs. 2d, 2e, and 2f). For the A and B bands of BSO:Cr crystals and the B band of BSO and BSO:Mn crystals, a boundary interval can be distinguished $T_c=420-480$ K. The curve $\alpha(T)$ traced in the reverse direction lies above for $T\leqslant T_c$ below for $T\geqslant T_c$ the curve $\alpha(T)$ traced in the forward direction. Cooling deepens the minimum in $\alpha(T)$ in the A band of BSO:Cr crystals (Fig. 2e).

The stepped dropoff in absorption in the A band could be due to emptying of electronic traps. The energies E_a^T and E_a^O of the traps could differ because of the electron–phonon interaction and the energy difference can be described in the configuration-coordinates model.[20]

The extrema of $\alpha(T)$ cannot be explained by ''transfer'' of electrons from shallower to deeper traps. In all probability, just as in the dependences $I_m(T_p)$ and $Q(T_p)$, they are determined by the change in the density of optically active defects as a result of association–dissociation processes, and the exponential shoulders of $\alpha(T)$ give activation energies for these processes that are close to those found from the dependences $I_m(T_p)$ and $Q(T_p)$ (see Table I). The fact that the maximum in $\alpha(T)$ of BSO:Mn crystals vanishes on cooling indicates that, at high temperatures T, an irreversible change occurs in the dissociated defects.

3. DISCUSSION

The high resistivity ($\sim10^{16}\,\Omega\cdot$cm) and high concentration of intrinsic point defects ($\sim10^{18}$ cm^{-1}) make BSO:Mn and BSO:Cr crystals compensated semiconductors. In this case quasidipoles in the form of associates of the type ''ionized donor–ionized acceptor'' could be responsible for the dipole mechanism of polarization, while unassociated centers are responsible for volume-charge polarization.

The kinetics of the dissociation and association of donor–acceptor pairs can be easily described as follows. Let pairs of donors and acceptors of a definite kind with concentration N_{pi} arise per unit time when a prescribed the polarization temperature T_p is reached. Ionized donors and acceptors, whose concentrations also equal n_i, enter into an interaction forming associates with concentration n_i. Then

$$dn_i/dt=N_{pi}-\beta_i n_i^2, \tag{1}$$

where β_i is a constant, which includes the probability of association. The solution of Eq. (1) has the form

$$n_i(t)=(N_{pi}/\beta_i)^{0.5}\{[\exp(2t/\tau_i)-1]/[\exp(2t/\tau_i)+1]\}, \tag{2}$$

where τ_i is the relaxation time and $n_i=0$ at $t_0=0$. As the donor levels become exhausted, thermal generation of pairs N_{pi} ceases, and the dissociation of associates becomes the dominant process:

$$dn_i/dt=-\beta_i n_i^2. \tag{3}$$

Measuring time from the moment $t^*=0$, for which $n_i=n_{0i}=(N_{pi}/\beta_i)^{0.5}$ we obtain

$$n_i=n_{0i}/(1+n_{0i}\beta_i t). \tag{4}$$

From the condition for halving of the pair concentration we obtain $\tau_i=(N_{pi}/\beta_i)^{-0.5}$. The relaxation-time distribution of the donor–acceptor pairs is manifested in the large width or

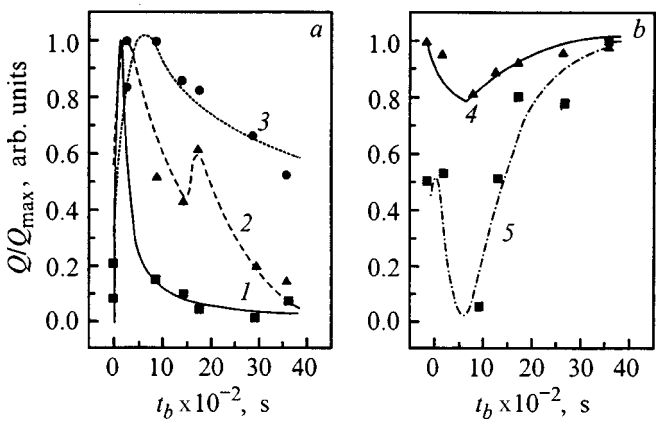

FIG. 3. Normalized, relative to the maximum values, dependences of the freed charge for the A group (a, *1*, *2*; b, *5*) and B group (a, *3*; b, *4*) of peaks of the TSD current of BSO:Cr (a, *1*–*3*), BSO:Mn (b, *5*), and BSO (b, *4*) crystals on the holding time $Q/Q_{max}(t_b)$. Dots — experimental values obtained with $T_p = 525$ (a, *1*), 423 (a, *2*; b, *2*), and 473 K (a, *3*; b,*2*); lines — computed values obtained for $\tau_i = 10^2 - 5 \times 10^3$ s.

the presence of several extrema of the function $\Sigma n_i(t_b) \sim Q(t_b)$. The functions $\Sigma n_i(t_b)/n_{0i}$ agree with the experimental dependences $Q/Q_{max}(t_b)$ for $\tau_i = 10^2 - 5 \times 10^3$ s (Fig. 3).

The presence of donor–acceptor pairs can be confirmed by studying their radiative recombination.[24] However, we note that such pairs have been used to explain the high photogalvanic activity in vacuum-annealed BSO crystals.[5]

[1] O. A. Gudaev, V. A. Detinenko, and V. K. Malinovskiĭ, Fiz. Tverd. Tela (Leningrad) **23**(1), 195 (1981) [Sov. Phys. Solid State **23**, 109 (1981)].
[2] O. A. Gudaev, V. A. Detinenko, A. P. Episeev, and V. K. Malinovskiĭ, Avtometriya **5**, 38 (1981).
[3] O. A. Gudaev, V. A. Detinenko, and A. P. Soklov, Avtometriya **5**, 34 (1983).
[4] O. A. Gudaev, V. A. Detinenko, and A. P. Sedel'nikov, Avtometriya **4**, 46 (1988).
[5] A. I. Grachev, M. P. Petrov, and M. V. Krasin'kova, Fiz. Tverd. Tela (Leningrad) **28**, 1530 (1986) [Sov. Phys. Solid State **28**, 864 (1986)].
[6] O. A. Gudaev, S. I. Demenko, V. A. Detinenko, É. É. Paul', Izv. Akad. Nauk SSSR, Neorg. Mater. **22**, 2070 (1986).
[7] V. K. Malinovskiĭ, O. A. Gudaev, V. A. Gusev, and S. I. Demenko, *Photoinduced Phenomena in Sillenites* [in Russian] (Nauka, Novosibirsk, 1990).
[8] I. Foldvari, L. E. Hallilburton, G. I. Edwards, and L. Otsi, Solid State Commun. **77**, 181 (1991).
[9] J. J. Martin, I. Foldvari, and G. A. Hunt, J. Appl. Phys. **70**, 7544 (1991).
[10] A. Ya. Volosov, V. Kh. Kostyuk, and A. Yu. Kudzin, Fiz. Tverd. Tela (Leningrad) **23**, 218 (1981) [Sov. Phys. Solid State **23**, 1281 (1981)].
[11] A. Hamri, M. Secu, V. Topa, and B. Briat, Opt. Mater. **4**, 197 (1995).
[12] E. P. Guenok, A. Yu. Kudzin, and G. Kh. Sokolyanskiĭ, Ukr. Fiz. Zh. **21**, 866 (1976).
[13] A. Yu. Kudzin, G. Kh. Sokolyanskiĭ, and A. S. Yudin, Fiz. Tverd. Tela (Leningrad) **33**, 981 (1991) [Sov. Phys. Solid State **33**, 562 (1991)].
[14] T. V. Panchenko, A. Yu. Kudzin, and V. Kh. Kostyuk, Izv. Akad. Nauk SSSR, Neorg. Mater. **19**, 1144 (1983).
[15] T. V. Panchenko, Yu. N. Potapovich, and G. V. Snezhnoĭ, Izv. Akad. Nauk SSSR, Ser. Fiz. **54**, 781 (1990).
[16] T. V. Panchenko, Yu. N. Potapovich, and G. V. Snezhnoĭ, Izmer. Tekh. **7**, 54 (1992).
[17] Yu. I. Ukhanov, *Optical Properties of Semiconductors* [in Russian] (Nauka, Moscow, 1977).
[18] F. Stern, Phys. Rev. **133**, 1653 (1979).
[19] Yu. A. Gorokhovatskiĭ and G. A. Bordovskiĭ, *Thermal-Activation Spectroscopy of High-Resistance Semiconductors and Dielectrics* [in Russian] (Nauka, Moscow, 1991).
[20] T. V. Panchenko, Fiz. Tverd. Tela (St. Petersburg) **40**, 452 (1998) [Phys. Solid State **40**, 415 (1998)].
[21] T. V. Panchenko and N. A. Truseeva, Ukr. Fiz. Zh. **29**, 1186 (1984).
[22] Yu. F. Gorokhovatskiĭ, *Principles of Thermal Depolarization Analyis* [in Russian] (Nauka, Moscow, 1981).
[23] A. Kessler and J. C. Caffin, J. Phys. C **5**, 1134 (1972).
[24] V. E. Loshkarev, A. V. Lyubchenko, and M. K. Sheĭkman, *Nonequilbrium Processes in Photoconductors* [in Russian] (Naukova Dumka, Kiev, 1981).

Translated by M. E. Alferieff

On the possibility of investigating the dispersion of the energy bands of a crystal using resonant x-ray emission spectra

M. A. Bunin*)

Scientific–Research Institute of Physics, Rostov-on-Don State University, 344090 Rostov-on-Don, Russia
(Submitted February 1, 1999)
Fiz. Tverd. Tela (St. Petersburg) **41**, 1597–1601 (September 1999)

It is shown that, when the dispersion of the energy bands of crystals is investigated by resonant x-ray emission (RXE), an ambiguity can arise in the determination of $\mathbf{k}_{tr}$ — the transition point in k space — as a result of the characteristic features of the band structure and the value of the matrix elements. It is proposed that calculations of the distribution of partial contributions to interband optical transitions in the Brillouin zone (BZ) be used as a means of obtaining a simplified estimate of $\mathbf{k}_{tr}$. The basic properties of this distribution are examined for lithium hydride, which is a convenient model object having a simple band structure and interband transitions which have been studied in detail. It is shown that the k points of the general position, which form a complex figure in the BZ, make the main contribution to the interband transitions. The contribution of high-symmetry points is much smaller mainly because of their small representativeness. This make it easier to understand the reason for the possible nonmonotonic variation of $\mathbf{k}_{tr}$ in RXE measurements of the dispersion of the energy bands of crystals or the sharp changes in the resonance-fluorescence intensity. © *1999 American Institute of Physics.* [S1063-7834(99)01309-X]

Since the publication of the well-known paper by Y. Ma[1] the methods of resonant x-ray spectroscopy (RXS) have developed so rapidly that it has not always been possible to make a comprehensive assessment of the difficulties arising with the use of the new possibilities of RXS and the problems in interpreting experimental data. These include investigation of the dependence $E(\mathbf{k})$ — the dispersion of the energy bands of crystals — on the basis of the RXE spectra. Its manifestation in silicon spectra was first noted by Ma.[2] These ideas were subsequently elaborated in Refs. 3–6. At first only the qualitative relation between $E(\mathbf{k})$ and the x-ray band intensities was investigated.[1–4] Thus, in Ref. 3, the changes of the intensity and position of the details in a graphite spectrum, as the frequency of the exciting monochromatic radiation $h\nu_{in}$ is varied, were attributed to the dispersion of the corresponding bands (for example, the band emanating from the M point — the saddlepoint for π and π^* bands[3]). The correspondence to states of definite k points was established from the law of conservation of momentum and by comparing with a calculation of $E(\mathbf{k})$ along the principal directions and high-symmetry points of the BZ. In silicon, similar work was performed[4] for the RXE spectra obtained from different crystallographic planes (RXE anisotropy). Six possible points of the BZ that satisfy the condition of momentum conservation were identified for the (111) plane — three close to L and three close to K. For (110) these are the Γ and X points, and for (100) they are the Γ, X, and W points. Both works employed in one form or another the long-held idea that the energies of the states of the high-symmetry points in the BZ (HP–BZ) correspond to maxima in the local partial densities of states, manifested in the x-ray emission bands. But, for example, even from the figures in Ref. 3 it is evident that the changes in the carbon spectra are unlikely to be so unequivocally determined by the dispersion of the bands only in HP–BZ. The same is also true of silicon spectra:[4] The choice of the coordinates of the x-ray transition point may not be so unique, since the law of conservation of momentum is an equation describing a family of planes containing not only the high-symmetry points of the BZ.

The trends observed in Refs. 3 and 4 qualitatively confirmed that the dispersion of the energy bands of crystals is manifested in RXE. Nonetheless great care must still be exercised in choosing $\mathbf{k}_{tr}$, since, compared to the point of the general position, the high-symmetry points may not make a large contribution to the intensity because of their small representativeness. For this reason, in searching for a correspondence between the shifts of the peaks in the spectrum and the change in the energy of a definite band (for example, as in Ref. 3), the k point of the general position should not be ruled out *a priori*.

The experimental $E(\mathbf{k})$ was determined in Ref. 5 for SiC. On the whole, it agreed quite well with the calculation of the energies for HP–BZ for the center of the valence band, but discrepancies, the reasons for which were not discussed, occurred at the valence-band top and bottom. In Ref. 6 it was proposed for Cu $K\beta_{2,15}$ and Ge $K\beta_5$ RXE that the dependence of the fluorescence intensity on $\mathbf{k}_{tr}$ and on the magnitude of the transferred momentum is due to the dispersion of the bands (Cu) and the magnitude of the matrix element (Ge). Unfortunately, this was not confirmed by calculations. The objective of the present work is to examine the possible sources of ambiguity in the choice of the coordinate of the x-ray transition point in investigations of the disper-

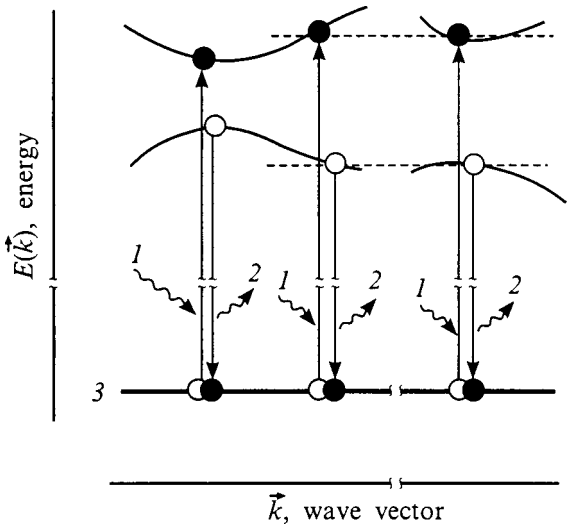

FIG. 1. Scheme of the resonant x-ray emission process: *1*—incident x-ray photon $h\nu_{\text{in}}$, *2*—emitted x-ray photon $h\nu_{\text{out}}$, *3*—core level E_{core}.

sion of the energy bands of crystals on the basis of resonant x-ray emission spectra, to determine the reasons for the discrepancy between experiment and the calculation of $E(\mathbf{k})$, and to propose a simplified method for estimating the possible values of $\mathbf{k}_{\text{tr}}$.

In RXE, x-ray fluorescent radiation is excited by monochromatic photons whose energy is close to the binding energy of a core level ($h\nu_{\text{in}} \approx E_{\text{core}}$). The process is described as one-step[5] absorption–emission (Fig. 1): The excitation radiation is absorbed by a core electron, the core electron is transferred to a free state directly above the Fermi level E_F, and an electron from the valence band fills the core vacancy, as a result of which an x-ray photon with energy $h\nu_{\text{out}}$ is emitted (reemission). The final state is an electron in the free state and a hole in the valence band.

The theoretical description of RXE is based on an analysis of emission–absorption process with inelastic resonant scattering of x rays (for example, Refs. 1–8 and references cited there)

$$F_{RIXS}(\omega_{\text{in}},\omega_{\text{out}}) = \sum_f \left| \sum_m \frac{\langle f|T|m\rangle\langle m|T|g\rangle}{E_m - E_g - \omega_{\text{in}} - i\Gamma} \right|^2 \delta(E_g + \omega_{\text{in}} - E_f - \omega_{\text{out}}), \quad (1)$$

where g, f, and m are, respectively, the ground, final, and intermediate states, E is the energy of the states, ω is the frequency of the incident (in) and emitted (out) radiations, T is the dipole transition operator, and Γ is the broadening associated with the lifetime of the intermediate state. If the electron–hole pair excited during resonant scattering is assumed to be completely delocalized, then absorption and reemission are coherently coupled. This leads to the law of conservation of momentum for the process as a whole

$$\mathbf{q} + \mathbf{k}_h - \mathbf{k}_e = \mathbf{G}, \quad (2)$$

where $\mathbf{k}_h$ and $\mathbf{k}_e$ are, respectively, the Bloch momentum vectors for a hole in the valence band and an electron in the conduction band and $\mathbf{q}=\mathbf{q}_{\text{in}}-\mathbf{q}_{\text{out}}$ is the momentum transferred to the electronic subsystem on scattering. This means that the structure of the electronic energy bands of the crystal and the wave vectors of the incident and emitted photons with the modulus of a reciprocal lattice vector $\mathbf{G}$ determine the points $\mathbf{k}_{\text{tr}}$ in the BZ where excitation of a core electron into a free state and emission from the valence band occur. This makes it possible to obtain information about the dispersion of the bands from the RXE spectra.

The experiment measuring $E(\mathbf{k})$ is based on manipulating the energy of the incident monochromatic radiation:[5] A core electron with energy E_{core} absorbs an x-ray photon $h\nu_{\text{in}}$ and is transferred to a free state with energy E_e

$$E_e = h\nu_{\text{in}} - E_{\text{core}}. \quad (3)$$

For soft x-rays, the momentum $\mathbf{q}$ transferred to the electronic subsystem is small compared with $\mathbf{k}_e$ — the wave vector of an electron excited to a free state in the conduction band

$$\mathbf{q} = \mathbf{q}_{\text{in}} - \mathbf{q}_{\text{out}} \ll \mathbf{k}_e, \quad (4)$$

and the transitions can be assumed to be vertical, as depicted in Fig. 1. The law of conservation of momentum (2) assumes the form[1)]

$$\mathbf{k}_e - \mathbf{k}_h + \mathbf{G} \approx 0. \quad (5)$$

If the excited electron and the core vacancy are uncoupled, then it can be assumed that E_e does not change after the vacancy decays. Then E_{in} and the structure of the conduction band, i.e., $E_e(\mathbf{k}_e)$, determined the possible electron $\mathbf{k}_e$ and hole $\mathbf{k}_h$ momenta in accordance with Eqs. (3)–(5) in the final state.[5] For substances with a band gap, the energy minimum $E_e=0$ corresponds to excitation of an electron to the lowest state at the conduction-band bottom. If the energy $h\nu_{\text{in}}$ in Eq. (3) is increased, then according to Refs. 3–5 the transition coordinates will change. This is the basis for the principle of obtaining $E(\mathbf{k})$ from the RXE [for example, for SiC (Ref. 5)].

Let us analyze the procedure for choosing $\mathbf{k}_{\text{tr}}$ in RXE. The vertical nature of the transition means that the reemission occurs at the same point $\mathbf{k}_0$ where an x-ray photon has been absorbed. When $\mathbf{k}_0$ is the conduction-band bottom, then there are no alternatives to it, since by definition this is the only band at this point. Let us increase $h\nu_{\text{in}}$ by $\Delta(h\nu_{\text{in}})$ and assume at first (for simplicity) that the reemission probability is independent of k, which means that one of the two matrix elements in Eq. (1) is constant. If not one but several free bands correspond to the new value of the excitation energy, then according to Eq. (1) the core electron will transfer to the one with the largest matrix element (of course, provided that the conditions (3)–(5) hold). For this reason, a smooth increase in excitation energy does not mean that the values of $\mathbf{k}_{\text{tr}}$ must vary just as smoothly by an amount determined by the dispersion of the only band emanating from $\mathbf{k}_0$, because in no way does it follow from Eqs. (3)–(5) that the next $\mathbf{k}_{\text{tr}}$ must definitely be close to the preceding one. Thus, a complication of the band structure easily admits a nonmonotonic variation of the coordinates of the transition point (see right side of Fig. 1). Most likely, this is the case that occurred for SiC, where the conduction-band bottom is located at the point X (Ref. 9).[2)] Just as in A^3B^5, in SiC the density of

states increases rapidly near the edges of the forbidden band, and as the excitation energy increases, higher conduction bands are drawn into the transitions.

If the probability of reemission from the valence states is not assumed to be constant, then the effect of the matrix elements in Eq. (1) is more difficult to estimate, but the possible nonuniqueness in the choice of $\mathbf{k}_{tr}$ in no way disappears. Only a direct nonempirical calculation of the distribution of the matrix elements in Eq. (1) over the BZ would guarantee uniqueness of such a choice. This requires either very complicated calculations or an approximation that makes it easier to estimate the spatial distribution of the probabilities of vertical transitions corresponding to the final state of RXE.

If the assumption that the intermediate state m is delocalized is valid, then the product of the matrix elements in Eq. (1) depends, first and foremost, on the wave functions of the ground g and final f states. The latter — an excited electron in a free state and a hole in the valence band — resembles completely the final state of an interband optical transition. For this reason, to a first approximation this analogy can be used to obtain a qualitative estimate of the distribution of the contributions to vertical transitions in RXE over the BZ. Then the complicated calculations based on Eq. (1) can be replaced by simpler calculations — for the intensities of vertical interband optical transitions, for which it is convenient to use the function $\varepsilon_2(\omega)$[3] given by[3)]

$$\varepsilon_2(\omega) \propto \frac{1}{\omega^2} \sum_{g,f} \int_{BZ} d\mathbf{k} |\langle f|T|g\rangle|^2 \delta(E_f - E_g - \omega). \qquad (6)$$

Relation (6) cannot be used directly in dispersion measurements to estimate $\mathbf{k}_{tr}$ from the RXE spectra, since contributions due to transitions between all admissable pairs of bands are summed at each point. We require the distribution of partial contributions to ε_2 over the BZ for a neighborhood $\Delta\Omega_{\mathbf{k}}$ of a certain point $\mathbf{k}$ in the BZ — $\varepsilon_2(\Delta\Omega_{\mathbf{k}})$, and transitions corresponding to a fixed frequency of a pair of bands must be distinguished in them. Thus, a local contribution from a pair of bands $g_{\mathbf{k}}f_{\mathbf{k}}$ to Eq. (6) at the point $\mathbf{k}$ is required. This can be called a local partial contribution $\varepsilon_2(g_{\mathbf{k}}, f_{\mathbf{k}})$, where

$$\varepsilon_2(\Delta\Omega_{\mathbf{k}}) \propto \sum_{g_{\mathbf{k}}, f_{\mathbf{k}}} \varepsilon_2(g_{\mathbf{k}}, f_{\mathbf{k}}). \qquad (7)$$

We note that, if the spectrum ε_2 near this point is formed by transitions only between two bands, then the left and right sides of relation (7) are identical.

The proposed approach is more convenient than only analyzing only transitions in RXE. When analyzing partial contributions to optical interband transitions, the validity of the old ideas concerning the correspondence between peaks in the spectra (optical, x-ray) and the states of bands at the high-symmetry points in the BZ can be checked at the same time. In this connection, it is useful to give a more general formulation of the problem, including investigation of the spatial distribution of partial contributions to the interband-transition spectrum over the BZ. Then the contribution of transitions with a definite frequency ω_{gf} at the point $\mathbf{k}$ (between one pair of bands $g_{\mathbf{k}}$ and $f_{\mathbf{k}}$) should be analyzed for the final state of the RXE process in Eq. (7). This is quite easy to do, since programs exist for performing band-structure calculations.

Strange as it may seem, such investigations have evidently never been performed for any substances, including those mentioned above.[3–6] Moreover, I know of no, even technically simpler, calculations of the distributions $\varepsilon_2(\Delta\Omega_{\mathbf{k}})$, knowledge of whose basic properties is very desirable to have before local transitions are considered. For this reason, it is first necessary to perform either a model calculation or to perform a calculation for a crystal whose fundamental optical absorption can be described by transitions between two bands. Then the analysis of the partial contributions to ε_2 will also be applicable to the more general problem.

Lithium hydride meets these requirements best. It has a simple lattice and its interband-transition spectrum, which agrees well with experiment, has been investigated in detail right up to $\omega \sim 20$ eV.[12] The function $\varepsilon_2(\omega)$ for lithium hydride was described by transitions from a single valence band to three upper bands; the main contribution was formed by transitions between two of them, the valence band and the lower conduction band. Using relation (7) for analysis of interband transitions in LiH will make it possible to obtain $\varepsilon_2(\Delta\Omega_{\mathbf{k}})$ and to examine the contributions of transitions between two specific bands at the same time. To solve the analogous problem for Si, Cu, Ge, SiC, or C,[3–6] a large number of bands need to be taken into account, complicating the picture without improving the clarity of the results. This is why lithium hydride was chosen for the calculation.

The method and results of a PPW band calculation for LiH are described in detail in Ref. 12. The histogram method, based on summing the partial contributions from points of a grid in k space, was used to calculate the functions $\varepsilon_2(\omega)$ and $\varepsilon_2(\Delta\Omega_{\mathbf{k}})$. The computational procedure is similar to that used in Ref. 12. Only contributions to $\varepsilon_2(\Delta\Omega_{\mathbf{k}})$ which are larger than $\sim 10-15\%$ of the maximum value were taken into account. This was completely sufficient to obtain the general picture; taking account small contributions makes the picture less clear without improving the information content. It was found that the ''brightest'' points form a completely ordered arrangement — a polyhedron (projections in Figs. 2a, 2b, and 2c), resembling Fermi surfaces in metals. The figure encompasses $\sim 80\%$ of the total intensity of the spectrum, and the points located in the interior of the BZ make the greatest contribution. Except for several small sections, it lies entirely inside the BZ, touching almost nowhere either the symmetric planes (of the type $XUW, \Gamma LUX, KLUW$) or points (Γ, X, U, W, ...). Figure 2 shows sections of the figure by seven planes. The plane *1*, closest to the XUW face, makes the largest contribution ($\sim 40\%$) to $\varepsilon_2(\Delta\Omega_{\mathbf{k}})$, and the plane *1*, to which the point L is closest, makes the smallest contribution. The distributions $\varepsilon_2(\Delta\Omega_{\mathbf{k}})$ were constructed for each plane (Fig. 2d); they form irregular surfaces. The values of the maximum coordinates of each one are shown in Fig. 2e. The position of the point where $\varepsilon_2(\Delta\Omega_{\mathbf{k}})$ assumes its maximum value (the

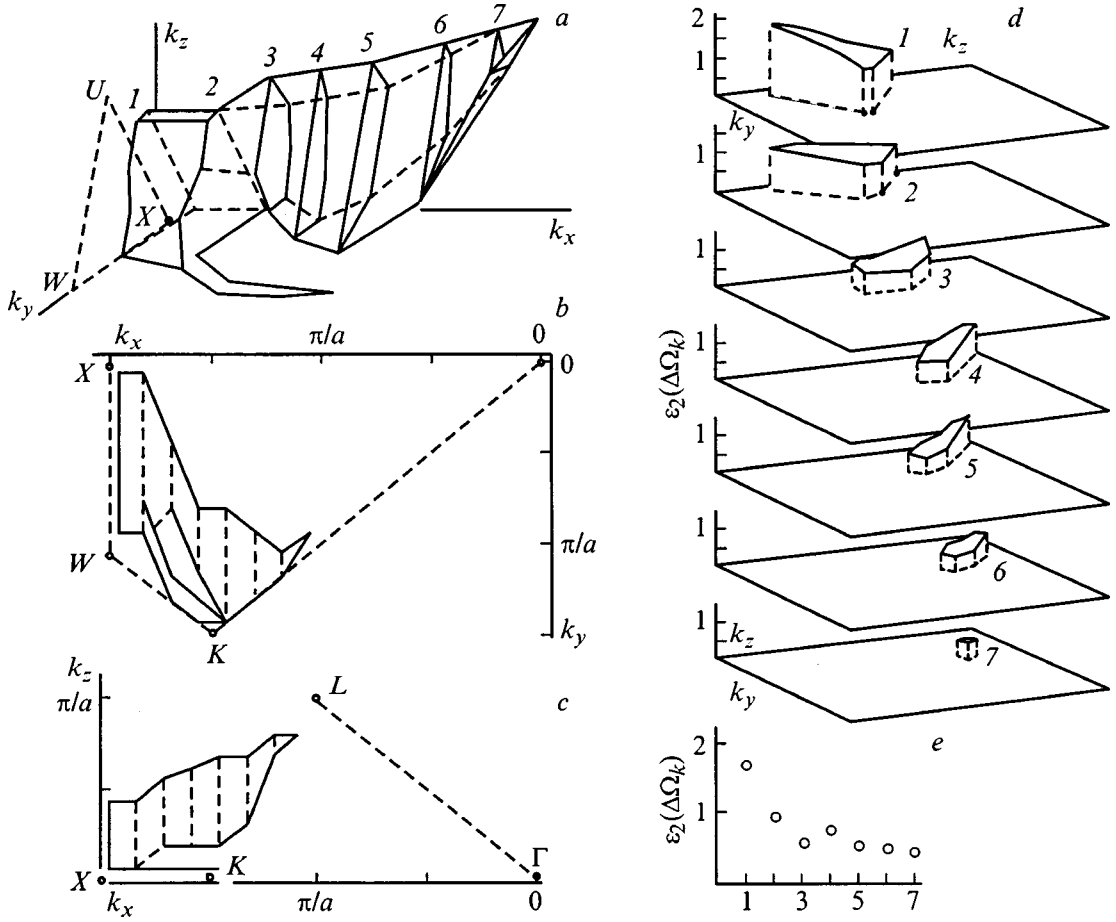

FIG. 2. Distribution of contributions to the intensity of interband transitions for various regions in k space of the BZ of a LiH crystal. a—Contour of the region inside the irreducible part of the BZ making the main contribution to the interband-transition spectrum of LiH. Several points in the figure are connected by dashed lines as a visual aid. The numbers *1–7* denote the planes of the sections; b, c—projections of the polyhedron shown in Fig. 2a on the coordinate planes; the dashed lines show the sections *2–7* and projections of the boundaries of the BZ; d—distributions of the contributions $\varepsilon_2(\Delta\Omega_{\mathbf{k}})$ for the sections *1–7*; e—values of the maximum ordinate for the sections shown in Fig. 2d.

plane *1* in Fig. 2d) is close to the coordinates of the conduction-band minimum.[13]

The example of lithium hydride shows that the intensity of interband transitions is distributed continuously over the BZ, without forming isolated ''bright spots,'' and varies relatively smoothly inside the BZ. Although transitions between the two bottom bands play the main role in LiH, the contribution of transitions to higher bands does not destroy the wholeness of the figure in Fig. 2a.

This result is not so unexpected: The contributions of high-symmetry points and planes to the intensity is small mainly because of their small representativeness, and their effect on the interband-transition spectrum is not determining. The regions making the largest contribution lie inside the BZ (compare the contributions of the planes *1–7* in Fig. 2d). This is of interest for RXE. These are the planes for which we are justified in comparing the band energies with the characteristic features of the experimental data on the density of states; the relation with the dispersion of the bands $E(\mathbf{k})$ should be sought for them first. Of course, similar data can be obtained by analyzing only the high-symmetry points, but then an error due to the nonuniqueness of the definition of a transition point in k space is more likely. Nevertheless, the tendencies in the function $E(\mathbf{k})$ will remain even in this case, as was observed in Refs. 3 and 4. Of course, in a different crystal the form of $\varepsilon_2(\Delta\Omega_{\mathbf{k}})$ will be different, but the qualitative description will most likely remain the same: The interband transition intensities form a complicated figure in k space and a substantial portion of the figure lies inside the BZ. The high-symmetry point can fall into this region, but this is by no means obligatory. Therefore the conjecture that the k point of the general position should be included in the analysis when performing measurements of $E(\mathbf{k})$ on the basis of RXE has been confirmed.

Let us compare these results with those of Refs. 5 and 6. Some possible reasons for the discrepancy observed in Ref. 5 between the experimental and computed dependences $E(\mathbf{k})$ have already been discussed above. Apparently, the contribution from transitions to other bands somewhat above the conduction-band bottom is substantial in SiC, as a result of which the choice of the coordinate of the point of the vertical transition need not be unique. (If the contributions of the matrix elements for ''competing'' bands differ sharply, then even the appearance of nonmonotonic features in $\varepsilon_2(\Delta\Omega_{\mathbf{k}})$ is not ruled out.) In Ref. 6, the large ($\sim$25%) narrowing of the Cu $K\beta_{2,15}$ band away from the L_1 point was attributed to the decrease in the combined density of states near this point. However, as can be easily verified from the figure in Ref. 6,

the dispersion of some bands emanating from this point is large. For this reason, for the transitions to occur from the same band as $\mathbf{k}$ varies, the excitation energy must vary rapidly, whereas it remained constant in the experiment. Then, transitions near L_1 can occur either to other bands or, if the change in the coordinate is small, only the tails of the corresponding wave functions will participate in the matrix elements (1) and the band width will become smaller. From the standpoint of the distribution $\varepsilon_2(\Delta\Omega_{\mathbf{k}})$, this means that most likely a neighborhood of the point L does not fall into it. The changes in the Ge $K\beta_5$ bands in Ref. 6 can also be explained on the basis of the properties of $\varepsilon_2(\Delta\Omega_{\mathbf{k}})$. Specifically, the influence of collective effects on the resonance fluorescence spectrum can be distinguished with a high degree of certainty. It is suggested that the contour of the surface $\varepsilon_2(\Delta\Omega_{\mathbf{k}})$ be calculated in the future for several substances from Refs. 3–6. This will make it easier to search for transition points in the RXE and to compare more reliably the experimental dependence $E(\mathbf{k})$ and the computed band energies.

*)E-mail: bunin@riphys.rnd.su

1) In the hard region of the spectrum the condition (4) is not satisfied, but it is still possible to study the dispersion of the bands.[6]

2) It is interesting that the nonuniqueness of the choice of the transition point in RXE is mentioned in a remark in Ref. 5, but it was not reflected in the discussion of the results.

3) We make no attempt to reduce the problem to the old problem of the correspondence between the energies of the peaks in the spectrum and the bands at the HP–BZ. This idea has long been used to interpret optical spectra, and it later took root in x-ray spectroscopy (for example, Ref. 10). Similar analogies were also pertinent at the early stage in the development of techniques for performing band calculations. As they improved, such comparisons were used only for substances with a very complicated band structure (for example, Ref. 11).

[1] Y. Ma, Phys. Rev. B **49**, 5799 (1994).
[2] Y. Ma, N. Wassdahl, P. Skytt, and J. Guo, J. Nordgren, P. D. Johnson, J.-E. Rubensson, T. Boske, W. Eberhardt, and S. D. Kewan, Phys. Rev. Lett. **69**, 2598 (1992).
[3] Y. Ma, K. E. Miyano, P. L. Cowan, Y. Aglitzkiy, and B. A. Karlin, Phys. Rev. Lett. **74**, 478 (1995).
[4] J. A. Carlisle, E. L. Shirley, E. A. Hudson, L. J. Terminello, T. A. Callcot, J. J. Jia, D. L. Ederer, R. C. C. Perera, and F. J. Himpsel, Phys. Rev. Lett. **74**, 1234 (1995).
[5] J.-E. Rubensson, J. Luning, S. Epstein, and W. Eberhardt, Appl. Phys. A: Mater. Sci. Process. **65**, 91 (1997).
[6] A. Kaprolat and W. Schulke, Appl. Phys. A: Mater. Sci. Process. **65**, 169 (1997).
[7] A. Cesar, F. Gel'mukhanov, Y. Luo, H. Agren, P. Skytt, P. Glans, J. Guo, K. Gunnelin, and J. Nordgrn, J. Chem. Phys. **106**, 3439 (1997).
[8] A. Kotani, J. Phys. IV **7**, C2–1 (1997).
[9] *Handbook of the Physical-Chemical Properties of Semiconductor Materials* [in Russian], edited by A. V. Novoselova (Nauka, Moscow, 1978), 338 pp.
[10] *X-Ray Spectra and Electronic Structure of Materials* [in Russian], edited by V. V. Nemoshkalenko (IMF AN Ukr. SSR, Kiev, 1969), 378 pp.
[11] M. A. Bunin, A. N. Gusatinskiĭ, V. I. Minin, Yu. I. Polygalov, A. S. Poplavnoĭ, and V. E. Tupitsyn, Fiz. Tekh. Poluprovodn. **15**, 1617 (1981) [Sov. Phys. Semicond. **15**, 937 (1981)].
[12] I. I. Geguzin, M. A. Bunin, and V. N. Datsyuk, Fiz. Tverd. Tela (Leningrad) **31**(12), 15 (1989) [Sov. Phys. Solid State **31**, 2035 (1989)].
[13] Ch. B. Lushchik, F. F. Gavrilov, G. S. Zavt, V. G. Plekhanov, and S. O. Cholakh, *Electronic Excitations and Defects in Lithium Hydride Crystals* [in Russian] (Nauka, Moscow, 1985), 214 pp.

Translated by M. E. Alferieff

Spin–spin interaction of Ni^{2+} ions in $ZnSiF_6 \cdot 6H_2O$

I. M. Krygin and A. D. Prokhorov*

Donetsk Physicotechnical Institute, Ukrainian Academy of Sciences, 340114 Donetsk, Ukraine
(Submitted February 1, 1999)
Fiz. Tverd. Tela (St. Petersburg) **41**, 1602–1608 (September 1999)

The angular dependences of the electron spin resonance spectrum of 1% Ni^{2+} ions in a $ZnSiF_6 \cdot 6H_2O$ matrix are investigated experimentally at 36 GHz and 4.2 K. Besides the main spectrum of the isolated ion, we observed a spectrum due to interacting pairs of Ni^{2+} ions, located in the first (nn) and second $(2n)$ coordination spheres and coupled by, besides the magnetic dipole–dipole interaction, isotropic exchange: $J_{nn}=(-197\pm 1)\times 10^{-4}$, $J_{2n\alpha}=(-5\pm 1)\times 10^{-4}$, and $J_{2n\beta}=(3\pm 2)\times 10^{-4}\,\mathrm{cm}^{-1}$. Lines due to other isolated Ni^{2+} ions, which have a different initial splitting D, are also present in the spectrum with intensity comparable to the pair spectrum. Low-symmetry distortions of the crystal field are observed, caused by a pair of impurity ions located close to one another. It is shown that the previously proposed interpretation is incorrect. © *1999 American Institute of Physics.*
[S1063-7834(99)01409-4]

To investigate an interacting pair of ions by ESR, it is very important that the spin–spin interaction (SSI) be sufficiently small compared to the measuring quantum. Then the maximum possible information about the SSI can be extracted from the spectrum. A spectrum due to pairs of this kind was first observed experimentally for $Ni^{2+}:ZnSiF_6 \cdot 6H_2O$.[1] Subsequently,[2] a detailed interpretation of the spectrum was given, according to which the spectrum contains lines due to three types of pairs in which the interacting ions are located in the first (nn), second $(2n)$, and third $(3n)$ configuration spheres and are coupled only by isotropic exchange, constituting -300×10^{-4}, $+130\times 10^{-4}$, and $-121\times 10^{-4}\,\mathrm{cm}^{-1}$, respectively. Later, the effect of hydrostatic compression on the same substance was investigated by ESR using the proposed interpretation of the spectrum,[3–7] and it was concluded that the isotropic exchange interaction J for the nn pair depends on the interion distance as $J=-5.81\times 10^{21}\exp(-8.55R)$. It can be concluded from the presence of citations to later works that the interaction of nickel ions in fluorosilicates only by means of isotropic exchange is considered to be a proven fact.

We note the following discrepancies concerning mainly Ref. 2 as the basic work.

1) The ESR spectrum of $Ni^{2+}:ZnSiF_6 \cdot 6H_2O$ pairs was studied only in one orientation, $\mathbf{H}_0 \| \mathbf{C}_3$, where the absorption spectrum is maximally simplified. However, in this case it is very risky to draw a conclusion about the existence of only an anisotropic interaction without investigating the angular dependence.

2) A magnetic dipole–dipole interaction (MDD) always exist between two magnetic dipoles, which the ions under investigation are. This interaction was neglected ''since the structure of nickel fluorosilicate is very close to cubic.''[2] Indeed, for isotropic g, which is the case for $Ni^{2+}:ZnSiF_6 \cdot 6H_2O$, the MDD is completely anisotropic and it does not contribute to the macroscopic magnetic properties in magnetically concentrated substances with cubic structure. But neglecting the MDD can lead to incorrect conclusions in investigations of an isolated pair of magnetic dipoles.

3) It follows from Ref. 2 that the initial splitting parameter D for pairs is different from D for an individual ion (D_1). Specifically, for an nn pair D_{nn} is 2.5% greater smaller than D_1, D_{2n} is 1.5% smaller, and D_{3n} is 7.8% smaller. It is obvious that a pair of impurity ions lying next to one another can give rise to stronger local distortions of the matrix than a single ion, so that D, which describes the crystal field, can be different for a single ion and from a pair of ions. The larger the distance between the impurity ions, the smaller the difference between D for a single ion and a pair of ions should be. In this connection, such a large difference between D_1 and D_{3n} is preplexing.

4) It follows from Fig. 2 of Ref. 6 that, under 10 kbar pressure, the difference between D_1 and D for pairs is already $+13\%$, -75%(!), and $+22\%$ for $nn, 2n$, and $3n$ pairs, respectively. This casts great doubt on the correctness of the interpretation of the experimental spectrum.

5) The pressure dependence predicted for the Curie temperature on the basis of Ref. 6 disagrees even in sign with that obtained experimentally in Ref. 8.

The reasons enumerated above, as well as at least as many reasons which have not been presented, give grounds for doubting the correctness of the conventional interpretation of the spectrum due to $Ni^{2+}:ZnSiF_6 \cdot 6H_2O$ pairs. The present work is devoted to a more thorough investigation of this material.

1. THEORY

The space group of zinc fluorosilicate is $R\bar{3}$. Since an octahedral cubic field with a trigonal component acts on a Ni^{2+} ion, the bottom energy levels are a spin doublet and a singlet. In this case the Hamiltonian of a single ion (effective spin $S=1$) with isotropic g can be written as

$$\hat{\mathbf{H}}=g\beta(\mathbf{H}\cdot\hat{\mathbf{S}})+B_2^0O_2^0, \tag{1}$$

where the first term describes the interaction of the spin with an external magnetic field and the second term describes the interaction with an axial component of the crystal field $D=3B_2^0$. According to Eq. (1), when the magnetic field is parallel to the C_3 axis and the energy of the measuring quantum is sufficiently high, the absorption spectrum should consist of two fine-structure lines corresponding to transitions $|1\rangle\leftrightarrow|0\rangle$ and $|-1\rangle\leftrightarrow|0\rangle$. For other orientations the Zeeman interaction mixes the $|+1\rangle$, $|0\rangle$ and $|-1\rangle$, $|0\rangle$ states, so that a ''forbidden'' transition should be observed in ''half'' fields.

The Hamiltonian of a pair of interacting ions can be written as

$$\hat{\mathbf{H}}=\hat{\mathbf{H}}_1+\hat{\mathbf{H}}_2+\hat{\mathbf{H}}_{12}, \tag{2}$$

where $\hat{\mathbf{H}}_1$ and $\hat{\mathbf{H}}_2$ are the Hamiltonians of the first and second single ions and $\hat{\mathbf{H}}_{12}$ is the interaction Hamiltonian. Since in the present case identical ions interact and the pair of impurity ions located next to one another can give rise to local distortions of the unit cell, in contrast to the Hamiltonian presented in Ref. 2, to describe the spectrum of the pairs it makes sense to use a Hamiltonian that takes account of the quite low-symmetric components of the crystal field

$$\hat{\mathbf{H}}_1=\hat{\mathbf{H}}_2=g\beta(\mathbf{H}\cdot\hat{\mathbf{S}})+B_2^0O_2^0+B_2^1O_2^1 + B_2^2O_2^2+C_2^1\Omega_2^1+C_2^2\Omega_2^2. \tag{3}$$

Using the generalized spin operators O_n^m, the spin–spin interaction Hamiltonian $\hat{H}_{12}$ can be written phenomenologically in the general form

$$\hat{\mathbf{H}}_{12}=\sum O_n^mP_{nq}^{ml}O_q^l, \tag{4}$$

where the summation is over the indices n,m,q, and l; m varies from $-n$ to n and l from $-q$ to q. For spin $S=1$ only the matrix elements of the operators O_1^m and O_2^m are different from zero, so that Eq. (4) simplifies to

$$\hat{\mathbf{H}}_{12}=\sum O_1^mP_{11}^{ml}O_1^l+\sum O_2^mP_{22}^{ml}O_2^l + \sum O_1^mP_{12}^{ml}O_2^l+\sum O_2^mP_{21}^{ml}O_1^l. \tag{5}$$

But even in this case 64 independent parameters P_{nq}^{ml} remain, too many to describe the experimental results.

The main contribution to the spin–spin interaction should be expected from terms which are linear in the spin. Therefore we shall confine ourselves to the first term in the expression (5). Since $O_1^{-1}=S_-$, $O_1^{+1}=S_+$, and $O_1^0=S_z$, it can be written as

$$\sum O_1^mP_{11}^{ml}O_1^l=\hat{\mathbf{S}}_1L_{12}\hat{\mathbf{S}}_2, \tag{6}$$

where the subscripts on the right-hand side enumerate the ions. The spin–spin interaction tensor L_{12}, in turn, can be decomposed into isotropic J, anisotropic A_{12}, and bilinear Q_{12} parts of the spin–spin interaction

$$L_{12}=K_{12}+Q_{12}=J+A_{12}+Q_{12};\quad \mathrm{Tr}\,A_{12}=0, \tag{7}$$

where J is a constant, A_{12} is a symmetric tensor, and Q_{12} is an antisymmetric tensor. The latter is also known as the ''Dzyaloshinskiĭ vector'' **D** with the components $D_x=Q_{yz}$, $D_y=Q_{xz}$, and $D_z=Q_{xy}$. Neglecting all other terms in Eq. (5), in the present work we described the spin–spin interaction by the Hamiltonian

$$\hat{\mathbf{H}}_{12}=\hat{\mathbf{S}}_1L_{12}\hat{\mathbf{S}}_2. \tag{8}$$

Various spin–spin interaction mechanisms, including exchange (Ex) and MDD, of which only the latter can be calculated with adequate accuracy, can contribute to L_{12}.

The Hamiltonian describing the MDD for two identical ions with isotropic g can be written as[9]

$$\hat{\mathbf{H}}^{MDD}=\beta^2R^{-3}g^2\{(1-3l^2)\hat{S}_{1x}\hat{S}_{2x}+(1-3m^2)\hat{S}_{1y}\hat{S}_{2y} + (1-3n^2)\hat{S}_{1z}\hat{S}_{2z}-3lm(\hat{S}_{1x}\hat{S}_{2y}+\hat{S}_{1y}\hat{S}_{2x}) - 3mn(\hat{S}_{1y}\hat{S}_{2z}+\hat{S}_{1z}\hat{S}_{2y})-3nl(\hat{S}_{1z}\hat{S}_{2x}+\hat{S}_{1x}\hat{S}_{2z})\}, \tag{9}$$

where R is the interionic distance, and l,m, and n are direction cosines of the line of interaction.

In a cubic crystal the ion located at a vertex of a cube has six nearest neighbors (nn pairs), whose lines of interaction are the edges of the cube; twelve neighbors in the second coordination sphere ($2n$ pairs) with lines of interaction lie along the face diagonals; and, eight neighbors in the third coordination sphere ($3n$ pairs), where the interaction lines lie along the body diagonals. In the substance under study, the cube is compressed along one of the body diagonals (the C_3 axis of the crystal), as a result of which some pairs become nonequivalent. Specifically, the line of interaction for half of the $2n$ pairs does not lie in the xy plane ($2n\alpha$ pairs) and compression of the unit cell changes the bond angle and shortens the interionic distance compared with $2n\beta$ pairs, for which the interaction line lies in the xy plane. A similar picture is observed for $3n$ pairs.

It follows from x-ray crystallographic investigations[10] that the lattice constant for $NiSiF_6\cdot 6H_2O$ (100% substitution) $d=6.21$ Å and the orthorhombic angle $\alpha=96.30°$; for $ZnSiF_6\cdot 6H_2O$ (pure matrix) $d=6.27$ Å and $\alpha=96.08°$. It is natural to suppose that for a unit cell distorted by a pair of impurity ions d and α cannot fall outside these limits, i.e., for pairs of ions Ni^{2+}:$ZnSiF_6\cdot 6H_2O$ $d=6.24\pm 0.03$ Å and $\alpha=96.20°\pm 0.12°$. On this basis, the computed interionic distances R and bond angles for various types of pairs are presented in Table I. The z axis of the laboratory coordinate system (LCS) is aligned along the C_3 axis of the crystal, and the line of interaction of one of the nn pairs lies in the xz plane of the LCS.

The contribution of the MDD to the tensor K_{12} was calculated in accordance with Eq. (9) in the proper coordinate system (PCS) for pairs of each type, specifically, the z axis is aligned along the C_3 axis of the crystal and the line of interaction of the corresponding pair of ions lies in the xz plane of the PCS, so that the parameters K_{xy} and K_{yz} for all types of pairs which are not presented in Table I are zero.

It follows from Table I that the MDD makes a contribution to the spin–spin interaction that is comparable to the

TABLE I. Interionic distances and bond angles for different types of pairs.

Type of pair	R, Å	θ, deg	φ, deg	K_{xx}^{MDD}	K_{yy}^{MDD}	K_{zz}^{MDD}	K_{yz}^{MDD}	Number of centers
nn	6.24±0.03	59.26±0.1	0, 120, −120	−107.8±1.9	88.6±1.3	19.2±1.0	−116.8±1.5	3
$2n\alpha$	8.33±0.05	40.06±0.11	60, −60, 180	−8.49±0.89	37.2±0.67	−28.7±0.22	−54.87±1.12	3
$2n\beta$	9.29±0.04	90	30, 90, 150	−53.72±0.62	26.86±0.31	26.86±0.31	0	3
$3n\alpha$	9.57±0.07	0	−	24.58±0.56	24.58±0.56	−49.2±1.11	0	1
$3n\beta$	11.19±0.05	73.44±0.06	60, 120, 240	26.98±0.36	15.36±0.19	11.62±0.17	−12.59±0.12	3

Note: The last column shows the number of magnetically nonequivalent centers. The nonzero parameters of the tensor K^{MDD} were calculated for $g=2.23$ and are given in units of 10^{-4} cm^{-1}.

results of Ref. 2, and this mechanism cannot be neglected. It likewise follows from Table I that if spectra from all three types of pairs (nn, $2n\alpha$, $2n\beta$, $3n\alpha$, and $3n\beta$) are indeed observed in the ESR spectrum of Ni^{2+}:$ZnSiF_6\cdot 6H_2O$, then five groups of lines, one group from each type of pair, should be observed in the parallel orientation ($\mathbf{H}_0\|\mathbf{C}_3$). When the external magnetic field deviates from C_3, each of them, with the exception of the one belonging to $3n\alpha$ pair, should split into three lines.

The spectrum can be additionally complicated for the follow reason. In the substance investigated, each paramagnetic ion is surrounded by a water octahedron, so that the ions should interact by indirect exchange. According to Ref. 10, the octahedra can be arranged in two ways, and if this can change the magnitude of the superexchange, then the number of groups should double.

2. EXPERIMENT

The investigations were performed using an 8-mm radiospectrometer at atmospheric pressure and 4.2 K temperature. The $ZnSiF_6\cdot 6H_2O$ single crystals with $1\%NiSiF_6\cdot 6H_2O$ impurity, grown from a water solution with decreasing temperature and used previously in Refs. 3–7, were used as the experimental samples.

In accordance with Eq. (1), for an arbitrary direction of the external magnetic field and symmetric relative to the value corresponding to $g=2.23$, two fine-structure lines of a single ion (the main resolved lines) are observed in the spectrum with ≈ 5 mT width according to the points of maximum curvature. The main allowed lines are accompanied by satellites with half the width and two orders of magnitude lower intensity. In weaker fields a weaker ''forbidden'' line (the main forbidden line) with ≈ 1.2 mT width is observed; it vanishes completely for $\mathbf{H}_0\|\mathbf{C}_3$, indicating that terms which are of lower symmetry than those presented in Eq. (1) are absent in the crystal field of the isolated ion. The main forbidden line is also surrounded by satellites, but their width is the same. Moreover, the satellites of the main forbidden line do not vanish for $\mathbf{H}_0\|\mathbf{C}_3$, which confirms the assumption that a pair of impurity ions induces quite low-symmetry components of the crystal field.

The position of the satellites, measured in the xz plane of the LCS, relative to the low-field main allowed line is displayed in Fig. 1 (dots). It follows hence that two types of satellites with fundamentally different angular dependence are present in the spectrum of the allowed transitions. Specifically, some satellites (*1–3* and *1′–3′*) split into three on rotation by $\theta=0$, while the others (a,b,c, and d) do not split, but rather approach the main line, following the same empirically obtained angular dependence, according to which the curves connecting the corresponding experimental points are drawn in Fig. 1,

$$\Delta H_i = A_i(3\cos^2\theta - 1), \tag{10}$$

where ΔH_i is the distance between the main line and the i-th satellite ($i=a,b,c,d$) and A_i are constants.

Additional investigations must be performed to make sense out of such a complicated angular dependence. Since the lines of the spectrum of forbidden transitions are much narrower and are less masked by one another and by the main line, their investigation should be quite fruitful for

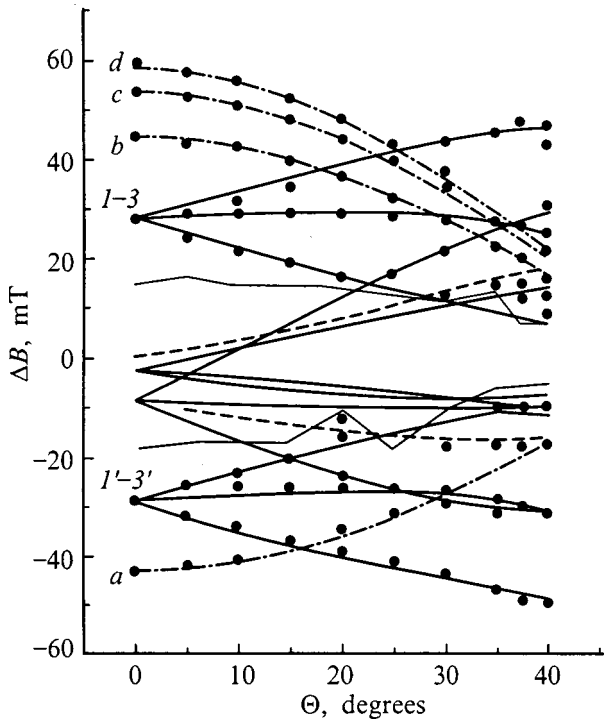

FIG. 1. Position of the satellites relative to the low-field main allowed line in the xz plane of the LCS. Dots—experiment, curves—calculation: solid lines (nn pairs) and dashed lines ($2n$ pairs) according to data from Table II and the expression (2); dot-dashed lines (isolated ions)—according to Eq. (10). For $2n$ pairs, only the curves that leave the zone covered by the main line at least in some range of angles are presented. The thin broken lines bound the region masked by the main line of the absorption spectrum. $T=4.2$ K, $\nu=34500$ MHz.

these purposes. It would be most informative and illuminating to investigate the angular dependence of the spectra in a cone relative to the C_3 axis. In this case, if lines from all types of pairs are indeed present in the spectrum, then the following picture should be expected: The spectrum of *nn* pairs (*nn* spectrum) is represented by three groups of lines, the extrema of whose angular dependence in accordance with the directions of the lines of interaction separated by 120° relative to one another; the $2n\alpha$ spectrum likewise consists of a rosette of three groups of lines, separated by an angle of 120° and turned away from the rosette of the *nn* spectrum by 60°; the rosette with twice the number of lobes and turned away from the *nn* spectrum by 30° should be expected from the $2n\beta$ pairs; the position of the lines in the spectrum of the $3n\alpha$ pair should not depend on the angle θ, and the number and direction of the lobes of the rosettes of the $3n\beta$ and $2n\alpha$ pairs should be the same and, in addition to a maximum amplitude with respect to the field should be expected from the *nn* spectrum and the minimum amplitude should be expected from the $3n$ spectrum.

It follows from Figs. 2a and 2b, where the dots show the experimentally obtained angular dependence of the forbidden transitions in the *xz* plane, that an angle θ in the range 20°–40° is optimal for the generatrix of the cone; for such an angle the lines of a pair spectrum are separated quite far from one another so that their masking by one another and by the main line is smallest.

The results of an experimental investigation of the spectrum of forbidden transitions in the cone $\theta = 29.5°$ is shown in Fig. 3 (dots). On the basis of the arguments presented above, there are grounds for believing that the points *1* and *1′*, *2* and *2′*, *3* and *3′* (group I) belong to the *nn* spectrum and the points *4* and *4′*, *5* and *5′*, *6* and *6′* (group II) belong to the $2n\alpha$ spectrum; there are no spectra from $2n\beta$, $3n\alpha$, and $3n\beta$ pairs. Lines similar to the lines *a*,*b*,*c*, and *d* in the spectrum of allowed transitions are also absent (Fig. 1).

3. ANALYSIS OF THE OBSERVATIONS

Since the Hamiltonian (2) cannot be diagonalized in its general form, a computer program was written which made it possible, for spectra of the forbidden and allowed transitions, to model the absorption spectrum on the basis of the parameters of the spin Hamiltonian and to find by the least-squares method the parameters of the same Hamiltonian on the basis of the input experimental spectra (up to 50 simultaneously).

3.1. Forbidden transitions

Simulation of the angular dependences presented in Figs. 2 and 3, assuming that the pair of ions interacting only via the MDD is in the same crystal field as the isolated ion, showed that in this case the ESR spectrum for pairs of any type should consist of four lines, to of which are weakly split and they should be masked in the real spectrum by a line of the spectrum of an isolated ion. For the $3n$ pairs all four lines should be masked, with the exception of the spectrum of the $3n\alpha$ pairs for $\theta < 20°$ in the spectrum of the forbidden transitions; group-II points are quite close to the calculation for the $2n\alpha$ spectrum, and *7* and *7′* (Fig. 2b) are close to the

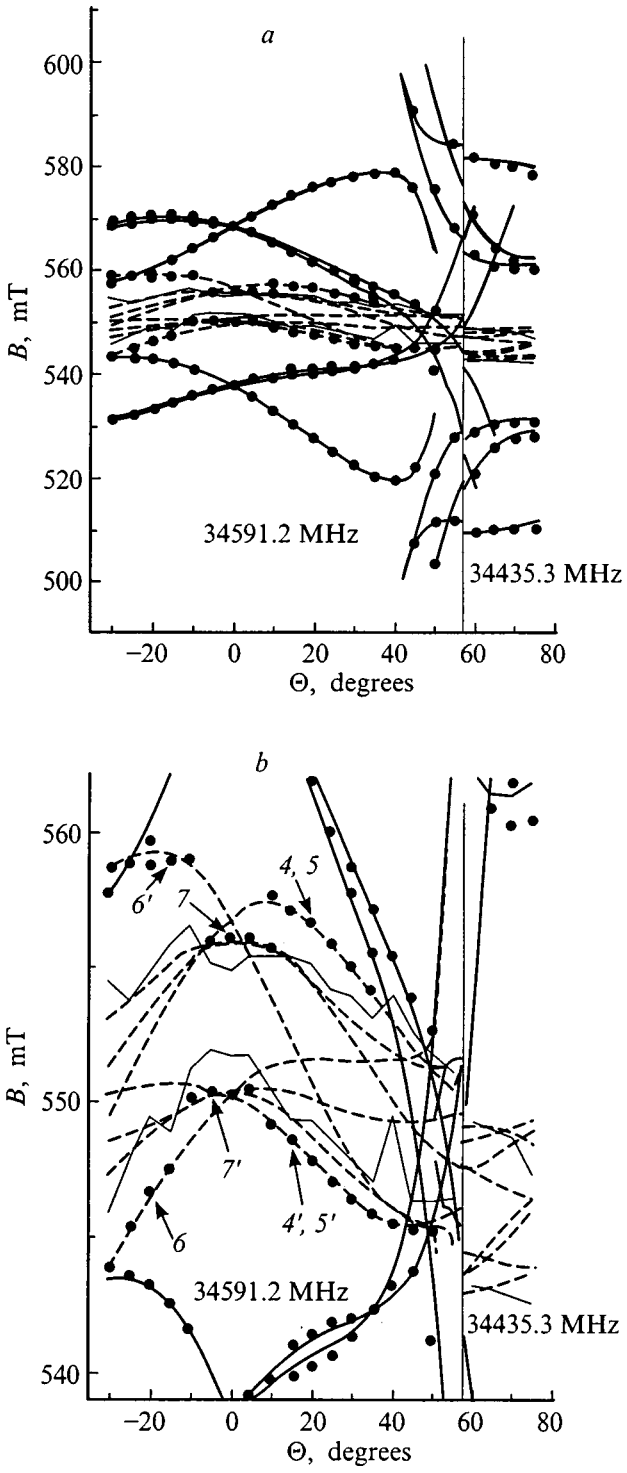

FIG. 2. a—Angular dependence of the spectrum of ''forbidden'' transitions in the *xz* plane of the LCS. Same remarks as in Fig. 1. b—Central part of Fig. 2a on an enlarged scale with respect to the field. Same remarks as in Fig. 1.

$2n\beta$ spectrum; the group-I points do not agree, even qualitatively, with the computational results for *nn* pairs.

The situation was radically improved by introducing into the analysis an isotropic SSI and lower-symmetry parameters of the crystal field (B_2^1 for $2n$ and B_2^1, C_2^1, and C_2^2 for *nn* pairs). No other parameters of the Hamiltonian (2) appreciably influence the agreement between experiment and the cal-

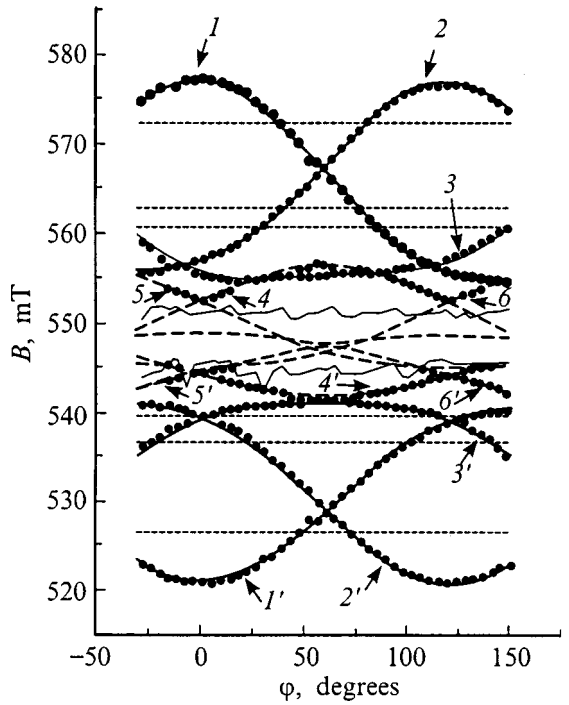

FIG. 3. Angular dependence of the spectrum of forbidden transitions in the cone $\theta=29.5°$. Dotted lines—angular dependence of the spectrum of nn, $2n$, and $3n$ pairs, calculated according to the results of Ref. 2. $\nu=34462.3$ MHz. All other remarks are the same as in Fig. 1.

culations. The results presented in Table II and all curves connecting the experimental points in Figs. 2 and 3 were obtained using them. Figure 3, where this is most clearly seen, also displays the computational results obtained on the basis of the results of Ref. 2. The complete disagreement with experiment demonstrates their incorrectness.

TABLE II. Parameters of the Hamiltonian (2), obtained for various types of pairs of Ni^{2+}:$ZnSiF_6\cdot 6H_2O$ ions.

Parameter	nn	$2n\alpha$	$2n\beta$
	Forbidden transitions. xz plane		
g	2.232±0.002	2.231±0.003	2.233±0.003
$3B_2^0$	−1384±32	−1356±87	−1342±361
B_2^1	189±37	−167±146	–
C_2^1	−105±41	–	–
C_2^2	83±28	–	–
J	−194±3	−6±2	3±2
	Forbidden transitions. Cone $\theta=29.5°$		
g	2.2321±0.0003	2.2319±0.0003	
$3B_2^0$	−1375±16	−1352±17	
B_2^1	81±31	−266±55	
C_2^1	−98±30	–	spectrum masked
C_2^2	37±54	–	by the main line
J	−198±1	−5±1	
	Allowed transitions. xz plane		
g	2.2299±0.0001	2.2319	2.2319
$3B_2^0$	−1398.1±0.5	−1372	−1372
B_2^1	155±3	−230	−230
C_2^1	−177±3	–	–
C_2^2	–	–	–
J	−197±1	−5	3

Note: Energies are given in units of $10^{-4}\,cm^{-1}$. The parameters that have not been presented are immaterial. The dipole contribution is presented in Table I. The confidence intervals were calculated at a 0.95 reliability level.

3.2. Allowed transitions

The results obtained make it possible to identify the spectrum of allowed transitions, and since the latter is much more sensitive to the parameters (2), they also yield more accurate information. However, this was found to be possible only for the nearest pair of interacting ions, since the spectrum of the $3n$ and $2n$ pairs in the experimental angular range is completely or almost completely hidden by the main line. The results of minimization are presented in Table II, and all curves with the exception of a,b,c, and d were obtained according to these results. It should be noted that the experimental spectrum contains too few points to make a statistical analysis of the data for $2n$ pairs, and for this reason the confidence interval is not indicated.

4. DISCUSSION

4.1. Spectrum of isolated ions

The spectrum of allowed transitions contains the satellites a,b,c, and d, whose angular dependence is fundamentally different from that of the lines identified as a pair spectrum. All lines in the spectrum of forbidden transitions have been identified and there are no analogs of the lines a,b,c, and d. What is their nature?

If a crystal field with an axial component D_1 acts on an isolated ion with effective spin $S=1$, then for a quantum with sufficient energy the angular dependence of the distance ΔH between the lines in the spectrum of allowed transitions can be described up to terms $D_1^2/h\nu$ by the expression (10), taking $A_i=D_1$. If the same paramagnetic ions, but in a crystal field D_2, are present in the sample, then lines from both spectra will be present in the spectrum. The distance between the low-field (or high-field) lines will likewise be described by expression (10), where $A_i=D_1-D_2$. On the other hand the position of the line of a forbidden transition, to within the accuracy presented above, does not depend on D, so that if the lines a,b,c, and d are due to isolated ions, for which D is different, then they should be absent in the spectrum of the forbidden transitions because they are superposed on one another, as is observed experimentally. Finally, the investigation of the angular dependence of the allowed transitions obtained in the cone $\theta=40°$ showed that the positions of the satellites examined are independent of the angle φ. These facts are completely sufficient to assert that these satellites, incorrectly identified in Ref. 2 as lines in a pair spectrum, are lines in the spectrum of isolated ions with D equal to -1789×10^{-4}, -873×10^{-4}, -781×10^{-4}, and $-732\times10^{-4}\,cm^{-1}$, respectively. We note that these spectra are not due to a concretion of single crystals of quite small volume, since this would be inconsistent wth the existence of a center with $D=-1789\times10^{-4}\,cm^{-1}$ and the independence of the positions of the lines of the spectrum from φ, but rather they are characteristic of the single crystal itself. Even

such a seemingly insignificant action as deuteration destroys this property: These lines are absent in the pair spectrum of the ions $Ni^{2+}:ZnSiF_6\cdot 6H_2O$.[3]

The ESR spectrum of $Ni^{2+}:ZnSiF_6\cdot 6H_2O$ is very sensitive to hydrostatic compression and, in the pressure range from 0 to 4 kbar, the initial splitting depends on the pressure as $D=(849.46P-1342)\times 10^{-4}\,cm^{-1}$ (Ref. 4), as a result of which the observed values of D can be realized if local regions under pressures 526, 549, 660, and 718 atm, respectively, are present in the single crystal. If this so, then why do these regions have sharp boundaries? After all, the width of the lines in this spectrum is the same as the width of the lines in the pair spectrum. Further, the volume of these regions, reflected in the intensity of the spectral lines, should decrease as the pressure deviates from the normal pressure. This appeared qualitatively in the intensity of the lines: 4:15:13:1, respectively; but, it is impossible to draw quantitative conclusions. Finally, as follows from Fig. 1, the number and position of these lines is not exactly the same as that found in Ref. 2. However, additional investigations, which fall outside the scope of our problem, are required to answer these and other questions.

4.2. Pair spectrum

The calculation of the confidence intervals presented in Table II neglected the uncertainty in the setting of the angles in the course of the experiment, and only the deviation of the experimental points from the computed curve was used. Therefore it is not surprising that the discrepancy between certain data for the crystal field parameters obtained from various angular dependences falls outside the confidence limits. Nonetheless these results make it possible to draw definite conclusions. It is clear from Table II that impurity ions lying close to one another (nn pairs) produce large distortions of the crystal field, manifested as an increase in B_2^0 and the appearance of low-symmetry terms. It is interesting to note that the term B_2^2, known as the ''rhombicity parameter,'' is absent for all types of pairs. As the distance between the ions increases ($2n$ pair), the distortions decrease, and substantial deviations from the crystal field parameters of an isolated ion can hardly be expected for strongly separated ions in a $3n$ pair. Further, as the interion distance increases from 6.24 Å for nn pairs up to 8.33 Å for $2n\alpha$ pairs (a factor of 1.33), the nondipole part of the spin–spin interaction represented only by an isotropic interaction decreases in absolute magnitude from $(-197\pm 1)\times 10^{-4}\,cm^{-1}$ to $(-5\pm 1)\times 10^{-4}\,cm^{-1}$, i.e., by almost a factor of 40, though this comparison is not entirely correct, since the bond angles also change in the process. The nondipole part continues to decrease from $2n\alpha$ to $2n\beta$ (9.29 Å) pairs, but now it decreases much more slowly and changes sign.

On this basis the following two conjectures can be made concerning the reasons why the spectrum of $3n\alpha$ pairs is absent in the experiment.

1) Since the crystal field does not contain low-symmetry components in the range of angles ($\theta<20°$) where such a spectrum could be observed, the transition probability is low and the spectrum is not observed because the lines are weak; because of the large interion distance the interaction between the ions is due essentially only to MDD ($J_{3n}=0$).

2) Since not only the interionic distance but also the bond angle have a large influence on the magnitude of the superexchange, besides MDD, the ions are coupled by isotropic exchange $J_{3n\alpha}=(18\pm 2)\times 10^{-4}\,cm^{-1}$. As calculations show, the lines of the spectrum coincide with the points *7* and *7′* (Fig. 2b) or are masked by the main line if J is larger.

On the basis of existing experimental results, it is impossible to draw a definite conclusion concerning the magnitude of the nondipole part of the interaction of $3n$ pairs. But the following has been proved.

1) The magnetic dipole–dipole interaction has a large effect on the ESR spectrum of interacting pairs of $Ni^{2+}:ZnSiF_6\cdot 6H_2O$ ions.

2) Isotropic exchange makes the main contribution to the nondipole part of the interaction. Its magnitude is $J_{nn}=(-197\pm 1)\times 10^{-4}$, $J_{2n\alpha}=(-5\pm 1)\times 10^{-4}$, and $J_{2n\beta}=(3\pm 2)\times 10^{-4}\,cm^{-1}$, and it does not depend on the position of the water octahedron. The contribution of other mechanisms is negligibly small.

3) In the material investigated, a pair of impurity ions produces very low-symmetry local distortions of the crystal field, which decrease as the distance between the impurity ions increases.

4) The interpretation offered in Ref. 2 for the pair spectrum, and then used in later works, is incorrect.

5) Regions with a volume of several percent with different values of B_2^0 are present in $Ni^{2+}:ZnSiF_6\cdot 6H_2O$.

Since quite close results ($J_{nn}=-193\times 10^{-4}\,cm^{-1}$) have been obtained for $Ni^{2+}:MgSiF_6\cdot 6H_2O$,[11] we shall make a comparison with the properties of concentrated nickel fluorosilicate. Following Ref. 2, we shall calculate the correction Θ in the Curie–Weiss law for the magnetic susceptibility, summing over all three coordination spheres, taking $J=0$ for the most distant neighbors:

$$\Theta=-\frac{S(S+1)}{3k}[z_{nn}J_{nn}+z_{2n\alpha}J_{2n\alpha}+z_{2n\beta}J_{2n\beta}+z_{3n\alpha}J_{3n\alpha}+z_{3n\beta}J_{3n\beta}]. \quad (11)$$

A calculation based on our data gives $\Theta=0.114\,K$ for $J_{3n\alpha}=J_{3n\beta}=0$ and 0.099 K for $J_{3n\alpha}=J_{3n\beta}=18\times 10^{-4}\,cm^{-1}$. The directly measured values of the paramagnetic Curie temperature are 0.1 K[12] and 0.111 K.[13] The magnetic specific heat CT^2/R, according to our data, is $0.0118\,K^2$ in both cases. Direct measurements give $0.0139\,K^2$ (Ref. 12).

In summary, comparison with macroscopic investigations does not give an unequivocal answer to the question of the value of J_{3n}, but it does demonstrate much better agreement with our data and with the results of Ref. 2 ($\Theta=0.117\,K$, $CT^2/R=0.0207\,K^2$).

We are sincerely grateful to our colleagues S. N. Lukin, for assistance and a discussion of the results, and G. Ya. Samsonova for growing high-quality single crystals.

*E-Mail: prohorov@pr.fti.ac.donetsk.ua

[1] S. A. Al'tshuller and R. M. Valishev, Zh. Éksp. Teor. Fiz. **48**, 464 (1965) [Sov. Phys. JETP **21**, 309 (1965)].
[2] R. M. Valishev, *Paramagnetic Resonance* [in Russian] (Kazan' University Press, Kazan', 1968), No. 3, p. 35.
[3] A. Yu. Kozhukhar', S. N. Lukin, G. A. Tsintsadze *et al.*, Prib. Tekh. Éksp., No. 4, 198 (1975).
[4] A. Yu. Kozhukhar', S. N. Lukin, and G. A. Tsintsadze, Fiz. Tverd. Tela (Leningrad) **17**, 1870 (1975) [Sov. Phys. Solid State **17**, 1231 (1975)].
[5] A. Yu. Kozhuhar and G. A. Tsintsadze, Phys. Lett. A **55**, 175 (1975).
[6] A. A. Galkin, A. Yu. Kozhukhar', and G. A. Tsintsadze, Zh. Éksp. Teor. Fiz. **70**, 248 (1976) [Sov. Phys. JETP **43**, 128 (1976)].
[7] A. Yu. Kozhukhar' and G. A. Tsintsadze, Fiz. Tverd. Tela (Leningrad) **17**, 3414 (1975) [Sov. Phys. Solid State **17**, 2234 (1975)].
[8] V. G. Bar'yakhtar, I. M. Vitebskiĭ, A. A. Galkin *et al.*, Zh. Éksp. Teor. Fiz. **84**, 1083 (1983) [Sov. Phys. JETP **57**, 628 (1983)].
[9] A. Abragam and B. Bleaney, *Electron Paramagnetic Resonance of Transition Ions* (Clarendon Press, Oxford, 1970; Mir, Moscow, 1972, 651 pp.).
[10] S. Ray, A. Zalkin, and D. Templeton, Acta Crystallogr., Sect. B: Struct. Crystallogr. Cryst. Chem. **29**, 2741 (1973).
[11] I. M. Krygin and A. D. Prokhorov, Fiz. Nizk. Temp. **20**, 396 (1994) [Low Temp. Phys. **20**, 316 (1994)].
[12] R. J. Benzie and A. H. Cooke, Proc. Phys. Soc. London, Sect. A **63**, 213 (1950).
[13] V. P. D'yakonov, G. G. Levchenko, I. M. Fita *et al.*, Zh. Éksp. Teor. Fiz. **87**, 2193 (1984) [Sov. Phys. JETP **60**, 1268 (1984)].

Translated by M. E. Alferieff

Volume effects in the theory of equilibrium and quasiequilibrium states of multicomponent solid solutions

M. A. Zakharov

Novgorod State University 173003 Novgorod, Russia
(Submitted April 21, 1999)
Fiz. Tverd. Tela (St. Petersburg) **41**, 1609–1613 (September 1999)

A phenomenological theory of equilibrium and quasiequilibrium states of multicomponent solid solutions is constructed taking account of volume effects. Quasiequilibrium states are characterized by the fact that only some of the conditions for thermal dynamic equilibrium of the system are satisfied. The short-range parts of the interatomic interactions are taken into account by introducing the proper volumes of the atoms based on a generalized lattice model. The long-range parts of the potentials are taken into account in the effective-field approximation. The equations for the quasiequilibrium components in the solutions are introduced taking account of the nonuniformity in the distributions of the less mobile nonequilibrium components. The conditions for spinodal decomposition of a solid solution with an arbitrary number of components in the equilibrium and quasiequilibrium cases are obtained. An equation for equilibrium spinodal decomposition of a three-component microheterogeneous solid solution is found. [S1063-7834(99)01509-9]

It is well known that the configurations of many condensed systems, including solid solutions,[1] spin glasses,[2,3] and so on, are not equilibrium systems because of the slowness of the restructuring processes. These systems are nonergodic, and they cannot be calculated on the basis of traditional statistical thermodynamics. The description of systems of this kind in the general case is an extremely difficult problem. The objective of the present work is to construct a phenomenological theory of nonequilibrium systems in the local-equilibrium approximation. We note that irreversible processes admit such a description at the ''hydrodynamic stage,'' where the conditions of total equilibrium in the system have still not been attained but local thermodynamic variables can already be introduced. The relation between the local thermodynamic variables is the same as in equilibrium thermodynamics.[4,5]

In most cases thermal equilibrium is reached most rapidly while mechanical and thermal equilibrium, as a rule, are reached most rapidly in liquid condensed systems. The slowest process is usually attainment of chemical equilibrium in the system.

An additional feature is present in the overwhelming majority of multicomponent solid solutions, viz., a hierarchy of atomic mobilities of the various components.[6,7] As a result, the conditions of chemical equilibrium (constancy of the chemical potential) for different components are reached in different time scales. Correspondingly, if the time elapsed from the moment the external thermodynamic conditions are established is much shorter than the longest of the relaxation times, then there is enough time for only some of the conditions of thermodynamic equilibrium to be satisfied in the system. We shall term such states of the system quasiequilibrium states.[8]

In Refs. 8 and 9 the quasiequilibrium states of solutions were analyzed on the basis of a generalized lattice model that takes account of volume effects which blur the concepts of a crystal lattice and occupation probabilities of ''sites'' in the lattice for different components. In this connection, the method of static concentration waves, proposed by Grivoglaz and Smirnov (see, for example, Ref. 11) and developed by Khachaturyan[12] in the absence of volume effects in uniform solutions, required correction. The extension to the case of nonuniform solutions (neglecting volume effects) has been made by A. I. Olemskiĭ[13] (see also Ref. 14).

Taking account of volume effects and the hierarchy of mobilities of components is the key factor for the development of a theory of the effect of mechanical stresses generated in the diffusion zone on the kinetics of diffusion processes. Thus, according to Refs. 15 and 16, mechanical stresses appear in the diffusion zone for two reasons — volume effects, giving rise to concentration stresses, and large differences in the atomic mobilities of the various components, generating diffusion stresses. The existing theories based on the classical theory of elasticity employ predominantly a macroscopic description (see, for example, Refs. 18 and 17), and their application on atomic scales, where the concept of mechanical stresses itself becomes meaningless, raises definite doubts. The concept of deformation for a solution whose components have appreciably different atomic dimensions becomes even more doubtful. A generalized lattice model, where the initial concepts are the specific volumes of the components, is better in this respect.

A phenomenological theory of quasiequilibrium ternary systems has been constructed in Ref. 8. Specifically, a ternary solid solution with a fixed (nonequilibrium) distribution of the least mobile component was examined, the condition for phase separation was found, and it was shown that there

exists a temperature range where opposing processes coexist in the system.

To develop a general theory we proceed from the fact that, when the external conditions (temperature, pressure, and so on) change, nonequilibrium phase transformations, whose characteristics can differ from those of equilibrium phase transitions, can occur in a system in quasiequilibrium. In this connection, the theory expounded below is unified, describing both equilibrium and nonequilibrium phase transformations in multicomponent solid solutions.

The formalism for taking account of volume effects and other restrictions in statistical thermodynamics is expounded in Sec. 1. As an example of the use of the apparatus developed, the system of equations for an equilibrium distribution of matter in condensed systems and the equation of equilibrium spinodal decomposition of a ternary solution are derived.

The relations obtained between the thermodynamic variables in the local-equilibrium approximation for investigated quasiequilibrium systems are used in Sec. 2.

1. EQUILIBRIUM STATES OF SOLUTIONS AND EQUILIBRIUM SPINODALS

Let us consider a solution of m components whose spatial distributions are given by the local particle number densities $n_1(\mathbf{r})$, $n_2(\mathbf{r})$, ..., $n_m(\mathbf{r})$. The Helmholtz free-energy functional F for a given thermodynamic system can be written in the self-consistent field approximation, taking account of only pair interactions, as

$$F=\frac{1}{2}\sum_{i,j=1}^{m}\int\int \mathcal{V}_{ij}(\mathbf{r}''-\mathbf{r}')n_i(\mathbf{r}'')n_j(\mathbf{r}')d\mathbf{V}''d\mathbf{V}' + T\sum_{i=1}^{m}\int n_i(\mathbf{r})\ln\left(\frac{n_i(\mathbf{r})}{n(\mathbf{r})}\right)dV, \tag{1}$$

where the first term is the configurational part of the free energy in the effective-field approximation, $\mathcal{V}_{ij}(\mathbf{r}''-\mathbf{r}')$ is the pair interaction potential of the particles of the i-th and j-th components located at the points $\mathbf{r}''$ and $\mathbf{r}'$, respectively; the second term is the entropy term of the free energy in the regular-solutions approximation; T is the temperature in energy units; the integration extends over the entire volume V of the system; and, $n(\mathbf{r})=\Sigma_{i=1}^{m}n_i(\mathbf{r})$ is the total particle number density.

We shall seek the extremum of the functional F under additional conditions. The first condition is a restriction on the densities of the components due to intense repulsion between atoms at short distances. In this connection, following Ref. 10, we introduce the ''proper'' volumes ω_i of the particles of the components of the system. We take account of the fact that the condition for each element of space to be occupied

$$\sum_{i=1}^{m}\omega_i n_i(\mathbf{r})-1=0, \tag{2}$$

which we shall call the principle of close packing, should hold at an arbitrary point in the solution. The introduction of proper volumes is an extreme form of taking account of the intense repulsion of particles at short distances. Specifically, we have an upper bound on the densities: $n_i(\mathbf{r})\leqslant 1/\omega_i$.

The second condition—the law of conservation of particle numbers for each component—is

$$\int n_i(\mathbf{r})dV-N_i=0, \tag{3}$$

where N_i the total number of particles of the i-th component in the system.

To find the extremum of the functional (1), taking account of Eqs. (2) and (3), we introduce the new functional (Lagrangian)

$$\Phi=F-\sum_{i=1}^{m}\mu_i\left[\int n_i(\mathbf{r})dV-N_i\right] - \int\Psi(\mathbf{r})\left[\sum_{i=1}^{m}\omega_i n_i(r)-1\right]dV, \tag{4}$$

where μ_i and $\Psi(\mathbf{r})$ are undetermined Lagrange multipliers (μ_i is the chemical potential of the i-th component).

Equating to zero the variational derivative $(\delta\Phi/\delta n_i(\mathbf{r}))_{n_j(\mathbf{r})}$, we find

$$\mu_i=\sum_{j=1}^{m}\int \mathcal{V}_{ij}(\mathbf{r}-\mathbf{r}')n_j(\mathbf{r}')dV' + T\ln\left(\frac{n_i(\mathbf{r})}{n(\mathbf{r})}\right)-\omega_i\Psi(\mathbf{r}). \tag{5}$$

Hence we obtain the condition for chemical equilibrium of the i-th component

$$\sum_{j=1}^{m}\int \mathcal{V}_{ij}(\mathbf{r}-\mathbf{r}')n_j(\mathbf{r}')dV' + T\ln\left(\frac{n_i(\mathbf{r})}{n(\mathbf{r})}\right)-\omega_i\Psi(\mathbf{r})=C_i, \tag{6}$$

where C_i are arbitrary constants.

Thus the closed system of equations describing total chemical equilibrium is

$$\sum_{j=1}^{m}\int \mathcal{V}_{ij}(\mathbf{r}-\mathbf{r}')n_j(\mathbf{r}')dV' + T\ln\left(\frac{n_i(\mathbf{r})}{n(\mathbf{r})}\right)-\omega_i\Psi(\mathbf{r})=C_i,$$

$$\sum_{i=1}^{m}\omega_i n_i(\mathbf{r})=1, \tag{7}$$

[The number of unknown functions in this system of nonlinear integral equations is $m+1$: $\Phi(\mathbf{r})$ and $n_i(\mathbf{r})$.]

A phase transition is always associated with the nonuniqueness of the Gibbs states.[18] This means that the system of equations (7) in the case of a phase transition should have a nonunique solution. For this reason, the criterion for a

phase transition in the system is the appearance of branch points of solutions as a function of the thermodynamic conditions.

Since we are interested in the spinodal decomposition of the solution, we shall examine a transition from a uniform into a nonuniform distribution of components. We represent the local concentrations of the components in the form

$$n_i(\mathbf{r}) = n_i^0 + \delta n_i(\mathbf{r}), \tag{8}$$

where $\delta n_i(\mathbf{r})$ is an infinitely small deviation of the local density of the i-th component from the equilibrium value n_i^0.

Linearizing with respect to $\delta n_i(\mathbf{r})$ and $\delta\Psi(\mathbf{r})$ and Fourier transforming the system (7) we find

$$\sum_{j=1}^{m} \tilde{\mathcal{V}}_{ij}\delta\tilde{n}_j + T\left[\frac{\delta\tilde{n}_i}{n_i^0} - \frac{\delta\tilde{n}}{n_0}\right] - \omega_i\delta\tilde{\Psi} = 0,$$

$$\sum_{i=1}^{m} \omega_i\delta\tilde{n}_i = 0, \tag{9}$$

(the overtilda denotes the Fourier transform of the function so labeled; the **k**-dependence of the Fourier transform is omitted here and in all subsequent formulas).

We represent this homogeneous system of algebraic equations, which is linear in $\delta\tilde{n}_i$ and $\delta\tilde{\Psi}$, in the matrix form

$$Ax = 0, \tag{10}$$

where

$$A = \begin{pmatrix} \tilde{\mathcal{V}}_{11}+\lambda_{11} & \cdots & \tilde{\mathcal{V}}_{1m}+\lambda_{1m} & -\omega_1 \\ \cdots & \cdots & \cdots & \cdots \\ \cdots & \cdots & \cdots & \cdots \\ \cdots & \cdots & \cdots & \cdots \\ \tilde{\mathcal{V}}_{m1}+\lambda_{m1} & \cdots & \tilde{\mathcal{V}}_{mm}+\lambda_{mm} & -\omega_m \\ -\omega_1 & \cdots & -\omega_m & 0 \end{pmatrix}, \tag{11}$$

$\lambda_{ij} = T((\delta_{ij}/n_j^0) - (1/n^0))$, δ_{ij} is a delta function, and

$$x = \begin{pmatrix} \delta\tilde{n}_1 \\ \vdots \\ \delta\tilde{n}_m \\ \delta\Psi \end{pmatrix} \tag{12}$$

At a branch point the system of integral equations (7) (and algebraic equations (9)) possesses a nontrivial solution, and therefore

$$\det A = 0. \tag{13}$$

Hence, specifically, the well-known result of Ref. 19 is obtained from Eq. (13) when the specific volumes of all components are the same.

For a ternary solution in total equilibrium, using the criterion (13) for decomposition and the explicit form of the matrix A (11), we obtain the equation of the spinodal

$$T^2 - \left(n_1^0 n_2^0 n_3^0 \gamma_1 + n^0 \sum_{i<j}^{3} \tilde{W}_{ij} n_i^0 n_j^0\right) T - \omega_1^2\omega_2^2\omega_3^2 n^0 n_1^0 n_2^0 n_3^0 \gamma_2 = 0, \tag{14}$$

where

$$\gamma_1 = \sum_{i\neq j, j\neq k, k\neq i}^{3} \left(\tilde{\mathcal{V}}_{ij}\omega_k(\omega_i+\omega_j-\omega_k) - \frac{1}{2}\tilde{\mathcal{V}}_{ii}\omega_j\omega_k\right),$$

$$\tilde{W}_{ij} = \omega_i^2\omega_j^2\left(2\frac{\tilde{\mathcal{V}}_{ij}}{\omega_i\omega_j} - \frac{\tilde{\mathcal{V}}_{ii}}{\omega_i^2} - \frac{\tilde{\mathcal{V}}_{jj}}{\omega_j^2}\right),$$

$$\gamma_2 = \sum_{i<j}^{3}\left(\frac{\tilde{\mathcal{V}}_{ij}^2 - \tilde{\mathcal{V}}_{ii}\tilde{\mathcal{V}}_{jj}}{\omega_i^2\omega_j^2}\right) + \sum_{i\neq j, j\neq k, k\neq i}^{3} \frac{\tilde{\mathcal{V}}_{ij}}{\omega_i\omega_j\omega_k} \times \left(\frac{\tilde{\mathcal{V}}_{kk}}{\omega_k} - \frac{\tilde{\mathcal{V}}_{jk}}{\omega_j}\right). \tag{15}$$

We note that $\tilde{W}_{ij}$ is the analog of the energy of mixing in the Gorskiĭ–Bragg–Williams theory taking account of the proper volumes of the components.

The equation (14) of the spinodal for a ternary solid solution is a generalization of the well-known Prigogine equation.[20] Without giving a detailed quantitative analysis of Eq. (14), we note nonetheless that, specifically, for binary solutions of the i-th and j-th components the critical temperature of phase separation is given by

$$T_c = n^0 n_i^0 n_j^0 \max_{\{\mathbf{k}\}} \tilde{W}_{ij}. \tag{16}$$

Here it is assumed that the criterion for decomposition of a binary solution in the Gorskiĭ–Bragg–Williams theory—the condition that the mixing energy is positive—is assumed to be satisfied.

2. QUASIEQUILIBRIUM STATES OF A MULTICOMPONENT SOLUTION

The theory of equilibrium states of multicomponent solid solutions presented in the preceding section taking account of the volume effects can be extended directly to quasiequilibrium states of the system. The distributions of the components which have reached an intermediate equilibrium on the time scales studied are described by equations of the type (6), and the distributions of the less mobile components of the system are given by fixed initial densities. The latter can always be assumed known initially.

We shall enumerate the components of the system in order of decreasing mobilities of their atoms. Let us consider the most general case of quasiequilibrium states of a solid solution. Let the first k ($k<m$) components of the system be in an intermediate equilibrium; the remaining $m-k$ components, by virtue of their lower atomic mobilites, play the role of a nonuniform medium. In this case, instead of the $m+1$ equations of the system (7) we have only the $k+1$ equations with $k+1$ unknown functions.

In investigations of the condition for decomposition of a quasiequilibrium solution, the critical temperature and compositions of the coexisting phases should depend on the con-

centrations of all low-mobility components, playing the role of a ''medium'' in the given quasiequilibrium state.

Let us find the condition of spinodal decomposition of a solid solution in a given quasiequilibrium state. We assume that all low-mobility components are distributed in the system slightly nonuniformly, fluctuating near their stationary values n_i^0. As a result of this assumption, the local densities of all components, both mobile and immobile, can be represented in the form (8). Linearizing a system similar to the system (7), taking account of Eqs. (8) and (9), with respect to $\delta n_i(\mathbf{r})$ and $\delta\Psi(\mathbf{r})$ and Fourier transforming, we obtain an inhomogeneous system of algebraic equations which is linear with respect to $\delta\tilde{n}_i$ and $\delta\tilde{\Psi}$, and which we write in the matrix form

$$Ax = B, \tag{17}$$

where

$$A = \begin{pmatrix} \tilde{\mathcal{V}}_{11}+\lambda_{11} & \cdots & \tilde{\mathcal{V}}_{1k}+\lambda_{1k} & -\omega_1 \\ \cdots & \cdots & \cdots & \cdots \\ \cdots & \cdots & \cdots & \cdots \\ \cdots & \cdots & \cdots & \cdots \\ \tilde{\mathcal{V}}_{k1}+\lambda_{k1} & \cdots & \tilde{\mathcal{V}}_{kk}+\lambda_{kk} & -\omega_k \\ -\omega_1 & \cdots & -\omega_k & 0 \end{pmatrix}, \tag{18}$$

$$x = \begin{pmatrix} \delta\tilde{n}_1 \\ \vdots \\ \delta\tilde{n}_k \\ \delta\tilde{\Psi} \end{pmatrix}, \quad B = \begin{pmatrix} \sum_{j=k+1}^{m} \left[-\tilde{\mathcal{V}}_{1j} + \frac{T}{n^0} \right] \delta\tilde{n}_j \\ \vdots \\ \sum_{j=k+1}^{m} \left[-\tilde{\mathcal{V}}_{kj} + \frac{T}{n^0} \right] \delta\tilde{n}_j \\ \sum_{j=k+1}^{m} \omega_j \delta\tilde{n}_j \end{pmatrix} \tag{19}$$

The existence of a nonequilibrium phase transition in the system, as already mentioned, is due to the nonuniqueness of the Gibbs states and the appearance of a branch point of the corresponding linearized system (in our case this system is Eq. (17)).

Since the system of equations is compatible, the ranks of the main A and expanded A' matrices of the system (17) are the same, and since the solutions of the system are not unique, rank $A<k+1$. As a result, we have

$$\Delta = 0, \quad \Delta_1 = 0, \quad \ldots \quad \Delta_{k+1} = 0, \tag{20}$$

where Δ is the determinant of the matmrix A, and Δ_i is the determinant of the matrix obtained by substituting the i-th column of the main matrix A by the column of free terms B.

The system (20) is the criterion for spinodal decomposition of an m-component solid solution, k components of which have reached an intermediate equilibrium; it also determines the nonequilibrium phase-transition temperature and the boundary of nonequilibrium metastability in the solution.

We note that for a uniform distribution of $m-k$ low-mobility nonequilibrium components the linear system (17) is homogeneous and the conditions $\Delta_i=0$ of the system (20) are clearly satisfied, as a result of which vanishing of the determinant Δ is a necessary and sufficient condition for spinodal decomposition of the solution.

An important feature of phase separation in a multicomponent solution in a quasiequilibrium state, in contrast to an equilibrium state, is the appearance of additional conditions of the form $\Delta_i=0$ (20). Thus, the condition for separation of an equilibrium solution $\Delta=0$ is inadequate for a phase transition to appear in a quasiequilibrium solution.

A quantitative analysis of the equation of the spinodal will be given in our next paper.

In closing, we list the main results of this work.

1) A unified phenomenological theory of the equilibrium and quasiequilibrium states of multicomponent solid solutions was constructed taking account of the proper volumes of the components in the local-equilibrium approximation.

2) The conditions for spinodal decomposition of these thermodynamic systems in an arbitrary quasiequilibrium state, including in the equilibrium state, were obtained.

3) The equation of the spinodal for an equilibrium ternary solution was derived taking account of volume effects.

[1] I. M. Lifshitz and G. I. Stepanova, Zh. Éksp. Teor. Fiz. **33**, 485 (1957) [Sov. Phys. JETP **6**, 379 (1958)].
[2] K. Binder and A. P. Young, Rev. Mod. Phys. **58**, 801 (1986).
[3] D. Chowdhury, *Spin Glasses and Other Frustrated Systems* (World Scientific, Singapore, 1986).
[4] S. de Groot and P. Mazur, *Nonequilibrium Thermodynamics* (North-Holland, Amsterdam, 1952; Mir, Moscow, 1964).
[5] K. P. Gurov, *Phenomenological Theory of Irreversible Processes* [in Russian] (Nauka, Moscow, 1978).
[6] B. S. Bokshteĭn, S. Z. Bokshteĭn, and A. A. Zhukhovitskiĭ, *Thermodynamics and Kinetics of Diffusion in Solids* [in Russian] (Metallurgiya, Moscow, 1974).
[7] B. Ya. Lyubov, *Diffusion Processes in Inhomogeneous Solids* [in Russian] (Mir, Moscow, 1981).
[8] M. A. Zakharov, Fiz. Tverd. Tela (St. Petersburg) **41**(1), 60 (1999) [Phys. Solid State **41**, 51 (1999)].
[9] A. Yu. Zakharov and S. V. Terekhov, Fiz. Met. Metalloved. **59**, 261 (1985).
[10] A. Yu. Zakharov and S. V. Terekhov, in *Mathematical Problems of Chemical Thermodynamics* [in Russian] (Nauka, Novosibirsk, 1985), p. 173.
[11] M. A. Krivoglaz and A. A. Smirnov, *The Theory of Alloys Undergoing Ordering* [in Russian] (GIFML, Moscow, 1958).
[12] A. G. Khachaturyan, *The Theory of Phase Transformations and the Structure of Solid Solutions* [in Russian] (Nauka, Moscow, 1974).
[13] A. I. Olemskiĭ, Izv. Vyssh. Uchebn. Zaved. Fiz. No. 9, 48 (1980).
[14] A. A. Katsnel'son and A. I. Olemskiĭ, *Microscopic Theory of Inhomogeneous Structures* [in Russian] (Moscow State University, Moscow, 1987).
[15] Ya. E. Geguzin, *The Diffusion Zone* [in Russian] (Nauka, Moscow, 1979)
[16] Ya. E. Geguzin and M. A. Grivoglaz, *The Motion of Macroscopic Inclusions in Solids* [in Russian] (Metallurgiya, Moscow, 1971).
[17] V. S. Eremeev, *Diffusion and Stresses* [in Russian] (Energoatomizdat, Moscow, 1984).
[18] H.-O. Georgi, *Gibbs Measures and Phase Transitions* [in Russian] (Mir, Moscow, 1992).
[19] D. de Fontaine, Solid State Phys., Adv. Res. Appl. **34**, 74 (1979).

Translated by M. E. Alferieff

Fine structure of the permittivity spectrum of a fluorite crystal

V. V. Sobolev and A. I. Kalugin

Udmurtian State University, 426034 Izhevsk, Russia
(Submitted February 15, 1999)
Fiz. Tverd. Tela (St. Petersburg) **41**, 1614–1615 (September 1999)

The experimental curve of the permittivity of fluorite is decomposed, for the first time, into 11 components in the range 10.5–18 eV (90 K) and 18 components in the range 10–35 eV (300 K) by the Argand diagram method. Three parameters are determined for each component: the energy at band maximum, the half-width of the band, and the oscillator strength. A scheme is proposed for the nature of the components of the permittivity of fluorite. © *1999 American Institute of Physics.* [S1063-7834(99)01609-3]

Fluorite CaF_2 is a model crystal of the difluoride group.[1] Many band calculations as well as calculations of the density of states and the spectrum of ε_2 in the band approximation have been performed for it.[1–7] However, thus far these calculations are contradictory, and they do not even determine the sequential order of the bands uniquely. For strongly ionic crystals, including CaF_2, excitonic effects are characteristic in a wide range of intrinsic absorption energies. They have not been studied theoretically. For this reason, the maxima of the reflection and ε_2 spectra of CaF_2 are discussed in a simplified manner using qualitative schemes for the combination of excitonic and interband transitions.[1,2,6–8] In this connection, it is especially urgent to investigate transition energies and transition probabilities irrespective of the nature of the transitions themselves.

Our objective in the present work is to determine a set of transitions and their energies and oscillator strengths for crystal CaF_2 in a wide range of intrinsic absorption energies. Using the Argand diagram method,[9,10] we decompose the experimental integrated permittivity curve ε_2 of fluorite from Ref. 8 into 18 elementary Lorentzian components in the range 10–18 eV at 300 K and into 11 components in the range 10.5–18 eV at 90 K. For brevity, only the three main parameters of each component — the energy E_i of the band maximum, the half-width of the maximum, and the oscillator strength f_i — are given in Table I. It should be underscored that, in the generally accepted approximation where the total permittivity is represented as a sum of contributions of Lorenzian oscillators, the Argand-diagram method we used makes it possible to decompose uniquely the integrated ε_2 and ε_1 spectra into a minimum number of bands without any adjustable parameters. Transitions with close energies but not necessarily of close nature are summed in each band. For this reason, they can be decomposed additionally into several components each on the basis of theoretical models of the possible fine structure of the bands. At 300 K eight bands are established in the region 12–18 eV. As temperature decreases to 90 K triplet (band No. 3) and doublet (band No. 7) splittings are observed. These bands can all be divided with respect to the temperature shift into two groups: with a large shift $\sim+(0.15-0.25)$ eV (bands Nos. 1, 2, 3‴, 7′) and with a very small shift $\sim+0.01$ (Nos. 6, 8), -0.01 (No. 5), and -0.02 eV (No. 4). The values of f_i are temperature-independent for bands Nos. 1, 3, and 7. Special theoretical calculations are required in order to solve the question of the nature of the temperature anomalies in f_i for other bands.

The top valence band of CaF_2 is due to the $2p$ state of the fluorine ion, and the bottom conduction band is due to the $3d$, $4s$, and $4p$ states of the calcium ion.[2–7] Qualitatively, in the energy-level scheme in the one-electron approximation, the components of ε_2 which we established for crystal CaF_2 are associated with transitions from $2p$ F^- into $3d$ Ca^{+2} (Nos. 1–3), $4s$ Ca^{+2} (Nos. 4–6), $4s$, $4p$ Ca^{+2} (Nos. 7 and 8), and $4p$ Ca^{+2} (Nos. 9–11) and from $3p$ Ca^{+2} into $3d$ Ca^{+2} and $4s$ Ca^{+2} (Nos. 12–18). The characteristic features of most of these components of the spectrum ε_2 of fluorite are easier to explain in the metastable-exciton model. A detailed discussion of the nature of the components of ε_2 requires calculations of bands and excitons in a wide range

TABLE I. The energies E_i (eV) of the maxima, the half-widths H_i (eV), and the oscillator strengths f_i of fluorite.

No.	E_i		H_i		f_i	
	300 K	90 K	300 K	90 K	300 K	90 K
1	12.38	12.59	0.79	0.56	0.46	0.43
2	12.94	13.13	1.11	0.45	0.75	0.37
3′	–	13.575	–	0.53	–	0.15
3″	–	13.71	–	0.27	–	0.05
3‴	13.77	13.92	0.58	0.46	0.54	0.38
4	14.21	14.19	0.48	0.46	0.10	0.05
5	14.57	14.56	0.41	0.63	0.05	0.17
6	15.36	15.37	0.99	0.70	0.37	0.27
7′	–	15.78	–	0.46	–	0.04
7	15.99	16.24	1.03	0.84	0.16	0.13
8	16.99	17.00	1.31	0.81	0.16	0.09
9	19.29	–	1.03	–	0.04	–
10	20.72	–	1.59	–	0.13	–
11	23.14	–	1.71	–	0.10	–
12	25.13	–	1.75	–	0.24	–
13	25.68	–	2.86	–	0.08	–
14	27.87	–	0.63	–	0.05	–
15	29.25	–	1.37	–	0.07	–
16	30.64	–	1.04	–	0.07	–
17	32.65	–	1.75	–	0.24	–
18	34.34	–	0.63	–	0.05	–

of fundamental absorption energies. We hope that the results of the present work will give a fundamentally new basis for performing substantially more accurate and complete calculations of the electronic structure of CaF_2.

We thank N. V. Starostin, R. A. Évarestov, and W. Y. Ching for reprints of their papers.

This work was supported by the Center for Fundamental Studies (St. Petersburg University).

[1] V. V. Sobolev, *Zones and Excitons of Metal Halides* [in Russian] (Shtiintsa, Kishinev, 1987).
[2] V. A. Ganin, M. G. Karin, V. K. Sidorin, K. K. Sidorin, N. V. Starostin, G. P. Starstev, and M. P. Shepilov, Fiz. Tverd. Tela (Leningrad) **16**, 3554 (1974) [Sov. Phys. Solid State **16**, 2313 (1974)].
[3] N. V. Starostin and M. P. Shepilov, Fiz. Tverd. Tela (Leningrad) **17**, 822 (1975) [Sov. Phys. Solid State **17**, 523 (1975)].
[4] R. A. Évarestov, I. V. Murin, and A. V. Petrov, Fiz. Tverd. Tela (Leningrad) **30**, 292 (1988) [Sov. Phys. Solid State **30**, 168 (1988)].
[5] L. K. Ermakov, P. A. Rodnyĭ, and N. V. Starostin, Fiz. Tverd. Tela (Leningrad) **33**, 2542 (1991) [Sov. Phys. Solid State **33**, 1435 (1991)].
[6] N. C. Amaral, B. Maffeo, and D. Guenzburger, Phys. Status Solidi B **117**, 141 (1983).
[7] F. Gan, Y.-N. Xu, M.-Z. Huang, W. Y. Ching, and J. G. Harrison, Phys. Rev. B **45**, 8248 (1992).
[8] J. Barth, R. L. Johnson, M. Cardona, D. Fuchs, and A. M. Bradshaw, Phys. Rev. B **41**, 3291 (1990).
[9] V. V. Sobolev and V. Val. Sobolev, Fiz. Tverd. Tela (St. Petersburg) **36**, 2570 (1994) [Phys. Solid State **36**, 1393 (1994)].
[10] V. V. Sobolev and V. V. Nemoshkalenko, *Methods of Computational Physics in Solid-State Theory. The Electronic Structure of Semiconductors* [in Russian] (Naukova Dumka, Kiev, 1988).

Translated by M. E. Alferieff

Ion-motion disorder in a tysonite superionic conductor from ^{19}F NMR data

A. F. Privalov and I. V. Murin

St. Petersburg State University, 198904 St. Petersburg, Russia
(Submitted February 25, 1999)
Fiz. Tverd. Tela (St. Petersburg) **41**, 1616–1620 (September 1999)

The disorder in ion motion in a LaF_3 superionic conductor with tysonite structure is determined from NMR spectra. The method is sensitive to dynamic effects with correlation times of $5\times10^{-3}<\tau<10^{-6}$ s. Within the 260–400-K interval, ion movement is observed only on one of the sublattices (F_1), and it exhibits a correlation time distribution. The shape of the distribution is well fitted by a log-Gaussian. The distribution in correlation times reflects noticeable spatial fluctuations of local potentials in the LaF_3 superionic conductor.
 [S1063-7834(99)01709-8]

Dynamic disorder on at least one of the ionic sublattices of a superionic conductor (SIC) is considered to be the main reason for the onset of a superionic phase.[1] Nevertheless practically all studies of ion motion in SICs are based on the concept of a thermally activated Arrhenius-type process with a single correlation time and a single activation energy. This approach describes well the macroscopic characteristics of a SIC, such as the coefficients of electrical conductivity and diffusion. However it is of little use in studies of the superionic conduction itself, because it totally eliminates from consideration dynamic disorder occurring on the microscopic scale. The practically complete absence of concrete literature data on disorder, even in comparatively well studied systems having the fluorite or tysonite structure, complicates our understanding of the processes accompanying the onset of the superionic state, is an obstacle to further progress in the theory of ionic transport, and, hence, slows the development of new materials with better electrophysical properties.

It should be pointed out that dynamic disorder in glasses and polymers has recently been studied in considerable detail by NMR, which is very sensitive to dynamic processes at the atomic level.[2] As one crosses over from the insulating to superionic phase in SICs, investigation of the disorder phenomenon becomes complicated by the slow correlation times, small distribution width, and, hence, by a fairly limited choice of applicable experimental techniques. Among them is the analysis of the temperature dependences of spin-lattice relaxation times,[3,4] NMR spectroscopy,[5] frequency-dependent electrical conductivity, and dielectric relaxation spectroscopy[6–8].

The temperature dependences of the spin-lattice relaxation times T_1 in SICs exhibit usually a considerable deviation from the behavior predicted by the Bloembergen–Purcell–Pound model, which assumes a single correlation time. Specifically, the dependence of $\ln T_1$ on reciprocal temperature is not symmetrical with respect to the minimum in T_1, and the proportionality $T_1\propto\omega_0^2$ breaks down in the low-temperature domain of this relation.[3,4] A model allowing a distribution in activation energies was proposed to account for this behavior of the relaxation times.[4] Similarly, the anomalous course of electrical conductivity $\sigma(\omega)$ in glassy $(Li_2S)_{0.56}(SiS_2)_{0.44}$ was successfully simulated by a Gaussian distribution of lithium-ion activation energies.[6] Unfortunately, this technique has a low sensitivity to the shape of the distribution function.[7] Even the simplest step-function distribution model, which obviously has little in common with reality, permits satisfactory description of the frequency dependence of electrical conductivity.[8] This is apparently connected with the lack of clearly pronounced features in the $T_1(T)$ or $\sigma(\omega)$ dependences and with the fact that, in order to find the shape of the distribution function, one has to approach the inverse problem by solving Fredholm's integral equation of the first kind, which makes the resultant function only weakly sensitive to variation of the starting experimental data. Therefore the shape of the distribution is usually prescribed *a priori* in the form of a mathematical function, with subsequent determination of its parameters. The phenomenological model of hopping relaxation developed to describe dynamic processes in superionic conductors makes use, in particular, of a scheme with two potential wells separated by a barrier, whose height was proposed to be Gaussian.[9] A similar distribution was invoked to interpret ^{7}Li NMR data on relaxation and electrical conductivity in $xLi_2S+(1-x)GeS_2$ glassy SICs.[10]

It should be noted that practically all disorder studies in SICs were carried so far on glassy SICs, where the intrinsic structural disorder simulates the potential relief and initiates inevitably dynamic disorder. In crystalline SICs, where a periodic potential field exists, one should expect a considerably weaker dynamic disorder, which apparently determines the phenomenon of superionic motion itself. Besides, the atomic coordinates in crystalline SICs can be determined precisely, which permits one, for instance, to simulate in detail NMR spectra and perform calculations on the atomic level. Therefore analysis of crystalline systems appears preferable. However in order to obtain information on disorder in these systems, one has to use methods specifically sensitive to this effect.

Because NMR is exclusively sensitive to the interaction of a nucleus with the local spin environment, the parameters

of NMR spectra depend substantially on spin motion. Spectral analysis permits one to derive information on ion-motion correlation times within the $10^{-6}-10^{-3}$-s range. NMR combines the merits of high sensitivity and large chemical shifts from structurally inequivalent atoms, thus enabling separation of spectral components due to different SIC sublattices.[11] This work reports a ^{19}F NMR spectroscopic study of ion-exchange disorder in LaF_3 superionic conductor with tysonite structure.

Tysonite has trigonal symmetry ($P\bar{3}c1$) with three structurally inequivalent fluorine sites (F_1, F_2, and F_3).[12–14] A variety of methods were used to study ion transport in LaF_3.[5,11,15–17] The fluorine anions were found to be inequivalent not only structurally but dynamically as well.[11] Ion motion in LaF_3 is known to involve Schottky defects.[15] Frenkel defects are likely to appear only at temperatures above 1000 K.[16] Below 400 K, ion motion occurs primarily on the F_1 sublattice.[5,18] This work analyzes ion motion within a temperature range from 260 to 400 K. The main attention is focused on studying the disorder in this process.

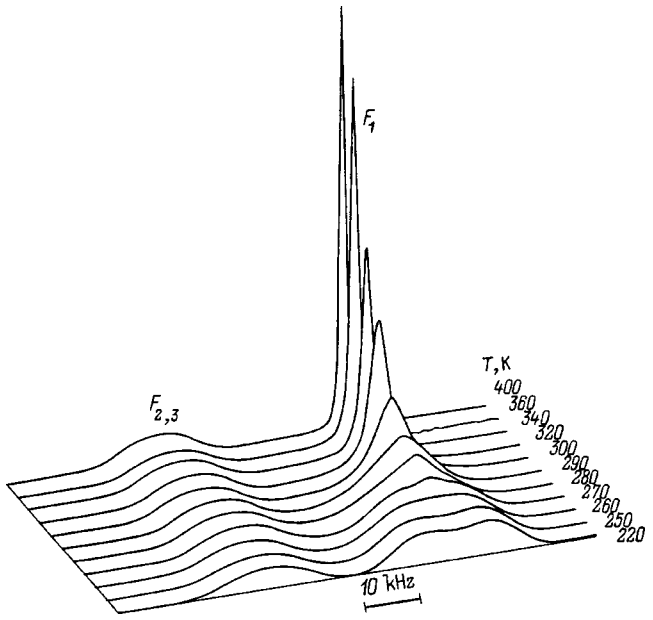

FIG. 1. Experimental ^{19}F NMR spectra of a LaF_3 single crystal, $B_0 \| c$ orientation, temperature range covered 220–400 K.

1. EXPERIMENT

The NMR spectra were obtained by Fourier transforming free-induction decay signals in a magnetic field of 7 T corresponding to the ^{19}F resonance frequency of 282 MHz. A BRUKER CXP300 pulsed Fourier spectrometer was used. The 90° pulse was 1 μs long permitting irradiation of a spectrum up to 500 kHz wide, which was considerably in excess of the actually measured spectrum (120 kHz).

The single-crystal LaF_3 sample used measured $3\times3\times7\ mm^3$. The crystal was oriented with a Laue diffractometer to an accuracy better than 1°. The sample temperature could be varied from 130 to 400 K, was determined to within 1 K, and stabilized to within ±0.1 K.

2. RESULTS AND INTERPRETATION

Figure 1 presents experimental NMR spectra of a LaF_3 single crystal, with its principal symmetry axis oriented parallel to the external magnetic field. The spectrum is seen to contain two components with integrated intensities in the ratio 2:1 and chemical shifts of -64 and 105 ppm relative to the reference signal from $CFCl_3$. As shown by NMR measurements performed in a strong magnetic field providing a high spectral resolution of chemical shift signals due to structurally inequivalent fluorine sublattices, the stronger component corresponds to the F_1 sublattice ions, and the weaker one, to combined signals produced by the F_2 and F_3 sublattices.[11,18] Homonuclear decoupling in ^{19}F using MREV-8 multiple-pulse high-resolution sequence did not permit one to resolve the F_2 and F_3 signals, whose chemical shift difference was estimated as not above 1.6 ppm.[14] The integrated component-intensity ratio is in full agreement with the occupation of the corresponding structural positions, namely, 12:(4+2). As follows from the angular dependences of the spectra, the chemical shift anisotropy is the largest when the principal optical axis of tysonite is parallel to the magnetic field, but nevertheless the shifts did not exhibit a noticeable splitting of the $F_{2,3}$ component, which implies that the F_2 and F_3 anions produce the same chemical shift anisotropies. Taking into account the insignificant difference between the F_2 and F_3 ion positions revealed by x-ray diffraction data,[12–14] this observation suggests that the structural inequivalence of the F_2 and F_3 ions is not reflected noticeably in NMR spectra. Because the line shape of the combined F_2 and F_3 component corresponding to the rigid-lattice one[11] was not affected by temperature variation, one may conclude that at least below 400 K the F_2 and F_3 ions behave dynamically in an equivalent manner and, in order to simplify our subsequent analysis, can be considered as belonging to a common sublattice $F_{2,3}$. At temperatures below 250 K, the spectrum does not undergo changes, i.e. the system may be treated as rigid, with ion-motion correlation times $\tau>1$ ms. As the temperature increases, ion motion sets in on the F_1 sublattice, which is evidenced by disappearance of the doublet structure and a dynamical narrowing of this particular component only. The component corresponding to the $F_{2,3}$ sublattices does not reveal any noticeable changes, which implies no ion exchange on them with correlation times $\tau<0.1$ ms. Because at temperatures up to 400 K motion is detected only on the F_1 sublattice, we performed an analysis of dynamic processes for the F_1 ions.

The shape of the ^{19}F NMR spectrum in a solid is determined by direct dipole-dipole interactions and chemical shifts. The LaF_3 structure was derived from x-ray diffraction measurements, and the fluorine anion positions in a rigid lattice are known to a high accuracy.[13,14] Calculation of pair dipole-dipole interactions in the LaF_3 spin system does not present any difficulties if the atomic positions and valence angles are known. Because the strongest dipole-dipole interactions on the F_1 sublattice (17 kHz) are substantially weaker than the difference in chemical shifts between the F_1 and $F_{2,3}$ components (50 kHz) and stronger than the dipole interactions between the F_1 and $F_{2,3}$ sublattices (3.6 kHz), the dy-

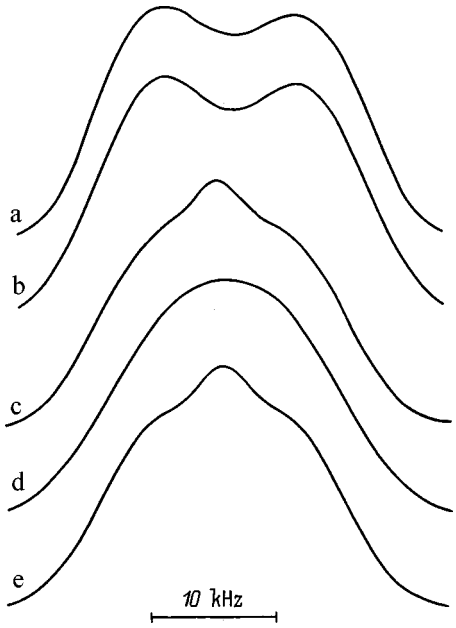

FIG. 2. NMR spectra of the F_1 sublattice: a — experimental at 220 K, b — calculated dipole spectrum for a rigid fluorine-lattice, c — experimental at 270 K, d — calculated for one correlation time of $\tau=35\,\mu$s, e — reconstructed with a log-Gauss time distribution with $\tau^c=30\,\mu$s and $\delta=0.8$.

namic processes in the F_1 sublattice may be treated as those in an isolated ion system.

Because exact calculation of NMR spectra of a solid is impossible due to the large number of interacting spins, we employed an approximate method[18,19]. In this method, the number of interacting spins for each nucleus is limited artificially based on the fact that magnetic interactions fall off with distance r proportionately to $1/r^3$, and that only interaction with the nearest neighbors turns out to be significant for determination of the NMR spectral shape. The dipole-dipole interactions in the spin system were classified in the order of decreasing magnitude. The calculation of the dipole spectrum due to two, three, etc. spins made in the decreasing order of the dipole-dipole interaction revealed that the spectral shape did not undergo any further changes starting with six spins. The interactions from 17 to 1.7 kHz, which dominate the shape of the interaction spectrum, were fully taken into account. The interactions with more distant spins, which result in an additional splitting of the already included energy levels by an amount corresponding to the next nonincluded interaction (1.5 kHz for the seventh spin and so on), were taken into account by additionally broadening the spectral component by a Gaussian. Calculation of the spectrum for the F_1 sublattice made disregarding the ion motion (Fig. 2b) gives a good agreement with experiment (Fig. 2a).

The ion exchange occurring under dynamic narrowing of the NMR line with increasing temperature was taken into account by solving Liouville's stochastic equation for the spin density matrix with an additional term describing the evolution of the spin ensemble in dynamic exchange.[20] The exchange process calculated for one, optimally chosen correlation time $\tau=35\,\mu$s, is presented graphically in Fig. 2d. As evident from a comparison of spectra 2c and 2d, the model spectrum 2d does not fit satisfactorily the experiment. Specifically, the experimental spectrum obtained at 270 K (Fig. 2c) exhibits a narrow central component which is lacking in the calculated spectrum. This experimental feature can be accounted for only by assuming coexistence of a fast and a slow exchanging spin ensemble. An analysis of two possible models taking into account the nonuniformity of ion exchange, namely, a model with two correlation times and another one with a distribution of correlation times revealed the latter to be preferable. We shall consider it in more detail.

The model assuming a distribution of correlation times assumes F_1 ions have different local environments, i.e., they are located at a potential relief with variable-height barriers. There is, accordingly, a dynamic distribution, which gives rise to a temperature-dependent correlation-time spectrum described by a distribution function $G(\tau)$. We used a limited set of correlation times τ_i $(i=1,2,\ldots,n)$, which extends over the range covered by the NMR method, $10^{-6}\leqslant\tau_i\leqslant10^{-3}$ s. To each τ_i corresponds a particular NMR spectral shape $f^{\rm cal}(\omega,\tau_i)$ calculated separately. The resultant NMR spectrum $f^{\rm cal}(\omega)$ is a superposition of individual spectra $f^{{\rm cal}(\omega,\tau_i)}$ taken with the corresponding weighting factors p_i

$$f^{\rm cal}(\omega)=\sum_{i=1}^{n} p_i f^{\rm cal}(\omega,\tau_i). \tag{1}$$

The p_i factors are unknown and are determined from the optimum fit of the calculated, $f^{\rm cal}(\omega)$, to experimental, $f^{\rm exp}(\omega)$, spectral shape. Because an experiment always contains noise and phase-correction errors, Eq. (1) was solved numerically. This equation was used to generate an overdetermined system of linear equations (2) of dimension $m\times n$

$$f^{\rm exp}(\omega_j)=\sum_{i}^{n} p_i f_i(\omega_j,t_i), \quad (j=1,2,\ldots m). \tag{2}$$

To obtain a stable solution, Eqs. (2) were solved by regularization.[21] The resultant set of parameters p_i for different temperatures, presented in Fig. 3 by sets of symbols, reflects the probability of the existence of a process with a given correlation time. The values of p_i obtained by such a model-independent method are fitted well by a log-Gauss function

$$G(\log(\tau))=A\exp\left[-\frac{1}{2}\left(\frac{\log\dfrac{\tau}{\tau^c}}{\delta}\right)^2\right] \tag{3}$$

shown by solid lines in Fig. 3. Equation (3) contains only two fitting parameters, the center of the distribution τ^c and its width $\delta=\frac{1}{2}\log(\Delta_2/\Delta_1)$, where Δ_1 and Δ_2 are the steepest-slope points of $G[\log(\tau)]$. Thus numerical calculation of the weighting factors p_i supports the validity of the model with a correlation-time distribution. The shape of the correlation-time distribution function determined by a model-independent method fits the log-Gauss function. The spectrum reconstructed by solving coupled equations (2) with the distribution function $G(\tau)$ having the parameters $\tau^c=30\,\mu$s and $\delta=0.8$ (Fig. 2e) practically coincides with the experi-

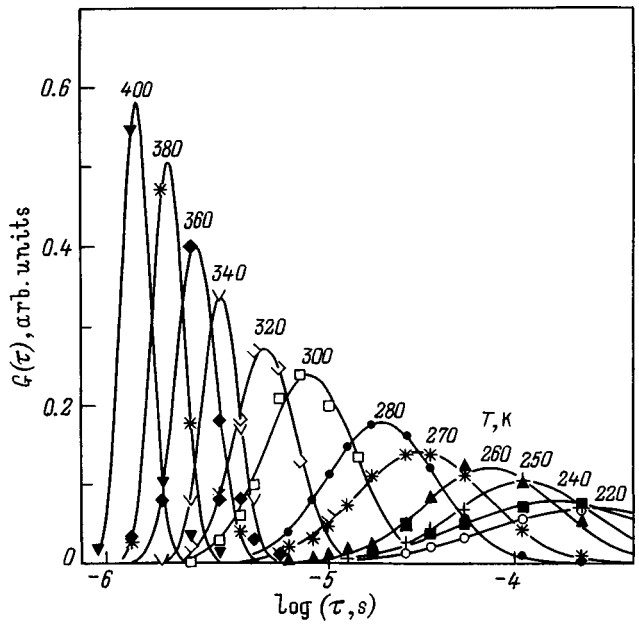

FIG. 3. Correlation time distribution $G(\tau)$ for the F_1 sublattice calculated for different temperatures. The lines are log-Gauss fitting functions.

mental one (Fig. 2c). Because distribution (3) contains only two fitting parameters, they can be determined with a high accuracy.

We believe that a distribution of correlation times is physically reasonable. For instance, a distribution of vacancies in a SIC gives rise to a distribution of potential barriers. If one assumes the processes involved to be thermally activated, a distribution in barrier height should entail that in correlation times. As the sample temperature increases, the center of the $G(\tau)$ distribution shifts toward shorter correlation times. The distribution becomes more narrow, which is typical of thermally activated processes. In accordance with the Arrhenius law, we have in this case

$$\tau = \tau_0 \exp(E_a/kT), \tag{4}$$

i.e. a distribution of correlation times transforms to that of potential barriers for ion jumps. The width δ and the center position τ^c of the $G(\tau)$ distribution plotted on a log scale depend linearly on reciprocal temperature. Our analysis shows a deviation from this behavior. The reason for this deviation lies possibly in that NMR detects processes occurring on the atomic level, and to explain the above result, one should take into account additional factors, such as cooperative effects. It should be pointed out that a similar behavior was discovered in many disordered systems.[22,23] Besides, the errors at the edges of the temperature range covered can be larger, because the correlation times may fall here outside the boundaries of dynamic sensitivity of the method, which we estimate in our case as $5\times10^{-3}<\tau<10^{-6}$ s.

Application of the molecular dynamics approach to an analysis of potential relief in lanthanum trifluoride appears promising for the interpretation of our results. In the initial stage, the barrier height distribution in a crystalline SIC was simulated successfully by a possible inhomogeneous spatial distribution of Schottky defects.[19] A more comprehensive analysis would require, however, further development of the technique used.

Work performed in project RFFI (Grant No. 96-03-33134).

[1] *Superionic Conductors*, edited by G. D. W. Mahan and W. L. Roth (Plenum, New York, 1980).
[2] E. Rössler, M. Taupitz, and H.-M. Vieth, J. Phys. Chem. **94**, 6879 (1990).
[3] D. Brinkmann, Magn. Reson. Rev. **14**, 101 (1989).
[4] S. H. Chung, K. R. Jeffrey, J. R. Stevens, and L. Börjesson, Solid State Ionics **40/41**, 279 (1990).
[5] A. F. Privalov, I. V. Murin, and H.-M. Vieth, Solid State Ionics **101/103**, 393 (1997).
[6] I. Svare, F. Borsa, D. R. Torgeson, and S. W. Martin, Phys. Rev. B **48**, 9336 (1993).
[7] J. R. Macdonald, Solid State Ionics **15**, 159 (1985).
[8] W. Schirmacher, Solid State Ionics **28/30**, 129 (1988).
[9] K. Funke, Prog. Solid State Chem. **22**, 111 (1993).
[10] K. H. Kim, D. R. Torgeson, F. Borsa, J. Cho, S. W. Martin, and I. Svare, Solid State Ionics **91**, 7 (1996).
[11] A. F. Privalov, H.-M. Vieth, and I. V. Murin, J. Phys. Chem. Solids **50**, 395 (1989).
[12] M. Mansmann, Z. Kristallogr. **122**, 375 (1965).
[13] B. Maximov and H. Schultz, Acta Crystallogr., Sect. B: Struct. Sci. **41**, 88 (1985).
[14] A. Zalkin and D. H. Templeton, Acta Crystallogr., Sect. B: Struct. Sci. **41**, 91 (1985).
[15] A. Sher, R. Solomon, K. Lee, and M. W. Muller, Phys. Rev. **144**, 593 (1966).
[16] P. E. Ngoepe, W. M. Jordan, C. R. A. Catlow, and J. D. Comins, Phys. Rev. B **41**, 3815 (1990).
[17] A. Belzner, H. Schultz, and G. Heger, Z. Kristallogr. **209**, 239 (1994).
[18] A. F. Privalov, H.-M. Vieth, and I. V. Murin, J. Phys.: Condens. Matter **6**, 8237 (1994).
[19] A. F. Privalov, A. Cenian, F. Dfujara, H. Gabriel, I. V. Murin, and H.-M. Vieth, J. Phys.: Condens. Matter **9**, 9275 (1997).
[20] J. I. Kaplan and G. Frenkel, *NMR of Chemically Exchanging Systems* (Academic, New York, 1980).
[21] W. H. Press, S. A. Teuklosky, W. T. Vetterling, and B. P. Flannery, *Numerical Recipes in C* (Cambridge Univ., Cambridge, 1992).
[22] I. Chang, F. Fujara, G. Hinze, H. Sillescu, and A. Tölle, J. Non-Cryst. Solids **172-174**, 674 (1994).
[23] E. Rössler, A. Kudlik, K.-U. Hess, D. B. Dingwell, A. P. Sokolov, and V. N. Novikov, Ber. Bunsenges. Phys. Chem. **100**, 1402 (1996).

Translated by G. Skrebtsov

DEFECTS. DISLOCATIONS. PHYSICS OF STRENGTH

Kinetics of the $\beta \rightarrow \alpha$ transformation and the hierarchical nature of structure defects in the two-phase state in the Pd–H system

A. A. Katsnel'son*) and M. A. Knyazeva

M. V. Lomonosov Moscow State University, 119899 Moscow, Russia

A. I. Olemskoĭ

Sumy State University, 244000 Sumy, Ukraine

(Submitted January 21, 1999)
Fiz. Tverd. Tela (St. Petersburg) **49**, 1621–1626 (September 1999)

Possible types of time dependences $p(t)$ describing the kinetics of the $\beta \rightarrow \alpha$ transformation in the Pd–H system are presented based on the theory of hierarchical structures. It is shown that one factor influencing the change in the time dependence $p(t)$ is the degree of regularity in the distribution of defects in the hierarchical complexes and the strength of the hierarchical coupling determining the number of hierarchically coupled levels. Analysis of the relations obtained and the experimental data made it possible to distinguish the most likely physical causes for the retardation of the $\beta \rightarrow \alpha$ transformation. © *1999 American Institute of Physics.* [S1063-7834(99)01809-2]

The problem of the interaction of hydrogen with metals and alloys is becoming increasing more pressing in connection with the use of hydrogen in many branches of technology. For example, the use of palladium–hydrogen systems in hydrogen energetics involves storage, transport, and extraction of hydrogen. The effect of hydrogen on service characteristics such as longevity and reliability of membranes used as filters for purifying hydrogen and separating its isotopes is extremely important. These applications make it necessary to study the mechanical properties of the Pd–H and Pd–Me–H systems determined by the phase composition[1] and state of the defect structure.[2,3] Specifically, it is found that the high-strength state is formed as a result of repeated cycling of the phase transformation.[1–3]

In recent years the idea has developed[4–6] that a strongly deformable crystal is a synergetic system, where the defect density is so high that collective effects show up in their behavior. This means that a coherent coupling is established in an ensemble of defects between the constituents of the ensemble, and this coupling leads to self-localized formation of the structural elements of a high level. Simple examples of this phenomenon are: clustering of vacancies leads to dislocation loops, clusters of dislocations transform into dislocation walls, and so on. As a result, a hierarchical system of defects arises and, since a definite relation exists between different structural levels, it is more accuracte to call it a hierarchically subordinated system.[4,6–9] A theory of hierarchical coupling is proposed in Ref. 9.

According to Refs. 10–14, a defect structure develops by generation of defects in the process of an $\alpha \leftrightarrow \beta$ transformation, leading to dilatation of the lattice. As a result of fine-scale fragments assembling into a large-scale structure, the evolution of a defect structure consists of a process in which a complex, hierarchically subordinated, system of defects arises. According to Ref. 15, the picture of the development of such a system of defects also depends on the phase state. We note that characteristic features of the kinetics of the reverse phase transformation are determined by the state of the defect structure.[12–14] It has been shown in Refs. 12, 14, and 16 that the time dependence of the volume fraction of the β phase does not reduce in the degassing process to very simple exponential-type relations, but rather it possesses a power-law or logarithmic dependence. In Refs. 12 and 16–18 it was determined that the $\beta \rightarrow \alpha$ transformation proceeds in multiple stages. It was established that the staged nature of the degassing process is associated with stagewise development of a defect structure.[19]

Our objective in the present work is to describe the kinetics of the reverse transformation $\beta \rightarrow \alpha$ on the basis of the concept of a hierarchical defect system arising in the two-phase system Pd–H.

This paper is organized as follows. In Sec. 1, the basic experimental data, generalizing the results of Refs. 12–19, are expounded and analyzed on the basis of ideas developed in Ref. 15, on the staged evolution of the defect structure. A discussion based on the theory of hierarchical structures[7] is given in Sec. 2. A number of basic relations are derived in the Appendix.

1. EXPERIMENTAL RESULTS

In Ref. 13 it was shown by x-ray diffraction that the kinetics of the $\beta \rightarrow \alpha$ transformation in Pd ribbons deformed by rolling is described by an exponential dependence, if the ribbons were saturated for 15 min by a current density 2.5 mA/cm^2. At the same time it was observed in these samples that the density of randomly distributed dislocations or large-radius dislocation loops increases appreciably during phase transformations. As the current density and saturation time

increase, the density of randomly distributed dislocations in the same samples increases up to critical values, above which assembly of these dislocations into dislocation walls (coherently coupled complexes) occurs.[15] In such samples the $\beta \rightarrow \alpha$ transformation process is observed to slow down. The form of the functions describing the kinetics of a $\beta \rightarrow \alpha$ transformation depends on the degree of development of the defect structure.

If dislocation pileups appear in the α phase,[13] then the kinetics of the $\beta \rightarrow \alpha$ transformation will follow the Kohlrausch law

$$p(t) = p_0 \exp[-t/t]^{\beta} \quad (t > t^*), \tag{1}$$

where p_0 is the initial content of the β phase, t^* is a characteristic time scale, and the constant $\beta = 0.8$.

For a cast sample and high current density,[12,18] the density of random dislocations reached such high values even in the saturation process that the dislocations assembled into walls. This leads to lower values of D (D is the size of the coherent scattering regions) and the formation of a cellular substructure in the α phase. A cellular substructure also formed in the β phase during degassing. The degassing process in this case was described by a power law[12,18]

$$p(t) = p_0 (t/t^*)^{-\gamma}, \quad (t > t^*). \tag{2}$$

The parameters are $\gamma = (0.575 \pm 0.030)$ and $t^* = (5.0 \pm 0.5)$ h. The β-phase content subsequently (after ~ 40 h) remained practically unchanged — a stage of stabilization of the β phase was observed.[18] At this stage the coherent scattering regions (CSRs) of the β phase increased in size — a transition was observed to the next stage of development of the hierarchical defect structure.[16]

When the initially deformed ribbon was cycled, the cellular substructure formed in the α phase during the first few cycles. In the last cycle, where the amount of the β phase is quite large ($\sim 90\%$), formation of dislocation walls was observed even in the β phase — after 4×10^3 h.[14] In this case D decreased by a factor of 2.5 — a cellular structure formed. The kinetics of the $\beta \rightarrow \alpha$ transformation was described by a logarithmic law[14,16]

$$p(t) = p_0 (\ln(t/t^*))^{-\alpha}, \tag{3}$$

where $\alpha > 0$ and t^* was found to be $t^* = (5.0 \pm 0.5) \times 10^3$ h.

We note that the logarithmic retardation of the $\beta \rightarrow \alpha$ transformation was observed at the stage of degassing where the CSRs in the α phase were already observed to increase in size — a block substructure formed.

With repeated cycling of a cast sample, a cellular substructure arose in both phases.[15] During degassing the formation of large blocks commenced after the last saturation (dislocation walls between substructural cells vanished), and this process occurred first in the β phase. At this stage the $\beta \rightarrow \alpha$ transformation process was described by a power law with exponent $\gamma = 0.29$ and characteristic time $t^* = 4 \times 10^3$ h.[14,16] The $\beta \rightarrow \alpha$ transformation process stopped after $\sim 4.5 \times 10^4$ h (the stage of stabilization of the β phase). Then nucleation of a block substructure in the β phase was observed.[15,16]

2. DISCUSSION

Since a dispersed mixture of α and β phases is formed upon saturation with hydrogen, the $\beta \rightarrow \alpha$ transformation process is limited not only by diffusion of individual hydrogen atoms but also by cooperative effects associated with the motion of an interphase boundary in the potential relief formed by the defect structure. As we have shown in a previous work,[12] for a uniform distribution of defects, characterized by density ρ and energy barrier $U \sim \rho$, the degassing process can be described by the Debye relation

$$p = p_0 \exp(-t/\tau), \tag{4}$$

where the relaxation time τ is determined by the rate of formation of α-phase nuclei

$$\tau \sim \exp(c/g^2 T) \exp(U/T), \tag{5}$$

where g is the difference of the specific free energies of the phases. Here the first exponential describes the thermodynamic aspect of a $\beta \rightarrow \alpha$ transformation and the second exponential is associated with the migration of the interphase boundary along the potential relief of the defect structure, characterized by barrier height U. We shall investigate only the kinetic aspect, which plays the dominant role in the interpretation of the experimental data presented.

In the very simple case of a uniform distribution of defects of one type, the microstrain $\varepsilon \sim \rho$ due to them is proportional to their density, which leads to the linear relation $U \sim \varepsilon \sim \rho$. However, such a case occurs for defects of any one type, for example, dislocations, precipitates of a phase, and so on. Analysis of the experimental data has shown[12–14] that the $\alpha \leftrightarrow \beta$ transformation, characterized by large accompanying distortions of the lattice, leads to the formation of various defects, which can be hierarchically subordinated. For example, vacancies combine into prismatic loops, edge dislocations assemble into small-angle walls, which in turn form cells, and so on. Each of these defect types corresponds to a hierarchical level n characterized by a barrier U_n and microstrain ε_n.

At each hierarchical level n the barrier height $U_n \sim \varepsilon_n$ is determined by the microstrain associated with the ratio of the scale factors l_n at different levels

$$\varepsilon_n = l_{n-1}/l_n. \tag{6}$$

For example, for single dislocations l_n corresponds to the radius of the nucleus, for walls it corresponds to the distance between dislocations, and so on.[20] Characteristically, as the value of n corresponding to a transition to a higher hierarchical level increases, the ratio l_{n-1}/l_n of the deformation scales should increase, since in this case the microstrain ε_1 increases (for example, grains make a larger contribution to the total strain than fragments, the latter make a larger contribution than blocks, and so on). Since the height U_n of the potential relief increases monotonically with the microstrain ε_n, the value of U_n should also increase with n.

To determine the dependence $U_n(\varepsilon_n)$ we shall present basic information about the theory of hierarchical structures.[7,9] It is convenient to turn to a geometric image —

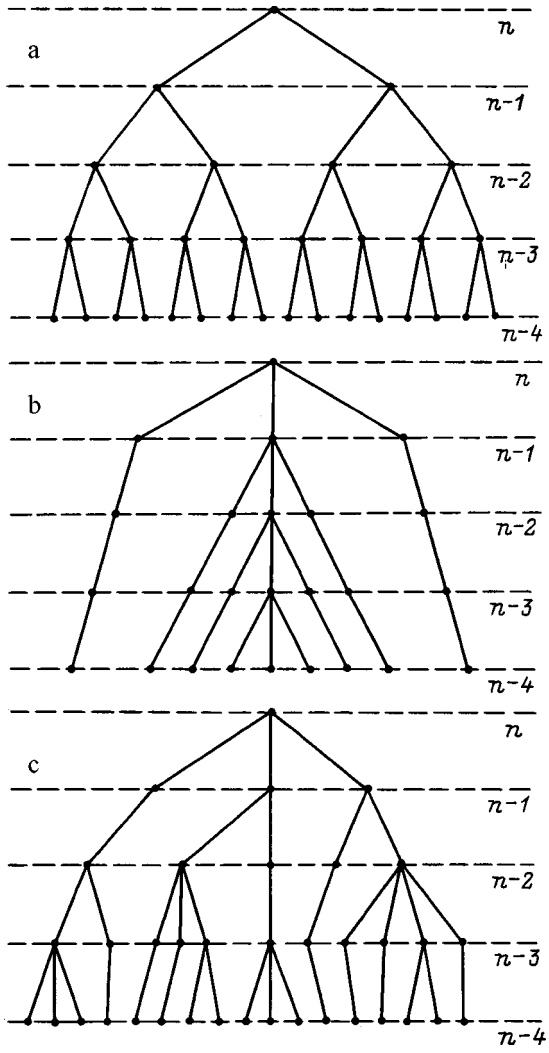

FIG. 1. Various types of hierarchical trees.

the Cayley tree, which makes it possible to represent the hierarchical coupling graphically (Fig. 1). Each hierarchical level of this tree corresponds to a given type of defect: The bottom level corresponds to individual dislocations, the next level corresponds to formed or small-angle walls, a higher level corresponds to cells, and so on, right up to the top level, characterizing by the behavior of the entire sample. Regular trees, for which the number of branches emanating from the nodes at each level is constant, are distinguished (see Fig. 1a). The opposite example is a tree shown in Fig. 1b for which only one node sprouts at each level. Real hierarchical systems correspond to irregular trees, of the type depicted in Fig. 1c, where a random variation of the branching structure is observed for nodes at a given hierarchical level and at different hierarchical levels.

For the defect structure under study a regular tree (see Fig. 1a) corresponds to an idealized situation where each type of defect in the upper level is formed as a result of the coherent assembly of an identical number of defects from the lower level. The situation corresponding to Fig. 1b means that at each level there exists a single distinguished group, which can assemble into a superdefect in a higher level. Finally, a tree of the type shown in Fig. 1c represents the real situation. We call attention to the fact that the microstrain ε_n, determined by the ratio of the scale factors l_n and l_{n-1} at different levels, characterizes the degree of the hierarchical coupling. Indeed, if dislocations with nuclei with radius l_0 do not form a small-angle wall, then the thickness of the wall $l_1=\infty$, and according to Eq. (6) the degree of hierarchical coupling $\varepsilon_1=0$. However, if the dislocations assemble with period $l_1<\infty$, then as the openness of the wall decreases, the hierarchical coupling $\varepsilon_1=l_0/l_1$ intensifies because of the decrease in the scale l_1. For the tree shown in Fig. 1c, a decrease in the degree of branching at a given node means that the superdefect formed by defects at the preceding level is more open than its neighbor, corresponding to a higher degree of branching.

As shown in the Appendix, for a regular tree (see Fig. 1a) the increase in barrier height U_n occurring with a change in the degree of hierachical coupling, whose magnitude is determined in our case by the microstrain ε_n, is exponentially strong

$$U_n=Q\exp(\varepsilon_n/\varepsilon_0). \tag{7}$$

For the opposite case, corresponding to Fig. 1b, a weak logarithmic dependence

$$U_n=Q\ln(\varepsilon_n/\varepsilon_0) \tag{8}$$

is observed.

Finally, for an irregular tree (see Fig. 1c) we have the power law

$$U_n=Q(\varepsilon_n/\varepsilon_0)^a, \quad a>0. \tag{9}$$

In the expressions (7)–(9) Q and ε_0 are characteristic values of the barrier height and microstrain.

It is important to keep in mind that the dependences presented are determined solely by the geometry of the Cayley tree and are not associated with other characteristics of the hierarchical coupling. In a real case the defects at different levels make a different contribution to the total deformation process. We shall take this into account in an analysis of two limiting cases — strong and weak hierarchical coupling. In the first case, corresponding to an infinite number of coupled levels, the distribution $w_s(\varepsilon_n)$ of hierarchical coupling over levels is a slowly varying function

$$w_s(\varepsilon_n)\sim(\varepsilon_n/\varepsilon_0)^{-D}, \tag{10}$$

where D is a positive parameter. For weak coupling, where the number of levels coupled is finite, exponentially rapid decay is realized

$$w_w(\varepsilon_n)\sim\exp\{-\varepsilon_n/\varepsilon_0\}, \tag{11}$$

where the scale ε_0 characterizes the depth of the hierarchical coupling.

When a hierarchical structure arises, the contribution of each level n is characterized by a specific degassing law $p_n(t)\sim\exp(-t/\tau_n)$ with relaxation time $\tau_n=\tau_0\exp(U_n/T)$, where the barrier height $U_n(\varepsilon_n)$ depends on the microstrain according to the relations (7)–(9).

TABLE I. Possible kinetic laws $p(t)$.

$p(t)$	$U_n \sim Q\ln\varepsilon_n$	$U_n \sim Q\varepsilon_n^a$	$U_n \sim Q\exp(\varepsilon_n)$
$w_w(\varepsilon_n)$	$\exp[(-t/t_0)^b]$, $b=(1+Q/T)^{-1}$	$\exp\{[(-T/Q)\ln(t/t_0)]^{1/a}\}$	$[(T/Q)\ln(t/t_0)]^{-1}$
$w_s(\varepsilon_n)$	t^{-c}, $c=DT/Q$	$[(T/Q)\ln(t/t_0)]^{-D/a}$	$[\ln(T/Q)\ln(t/t_0)]^{-D}$

Each of these levels makes an additive contribution with weight $w(\varepsilon_n)$, given by the distributions (10) and (11). As a result, the complete degassing law can be written as a sum over the levels

$$p(t)=\sum_n w(\varepsilon_n)\exp\{-(t/\tau_0)\exp(-U(\varepsilon_n)/T)\}, \qquad (12)$$

where τ_0 is the characteristic relaxation time at the lower level. The possible types of functions $p(t)$ corresponding to various combinations of the dependences $U_n(\varepsilon_n)$ and $w(\varepsilon_n)$ were found on the basis of Ref. 7. These types are indicated in Table I. The main feature of the dependences obtained is that they decrease with increasing t much more slowly than a Debye exponential $\exp(-t/\tau_0)$. For weak hierarchical coupling $w_w(\varepsilon_n)$, logarithmic growth of the barrier height $U_n(\varepsilon_n)$ gives the weakest retardation, which is characterized by an extended Kohlrausch exponential. A power-law function $U_n(\varepsilon_n)$ leads to a quasipower-law form (for $a=1$ we obtain $p(t)\propto t^{-T/Q}$). Finally, for an exponential dependence $U_n(\varepsilon_n)$ a logarithmic retardation of degassing should be observed. The types of functions $p(t)$ transform in a similar manner when sorting through the relations $U_n(\varepsilon_n)$ for strongly hierarchical coupling $w_s(\varepsilon_n)$. Here a shift is observed in the direction of even greater retardation of the degassing law: A power-law function $p(t)$ arises even with logarithmic growth of the barrier heights $U_n(\varepsilon_n)$, logarithmic retardation appears with power-law growth, and double-logarithmic retardation, attesting to almost complete stoppage of the degassing process, appears with exponential growth. It is interesting that as weak hierarchical coupling passes into strong coupling, the form of the degassing law can remain the same, if at the same time the rate of growth of the barrier heights U_n with increasing deformation ε_n decreases.

As is evident from the Appendix (see also Ref. 9), the transition from an exponential function $U_n(\varepsilon_n)$ to a power-law function and then to a logarithmic function (this corresponds to going from right to left in the table) corresponds to an increase in the degree of irregularity of the hierarchical tree. Correspondingly, the transition from the top to bottom row signifies an increase in the number of hierarchically coupled levels. For this reason, the transformation of degassing laws which has been presented above means that their retardation occurs either with an increase in the degree of regularity in the hierarchical formation of defects or with an increase in the number of hierarchically coupled levels of the defect structure. For certain different combinations of functions $w(\varepsilon_n)$ and $U_n(\varepsilon_n)$ the degassing laws can be identical. Let us examine, for example, the transition from the last column in the first row of the table to the next to last column of the second row. In the first case we have weakly coupled but regularly arranged defects, and in the second case a system of irregularly arranged but strongly coupled defects is realized. It is evident that systems of weakly coupled but regularly distributed defects and strongly coupled but irregularly distributed defects lead to the same degassing laws.

The main feature in selecting samples, whose investigations are reported in Sec. 2, is that in the process of evolution a different defect structure is formed at phase transitions in the samples. Thus, in ribbons subjected initially to the weakest saturation with hydrogen, the restructuring of the defect substructure reduces to an increase in the density of randomly distributed defects. In a ribbon where the hydrogen-saturation time is much longer, apparently one can already talk about the formation of a new structural level in the form of dislocation pileups. A large increase in the current density during saturation of a massive sample leads to the formation of a cellular substructure of the α phase even during the saturation process. During the subsequent degassing a cellular substructure also forms in the β phase. The richest picture of evolution of a defect structure occurs in a cast sample, prepared by repeated cycling of the saturation process with current densities which are just as high. Here the successive formation of a cellular structure in the α and β phases occurs even during cycling; then fragmentation of the β phase due to merging of the cells is observed during degassing; finally, the fragmentation process starts in the volume of the α phase.

The experimental data on ribbons saturated once[13] show that the saturation time t_s influences the picture of nucleation of a hierarchical level of the defect structure. Judging from the time dependence of the microstrains, it occurs only in the α phase of the sample with the maximum value of t_s. In the hydride phase the density of random dislocations and walls is negligibly small and does not change in the course of degassing. The degassing law observed in experiments reduces to a Kohlrausch exponential, which can be obtained only with logarithmic growth of the barrier heights $U_n(\varepsilon_n)$ and a small number of hierarchically coupled levels. Hence it can be concluded that the structural level formed consists of a collection of different types of open dislocation formations. Most likely they are tangles of dislocations.

A cast sample saturated once at high current densities is characterized by power-law degassing.[12,18] Investigations of the substructure parameters D and ε show that here, in contrast to saturated ribbons, the formation of a cellular substructure in the α phase has already been completed by the start of the degassing process, while in the volume of the β phase it forms during the degassing process. As is evident from Table I, a power-law function $p(t)$ can be realized for weak and strong hierarchical coupling. A cellular substructure appears in the α phase during saturation, while in the β phase it appears during degassing. The next structural level (fragments) engages in the β phase already at the stabilization stage, where the content of the β phase remains essentially unchanged. For this reason, it can be assumed that the determining factor for the kinetics of the $\beta\rightarrow\alpha$ transformation is the formation of a well-formed cellular substructure characterized by power-law growth of the barrier heights

$U_n(\varepsilon_n)$. Next, the degassing process slows down. This can be attributed either to intensification of hierarchical coupling or a transition to a stronger dependence $U_n(\varepsilon_n)$. According to Table I, in both cases the degassing law assumes a more slowly decaying form.

The transition from a once-saturated cast sample to a cycled sample can be represented as a further evolution of the defect structure in the former, since in the latter the initial state is the same as the final state in the former. As a result of cycling, a cellular structure arises in the sample not only in the α but also in the β phase. The subsequent degassing process leads to fragmentation of the β phase first, as a result of merging of cells most likely because of migration of dislocation walls, and then fragmentation in the α phase. Thus, in the course of a $\beta \rightarrow \alpha$ transformation hierarchical levels of fragments are engaged first in the β phase and then in the α phase. However, this does not change the degassing law, which has a power-law form. This circumstance can be attributed to the fact that together with the formation of new levels, due to intensification of the hierarchical coupling, we switch from a power-law to logarithmic dependence $U_n(\varepsilon_n)$.

In summary, the basic types of dependences, obtained in the present work based on the theory of hierarchical structures, of the height U of potential barriers dependence on the microstrain ε, made it possible to describe the diversity of degassing laws $p(t)$. Analysis showed that the transformation of the degassing laws can be due to a change in the degree of regularity in the hierarchical formation of defects and to a change in the number of hierarchical levels of the defect structure.

A change in the degree of regularity of the distribution of hierarchically coupled defects and a change in the number of coupled structural levels result in a change in the entropy of the nonequilibrium system of defects. In this respect the appearance of a hierarchical defect structure can be attributed to self-organization of defects in a nonequilibrium medium in metastable dissipative structures as a result of entropy dissipation.

3. APPENDIX

We shall derive the basic relations (7)–(9), representing the dependence $U(\varepsilon)$ of the characteristic height of the potential relief on the microstrain. To this end it is convenient to switch from enumeration of hierarchical levels from bottom to top using the index n, which is convenient for determining the microstrain (6), to enumeration $k=N-n$ from top to bottom, reflecting the direction of development of the hierarchical coupling (N is the total number of levels). We start with the recurrence relation

$$U_{k-1}=U_k+W/N_k, \tag{A1}$$

according to which the difference $\Delta U_k \equiv U_k - U_{k-1}$ of the heights at neighboring levels is inversely proportional to the number N_k of nodes at the level k (W is a positive constant). Replacing the finite difference $\Delta U_k \equiv \Delta U_k/\Delta k$, $\Delta U_k \Delta k = 1$, by the derivative $dU(k)/dk$, we obtain in the continuum limit $k \rightarrow \infty$

$$U(k)=U_0-W\int dk/N(k), \tag{A2}$$

where U_0 is the integration constant.

As one can see from Fig. 1a, in the case of a regular tree we have $N(k)=j^k$, where j is the degree of branching, and the expression (A2) leads to the dependence (7), if a linear approximation $\varepsilon_n=An$ is used and $U_0=0$, $\varepsilon_0=A/\ln j$, and $Q=(W/\ln j)\exp(-\varepsilon_N \ln j/A)$. Correspondingly, for a degenerate tree (Fig. 1b) $N(k)=k(j-1)+1\approx k(j-1)$, and we obtain the logarithmic dependence (8), where $Q=bW/(j-1)$, if $U_0=(W/(j-1))\ln N$, $(\varepsilon/\varepsilon_0)^b=N/k$, and b and ε_0 are positive constants. Finally, for an irregular tree (Fig. 1c) the power-law function $N(k)=Bk^b$ can be used. Assuming a similar coupling $(\varepsilon_0/\varepsilon)^c=N/k$ this function leads to the dependence (9), where $U_0=0$, $Q=WN^{1-b}/B(b-1)$, $a=(b-1)c$, $B>0$, $b>1$.

This work was partially supported by grant No. 1-1004 from the program ''Universities of Russia — Fundamental Studies.''

*)E-mail: albert@solst.phys.msu.su

[1] V. A. Gol'tsov, N. I. Timofeev, and I. Yu. Machikina, Fiz. Met. Metalloved. **46**, 502 (1978).
[2] V. A. Gol'tsov, N. I. Timofeev, and I. Yu. Machikina, Dokl. Akad. Nauk SSSR **253**, 1080 (1977).
[3] G. P. Revkevich and S. V. Sveshnikov, in *Abstracts of Reports at the 4th All-Union Seminar on Hydrogen in Metals* (1984), Part 2, p. 199.
[4] V. E. Panin, V. A. Likhachev, and Yu. V. Grinyaev, *Structural Levels of Deformation in Solids* (Nauka, Novosibirsk, 1985), 226 pp.
[5] V. V. Rybin, *Large Plastic Deformations and Fracture of Metals* [in Russian] (Metallurgiya, Moscow, 1986), 223 pp.
[6] V. E. Panin and T. F. Elsukova, *Synergetics and Fatigue Fracture of Metals* [in Russian] (Nauka, Moscow, 1989), p. 113.
[7] A. I. Olemskoĭ and I. A. Sklyar, Usp. Fiz. Nauk **162**(6), 29 (1992) [Sov. Phys. Usp. **35**, 455 (1992)].
[8] N. A. Koneva, É. V. Kozlov, and L. I. Trishkina, Metallofizika (Kiev) **13**(10), 49 (1991).
[9] A. I. Olemskoi and A. B. Kiselev, Phys. Lett. A **247**, 221 (1998).
[10] H. C. Jamieson, G. C. Weatherly, and F. D. Manchester, J. Less-Common Met. **50**, 85 (1976).
[11] V. A. Gol'tsov and B. A. Lobanov, Dokl. Akad. Nauk SSSR **283**, 598 (1985) [Sov. Phys. Dokl. **30**, 613 (1985)].
[12] G. P. Revkevich, A. I. Olemskoĭ, A. A. Katsnel'son, and V. M. Khristov, Fiz. Met. Metalloved. **12**(3), 71 (1990).
[13] G. P. Revkevich, M. A. Knyazeva, A. I. Olemskoĭ, and A. A. Katsnel'son, Fiz. Met. Metalloved. , No. 9, 43 (1992).
[14] G. P. Revkevich, A. I. Olemskoĭ, A. A. Katsnel'son, and M. A. Knyazeva, Fiz. Met. Metalloved. **76**(7), 101 (1993).
[15] A. A. Katsnel'son, M. A. Knyazeva, A. I. Olemskoĭ, and G. P. Revkevich, Fiz. Tverd. Tela (St. Petersburg) **39**, 1275 (1997) [Phys. Solid State **39**, 1132 (1997)].
[16] G. P. Revkevich, A. I. Olemskoĭ, A. A. Katsnel'son, and M. A. Knyazeva, Fiz. Met. Metalloved. **79**(2), 87 (1995).
[17] G. P. Revkevich, S. V. Sveshnikov, and A. A. Katsnel'son, Izv. Vyssh. Uchebn. Zaved. Fiz. No. 6, 117 (1988).
[18] G. P. Revkevich, V. M. Khristov, and A. A. Katsnel'son, Vestn. Mosk. Univ., Fiz., Astron. **29**(3), 72 (1988).
[19] A. A. Katsnel'son, M. A. Knyazeva, A. I. Olemskoĭ, and G. P. Revkevich, Vestn. Mosk. Univ., Fiz., Astron. **38**(6), 46 (1997).
[20] A. M. Kosevich, *Physical Mechanics of Real Crystals* [in Russian] (Naukova Dumka, Kiev, 1981), 327 pp.

Translated by M. E. Alferieff

Transformation of interfaces in nanoamorphous solids

A. L. Kolesnikova and I. A. Ovid'ko

Institute for Problems in Mechanical Engineering, Russian Academy of Sciences, 199178 St. Petersburg, Russia

A. E. Romanov

A. F. Ioffe Physicotechnical Institute, Russian Academy of Sciences, 194021 St. Petersburg, Russia
(Submitted February 3, 1999)
Fiz. Tverd. Tela (St. Petersburg) **41**, 1627–1629 (September 1999)

A model is proposed for the diffusive smearing of interfaces of different geometries in metal nanoglasses. It is shown that the smearing of planar interfaces occurs faster than that of triple junctions, which, in turn, takes place faster than that of the nodes. This accounts for the variation of the mean positron lifetime in metal nanoglasses induced by thermal treatment.
 [S1063-7834(99)01909-7]

Metal nanoglasses (nanoamorphous metals) are a new class of nanostructural solids exhibiting unique properties and structure.[1–5] Metal nanoglasses are solids consisting of amorphous metal nanoparticles ($\leqslant 15$ nm in size) separated by interfaces. The interfaces have also an amorphous structure and have a lower atomic density than that of nanoparticles. In other words, metal nanoglasses are glasses with nanoscale spatial atomic-density nonuniformities. Metal nanoglasses transform with time to conventional metal glasses with approximately uniform spatial atomic-density distribution.[1] Such transformations are considered to be related with diffusive smearing of interfaces. The main objective of this work is to construct a model of the diffusive smearing of interfaces, their junctions, and nodes in metal nanoglasses, which result in transformation of such glasses into conventional metal glasses.

Considered in terms of the proposed model, metal nanoglasses contain interface configurations of three main types: interfaces themselves, their triple junctions, and triple-junction nodes (i.e., the regions where the triple junctions connect). The interfaces, the triple junctions, and the nodes are simulated, respectively, as planar regions of finite width, cylinder-shaped regions, and spherically shaped regions, in which the free-volume atomic density is lower than that in amorphous nanoparticles. The interface configurations under study have essentially differing geometries, sizes, and atomic densities, which accounts for substantial differences in the diffusive smearing of such configurations. The specific features of the diffusive smearing of interfaces, triple junctions, and nodes are analyzed below in the corresponding Sections. The paper concludes with a general discussion of the results obtained and a summary.

1. DIFFUSIVE INTERFACE SMEARING IN METAL NANOGLASSES

Within our model, the main characteristic reflecting nanoscale spatial nonuniformities in the metal-glass structure is the atomic density $\rho(x,y,z,t)$ (here x,y,z are spatial coordinates), which evolves with time t. Due to the symmetry in the distribution of atomic density ρ along the interface plane, we shall restrict ourselves in the consideration of the specific features of the diffusive interface smearing to analyzing a one-dimensional pattern with a function $\rho(x,t)$ depending only on time t and spatial coordinate x along the interface plane normal. The interface smearing is described here as a smoothening of the originally spatially-nonuniform function $\rho(x,t)$ prescribed at the initial time $t=0$. Thus the diffusive interface smearing is described by the following diffusion equation:

$$\frac{\partial \rho}{\partial t} = D\frac{\partial^2 \rho}{\partial x^2}, \tag{1}$$

where $\rho(x,t)=\rho_b+\Delta\rho(x,t)$, and the initial and boundary conditions are defined, respectively, as

$$\Delta\rho(x,0)=\Delta\rho_1[H(x+d)-H(x-d)], \quad \Delta\rho|_{x\to\infty}\to 0. \tag{2}$$

Here D is the diffusion coefficient, $\Delta\rho_1=\rho_1-\rho_b$, ρ_b is the atomic density of nanoparticles adjoining the interface, ρ_1 is the initial atomic density of the interface, $H(x)=0$ for $x<0$ and $H(x)=1$ for $x>0$, and the $[-d,d]$ interval corresponds to the initial (unsmeared) interface of width $2d$. Conditions (2) are approximate, because real nanoparticles have finite dimensions. However the choice of the initial and boundary conditions in the form (2), on the one hand, permits a substantial simplification in the discussion of the results obtained with the model, and, on the other, it does not affect noticeably these results.[1)] In our case [conditions (2)], the solution of Eq. (1) can be written[6]

$$\Delta\rho(t,x)=\frac{\Delta\rho_1}{2}\left[\operatorname{erf}\left(\frac{d-x}{2\sqrt{Dt}}\right)+\operatorname{erf}\left(\frac{d+x}{2\sqrt{Dt}}\right)\right], \tag{3}$$

where $\operatorname{erf}(z)$ is the standard error function.

The main parameter of the diffusive interface smearing is the time τ_1 in which it occurs. We define τ_1 more exactly as a time interval during which the minimum of the $\rho(x,t)$

profile reaches the value $\rho(0,\tau_1)=\rho_b+0.2\Delta\rho_1$, where $\Delta\rho_1<0$. For the characteristic values $D=10^{-21}$ m^{2}s^{-1} (for $Fe_{91}Zr_9$ at a temperature $T=700$ K),[7] $d=5\times10^{-10}$ m, and $\rho_1=0.8\,\rho_b$, numerical solution of Eq. (3) yields $\tau_1\approx2000$ s.

2. DIFFUSIVE SMEARING OF TRIPLE INTERFACE JUNCTIONS IN METAL NANOGLASSES

To a first approximation, we simulate triple interface junctions in metal nanoglasses by cylindrical regions with a low atomic density ρ. Taking into account the cylindrical symmetry of the model case under study, ρ can be effectively defined as a function of time t and of one cylindrical coordinate r: $\rho=\rho(r,t)$. The diffusive smearing of a triple junction is described in these conditions as a smoothing of the originally spatially-nonuniform function $\rho(r,t)$ in the radial direction r. Then the $\rho(r,t)$ function obeys the following diffusion equation:

$$\frac{\partial\rho}{\partial t}=D\left(\frac{\partial^2\rho}{\partial r^2}+\frac{1}{r}\frac{\partial\rho}{\partial r}\right), \tag{4}$$

where $\rho(r,t)=\rho_b+\Delta\rho(r,t)$, and the initial and boundary conditions can be written, respectively:

$$\Delta\rho(r,0)=\Delta\rho_2 H(r_0-r), \quad \Delta\rho|_{r\to\infty}\to0. \tag{5}$$

Here $\Delta\rho_2=\rho_2-\rho_b$ ($\Delta\rho_2<0$), and r_0 and r_2 are, respectively, the radius and initial atomic density of the triple junction. The solution to Eqs. (4) and (5) is the function[6]

$$\Delta\rho(r,t)=\frac{\Delta\rho_2}{2Dt}\int_0^{r_0}\exp\left(-\frac{r^2+\hat{r}^2}{4Dt}\right)I_0\left(\frac{r\hat{r}}{2Dt}\right)\hat{r}\,d\hat{r}, \tag{6}$$

where I_0 is the modified Bessel function.

The main parameter of the diffusive smearing of a triple interface junction is the characteristic time τ_2 of smoothening of the initial distribution of ρ. We can define τ_2 more exactly as a time interval during which the minimum of the $\rho(r,t)$ profile becomes equal to $\rho_b+0.2\Delta\rho_2$. For the characteristic values $D=10^{-21}$ m^{2}s^{-1}, $r_0=10^{-9}$ m, and $\rho_2=0.5\rho_b$, numerical solution of Eq. (6) yields $\tau_2\approx4000$ s.

3. DIFFUSIVE SMEARING OF INTERFACE JUNCTIONS IN METAL NANOGLASSES

To a first approximation, the interface nodes (the regions where triple interface junctions connect) are simulated as spherical regions with a low atomic density. Taking into account the spherical symmetry of the model case under study, ρ can be defined effectively as a function of time t and one spherical coordinate R, i.e., $\rho=\rho(R,t)$. The diffusive node smearing is described as a smoothing of an originally spatially-nonuniform function $\rho(R,t)$ in the radial R direction, with the $\rho(R,t)$ function obeying the following diffusion equation

$$\frac{\partial\rho}{\partial t}=D\left(\frac{\partial^2\rho}{\partial R^2}+\frac{2}{R}\frac{\partial\rho}{\partial R}\right), \tag{7}$$

where $\rho(R,t)=\rho_b+\Delta\rho(R,t)$, and the initial conditions are given, accordingly, in the form

$$\Delta\rho(R,0)=\Delta\rho_3 H(R_0-R), \quad \Delta\rho|_{R\to\infty}\to0. \tag{8}$$

Here $\Delta\rho_3=\rho_3-\rho_b$ ($\Delta\rho_3<0$), and R_0 and ρ_3 are, respectively, the radius and atomic density of the sphere-shaped node. The solution of Eqs. (7) and (8) is the function[6]

$$\Delta\rho(R,t)=\frac{\Delta\rho_3}{2\sqrt{\pi Dt}R}\int_0^{R_0}\left[\exp\left(-\frac{(R-\xi)^2}{4Dt}\right)-\exp\left(-\frac{(R+\xi)^2}{4Dt}\right)\right]\xi\,d\xi. \tag{9}$$

The main parameter of the diffusive interface smearing is the characteristic time of smoothening of the initial ρ distribution. We can define τ_3 more exactly as the period during which the minimum of the $\rho(R,t)$ function reaches a value $\rho_b+0.2\Delta\rho_3$. For the characteristic values $D=10^{-21}$ m^{2}s^{-1}, $R_0=2.5\times10^{-9}$ m, and $\rho_3=0.5\rho_b$, numerical solution of Eq. (9) yields $\tau_3\approx2\times10^5$ s.

4. DISCUSSION OF RESULTS

Thus the diffusive smearing of interfaces, their triple junctions, and nodes is characterized by the τ_1, τ_2, and τ_3 times, respectively. Our model calculations yield the following inequality: $\tau_1<\tau_2<\tau_3$. This inequality implies that the interfaces smear faster than the triple junctions, and the latter, in their turn, spread out faster than the interface nodes.

This result accounts for the experimental data[1] on positron lifetimes in metal nanoglasses. Indeed, as follows from these experiments,

(1) Metal nanoglasses have two characteristic average positron lifetimes, $t_1=196$ ps and $t_2=489$ ps, which correspond to positron capture in vacancy-like and in large free volumes. The time t_1 is the same as in conventional (homogeneous) metal glasses, which permits one to assign t_1 to positron capture in vacancy-like free volumes inside amorphous nanoparticles (which have the same atomic density as the conventional metal glasses), and t_2, to positron capture in large free volumes present in interfaces, their junctions, and nodes.

(2) In thermally treated metal nanoglasses t_2 transforms to the so-called t_2 component of the positron lifetime, with $t_3>t_2$. The t_3-component intensity decreases with increasing thermal-treatment time, whereas the average value of t_3 increases. As the temperature of the treatment increases, the rate of the t_3-component intensity falloff increases.

Within the proposed model, the transition from the t_2 to the t_3 component and the decrease of the t_3-component intensity is associated with the (fast) diffusive smearing of the interfaces. The average value of t_3 grows with the treatment time, because (a) the comparatively small regions (interfaces, triple junctions) with a low atomic density smear faster than the larger regions (interface nodes) do, with the result that the relative contribution of the latter to the positron capture and annihilation increases; (b) larger regions with low atomic density are characterized by longer positron lifetimes. The effect of the thermal-treatment temperature on the rate of t_3 intensity variation (see the experimental data of Ref. 2)

finds a straightforward explanation as due to temperature-controlled diffusive smearing of the interfaces, their junctions, and nodes.

Thus the model proposed in this work describes structural transformations of metal nanoglasses as associated with diffusive smearing of interfaces, their triple junctions, and nodes. It is shown that, for characteristic values of the metal-nanoglass parameters, the diffusive smearing of interfaces occurs faster than that of their triple junctions, and the latter, faster than that of interface nodes. The proposed model explains the trends in the evolution of the average positron lifetime in metal nanoglasses under thermal treatment.

It should be pointed out that this model is based on fairly crude approximations (the interfaces are simulated by planar regions, the triple junctions, by cylindrical, and the nodes, by spherical regions). These approximations however, are, realistic for our purposes, namely, for revealing the main trends in evolution of the structure of metal nanoglasses taking into account available experimental data.[1] The matter is that these experimental results[1] do not permit a detailed study of the structural evolution of metal nanoglasses. They were derived from the average positron lifetime, which characterizes only indirectly the changes in the structure and, hence, reveals the trends rather than details in the evolution. Taking into account the indirect nature of these experimental data, the present work puts forward a somewhat crude model, which can serve, however, as an efficient basis for a further detailed theoretical description of the structural transformation of metal nanoglasses.

Partial support of the Russian Fund for Fundamental Research (Grant 98-02-16075), Office of the US Naval Research (''The Fundamentals of Nanostructured Interfaces of Hybrid Multilayer Coatings'' project), and of the Scientific Council ''Physics of Solid-State Nanostructures'' (Grant 97-3006) is gratefully acknowledged.

[1)]As follows from our calculations, the numerical solutions of Eq. (1) obtained for (2) and more realistic conditions differ insignificantly.

[1] R. Wurschum, M. Rollinger, H. Kisker, A. Rauchle, B. Damson, and H.-E. Schaefer, Nanostruct. Mater. **6**, 377 (1995).
[2] J. Jing, A. Krämer, R. Birringer, H. Gleiter, and U. Gonser, J. Non-Cryst. Solids **113**, 167 (1989).
[3] J. Weissmüller, R. Birringer, and H. Gleiter, Phys. Lett. A **145**, 130 (1990).
[4] R. S. Averback, H. Hahn, H. J. Höfler, and J. C. Logas, Appl. Phys. Lett. **57**, 1745 (1990).
[5] R. Wurschum, W. Greiner, R. Z. Valiev, M. Rapp, W. Sigle, O. Schneeweiss, and H.-E. Schaefer, Scr. Metall. Mater. **25**, 2451 (1991).
[6] V. F. Zaĭtsev and A. D. Polyanin, *Partial Differential Equations: Exact Solutions. A Handbook* [in Russian] (MPO, Moscow, 1996).
[7] H. Kronmüller, W. Frank, and A. Horner, Mater. Sci. Eng., A **133**, 410 (1991).

Translated by G. Skrebtsov

First-principles investigation of thermal point defects in B2 NiAl

A. Yu. Lozovoĭ, K. V. Ponomarev, and Yu. Kh. Vekilov

Moscow State Institute of Steels and Alloys, 117936 Moscow, Russia

P. A. Korzhavyĭ and I. A. Abrikosov

Uppsala University, S-75121 Uppsala, Sweden
(Submitted March 19, 1999)
Fiz. Tverd. Tela (St. Petersburg) **41**, 1630–1636 (September 1999)

The equilibrium concentrations of thermal defects are calculated in the mean-field approximation for the configurational entropy. The stable configurations of point defects in NiAl are discussed. © *1999 American Institute of Physics.* [S1063-7834(99)02009-2]

The intermetallic compound NiAl is widely used in aircraft manufacture, electronics, chemical catalysis, and elsewhere on account of its unique physical, chemical, and mechanical properties.[1,2] A large number of theoretical investigations of the electronic structure,[3–6] the optical properties,[7–11] the nature of interatomic interactions,[12,13] and the energetics of defects in the crystal structure[14–16] of this compound have been performed in the last 20 years. The structure of thermal defects in NiAl is very unusual and is a subject of experimental and theoretical investigations. Until very recently it was believed that the main thermal excitation in NiAl is a triple defect (two vacancies in the nickel sublattice plus an antistructural defect: a Ni atom in the aluminum sublattice).[1,2] The equilibrium concentrations of defects in NiAl at 1300 K calculated from first principles[14] confirm this picture of thermal excitations for nickel-enriched and stoichiometric NiAl. However, the high density of Al atoms in the nickel sublattice and the virtually complete absence of Ni atoms in the aluminum sublattice at high temperatures in aluminum-enriched NiAl that were obtained in the calculation in Ref. 14 and were observed experimentally in Ref. 17 do not agree with the idea of a triple-defect type thermal excitation for this range of compositions of NiAl.

In the present paper the equilibrium concentrations of thermal defects in NiAl are determined from first principles as a function of the composition of an alloy based on NiAl.

1. COMPUTATIONAL METHOD

In the present work the formation enthalpies of point defects were calculated using cubic supercells based on the B2 structure with 54 sites $(3\times3\times3)$ and one defect per supercell. The pair-interaction energies of the defects were calculated using supercells with 108 sites $(3\times3\times6)$ with two defects per supercell.

First-principles calculations for such large supercells are needed in order to rule out nonphysical interactions between defects. The increase in computational time, characteristic of standard band methods, $t\sim N^3$, makes it impossible to perform a calculations of the total energy for supercells with 108 sites in an acceptable period of time. For this reason, methods for calculating the electronic structure and the total energy, where the computing time t increases linearly with the number N of sites, in a supercell are preferable. In the present work we used the method of a locally self-consistent Green's function,[18,19] for which the computing time scales linearly with the number of sites, in a new formulation that takes account of a correction to the one-electron potential and total energy for the electrostatic interaction of multipole charges of atomic spheres.[20]

The main reason why nonspherical corrections to the potential and Madelung energy were taken into account in the present work is that the calculations of the total energy must be performed for subtraction alloys (in the substitution case, to calculate the energetics of defects it is sufficient to take account of the standard monopolar contributions to the potential and Madelung energy). Specifically, taking account of multipole contributions makes it possible to calculate the formation enthalpy of vacancies in pure metals,[20] while standard calculations in the atomic-sphere approximation (ASA) usually overestimate this quantity by a factor of 2–2.5,[21] The ASA error arises as a result of spherically-symmetric averaging of the electron density in the atomic spheres. This approximation works well for lattice sites where the symmetry of the local atomic environment is high. For sites where lattice defects (specifically, vacancies) destroy the symmetry of the local environment, this approximation becomes a source of error. For NiAl our preliminary calculations performed using the standard ASA gave an incorrect result for the ground state of the aluminum-enriched alloys NiAl because too high a value was obtained for the vacancy-formation energy. If the atomic-sphere approximation is supplemented by nonspherical corrections to the potential and Madelung energy (for brevity, we shall name this approximation ASA+M), the ground state in NiAl is reproduced correctly.

2. DEFECTS AT ZERO TEMPERATURE

In this section we shall consider the structure of defects in NiAl of arbitrary stoichiometry in the ground state, i.e., at zero temperature $(T=0)$ and zero pressure $(p=0)$. This structure is analyzed in detail in Ref. 22. We shall consider single-phase nonstoichiometric NiAl with a fixed concentra-

tion, $Ni_{1/2-\delta}Al_{1/2+\delta}$, where δ is the deviation from stoichiometry. The distribution of the components of the alloy (Al and Ni atoms and vacancies, $i=\{Al, Ni, V\}$) over the two sublattices ($\alpha \neq Al, Ni$) in the ground state is determined by the minimum of the enthalpy $\mathcal{H}$ of the entire system in which the number of atoms, $N_{at}=n_{Al}+n_{Ni}$, is fixed while the number of lattice sites, $N=N_{at}+n_V$, can vary. To determine the structure of the ground state of the alloy in the thermodynamic limit ($N_{at}\to\infty$), the enthalpy per atom

$$H=\lim_{N_{at}\to\infty}\frac{\mathcal{H}}{N_{at}}, \tag{1}$$

must be compared for different configurations of the alloy. The results of calculating the total energy performed in the present work were rescaled, therefore, to the standard formation enthalpies of alloys with respect to the standard states of the pure components (fcc nickel and aluminum)

$$H^0=E^{tot}_{Ni_{1/2-\delta}Al_{1/2+\delta}}-(1/2-\delta)E^{tot}_{Ni}-(1/2+\delta)E^{tot}_{Al}. \tag{2}$$

All total energies (per atom), E^{tot}, correspond to equilibrium volumes determined from the condition $p=0$. The extensive properties are normalized in this work per atom and not per lattice site, since the number of lattice sites in the present case is not fixed. Correspondingly, the atomic concentrations, $x_{i_\alpha}=n_{i_\alpha}/N_{at}$ and $x_i=\Sigma_\alpha x_{i_\alpha}$, where n_{i_α} is the number of sites in the α sublattice that are occupied by the component i, are used to characterize the configurations of the alloy. We note that the total atomic concentrations of the Al or Ni atoms in the alloy do not depend on the specific distribution of atoms in vacancies between the two sublattices, i.e., $x_{Al}=1/2+\delta$ and $x_{Ni}=1/2-\delta$. The use of concentrations determined per lattice site, $c_{i_\alpha}=n_{i_\alpha}/N_\alpha$, becomes more convenient when analyzing the distribution of the alloy components over sublattices with a fixed vacancy density. Here $N_\alpha=1/2N$ is the number of sites in the α sublattice which, in the case at hand, becomes fixed. The atomic and site configurations are related as $c_{i_\alpha}=2x_{i_\alpha}/(1+x_V)$.

In the general case, however, it is more natural to use atomic concentrations, especially for subtraction alloys, where the vacancy concentration can reach 10 at.%. It is the atomic concentrations that appear in the definition of the formation enthalpy of a defect

$$H^F_d=\frac{\partial\mathcal{H}^0}{\partial n_d}=\frac{\partial H^0}{\partial x_d}, \tag{3}$$

where the index d specifies the point defect. In our calculations four types of characteristic point defects in NiAl were considered: two antistructural atoms, $d=\{Ni_{Al}, Al_{Ni}\}$, and two vacancies, $d=\{V_{Al}, V_{Ni}\}$. For specific calculations Eq. (5) was written in terms of finite differences

$$H^F_d=\frac{H^0_d-H^0_{NiAl}}{x_d}, \tag{4}$$

where H^0_{NiAl} and H^0_d are the standard formation enthalpies (per atom) of perfect NiAl, and a supercell based on NiAl, containing one of the four intrinsic point defects, respectively, was used. The atomic concentration of defects x_d was 1/54 for antistructural atoms and 1/53 for vacancies.

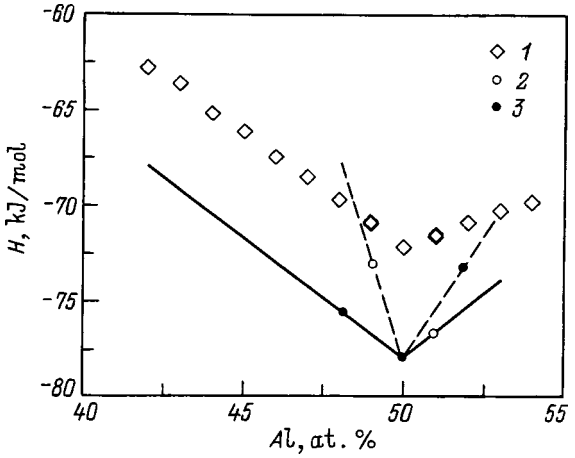

FIG. 1. Standard formation enthalpy of NiAl as a function of the composition of the alloy. *1*—Experimental data,[23] *2*, *3*—computed enthalpies, *2*—subtraction alloys, *3*—substitution alloys. Solid lines—formation enthalpy of the alloys NiAl in the ground state, dashed lines—enthalpies of unstable alloys.

The standard formation enthalpies of stoichiometric B2 NiAl and four nonstoichiometric alloys each containing four intrinsic point defects per supercell are presented in Fig. 1, which also shows the experimental formation enthalpies obtained by Henig and Lukas[23] for NiAl alloys. Assuming the defects to be noninteracting, the formation enthalpy of the alloy should be a linear function of the atomic concentrations of defects. The linear dependences of the formation enthalpies of the alloys NiAl for cases where the deviation from stoichiometry is due to one of four intrinsic point defects are shown in Fig. 1 (straight lines). They form two branches of alloys on each side of the exact stoichiometric composition: One corresponds to substitution alloys containing antistructural defects and the other corresponds to subtraction alloys containing structural vacancies.

The computational results presented in Fig. 1 show that the lower branch of the formation enthalpy of nickel-enriched alloys NiAl corresponds to substitution alloys, while in the case of excess aluminum the branch corresponding to subtraction alloys containing structural vacancies has the lowest formation enthalpy. As one can see, the slopes of the concentration dependences for the computed formation enthalpy of stable (possessing a lower formation enthalpy) nonstoichiometric alloys NiAl and the experimental formation enthalpy are close, while the slope of the formation-enthalpy branches corresponding to unstable alloys differ substantially from experiment.

The computed formation enthalpies of isolated defects as well as the formation enthalpies of complex, concentration-preserving defects are presented in Table I.

The binding energies of all possible pairs of point defects in NiAl were calculated in the present work using supercells with 108 sites, where two defects were placed first at the maximum distance from one another and then brought to the closest possible distance. The computational results are

TABLE I. The formation enthalpies of isolated defects, concentration-conserving defect complexes, and interbranch excitations in NiAl.

Name	Designation or quasichemical reaction	H_d^F, eV
	Intrinsic point defects	
Ni in Al	Ni_{Al}	1.30
Al	V_{Al}	2.69
Al in Ni	Al_{Ni}	2.64
Vacancy in Ni	V_{Ni}	0.70
	Complex concentration-conserving defects	
Triple (T)	$0 \rightarrow 2V_{Ni} + Ni_{Al}$	2.70
Divacancy (D)	$0 \rightarrow V_{Al} + V_{Ni}$	3.39
Volume (E)	$0 \rightarrow Ni_{Al} + Al_{Ni}$	3.94
Triple Al (TA)	$0 \rightarrow 2V_{Al} + Al_{Ni}$	8.02
	Interbranch excitation	
Interbranch Ni (IN)	$Ni_{Al} \rightarrow 2V_{Al}$	4.08
Interbranch Al (IN)	$2V_{Ni} \rightarrow Al_{Ni}$	1.24

presented in Table II. A positive binding energy corresponds to repulsion between defects.

3. DEFECTS AT FINITE TEMPERATURE

In the present section a statistical analysis is made of thermal defects in NiAl. The method is described, the results of numerical minimization of the Gibbs free energy are presented, and the structure of defects in NiAl at 1300 K is analyzed. The entire analysis is performed for noninteracting defects, and the possible influence of interactions between defects is discussed at the end of the section.

3.1. Numerical simulation method

In the present work the following method was used to calculate the equilibrium concentrations in the binary alloy B2 NiAl at finite temperature. The distribution of atoms of different kinds and vacancies over the two sublattices of the nonstoichiometric alloy $Ni_{1/2-\delta}Al_{1/2+\delta}$ can be described uniquely using the following four parameters:

1. The deviation from stoichiometry, δ.

2. The vacancy concentration (per site), $c_V = (c_{V_{Ni}} + c_{V_{Al}})/2$.

3. The long-range order parameter for Ni, $\eta_{Ni} = c_{Ni_{Ni}} - c_{Ni_{Al}}$.

TABLE II. Binding energies of all possible defects in NiAl.

Defect pair	Distance	H_{2d}^F eV
$Ni_{Al} + Al_{Ni}$		−0.55
$V_{Al} + Al_{Ni}$	$a\sqrt{3}/2$	−0.62
$Ni_{Al} + V_{Ni}$		0.05
$V_{Al} + V_{Ni}$		−0.02
$Ni_{Al} + Ni_{Al}$		0.16
$Ni_{Al} + V_{Al}$	a	0.14
$V_{Al} + V_{Al}$		0.05
$Al_{Ni} + Al_{Ni}$		0.12
$Al_{Ni} + V_{Ni}$	a	0.07
$V_{Ni} + V_{Ni}$		0.14

Note: A positive binding energy corresponds to repulsion of defects.

4. The long-range order parameter for Al, $\eta_{Al} = c_{Al_{Al}} - c_{Al_{Ni}}$.

The concentrations of the components of the alloy (per site) can be expressed in terms of these four parameters as follows:

$$c_{Al_{Al}} = (1/2 + \delta)(1 - c_V) + \eta_{Al}/2,$$

$$c_{Al_{Ni}} = (1/2 + \delta)(1 - c_V) - \eta_{Al}/2,$$

$$c_{Ni_{Ni}} = (1/2 - \delta)(1 - c_V) + \eta_{Ni}/2,$$

$$c_{Ni_{Al}} = (1/2 - \delta)(1 - c_V) - \eta_{Ni}/2,$$

$$c_{V_{Al}} = c_V - (\eta_{Al} - \eta_{Ni})/2,$$

$$c_{V_{Ni}} = c_V + (\eta_{Al} - \eta_{Ni})/2.$$

For an alloy whose composition is fixed by the parameter δ it is necessary to find the global minimum of the Gibbs free energy, $G^0 = H^0 - TS$, where the standard formation enthalpy, according to Eqs. (3) and (4), is a linear function of the atomic concentrations of the defects

$$H^0 = H^0_{NiAl} + \sum_d H_d^F x_d . \tag{5}$$

In the present work the mean-field approximation is used for the configurational entropy (per atom):

$$S = \frac{-1}{2(1-c_V)} \sum_\alpha \sum_i c_{i_\alpha} \ln c_{i_\alpha} = (1 + x_V)\ln\left(\frac{1+x_V}{2}\right) - \sum_\alpha \sum_i x_{i_\alpha} \ln x_{i_\alpha}. \tag{6}$$

The calculation of the equilibrium concentrations of defects is performed as follows. For fixed δ, an initial approximation is made for the vacancy concentration c_V, after which the equilibrium distribution of vacancies and kinds of atoms between the two sublattices is found by optimizing the values of the long-range order parameters η_{Ni} and η_{Al}. To optimize the long-range order parameters a first-principles calculation is performed of the total energy of the partially ordered alloy for different values of η_{Ni} and η_{Al}, and the minimum of the total energy is found. (The problem of the distribution of a third impurity, in our case vacancies, over the sublattices of a binary ordered alloy has been investigated in detail in Ref. 24.) The procedure is repeated for different values of c_V, and in this manner a global minimum of the Gibbs free energy is found. It should be noted that, for a fixed concentration of the alloy within the single-phase region, there is no need to use the grand canonical ensemble to find the equilibrium concentration of defects (compare, however, with the approach used in Ref. 14).

3.2. Thermal defects

The equilibrium atomic concentrations x_d of defects in NiAl at 1300 K computed in the present work are shown in Fig. 2 as a function of the stoichiometry of the alloy, fixed by the parameter δ. The main defects in the alloys NiAl with excess nickel are Ni atoms in the aluminum sublattice and, in

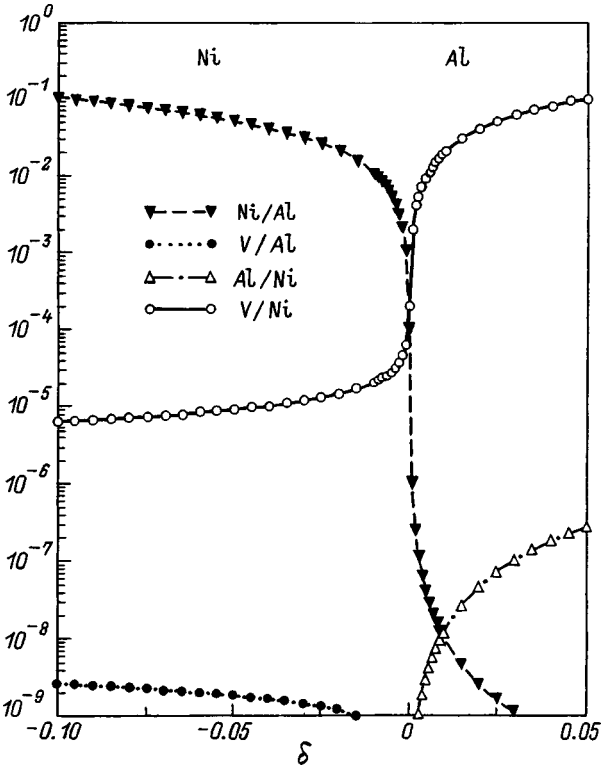

FIG. 2. Equilibrium concentrations of defects in NiAl at 1300 K as a function of the deviation δ from stoichiometry ($\delta>0$ — enrichment with aluminum).

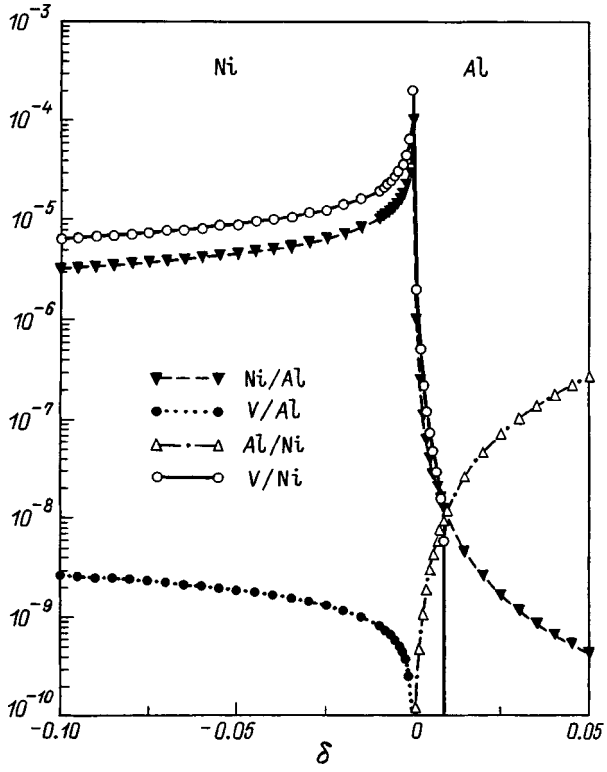

FIG. 3. Equilibrium concentrations of thermal defects in NiAl at 1300 K as a function of the deviation δ from stoichiometry.

alloys with excess aluminum, the most common defects are vacancies in the nickel sublattice. Many of these defects are structural defects, whose concentration is determined by the deviation from exact stoichiometry. In this connection it was of interest to separate thermal defects, which appear at finite temperature, from structural defects present in the ground state

$$x_d^t = x_d - x_d^0, \tag{7}$$

where x_d^t is the concentration of thermal defects. The atomic concentrations of thermal defects in NiAl at 1300 K are shown in Fig. 3. To understand the structure obtained for the thermal defects it is necessary to take account of the fact that, in an ordered compound having a fixed composition, thermal excitations are possible only in the form of complex defects conserving the concentration so that

$$x^t_{\mathrm{Ni_{Al}}} + x^t_{\mathrm{Al_{Ni}}} - 2(x^t_{V_{\mathrm{Al}}} + x^t_{V_{\mathrm{Ni}}}) = 0. \tag{8}$$

Particular cases of such thermal excitations are complex, concentration-conserving defects and interbranch excitations, enumerated in Table I. It has been generally assumed that the main thermal excitation in NiAl is a triple defect. Indeed, our calculations show that the most common thermal defects in stoichiometric and nickel-enriched NiAl are vacancies in the nickel sublattice and Ni atoms in the aluminum sublattice, which comprise a triple defect.

However, in alloys with excess aluminum the concentration of thermal Ni atoms in the aluminum sublattice becomes unexpectedly low, but Al atoms appear in the nickel sublattice in relatively large quantities. The behavior of the vacancy concentration in the nickel sublattice is even more interesting. At first it decreases rapidly with increasing deviation from stoichiometry. Then, when the parameter δ exceeds 0.01, the concentration of thermal vacancies in the nickel sublattice becomes negative. This means that the concentration of nickel vacancies in aluminum-enriched NiAl alloys decreases with temperature. Such behavior of the thermal-defect structure in aluminum-enriched NiAl alloys can be attributed only to interbranch Al excitation, which consists in the vanishing of two nickel vacancies and the formation of one antistructural Al atom instead (see Table I).

We shall show statistically that a triple defect is the primary thermal excitation in nickel-enriched alloys and in stoichiometric NiAl, while interbranch Al excitation is the primary thermal excitation in aluminum-enriched NiAl alloys. To this end the computed concentration ratios of thermal defects

$$R_T = \frac{1}{2}\frac{x^t_{V_{\mathrm{Ni}}}}{x^t_{\mathrm{Ni_{Al}}}} \quad \text{and} \quad R_{IA} = -\frac{1}{2}\frac{x^t_{V_{\mathrm{Ni}}}}{x^t_{\mathrm{Al_{Ni}}}} \tag{9}$$

are shown in Fig. 4. The ratio R_T should be close to 1 for primary thermal excitations of the ternary defect type, while R_{IA} should be close to 1 for primary thermal excitations of the interbranch Al excitation type. Thus we find that the thermal excitations in NiAl alloys at 1300 K are triple defects for $\delta<0.01$ and interbranch Al excitations for $\delta>0.01$. At the boundary between these two concentration ragnes the thermal excitations are exchange defects (see Table I).

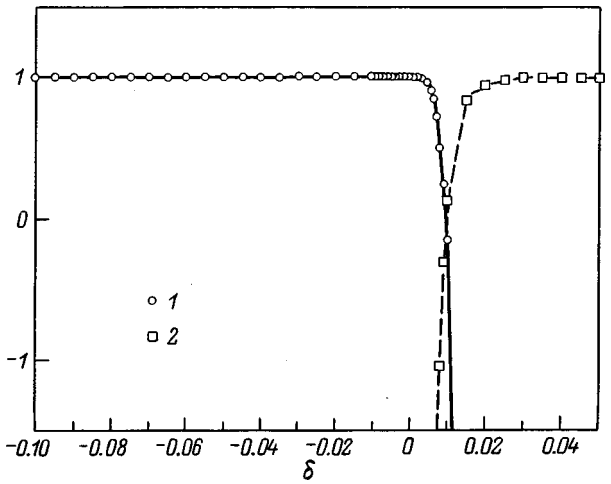

FIG. 4. Ratios of the concentrations of thermal defects (see text). *1*—Triple defects, *2*—interbranch Al excitations.

Thus, the presence of Al atoms in the nickel sublattice in aluminum-enriched NiAl alloys at finite temperature is a result of thermal interbranch Al excitations. According to our results, the concentration of antistructural Al atoms can reach 10^{-6} in Al-rich alloys at 1300 K, while according to the results of Ref. 14 their concentration should be much higher. Nonetheless, the results of both first-principles calculations are in qualitative agreement with the fact that interbranch Al excitations are the dominant thermal defects in aluminum-enriched NiAl.

The total concentration of point thermal defects can be determined as the difference of the total concentration of all types of point defects (structural and thermal) and the total concentration of structural defects in the ground state. This difference is shown in Fig. 5. The total number of thermal defects in nickel-enriched NiAl alloys is almost constant and much less than the number of structural defects, $O(\delta)$. The total concentration of thermal defects near the stoichiometric composition becomes relatively high (3×10^{-4} for $\delta=0$). This anomaly is due to the absence of structural defects in the ground state of stoichiometric NiAl, and therefore a high concentration of thermal defects arises at high temperatures on account of the contribution from the configurational entropy (Eq. (6)).

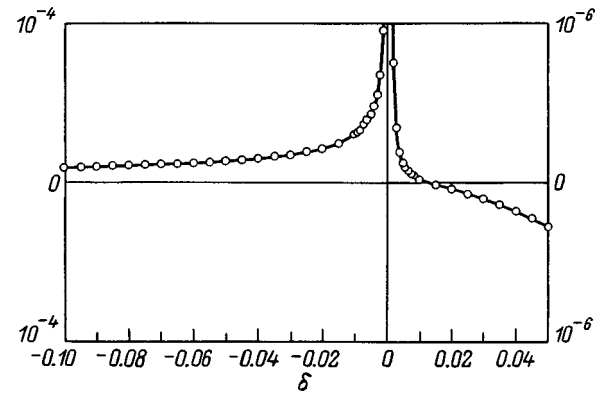

FIG. 5. Total concentration of thermal defects in NiAl at 1300 K.

The most interesting anomaly obtains for aluminum-rich NiAl alloys, where the total number of point defects decreases with temperature, on account of the fact that the main thermal excitation in this region (interbranch Al excitation) consists in vanishing of two vacancies and the production of only a single antistructural defect. A thermal excitation of this type is due to the nonlinear character of the entropy contribution. An increase in the distance between two defects, whose concentration in the ground state is already quite high, decreases the configurational entropy only negligibly (and can even increase it if the vacancies form an ordered structure in the ground state), while the formation of an antistructural defect (Al atom in the nickel sublattice) strongly increases the entropy. As a result, the total number of point defects decreases with temperature but the configurational entropy increases on account of the increase in the structural diversity of defects (diversification). Therefore, if the deviation from stoichiometry in aluminum-enriched NiAl alloys at zero temperature is due only to structural vacancies, at finite temperatures, a definite number of antistructural aluminum atoms is formed as a result of interbranch Al excitations.

3.3. Complexes of thermal defects

We shall now examine the possible effect of interactions between defects on the structure of the primary and secondary thermal defects in NiAl. First, the results of first-principles calculations of the interaction energies of defects in NiAl, obtained in the present work (see Table II), confirm the existing viewpoint[1] that the components of a triple defect (two vacancies and one antistructural defect) exist independently in NiAl, without forming a bound complex.

The interactions of point defects separated by a very short interatomic distance, $a\sqrt{3}/2$, are strong and attractive in the following two cases. Calculations show that strong attraction exists between the components of an exchange defect, and therefore the exchange pair $Ni_{Al}+Al_{Ni}$ should exist as a bound complex. The decrease in the formation enthalpy of an exchange defect as a result of the interaction of its constituent parts is still insufficient for an exchange effect to become the main thermal excitation in aluminum-rich NiAl alloys. However, the observed interaction can lead to the formation of a separate zone between stoichiometric NiAl and concentrated NiAl with excess aluminum, where an exchange defect will be the dominant thermal excitation.

A strong attractive interaction was also found for the pair $Al_{Ni}+V_{Al}$. However, as Fig. 2 shows, these two defects never coexist in the equilibrium state in NiAl with any concentration. The formation enthalpy of such a pair of defects is so high that the effect of a strong interaction between the defects in a pair on the final structure of the equilibrium concentrations of thermal defects is negligible. However, the attraction between Al atoms in the nickel sublattice and an aluminum vacancy could be important for understanding kinetic processes in NiAl, such as diffusion.

In summary, we can draw the following conclusions.

The equilibrium concentrations of thermal defects were calculated by minimizing the Gibbs free energy in the mean-

field approximation for the configurational entropy. It was shown that the primary thermal defects in stoichiometric NiAl and in NiAl alloys with excess nickel are triple defects, while in aluminum-rich alloys they are interbranch Al excitations. Since interbranch Al excitations consist of the removal of two vacancies from the nickel sublattice and the creation instead of only one antistructural Al atom in the nickel sublattice, the number of vacancies, just as the total number of point defects, should decrease with temperature in aluminum-rich NiAl alloys.

It can be concluded on the basis of the computed interaction energies of the defects that all three components of a triple defect exist independently in NiAl, without forming a bound complex. Conversely, a strong interaction was found for the following pairs of defects in NiAl: a Ni atom in the aluminum sublattice — an Al atom in the nickel sublattice and also a vacancy in the Al sublattice — an Al atom in the nickel sublattice. Therefore exchange defects in NiAl should form bound complexes, which can be the dominant thermal excitations in the finite concentration range between stoichiometric NiAl and concentrated NiAl with excess aluminum. Although the analysis performed in the present paper shows that the interactions between defects have only a secondary influence on the equilibrium structure of the defects, they could be important for understanding kinetic processes and metastable groupings of defects in NiAl.

This work was partially supported by the ''Surface Atomic Structures'' program of the Ministry of Education of the Russian Federation (No. 3.13.99), a ''First-Principles Investigation of the Distribution of Impurities and Their Charge State over Sublattices in Semiconductors'' grant, and the Russian Fund for Fundamental Research (grant No. 98-02-16419).

[1] D. B. Miracle, Acta Metall. Mater. **41**, 649 (1993).
[2] R. D. Noebe, R. R. Bowman, and M. V. Nathal, Int. Mater. Rev. **38**, 193 (1993).
[3] D. Hackenbracht and J. Kübler, J. Phys. F **10**, 427 (1980).
[4] J. M. Koch and C. Koenig, Philos. Mag. B **54**, 177 (1986); J. M. Koch and C. Koenig, Philos. Mag. B **55**, 359 (1987); J. M. Koch and C. Koenig, Philos. Mag. B **57**, 557 (1988).
[5] J. Zou and C. L. Fu, Phys. Rev. B **51**, 2115 (1995).
[6] C. A. Botton, G. Y. Guo, W. M. Temmerman, and C. J. Humphreys, Phys. Rev. B **54**, 1682 (1996).
[7] D. J. Peterman, R. Rosei, D. W. Lynch, and V. L. Moruzzi, Phys. Rev. B **21**, 5505 (1980).
[8] V. E. Egorushkin, A. I. Kul'mentyev, and P. E. Rubin, Solid State Commun. **57**, 821 (1986).
[9] D. Knab and C. Koenig, J. Phys.: Condens. Matter **2**, 465 (1990).
[10] K. J. Kim, B. N. Harmon, and D. W. Lynch, Phys. Rev. B **43**, 1948 (1991).
[11] O. V. Faberovich, S. V. Vlasov, K. I. Portnoi, and A. Yu. Lozovoi, Physica B **182**, 267 (1992).
[12] T. Hong and A. J. Freeman, Phys. Rev. B **43**, 6446 (1991).
[13] Z. W. Lu, S.-H. Wei, and A. Zunger, Acta Metall. Mater. **40**, 2155 (1992).
[14] C. L. Fu, Y.-Y. Ye, M. H. Yoo, and K. M. Ho, Phys. Rev. B **48**, 6712 (1993).
[15] C. L. Fu, Phys. Rev. B **52**, 3151 (1995).
[16] N. I. Medvedeva, O. N. Mryasov, Yu. N. Gornostyrev, D. L. Novikov, and A. J. Freeman, Phys. Rev. B **54**, 13 506 (1996).
[17] M. Kogachi, Y. Takeda, and T. Tanahashi, Intermetallics **3**, 129 (1995).
[18] I. A. Abrikosov, A. M. N. Niklasson, S. I. Simak, B. Johansson, A. V. Ruban, and H. L. Skriver, Phys. Rev. Lett. **76**, 4203 (1996).
[19] I. A. Abrikosov, S. I. Simak, B. Johansson, A. V. Ruban, and H. L. Skriver, Phys. Rev. B **56**, 9319 (1997).
[20] P. A. Korzhavyi, I. A. Abrikosov, B. Johansson, A. V. Ruban, H. L. Skriver, in press.
[21] T. Beuerle, R. Pawellek, C. Elsässer, and M. Fähnle, J. Phys.: Condens. Matter **3**, 1957 (1991).
[22] P. A. Korzhavyĭ, I. A. Abrikosov, A. Yu. Lozovoĭ, K. V. Ponomarev, and Yu. Kh. Vekilov, Materialovedenie **12**, 32 (1998).
[23] E.-T. Henig and H. L. Lukas, Z. Metallkd. **66**, 98 (1975).
[24] A. V. Ruban and H. L. Skriver, Phys. Rev. B **55**, 856 (1997).

Translated by M. E. Alferieff

Misfit disclinations at crystal/crystal and crystal/glass interfaces

I. A. Ovid'ko

Institute for Problems in Mechanical Engineering, Russian Academy of Sciences, 199178 St. Petersburg, Russia

(Submitted February 8, 1999)
Fiz. Tverd. Tela (St. Petersburg) **41**, 1637–1643 (September 1999)

Theoretical concepts have been developed for a new type of misfit defects, misfit disclinations, at crystal/crystal and crystal/glass interfaces. It is shown, in particular, that the formation of misfit disclinations is an efficient physical micromechanism of misfit stress relaxation at crystal/crystal interfaces. A model describing misfit disclinations at crystal/glass interfaces has been constructed. The energy characteristics of phase boundaries with misfit disclination ensembles are estimated. © *1999 American Institute of Physics.* [S1063-7834(99)02109-7]

Misfit stresses arise in heteroepitaxial systems as a result of a geometric mismatch between the film and substrate lattices. In most cases, (partial) misfit-stress relaxation occurs through formation of misfit dislocations (MD), which make up planar arrays parallel to the interface between the film and the substrate (see, e.g., Refs. 1–4). This work proposes and studies theoretically an alternate micromechanism of misfit-stress relaxation, namely, through formation of specific internal interfaces (MD walls or high-angle grain boundaries) and of disclinations at the junctions of the crystal/crystal interfaces and low- or high-angle film grain boundaries. A theoretical model describing misfit disclinations in composite crystal/glass systems is also proposed.

1. MISFIT DISCLINATIONS IN CRYSTALLINE FILMS (DEFINITION)

Consider as a model system a solid-state system consisting of a thin, elastically-isotropic crystalline film of thickness h and of a semi-infinite, elastically-isotropic crystalline substrate. For the sake of simplicity we shall restrict ourselves to the case of one-dimensional mismatch characterized by a parameter $f=(a_2-a_1)/a_1<0$, where a_1 and a_2 are the substrate and film lattice parameters, respectively. The shear modulus G and the Poisson ratio ν are assumed to be the same for the substrate and the film.

Consider this solid-state system in the absence of MDs. Because of a geometric mismatch between the film and substrate lattices, the film is elastically distorted and can be characterized by an elastic homogeneous strain $\varepsilon^*=-f$. For $f<0$, the film is subjected to tensile misfit stresses ($\varepsilon^*>0$). In a general case, their efficient relaxation can be achieved by creating in the film defects associated with introduction of excess material.

A ''standard'' micromechanism of relaxation of the misfit stress (or of the mismatch f) involves generation of MDs, which, when in thermodynamic equilibrium, make up a planar array parallel to the phase boundary.[1–5] Considered in terms of the continuum theory of defects, creation of MDs means introduction into the film of ''excess'' material in the form of half-planes bounded by MD lines (Fig. 1a).

We believe that introducing into the film an ''excess'' material in the form of wedges bounded by (wedge) disclination lines, i.e., of rotational-type defects (Fig. 1b), could be an efficient alternative to this micromechanism. We shall call such defects in what follows misfit disclinations.

The specific features of the misfit disclinations are determined by the crystalline structure of the film. The misfit disclination lines can bound either the finite dislocation walls or grain boundaries in the film. A theoretical analysis of the first and second cases is performed.

2. MISFIT DISCLINATIONS BOUNDING MISFIT DISLOCATION WALLS IN CRYSTALLINE FILMS

Following the above conclusions, we assume an alternative to the standard micromechanism of misfit stress relaxation through generation of a planar MD array (Fig. 1a) to be formation of MD walls bounded by misfit disclination lines (Fig. 2). By which of the above micromechanisms the misfit stresses relax depends on the kinetic factors (associated, in particular, with the film deposition technology used) and the degree of misfit stress relaxation in the final equilibrium state.

To evaluate the extent of misfit stress relaxation in the case of MD walls (Fig. 2), estimate the elastic energy density (per unit phase-boundary area) W of the film/substrate system with periodically arranged identical MD walls. The walls are considered to be regular, i.e., one assumes the

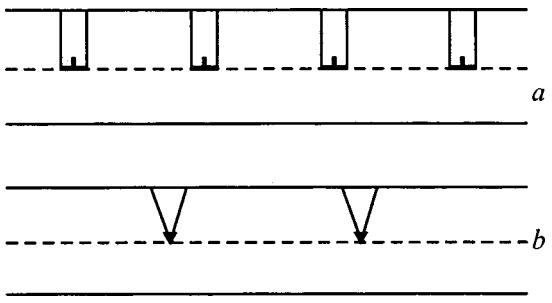

FIG. 1. Misfit defects in the interface: (a) misfit dislocations, (b) misfit disclinations.

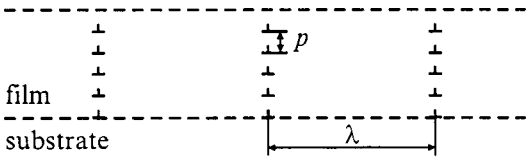

FIG. 2. Misfit dislocation walls in a crystalline film bounded by misfit disclinations.

Burgers vector b to be the same for all MDs, and distance p between the adjacent MDs is the same in each wall. The specific features of an MD wall (Fig. 2) at equilibrium are an efficient screening of the fields of the MDs making up the wall and a finite wall length. The latter accounts for the existence of a misfit disclination, which is the source of disclination-type stress fields at the point of wall termination at the phase boundary.

To a first approximation (corresponding to that of Matthews[1,6]), the energy density W has three main components:

$$W \approx W^f + W^\omega + W^d. \tag{1}$$

Here W^f is the density of the intrinsic elastic energy of residual misfit, and W^d and W^ω are, accordingly, the elastic energy densities of the misfit disclinations and of the MD walls.

Consider the quantity W^f. In a general case (for films of finite thickness), MDs accommodate only partially the f mismatch, which accounts for the presence of residual homogeneous elastic strain $\varepsilon = -(f - B/\lambda)$, where B is the total MD Burgers vector in the wall, and λ is the distance between the walls. B/λ is the part of the initial misfit which is accommodated through MD formation. The MD wall parameters in our model (Fig. 2) determine the $B = hb/p$ relation (where h/p is the number of MDs in the wall), thus yielding

$$\varepsilon = -(f - (h\,b/p\,\lambda)). \tag{2}$$

Inserting Eq. (2) into the well-known[1–4] expression for the energy of homogeneous strain of a film of thickness h, we obtain the following relation for W^f

$$W^f = 2\,G\,\frac{1+\nu}{1-\nu}(f - (h\,b/p\,\lambda))^2 h. \tag{3}$$

The MD wall energy density, without including the contribution due to misfit disclinations, is given by the expression known from dislocation theory (see, e.g., Ref. 7)

$$W^\omega = \frac{G\,b^2\,h}{4\,\pi(1-\nu)p\,\lambda}\left(\ln\frac{R}{r_0} + Z\right). \tag{4}$$

Here R is the radius of MD stress-field screening in a wall ($R \approx p$), r_0 is the MD core radius ($r_0 \approx a_2$), and Z is a factor taking into account the MD core contribution to the elastic energy density ($Z \approx 1$).

Within the model under study (Fig. 2), all misfit disclinations are characterized by the same strength $\omega \approx b/p$ ($\ll 1$), which is determined in a standard way[8] by the MD wall parameters as the strength of a disclination bounding the dislocation wall. The stress fields of disclinations localized near a free surface (in our case, separated from the free surface through a distance h) are screened by such a surface. The effective disclination-field screening radius in our model is h. In view of this, we use the well-known expression[8] for the elastic energy density of a wedge disclination in half-space to obtain the following relation for the density of self-energy of misfit disclinations distributed along an interface with a linear density λ^{-1}

$$W^d \approx \frac{G\,\omega^2 h^2}{4\,\pi(1-\nu)\lambda} \approx \frac{G\,b^2 h^2}{4\,\pi(1-\nu)p^2\,\lambda}. \tag{5}$$

Note that elastic interaction between misfit disclinations is negligible, because the disclination-field screening radius h in the model under study (Fig. 2) is smaller than the distance λ between the disclinations. This permits us to neglect the contribution of this interaction to W.

Using the relations $R \simeq p$ and $r_0 \approx a_2$, we derive from Eqs. (1)–(5) the following expression for the elastic energy density of a heteroepitaxial system with MD walls:

$$W \approx 2\,G\,\frac{1+\nu}{1-\nu}\varepsilon^2 h + \frac{G\,b(\varepsilon+f)}{4\,\pi(1-\nu)}[\ln(p/a_2) + Z] + \frac{G\,b\,h(\varepsilon+f)}{4\,\pi(1-\nu)p}. \tag{6}$$

Minimization of W with respect to ε yields the equilibrium value of the residual elastic strain in a film

$$\varepsilon_{eq} = \frac{b}{16\,\pi(1+\nu)h}[\ln(p/a_2) + Z + (h/p)]. \tag{7}$$

The critical thickness h_c at which the existence of MD walls is energetically preferable compared to the coherent state is obtained by setting $\varepsilon_{eq} = f$ in Eq. (7)

$$h_c = \frac{b\,p[\ln(p/a_2) + Z]}{16\,\pi f(1+\nu)p + b}. \tag{8}$$

The elastic energy density of a heteroepitaxial system with MD walls (6) for the case of $h/p > 1$ (the condition always satisfied in our model) is larger than the elastic energy density W_0 of a heteroepitaxial system with a planar array of MDs with the same total Burgers vector (Fig. 1a), which in Matthews' approximation is given by the well-known[1,6] expression

$$W^0 = 2\,G\,\frac{1+\nu}{1-\nu}\varepsilon^2 h + \frac{G\,b(\varepsilon+f)}{4\,\pi(1-\nu)}[\ln(p/a_2) + Z]. \tag{9}$$

It thus follows that planar MD arrays (Fig. 1a) are more equilibrium configurations than MD walls (Fig. 2). This conclusion is supported by numerous observations (see, e.g., Refs. 1–4) of planar MD arrays in heteroepitaxial systems under equilibrium conditions.

Nevertheless, because in order to emerge out of a dislocation wall the dislocation has to overcome an energy barrier[7], the MD walls considered here are quasiequilibrium and, hence, fairly stable configurations. Such MD walls can form in nonequilibrium conditions, specifically in coalescence of nucleating island films. This accounts for the ex-

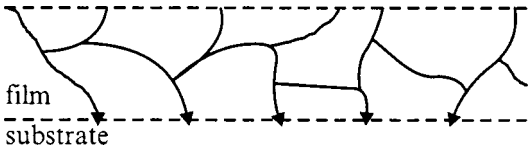

FIG. 3. Misfit disclinations (triangles) at the interface between a substrate and a polycrystalline (or nanocrystalline) film.

perimental data (see, e.g., Ref. 2) on the formation of specific interfaces, which affect the physical properties of films, in films produced in coalescence of islands.

It should be noted that, besides the walls of complete MDs, one can generally envisage formation of walls of partial MDs. A thorough analysis of this case is outside the scope of the present work.

3. MISFIT DISCLINATIONS IN POLYCRYSTALLINE AND NANOCRYSTALLINE FILMS

Consider a solid-state system consisting of a polycrystalline or nanocrystalline film of thickness h and a single-crystal semi-infinite substrate (Fig. 3). Following the conclusions drawn from a general consideration of the micromechanisms of misfit stress relaxation (Sec. 2), we assume that such stresses in the heteroepitaxial system under study can be efficiently relieved through misfit disclinations at the points where grain boundaries meet with the interface (Fig. 3).

We estimate the elastic energy density $\tilde{W}$ of a film/substrate system with an ensemble of misfit disclinations at the interface separating the substrate from a polycrystalline (nanocrystalline) film with a characteristic grain size d. For simplicity, we shall limit ourselves to a model within which all misfit disclinations are characterized by the same strength ω and are located along the interface periodically with a period d (Fig. 3). In these conditions, the energy density $\tilde{W}$ has, in a first approximation, three main components:

$$\tilde{W}=\tilde{W}^f+\tilde{W}^d+\tilde{W}^{\mathrm{int}}, \tag{10}$$

where $\tilde{W}^f$ is the density of elastic self-energy of the residual misfit, and $\tilde{W}^d$ and $\tilde{W}^{\mathrm{int}}$ are, respectively, the densities of the misfit disclination elastic self-energy and of the disclination interaction energy. $\tilde{W}^f$ is given by the expression

$$\tilde{W}^f=2\,G\frac{1+\nu}{1-\nu}\,\tilde{\varepsilon}^2\,h, \tag{11}$$

where $\tilde{\varepsilon}$ is the residual elastic strain in a film with misfit disclinations. Using the well-known expression[8] for the elastic self-energy of a wedge disclination near a free surface, we come to the following relation for the density of elastic self-energy of misfit disclinations distributed along an interface with a linear density d^{-1}

$$\tilde{W}^d\approx\frac{G\,\omega^2\,h^2}{4\,\pi(1-\nu)d}. \tag{12}$$

Estimate now the energy density of elastic interaction between misfit disclinations, $\tilde{W}^{\mathrm{int}}$, present in Eq. (10). To do this, we use the well-known expression for the pair interaction energy between two (i and j) parallel wedge disclinations at a distance h from the free surface[8]

$$E_{ij}=\frac{G\,\omega_i\,\omega_j}{2\,\pi(1-\nu)}\left[h^2+\frac{r_{ij}^2}{4}\ln\frac{r_{ij}^2}{4\,h^2+r_{ij}^2}\right], \tag{13}$$

where r_{ij} is the distance between disclinations, ω_i and ω_j are the strengths of the ith and jth disclinations, respectively, and i and j are integers labeling the disclinations. In our model

$$r_{ij}=d|i-j|,\quad \omega_i=\omega_j=\omega. \tag{14}$$

Consider N misfit disclinations located within a finite portion of length Nd ($N\gg 1$) of an infinite (model) interface. Because the stress fields of disclinations located at a distance h from the free surface are screened efficiently with a screening radius $\approx h$,[8] the total interaction energy of the ith disclination with other misfit disclinations can be written [taking into account Eqs. (13) and (14)]

$$E_i\approx\frac{G\,\omega^2}{2\,\pi(1-\nu)}\left[h^2+2\sum_k\frac{d^2\,k^2}{4}\ln\left(\frac{d^2\,k^2}{4\,h^2+d^2\,k^2}\right)\right], \tag{15}$$

where $k=|i-j|=1,2,\ldots,[h/d]$, and $[h/d]$ is the integral part of the h/d ratio. The sum of the energies E_i for all disclinations within the chosen part of the interface of length Nd is NE_i. Whence, taking into account Eq. (15), one obtains the expression for the density of misfit-disclination interaction energies:

$$\tilde{W}^{\mathrm{int}}=\frac{N\,E_i}{N\,d}\approx\frac{G\,\omega^2}{2\,\pi(1-\nu)d}\left[h^2+\frac{1}{2}\sum_{k=1}^{[h/d]}d^2\,k^2\times\ln\left(\frac{d^2\,k^2}{4\,h^2+d^2\,k^2}\right)\right]. \tag{16}$$

Consider in more detail two important particular cases, namely, films with $d/h>1$ and $d/h\ll 1$.

(1) *Films with a characteristic ratio* $d/h>1$. In this case the interaction between misfit disclinations is negligible, i.e. $\tilde{W}^{\mathrm{int}}\ll\tilde{W}^f,\tilde{W}^d$. Then the density of elastic energy $\tilde{W}$ of the system under study, taking into account Eqs. (10)–(12), can be written

$$\tilde{W}\approx 2\,G\frac{1+\nu}{1-\nu}\tilde{\varepsilon}^2\,h+\frac{G\,\omega^2\,h^2}{4\,\pi(1-\nu)d}. \tag{17}$$

To find an explicit dependence of $\tilde{W}$ on $\tilde{\varepsilon}$, consider the relation between the disclination strength ω and residual strain $\tilde{\varepsilon}$. Introduction of a wedge disclination of strength ω into a film is equivalent of inserting there ''excess'' material in the form of an isosceles triangle with a base $2h\tan(\omega/2)$. (In the case under study, $\omega\ll 1$ and, as a consequence, $2h\tan(\omega/2)\approx h\omega$.) As a result, the misfit disclinations distributed with a linear density d^{-1} along the interface accommodate part of the original mismatch characterized by the quantity $h\omega/d$. Hence one can write the following relation between $\tilde{\varepsilon}$ and ω:

$$\tilde{\varepsilon} \approx -(f-(h\,\omega/d)). \tag{18}$$

Taking into account Eqs. (17) and (18), the condition of a minimum of $\tilde{W}$ with respect to $\tilde{\varepsilon}$ yields the equilibrium residual elastic strain in the film

$$\tilde{\varepsilon}_1 \approx -\frac{f\,d}{8\,\pi(1+\nu)h+d}. \tag{19}$$

The critical thickness $\tilde{h}_c$ starting from which the presence of misfit disclinations is energetically preferable (compared to their absence) is found by setting $\tilde{\varepsilon}_1=-f$ in Eq. (19), i.e. $\tilde{h}_c=0$. Thus the presence of misfit disclinations in a film with a characteristic ratio $d/h>1$ is energetically preferable for any thickness $h>0$.

(2) *Films with a characteristic ratio* $d/h \ll 1$. (This case, in particular, relates to nanocrystalline films.) In such films interaction among misfit disclinations contributes noticeably to the film characteristics. Therefore we shall estimate the energy density $\tilde{W}^{\rm int}$ of disclination interaction. Because $d/h \ll 1$, the summation in Eq. (16) can be approximated with integration to obtain

$$\tilde{W}^{\rm int} \approx \frac{G\omega^2h^2}{2\,\pi(1-\nu)d}\left[1+\frac{1}{2}\int_0^1 y^2\ln\left(\frac{y^2}{4+y^2}\right)dy\right] \approx \frac{2\,G\,\omega^2\,h^2}{5\,\pi(1-\nu)d}, \tag{20}$$

where $y=kd/h$ for $h/d \ll 1$.

Equations (10)–(12), (19), and (20) permit one to find the elastic energy density of a heteroepitaxial system with a polycrystalline (nanocrystalline) film characterized by the ratio $d/h \ll 1$:

$$\tilde{W} \approx 2\,G\,\frac{1+\nu}{1-\nu}\tilde{\varepsilon}^2h+\frac{13\,G\,d(\tilde{\varepsilon}+f)^2}{20\,\pi(1-\nu)}. \tag{21}$$

Minimizing $\tilde{W}$ with respect to $\tilde{\varepsilon}$ yields the equilibrium residual elastic strain

$$\tilde{\varepsilon}_2 \approx -\frac{13\,f\,d}{40\,\pi(1+\nu)\,h+13\,d}. \tag{22}$$

Substituting f in place of $\tilde{\varepsilon}_2$ in Eq. (22), we find for the critical thickness $h_c=0$. Thus the presence of misfit disclinations with a characteristic ratio $d/h \ll 1$ is energetically preferable from the beginning of film formation (deposition).

We see that formation of misfit disclinations at the junctions of the interface with grain boundaries is an efficient micromechanism of misfit stress relaxation.

4. DISCLINATIONS AT THE CRYSTAL/GLASS INTERFACE

Composite solid-state (including thin-film) systems of the crystal/glass type, which enjoy widespread application in diverse high technologies, have been a subject of intensive studies (see, e.g., Refs. 9–11). The physical, chemical, and mechanical properties of such composites depend substantially on the crystal/glass interface, which accounts for the particular interest expressed in investigation of such interfaces. A recent publication presented an estimate of the energy characteristics of crystal/glass interfaces within a thermodynamic approach which neglected the geometric mismatch between the crystalline and amorphous structures.[12] At the same time it is well known that the influence of mismatch on the interface characteristics is dominant even in the case where such interfaces separate crystalline phases with similar structures.[1–5] Because the essentially different (crystalline and amorphous) phases are separated by crystal/glass interfaces, it can be expected that geometric mismatch at such interfaces gives rise to strong distortions in the regions adjacent to the interfaces and to high-density ensembles of misfit defects. This Section puts forward a theoretical description of misfit defects at the crystal/glass interfaces and estimates the elastic energy of the latter.

For simplicity we shall restrict our consideration to the situation where most of the faces of the glass structural units (geometric models of atomic clusters characteristic of a given structure) have the same topology as those of the structural units of the crystal. This permits one to treat the crystal/glass interface as a semicoherent boundary, i.e., one made up of coherent (defect-free) and incoherent parts. We assume also, by analogy with the definition of crystal/crystal semicoherent interfaces,[1–4] that within coherent parts the structural units of the crystal and of the glass join in a coherent manner, i.e. without forming topological defects, whereas incoherent regions represent topological defects of the interface. Within this description, interfaces separating metal glasses from fcc or bcc crystals may serve as an illustration of the crystal/glass semicoherent interfaces [because, according to Refs. 13–15, the faces of structural units of both metal glasses and of fcc (bcc) crystals have a topology of triangles and quadrangles, which are the faces of tetrahedral and octahedral pyramids simulating the characteristic atomic clusters of glasses and crystals].

The major structural features of metal and covalent glasses are the absence of long-range translational order and the presence of medium-scale structural homogeneity and frozen-in local distortions in the glass structure.[16] These structural features, as well as the main physical and mechanical properties of glasses, are well described in terms of the so-called disclination models, which treat glasses as solids with randomly distributed disclinations,[14–21] i.e., defects distorting the long-range translational order and creating local distortions in glasses. Such disclinations make up usually low-energy configurations with screened stress fields,[14–21] and this accounts for the medium-scale structural homogeneity of glasses.

Consider a semicoherent interface between a crystal and glass, representing a solid-state system with disclinations which are randomly distributed in the bulk of the glass and emerge onto its surface, specifically onto an interface (Fig. 4). The interface lies actually inside the crystal/glass composite (Fig. 4b and 4c). At the same time, according to the law of disclination charge conservation,[8] disclinations cannot terminate inside a solid; they either emerge at a free surface or form disclination loops. This leads us to the following conclusion: disclinations emerging onto the interface should either pass through the crystal bulk to reach the free surface

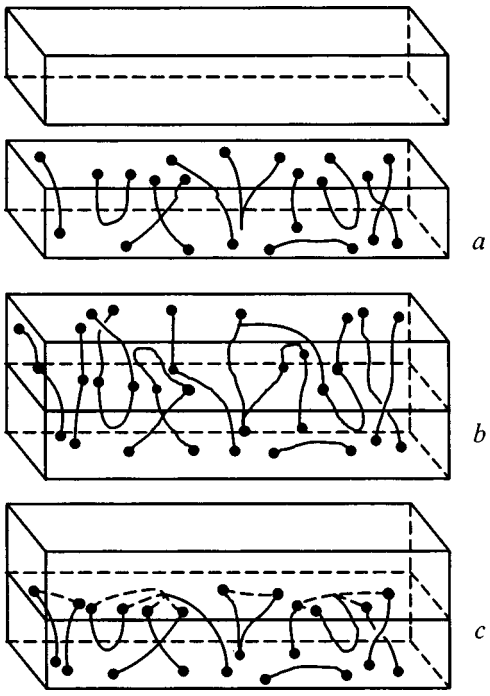

FIG. 4. Crystal/glass composite. (a) Glass (below) with disclinations (solid lines) and crystal (above) before the composite formation, (b) amorphization of the crystalline phase, (c) misfit disclinations (dashed lines) in the interface.

of the crystal/glass composite (Fig. 4b) or form loops with segments at the interface (Fig. 4c).

The first variant (Fig. 4b) corresponds to amorphization of a crystal. The second variant (Fig. 4c) which is most widespread results in formation of new disclination segments in the interface, or, in other words, in formation of specific misfit defects. Such defects are localized in the interface plane and connect the points of emergence (from the bulk of the glass) of disclinations onto the interface (Fig. 4c). The misfit defects under study here represent actually a continuation of the disclination lines, and are also disclinations with the same Frank vectors (disclination charges) $\boldsymbol{\omega}$ as those reaching the interface. Note, however, that the lines of the specific misfit defects are at a nonzero angle (i.e. tilted) to the lines of the original disclinations and, hence, to their and own Frank vectors. This is what determines the difference of the specific misfit defects as disclinations from the original ''bulk'' species (i.e. disclinations in the amorphous bulk) making up lines whose continuations the former are. In particular, wedge ''bulk'' disclinations transform into the twist species at the interface.

Estimate the density (per unit area of the interface) of elastic energy W^{sp} of these specific misfit defects, the misfit disclinations. In most cases, bulk disclinations in glasses are randomly distributed, closely spaced, and their stress fields are screened (at small distances) through interaction with one another.[14–21] As a consequence, the misfit disclinations (which are a continuation of bulk disclination lines) also form usually at the crystal/glass interface a disordered ensemble characterized by a high disclination density and consisting of low-energy configurations with screened stress fields. Such ensembles of misfit disclinations create elastic distortions in the layer adjoining the interface plane and having a thickness λ' equal to the characteristic elastic-field screening scale of disclination configurations in glass. The density of elastic energy of such a layer per unit of its volume is close to that of the elastic distortion energy E^a in the amorphous phase. Hence the elastic energy density of misfit disclinations per unit area of the interface W^{sp} can be approximated by

$$W^{sp} \approx \lambda' E^a. \tag{23}$$

As follows from neutron diffraction measurements in metal glasses,[22] the characteristic scale of the ''frozen-in'' inhomogeneities is ≈ 1.5 nm. In terms of the disclination approach to the glass structure,[14–21] this is equal to the characteristic elastic-field screening scale of disclination configurations λ', i.e. $\lambda' \approx 1.5\,\text{nm} \approx 5\tilde{a}$ (where $\tilde{a}$ is the average interatomic distance in glass). The quantity $E^a \approx (1/83 - 1/63)G$, where G is the shear modulus (see Ref. 23 and the references therein). Thus Eq. (23) yields an approximate estimate $W^{sp} \approx (0.06-0.08)G\tilde{a}$.

Besides W^{sp}, the energy density W^{dil} associated with misfits of dilatation nature also contributes to the density of the total elastic energy W^{tot} of the interface. The point is that the mismatch between the lattice parameters a_x and a_y of the crystalline phase in the interface plane, on the one hand, and the interatomic distances in glass, on the other, give rise to dilatation misfit stresses, similar to the case of the crystal/crystal interface. To a first approximation, dilatation misfit in the crystal/glass model system with infinite dimensions is characterized by (average) misfit parameters $f_x = 2(\tilde{a} - a_x)/(\tilde{a} + a_x)$ and $f_y = 2(\tilde{a} - a_y)/(\tilde{a} + a_y)$ (where $\tilde{a}$ is the average interatomic distance in glass), which for the sake of simplicity are subsequently assumed to be equal, $f_x = f_y$. Consider the situation where the dilatation misfit is completely accommodated by perpendicular arrays of misfit dislocations with Burgers vectors $b' = a_x = a_y$ created at the interface (the ''standard'' micromechanism of dilatation misfit relaxation). The corresponding density of elastic energy W^{dil} can be written in Matthews' approximation in the form

$$W^{dil} \approx \frac{G\,b'\,f}{2\,\pi(1-\nu)}\left(\ln\frac{b'}{f\,r_0}+1\right), \tag{24}$$

where r_0 is the core radius of misfit dislocations ($r_0 \approx b'$), and b'/f is the average distance between misfit dislocations in each dislocation array and, accordingly, the effective screening radius of the stress fields of such dislocations. For the characteristic parameters $\nu = 0.33$, $b' \approx \tilde{a} \approx 3 \times 10^{-10}$ m, $f = 10^{-3}$ and 10^{-1}, we obtain from Eq. (24) $W^{dil} \approx 0.002$ and $\approx 0.1\,G\tilde{a}$, respectively.

Thus within the proposed model the density of the total elastic energy $W^{tot} = W^{sp} + W^{dil}$ of the crystal/glass interface can be estimated as

$$W^{tot} \approx k\,G\,\tilde{a}, \tag{25}$$

where $k = 0.06 - 0.18$. A comparison of W^{tot} with the energy densities of high-angle grain boundaries W^{gb} (see, e.g., Ref.

24) shows that in a general case W^{tot} can be either larger or smaller than W^{gb}, depending on the actual geometric and structural grain-boundary parameters.

Thus the concept of misfit disclinations turns out to be efficient in describing defect structures of the crystal/crystal and crystal/glass interfaces. Indeed, creation of misfit disclinations at the junctions of crystal/crystal interfaces with (low- and high-angle) grain boundaries represents an efficient micromechanism of misfit stress relaxation, which must be taken into account when studying the structure and properties of crystal/crystal composite systems, particularly in single-crystal-film–polycrystalline (or nanocrystalline)-film. The above theoretical analysis shows also that misfit disclinations are inherent elements of crystal/glass interfaces. The existence of such disclinations is due to the presence of disclinations in the bulk of glass.

It should be pointed out that the above calculations of the characteristics of the crystal/crystal and crystal/glass interfaces are approximate and need refinement. At the same time the models developed here may serve as an efficient basis for a purposeful experimental investigation and subsequent, more detailed theoretical analysis of the interface structure.

The author is indebted to M. Yu. Gutkin, S. A. Kukushkin, and A. E. Romanov for fruitful discussions.

Partial support of the Russian Fund for Fundamental Research (Grant 98-02-16075), Office of the US Naval Research (''The Fundamentals of Nanostructured Interfaces of Hybrid Multilayer Coatings'' project), and of the Volkswagen Stiftung is gratefully acknowledged.

[1] Yu. A. Tkhorik and L. S. Khazan, *Plastic Deformation and Misfit Dislocations in Heteroepitaxial Systems* [in Russian] (Naukova Dumka, Kiev, 1983).

[2] V. M. Ievlev, L. I. Trusov, and V. A. Kholmyanskiĭ, *Structural Transformations in Thin Films* [in Russian] (Metallurgiya, Moscow, 1988).

[3] G. Möbus, E. Schumann, G. Dehm, and M. Rühle, Phys. Status Solidi A **150**, 77 (1995).

[4] S. C. Jain, A. H. Harker, and R. A. Cowley, Philos. Mag. A **75**, 1461 (1997).

[5] I. A. Ovid'ko, in *Nanostructured Materials: Science and Technology*, NATO ASI Ser., edited by G. M. Chow and N. I. Noskova (Kluwer, Dordrecht, 1998), p. 183.

[6] J. W. Matthews, J. Vac. Sci. Technol. **12**, 126 (1975).

[7] J. P. Hirth and J. Lothe, *Theory of Dislocations* (McGraw-Hill, New York, 1968; Atomizdat, Moscow, 1972).

[8] V. I. Vladimirov and A. E. Romanov, *Disclinations in Crystals* [in Russian] (Nauka, Leningrad, 1986).

[9] X. Pan, J. Am. Ceram. Soc. **79**, 2975 (1996).

[10] S. Veprek, M. Haussmann, and S. Reiprich, in *Metastable Phases and Microstructures*, MRS Symp. Proc. Vol. 400, edited by R. Bormann, G. Mazzone, R. D. Shull, R. S. Averback, and R. F. Ziolo (MRS, Pittsburg, 1996), p. 261.

[11] M. Yu. Gutkin and I. A. Ovid'ko, Nanostruct. Mater. **2**, 631 (1993).

[12] R. Benedictus, A. Böttger, and E. J. Mittemeijer, Phys. Rev. B **54**, 9109 (1996).

[13] T. Ninomiya, in *Topological Disorder in Condensed Matter*, edited by G. Toulouse (Springer, Berlin, 1983), p. 40.

[14] I. A. Ovid'ko, *Defects in Condensed Media: Glasses, Crystals, Quasicrystals, Liquid Crystals, and Superfluid Liquids* [in Russian] (Znanie, Leningrad, 1991).

[15] I. A. Ovid'ko, Metallofizika (Kiev) **11**(2), 35 (1989).

[16] N. Rivier, Adv. Phys. **36**(2), 95 (1987).

[17] N. Rivier, Philos. Mag. **40**, 859 (1979).

[18] J.-F. Sadoc and N. Rivier, Philos. Mag. B **55**, 537 (1987).

[19] M. Kléman and J.-F. Sadoc, J. Phys. (France) Lett. **40**, 569 (1979).

[20] D. R. Nelson, Phys. Rev. B **28**, 5515 (1983).

[21] M. Yu. Gutkin, I. A. Ovid'ko, and A. E. Romanov, Radiat. Eff. Defects Solids **129**, 239 (1994).

[22] E. Nold, S. Steeb, and P. Lamperter, Z. Naturwiss A **35**, 610 (1980).

[23] R. G. Morris, J. Appl. Phys. **50**, 3250 (1979).

[24] A. P. Sutton and R. W. Balluffi, *Interfaces in Crystalline Materials* (Clarendon Press, Oxford, 1995).

Translated by G. Skrebtsov

Distinctive features of the change in structural state and internal stresses present in shear bands of single-crystal zinc

M. E. Bosin

Khar'kov State Polytechnical University, 310002 Khar'kov, Ukraine

F. F. Lavrent'ev and V. N. Nikiforenko

Physicotechnical Institute of Low Temperature, Ukrainian Academy of Sciences, 310167 Khar'kov, Ukraine
(Submitted October 9, 1998; accepted February 12, 1999)
Fiz. Tverd. Tela (St. Petersburg) **41**, 1644–1646 (September 1999)

Transmission electron microscopy is used to study the dislocation structure of strained zinc crystals. It is shown that shear bands in this material consist of dipoles and individual dislocation loops. A connection is established between internal stresses and the corresponding dislocation structure of the shear band. © *1999 American Institute of Physics.* [S1063-7834(99)02209-1]

A problem of current interest to physicists who study hardness and plasticity is to identify the mechanisms responsible for shear-band formation and hardening in metals and alloys.[1–3] A necessary prerequisite for solving this problem is to investigate the dislocation structure of elementary local shears and how the magnitude of local internal stresses changes in various slip systems. Note that, despite the large number of studies of the structural state of deformed crystals,[3] a number of unresolved questions remain regarding identification of structural states and their and associated internal stresses. In this paper transmission electron microscopy (TEM) is used to study the dislocation structure and internal stresses in shear bands of deformed single-crystal zinc.

1. OBJECT AND METHODS OF INVESTIGATION

The crystals we studied were grown from single-crystal zinc with purity 99.997% by directed crystallization from a melt.[4] The samples were deformed by simple shear in the system $(0001)[11\bar{2}0]$. The TEM studies were made over the planes $(1\bar{1}00)$ and (0001). The samples used in transillumination electron-microscopy studies were cut by electroerosion into disks with diameter 3 mm and thickness 0.5 mm, whose central portions, after being thinned down electrochemically to a thickness of 1000 Å, were transparent to electrons with energies of 100 kV. Their dislocation structures were studied using IEM-100U and JEM-7A electron microscopes.

2. RESULTS AND DISCUSSION

TEM studies showed that the original structural state of these zinc crystals was characterized by a large number of dislocation loops with radii $r=0.3\ \mu$m. After deformation by simple shear in the system $(0001)[11\bar{2}0]$, basal slip bands formed. Figure 1, which shows a TEM pattern in the cross section of the plane $(1\bar{1}00)$, reveals that the basal slip macroband consists of fine basal slip lines with a line density along [0001] of $\rho_B=10^4\ \text{mm}^{-1}$. In this case, dipoles and basal dislocation loops can be seen in the (0001) planes with radii $r_0=0.14\ \mu$m. These are also easily seen in Fig. 2, where a TEM image is shown in the cross section of the plane (0001). From Fig. 1 it is clear that the dipoles are generated by edge basal dislocations with a height $h=4-60$ nm and length $0.13-1\ \mu$m. The distance between dipoles $L_d\sim 1\ \mu$m. In order to study the internal stresses in the basal slip system, we used the expression

$$\tau_0=\frac{\alpha Gb}{r_0}=17.4\ \text{MPa}, \tag{1}$$

where $\alpha=0.24$ is the coefficient of basal dislocation-dislocation interactions; $G=3.8\times10^4$ MPa is the shear modulus, $b=2.67\times10^{-10}$ m is the Burgers vector of the basal dislocations, and r_0 is the radius of curvature of the basal dislocations. The internal stress fields caused by the dipole structure are strongly compensated. In order to estimate the internal long-range stresses of the dipole structure we used the relation

$$\tau_G=\frac{Gbh}{2\pi L_d}=0.097\ \text{Pa}, \tag{2}$$

where $L_d=1\ \mu$m and $h=60$ nm. The small value of the quantity τ_G is due to the compensation of the dipole stress fields. In order to destroy the dipole structure we require a stress

$$\tau_c=\frac{Gb}{8\pi(1-\nu)h}=9.61\ \text{MPa}, \tag{3}$$

where $h=60$ nm and $\nu=0.3$ is the Poisson coefficient. Comparison of Eqs. (2) and (3) showed that the stress required to destroy the dipole structure is significantly larger than the internal stresses caused by the dipole structure. We note that, for basal slip, components of a shear stress appear in a pyramidal slip system, which leads to activation of pyramidal slip. The value of this stress can be estimated from the expression

$$\tau_p=\tau_b n\cos\varphi=4.7\ \text{MPa}, \tag{4}$$

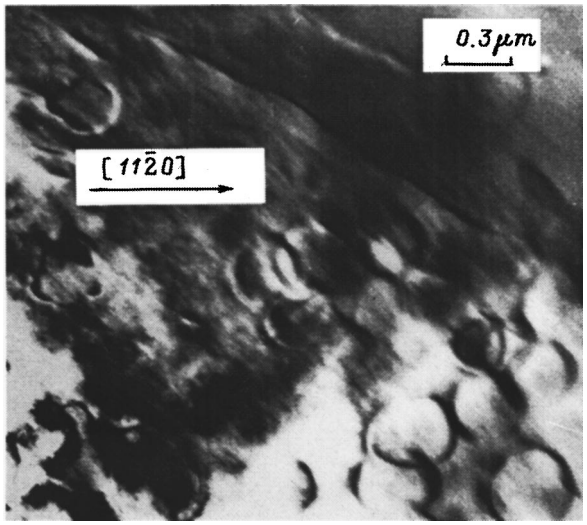

FIG. 1. TEM picture in $(1\bar{1}00)$ cross section of the dislocation structure after basal slip in zinc crystals of up to $\varepsilon = 10\%$.

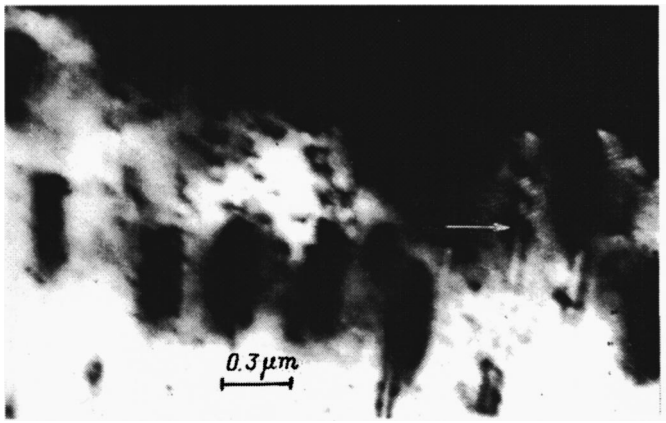

FIG. 3. TEM picture of pyramidal screw dislocations involving large local shears ($\varepsilon_L = 6 \cdot 10^3\%$) observed *in situ* in zinc crystals within the plane-(0001) cross section. The arrow indicates a point where of the screw components of the pyramidal dislocations bend around.

where $\tau_b = 1$ MPa is the applied shear stress in the basal slip system, $n = 10$ is the number of basal dislocations in the piled-ups, and $\varphi = 62°$ is the angle between planes (0001) and $(11\bar{2}2)$. The stress estimated in Eq. (4) is 5 times larger than the starting stress for motion of pyramidal dislocations. The presence of basal and pyramidal dislocations is due to ongoing reactions of type

$$\frac{1}{3}[2\bar{1}\bar{1}3]^{(\bar{2}112)}_{4.46} + \frac{1}{3}[2\bar{1}\bar{1}3]^{(2\bar{1}\bar{1}3)}_{4.46} \rightarrow \frac{2}{3}[2\bar{1}\bar{1}0]^{(0001)}_{4.00}. \quad (5)$$

The labels in the upper right show the planes in which the dislocations lie, while the labels in the lower right give the relative dislocation energies (the ratio of the square of the Burgers vector to the square of the lattice parameter).

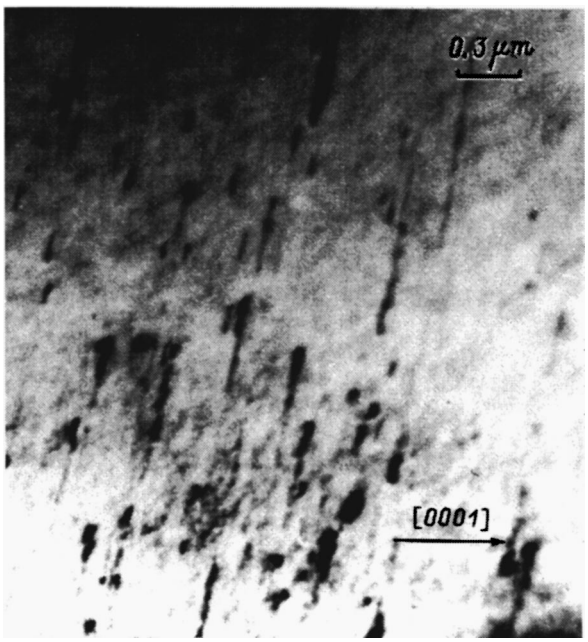

FIG. 2. TEM picture of the dislocation structure in the (0001) plane cross section of zinc crystals under strains of up to $\varepsilon = 10\%$.

Loops of prismatic dislocations corresponding to the reaction (5) are shown in Fig. 2. It is important to note that a prismatic dislocation is sessile, which gives rise to its considerable contribution to strain hardening of hcp metals. Figure 3 shows a TEM image of slip bands in the plane $(11\bar{2}2)$ observed in plane (0001). It is clear that pyramidal slip bands are located along the direction $[11\bar{2}0]$; within them we see bent screw components of the pyramidal dislocations, along whose radius of curvature we can estimate the internal stress τ_p. For pyramidal slip, $\alpha_p = 1$, $G_p = 4 \times 10^4$ MPa, $b_p = 5.6 \times 10^{-10}$ m is the Burgers vector of the pyramidal dislocation, and $r_p = 0.025\ \mu$m is the radius of curvature of the screw component of the pyramidal dislocations (estimated from Fig. 3). From all this we obtain $\tau_p = 896$ MPa. This large internal stress corresponds to a $6 \times 10^3\%$ strain, which is present in the sample shown in Fig. 3. This large value of shear strain is caused by the transformation of basal dislocations into pyramidal dislocations.

Thus, our TEM studies have enabled us to identify the characteristic structural states that form in various slip systems of strained single-crystal zinc. We have determined the characteristic structural elements of basal, prismatic, and pyramidal slip, and have estimated the value of internal stresses generated in these states.

The authors are grateful to I. Tretyak for assistance with the TEM experiments.

[1] B. I. Smirnov, Fiz. Tverd. Tela (St. Petersburg) **36**, 2037 (1994) [Phys. Solid State **36**, 1112 (1994)].
[2] A. Luft, Prog. Mater. Sci. **1**, 629 (1991).
[3] N. A. Tyapunina, G. V. Bushueva, and G. A. Zinenkova, *Physics of Crystals with Defects* [in Russian] (Moscow State Univ. Publ., Moscow, 1986), p. 239.
[4] Yu. G. Kazarov and F. F. Lavrentev, Cryst. Res. Technol. **18**, 107 (1983).

Translated by Frank J.Crowne

MAGNETISM AND FERROELECTRICITY

Magnetostriction in the vicinity of spin-reorientation phase transitions in single-crystal $DyFe_{11}Ti$

S. A. Nikitin,*) I. S. Tereshina, and N. Yu. Pankratov

M. V. Lomonosov Moscow State University, 119899 Moscow, Russia
(Submitted November 17, 1998)
Fiz. Tverd. Tela (St. Petersburg) **41**, 1647–1649 (September 1999)

The field, temperature, and angular dependences of longitudinal $\lambda_\parallel$ and transverse $\lambda_\perp$ magnetostriction in single-crystal $DyFe_{11}Ti$ are investigated. Tensometric measurements were made in the temperature range from 78 to 300 K in magnetic fields up to 12 kOe. Measurements of the magnetostriction of single-crystal $DyFe_{11}Ti$, $YFe_{11}Ti$, and $LuFe_{11}Ti$ imply that the sublattice of $3d$ transition metals makes only a small contribution to the magnetostriction in compounds $RFe_{11}Ti$, and that the primary contribution to the magnetostriction of these compounds comes from the rare-earth metal sublattice. The primary microscopic mechanism for magnetostriction is single-ion magnetostriction caused by the interaction of the anisotropic orbital electron cloud around the Dy^{3+} magnetic ion with the crystal field of the lattice. © *1999 American Institute of Physics.* [S1063-7834(99)02309-6]

In recent years, the phenomenon of spin reorientation has attracted the interest both of theoretical physicists, who seek to confirm the fundamental assumptions of their theoretical models,[1,2] and of experimental physicists looking for possible engineering applications of this phenomenon. In a previous paper[3] we investigated this phenomenon in single-crystal $DyFe_{11}Ti$ by measuring the angular and field dependences of the mechanical torque acting on a sample placed in a magnetic field. We showed for this compound that there are two spin-reorientation phase transitions: a second-order transition at $T_1 = 250$ K and a first-order transition at $T_2 = 122$ K. These data are in agreement with the results of Refs. 4 and 5.

New information regarding the nature of these transitions can be obtained by studying magnetoelastic effects. To this end, we have investigated magnetostriction in single crystals of $DyFe_{11}Ti$ near these spin-reorientation phase transitions by tensometric methods.

1. EXPERIMENTAL METHOD

The technology for obtaining single crystals and the method used to measure magnetostriction were described previously in Ref. 6. We measured the temperature, field, and angular dependences of the magnetostriction for single-crystal samples in the form of disks with diameter ~ 4 mm and thickness ~ 0.5 mm along the [001] and [100] crystallographic directions in magnetic fields up to 13 kOe within the temperature range 78–300 K. The absolute error of our magnetostriction measurements was 1×10^{-6}.

2. EXPERIMENTAL RESULTS AND DISCUSSION

Figure 1 shows temperature dependences of the longitudinal ($\lambda_\parallel > 0$) and transverse ($\lambda_\perp < 0$) magnetostrictions. A tensometer was glued to the surface of a disk parallel to the c axis. The magnetic field was applied parallel ($\lambda_\parallel$) and perpendicular ($\lambda_\perp$) to the **c** axis. From Fig. 1 it is clear that when the sample is heated in the temperature range 78–100 K, a rapid increase in $\lambda_\parallel(T)$ is observed. The maximum value of the magnetostriction is reached in the temperature range 100–140 K. This is the temperature range in which the spin-reorientation phase transition of first order is observed.[3–5] According to our data,[3] the angle $\mathbf{M}_s$ (i.e., the angle between the magnetic moment of the sample **c** and the c-axis) at $T_2 = 122$ K changes discontinuously from 90° to 45° (see the inset to Fig. 1). As the temperature is further increased, the angle θ varies smoothly and for $T_1 \geqslant 250$ K it becomes equal to zero. From Fig. 1 it is clear that the longitudinal magnetostriction in fields $\mathbf{H} \| \mathbf{c}$ is a maximum near

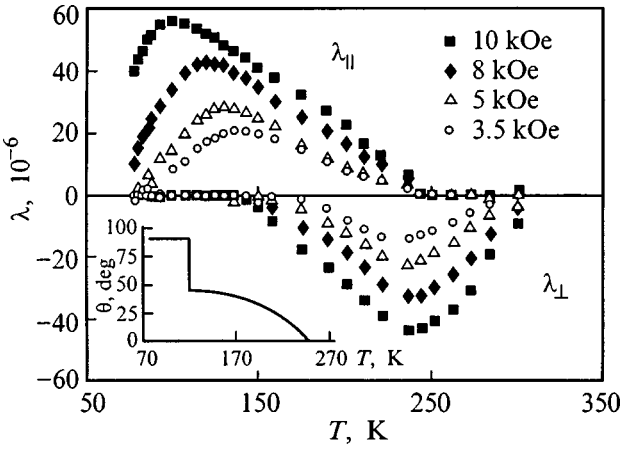

FIG. 1. Temperature dependence of the longitudinal $\lambda_\parallel$ and transverse $\lambda_\perp$ magnetostriction of single-crystal $DyFe_{11}Ti$ in various magnetic fields.

T_2. Here the effective magnetic anisotropy field is small, and an external magnetic field applied along the **c**-axis causes rotation of the magnetic moments out of the basal plane ($\theta = 90°$) in the direction of the magnetic field, which also leads to a strong increase in the magnetostriction. As the field increases, the maximum in the curve $\lambda_\parallel(T)$ shifts towards lower temperatures, probably because the transition temperature T_2 decreases with increasing field. From Fig. 1 it follows that in a field of 3.5 kOe $\lambda_\parallel$ is a maximum at 130 K, whereas in a field $H=10$ kOe this maximum is observed at $T\sim 100$ K. Heating the sample so that $T>T_2$ leads to a smooth falloff in $\lambda_\parallel$, which for all values of the applied field ends at a temperature $T_1=250$ K. In this temperature range the angle θ decreases smoothly (see the inset to Fig. 1) starting at a temperature $T_2=122$ K. At $T_1=250$ K, the angle θ becomes equal to zero, and $\lambda_\parallel$ has a very small value for $T>T_1$. The experimental data (Fig. 1) indicate a second-order phase transition near T_1, where the magnetic moments rotate smoothly in the direction of the **c** axis. Now, $\mathbf{M}_s \| \mathbf{c}$ when $T_1>250$ K; therefore, in fields $\mathbf{H}\|\mathbf{c}$, no torque-related processes can occur, and hence there is no noticeable contribution to the value of $\lambda_\parallel$.

In the temperature range 80–140 K there is practically no measureable transverse magnetostriction $\lambda_\perp$ along the **c** axis for fields $\mathbf{H}\|\mathbf{c}$ (see Fig. 1). Here a field directed along the axis of easy magnetization can induce only processes involving translation of domain boundaries of 180° domains. These processes do not contribute to the transverse magnetostriction, due to the even character of this effect. For $T>140$ K the magnetostriction $\lambda_\perp$ becomes negative. In this case the magnetic moment $\mathbf{M}_s$ leaves the basal plane and forms an angle $(\pi/2-\theta)$ with it. Under the action of a field $\mathbf{H}\perp\mathbf{c}$, $\mathbf{M}_s$ rotates in the direction of the basal plane, a consequence of which is the appearance of a rotational magnetostriction $\lambda_\perp$ that is sizeable in magnitude. It increases in absolute value for $T>140$ K, reaches a maximum in the region $T\sim 250$ K, and then decreases smoothly.

The spontaneous magnetostriction along the **c** axis (i.e., spontaneous magnetostriction-induced strain in the sample) of a crystal with a tetragonal crystal lattice can be calculated using the expression[7]

$$\lambda_c=\lambda_2^{\alpha,0}+\lambda_2^{\alpha,2}(\cos^2\theta-1/3), \tag{1}$$

where $\lambda_2^{\alpha,0}$ and $\lambda_2^{\alpha,2}$ are magnetostriction constants and θ is the angle the magnetic moment $\mathbf{M}_s$ makes with the tetragonal **c** axis. In fields $\mathbf{H}\|\mathbf{c}$ large enough to orient $\mathbf{M}_s$ along the **c** axis, the spontaneous magnetostriction becomes equal to

$$\lambda_c|_{\theta=0}=\lambda_2^{\alpha,0}+2/3\lambda_2^{\alpha,2}. \tag{2}$$

Consequently, the longitudinal magnetostriction induced by the field along the **c** axis caused by rotation processes will equal

$$\lambda_{\parallel c}=\lambda_c-\lambda_c|_{\theta=0}=-\lambda_2^{\alpha,2}(1-\cos^2\theta). \tag{3}$$

From Eq. (1) it also follows that during the rotational processes the transverse magnetostriction $\lambda_\perp$ measured along the **c**-axis in a field $\mathbf{H}\|\mathbf{c}$ equals

$$\lambda_{\perp c}=\lambda_c-\lambda_c|_{\theta=\pi/2}=\lambda_2^{\alpha,2}\cos^2\theta. \tag{4}$$

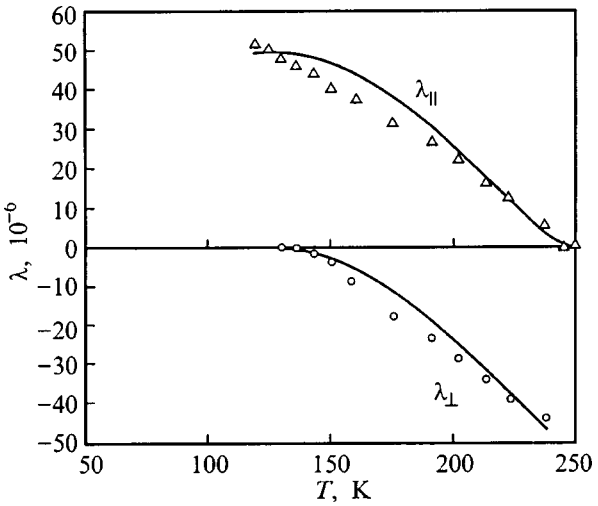

FIG. 2. Temperature dependence of the longitudinal $\lambda_\parallel$ and transverse $\lambda_\perp$ magnetostriction of single-crystal $DyFe_{11}Ti$ in a magnetic field $H=10$ kOe in the neighborhood of the spin-reorientation phase transition, and theoretical curves obtained from Eqs. (3) and (4).

Plots of the quantities $\lambda_{\parallel c}$ and $\lambda_{\perp c}$ obtained from the theoretical expressions (3) and (4) are shown in Fig. 2. The values of the angle θ were set equal to those we determined in our previous paper Ref. 3. It is clear that theory and experiment are in agreement, allowing us to conclude that magnetostriction in $DyFe_{11}Ti$ near the spin-reorientation phase transition is due to rotation of the magnetic moment under the action of the field. The value of the magnetostriction constant $\lambda_2^{\alpha,2}$ found from the dependences of $\lambda_{\parallel c}$ and $\lambda_{\perp c}$ on temperature and the angle θ equals $\lambda_2^{\alpha,2}\sim -1\times 10^{-4}$, which coincide with results presented in Ref. 5 where they were determined from thermal expansion.

Figure 3 shows the field dependences of the longitudinal magnetostriction $\lambda_\parallel(H)$ for the compound $DyFe_{11}Ti$. From Fig. 3 it is clear that at temperatures $T=78$ and 86 K there is no saturation of the isotherms of magnetostriction $\lambda_\parallel(H)$,

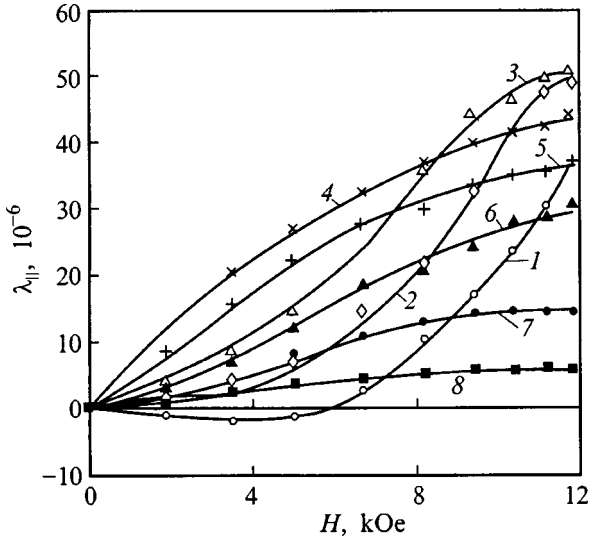

FIG. 3. Isotherms of the longitudinal magnetostriction $\lambda_\parallel$ in single-crystal $DyFe_{11}Ti$. *T*, K: *1* — 78, *2* — 86, *3* — 100, *4* — 143, *5* — 158, *6* — 190, *7* — 221, *8* — 236.

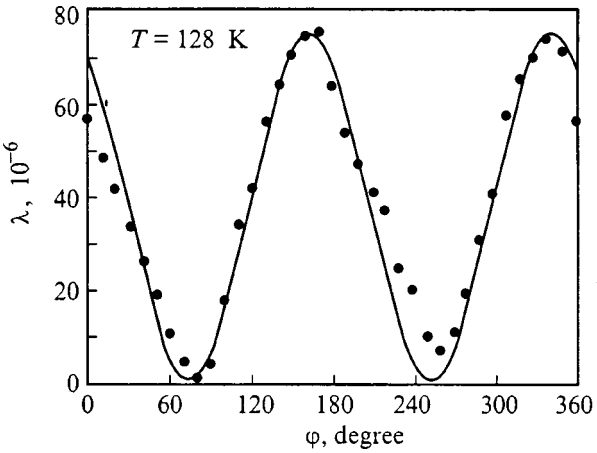

FIG. 4. Angular dependence of magnetostriction in a $DyFe_{11}Ti$ single crystal in the (100) plane at $T=128$ K, measured in a magnetic field $\mathbf{H}=11$ kOe (black dots), and a theoretical curve obtained from Eq. (5).

which indicates a large value of the magnetic anisotropy. Furthermore, when $T>120$ K the $\lambda_{\parallel}(H)$ curves exhibit a tendency to saturate in the neighborhood of the spin-reorientation phase transition, where the value of the effective magnetic anisotropy field decreases. Also noteworthy is the existence of a threshold field $H_{\rm thr}$, starting with which $\lambda_{\parallel}(H)$ increases rapidly in the temperature range 78–100 K, since for $H>H_{\rm thr}$ the magnetic moment $\mathbf{M}_s$ of the compound begins to deviate towards the **c** axis. It is clear from Fig. 3 that the higher the temperature, the smaller the value of the threshold field.

When we investigated the angular dependences of the magnetostriction $\lambda(\varphi)$, where φ is the angle between the direction of measurement of the magnetostriction (the detector was glued parallel to the *c*-axis) and the direction of the external magnetic field, we found that all the curves have a period equal to π. However, the shape of the curves undergoes a considerable transformation as the temperature and field are varied. Figure 4 shows the curve $\lambda(\varphi)$ measured at a temperature $T=128$ K in a field $H=11$ kOe. From the figure it is clear that for all values of the angle φ the magnetostriction $\lambda(\varphi)$ is positive. As the temperature increases, as our experiments show, the curves shift smoothly downward, and for $T>250$ K their values are negative almost everywhere, which correlates very well with the functions $\lambda_{\parallel}(T)$ and $\lambda_{\perp}(T)$. The angular dependence of the magnetostriction $\lambda(\varphi)$ measured along the **c** axis can be described by the following expression:

$$\lambda_c(\varphi)=\lambda_2^{\alpha,2}\cos^2\varphi+\lambda_T(T), \tag{5}$$

where $\lambda_T(T)$ is a quantity that depends on temperature and which takes into account the magnetostriction-induced strain due to thermal expansion and the domain structure.

According to literature data,[8,9] the compound $DyFe_{11}Ti$ can be viewed as a two-sublattice magnet: in this case, both sublattices, i.e., the rare-earth metal sublattice and the $3d$ transition metal sublattice, contribute to the magnetostriction. We have measured the longitudinal $\lambda_{\parallel}(T,H)$ and transverse $\lambda_{\perp}(T,H)$ magnetostrictions of single crystals of $YFe_{11}Ti$ and $LuFe_{11}Ti$. The ions of yttrium and lutetium do not have magnetic moments; therefore, the results obtained allow us to study the magnetostriction due only to the $3d$ transition metal sublattice. We have found that the magnetostriction λ for the compounds $YFe_{11}Ti$ and $LuFe_{11}Ti$ is an order of magnitude smaller than its value for $DyFe_{11}Ti$. Consequently, the iron sublattice gives a negligibly small contribution to magnetostriction in $RFe_{11}Ti$ compounds. From this we may conclude that the magnetostriction in the neighborhood of spin reorientation in $DyFe_{11}Ti$ single crystals is actually due to rotation of the magnetic moment of the rare-earth metal sublattice. The primary microscopic mechanism for magnetostriction is probably single-ion magnetostriction caused by the interaction of the anisotropic orbital electron cloud of the magnetic Dy^{3+} ion with the crystal field of the lattice.[7,10] Analogous results were obtained in Refs. 11 and 12 for a single-crystal $TbFe_{11}Ti$.

Thus, our experimental results indicate that the spin-reorientation phase transitions and processes involving rotation of the magnetic moment strongly influence the temperature, field, and angular dependences of magnetostriction in single crystals of $DyFe_{11}Ti$.

This work was funded by a federal program for the support of science education schools (Grant No. 96-15-96429) and a grant from the Russian Fund for Fundamental Research (No. 96-02-18271).

*)E-mail: nikitin@rem.phys.msu.su

[1] A. A. Kazakov and N. V. Kudrevatykh, J. Alloys Compd. **191**, 67 (1993).
[2] M. D. Kuz'min, Phys. Rev. B **46**, 8219 (1992).
[3] I. S. Tereshina, I. V. Telegina, and K. P. Skokov, Fiz. Tverd. Tela (St. Petersburg) **40**(4), 699 (1998) [Phys. Solid State **40**, 643 (1998)].
[4] B.-P. Hu, H.-S. Li, J. M. D. Coey, and J. P. Gavigan, Phys. Rev. B **41**, 2221 (1990).
[5] A. V. Andreev, M. I. Bartashevich, N. V. Kudrevatykh, S. M. Razgonyaev, S. S. Sigaev, and E. N. Tarasov, Physica B **167**, 139 (1990).
[6] V. Yu. Bodriakov, T. I. Ivanova, S. A. Nikitin, and I. S. Tereshina, J. Alloys Compd. **259**, 265 (1997).
[7] S. A. Nikitin, *Magnetic Properties of Rare-Earth Metals and Their Alloys* [in Russian] (Moscow State Univ. Publ., Moscow, 1989).
[8] X. C. Kou, T. S. Zhao, R. Grossinger, H. R. Kirchmayr, X. Li, and F. R. de Boer, Phys. Rev. B **47**, 3231 (1993).
[9] K. Yu. Guslienko, X. C. Kou, and R. J. Grossinger, J. Magn. Magn. Mater. **150**, 383 (1995).
[10] K. P. Belov, *Magnetostriction Phenomena and Their Engineering Applications* [in Russian] (Nauka, Moscow, 1987).
[11] A. A. Kazakov, N. V. Kudrevatykh, and P. E. Markin, J. Magn. Magn. Mater. **146**, 208 (1995).
[12] S. A. Nikitin, T. I. Ivanova, and I. S. Tereshina, Neorg. Mater. **34**, 1 (1998).

Translated by Frank J. Crowne

Investigation of the magnetic properties of chains with alternating ferro- and antiferromagnetic exchange interactions in the Heisenberg model with spin $S=1/2$

S. S. Aplesnin and G. A. Petrakovskiĭ

L. V. Kirenskiĭ Institute of Physics, Siberian Branch, Russian Academy of Sciences, 660036 Krasnoyarsk, Russia

(Submitted December 8, 1998)
Fiz. Tverd. Tela (St. Petersburg) **41**, 1650-1651 (September 1999)

The quantum Monte Carlo method is used to calculate the susceptibility and pairwise spin-spin correlation functions of chains with alternating ferro (K)- and antiferromagnetic (J)-exchange interactions within the Heisenberg model with spin $S=1/2$. From the susceptibility, the energy gap between the ground state and excited triplet states is determined for arbitrary ratios K/J. The value of the gap coincides with the Haldane gap for spin $S=1$ when $K/J>1.25$.
 [S1063-7834(99)02409-0]

The magnetic properties of one-dimensional antiferromagnetic chains are of interest both from an experimental[1,2] and from a theoretical point of view.[3] A question of fundamental interest is Haldane's hypothesis[4] regarding the qualitative difference between the ground states of antiferromagnets having integer and half-integer values of the spin: for half-integer spins there exist gapless magnetic excitations,[4] while for integer spins there is a gap in the excitation spectrum,[5,6] which was later observed experimentally.[7] For $S=1$ spins, values of the gap $g=0.41049$ and correlation radius $\xi=6.2$ have been determined by various methods: analytically, using perturbation theory,[8] by Monte Carlo,[9] and by exact diagonalization for small chains.[10]

Let us consider an antiferromagnetic chain consisting of coupled dimers. Then we can obtain a Haldane gap by alternating ferro- and antiferromagnetic interactions on a chain of spins with $S=1/2$. In the limit of strong ferromagnetic coupling ($K\to\infty$), the dimers are in the lowest triplet state, and the chain of spins with $S=1/2$ can be reduced to an effective antiferromagnetic chain with spins $S=1$. In the other limiting case ($K\to 0$), a gas of antiferromagnetic dimers is realized which also exhibits an energy gap between the singlet and triplet state, equal to the value of the antiferromagnetic exchange.

The question of magnetic behavior of chains and the value of the gap for arbitrary ratios of the exchange constants K/J remains open. In this paper we solve the problem as formulated by the quantum Monte Carlo method in the Heisenberg model with spin $S=1/2$. The Hamiltonian has the form

$$H=-2J\sum_{i=1}^{N/2} S_{2i-1}S_{2i}-2K\sum_{i=1}^{N/2} S_{2i}S_{2i+1}-h\sum_{i=1}^{N} S_i,$$

where $J<0$, $K>0$ are the ferro- and antiferromagnetic interactions respectively, N is the number of spins in the chain, and h is an external magnetic field.

A detailed description of the quantum Monte Carlo method, using the Trotter equation and corresponding expressions for computing the susceptibility, heat capacity, and pairwise spin-spin correlation functions, was presented in a previous paper.[11] In our Monte Carlo calculations, periodic boundary conditions were used along the Trotter direction (m) and along the chain. The number of spins in a chain was $L=200$, with $m=16$, 32, and 64. The number of Monte Carlo steps for one spin varied from $M=6000$ to 20000. One step was determined by the rotation of all the spins on a lattice of size $L\times 2m$. The mean-square errors for the energy and susceptibility were ~ 1 and $\sim 6\%$ respectively. The systematic error arising from the finite Trotter number, which takes into account the noncommutative nature of the operators, was proportional to $\sim 1/(mT)^2$.

The heat capacity, susceptibility, and spin correlation functions for an isotropic antiferromagnetic chain are in good agreement with known exact calculations and were given in Ref. 11. The magnetic susceptibility of a chain with alternating exchange interactions equals zero as $T\to 0$. Figure 1 shows the temperature dependence of the susceptibility for certain values of the ratio of exchange constants K/J and Trotter numbers. As the ferromagnetic coupling increases, the maximum in the susceptibility increases as well, and at low temperatures $T/J<1$ it is well described by the relation $\chi(T)=A\exp(-g/T)$, where g is the value of the gap between the ground and excited triplet states. The inset to Fig. 1 shows the susceptibility plotted on a logarithmic scale versus the inverse value of the temperature for various values of m. It is clear from Fig. 1 that quantum effects are correctly taken into account for these Trotter numbers, and within the limits of error for the susceptibility they are well described by a linear dependence.

The magnitude of the energy gap decreases with increasing ferromagnetic exchange, and for $K/J>1.25$ it is practically independent of the value of K (Fig. 2). It is probably the computed value of K for ferromagnetic coupling that is critical. Thus, the spin-spin correlation functions between nearest neighbors and next-to-nearest neighbors is negative for the whole temperature range when $K/J<1.25$, while for $K/J>1.25$ there is a certain temperature at which $\langle S^z(0)S^z(r=1)\rangle$ changes sign from negative to positive, as shown in Fig. 3. Probably this is caused by removing the

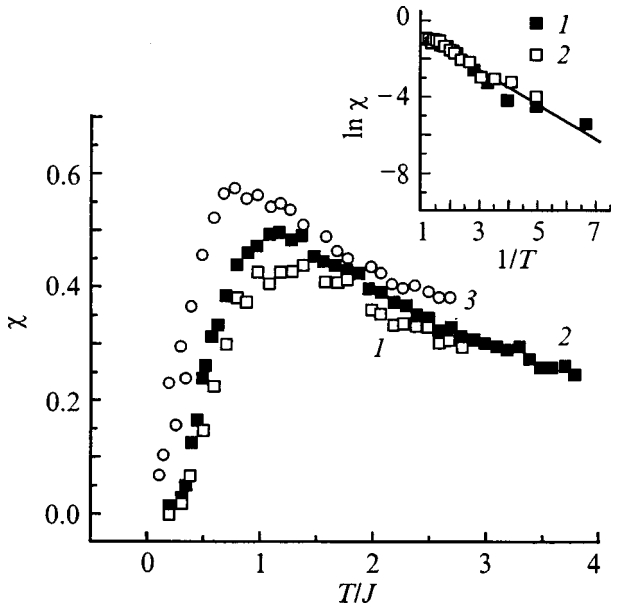

FIG. 1. Temperature dependence of the magnetic susceptibility of a chain with alternating ferro- and antiferromagnetic exchange constants when $K/J=-0.25$ (*1*), 1 (*2*), 3 (*3*). The inset shows the logarithm of the susceptibility plotted versus $1/T$ for $K/J=1$, $m=64$ (*1*), 32 (*2*).

degeneracy between the three multiplets of the ferromagnetic dimer with $S^z=\pm 1$ and 0, due to the antiferromagnetic interaction between them. With increasing J/K, the splitting between these multiplets increases. Thus, a one-dimensional

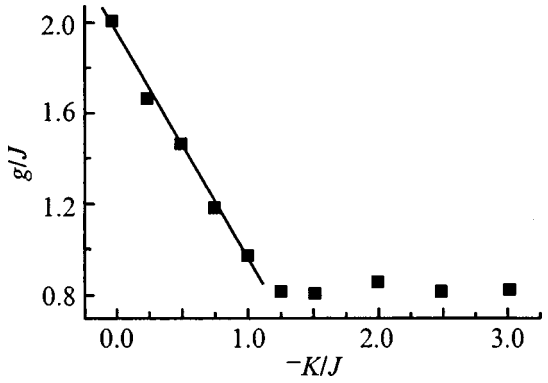

FIG. 2. Dependence of the energy gap between the ground and excited triplet states on the ratio of exchange constants K/J.

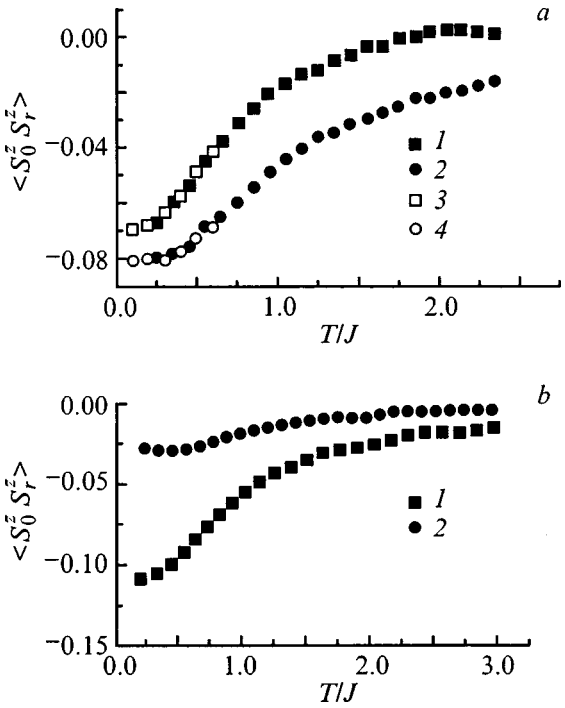

FIG. 3. Temperature dependence of the spin-spin correlation function for $K/J=-2$ (a), -0.5 (b), at distances $r/a=1$ (*1,3*), $r/a=2$ (*2,4*), $m=32$ (*1,2*), $m=64$ (*3,4*).

chain with alternating ferro- and antiferromagnetic exchanges has a gap in the energy of spin triplet excitations, whose value does not depend on the value of the ferromagnetic exchange for $K/J>1.25$, and equals the value of the Haldane gap when $S=1$.

[1] Manaka Hirotaka and Yamada Isao, J. Phys. Soc. Jpn. **66**, 1908 (1997).
[2] N. Motoyama, H. Eisaki, and S. Uchida, Phys. Rev. Lett. **76**, 3212 (1996).
[3] J. C. Bonner and M. E. Fisher, Phys. Rev. **135**, 640 (1964).
[4] F. D. M. Haldane, Phys. Rev. Lett. **50**, 1153 (1983).
[5] S. Yamamoto and S. Miyashita, Phys. Rev. B **48**, 9528 (1993).
[6] U. Schollwock and T. Jolicoeur, Europhys. Lett. **30**, 493 (1995).
[7] J. P. Renard, M. Verdaguer, and L. P. Regnault, J. Appl. Phys. **63**, 3538 (1988).
[8] D. V. Khveshchenko and A. V. Chubukov, Zh. Éksp. Teor. Fiz. **93**, 1088 (1987) [Sov. Phys. JETP **66**, 613 (1987)].
[9] M. P. Nightingale and H. W. J. Blote, Phys. Rev. B **33**, 659 (1986).
[10] O. Golinelli, T. Jolicoeru, and R. Lacore, Phys. Rev. B **50**, 3037 (1994).
[11] S. S. Aplesnin, Fiz. Tverd. Tela (St. Petersburg) **38**, 1868 (1996) [Phys. Solid State **38**, 1031 (1996)].

Translated by Frank J. Crowne

Parametric excitation of spin waves in strongly anisotropic uniaxial ferrites

A. G. Gurevich, A. V. Nazarov, and O. A. Chivileva

A. F. Ioffe Physicotechnical Institute, Russian Academy of Sciences, 194021 St. Petersburg, Russia

V. V. Petrov

Research Institute DOMAIN, 196084 St. Petersburg, Russia
(Submitted January 15, 1999)
Fiz. Tverd. Tela (St. Petersburg) **41**, 1652–1659 (September 1999)

The thresholds of parametric spin-wave excitation are measured in a $Ba_2Zn_2Fe_{12}O_{22}$ easy-plane ferrite at a pumping frequency of 36 GHz in the temperature range from 5 to 350 K at different angles between the external dc magnetic field and the anisotropy axis, where the pumping is, in a general case, oblique. The dependences of the spin-wave damping parameter on wave number, temperature, and the angle between the spin-wave propagation direction and the anisotropy axis have been found. The results of measuring the ferromagnetic resonance parameters in this ferrite and an easy-axis $Ba(Fe_{0.95}Sc_{0.05})_{12}O_{19}$ ferrite are presented. Conclusions on the relaxation processes in strongly anisotropic hexagonal ferrites are made. © *1999 American Institute of Physics.* [S1063-7834(99)02509-5]

The smallest uniform ferromagnetic-resonance linewidths ΔH_0 achieved presently in strongly anisotropic hexaferrites (they may be considered uniaxial with a fairly good accuracy) are a few tens of Oe. At the same time these substances are of considerable interest, including their possible potential application as promising magnetic materials for use in the short-wavelength part of the microwave range. It is the small ΔH_0 that is their most attractive characteristic. To achieve it, one has to understand the specific features of relaxation in these substances.

In experimental investigation of relaxation processes in ferrites one traditionally makes use of parametric spin-wave excitation, specifically under longitudinal pumping (with an ac magnetic field parallel to constant magnetization).[1] The theory of such excitation of spin waves in uniaxial ferrites was developed in Ref. 2. According to this theory, the spin waves excited in first-order processes (i.e., with the spin-wave frequency $\omega_k=\omega/2$, where ω is the pump frequency) in an external dc magnetic field H_{e0} less than the critical field H_c have a wave number

$$k=\sqrt{(H_c-H_{e0})/\eta}, \tag{1}$$

and propagate at an angle $\theta_k=90°$ to the direction of constant magnetization $\mathbf{M}_0$ (η is the nonuniform-exchange constant). For $H_{e0}>H_c$, theory[2] predicts excitation of waves with $k\to 0$ and $\theta_k<90°$.

The critical field H_c in uniaxial ferrites can be written[2]

$$H_c=-\frac{1}{2}(4\pi M_0+|2H_A|) + \sqrt{\left(\frac{\omega}{2\gamma}\right)^2+\frac{1}{4}(4\pi M_0+|2H_A|)^2}, \tag{2}$$

and the threshold amplitude of the ac magnetic field h for $H_{e0}<H_c$, where $\theta_k=90°$,

$$h_{\text{thr}}=\min\left\{\frac{\omega\Delta H_k}{\omega_M+\gamma|2H_A|}\right\}. \tag{3}$$

Here ΔH_k is the spin-wave damping parameter (the width of the resonance curve), $\omega_M=4\pi\gamma M_0$, and $H_A=K_1/M_0$ is the anisotropy field (K_1 is the anisotropy constant).

The theory of Ref. 2 was based on the assumption that the magnetization $\mathbf{M}_0$ is parallel to $\mathbf{H}_{e0}$, and, hence, that the ac magnetic field parallel to $\mathbf{H}_{e0}$ is parallel also to $\mathbf{M}_0$. For easy-axis ferrites this assumption is valid (see, e.g., Ref. 3) if $\mathbf{H}_{e0}$ is aligned with the easy axis or, for fields in excess of the anisotropy field, lies in the hard plane. For easy-plane ferrites it is met if $\mathbf{H}_{e0}$ lies in the easy plane or, for a field exceeding the anisotropy field, is along the hard axis; in the latter case, however, the field direction is very critical. For an arbitrarily oriented external dc field $\mathbf{H}_{e0}$, the constant magnetization is not parallel to $\mathbf{H}_{e0}$, and in these conditions the pumping is oblique even for the ac field $\mathbf{h}$ parallel to $\mathbf{H}_{e0}$, and parametric excitation occurs under combined action of the ac field parallel to $\mathbf{M}_0$ and uniform-precession magnons. Such excitation was studied for isotropic and weakly anisotropic cubic ferrites.[4,5]

Oblique pumping is of particular interest for strongly anisotropic ferrites, because purely longitudinal pumping under an arbitrarily oriented dc field is very difficult to achieve in such materials. Parametric spin-wave excitation in strongly anisotropic uniaxial ferrites under oblique pumping was treated theoretically in Ref. 6.

Parametric excitation of spin waves was used in experimental studies (see, e.g., Refs. 7 and 8) of relaxation in easy-plane uniaxial ferrites, but only in the case of an external dc field lying in the easy plane, the conditions in which the pumping was purely longitudinal.

The main objective of this work was an experimental investigation of relaxation processes in strongly anisotropic

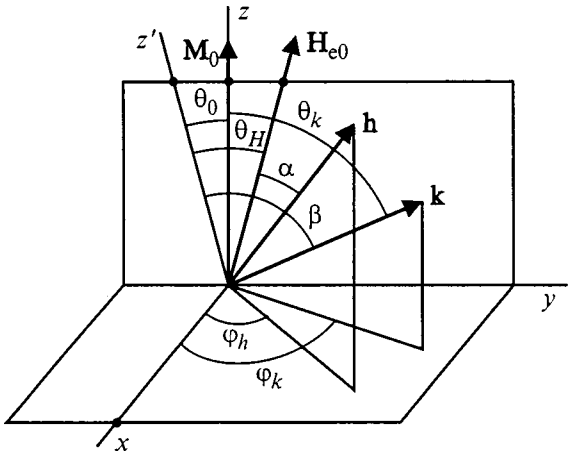

FIG. 1. Coordinate frame axes and angles.

uniaxial ferrites through parametric excitation of spin waves under oblique pumping.

1. PARAMETRIC EXCITATION OF SPIN WAVES IN UNIAXIAL FERRITES: CALCULATIONS

We are presenting here the results of calculations based on the theory of Ref. 6, which will be used subsequently for interpretation of experimental data. We consider parametric excitation of first-order spin waves in a sphere of a nonconducting uniaxial ferromagnet with easy axis ($K_1>0$) or easy plane ($K_1<0$), for an arbitrary orientation of the external dc magnetic field $\mathbf{H}_{e0}$ with respect to the anisotropy axis, and an arbitrary angle between $\mathbf{H}_{e0}$ and an ac linearly polarized magnetic field $\mathbf{h}$ of frequency ω (Fig. 1). The direction of constant magnetization $\mathbf{M}_0$ is determined by the condition of equilibrium, and the threshold ac field amplitude $h_{\rm thr}$ is found by solving the Landau–Lifshits equation taking into account the effective anisotropy field. One obtains finally the following expression

$$h_{\rm thr}=\min\left\{\frac{\omega_k\Delta H_k}{\omega_M|W_k|}\right\}. \tag{4}$$

Here

$$W_k=\frac{1}{4}(A_k+\xi_a+\omega_k)\left[2\exp(i\varphi_k)\sin 2\theta_k+\frac{iN_{23}^a}{\pi}\right]\tau_{01}$$
$$+\frac{1}{4}(A_k+\xi_a-\omega_k)\frac{[B_k\exp(2i\varphi_k)-\eta_a]^2}{|B_k\exp(2i\varphi_k)-\eta_a|^2}$$
$$\times\left[2\exp(-i\varphi_k)\sin 2\theta_k-\frac{iN_{23}^a}{\pi}\right]\tau_{02}+[B_k$$
$$\times\exp(2i\varphi_k)-\eta_a]\left[\frac{\cos\theta_h}{\omega_M}-\frac{\tau_{01}}{2}\exp(-i\varphi_k)\sin 2\theta_2\right.$$
$$\left.-\frac{\tau_{02}}{2}\exp(i\varphi_k)\sin 2\theta_k+\frac{i}{2\pi}(\tau_{01}-\tau_{02})N_{23}^a\right], \tag{5}$$

ω_k is the spin-wave frequency (which is equal to $\omega/2$ for first-order processes):

$$\omega_k^2=(A_k+\xi_a)^2-|B_k\exp(2i\varphi_k)-\eta_a|^2, \tag{6}$$

and the expressions for the quantities entering Eqs. (5) and (6) have the following form

$$A_k=\omega_H-\frac{\omega_M}{3}+\eta k^2+\frac{\omega_M}{2}\sin^2\theta_k, \quad B_k=\frac{\omega_M}{2}\sin^2\theta_k,$$

$$\omega_H=\gamma H_{e0}\cos(\theta_H-\theta_0), \quad \xi_a=\frac{\omega_M}{8\pi}(N_{22}^a-2N_{23}^a),$$

$$\eta_a=\frac{\omega_M}{8\pi}N_{22}^a,$$

$$\tau_{01,02}\frac{\sin\theta_h}{2\sqrt{2\omega_a}}\left[\frac{\sqrt{\omega_a+\omega_1}}{\omega_a\mp\omega}\exp(i\psi_h)-\frac{\sqrt{\omega_1-\omega_a}}{\omega_a\pm\omega}\exp(-i\psi_h)\right],$$

$$\omega_a=\sqrt{\omega_1^2-\eta_a^2}, \quad \omega_1=\omega_H+\xi_a, \quad \tan\psi_h=\frac{h_y}{h_x}\frac{\omega_1+\eta_a}{\omega_a}.$$

Here θ_k and φ_k are the polar and azimuthal angles of the spin-wave wave vector, θ_h and φ_h are the angles of the $\mathbf{h}$ vector, and θ_H is the angle between the external field $\mathbf{H}_{e0}$ and the anisotropy axis.

The spin-wave dispersion law (6) and the relation $\omega_k=\omega/2$ permit one to obtain the boundaries of the regions of ω, H_{e0}, and of the angle θ_H within which first-order parametric excitation is possible. The lower frequency boundaries of the ω, H_{e0}, and θ_H regions are derived from the condition

$$\omega_k(H_{e0},\ \theta_H,\ k=0,\ \theta_k=0)=\omega/2. \tag{7}$$

Figure 2 shows these boundaries for the two crystals studied in this work. One readily sees that a first-order process at a frequency of 36 GHz is possible in an easy-axis crystal only within a narrow interval of θ_H angles close to the hard axis, and in an easy-plane crystal it can be realized for any θ_H angle.

The values of h_{thr} and the parameters of the excited spin waves should be found by minimizing Eq. (4). Note that the ΔH_k quantity cannot be considered constant; it certainly depends on k and the orientation of the $\mathbf{k}$ vector relative to $\mathbf{M}_0$ (i.e., on the angles θ_k and φ_k) and to the anisotropy axes. These dependences are not known *a priori*. They can be found from an experiment by measuring h_{thr} as a function of H_{e0} and θ_H. However when analyzing these experiments, one should use the results of the minimization. This makes the problem self consistent and extremely complex.

As a first approximation, we carried out minimization for a constant ΔH_k, i.e. we minimized the $h_{thr}/\Delta H_k$ ratio with respect to two of the k, θ_k, and φ_k parameters coupled through the relation (7).

For each value of H_{e0} and θ_H, the angles θ_k and φ_k were varied with a step of 0.5°, and one looked for the minimum values of h_{thr} and the corresponding values of k, θ_k, and φ_k. Figure 3 displays the results of such a minimization for an easy-plane crystal in the case where the angle α between the ac field $\mathbf{h}$ and the external dc field $\mathbf{H}_{e0}$ (Fig. 1) is 0°. It is this case of ''quasi-longitudinal'' pumping that was realized in the experiment.

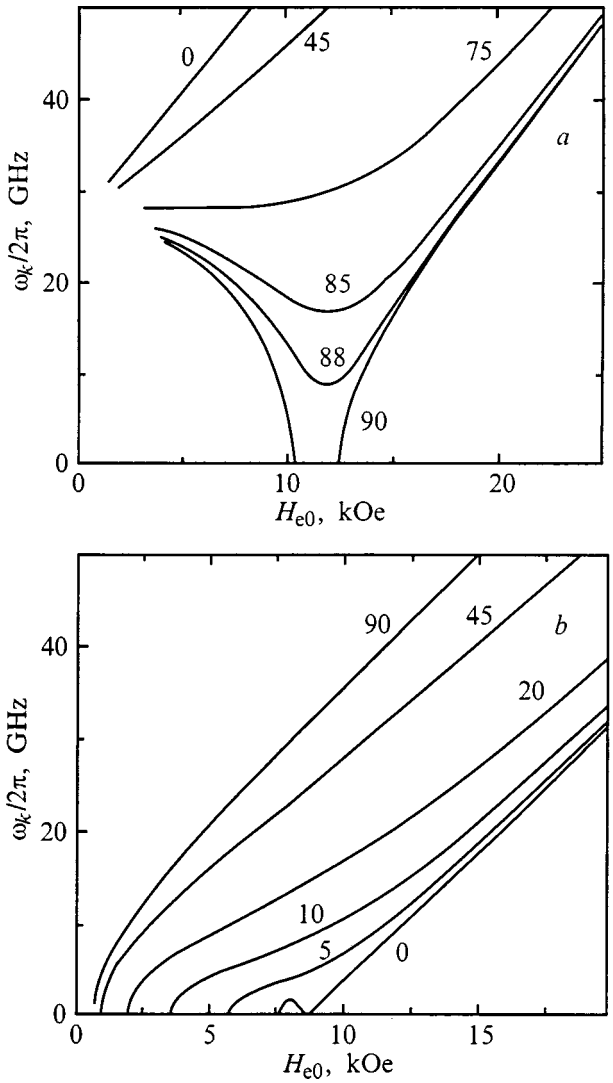

FIG. 2. Spectra of spin waves with $k=0$ and θ_k in (a) easy-axis and (b) easy-plane uniaxial ferrites. The values of $2H_A$ and M_0 are chosen equal to those for the crystals studied experimentally in this work (see Table I). The numbers adjoining the curves are θ_H angles in degrees.

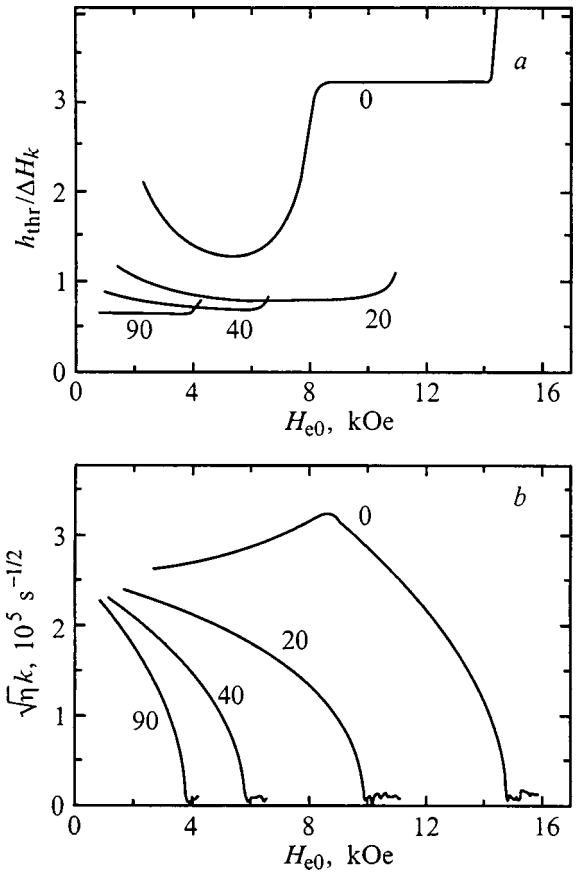

FIG. 3. Calculated dependences of (a) the threshold amplitude of the ac magnetic field (in units of the spin-wave damping parameter) and (b) the wave number of spin waves excited in Zn_2Y on the magnitude and direction of the external dc magnetic field. The numbers adjoining the curves are θ_H angles in degrees.

2. SAMPLES

The samples used in the study were $Zn_2Ba_2Fe_{12}O_{22}$ (Zn_2Y) easy-plane and $Ba(Fe_{0.95}Sc_{0.05})_{12}O_{19}$ easy-axis single-crystal hexaferrites (scandium was added to reduce the anisotropy constant). All crystals were doped slightly with Mn (~ 0.25 wt. %) to reduce the number of Fe^{2+} ions which lead to a growth of magnetic losses.[9]

The crystals were grown by crystallization from a melt solution.[10] A boron–barium solvent was used. The seed crystals were mounted on a rotating holder, which permitted one to increase the growth rate and obtain fairly large (up to 20 mm) and well-faceted crystals. The melt was heated to a temperature slightly in excess of the saturation point and maintained at this temperature for 10 hours, after which the temperature was reduced by a prescribed program with a gradient of 1–3 K/cm.

Spherical samples were prepared in the following way.[10] The crystals were cut into cubic blanks, of which spheres with a diameter of 0.5–0.8 mm were fabricated by turning between two abrasive tools. They were subsequently rough ground with successively finer grit abrasives and polished in the same way with the grit size reduced from 14 to 1 μm.

The Zn_2Y spheres were oriented with the use of x-ray diffraction technique. The $Ba(Fe_{0.95}Sc_{0.05})_{12}O_{19}$ samples, which, from x-ray diffraction data, had a mosaic structure with the angles between the block axes of $\sim 0.5°$, were oriented by a magnetic method.[11] Next the samples were pasted onto quartz-tube or beryllium-oxide rod holders, whose axis (x axis in Fig. 1) was perpendicular to the anisotropy axis, and around it the samples were rotated in the measurements. The accuracy of orientation (after the pasting) and of setting the sample rotation angle were not worse than 1°.

The sample parameters were measured by the microwave techniques (see Sections 3 and 4) and are presented in Table I.

3. MEASUREMENT TECHNIQUES

The experimental scheme is shown in Fig. 4. As generator *3* a magnetron[1)] was used, which could be tuned within the range of 36 GHz $\pm$ 2% and produced 200 W in cw (under proper cooling) or pulsed regime. 3.5-kV negative voltage pulses 20 μs long were applied to the magnetron with a repetition frequency of 40 Hz from the modulator

TABLE I. Parameters of the ferrites studied.

Composition	$4\pi M_0$, G	$2H_A$, kOe	T_C, °C
$Ba_2Zn_2Fe_{12}O_{22}$	2500	−8.6	104
$Ba(Fe_{0.95}Sc_{0.05})_{12}O_{19}$	4500	11	445

Note: The crystals contained ~0.25 wt. % Mn. The values of $4\pi M_0$ and $2H_A$ are for room temperature.

capacitor *2*. For such a pulse duration, one could neglect the voltage variation at the magnetron during the pulse while at the same time disregarding the error caused by a finite time of growth of the parametric spin waves.[13]

The microwave power was fed through valve *4*, precision polarizing attenuator *6*, and circulator *8* (with decoupling of ~40 dB) into cryostat *10* or, when measuring the incident power, into a thermistor-based power meter *11*. The measuring cell of the cryostat was a rectangular TE_{102} cavity *13* coupled to the waveguide through a hole. The coupling was adjusted by means of piston *15*, which for the time of measurements was placed outside the cryostat. The cavity was not readjusted, and the tuning was effected by varying properly the magnetron frequency. The cryostat design permitted one to rotate the cavity with the sample through 90° with respect to the dc magnetic field direction and turn the sample around the cryostat axis from the outside during the measurements. The power reflected from the sample-containing cavity was fed into crystal detector *17* via circulator *8* and polarizing attenuator *16*. The pulse envelope was visualized on oscillograph *18*.

The frequency was measured roughly with a resonant wavemeter *9*, and precisely, with a Ch5-13 frequency meter *19*. The dc magnetic field was generated by electromagnet *20* (with a pole piece diameter of 80 mm and a gap of 20 mm)

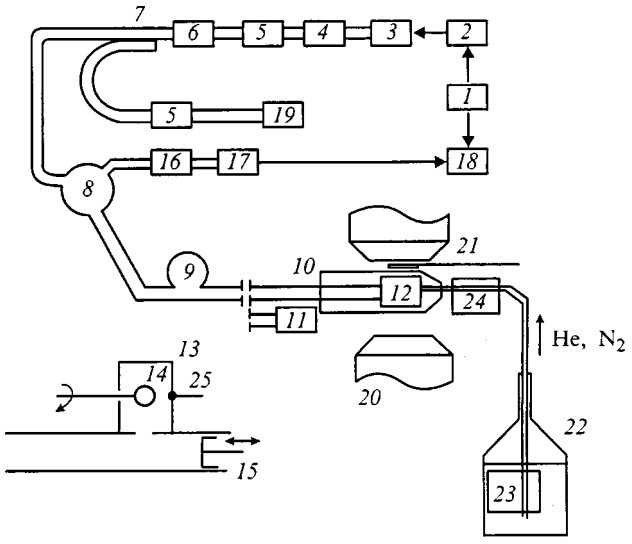

FIG. 4. Scheme of the measuring setup. *1*—Master pulse generator, *2*—modulator, *3*—magnetron, *4*—valve, *5*—attenuator, *6*—polarizing attenuator, *7*—directional coupler, *8*—circulator, *9*—voltmeter, *10*—cryostat, *11*—power meter, *12*—measuring cell (shown in the inset), *13*—cavity, *14*—sample, *15*—piston, *16*—polarizing attenuator, *17*—detector, *18*—oscillograph, *19*—frequency meter, *20*—electromagnet, *21*—Hall sensor, *22*—Dewar flask, *23* and *24*—furnaces, *25*—thermocouple.

supplied from a stabilized power source. The magnetic field was measured with a Hall film sensor *21* attached to the pole piece. It was calibrated using ferromagnetic resonance in an oriented YIG sphere.

The temperature was set within the 5–350-K range in a steady-state regime by blowing helium or (from 100 to 350 K) nitrogen vapor from Dewar flasks with the use of furnaces *23* and *24*. The temperature was measured with a copper–copper-iron thermocouple in the cavity wall.

The threshold of parametric spin-wave excitation can be established from a pulse envelope distortion,[1] the onset of self-modulation (see, e.g., Ref. 3), or a deviation from the linear dependence of the output on input power.[12] In our case, all three methods (in the cases where modulation set in immediately above the threshold) yielded the same results within experimental error, and one used primarily the first method.

The ac magnetic field in the cavity at the sample position is related[3] to the power P_{in} incident on the cavity through[2)]

$$h^2=\frac{8\pi\xi}{\omega V}Q_0(1-|\Gamma|^2)P_{\rm in}. \tag{8}$$

Here ξ is the ratio of the squared field at a given point to the mean squared field in the cavity, Q_0 is the intrinsic cavity Q factor, V is the cavity volume, and Γ is the reflection coefficient.

The largest error in $h_{\rm thr}$ is due to determination of $P_{\rm in}$ and Q_0. The power at the cryostat input (for a certain position of the polarizing attenuator *6*) was measured with the thermistor-based power meter approximately to within 10%. $P_{\rm in}$ was determined with due account of the cryostat waveguide losses (~1.5 dB). In subsequent threshold-field measurements, the power readings were made using attenuator *6* practically without introducing additional errors.

The quality factor Q_0 was derived from the frequency detuning corresponding to a given increase of the reflection coefficient in absolute magnitude relative to its lowest value, which was reached by tuning the magnetron to resonance with piston *14*. This was done by means of the expression obtained when the measuring cell *12* (Fig. 4) is replaced with its equivalent scheme. In our case the quantity $|\Gamma|_{\rm min}$, as well as naturally the frequency detuning $\alpha=2\delta\omega/\omega_{\rm res}$, could be considered small, which yielded the following simple relation

$$Q_0=2|\Gamma|/(\alpha\sqrt{1-|\Gamma|^2}). \tag{9}$$

The scatter in measurements of Q_0 made at different values of $|\Gamma|$ in the region from 6 to 12 dB (with respect to the maximum value of $|\Gamma|$) was not more than 10%. The quality factor Q_0 is temperature dependent and varies from sample to sample, and therefore it was checked in each measurement of h_{thr}. Estimates showed the total measurement error for h_{thr} to be ~10%.

To find the effective anisotropy field $2H_A$ and the resonance-curve width ΔH_0, ferromagnetic resonance measurements were performed, for which purpose the measuring cell *12* was replaced by a shorted waveguide section, with the sample placed at a distance of $\lambda/2$ from the waveguide face end. The width of the curve was measured at the level

determined in accordance with Ref. 14, and the values of $2H_A$ were determined from the measured resonance fields using the expressions presented, for instance, in Ref. 3. The constant magnetization was found from measurements of the threshold fields (see Section 4).

4. EXPERIMENTAL RESULTS

The ferromagnetic resonance parameters in the $Ba(Fe_{0.95}Sc_{0.05})_{12}O_{19}$ easy-axis crystal were measured at various orientations of the external dc field. The quantity $(H_{e0})_{\rm res}$ was found to grow rapidly for $\theta_H > 45°$. As mentioned in Section II, these crystals had a mosaic structure, and the increase in the steepness of the slope of the $(H_{e0})_{\rm res}$ dependence on θ_H should have resulted in a growth of ΔH_0 for $\theta_H > 45°$, and this is what was actually observed. The fairly large values of ΔH_0 for $\theta_H < 45°$ were also apparently due to a considerable extent to the mosaic structure.

Parametric first-order spin-wave excitation in the $Ba(Fe_{0.95}Sc_{0.05})_{12}O_{19}$ ferrite at the frequency used by us can occur, as evident from Fig. 2, only within a very narrow angular interval $\theta_H \cong 85-90°$. For these angles ΔH_k, while being probably smaller than ΔH_0, is nevertheless large, and parametric excitation may not be initiated because of insufficient power. Indeed, we have not succeeded in observing it in these crystals.

The measurements of ferromagnetic resonance in the Zn_2Y easy-plane ferrite were carried out in the 10–350-K temperature range. The temperature dependences of the anisotropy field $2H_A$ derived from the measured resonance fields, and the values of ΔH_0 for this crystal are plotted in Fig. 5. The temperature dependence of the anisotropy field is seen to be nonmonotonic. The same figure shows the temperature dependence of constant magnetization M_0 derived from threshold field measurements (see below).

The $\Delta H_0(T)$ relation exhibits a broad minimum at $T \cong 150$ K. The low-temperature rise may be due to a certain extent to the increasing contribution of inhomogeneities (because of the increase of M_0), but its main cause is undoubtedly the influence of the rapidly relaxing ions, most likely of Fe^{2+}. The high-temperature increase of ΔH_0 originates probably from fluctuations; interestingly, it starts far from the Curie temperature (which is 377 K). The comparatively large value of the minimum ΔH_0 (Fig. 5) is due primarily to inhomogeneities, including possibly the mosaic structure, which is not detected by x-ray diffraction for axial misalignments less than $20'$.

The threshold field measurements were performed with the ac field parallel to the dc external field $\mathbf{H}_{e0}$ (quasi-longitudinal pumping) for different magnitude and orientations of $\mathbf{H}_{e0}$ and different temperatures. For illustration, Fig. 6 presents graphs of $h_{\rm thr}$ against H_{e0} measured at different θ_H. One sees, first of all, that parametric spin-wave excitation occurs also within the field interval ($H_{e0} < 1$ kOe) where domains exist, and without a substantial increase in the threshold. For high fields, a correlation is seen between the measured and calculated dependences (Fig. 3). Specifically, the calculated values agree well with experiment for fields where $h_{\rm thr} \to \infty$.

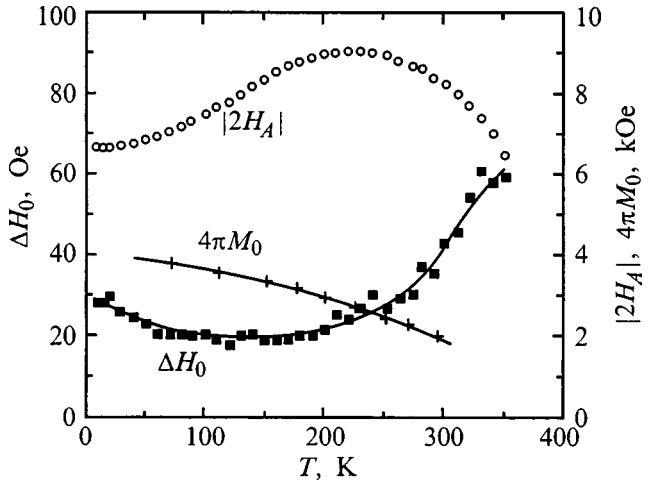

FIG. 5. Temperature dependences of the static parameters and ferromagnetic-resonance linewidth in a Zn_2Y sphere at a frequency of 36 GHz.

The transition from the measured $h_{\rm thr}(H_{e0}, \theta_H)$ relationships to $\Delta H_k(k)$ dependences for $\theta_H = 90°$ (the case of purely longitudinal pumping) was done using Eqs. (1)–(3) and the values of M_0 and $2H_A$ for the corresponding temperatures. The temperature dependence of $\Delta H_{k \to 0}$ thus obtained is displayed in Fig. 7. A comparison of this dependence with the ΔH_0 relation (Fig. 5) shows that the values of $\Delta H_{k \to 0}$, as expected, are considerably smaller than ΔH_0. One of the reasons for this is the twice smaller frequency of the parametric spin waves. However the main reason is that the inhomogeneities, although affecting parametric spin-wave excitation (see, e.g., Ref. 3), nevertheless do not contribute additively to ΔH_k. At the same time the low-temperature increases of ΔH_k and ΔH_0 differ only insignificantly. This bears out the assumption that the low-temperature rise is due to the contribution of rapidly relaxing ions.

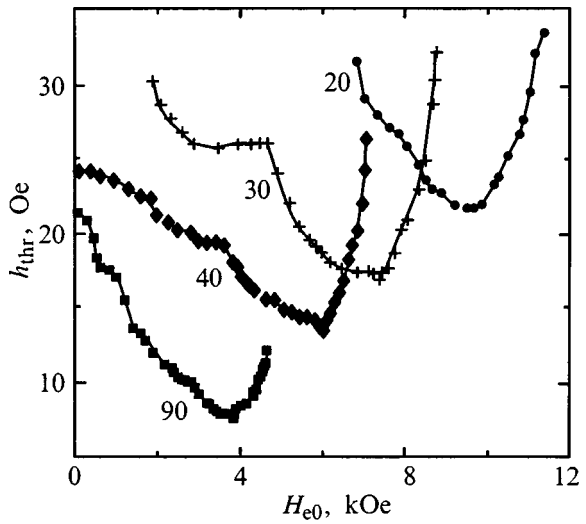

FIG. 6. Dependences of the threshold amplitude of the ac magnetic field on the magnitude and direction of the external dc magnetic field for a Zn_2Y sphere. Pumping frequency 36 GHz, temperature 150 K. The numbers adjoining the curves are θ_H angles in degrees.

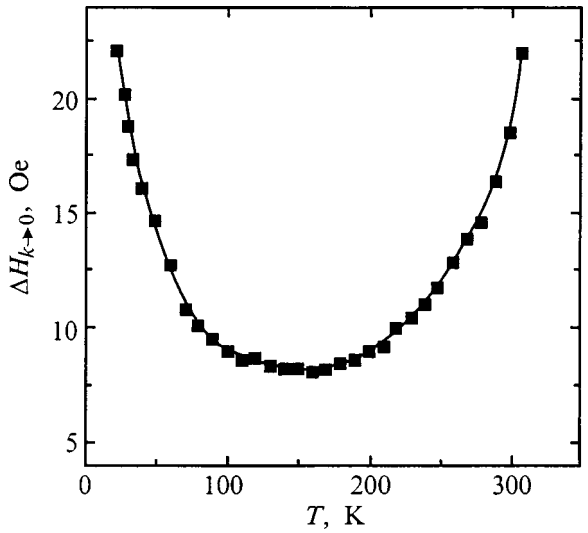

FIG. 7. Temperature dependence of $\Delta H_{k\to 0}$ in Zn_2Y for $\theta_H=90°$. Pumping frequency 36 GHz.

The calculation of the ΔH_k dependence on k, even for $\theta_H=90°$, the case where one can use the simple expressions (1)–(3), is complicated by the fact that the nonuniform-exchange constant η for Zn_2Y is unknown. To estimate k, we accepted $\eta=0.04$, a value only one half that for the YIG, based on the Curie temperature for the Zn_2Y crystal (377 K) being lower than that for YIG, and on the average distance between magnetic ions being somewhat larger.

Figure 8 plots the difference $(\Delta H_k-\Delta H_{k\to 0})$ against k for $T=$ const, and against T for constant k. One readily sees that ΔH_k grows with increasing T and k faster than by a linear law. This gives one some grounds to assume that this growth is due to the contribution of the intrinsic four-magnon relaxation process. It should be pointed out, however, that both the calculations and experiment[3] suggest that this contribution in YIG was substantially smaller. Thus the question of the contribution of four-magnon processes in hexagonal ferrites requires further investigation.

The calculations of ΔH_k for the case of $\theta_H<90°$, where the pumping is oblique, was done using the results of the calculations based on the theory of Ref. 6 (see Section 1). The calculated dependences of ΔH_k on k are shown graphically in Fig. 9; they were obtained using the above value $\eta=0.04$. As seen from the figure, for small k (i.e. large H_{e0}) ΔH_k increases strongly with decreasing θ_H, i.e., as the direction of the dc field and, hence, of the constant magnetization $\mathbf{M}_0$ deviates from the easy plane. For large k, i.e. for small H_{e0}, the difference between the values of ΔH_k for different θ_H becomes smaller. This behavior can be due to the strong dependence of the spin-wave damping parameter on the direction of spin-wave propagation relative to the anisotropy axis. Indeed, for a high H_{e0} field a change in its direction turns strongly $\mathbf{M}_0$ and, hence, the direction of propagation of parametric spin waves with respect to the anisotropy axis, which, because of the damping parameter being strongly anisotropic, affects considerably its magnitude. For small H_{e0}, this influence is small.

The anisotropy in the spin-wave damping parameter is of considerable interest for understanding the relaxation processes. This prompted a calculation of the dependence of ΔH_k on the angle β between the **k** vector and the anisotropy axis (the z' axis in Fig. 1) using the data in Fig. 9. The β angles were calculated using the θ_0 angles found from the

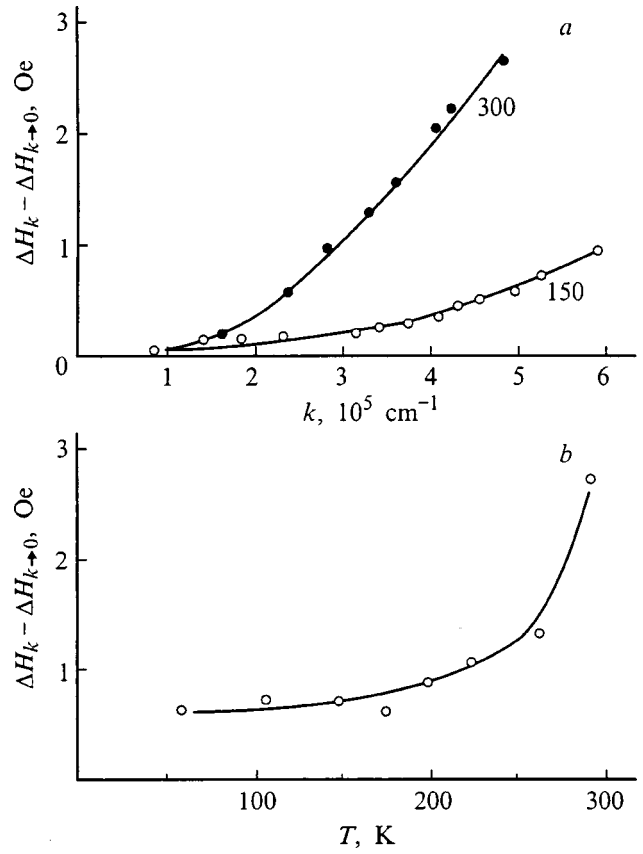

FIG. 8. Dependences of the difference $\Delta H_k(k)-\Delta H_{k\to 0}$ in Zn_2Y (a) on wave number k for the temperatures (in K) specified at the curves, and (b) on temperature for $k=5\times 10^5$ cm^{-1}. Pumping frequency 36 GHz.

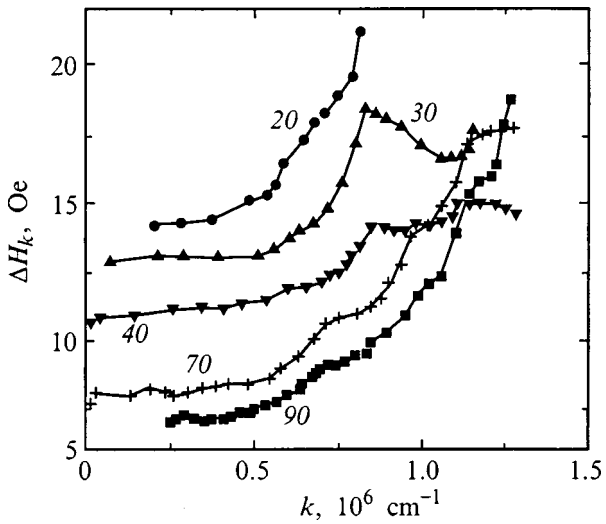

FIG. 9. Dependences of ΔH_k in Zn_2Y on wave number for different orientations of the external dc field $\mathbf{H}_{e0}$. Pumping frequency 36 GHz, temperature 150 K. The numbers adjoining the curves are the angles θ_H between $\mathbf{H}_{e0}$ and the anisotropy axis (in deg).

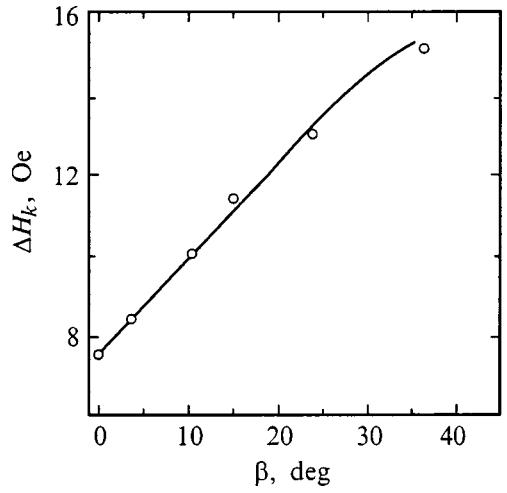

FIG. 10. Dependence of ΔH_k in Zn_2Y on the angle between the direction of spin-wave propagation and the anisotropy axis for a constant wave number $k=5\times10^5$ cm^{-1}. Pumping frequency 36 GHz, temperature 150 K.

equilibrium condition and the angles θ_k and φ_k obtained in threshold-field minimization. The results of this calculation are displayed in Fig. 10. One readily sees that ΔH_k depends strongly on the angle between the direction of spin-wave propagation and the anisotropy axis, and that this dependence is close to linear (for reasons remaining as yet unclear).

Thus our measurements of the thresholds of parametric spin-wave excitation in a strongly anisotropic Zn_2Y ferrite were carried out for the first time for different orientations of an external dc magnetic field, including the angles at which the pumping was oblique. The calculations of the damping parameter of the excited spin waves and of their wave vector from these measurements were based on a recently developed theory[6] of parametric spin-wave excitation in strongly anisotropic ferrites under oblique pumping.

The threshold fields, as well as the ferromagnetic-resonance parameters, were measured within a broad temperature range, which permitted one to draw conclusions on the contributions of various mechanisms to the damping parameter of strongly anisotropic ferrites. We are presenting here a few of them.

The superlinear growth of the spin-wave damping parameter ΔH_k with increasing wave number and temperature gives one grounds to conjecture the existence of a contribution of an intrinsic four-magnon relaxation process. A final conclusion in this respect could be made, however, only after a quantitative comparison of the expected value of this contribution with calculations.

One cannot question the considerable contribution of fast-relaxing ions, apparently of Fe^{2+}, which, as could be expected, is approximately the same for uniform precession and spin waves.

Among the inhomogeneities providing the major contribution to ΔH_0 and affecting also, although in a lesser degree, ΔH_k, is the mosaic structure, which was detected independently in an easy-axis crystal but existed apparently in the Zn_2Y crystals as well. Thus eliminating the mosaic in the crystal structure is one of the ways of reducing the magnitude of ΔH_0 in single crystals of strongly anisotropic ferrites, which is a necessary condition for their wide application in the short-wavelength part of the microwave range.

An important result of this work is determination of the spin-wave damping parameter in strongly anisotropic ferrites for different angles between the external dc field and the anisotropy axis. Because minimization yields also the direction of propagation of parametric spin waves, one obtains in this way a possibility to find the dependence of the damping parameter on the direction of their propagation relative to the anisotropy axis, i.e. to determine the spin-wave damping anisotropy. In this work this possibility has been realized for the first time for a strongly anisotropic ferrite.

It should be noted, however, that the threshold-field minimization by the theory[6] used in this work was made under the assumption of a constant ΔH_k, and therefore all the results, including those on the angular dependence of ΔH_k, are valid only to a first approximation. Calculation to higher-order approximations, i.e., minimization taking into account the dependences of ΔH_k on the parameters of the excited spin waves derived in the lower-order approximations, is a topical problem. Its solution will show the extent to which this process is convergent and yield refined values of the spin-wave damping parameter.

The authors are indebted to K. S. Luzgin for the development of the modulator for the measuring setup, to R. I. Zvereva for assistance in growing the crystals, to N. N. Syrnikova for sample orientation by x-ray diffraction, and to N. I. Pogodin for providing the Hall sensor developed by him. The authors consider it their duty to point out that this work would have been impossible without the unique magnetron developed by A. V. Atlasman.

[1)]The magnetrons were developed by A. V. Atlasman, fabricated on order of the Ioffe Institute, and used for the first time in the study Ref. 12.
[2)]There is a misprint in Eq. (10.53) in Ref. 3, which is equivalent to Eq. (8) of this work, namely, there should be $(1+q)^2$ in the denominator.

[1] E. Schlömann, J. J. Green, and U. Milano, J. Appl. Phys. **31**, 386S (1960).
[2] I. Bady and E. Schlömann, J. Appl. Phys. **33**, 1377 (1962); E. Schlömann, R. I. Joseph, and I. Bady, *ibid.* **34**, 672 (1963).
[3] A. G. Gurevich and G. A. Melkov, *Magnetic Oscillations and Waves* [in Russian] (Nauka, Moscow, 1996).
[4] Yu. M. Yakovlev, Fiz. Tverd. Tela (Leningrad) **10**, 2431 (1968) [Sov. Phys. Solid State **10**, 1911 (1968)].
[5] Yu. M. Yakovlev and Yu. N. Burdin, Fiz. Tverd. Tela (Leningrad) **16**, 466 (1974) [Sov. Phys. Solid State **16**, 299 (1974)].
[6] A. V. Nazarov and A. G. Gurevich, Zh. Tekh. Fiz. **68**(5), 65 (1998) [Tech. Phys. **43**, 539 (1998)]; *ibid.* **69**(9) (1999) (in press).
[7] J. J. Greene and B. J. Healy, J. Appl. Phys. **34**, 1285 (1963).
[8] S. Dixon, Jr., J. Appl. Phys. **34**, 3441 (1963).
[9] R. O. Savage, Jr., S. Dixon, Jr., and A. Tauber, J. Appl. Phys. **36**, 873 (1965).
[10] V. V. Petrov and R. I. Zvereva, *Proceedings of the 6th International Conference on Ferrites* (Tokyo, 1992), p. 1317.
[11] V. V. Petrov, V. I. Salyganov, and G. M. Galaktionova, Élektron. Tekh. Ser. I, SVCh Élektron. No. 8, 64 (1982).
[12] L. Kraus, A. N. Anisimov, A. G. Gurevich, and A. V. Atlasman, JETP Lett. **37**, 123 (1983).
[13] E. Schlömann, J. Appl. Phys. **34**, 1998 (1963).
[14] A. G. Gurevich, Radiotekh. Elektron. **8**, 780 (1963).

Translated by G. Skrebtsov

Low-temperature electronic and magnetic transitions in the antiferromagnetic semiconductor $Cr_{0.5}Mn_{0.5}S$

G. A. Petrakovskiĭ, L. I. Ryabinkina, D. A. Velikanov, S. S. Aplesnin, G. M. Abramova, N. I. Kiselev, and A. F. Bobina

L. V. Kirenskiĭ Institute of Physics, Siberian Branch, Russian Academy of Sciences, 660036 Krasnoyarsk, Russia

(Submitted November 17, 1998)
Fiz. Tverd. Tela (St. Petersburg) **41**, 1660–1664 (September 1999)

Experimental-theoretical studies were carried out of the electrical and magnetic properties of the antiferromagnetic semiconductor $Cr_{0.5}Mn_{0.5}S$ in the temperature range 4.2–300 K. A magnetic antiferromagnetic-ferrimagnetic phase transition was observed along with a semimetal-semiconductor electronic transition. Monte Carlo calculations indicate that the changes in the type of magnetic ordering and conductivity are due to the cooperative Jahn–Teller effect caused by the Cr^{2+} ions. © *1999 American Institute of Physics.* [S1063-7834(99)02609-X]

At present, compounds with perovskite structure similar to $La_{1-x}Me_xMnO_3$ (where Me=Ca, Ba, Sr, etc.) are being studied intensely.[1] These compounds are interesting because they exhibit giant magnetoresistance and magnetically and electronically nonuniform states that preserve the compounds' crystallographically uniform structure. Since the mechanisms for magnetic biphase behavior and electronic stratification are not clear at this time, there is interest in studying compounds with a different crystal lattice but with similar physical properties.

The compound $Cr_{0.5}Mn_{0.5}S$ is a strongly doped antiferromagnetic semiconductor, belonging to the group of sulfides $Me_xMn_{1-x}S$ (where Me is a 3*d* metal), which crystallize in the cubic NaCl lattice.[2] Like the rare-earth manganite compounds, the $Me_xMn_{1-x}S$ sulfides exhibit changes in the type of conductivity and magnetic order as the concentration of 3*d* metal is varied. Thus, with Me=Fe, as x increases the magnetic order changes from antiferromagnetic to ferromagnetic, which precedes an electronic semiconductor-semimetal transition (at $x_c \sim 0.4$).[3] In the system $Cr_{0.5}Mn_{0.5}S$ ($0<x<0.67$), however, no noticeable change in the magnetic order is observed in the vicinity of the concentration-induced semiconductor—semimetal transition ($x_c \sim 0.67$). The semimetallic sulfides retain their antiferromagnetic order with increasing Néel temperature T_N up to ~ 175 K for $x \approx 0.5$ ($T_N \sim 148$ K for $x=0$).[4,5] Measurements of the magnetic susceptibility,[4] along with EPR data[6] and neutron-diffraction measurements,[7] indicate that increases in the Néel temperature with a simultaneous decrease (in absolute value) in the negative paramagnetic Curie temperature do not exclude the possible formation within the $Me_xMn_{1-x}S$ sulfides of a magnetically nonuniform state in the temperature range $T<T_N$ and a transition to a ferromagnetic state with changes in the temperature or magnetic field.

In this paper we investigate experimentally and theoretically the magnetic and electrical properties of the antiferromagnetic semiconductor $Cr_{0.5}Mn_{0.5}S$ in the temperature range 4.2–300 K in order to study the low-temperature ($T<77$ K) electronic and magnetic states of this compound.

1. EXPERIMENTAL RESULTS

Polycrystalline samples were synthesized from pure elements (electrolytic Mn, Cr and S with purity 99.999%) in vacuum quartz ampules over the course of a week. The temperature dependences of the electrical resistance of these samples were measured at constant current by a potentiometer method in the temperature range 4.2–300 K. The measurements of the magnetization in the range 4.2–100 K were made using a superconducting quantum interference (SQUID) magnetometer in fields up to 8 Oe.

According to *x*-ray structural data, our samples of $Cr_{0.5}Mn_{0.5}S$ were solid solutions with the fcc NaCl lattice characteristic of α MnS. Replacement of Mn ions with Cr ions is accompanied by compression of the cubic unit cell and decrease in the lattice parameter from $a=5.222$ (α MnS) to 5.165 Å while preserving the NaCl structure. Additional phases were not observed in the solid solution $Cr_{0.5}Mn_{0.5}S$.

Figure 1a shows the temperature dependence of the electrical resistivity $\rho(T)$ for $Cr_{0.5}Mn_{0.5}S$. The behavior of $\rho(T)$ in the range 77–300 K agrees with the data of Ref. 5 and corresponds to the semimetallic type of conductivity, i.e., the compound is in the degenerate- semiconductor state. In the range below ~60 K a rapid increase (by an order of magnitude) in the electrical resistivity is observed, along with an anomalous change in the temperature coefficient of the resistivity $d\rho/dT$ (Fig. 1b). In this case the activation energy of the conductivity E_a changes discontinuously with decreasing temperature from 0.04 to 0.01 eV in the neighborhood of T_N, and then decreases continuously down to ~0.003 eV in the range below ~60 K (Fig. 1c).

Figure 2 shows temperature dependences of the magnetization of $Cr_{0.5}Mn_{0.5}S$ samples measured in the range 4.2–100 K, some cooled in zero magnetic field (ZFC samples, see curve *1*) and some in a field $H=8$ Oe (FC samples, see curve *2*). It is clear from the figure that the material enters a state with spontaneous magnetization at $T_c \approx 66$ K. The behavior of the ZFC magnetization is typical of the initial susceptibility of a ferromagnet (the Hopkinson effect).[8] In the

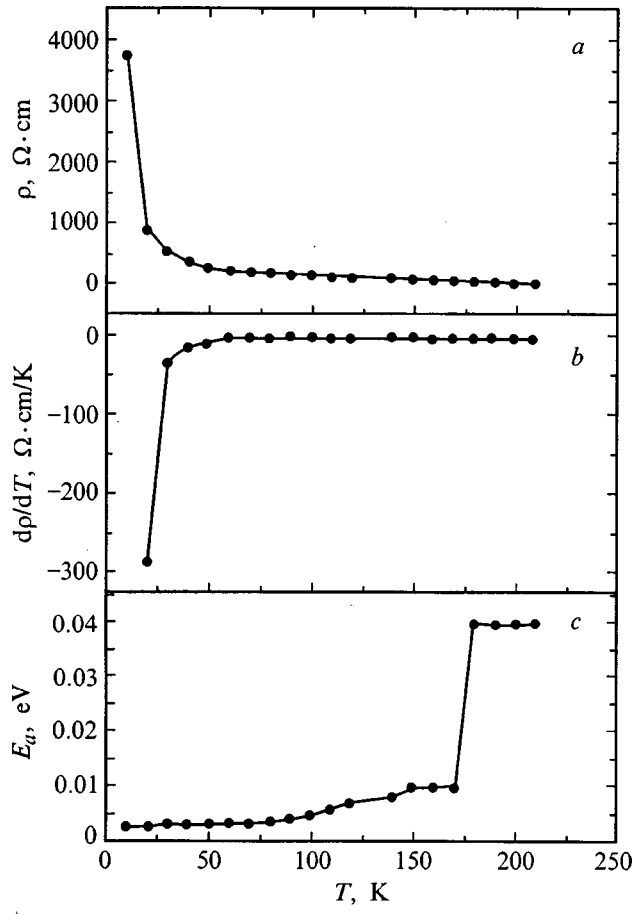

FIG. 1. Temperature dependences of the electrical resistivity ρ (a), the temperature coefficient of the resistivity $d\rho/dT$ (b), and the activation energy of the conductivity E_a (c) for $Cr_{0.5}Mn_{0.5}S$.

vicinity of ~35 K the ZFC magnetization curves exhibit an additional weakly expressed maximum. Below this temperature, the FC magnetization decreases with decreasing temperature.

2. DISCUSSION OF RESULTS

Analysis of the magnetic properties based on Monte Carlo calculations show that the behavior of the magnetization of $Cr_{0.5}Mn_{0.5}S$ in the 4.2–300 K range cannot be described in terms of magnetic ordering mechanisms that take into account two- and four-spin exchange interactions, which are normally used to describe the properties of the magnetically ordered state.[9,10] These calculations show that the behavior of the spontaneous moment in the fcc lattice of $Cr_{0.5}Mn_{0.5}S$ is due to the cooperative Jahn–Teller effect caused by the Cr^{2+} ions.

The ground state of Cr^{2+} ions in a lattice with cubic symmetry is characterized by twofold orbital degeneracy. In this case, two types of interactions are possible. The first is an interaction of the degenerate orbitals with the lattice. Here Pauli matrices for the effective spin τ are introduced in order to describe the orbital wave functions e_g.[11] The ordering of the pseudospins (orbitals) is accompanied by a structural phase transition. The second is an interaction between orbitals, which depends on the spins and is a function of the pseudospin exchange integral $J_s = J_s^0 + J_m\langle \tau_g \tau_{g+r}\rangle$.[11] Here J_s^0 is the exchange interaction integral between spins, and J_m is an interaction parameter between spins and orbitals. If $J_s^0 < 0$ and $J_m < 0$, it is possible for a critical temperature to exist at which the sign of the exchange interaction between the spins changes from negative to positive.

Let us assume that the variation of the pseudospin correlation function with temperature is analogous to that of spin-spin correlation function in the magnetically ordered phase, i.e., $|\langle \tau_g \tau_{g+r}\rangle| \sim (1 - T/T_N)^{2\beta}$, where β is a critical index for the magnetization; it is known that $\beta = 0.35$. As a result, the exchange interaction between nearest neighbor chromium ions depends on temperature like $J_{Cr-Cr} = J^0_{Cr-Cr} + J_m(1 - T/T_N)^{2\beta}$, where J_m is a fitting parameter determined from the condition that the exchange constant J_{Cr-Cr} should change sign at a certain critical temperature T_c. The temperature T_c corresponds to the appearance of ferromagnetic ordering. As a rule, the ordering temperature of the orbitals should coincide with the temperature of a structural transition and the Néel temperature T_N. In fact, *x*-ray analysis indicates that a lattice distortion analogous to the distortion at T_N observed in α MnS does indeed occur at $T_N \approx 175$ K in the solid solution $Cr_{0.5}Mn_{0.5}S$.[12] In this temperature range we observe[4] a 10% discontinuity in the susceptibility.

In our Monte Carlo calculations we used a lattice model of the solution $Cr_{0.5}Mn_{0.5}S$ with six exchange interaction parameters between the classical spins $S_{Mn} = 2.5\mu_B$ and $S_{Cr} = 2\mu_B$ (Mn–Mn, Cr–Cr, and Mn–Cr in the first and second coordination spheres). Some of these exchange interaction parameters were determined previously[4] from the concentration dependence of the Néel temperature for $Cr_xMn_{1-x}S$ ($0 < x < 0.67$): $J_{MnCr}/J_{MnMn} = -0.4$, $K_{Mn-Cr}/J_{MnMn} = -1.9$, and $K_{MnMn}/J_{MnMn} = -1.8$. The Cr–Cr exchange interaction parameters for the first and second coordination spheres are determined in the present paper. For an fcc lattice consisting of $N = 4 \times 12^3$ sites we calculated the magnetization, the susceptibility, the Edwards–Anderson parameter $q_\alpha = (1/N)\sqrt{\sum_{i=1}^{N}\langle S_i^\alpha\rangle^2}$ ($\alpha = x,y,z$), and the magnetic static structure factor along the cube edges and diagonals of the planes. Based on these characteristics, we determine the transition temperature from the antiferromagnetic state to a ferrimagnetic state with a spontaneous moment $m \approx (1/3)S_{Cr}\mu_B$ for $T \to 0$. The magnetic Hamiltonian for the solid solution $Cr_{0.5}Mn_{0.5}S$ can be written in the form

$$H = -\sum_{\alpha,\beta=Cr,Mn} I_{\alpha\beta} \sum_{i=1}^{N} \sum_{\Delta=1}^{Z_1} P_\alpha(i) P_\beta(i+\Delta) S_\alpha(i) S_\beta(i+\Delta) - \sum_{\alpha,\beta} K_{\alpha\beta} \sum_{i=1}^{N} \sum_{h=1}^{Z_2} P_\alpha(i) P_\beta(i+h) S_\alpha(i) S_\beta(i+h) - \sum_{\alpha} H \sum_{i} P_\alpha(i) S_\alpha^z(i),$$

where $I_{\alpha\beta}$ and $K_{\alpha\beta}$ are exchange interaction integrals between nearest neighbors ($Z_1 = 6$) and next-nearest neighbors ($Z_2 = 12$), H is the external magnetic field, and the projection operator $P_\alpha(i)$ equals unity at sites occupied by spin S_α.

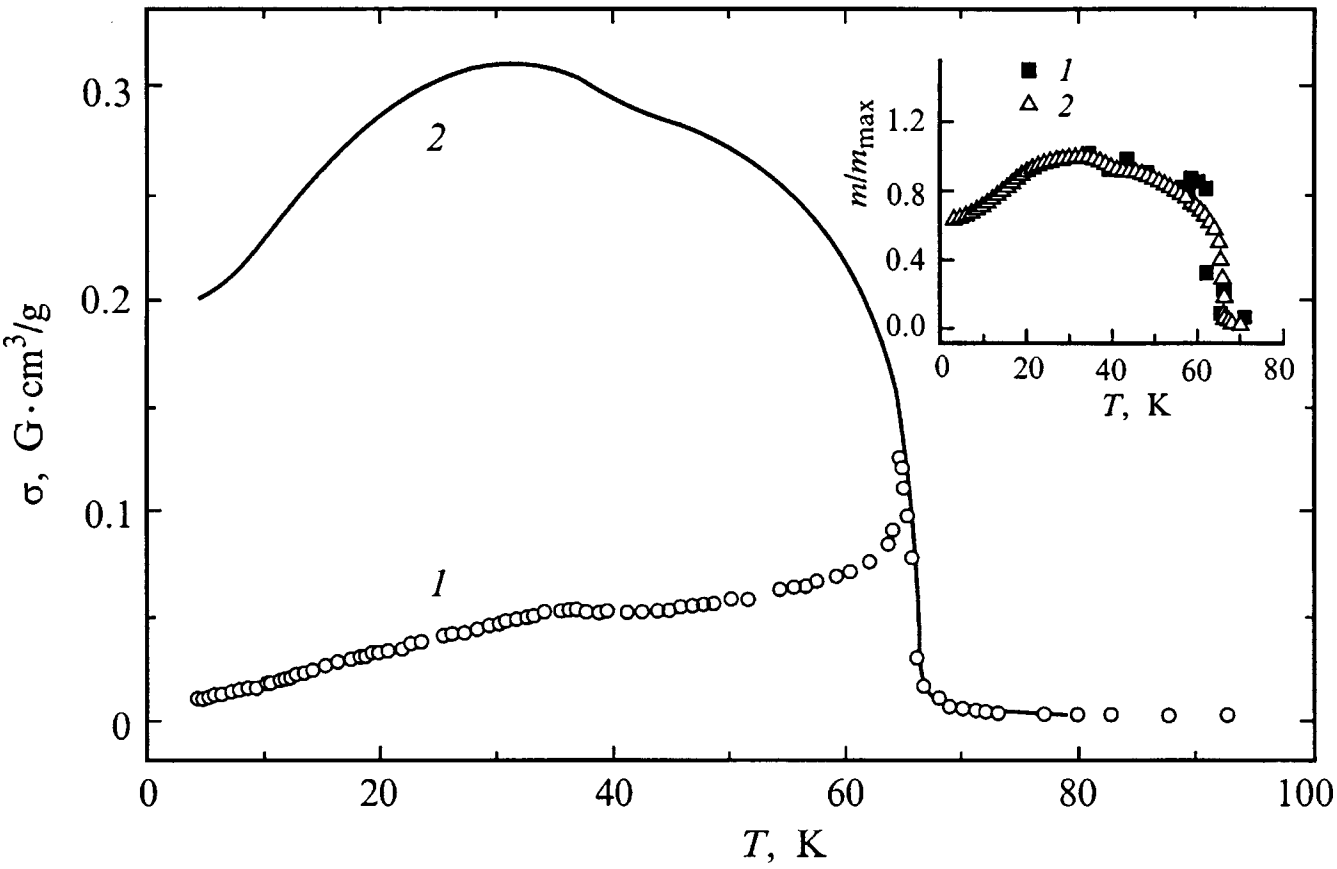

FIG. 2. Temperature dependences of the magnetization σ for samples cooled in zero magnetic field (ZFC—curve *1*) and in a field of 8 Oe (FC—curve *2*) for $Cr_{0.5}Mn_{0.5}S$. The inset shows the temperature dependence of the normalized value of the magnetic moment: *1*—calculated by the Monte Carlo method, *2*—experiment.

According to these calculations, the dependence of the Fourier spectrum of the pairwise spin correlation function on wave vector in the antiferromagnetic temperature range ($66 \pm 5 < T < 180 \pm 10$) K exhibits two maxima: at $q=0$ and π/a in the direction [101], as is shown in the inset to Fig. 3a. This indicates that spins in the four sublattices located at the vertices of a tetrahedron are pairwise antiparallel (Fig. 4a). The first effect of decreasing the temperature is propagation of the long-range ferromagnetic order along the spins of the chromium ions. Below $T \leqslant 130$ K, ordering of the moments of the manganese ions contributes to the magnetic structure factor, leading to a considerable increase in the magnitude $S(q)$ and the appearance of a modulation of the magnitude of the antiferromagnetism vector in the direction [101] with $q=\pi/12a$. The quantity $S(q)$ calculated by the Monte Carlo method exhibits a satellite peak at temperatures below ~140 K. For $T_c = 65 \pm 5$ K, the intensity of the magnetic structure factor at $q=\pi/a$ (curve *1* in Fig. 3a) reduces to zero, and a peak in $S(q)$ forms at $q = 0$ (curve *1* in Fig. 3b), i.e., ferromagnetic order is established along two directions of the planes (Fig. 4b), which leads to the formation of a spontaneous moment. The temperature dependence of the magnetic moment calculated by the Monte Carlo method (the inset to Fig. 2) is in good agreement with the experimental results. At T_c, the lifting of orbital degeneracy causes the sign of the exchange interaction between chromium ions J_{Cr-Cr} to change from negative to positive. By comparing the experimental and theoretical values of T_c and T_N, we can determine the value of the exchange constants between Cr–Cr ions: $J_{Cr-Cr}/J_{MnMn} = -2.7$, $K_{Cr-Cr}/J_{MnMn} = 6$, and $J_m/J_{MnMn} = -2.5$, where $J_{MnMn} = (7.8 \pm 0.3)$ K.

From our calculations of the magnetic structure factor it follows that the ions of chromium and manganese are located randomly in the lattice and form two infinite clusters containing chromium and manganese respectively. The Edwards–Anderson parameter (Fig. 5) exceeds the value of the magnetic structure factor by a few times. This indicates that independent finite clusters are also contained in the material and randomly distributed. The temperatures of the paramagnetic-antiferromagnetic (T_N) and antiferromagnetic-ferrimagnetic (T_c) phase transitions determined from the temperature dependences of the Edwards–Anderson parameter (Fig. 5) are in good agreement with the data obtained from the magnetic structure factor: $T_N \approx 180 \pm 10$ K, $T_c \approx 70 \pm 6$ K.

The decrease in magnetic moment at low ($T < 30$ K) temperatures and the temperature hysteresis of the magnetic moments of ZFC and FC samples are probably due to the formation of domain structures in weak magnetic fields. It is also known that the original α MnS exhibits a structural transition at $T \approx 25$ K.[13] This transition is probably preserved in the solid solution $Cr_{0.5}Mn_{0.5}S$ as well, leading to a change in the exchange constants between Mn ions due to lattice distortion and the appearance of non-Heisenberg types of

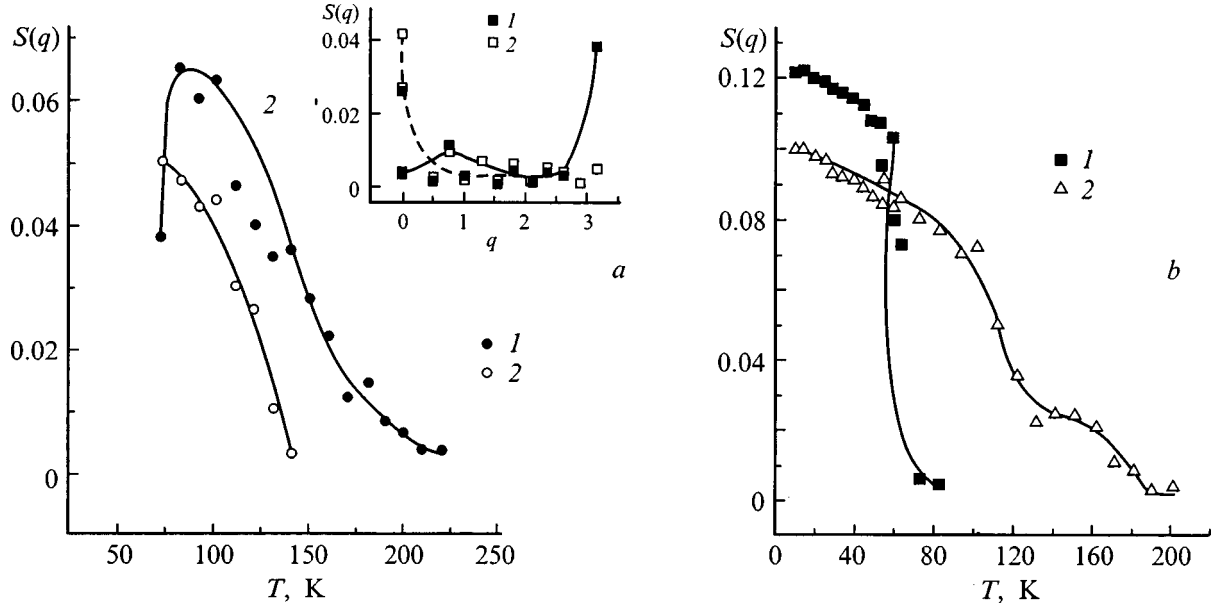

FIG. 3. Temperature dependence of the magnetic structure factor $S(q)$. a: Curve *1*—$q=\pi/a$ in the direction [101]; curve *2*—$q=\pi/12a$ in the direction [011]; b: curve *1*—$q=0$ in the direction [101]; curve *2*—$q=0$ in the direction [110]. The inset shows the Fourier spectrum of the pairwise spin correlation function for the direction [101] (*1*) and [110] (*2*) at a temperature 115 K.

interactions, for example biquadratic and four-spin. This causes the modulus of the spin on a site to contract, thereby decreasing the noncollinearity of the spins. Our Monte Carlo calculations show that this structural transition can decreasse the exchange parameter J_{MnMn} by a factor of 2, which in turn decreases the magnetization by about 15% at 4 K.

Based on this model we can predict two effects. In a magnetic field, the sign of the spin-spin correlation function $\langle S_g S_{g+r}\rangle$ changes from negative to positive at a distance $r/a=1$ in the vicinity of the Néel temperature, increasing the exchange interaction between orbitals $J_\tau=J_\tau^0+J_m\langle S_g S_{g+r}\rangle$, which in turn increases the temperature for orbital ordering. This will enhance the orbital correlations $\langle \tau_g \tau_{g+r}\rangle$ and decrease the exchange interaction between chromium atoms, leading to a decrease in the Néel temperature and an increase in the Curie temperature for ferrimagnetism with increasing field. As a result, in strong magnetic fields there should exist a tetracritical point where the phase transition lines T_c and T_N are in contact. Uniaxial pressure along a principle diagonal of the cube should lead to an analogous effect.

In light of these magnetic calculations, we can explain the behavior of the electrical resistance of $Cr_{0.5}Mn_{0.5}S$ in the following way. According to Ref. 5, the temperature behavior of the electrical resistivity of the sulfides $Cr_xMn_{1-x}S$ arises from changes in the activation energy of the conductivity E_a due to a red shift in the mobility edge E_c caused by the contribution of the ferromagnetic component of the exchange interaction in the second coordination sphere of the NaCl lattice. In this picture, the Fermi level E_F is located in the vicinity of the *d* atom-like states of the chromium atoms

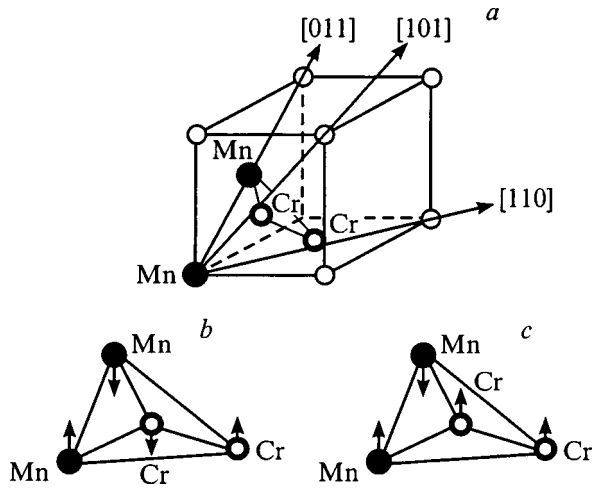

FIG. 4. Sketch of magnetic order in the solid solution $Cr_{0.5}Mn_{0.5}S$: a—unit cell of the fcc lattice; b—antiferromagnet ($T>T_c$); c—ferrimagnet ($T<T_c$).

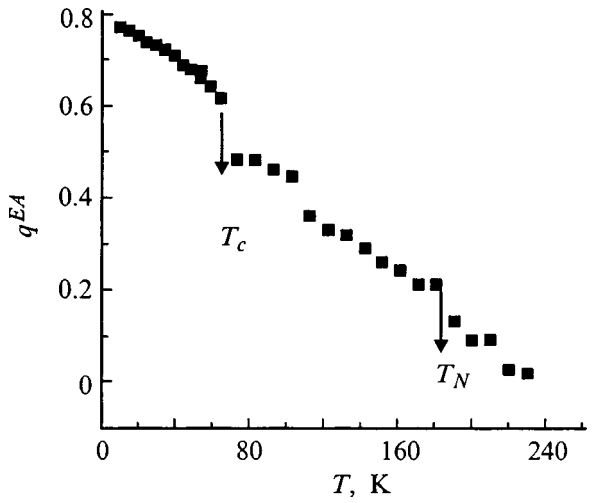

FIG. 5. Temperature dependence of the Edwards–Anderson parameter q^{EA} for the longitudinal components of the spin.

and the top of the valence $p-d$ hybridized band. The shift δE_c in $Cr_{0.5}Mn_{0.5}S$ as it enters the antiferromagnetic phase $E_{a\mathrm{PM}}-E_{a\mathrm{AFM}}\approx 0.05$ eV, and the activation energy of the conductivity below the Néel temperature reaches values of ~ 0.01 eV. As the temperature decreases, the shift δE_c is probably increased by the appearance of a contribution from the ferromagnetic exchange interaction in the first coordination sphere. This leads to a still larger decrease in the conductivity activation energy. However, the Jahn–Teller transition lifts the orbital degeneracy of the *d* levels of chromium ions located near the valence band, and the splitting between e_g sublevels increases as the magnitude of the exchange field in the ferromagnetic phase increases. As a result of this splitting, the Fermi level can end up in an energy range with lower density of states, increasing the magnitude of the electrical resistance despite the fact that $E_c \sim E_F$.

Thus, at low temperatures the antiferromagnetic semiconductor $Cr_{0.5}Mn_{0.5}S$ exhibits a magnetic transition from antiferromagnet to ferrimagnet, and an electronic transition from a semimetallic to a semiconducting phase. The mechanisms for these transitions can be explained by the cooperative Jahn–Teller effect caused by Cr^{2+} ions.

The authors are grateful to E. V. Kuz'min for useful discussions of this work.

[1] E. L. Nagaev, Usp. Fiz. Nauk **166**(8), 833 (1996).
[2] G. A. Petrakovskiĭ, G. V. Loseva, L. I. Ryabinkina, and S. S. Aplesnin, J. Magn. Magn. Mater. **140–144**, 147 (1995).
[3] G. A. Petrakovskiĭ, S. S. Aplesnin, G. V. Loseva, L. I. Ryabinkina, and K. I. Yanushkevich, Fiz. Tverd. Tela (Leningrad) **33**, 406 (1991) [Sov. Phys. Solid State **33**, 233 (1991)].
[4] G. A. Petrakovskiĭ, S. S. Aplesnin, G. V. Loseva, and L. I. Ryabinkina, Fiz. Tverd. Tela (Leningrad) **31**, 172 (1989) [Sov. Phys. Solid State **31**, 642 (1989)].
[5] G. V. Loseva, L. I. Ryabinkina, and S. G. Ovchinnikov, Fiz. Tverd. Tela (Leningrad) **31**, 45 (1989) [Sov. Phys. Solid State **31**, 375 (1989)].
[6] G. V. Loseva, L. I. Ryabinkina, L. S. Emel'yanova, and A. V. Baranov, Fiz. Tverd. Tela (Leningrad) **22**, 3698 (1980) [Sov. Phys. Solid State **22**, 2165 (1980)].
[7] P. Burlet and E. F. Bertaut, C. R. Acad. Sci. (Paris) B **264**, 323 (1967).
[8] S. I. Vonsovskiĭ, *Magnetism* [in Russian] (Nauka, Moscow, 1971), p. 831.
[9] E. L. Nagaev, *Physics of Magnetic Semiconductors* [in Russian] (Nauka, Moscow, 1979).
[10] E. L. Nagaev, *Magnets with Compound Exchange Interactions* [in Russian] (Nauka, Moscow, 1988).
[11] K. I. Kugel' and D. I. Khomskiĭ, Usp. Fiz. Nauk **136**, 621 (1982) [Sov. Phys. Usp. **25**, 231 (1982)].
[12] H. H. Heikens, G. A. Wiegers, and C. F. van Bruggen, Solid State Commun. **24**, 205 (1977).
[13] E. F. Bertaut, F. Sayetat, F. Tcheou, G. Bassi, and R. Georges, C. R. Acad. Sci. (Paris) **270B**, 704 (1970).

Translated by Frank J. Crowne

Temperature dependence of the giant magnetostriction of submicrocrystalline dysprosium

Kh. Ya. Mulyukov, I. Z. Sharipov, and G. F. Korznikova

The Institute for Problems in Superplasticity of Metals, Russian Academy of Sciences, 450001 Ufa, Russia
(Submitted November 24, 1998; accepted for publication February 25, 1999)
Fiz. Tverd. Tela (St. Petersburg) **41**, 1665–1667 (September 1999)

The temperature dependence of the magnetostriction of Dy was measured in various structural states. A submicrocrystalline state was created by intense plastic deformation on Bridgman anvils. Intermediate- and large-grain states were obtained by annealing samples in a vacuum at 573 and 873 K respectively. In the large-grain state, plots of the magnetostriction versus temperature exhibit a kink at around 85 K, which is evidence of a magnetic phase transition from ferromagnetism to helical antiferromagnetism. In the submicrocrystalline state these curves have no kinks and decrease smoothly to zero at high temperatures. This is interpreted as the absence of helical antiferromagnetic order in the sample. © *1999 American Institute of Physics.* [S1063-7834(99)02709-4]

In previous papers, researchers have found significant differences in some magnetic properties of rare-earth ferromagnets in the submicrocrystalline and large-grain structural states. Thus, for example, it has been established that, when Dy is in the submicrocrystalline structural state, its magnetization decreases by roughly a factor of 10,[1] and its coercive field increases from zero in the large-grain state to 200 kA/m.[2] Furthermore, helical antiferromagnetic ordering, which is usually observed in the temperature range 85–179 K,[3] does not appear.[1,2] Our studies of the dependence of the giant magnetostriction on structural state in Ref. 4 also indicate the absence of helical antiferromagnetic ordering in submicrocrystalline Dy. The complicated hysteresis loop we obtained in the latter paper for the magnetostriction, which corresponds to an intermediate structural state, was tentatively interpreted there as evidence of the coexistence of ferromagnetic and helical antiferromagnetic orderings within a certain range of temperatures. In subsequent papers.[5,6] we also observed a sizable change in the temperatures for magnetic phase transformations in rare-earth ferromagnets having submicrocrystalline structure.

An interesting way to identify the physical mechanism that gives rise to the magnetic properties of Dy is to study the temperature dependence of its magnetostriction in various structural states. In this paper we present the results of these investigations.

1. EXPERIMENTAL METHOD

Our investigations were carried out on samples of Dy with a 99.9% purity. The submicrocrystalline structure was obtained by intense plastic deformation of Dy films on Bridgman anvils under pressures of 0.5 GPa at room temperature. Intermediate- and large-grained states were obtained by annealing in a vacuum of 1.3×10^{-3} Pa at 573 and 873 K respectively.

The longitudinal magnetostriction was measured in the same sample using an apparatus described in Ref. 7. The length of the sample in question was 7.8 mm. Temperature was measured using a copper thermal resistor mounted on the sample being studied. The temperature dependence of the magnetostriction $(\lambda(T))$ was obtained by subtracting the value of the thermal expansion of the sample being measured before the magnetic field was applied from its value within a magnetic field.

2. EXPERIMENTAL RESULTS

Figure 1 shows curves $\lambda(T)$ for the submicrocrystalline state, plotted for various values of the magnetic field intensity (H). The nature of all the curves is practically the same. The difference lies in the fact that, as the magnetic field intensity increases, an increase occurs both in (H) and in the temperature at which the magnetorestriction reduces to zero.

Annealing the sample at 573 K leads to a radical change in the course of the curves $\lambda(T)$ (Fig. 2). First of all, a considerable increase in the magnitude of λ is observed. Secondly, after dropping almost to zero at a certain temperature, λ once more begins to increase, passes through a flattened maximum, and finally becomes equal to zero at a low temperature around 180 K. As in the previous case, increasing the magnetic field intensity causes a considerable increase both in λ and in the temperature at which it drops to zero for the first time. However, for all values of H, λ goes to zero at practically the same temperature after it passes through its maximum. Curves *1* and *2* exhibit weak kinks at 85 K.

After high-temperature (873 K) annealing of the sample (Fig. 3) the functions $\lambda(T)$ differ from the curves discussed above. The differences basically reduce to the following: the kink in curves *1* and *2* at 85 K becomes more marked, the temperature at which λ equals zero shifts towards lower values and, in contrast to the curves for the previous state of the structure, no additional maximum is observed.

Finally, we should pause to examine curve *4* in all three figures. These curves were plotted for all the structural states after a short-time exposure to a magnetic field intensity

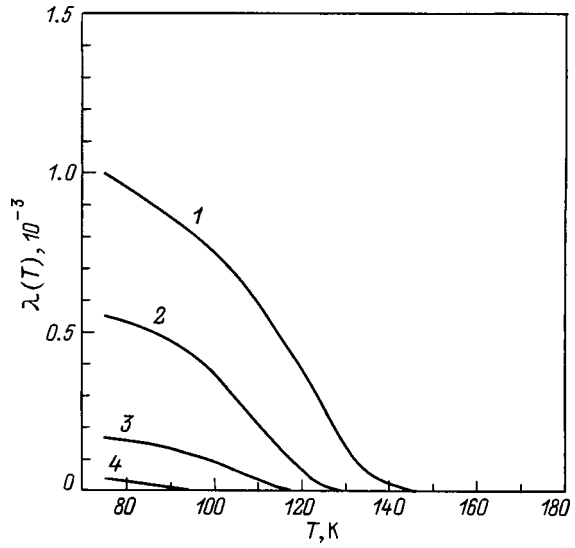

FIG. 1. Plots of magnetostriction versus temperature for Dy in its submicrocrystalline state plotted at various fields. H, kA/m: *1* — 620, *2* — 320, *3* — 130, *4* — 0 (in a state with residual magnetization).

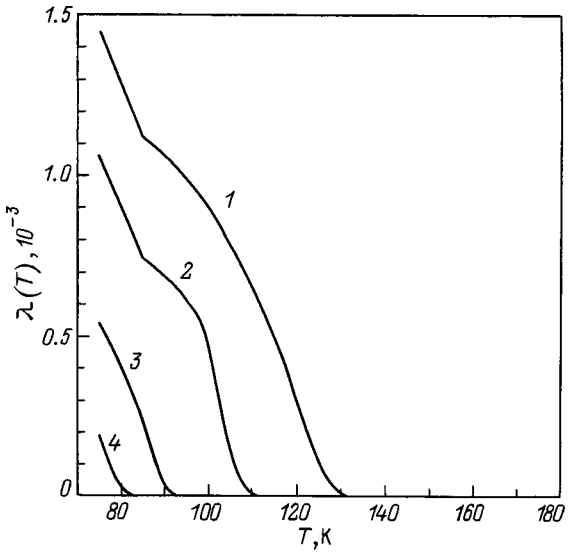

FIG. 3. Plots of magnetostriction versus temperature for Dy after annealing at 873 K, taken at the same fields as in Fig. 1.

$H=$ 800 kA/m, which endows the states with residual magnetization. It is clear from the figures that after the magnetic field is switched off the sample is left with a residual increase in length for all structural states. Whereas this increase is rather small in the submicrocrystalline state, it becomes sizable after annealing. The curve *4* that corresponds to a sample annealed at 573 K (see Fig. 2) exhibits a sharp maximum at 85 K. Moreover, in contrast to curves *1–3*, the flattened maximum in the temperature range 110–180 K is not observed on curve *4*.

Thus, for various structural states of the same sample, the curves $\lambda(T)$ have entirely different forms. What is the origin of this difference? Obviously, it is connected with peculiarities in the structure of each of the states. Electron-microscopy shows that the structure in the submicrocrystalline state consists of microcrystallites with sizes no larger than 200 nm, and the density of dislocations is $10^{12}\,\mathrm{cm}^{-2}$. *X*-ray structural analysis does not reveal any other phase states either in the submicrocrystalline or large-grain crystalline states. We report the results of this structural analysis in more detail in Ref. 1.

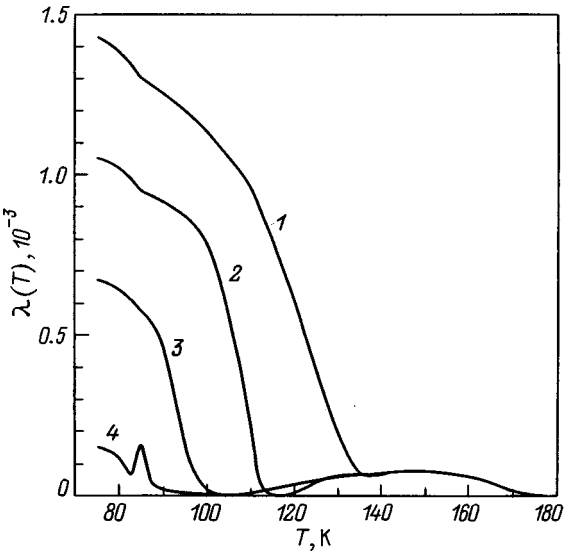

FIG. 2. Plots of magnetostriction versus temperature for Dy after annealing at 573 K, taken at the same fields as in Fig. 1.

3. DISCUSSION OF RESULTS

We wish to emphasize before all else that our measurements of the magnetostriction were made at field intensities below the critical field, since fields higher than the critical field destroy the helical antiferromagnetic ordering (for Dy we have $H_{cr}=880$ kA/m; see Ref. 3). This allows us to identify peculiarities in the way this type of ordering affects the magnetostriction of Dy in the various structural states.

Let us consider the usual large-grain crystalline state. The kinks on curves *1* and *2* are obviously connected with the ferromagnetic-helical antiferromagnetic transition. The nonzero magnetostriction above 85 K arises from reconstruction of the helical antiferromagnetic order driven by the external magnetic field. Evidence of this is the fact that the temperature at which λ reduces to zero increases with increasing H. Consequently, the larger H is, the higher is the temperature up to which it can keep the magnetic moments of the atoms parallel to the field.

Turning from the ordinary large-grain state to the state with submicrocrystalline structure, we begin by noting that λ decreases considerably. These smaller values of λ are probably evidence that some portions of the volume in the submicrocrystalline structure cannot support ferromagnetic ordering at all, due to the high density of defects. In fact, a high density of defects should lead to a change in the equilibrium interatomic distances. Fluctuations of these interatomic distances can change not only the magnitude but also the sign of the exchange interaction. As a result, the medium can enter the so-called ''spin-glass state,'' characterized by a random (noncollinear) distribution of atomic magnetic moments.[8]

We mentioned above that the curves $\lambda(T)$ corresponding to the submicrocrystalline state exhibit no kink at 85 K and decrease smoothly to zero at very high temperatures. The absence of the kink indicates that a sample in the submicrocrystalline structural state exhibits no helical antiferromagnetic order anywhere within the temperature range we are looking at below its transition to the paramagnetic state. Probably this is associated with the impossibility of generating magnetic systems as complicated as helical antiferromagnetic order in crystals of such small size. We were led to an analogous conclusion in Refs. 1, 2, and 9. In describing the results of our investigations, we mentioned above that the values of temperature at which λ reduces to zero do not coincide in the large-scale and submicrocrystalline states, although measurements were made at the same values of H. Thus, in the submicrocrystalline state λ decreases to zero at 140 K when $H=620\,\mathrm{kA/m}$. However, this temperature is not the Curie point of the magnetic phase, since it depends on the value of H. In this case, the external magnetic field apparently imposes a preferred orientation on the magnetic moments of the atoms.

The high-temperature maximum observed on the curves $\lambda(T)$ after annealing at 573 K is in all probability caused by nonuniformity of the structure. During annealing, recrystallization begins, leading not only to an increase in the size of the crystallites but also to repair of their structure. In crystallites whose dimensions correspond to a perfect structure, the conditions for generating helical antiferromagnetic order can arise. In this case some portion of unrecrystallized volume will remain, in which the ferromagnetic order that was present before the recrystallization is preserved. The maximum in the magnetostriction observed in the temperature range from 100 to 170 K is apparently caused by a phase that appears within this temperature range.

Finally, we wish to emphasize that the course of curves *4* in all the figures confirms the explanation of our results given above. In fact, for the large-grain state this curve goes to zero at 85 K, i.e., λ arises only from the residual magnetization of the ferromagnetic order, and without an external field, there is no destruction of the helical antiferromagnetic order. In the submicrocrystalline state, λ disappears for all temperatures above 85 K. In this case the disappearance of λ is caused not by the appearance of helical antiferromagnetic order, but rather the effect of temperature on the residual magnetization. The sharp peak that appears on curve *4* in the intermediate structural state is not entirely understood yet.

In conclusion we are grateful to S. A. Nikitin for providing the pure dysprosium.

[1] Kh. Ya. Mulyukov, G. F. Korznikova, and S. A. Nikitin, Fiz. Tverd. Tela (St. Petersburg) **37**, 2481 (1995) [Phys. Solid State **37**, 1359 (1995)].
[2] Kh. Ya. Mulyukov, G. F. Korznikova, and S. A. Nikitin, J. Appl. Phys. **79**, 8584 (1996).
[3] S. A. Nikitin, *Magnetic Properties of Rare-Earth Metals and Their Alloys* [in Russian] (Moscow State Univ. Publ., Moscow, 1989).
[4] Kh. Ya. Mulyukov, I. Z. Sharipov, and S. A. Nikitin, Fiz. Met. Metalloved. **81**, 70 (1996).
[5] Kh. Ya. Mulyukov, G. F. Korznikova, I. Z. Sharipov, and S. A. Nikitin, Fiz. Tverd. Tela (St. Petersburg) **38**(12), 3602 (1996) [Phys. Solid State **38**, 1963 (1996)].
[6] Kh. Ya. Mulyukov, I. Z. Sharipov, and G. F. Korznikova, Fiz. Met. Metalloved. **83**(1), 89 (1997).
[7] I. Z. Sharipov and Kh. Ya. Mulyukov, Prib. Tekh. Éksp. **5**, 143 (1996).
[8] I. Ya. Korenblit and E. F. Shender, Izv. Vyssh. Uchebn. Zaved. Fiz. **10**, 23 (1984).
[9] Kh. Ya. Mulyukov, I. Z. Sharipov, and S. A. Nikitin, Fiz. Tverd. Tela (St. Petersburg) **38**, 1629 (1996) [Phys. Solid State **38**, 899 (1996)].

Translated by Frank J. Crowne

Fluctuation-induced broadening of Mn^{2+} EPR lines in the incommensurate phase of Rb_2ZnCl_4 crystals

M. P. Trubitsyn

Dnepropetrovsk State University, 320625 Dnepropetrovsk, Ukraine
(Submitted December 29, 1998)
Fiz. Tverd. Tela (St. Petersburg) **41**, 1668–1674 (September 1999)

The EPR spectra of Mn^{2+} ions in Rb_2ZnCl_4 crystals is investigated in the vicinity of the transition from the paraelectric phase to an incommensurate modulated phase. When these crystals are cooled below the transition temperature $T_i = 304$ K, a splitting of the resonance lines is observed in the singular spectrum. A one-harmonic model is used to discuss the contributions that fluctuations in the amplitude and phase of the incommensurate displacement wave make to the local width of the singular spectra. It is shown that anomalies in the local width of the low-temperature singular peaks observed in the vicinity of T_i are caused by amplitude fluctuations. © *1999 American Institute of Physics.* [S1063-7834(99)02809-9]

When a material undergoes a transition from a high-temperature paraelectric phase to a low-temperature modulated incommensurate phase, the appearance of an incommensurate wave of lattice displacements below the transition point T_i leads to a loss of translational periodicity along the modulation axis. As a result, when samples of such a material are cooled below T_i, discrete magnetic resonance lines observed in the commensurate paraelectric are transformed into a quasicontinuous distribution of resonance fields (frequencies) bounded on each side by maxima in the absorption intensity (singular peaks).[1,2] As T_i is approached from above, the condensation of pairs of soft modes that are degenerate in the paraelectric phase leads to lifting of the degeneracy and the appearance of two modes in the vibrational spectrum of the incommensurate crystal, which, in the harmonic approximation, are comparable to oscillations in the amplitude and phase of the wave of incommensurate displacements.[1,3]

In this paper we investigate EPR lines of Mn^{2+} centers isovalently substituting for Zn^{2+} ions in the lattice of Rb_2ZnCl_4 crystals.[4,5] In the paraelectric phase, the crystal lattice of Rb_2ZnCl_4 corresponds to space group $D_{2h}^{16} - Pnam$ $(b>a>c)$. A sample of this material cooled below $T_i = 303$ K enters an incommensurate phase, accompanied by the appearance of periodic structural distortions with wave vectors $\mathbf{q}_i = (1/3 - \delta)\mathbf{a}^*$.[6,7] In the paraelectric phase, Mn^{2+} centers are located on the mirror plane (**ab**) and have multiplicity $k_m = 2$. The fine structure of the Mn^{2+} spectra can be described within the quasirhombic approximation using the following values of parameters of the spin Hamiltonian: $g = 2.004$, $|D| = 449 \times 10^{-4}$ cm^{-1}, $|E| = 85 \times 10^{-4}$ cm^{-1}.[5] The transition to the incommensurate phase locally disrupts the mirror plane (**ab**), and a splitting of the resonance lines in the singular spectrum can be measured experimentally. This is evidence that the point symmetry of the paramagnetic centers has decreased to triclinic. The goal of this paper is to study how fluctuations in the modulated wave contribute to the local width of the singular spectra.

1. EXPERIMENTAL RESULTS

The samples under study were made in the form of parallelepipeds with dimensions $2 \times 2 \times 3$ mm^3 from single crystals grown by the Czochralsky method.[5] The EPR spectra were measured at *X*-band. The temperature of the samples was regulated by heating in liquid nitrogen vapor and stabilized to an accuracy of 0.1 K.

At the measurement temperatures, the high-field electronic transition $|M_S| = 3/2 \leftrightarrow 5/2$ was detected, both with the external magnetic field **H** oriented along the **a** axis and with (**H**) slightly misoriented from **a** in the direction of the **c** axis. The temperature dependences of the corresponding hyperfine sextet measured as the sample was cooled through the transition are shown in Figs. 1 and 2a.

For the principal orientation $\mathbf{H} \| \mathbf{a}$ (Fig. 1), the group of lines under study did not change noticeably as the temperature approached the transition point from above. Below $T_i = 304.4$ K a smooth splitting of the sextet was observed. Each of the hyperfine components transforms into its own singular contour, and six singular spectra are observed in the incommensurate phase, shifted relative to each other by the value of the hyperfine constant. The magnitude of the singular peak splitting increases with decreasing temperature, until it exceeds the spacing between neighboring hyperfine lines (~ 8 mT) below $\sim T_i - 10$ K. It is clear from Fig. 1 that, when the samples are cooled to within the range of the incommensurate phase, the position of the high-field sextet of singular peaks depends only slightly on temperature, whereas the low-field group of peaks shifts appreciably toward lower fields. Also noteworthy is an asymmetry of high- and low-field singularities corresponding to an isolated hyperfine component, which manifests itself as differences in their local widths.

When the external magnetic field **H** is inclined to the **a** axis by 7° (Fig. 2a), the temperature-induced transformation of these spectra occurs more abruptly in the neighborhood of the phase transition. As T_i^+ is approached from above, the hyperfine sextet broadens significantly, due to the contribu-

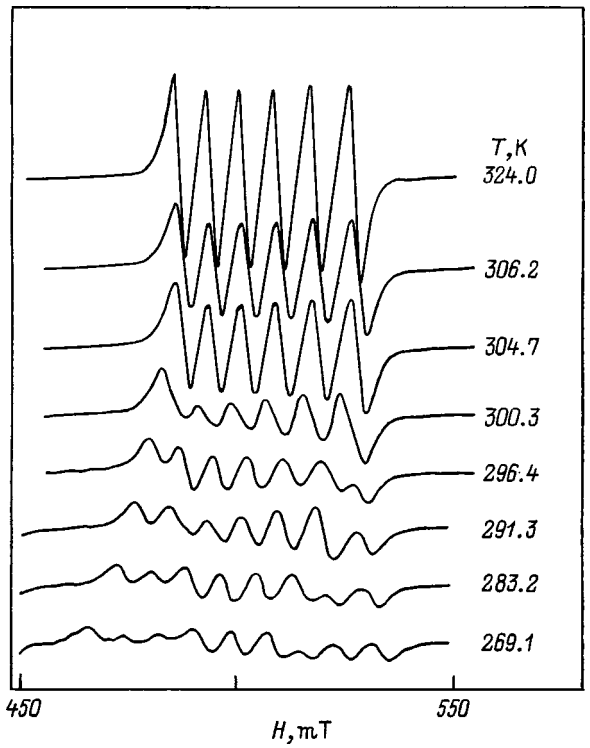

FIG. 1. Fragment of EPR spectra from a $Rb_2ZnCl_4:Mn^{2+}$ crystal corresponding to the hyperfine group $|M_S|=3/2\leftrightarrow 5/2$, in the neighborhood of $T_i=$ 304.4 K. $\mathbf{H}\|\mathbf{a}$.

tion of low-frequency fluctuations of the order parameter.[8,9] Below T_i^+, each of the hyperfine components splits into a spectrum bounded by two singular peaks. For this orientation the positions of both singularities depend strongly on temperature. Both groups of singular peaks exhibit anomalies in the local widths near T_i^-: this anomaly is more striking for the low-field singular sextet. It is characteristic that for the oblique orientation the asymmetry of the singular spectrum manifests itself more clearly, and is observed both in the immediate vicinity of the transition point and also at temperatures further into the incommensurate-phase temperature range.

In Ref. 10 it was shown that a satisfactory description of the temperature behavior of the positions of the singular peaks corresponding to the transition $|M_S|=3/2\leftrightarrow 5/2$ in the high- temperature range of the incommensurate phase for crystals of $Rb_2ZnCl_4:Mn^{2+}$ can be obtained based on a simple ''local'' model.[1] However, it is not possible to explain the asymmetry in the singular spectra (Figs. 1 and 2a) within the framework of an approximation involving a ''rigid'' lattice, which only incorporates the dependence of the position of the resonance signals on the phase of the modulated wave. It is obvious that since the local width of the resonance contains fluctuation-induced components, it also must be a function of the phase of the incommensurate wave. We believe that once this dependence is included we will be able to describe the asymmetric shape of the spectral contour and identify the contributions of amplitude and phase fluctuations to the local width of the singular spectrum.

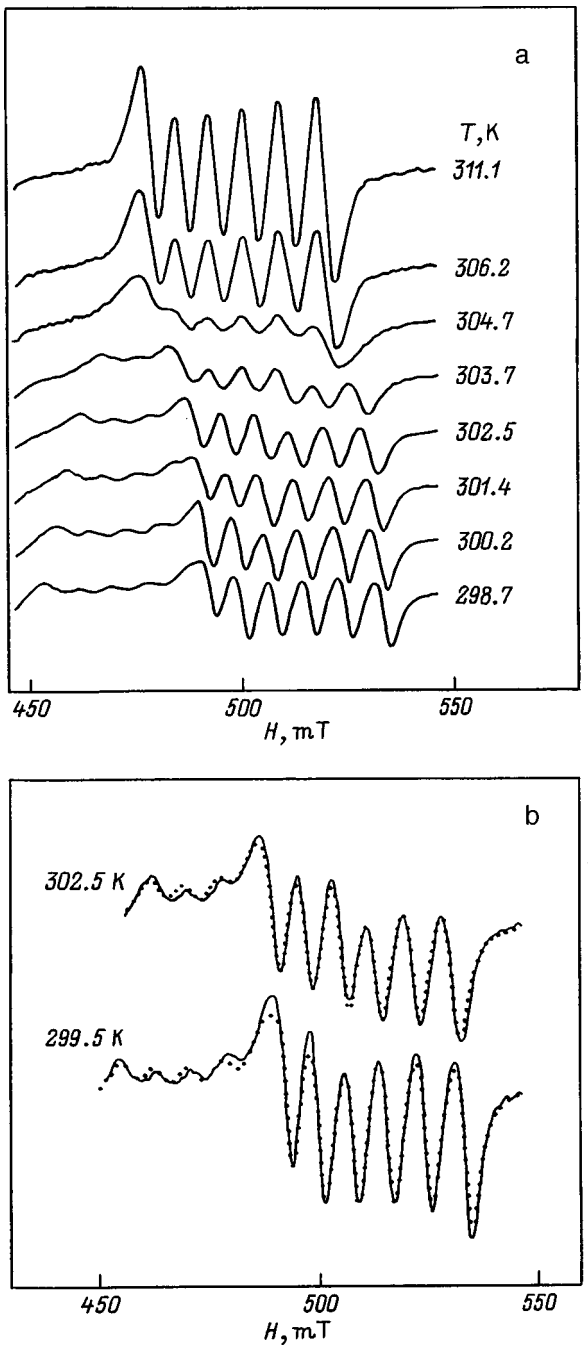

FIG. 2. a—hyperfine group $|M_S|=3/2\leftrightarrow 5/2$ for a sample cooled through the transition. $\angle\mathbf{H,a}=7°$, $\mathbf{H}\perp\mathbf{b}$; b—experimental spectra are solid curves, the dots are calculated.

2. FLUCTUATIONAL CONTRIBUTIONS TO THE LOCAL WIDTH OF THE SINGULAR SPECTRUM

In describing EPR spectra from a sample in the modulated phase, we can treat the wave of incommensurate displacements **U** as a ''perturbing'' parameter, in which case the corresponding spin Hamiltonian can be written in the form

$$\mathscr{H}_{INC}=\mathscr{H}_{PP}+U\mathscr{H}'. \tag{1}$$

Here $\mathscr{H}_{PP}$ is the quasirhombic spin Hamiltonian used previously[5] to describe the spectra of Mn^{2+} in the paraelec-

tric phase with the parameters listed above; the ''perturbing'' spin Hamiltonian $\mathscr{H}'$ contains ''triclinic'' spin operators that are responsible for the decrease in local symmetry of the active centers below T_i.[11] In accordance with Eq. (1), the resonance fields can be written in the form of an expansion in powers of the time-dependent incommensurate order parameter $U(t)=U_0+\delta U(t)$:

$$H_R(t)=H_0+AU+\frac{1}{2}BU^2+\ldots$$
$$=\left[H_0+AU_0+\frac{1}{2}B(U_0^2+\langle\delta U^2\rangle)\right]$$
$$+\left\{(A+BU_0)\delta U+\frac{1}{2}B(\delta U^2-\langle\delta U^2\rangle)\right\}. \quad (2)$$

In Eq. (2), H_0 corresponds to the position of the resonance line in the paraelectric phase, and is calculated from the spin Hamiltonian $\mathscr{H}_{PP}$. The expansion parameters A,B depend on the position of the active center in the unit cell and the direction of the external magnetic field relative to the crystal axes. In this case the coefficient A for the linear term is determined by the diagonal matrix elements, while the parameter B in the quadratic term contains nondiagonal matrix elements of the ''perturbing'' spin Hamiltonian $\mathscr{H}'$. On the second line of (2) we have rewritten the expansion, using brackets to separate the static and dynamic parts. The static part determines the shift in the position of the resonance induced by the order parameter, while the dynamic part describes the contribution of fluctuations to the width and shape of the resonance line.

Since, in the high-temperature range of the incommensurate phase, the structural displacements are determined by the first harmonic of the modulation wave, the order parameter can be written $U=\rho\cos\varphi(z)$, where $\rho=\text{const}(z)$, $\varphi=q_1z+\psi_0$. Taking Eq. (2) into account, the position of the singular peaks is determined from the condition[1]

$$|d\langle H_R\rangle/d\varphi|=0.$$

The contributions of fluctuations to the local width of the singular spectrum can be expressed in terms of the second moment of the resonance signal, corresponding to a preset value of the phase of the modulated wave:

$$\delta H^2=4(\langle H_R^2\rangle-\langle H_R\rangle^2).$$

In discussing the local width of the resonance, we must take into account that the soft-mode dynamics are usually overdamped near the transition point. Hence, the spin—lattice relaxation is determined by one-phonon processes and, in discussing the critical contributions to the dynamic part (2), it is sufficient to retain terms that are linear in the fluctuations of the critical variable $\delta U=\delta\rho\cos\varphi_0-\delta\varphi\sin\varphi_0$, where the amplitude and phase are written in the form of a sum of static and fluctuating parts $\rho(t)=\rho_0+\delta\rho(t)$, $\varphi(t)=\varphi_0+\delta\varphi(t)$. The dynamic two-phonon term $\{1/2B(\delta U^2-\langle\delta U^2\rangle)\}$ in Eq. (2) can be neglected near the transition. Moreover, if we consider only the long-wavelength part of the spectrum near the critical value q_i, we may treat the parameters A and B as independent of the wave vector of the order-parameter fluctuations. Consequently, they may be taken to be the same for the static and dynamic parts of the expansion (2).

If we can neglect the quadratic term in Eq. (2) ($B=0$), the spectral contour is bounded by two singular peaks, corresponding to active centers that are maximally displaced in the wave of incommensurate distortion. The positions of these singular peaks are given by the expressions

$$H_{L1,L2}=H_0\pm H_1, \quad (\varphi_0=0,\pi);$$
$$H_1=A\rho_0\sim(T_i-T)^{\beta}, \quad (3a)$$

where β is the critical index of the order parameter. From Eq. (3a) it is clear that cooling displaces the singular peaks symmetrically with respect to H_0, in agreement with the increase in amplitude ρ_0. For linear coupling of the resonance fields to the order parameter, the dependence of the local width on the phase φ_0 in the dynamic limit[1,12] can be written in the form

$$\delta H(\varphi_0)\sim h_1^2\{\Delta_\rho(0)\cos^2(\varphi_0)+\Delta_\varphi(0)\sin^2(\varphi_0)\},$$
$$h_1=H_1/\rho_0. \quad (3b)$$

Here $\Delta_{\rho,\varphi}(0)$ are parameters related to the spectral density of the amplitude and phase fluctuations. Since for linear coupling the resonance fields are determined by the diagonal matrix elements of the spin Hamiltonian $\mathscr{H}'$, the critical contributions to the line width reflect the spectral density of fluctuations at zero frequency.[13] Expression (3b) shows that it is the amplitude fluctuations that make the maximum contribution to the local width of the singular peaks $H_{L1,L2}$ in Eq. (3a), whereas the contribution of phase fluctuations is a maximum in the central flattened portion of the singular spectrum $H_R=H_0(\varphi_0=\pm\pi/2)$.

If the linear term in Eq. (2) is forbidden by symmetry constraints ($A=0$), the spectral contour is bounded by two singular peaks corresponding to undisplaced ($\varphi_0=\pm\pi/2$) and maximally displaced ($\varphi_0=0,\pi$) active centers in the modulated wave

$$H_{Q1}=H_0, \quad (\varphi_0=\pm\pi/2);$$
$$H_{Q2}=H_0+\frac{1}{2}H_2, \quad (\varphi_0=0,\pi);$$
$$H_2=B\rho_0^2\sim(T_i-T)^{2\beta}. \quad (4a)$$

The position of the singular peak H_{Q1} corresponds to the position of the line H_0 in the high-temperature phase, whereas the other peak H_{Q2} moves relative to H_0 as the sample is cooled with a shift proportional to the square of the amplitude $\rho_0^2\sim(T_i-T)^{2\beta}$. If we retain only the term containing the first power in δU in the dynamic part of (2), we can obtain the local width in the limit of rapid fluctuations:[12]

$$\delta H(\varphi_0)\sim h_2^2\{\Delta_\rho(\omega_{RES})\cos^4(\varphi_0)$$
$$+\Delta_\varphi(\omega_{RES})\cos^2(\varphi_0)\sin^2(\varphi_0)\},$$
$$h_2=H_2/\rho_0. \quad (4b)$$

For quadratic coupling to the order parameter, the resonance fields are determined by the nondiagonal matrix elements of

the spin Hamiltonian $\mathscr{H}'$. Therefore the parameters $\Delta_{\rho,\varphi}(\omega_{RES})$ in Eq. (4b) are a measure of the spectral density of local fluctuations at EPR frequencies $\omega_{RES}\sim 10^{10}$ Hz.[13] According to Eqs. (4a) and (4b), amplitude fluctuations contribute to the local width of the singular peak H_{Q2}, whereas the contribution of phase fluctuations will be a maximum in the middle part of the singular spectrum for $H_R=H_0+(1/4)H_2$ ($\varphi_0=\pm\pi/4$). In this case the local width of the peak H_{Q1} ($\varphi_0=\pm\pi/2$) does not contain fluctuation-induced contributions, and is determined by noncritical processes.

If it is necessary simultaneously to include the linear and quadratic terms in Eq. (2), where the linear term dominates ($H_1>|H_2|$), as we enter the incommensurate phase, the spectrum will be bounded by two singular peaks

$$H_{L1,L2}=H_0\pm H_1+\frac{1}{2}H_2, \quad (\varphi_0=0,\pi). \tag{5a}$$

In discussing fluctuation-induced contributions we must keep in mind that the dynamic component of the linear term is determined by the spectral density of quasistatic fluctuations, whereas the dynamic part of the quadratic term is determined by fluctuations with the resonance frequencies $\sim 10^{10}$ Hz. We can simplify the expression for the local width by assuming that the spectral density of the critical fluctuations does not change appreciably in the frequency range $0-0.32\,\mathrm{cm}^{-1}$ ($\sim 10^{10}$ Hz). For Rb_2ZnCl_4 this requirement is probably satisfied within a wide temperature interval around T_i, where the soft mode is strongly over- damped.[14] Then we can obtain the following expression for the local width in the limit of rapid motion:

$$\delta H(\varphi_0)\sim(h_1+h_2\cos(\varphi_0))^2\{\Delta_\rho\cos^2(\varphi_0)+\Delta_\varphi\sin^2(\varphi_0)\}. \tag{5b}$$

From this it is clear that, when the linear term in Eq. (2) dominates, we will see two linearly-split singular peaks in the incommensurate phase as well, whose local widths will differ considerably due to the quadratic contribution. For peak H_{L1} ($\varphi_0=0$) the local width $\delta H_{L1}\sim(h_1+h_2)^2\Delta_\rho$, whereas for H_{L2} ($\varphi_0=\pi$) the width $\delta H_{L2}\sim(h_1-h_2)^2\Delta_\rho$.

The quantities $\Delta_{\rho,\varphi}$ entering into Eqs. (3b)–(5b) are related to the corresponding susceptibilities $\chi_{\rho,\varphi}$ of the amplitude and phase modes and, in the dynamic approximation,[12] can be written in the form

$$\Delta_\alpha\sim k_BT\sum_q\chi_\alpha^2(q),$$

where k_B is Boltzmann's constant, $\alpha=\rho,\varphi$, and the summation runs over wave vectors in the Brillouin zone. By writing χ_α in the form of the susceptibility of a harmonic oscillator with damping, it can be shown that the contribution of the amplitude mode depends critically on nearness to the transition temperature: $\Delta_\rho\sim(T_i-T)^{-\nu}$ (where ν is the critical index of the correlation length).[1,12] Conversely, the contribution of the phase mode is temperature independent. For an ideal incommensurately modulated structure the susceptibility χ_φ is infinitely large at a critical value of the wave vector q_i over the whole temperature range of the incommensurate phase for which the single-harmonic approximation is valid. When ''pinning'' of the modulated wave is possible due to imperfections in the structure, a gap appears in the spectrum of phase fluctuations. In this case the susceptibility χ_φ and, accordingly, the contribution Δ_φ of phase fluctuations to the local width of the EPR signal is, as before, temperature-independent and determined by the width of the gap in the spectrum of phase modes.[1,3]

In the next section we will show that the relations presented here allow us to describe the primary features of the experimental spectra (Figs. 1 and 2a).

3. PROCESSING OF SPECTRA AND DISCUSSION OF RESULTS

Modeling the experimental spectra in the paraelectric phase is done by convolving the derivative of a Lorentzian function with a Gaussian distribution. The output parameters of this processing procedure—the line position, and its homogeneous and inhomogeneous broadening components—allowed us to achieve a good agreement between calculated and experimental spectra.[9]

In modeling spectra in the incommensurate phase, it clearly would be advantageous to use the procedure of convolving a Lorentzian with a Gaussian, in order to identify the static and dynamic contributions to the local width of the singular spectrum. However, when this approach is used in practice the fitting procedure includes a large number of parameters, the reliability of whose determination is significantly degraded. Therefore, we assume that an isolated active center corresponds to a Lorentzian with a position H_R and width δH determined by the amplitude and phase of the incommensurate wave. The spectral form is modeled according to the method of least squares with the help of the expression

$$\int_0^{2\pi}L\{[H-H_R(\varphi_0)]/\delta H(\varphi_0)\}d\varphi_0. \tag{6}$$

Since (**ab**) is a plane of symmetry for the Mn^{2+} centers, which is disrupted when the sample enters the incommensurate phase, for the magnetic field orientation $\mathbf{H}\|\mathbf{a}$ the linear term in the expansion (2) is forbidden. The temperature dependence of the position of the singular peaks (the inset to Fig. 3) agrees in its primary features with expressions (4a): the position of the high-field singularity H_{Q1} corresponds approximately to the drift H_0, extrapolated in the incommensurate phase, whereas the other singularity H_{Q2} shifts at low fields (H_2, $B<0$).[10] In modeling spectra obtained in the incommensurate phase with $\mathbf{H}\|\mathbf{a}$, we write the local width in Eq. (6) in a form analogous to Eq. (4b):

$$\delta H(\varphi_0)=\delta H_{BGR}+[\delta H_\rho\cos^4(\varphi_0)+\delta H_\varphi\cos^2(\varphi_0)\sin^2(\varphi_0)]. \tag{7}$$

In Eq. (7) we have expressed the contributions of the amplitude and phase fluctuations in terms of $\delta H_{\rho,\varphi}$. The quantity δH_{BGR} serves as a background component that is independent of φ_0 and which gives a uniform contribution to the width of the singular spectrum as a whole. It should be noted that in this method of analyzing the line shapes we can determine the local width of the singular peaks with satisfac-

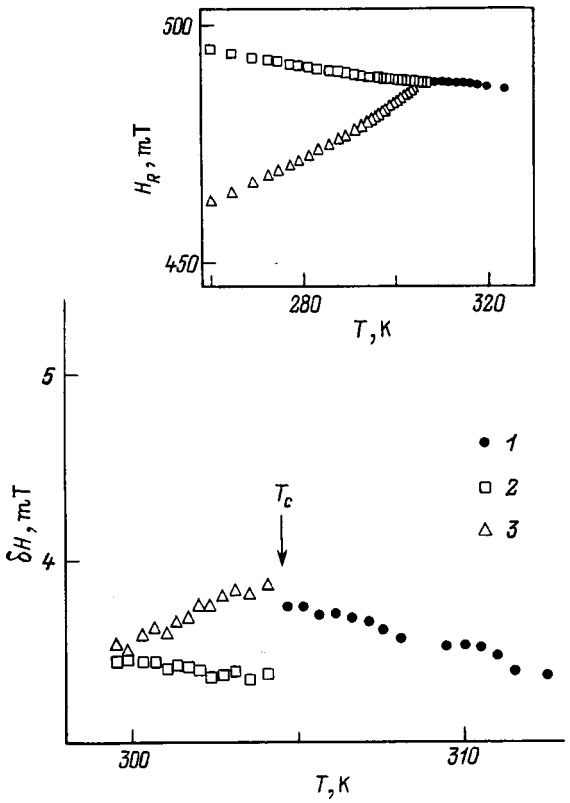

FIG. 3. Temperature dependence of the width of the hyperfine component of the transition $|M_S|=3/2\leftrightarrow 5/2$ above T_i (*1*) and the local widths of the singular peaks δH_{Q1} (*2*) and δH_{Q2} (*3*) below T_i. $\mathbf{H}\|\mathbf{a}$. The inset shows the temperature dependence of the positions of the hyperfine lines above T_i and the singular peaks H_{Q1}, H_{Q2} in the incommensurate phase.

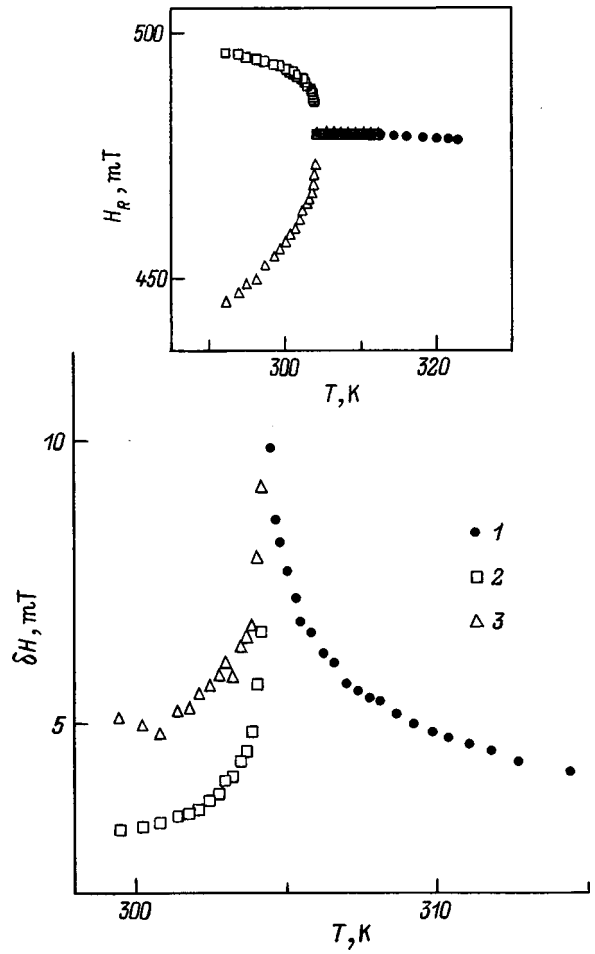

FIG. 4. Temperature dependence of the width of the line (*1*) above T_i and the local widths of the singular peaks δH_{L1} (*2*) and δH_{L2} (*3*) below T_i. $\angle\mathbf{H},\mathbf{a}=7°$, $\mathbf{H}\perp\mathbf{b}$. The inset shows the temperature dependence of the position of the lines in the paraelectric phase and the singular peaks H_{L1}, H_{L2} in the incommensurate phase.

tory accuracy. According to Eqs. (5) and (7), the local width of peak H_{Q1} ($\varphi_0=\pm\pi/2$) is determined by the background component

$$\delta H_{Q1}=\delta H_{BGR}.$$

Conversely, the local width of peak H_{Q2} ($\varphi_0=0,\pi$) is determined by the sum

$$\delta H_{Q2}=(\delta H_{BGR}+\delta H_\rho)$$

and accordingly should reflect the critical behavior of the amplitude fluctuations as T_i^- is approached. The contribution from phase fluctuation δH_φ is important only for the central flattened portion of the incommensurate spectrum. In modeling the line shape, the mean-square deviation of the calculated spectra from the experimental values is not very critical compared to variations in δH_φ. Therefore, the modeling procedure does not allow us to determine reliably the parameter δH_φ and arrive at any conclusions about its temperature dependence. In fitting the calculated spectra, the quantity δH_φ varies statistically relative to an average value of ~ 0.2 mT in the temperature interval under study.

The dependences we obtained for the local widths δH_{Q1} and $\delta H_{Q2}$of the singular peaks are shown in Fig. 3. Above T_i this figure shows the dependence of the total width of the hyperfine component. It is clear that, as we approach the transition point from above, the lines undergo very little broadening due to the contribution of nondiagonal matrix elements of the spin Hamiltonian $\mathscr{H}'$.[9] The local width δH_{Q2} of the low-field singularity near T_i^- also undergoes a weak anomaly due to the contribution of amplitude fluctuations. The width δH_{Q1} of the high-field singular peak is practically independent of temperature, which is a natural result of the absence of any fluctuating components.

For the oblique orientation $\angle\mathbf{Ha}=7°$ the linear term in Eq. (2) is no longer forbidden, and the latter becomes the dominant contribution to the position of the singular peaks, whose temperature dependence (see Fig. 4 inset) is well described by relations (5a).[10] In modeling the spectra for the local width we use the following expression analogous to Eq. (5b):

$$\delta H(\varphi_0)=\delta H_{BGR}+[h_1/h_2+\cos(\varphi_0)]^2\{\delta H_\rho\cos^2(\varphi_0)+\delta H_\varphi\sin^2(\varphi_0)\}. \quad (8)$$

It is obvious that when the linear term is zeroed out ($h_1=0$) Eq. (8) reduces to Eq. (7), which we used to process the spectra measured in the principal orientation of the external magnetic field. The ratio of parameters h_1/h_2 is determined by the positions of the singular peaks in accordance with Eq. (5c).[10] A comparison of the calculated spectra with the ex-

perimental spectra is shown in Fig. 2b. As in previous cases, analysis of the shape of the singular spectra allows us to determine only the widths of the singular peaks with reasonable accuracy which, in accordance with Eq. (8), are given by the expressions

$$\delta H_{L1,L2} = \delta H_{BGR} + [h_1/h_2 \pm 1]^2 \delta H_\rho, \quad (\varphi_0 = 0, \pi). \tag{9}$$

The data obtained are shown in Fig. 4. As we cool toward the transition point from above, the resonance line undergoes a marked anomaly in width, which, as shown in Ref. 9, is caused by an increase in the spectral density of low-frequency fluctuations. Below T_i both singular peaks also exhibit anomalous widths. Although the use of Eq. (6) to analyze the line shape in the incommensurate phase prevents us from separating the homogeneous and inhomogeneous components of the anomalous contribution to the local width, it is natural to assume that the width of the peaks below T_i is also caused by quasistatic amplitude fluctuations. It is remarkable that the low-field singular peak is characterized by a large local width both in the immediate vicinity of the transition point and as we move away from it. Based on Eq. (9), we can explain this by the differing signs of the parameters $h_1 > 0$, $h_2 < 0$, evidence for which is the temperature behavior of the position of the singular peaks (the inset to Fig. 4).[10]

The results of processing these experimental spectra are qualitative in nature. The expressions used to model the spectra for the local width were obtained in the limit of rapid fluctuations,[12] and do not take into account effects of inhomogeneous broadening. Therefore, they allow us only to make judgements regarding the primary outline and sources of the fluctuation-induced broadening of singular spectra.

In a previous paper,[15] Kazba and Fayet investigated the local width of EPR spectra of Mn^{2+} ions in crystals of Rb_2ZnCl_4 in their incommensurate phase. The singular spectra they obtained, for both principal and oblique orientations of the external field, were discussed using a model with an exclusively linear contribution to the local width, i.e., expressions of the form Eq. (3b) were used to process the spectra. This assumes that the local width of one of the singular peaks both principal and oblique field orientations is determined by the contribution from amplitude fluctuations, and of other by the contribution from phase fluctuations. Based on the temperature dependence of the local width of the singular peaks, these authors infer certain properties of the latter, namely that the contribution from amplitude fluctuations exhibits critical behavior while the contribution of the phase mode is temperature-independent.

In contrast, the results of this paper were obtained by assuming that one-phonon processes dominate in the vicinity of the transition point. The expressions we have derived here show that for an external magnetic field in principal orientation, which ensures quadratic coupling of the resonance fields to the order parameter, the width of one of the peaks is determined only by fluctuations in the amplitude of the incommensurate wave. The width of the other peak is unrelated to fluctuation-induced contributions to the phase mode, as assumed in Ref. 15. Rather, it is a product of insignificant background mechanisms, and thus gives no evidence of anomalies near T_i. Analysis of spectra measured in obliquely oriented fields also indicate that expressions of the form Eq. (3b), which were used in Ref. 15, are inapplicable since the influence of the quadratic term responsible for asymmetry of the singular spectrum cannot be neglected. We can summarize our data by saying that for all the external-field orientations we studied, anomalies in the local width of singular peaks near T_i^- were determined by amplitude fluctuations only. Modeling of the shape of the experimental spectra does not allow us to reliably conclude anything about the behavior of the contribution of the phase mode to the local width of the EPR signal. In investigations of this kind the advantages of Fourier radiospectroscopy over traditional methods of EPR measurements are especially obvious.

[1] R. Blinc, Phys. Rep. **79**, 331 (1981).
[2] K. A. Müller and J. C. Fayet, in *Structural Phase Transitions II*, edited by K. A. Müller and H. Thomas (Springer-Verlag, Berlin, 1991) **45**, p. 1.
[3] A. D. Bruce and R. A. Cowley, *Structural Phase Transitions* (Taylor and Francis, Philadelphia, Pa., 1981; Mir, Moscow, 1984).
[4] M. Pezeril, J. Emery, and J. C. Fayet, J. Phys. (France) Lett. **41**, L-499 (1980).
[5] T. M. Bochkova, O. E. Bochkov, S. A. Flerova, and M. P. Trubitsyn, Fiz. Tverd. Tela (Leningrad) **26**, 2170 (1984) [Sov. Phys. Solid State **26**, 1315 (1984)].
[6] K. Gesi and M. Iizumi, J. Phys. Soc. Jpn. **46**, 697 (1979).
[7] K. Itoh, A. Hinasada, H. Matsunaga, and E. Nakamura, J. Phys. Soc. Jpn. **52**, 664 (1983).
[8] A. Kaziba, M. Pezeril, J. Emery, and J. C. Fayet, J. Phys. (France) Lett. **46**, L-387 (1985).
[9] M. P. Trubitsyn, V. I. Pastukhov, and T. M. Bochkova, Fiz. Tverd. Tela (St. Petersburg) **41**, 122 (1999) [Phys. Solid State **41**, 108 (1999)].
[10] M. P. Trubitsyn, Fiz. Tverd. Tela (St. Petersburg) **41**, 691 (1999) [Phys. Solid State **41**, 624 (1999)].
[11] S. A. Al'tshuler and B. M. Kozyrev, *Electron Paramagnetic Resonance of Compounds of Transition Elements* (Nauka, Moscow, 1972; Halsted, New York, 1975),
[12] Th. Von Waldkirch, K. A. Müller, and W. Berlinger, Phys. Rev. B **7**, 1052 (1973).
[13] G. F. Reiter, W. Berlinger, K. A. Müller, and P. Heller, Phys. Rev. B **21**, 1 (1980).
[14] M. Quilichini, J. P. Mathein, M. Le Postollec, and M. Toupry, J. Physique **43**, 787 (1982).
[15] A. Kaziba and J. C. Fayet, J. Physique **47**, 239 (1986).

Translated by Frank J. Crowne

Electron emission in ferroelectrics for different values of the coercive field

A. S. Sidorkin, N. Yu. Ponomarëva, and S. D. Milovidova

Voronezh State University, 394693 Voronezh, Russia
(Submitted January 20, 1999)
Fiz. Tverd. Tela (St. Petersburg) **41**, 1675–1678 (September 1999)

Results are presented of experimental studies of electron emission from single crystals of triglycine sulfate, nominally pure and doped with Cr^{3+}. The relation between the parameters of the processes of switching and electron emission from ferroelectrics by a coercive field and the threshold field for the onset of emission is investigated. It is shown that the temperature and concentration dependences of the threshold field can be explained by the corresponding dependences of the coercive field. © *1999 American Institute of Physics.* [S1063-7834(99)02909-3]

Active studies of ferroelectrics by the method of exoelectron emission were begun at the end of the 1970's. Despite the unflagging scientific and practical interest in this problem, efforts to achieve a satisfactory picture of the onset of electron emission from ferroelectrics has not yet been crowned with success. At present, there has developed a rather long-standing opinion regarding the connection between switching processes in ferroelectrics and the emission effect. It is supported by a number of factors. First, emission is observed, as a rule, only in the ferroelectric phase, where spontaneous polarization is present.[1,2] Second, it appears not simply in the presence of the polar state in the sample, but also under ''freshly prepared'' conditions.[3] Specifically, decay of the emission intensity is described by an exponential law provided the polar state is stable with a relaxation time on the order of several seconds or minutes depending on the observed material.[4,5] in addition, emission is always observed upon repolarization of the sample[6] in a high-frequency field, where the condition of ''freshness'' of the polar state is unquestionably fulfilled.

Taking into account the possibility of charge screening by spontaneous polarization on the surface of the sample by free charge carriers located in the bulk of the material or on its surface, it is natural to assume that the reason for the observed emission is the total uncompensated charge, which appears near the surface of the material when the polar state of the sample is changed. This conjecture, made in Ref. 3 in an attempt to elucidate the nature of thermal emission of electrons in ferroelectrics for emission stimulated by switching was corroborated in Ref. 7 by parallel observations of the emission current and the stimulating electric field. It was shown there that the emission signal is observed only during that half-period of the variation of the external variable field, when a negative uncompensated charge appears near the surface of the sample that is active during emission.

The results of the present work provide new demonstrations of the connection between the phenomena of electron emission from ferroelectrics and switching processes in these materials. Specifically, we discuss the correlation between the most important parameters of these processes—the coercive field of the sample and the threshold field for the onset of emission.

1. MEASUREMENT METHOD AND EXPERIMENTAL RESULTS

The experimental studies of emission reported in this paper were performed on single crystals of nominally pure triglycine sulfate (TGS) and a crystal of TGS doped with chromium in four different concentrations. These doped crystals were grown from solutions with Cr^{3+} ion dopant levels of 0.1, 0.3, 0.6, and 1 molar percent in solution.

The measurements of the emission current density j_{em} were made using the standard method in a vacuum of 6.5×10^{-3} Pa on polar-cut samples with an area of $20-30\,mm^2$ and a thickness of 1 mm with gold-leaf electrodes. Electron emission was measured in the gap region in one of the electrodes. The width of the gap was approximately 1 mm. As the stimulating field we used a sinusoidal electric field with a frequency of 50 Hz. The experiments were conducted in the heating regime (passage through the Curie point T_c starting from the ferroelectric phase) and the cooling regime (passage through T_c starting from the paraelectric phase) in the temperature interval $25-55\,^{\circ}C$. In both cases, the rate of change of the temperature was approximately $0.5\,^{\circ}C$/min.

Our experiments gave the following results. In all of the samples electron emission was recorded directly in the ferroelectric phase at temperatures ranging from the onset of emission T_{beg} to the Curie point T_c (Fig. 1). In these measurements, regardless of the magnitude of the external field stimulating switching in the sample, the position of the high-temperature boundary of the temperature interval in which emission was observed remained unchanged and coincided approximately with the Curie point in the pure material. At the same time, like in samples of the weak ferroelectric lithium heptagermanate,[5] the position of the low-temperature boundary T_{beg} in the investigated crystals depended substantially on the amplitude of the stimulating field, falling with growth of the latter.

Curves of the temperature dependence of the coercive field, calculated from the dielectric hysteresis loops, are dis-

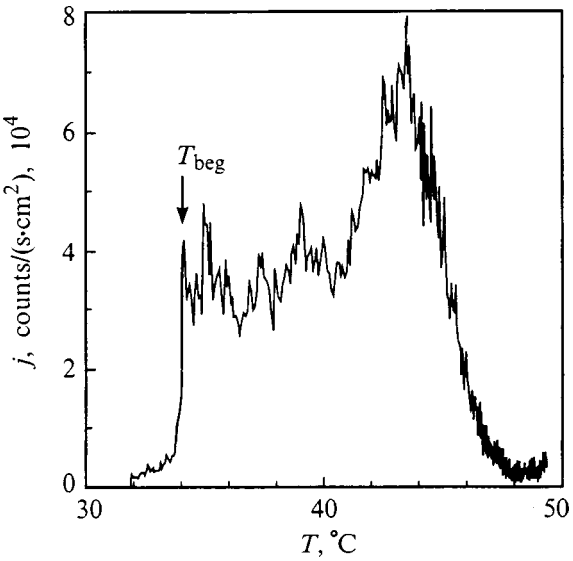

FIG. 1. Temperature dependence of the current density of the electron emission stimulated by switching on a single crystal of TGS. $E = 780$ V/cm.

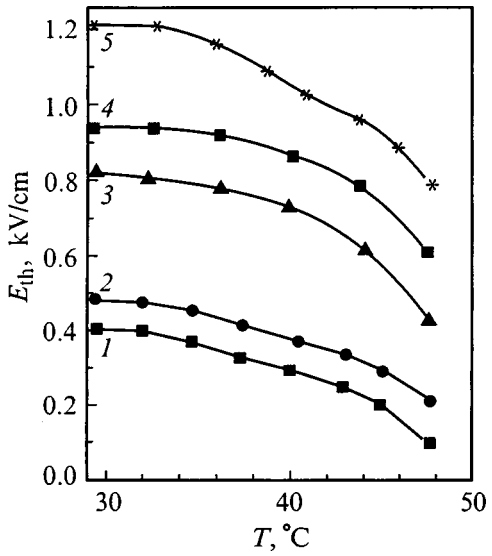

FIG. 3. Temperature dependence of the threshold field E_{th} of single crystals of TGS with different chromium impurity concentrations: *1, 2, 3, 4, 5* — 0, 0.1, 0.3, 0.6, 1.0 mol.% in solution.

played in Fig. 2. As can be seen from Fig. 2, an increase in the concentration of the chromium impurity leads to a proportionate growth in the numerical value of the coercive field for all defective crystals. Similar experimental curves were also obtained for the threshold field E_{th} for the onset of emission. According to Fig. 3, the threshold field E_{th} is also a decreasing function of temperature in the region corresponding to the ferroelectric phase. In this region, while mimicking the shape of the coercive field E_c, the threshold field exceeds it somewhat. In addition, the concentration dependence of the threshold field E_{th} is similar to the corresponding dependence for the coercive field E_c, thereby confirming our hypothesis of a correlation between the threshold and coercive fields of the material.

Increasing the impurity concentration in the chromium-doped TGS samples for a given amplitude of the stimulating field leads to a shift of the low-temperature boundary of the existence region of emission T_{beg} toward higher temperatures (Fig. 4).

2. DISCUSSION

The explanation of our results agrees well with the scheme proposed above. The presence of electron emission only in the polar phase is another confirmation of its connection with spontaneous polarization. In the ordinary state, the bound states formed as a result of breakoff of the spontaneous polarization vector at the surface of the sample are compensated by free charges in surface states. Violation, for one or another reason, of the balance of charges near the surface

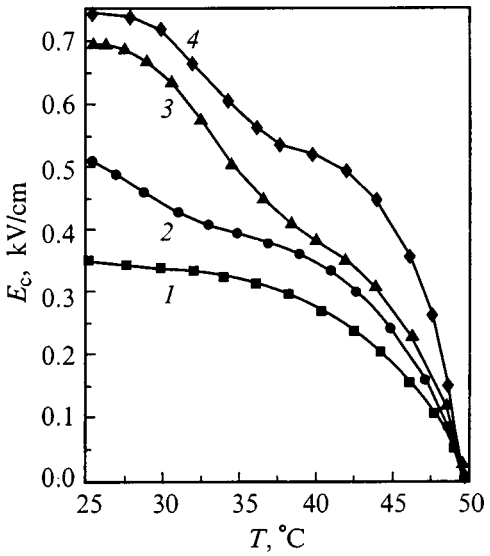

FIG. 2. Temperature dependence of the coercive field E_c in single crystals of TGS with different chromium impurity concentrations: *1, 2, 3, 4* — 0, 0.1, 0.3, 0.6 mol.% in solution.

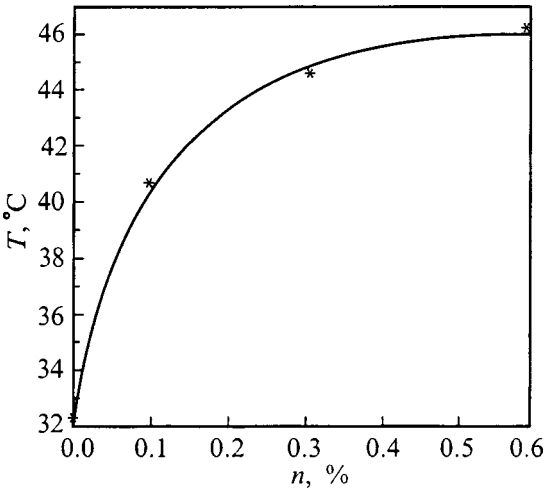

FIG. 4. Variation of the low-temperature boundary of the emission interval in a single crystal of TGS as a function of the chromium impurity concentration.

leads to the appearance of an electric field (as a result of the imbalance of charges), which induces electron emission from the sample if it is favorably directed.

One way of creating uncompensated charges on the surface of a ferroelectric is to repolarize it. As was shown by direct measurements in Ref. 5, which investigated the weak ferromagnet lithium heptagermanate, the emission effect induced by switching of the ferroelectric appears when the applied field exceeds the coercive field, i.e., when the switching process begins. This point, in our view, is convincingly confirmed by the new experimental data presented above on the threshold fields for emission from a ferroelectric.

Indeed, as follows from experiment, increasing the Cr^{3+} impurity concentration and the coercive field E_c at the same time (Fig. 2) leads to a parallel increase in the values of the threshold fields E_{th} (Fig. 3) over the entire temperature interval of the ferroelectric phase for all of the investigated crystals.

A correlation between the coercive field and the threshold field for the onset of emission also exists on the level of the numerical values. It is actually well known that the coercive field is very strong in weak ferroelectrics, reaching values $\sim 5-25$ kV/cm near T_c, which is approximately 1–2 orders of magnitude higher than the values of the given field, measured under similar conditions in classical ferroelectrics, in particular, single crystals of triglycine sulfate. As was shown in Ref. 5, the values of the threshold fields for a weak ferroelectric are also very high and reach values on the order of several kV/cm even near the phase transition temperature. On the contrary, according to our data for pure TGS and also TGS crystals doped with Cr^{3+} the corresponding values of E_{th} and E_c are at least one order of magnitude lower in comparison with weak ferroelectrics.

It is well known that the coercive field grows as the temperature is lowered starting at the Curie temperature. Obviously, at some temperature below T_c the electric field applied to the sample is already insufficient to switch the sample and, consequently, to excite the emission effect. As a result, the existence region of emission in the ferroelectric phase should be limited to a temperature interval starting at T_c and running approximately to the temperature at which the coercive field E_c is equal to the applied field (Fig. 5).

Our study of actual numerical values and the temperature dependence of the coercive field $E_c(T)$ for the weak ferroelectric lithium heptagermanate, and also for nominally pure and doped single crystals of triglycine sulfate, shows that this explanation is completely adequate to understand the boundedness of the temperature interval in the ferroelectric phase in which emission exists. The point is that when the amplitude of the switching field is increased to values exceeding the coercive field, the possibility arises, depending on the temperature dependence of E_c, of switching in the lower-temperature region, which leads to an extension of the temperature interval of the existence of emission into the low-temperature region (Fig. 5).

Another way of varying the coercive field in the sample is to vary the level of the dopant impurity. As follows from experiment, increasing the impurity concentration leads to a growth of the coercive field in comparison to its value in the defect-free material over the entire temperature interval of existence of the ferroelectric phase. As a result, for the same value of the external switching field, the temperature interval in which the sample can be switched by a given applied field will obviously narrow with growth of the impurity concentration due to the shift of its lower boundary toward lower temperatures (Fig. 2).

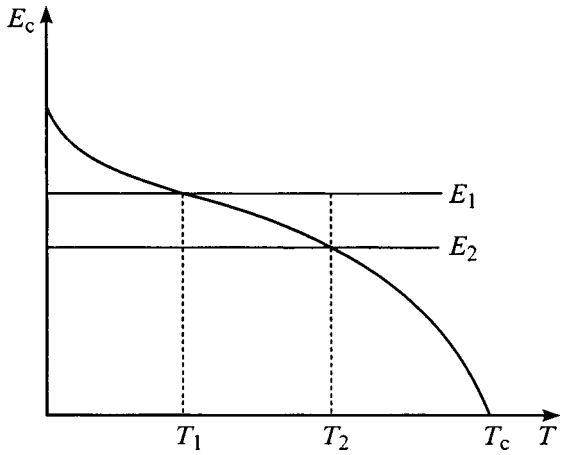

FIG. 5. Variation of the low-temperature boundary of the emission interval as a function of the amplitude of the stimulated wave.

The results of the present work demonstrate the existence of a clear correlation between the coercive field and the threshold field for emission. Both fields can be varied by different means: by substituting one ferroelectric material for another (weak or ordinary ferroelectric), by varying the temperature of the sample, and finally, by varying the defect level of the material. The possibility of employing all three factors in concert creates the possibility of configuring the temperature interval of emission as desired, which is obviously important for practical applications of this effect.

This work was carried out with the partial support of Grant No. 2801 under the program ''Universities of Russia—Basic Research.''

[1] K. Biedrzycki, Phys. Status Solidi A **109**, K79 (1988).
[2] H. Gundel, J. Handerek, and H. Riege, J. Appl. Phys. **69**, 975 (1991).
[3] A. M. Kostsov, A. S. Sidorkin, V. S. Zal'tsberg, and S. P. Gribkov, Fiz. Tverd. Tela (Leningrad) **24**, 3436 (1982) [Sov. Phys. Solid State **24**, 1952 (1982)].
[4] A. S. Sidorkin, A. M. Kostsov, V. S. Zal'tsberg, and S. P. Gribkov, Fiz. Tverd. Tela (Leningrad) **27**, 2200 (1985) [Sov. Phys. Solid State **27**, 1320 (1985)].
[5] A. S. Sidorkin, P. V. Loginov, A. M. Savvinov, A. Yu. Kudzin, and N. Yu. Korotkova, Fiz. Tverd. Tela (St. Petersburg) **38**, 624 (1996) [Phys. Solid State **38**, 344 (1996)].
[6] G. I. Rozenman, V. A. Okhapkin, Yu. L. Chepelev, and V. Ya. Shur, JETP Lett. **39**, 477 (1984).
[7] K. Biedrzycki and B. Bihan, Ferroelectrics **124**, 1201 (1992).

Translated by Paul F. Schippnick

LATTICE DYNAMICS. PHASE TRANSITIONS

Thermal flicker noise in dissipative processes of pre-melting of crystalline materials

L. A. Bityutskaya and G. D. Seleznev

Voronezh State University, 394693 Voronezh, Russia
(Submitted August 3, 1998; accepted December 29, 1998)
Fiz. Tverd. Tela (St. Petersburg) **41**, 1679–1682 (September 1999)

A spectral analysis is performed of fluctuations in the liberation of heat in the pre-melting regime of Cu, Sb, Ge, and KCl. It is shown for the first time that the observed thermal fluctuations can be identified as two-level thermal flicker noise. Characteristic parameters of the thermal fluctuations of transitional processes in the melting of crystalline materials are introduced.
 [S1063-7834(99)03009-9]

Flicker noise, which has been known already for more than a half-century, has in recent years continued to attract attention.[1–5] This has been motivated largely by the growing interest in problems of irreversibility, nonlinearity, and self-organization as the fundamental role of flicker noise in the these problems has become increasingly obvious. First recorded as electrical noise in electronic and semiconductor devices ($p-n$ junctions, transistors, and metal–semiconductor contacts),[4,5] flicker noise has since been detected in processes of the most diverse nature from fluctuations of the membrane potential of the living cell and vibrations of the earth's core to music.[1,3] In Refs. 6–9, Bityutskaya and Mashkina detected thermal fluctuations of flicker type, arising in nonequilibrium phase transitions, specifically during melting of crystalline materials in dynamic regimes. The physical nature of these fluctuations is as yet unclear. The aim of the present work was a spectral analysis of thermal fluctuations during isothermal holding in the pre-melting stage of the crystalline materials copper, antimony, germanium, and potassium chloride.

1. EXPERIMENTAL METHOD AND DATA PROCESSING

A study of transitory processes during melting of crystalline materials was performed using digital differential thermal analysis (DTA).[10,11] When 2-gram samples of the materials under investigation were heated at a constant rate exceeding 1 K/min near the melting point, within a neighborhood of a few tens of degrees, processes were observed which were accompanied by the liberation of heat. These processes were manifested on the DTA thermograms in the form of positive thermal ''pulses'' with sharp boundaries (Fig. 1). Against the background of these ''pulses'' we observed low-frequency fluctuations of the liberation of heat, recorded by a differential thermocouple as temperature variations ΔT. If the temperature of the investigated material was fixed in the region of such a thermal ''pulse'' (the point T^* in Fig. 1), then, upon extended isothermal holding, the observed thermal fluctuations continued and even grew (Fig. 2). From these measurements we obtained two sets of counts from the differential thermocouple: the running temperature of a reference and the fluctuating difference between the sample and the reference, expressed in μV. Using a Pt−Pt/Rh thermocouple 10 μV corresponds to 1°K. For the investigated group of materials the variances of the recorded macroscopic thermal fluctuations given in Table I significantly exceed the variance of the intrinsic noise of the apparatus, equal to 0.13 μV, which testifies to the physical nature of the observed fluctuations. The measuring apparatus had a controllable transmission band up to 1 Hz. We analyzed the DTA datafile of pre-melting isotherms of copper, antimony, germanium, and potassium chloride. The characteristic length of the isothermal holding times was 30 minutes, and the number of readings was typically 1000−1500.

The isothermal fluctuations were subjected to digital spectral analysis. The data processing implemented a special program which made use of the Welch periodogram method.[12] This method is efficient for estimating the spectral power density.

Note that usually the results of carrying out a spectral analysis of random processes[5,12] are presented as the dependence of the magnitude of the spectral power density S on frequency f. Let $x(t)$ be a stationary accidental process recorded during a time T. The corresponding Fourier transform is $X(j\omega)$, where $\omega=2\pi f$. The spectral power density (unilateral) of this process is defined, according to Ref. 4, by

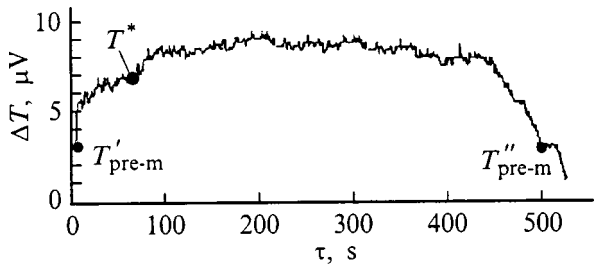

FIG. 1. DTA thermogram of pre-heating of copper, $T'_{\text{pre-m}}$ and $T''_{\text{pre-m}}$ are the temperatures of onset and termination of pre-melting.

TABLE I. Spectral characteristics of thermal fluctuations during isothermal holding in the pre-melting regime.

Material	Temperature of isothermal holding, °C	Variance, μV^2	Spectral characteristics			
			α_A	α_B	α_B/α_A	f_c, Hz
Cu	1047	3.56	1.25	0.38	0.30	0.085
Sb	584	0.78	1.4	0.42	0.30	0.042
Ge	949	2.94	1.02	0.5	0.50	0.056
KCl	762	2.47	1.1	0.52	0.47	0.115

$$S(j\omega)=\lim_{T\to\infty}\frac{2|X(j\omega)|^2}{T}. \quad (1)$$

The quantity $S(j\omega)$ is taken as an energy characteristic of the process since the amplitudes of the oscillations of its spectral components $|X(j\omega)|$ enter into expression (1) to the second power. However, the thermal fluctuations considered in the present work are themselves releases of heat energy, and in this case their spectral density, which we denote as $S^*(j\omega)$, must be represented by an expression in which the absolute values of the amplitudes must enter to the first power

$$S^*(j\omega)=\lim_{T\to\infty}\frac{2|X(j\omega)|}{T}. \quad (2)$$

2. RESULTS AND DISCUSSION

For all of the investigated materials, the spectrum in log–log coordinates takes the form of two segments *A* and *B* which can be fit by straight lines, whose absolute values of the slopes of $\alpha_A>1$ and $\alpha_B<1$, and the critical frequency at which the slope changes, f_c (Fig. 3), are listed in Table I. A hyperbolic dependence of the spectral density on the frequency is characteristic of the fluctuation process known as flicker noise.[5] (Such a dependence can be written $S(j\omega)=C|f|^{-\alpha}$, and in log–log coordinates appears as a straight line.) The presence of two approximately rectilinear segments *A* and *B* in the spectra of all the investigated materials revealed in the present work allows us to assert that the thermal fluctuations observed under isothermal conditions in the pre-melting temperature interval of crystalline materials can be identified as two-level thermal flicker noise. Two-level flicker noise was also observed in experiments on electric current fluctuations,[13] but in, contrast to thermal fluctuations, the reverse relation held between the slopes: $\alpha_A<\alpha_B$. It may be conjectured that the presence of two segments in the spectra of thermal fluctuations observed under isothermal conditions was caused by the presence of two levels of a common physical process giving rise to these fluctuations.

Let us consider possible reasons for the appearance of the thermal flicker noise observed in the experiments. Equilibrium and nonequilibrium flicker noise differ. Equilibrium flicker noise is observed in systems found in a state of statistical equilibrium and is associated with the presence of anomalous Brownian motion, i.e., Brownian motion which violates the Einstein relation, where the mean-square displacement of the diffusing particle is proportional to the time.[2] Non-equilibrium flicker noise arises during stationary, dissipative processes and is a result of fluctuations of the dissipative parameters of the system—resistances, conductances, etc., which determine the magnitudes of the irreversible processes under given nonequilibrium conditions.[3] In this case, flicker noise looks like avalanche fluctuations of these processes, described by a model of self-organizational criticality.[14] Both equilibrium and nonequilibrium flicker noise are associated with the appearance in the system of long-lived temporal correlations, temporal ordering, and self-organization.[2]

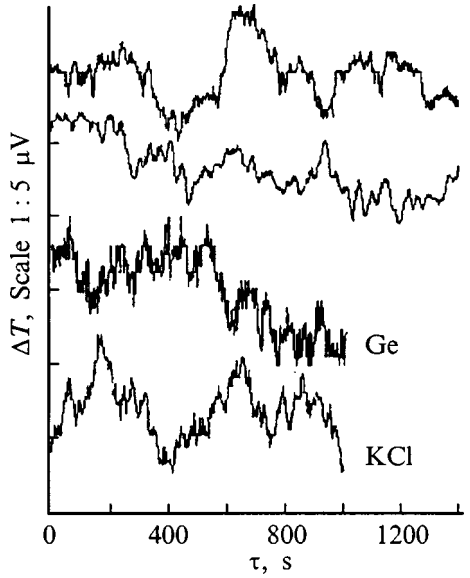

FIG. 2. Fluctuations of the liberation of heat in Cu, Sb, Ge, and KCl in the isothermal pre-melting regime.

Under the conditions of our experiment, the material is found in a stationarily excited state as a result of the occurrence of a nonequilibrium phase transition—pre-melting. According to Prigogine, nonequilibrium phase transitions are characterized by the occurrence of dissipative processes, the appearance of which presupposes as its main conditions an open system out of equilibrium. In our case, the passage of the system out of equilibrium arises as a result of anharmonism of the vibrations of the crystalline lattice in the pre-melting stage in dynamic regimes due to an abrupt growth of the vacancy concentration. Openness here is understood in a wider sense: not only as exchange of energy between the system and its environment, but also as an energy interaction of two of its subsystems: atomic and phonon. Under conditions of strong anharmonism, this interaction leads to a qualitative transformation of both the phonon subsystem and the atomic subsystem of the crystal. A decrease in the intensity of the phonon vibrations of the crystalline lattice during heating and even their complete disappearance at temperatures near the melting temperature was observed in experiments on Raman light scattering of crystalline NaOH.[15–18] In artificial and natural materials the appearance of flicker noise has been linked with the appearance of long-lived temporal correlations leading to degradation, deformation, and destruction of the materials.[1,2] It may be surmised that the appearance of thermal flicker noise is evidence of a structural

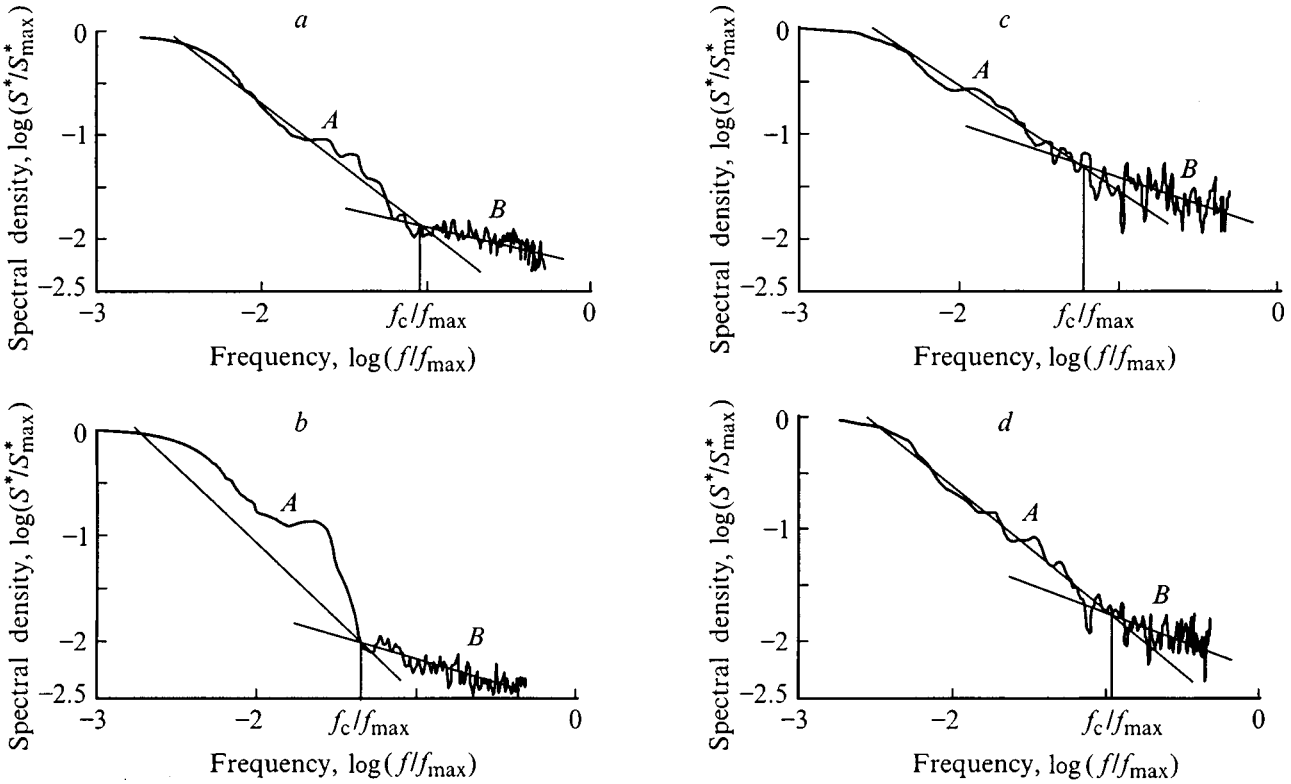

FIG. 3. Dependence of the relative spectral density of the fluctuations $\log(\overline{S^*}/\overline{S^*_{max}})$ on the relative frequency $\log(f/f_{max})$, where f_{max} and $\overline{S^*_{max}}$ are the maximum values for Cu (a), Sb (b), Ge (c), and KCl (d); log–log plot.

rearrangement in the pre-melting stage. This hypothesis is confirmed by electron-diffraction studies of the structure of metals in dynamic regimes near the melting temperature.[19] In these studies, continuous recording of rapidly varying diffraction patterns was carried out during heating of metallic films at heating rates of $20-25\,\mathrm{K}\cdot\mathrm{min}^{-1}$. By direct observations, the dynamic structure of transitional temperature regions was determined in which disordering of lattice sites and changes in the symmetry of the crystalline lattice arise. In particular, in a melting *hcc* metal the emergence of icosahedral formations was observed.

One property of flicker noise is well known—its self-similarity over different time scales.[4] This property manifests its fractal structure. If the fracticality of thermal flicker noise is judged as the appearance of dynamic fracticality of the structure of the material in the pre-melting state,[1] then its appearance is evidence of the formation of a dynamic pre-melting mesophase.

To summarize, we may draw the following conclusions from the above study.

1) The appearance of thermal flicker noise during dissipative processes of pre-melting of crystalline materials in dynamic regimes is universal and does not depend on the type of chemical bond or the structure of the material.

2) The flicker-noise parameters—the spectral density exponents α_A and α_B and the critical frequency f_c—are characteristic parameters of dissipative transitory processes taking place during melting and accompanied by a structural rearrangement with the formation of a fractal pre-melting mesophase.

This work was carried out with the support of the Russian Fund for Fundamental Research (Grant No. 98-03-32406).

[1] S. F. Timashev, Ross. Khim. Zh. **41**(3), 17 (1997).
[2] A. S. Vrachev, *Noise and Degradation Processes in Semiconductor Devices: Reports of Scientific-Technical Seminar. MNTORÉS A. S. Popov* [in Russian] (Moscow, 1995), p.43.
[3] Yu. L. Klimontovich, *Statistical Theory of Open Systems* [in Russian] (TOO ''Yanus,'' Moscow, 1995).
[4] G. N. Bochkov and Yu. E. Kuzovlev, Usp. Fiz. Nauk **141**(1), 151 (1983) [Sov. Phys. Usp. **26**, 829 (1983)].
[5] M. Buckingham, *Noise in Electronic Devices and Systems* (Ellis Horwood Limited, Chichester, 1983).
[6] L. A. Bityutskaya and E. S. Mashkina, Pis'ma Zh. Tekh. Fiz. **21**(17), 85 (1995) [Tech. Phys. Lett. **21**, 720 (1995)].
[7] L. A. Bityutskaya and E. S. Mashkina, Pis'ma Zh. Tekh. Fiz. **21**(18), 8 (1995) [Tech. Phys. Lett. **21**, 728 (1995)].
[8] L. A. Bityutskaya and E. S. Mashkina, Pis'ma Zh. Tekh. Fiz. **21**(20), 30 (1995) [Tech. Phys. Lett. **21**, 828 (1995)].
[9] L. A. Bityutskaya and E. S. Mashkina, Pis'ma Zh. Tekh. Fiz. **21**(24), 90 (1995) [Tech. Phys. Lett. **21**, 1032 (1995)].
[10] W. W. Wendlandt, *Thermal Methods of Analysis*, 2nd ed. (Wiley, New York, 1974).
[11] L. A. Bityutskaya and G. D. Seleznev, Pis'ma Zh. Tekh. Fiz. **24**(14), 24 (1998) [Tech. Phys. Lett. **24**, 551 (1998)].
[12] S. L. Marple, Jr., *Digital Spectral Analysis with Applications* (Prentice-Hall, Englewood Cliffs, New Jersey, 1987).
[13] R. F. Voss and J. Clarke, Phys. Rev. B **13**, 556 (1976).

[14] P. Bak, C. Tang, and K. Wiesenfeld, Phys. Rev. A **38**, 780 (1988).
[15] L. A. Zhukova, Rasplavy **4**, 29 (1990).
[16] L. A. Zhukova, Rasplavy **6**, 15 (1991).
[17] L. A. Zhukova, Rasplavy **5**, 15 (1992).
[18] L. A. Zhukova, Rasplavy **2**, 95 (1995).
[19] I. D. Zakir'yanova, A. P. Khaĭmenov, V. A. Khokhlov, and V. A. Kochedykov, Rasplavy **3**, 45 (1997).

Translated by Paul F. Schippnick

Phase transition in the layered perovskite $CsScF_4$ induced by hydrostatic pressure

K. S. Aleksandrov, A. N. Vtyurin, and I. V. Shmygol'

L. V. Kirenskiĭ Institute of Physics, Siberian Branch, Russian Academy of Sciences, 660036 Krasnoyarsk, Russia

S. V. Goryaĭnov

Unified Institute of Geology, Geophysics, and Mineralogy, Siberian Branch, Russian Academy of Sciences, 630090 Novosibirsk, Russia

(Submitted December 21, 1998)
Fiz. Tverd. Tela (St. Petersburg) **41**, 1683–1685 (September 1999)

Using polarization microscopy and Raman scattering, we have discovered a new phase transition in the layered perovskite crystal $CsScF_4$ under a hydrostatic pressure around 6 GPa. The proposed space group of the high-pressure phase is C_{2h}^2, $Z=4$. © *1999 American Institute of Physics.* [S1063-7834(99)03109-3]

Layered perovskite-like crystals are a traditional models for studying the mechanisms of phase transition; at the same time, numerous practical applications are associated with them (see, e.g., Refs. 1 and 2). The $CsScF_4$ crystal is a typical representative of this family. According to x-ray structural data and measurements of the macroscopic characteristics of this crystal,[3] the structure of its high-temperature phase (space group D_{4h}^1, $Z=1$; see Fig. 1) consists of four layers of linked ScF_6 octahedra, separated by Cs^+ ions. Upon cooling below 475 K a first-order transition of displacement type occurs, similar to a second-order transition, to the phase D_{4h}^5 with a doubling of the unit cell and, upon further cooling below 317 K, to the rhombic phase D_{2h}^{13}, $Z=4$ (Refs. 3 and 4). This sequence of phase transitions is unusual for cesium-containing perovskites[1,2] and is analogous to that observed in $RbAlF_4$ (Refs. 5 and 6).

In a $KAlF_4$ crystal, which is isomorphic to $RbAlF_4$, a transition to the phase C_{2h}^2, $Z=4$ is also observed at 260 K, and also at room temperature under a hydrostatic pressure around 0.25 GPa;[7] however, efforts to observe an analogous transition in $RbAlF_4$, and over a wide temperature interval in $CsScF_4$ (Refs. 3 and 4), have not yielded positive results. It was in response to this situation that the present study of the effect of high hydrostatic pressures on $CsScF_4$ was undertaken.

Samples of $CsScF_4$ were investigated under conditions of high (up to 10 GPa) hydrostatic pressure on a setup with diamond anvils similar to the one used in Refs. 7 and 8, at room temperature. We investigated samples of the same crystallization as in Refs. 1 and 4; the diameter of the chamber with the sample was 0.25 mm, and its height—0.1 mm. In light of the pronounced layered structure of the crystal, the samples were oriented in the chamber so that observation takes place along the four-fold axis of the tetragonal phases of the crystal (the Z axis in Fig. 1). The pressure was determined with an accuracy of 0.05 GPa from the shift of the luminescence band of a ruby microcrystal[8,9] placed alongside the sample. As the pressure-transmitting medium we used a mixture of ethyl and methyl alcohols or glycerin. Raman scattering spectra were excited by radiation from an Ar^+ laser (514 nm, 0.5 W) and recorded on an OMARS 89 (Dilor) multichannel spectrometer. In light of the small dimensions of the sample and the strong diffuse scattering from its domain structure, we recorded the high-frequency (300–600 cm^{-1}) part of the spectrum, where the valence vibrations of the Sc–F bound of the axial fluorine atoms (F3–Sc–F4 in Fig. 1). From the characteristic low-frequency shift of the analogous vibration line of Al–F we probed the phase transition in $KAlF_4$ (Ref. 7). Simultaneously, we observed the domain structure of the sample with the help of a polarizing microscope.

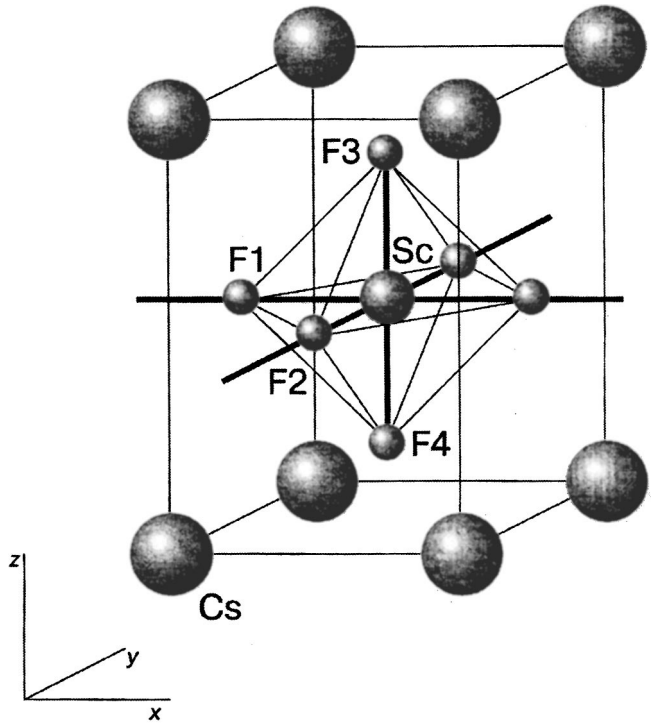

FIG. 1. Structure in one unit cell of the high-temperature phase of $CsScF_4$

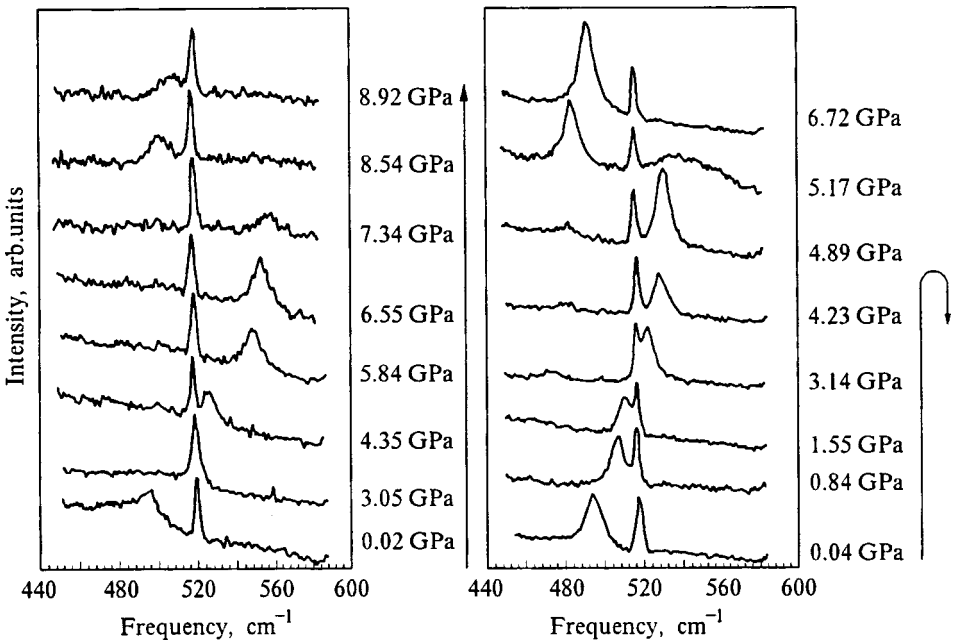

FIG. 2. Variations of the Raman scattering spectra under pressure. The narrow 520 cm^{-1} line in the center is the reference line of the gas-discharge. The arrows to the right show the direction of variation of the pressure with which the experimental points were approached.

We carried out two series of measurements: in the one case the pressure was increased monotonically with stops to record the spectra; in the other case, before recording the spectra we lowered the pressure by 0.5–1 GPa to estimate the magnitude of possible hysteretic effects.

At normal pressure the crystal is found in the rhombic phase D_{2h}^{13}. In the indicated spectral region one intense line is observed at 495 cm^{-1}; a weakly expressed, uncolored system of 90-degree domains is visible in the microscope. As the pressure is increased, the system of domains acquires more contrast (which corresponds to departure from the point of the $D_{4h}^{5} \rightarrow D_{2h}^{13}$ transition) and the frequency of the observed line grows linearly (7.8 cm^{-1}/GPa).

In the region above 6 GPa the picture changes abruptly. A new domain structure appears suddenly, as if with a jump: the orientation of the domain walls remains the same as before, but the new structure has a bright interference color, and the domains are larger. With further increase of the pressure, the interference colors change in a continuous fashion. In this case, a dramatic broadening and decrease in the intensity of the observed line take place (Fig. 2); in the series of measurements with continuous increase of the pressure, this happens at 6.6 GPa, the width of the line increases by four- to fivefold up to 40–50 cm^{-1}, while above 8.5 GPa the line is no longer observed. In the runs with partial lowering of the pressure the corresponding jump takes place at 5.6 GPa, and this line disappears completely at 7.5 GPa. In both cases, the position of the maximum of this wide line changes very little with pressure: 1.8 cm^{-1} GPa. At the same time, a new intense line at a lower frequency, 490 cm^{-1}, appears in the spectrum immediately after the transition and with further increase of the pressure shifts linearly upward (7.5 cm^{-1}/GPa).

The observed transition has a pronounced hysteresis of 1–1.5 GPa, which is clearly visible in Fig. 2, and is reversible. The appearance of interference coloring of the domains and its continuous variation are indications of low symmetry (not higher than monoclinic) of the newly formed phase, which allows variation of the orientation of the optical indicatrix. The shift of the frequency of the Sc–F valence vibration toward lower frequencies correlates with the presumed structure of the phase, C_{2h}^{2}, in which a shift of perovskite-like layers leads to an increase in the distances between fluorine atoms of neighboring layers and a decrease in the corresponding force constant (Fig. 3). An analogous low-frequency shift was observed during the transition to this phase in the spectrum of $KAlF_4$ (Ref. 7). Such a strong dis-

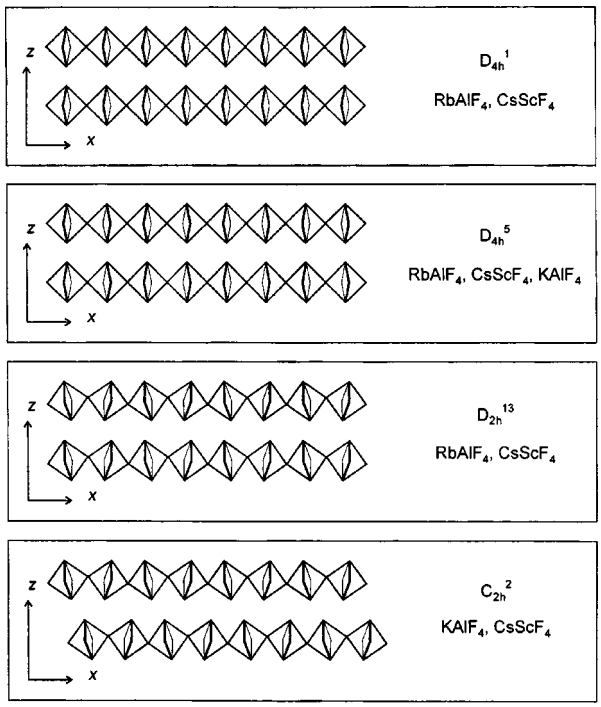

FIG. 3. Packing diagram of the ScF_6 octahedra in different phases of $CsScF_4$ and isomorphic crystals.

tortion of the structure during the transition should lead to formation of pronounced domain walls and a large number of defects, which can explain the pulling of the high-frequency line above the transition point.

To sum up, the above study has made it possible for the first time to observe the transition to the new low-symmetry phase of $CsScF_4$ induced by hydrostatic pressure around 6 GPa. The first-order transition is accompanied by a hysteresis of 1–1.5 GPa. All the observed experimental facts agree with the assertion that the observed phase is isomorphic to the high-pressure phase of $KAlF_4$ with space group C_{2h}^2, $Z=4$.

The authors are grateful to A. P. Shebanin for assitance with the experimental measurements.

This work was carried out with the support of the Russian Fund for Fundamental Research (Grant No. 96-15-96700), and was also partially supported within the framework of a grant from INTAS–RFBR (No. IR-97-0177).

[1] K. S. Aleksandrov, A. T. Anistratov, B. V. Beznosikov, and N. V. Fedoseeva, *Phase Transitions in* ABX_3 *Crystals* [in Russian] (Nauka, Novosibirsk, 1981).
[2] K. S. Aleksandrov and B. V. Beznosikov, *Perovskite-like Crystals* [in Russian] (Nauka, Novosibirsk, 1997).
[3] K. S. Aleksandrov, V. N. Voronov, A. I. Kruglik, S. V. Mel'nikova, and I. N. Flerov, Fiz. Tverd. Tela (Leningrad) **30**, 3325 (1988) [Sov. Phys. Solid State **30**, 1911 (1988)].
[4] A. N. Vtyurin, A. S. Krylov, I. V. Shmygol', and A. P. Shebanin, Fiz. Tverd. Tela (St. Petersburg) **39**, 717 (1997) [Phys. Solid State **39**, 632 (1997)].
[5] K. S. Aleksandrov, Kristallografiya **32**, 661 (1987) [Sov. Phys. Crystallogr. **32**, 387 (1987)].
[6] A. Bulou, M. Roussean, J. Nouett, and B. J. Hennion, J. Phys.: Condens. Matter **1**, 4553 (1989).
[7] Q. Wang, G. Ripault, and A. Bulou, Phase Transit. **53**, 1 (1995).
[8] S. V. Goryainov and I. A. Belitsky, Phys. Chem. Miner. **22**, 443 (1995).
[9] R. G. Munro, G. J. Piermarini, S. Block, and W. B. Holzapfel, J. Appl. Phys. **57**, 165 (1985).

Translated by Paul F. Schippnick

Specific heat of the elpasolite Pb_2MgWO_6

I. N. Flërov*) and M. V. Gorev

L. V. Kirenskiĭ Institute of Physics, Siberian Branch, Russian Academy of Sciences, 660036 Krasnoyarsk, Russia

Ph. Sciau

Centre d'Elaboration des Matériaux et d'Etudes Structurales, CNRS, 31055 Toulouse, France
(Submitted January 26, 1999)
Fiz. Tverd. Tela (St. Petersburg) **41**, 1686–1688 (September 1999)

The specific heat of Pb_2MgWO_6 has been measured in the temperature interval 83–370 K. An anomaly in the specific heat associated with the phase transition at $T_0 = 312.8$ K has been discovered. The thermodynamic parameters of the structural phase transition $Fm3m - Pmcn$ have been determined. © *1999 American Institute of Physics.* [S1063-7834(99)03209-8]

There exists a wide class of oxygen compounds with general formula $A_2BB'O_6$, which undergo structural phase transitions of diverse nature, including transitions associated with compositional ordering of the cations B and B′. The degree of ordering of the cations has a substantial affect both on the physical properties of the compound and on the nature of the structural transformations taking place in it.[1] The temperature of compositional ordering is determined, first of all, by the difference in the charges and dimensions of the ordering ions. $Pb_2B^2WO_6$ compounds, as a rule, are ordered mainly due to the significant difference in the charges of the B^{2+} and W^{6+} ions and in the high-temperature phase have elpasolite structure (an ordered perovskite, space group $Fm3m$).[1] Depending on the size of the B^{2+} ion in these compounds, distorted phases of varied symmetry can be realized by a change in the temperature. Elpasolite with Mg as the B ion undergoes transitions to the antiferroelectric state,[2] which is preceded in the compound having Co as the B ion by an incommensurate phase in a wide temperature interval.[3] Substitution of the cobalt ion by cadmium leads to a substantial growth in the temperature of loss of stability of the original cubic phase.[4]

Despite active research into oxygen elpasolites by various methods, detailed information about their thermodynamic properties and their behavior during phase transitions are lacking. What information about them exists was obtained for isolated representatives of the family and, as a rule, using a differential scanning calorimeter; only in Ref. 5 was Pb_2MgWO_6 investigated using an adiabatic calorimeter, but only in a limited temperature interval (275–311 K) in the vicinity of the phase transition at $T_0 = 303.5$ K. At the same time, from the temperature dependence of the relative elongation and volume,[2,6] it follows that additional thermodynamic parameters associated with the phase transition (thermal expansion coefficient, specific heat) should be present over a significant wider temperature interval. Reference 5 investigated a ceramic material in which, so the authors maintained, the existence of an inhomogeneous composition is possible. It is entirely possible that this is precisely the reason the temperature of the phase transition in this sample[5] proved to be lower than its value determined in other studies (312 K, Ref. 1). The structure of the initial cubic phase and the distorted phase of Pb_2MgWO_6 was resolved in Ref. 7. The symmetry of the low-temperature phase turned out to be orthorhombic with space group $Pmcn$. In a Raman light-scattering study on a powder sample of Pb_2MgWO_6, a soft mode was discovered in the $Pmcn$ phase, condensing in the center of the Brillouin zone.[8] This gave cause to believe that a phase transition of displacement type is realized in this compound. At the same time, the diffuse Raman signal observed in the cubic phase indicated that there is also a contribution to the mechanism of the phase transition from phenomena apparently associated with ordering of lead and oxygen atoms,[8] which according to the structural studies are disordered in the cubic phase over several local sites.[7]

The Raman scattering spectra and the dielectric constant were later examined in greater detail in single-crystal Pb_2MgWO_6 (Ref. 9). The results of this study confirm the hypothesis made in Ref. 8 of a double mechanism of this phase transition. On the other hand, it is asserted that there exists in this compound a phase intermediate between the cubic paraelectric phase and the orthorhombic antiferroelectric phase, and a second phase transition occurs in the region 220–240 K.

The present paper reports a careful study of the specific heat of elpasolite Pb_2MgWO_6 over a wide temperature range with the aim of elucidating the nature of its behavior and determining its thermodynamic parameters such as the existence interval of the excess specific heat, entropy difference, and hysteresis of the phase transition temperature.

Specific-heat measurements were performed on the powder sample used earlier in experiments to refine the structure of the compound[7] and in the Raman light scattering studies.[8] An analysis of the x-ray diffraction patterns showed that impurities are absent in the sample which would have come from the initial ingredients used in the solid-state synthesis, and that foreign phases are absent as well.[8] It was also established that disorder is absent in the distribution of Mg^{2+} and W^{6+} ions occupying the sites at the centers of the corresponding octahedra.[7] The sample in powdered form pos-

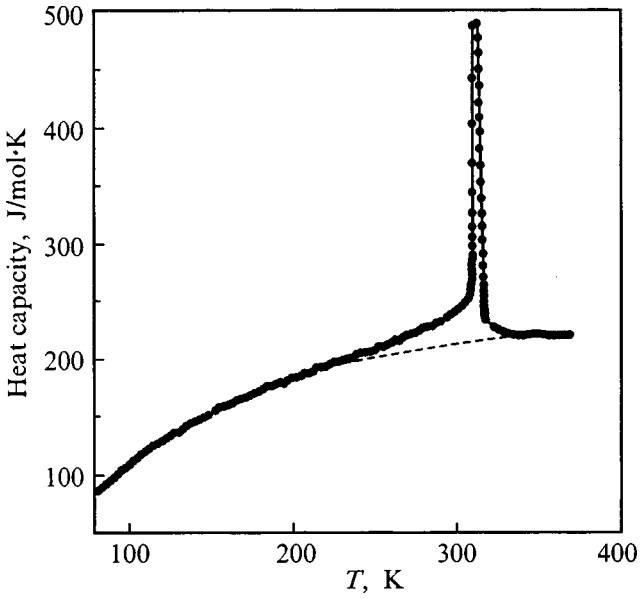

FIG. 1. Temperature dependence of the specific heat of Pb_2MgWO_6. The dashed curve is the lattice specific heat.

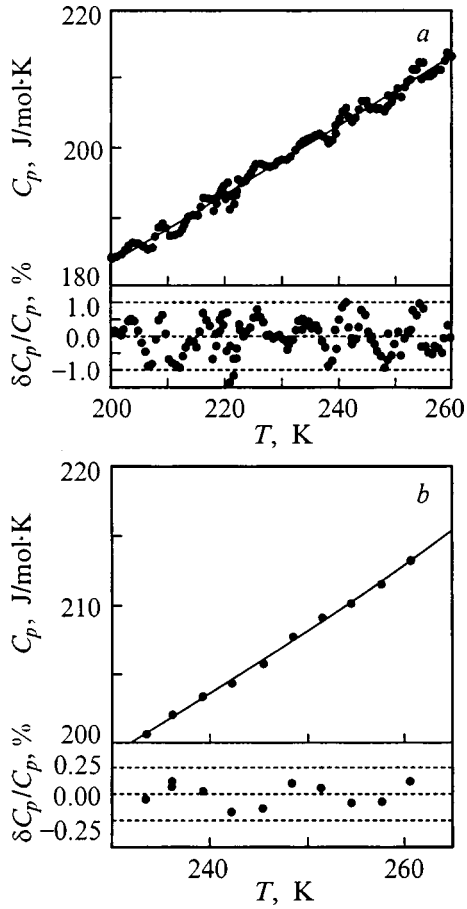

FIG. 2. Specific heat of Pb_2MgWO_6 in the region of the second phase transition suggested in Ref. 9, measured using the methods of continuous (a) and discrete (b) heating, with deviations of the experimental points from the corresponding smoothed curves.

sesses the advantage that it is free of the mechanical stresses which inevitably arise in a ceramic during hot pressing.

The specific heat was examined in the interval 83–370 K with the use of an adiabatic calorimeter in the regimes of discrete and continuous heating/cooling. A powder sample of Pb_2MgWO_6 with mass 4.297 g was placed in an indium container which was sealed in a helium atmosphere. Below 300 K the measurements were performed using a liquid-nitrogen bath, and in the interval 290–370 using an ice bath. The temperature regions of the phase transitions were examined with the help of low-static thermograms with low rates of variation of temperature $dT/dt = \pm 4\times10^{-4}$ K/s.

Results of the measurement of the specific heat $C_p(T)$ are plotted in Fig. 1. One specific-heat anomaly is revealed, with a maximum at 313.1 ± 0.5 K.

Figures 2a and 2b present results of a specific-heat measurement in the temperature region where some peculiarities in the Raman spectra and in the behavior of the dielectric constant were observed in Ref. 9 and interpreted as being associated with a second phase transition in Pb_2MgWO_6. The relatively small and uniform spread of the experimental points from the smoothed curve of $C_p(T)$, both in the series of continuous heating and in the series of discrete heating, allows us to state unambiguously that there are no anomalies in the specific heat in the investigated sample in the temperature interval 200–250 K, at least within the limits of 1.0 J/mol·K, which amounts to 0.5% of the total specific heat of the compound.

Thermographic studies of temperature regions centered on the phase transition $Fm3m-Pmcn$ allowed us to refine the transition temperature to $T_0 = 312.8\pm0.2$ K, which is in satisfactory agreement with the data of Ref. 2, and also enabled us to determine its hysteresis $\delta T_0 = 2.45\pm0.2$ K (Fig. 3). From the thermograms we also calculated the latent heat (or jump in the enthalpy at the phase transition), which is equal to $\delta H_0 = 2340\pm200\ \mathrm{J\cdot mol^{-1}}$, and the corresponding change in the entropy $\delta S_0 = \delta H_0/T_0 = 7.48 \pm 0.52\ \mathrm{J\cdot mol^{-1}\cdot K^{-1}}$. The quantities δH_0 and δT_0 in the sample investigated in this study turned out to be two times larger than the values obtained in Ref. 5. This also testifies on behalf of a higher degree of perfection of the powder sample in comparison with a ceramic sample since a decrease in δH_0 and δT_0 from one sample to another of the same compound $A_2BB'O_6$ can be due to a ''washing out'' of the phase transition as a consequence of the presence in the sample of significant mechanical stresses and/or a disruption of the degree of ordering of the B and B′ ions.

The effect of hydrostatic pressure on the anomaly in the dielectric constant at the phase transition in Pb_2MgWO_6 was investigated in Refs. 10 and 11. The data of different authors differ quite significantly: $dT_0/dp = -0.59$ (Ref. 10) and -0.38 K/GPa (Ref. 11). Using this information and the value of δS_0 determined in the present work, it is possible to use the Clapeyron–Clausius equation $dT_0/dp = (\delta V_0/V)/\delta S_0$ to calculate the jump in the volume at the phase transition point, which turns out to lie within the limits $(\delta V_0/V) = -(3.7-5.7)\times10^{-3}$ for the two values of dT_0/dp corresponding to the data of Refs. 11 and 10. Experimentally, it has been found that $(\delta V_0/V) = -2.6\times10^{-3}$ (Ref. 11) and -4.7×10^{-3} (Ref. 6).

To calculate the integral thermodynamic characteristics

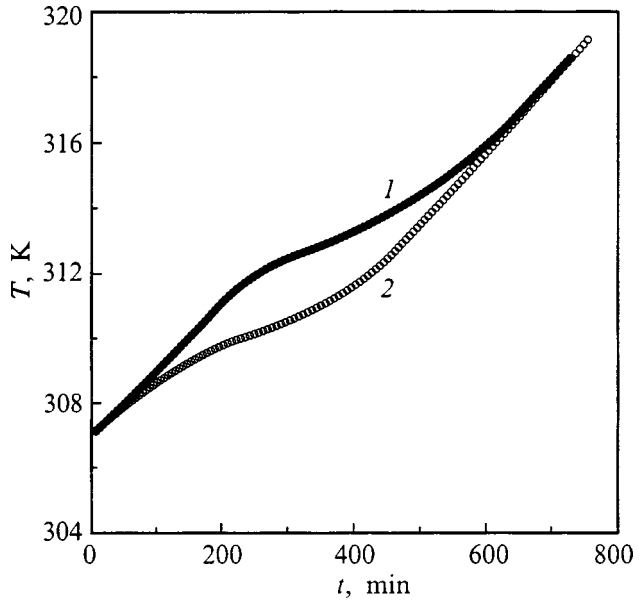

FIG. 3. Thermograms recorded during the heating (*1*) and cooling (*2*) in the vicinity of the $Fm3m-Pmcn$ phase transition in Pb_2MgWO_6.

of the phase transition between the cubic and orthorhombic phases, it was necessary to separate out the anomalous contribution $\Delta C_p(T)$, defined as the difference between the total $C_p(T)$ and lattice $C_{\text{lat}}(T)$ specific heats. The latter was determined by fitting the experimental data far from the phase transition temperature T_0 by the Debye and Einstein functions $C_{\text{lat}}(T)=A_1D(\theta_D/T)+A_2E(\theta_E/T)$ and is represented by the dashed line in Fig. 1. By varying the datasets for the high- and low-temperature phases included in the processing, we determined optimal values of the constants $A_1=391.4\,\text{J}\cdot\text{mol}\cdot\text{K}$, $A_2=113.0\,\text{J}\cdot\text{mol}\cdot\text{K}$, $\theta_D=262.3\,\text{K}$, and $\theta_E=552.7\,\text{K}$. The temperature interval in which the anomalous specific heat occurs turned out to be quite wide: from 200 to 345 K, which is in satisfactory agreement with the thermal expansion data of Ref. 6.

The excess entropy of the phase transition was calculated by integrating the function $(\Delta C_p/T)(T)$. The total entropy difference associated with the phase transition is $\Delta S_0=13.00\pm1.05\,\text{J}\cdot\text{mol}^{-1}\cdot\text{K}^{-1}$. The ratio $\delta S_0/\Delta S_0=0.58$ indicates that the $Fm3m-Pmcn$ phase transition in Pb_2MgWO_6, although first order, is quite close to the tricritical point.

While refining the structure of the cubic phase, we noticed that the best values of the various *R*-factors correspond to the situation where the lead atoms are disordered over several equivalent sites.[7] At the same time, these quantities turned out to be very similar to each other for the possible displacements of the lead atoms in the ⟨100⟩, ⟨110⟩, and ⟨111⟩ directions leading to 6, 12, and 4 equivalent sites, respectively. In the orthorhombic phase, along with small rotations and weak distortions of the octahedra, we indeed discovered a displacement of the lead atoms along the $[010]_p$ axis of the pseudocubic cell. Thus, the structural data suggest that the contribution to the entropy difference associated with the $Fm3m-Pmcn$ phase transition in Pb_2MgWO_6 due to ordering of the lead atoms should be $\Delta S/R=\ln 6=1.79$. The entropy difference determined in the present work, $\Delta S_0/R=1.56\pm0.13$, turns out to be less than this value, but larger than $\ln 4$. As for the change in the entropy due to rotation of the octahedra, this quantity, as was shown in Ref. 12, is not large as a rule.

This work was carried out with the financial support of the Russian Fund for Fundamental Research (Grants No. 96-15-96700 and 97-02-16277).

*)E-mail: flerov@iph.krasnoyarsk.su

[1] A. A. Bokov, Izv. Ross. Akad. Nauk, Ser. Fiz. **57**(6), 25 (1993).
[2] G. A. Smolenskiĭ, N. N. Kraĭnik, and A. I. Agranovskaya, Fiz. Tverd. Tela (Leningrad) **3**, 981 (1961) [Sov. Phys. Solid State **3**, 714 (1961)].
[3] W. Brixel, M. L. Werk, P. Fischer, W. Bührer, J.-P. Rivera, P. Tissot, and H. Schmid, Jpn. J. Appl. Phys., Suppl. **24**(2), 242 (1985).
[4] Ph. Sciau and D. Grebille, *Aperiodic'94, Proceedings of the International Conference on Aperiodic Crystals* (World Scientific, Singapore, 1994), p. 460.
[5] B. A. Strukov, K. A. Minaeva, T. L. Skomorokhova, and V. A. Isupov, Fiz. Tverd. Tela (Leningrad) **8**, 972 (1966) [Sov. Phys. Solid State **8**, 740 (1966)].
[6] G. Baldinozzi, Ph. Sciau, and P.-A. Buffat, Solid State Commun. **86**, 541 (1993).
[7] G. Baldinozzi, Ph. Sciau, M. Pinot, and D. Grebille, Acta Crystallogr., Sect. B: Struct. Sci. **51**, 668 (1995).
[8] G. Baldinozzi, Ph. Sciau, and A. Bulou, J. Phys.: Condens. Matter **7**, 8109 (1995).
[9] A. Kania, E. Jahfel, G. E. Kugel, K. Roleder, and M. Hafid, J. Phys.: Condens. Matter **8**, 4441 (1996).
[10] I. N. Polandov, Fiz. Tverd. Tela (Leningrad) **5**, 1147 (1963) [Sov. Phys. Solid State **5**, 838 (1963)].
[11] N. Yasuda, S. Fujimoto, and T. Yoshimura, J. Phys. C **19**, 1055 (1986).
[12] I. N. Flerov, M. V. Gorev, K. S. Aleksandrov, A. Tressaud, G. Grannec, and M. Couzi, Mater. Sci. Eng. **24**, 81 (1998).

Translated by Paul F. Schippnick

Field theory of fluctuations during phase transitions

A. I. Olemskoĭ*) and V. A. Brazhnyĭ†)

Sumy State University, 244007 Sumy, Ukraine
(Submitted October 27, 1998; accepted February 10, 1999)
Fiz. Tverd. Tela (St. Petersburg) **41**, 1689–1692 (September 1999)

The evolution of the most probable amplitudes of the hydrodynamic mode is investigated in the self-consistent scheme. Fluctuations of the amplitude of the conjugate force are also investigated. © *1999 American Institute of Physics.* [S1063-7834(99)03309-2]

The influence of fluctuations on the nature of a phase transition has been studied intensely for decades (see Refs. 1 and 2). The current concept is based on the similarity hypothesis, according to which the behavior of the correlators of fluctuating quantities takes on a universal character in the critical region which has been studied with the help of field methods.[3] It is characteristic that efforts in this direction have considered the behavior of mean quantities rather than the most probable quantities. Thus, the Landau theory[4] examines the self-consistent variation of the order parameter reduced to the first moment $\langle\psi\rangle$ of the fluctuating amplitude ψ of the hydrodynamic mode. In the mean-field approximation, the quantity $\langle\psi\rangle$ does not depend on the intensity of the fluctuations, whose role reduces to that of a trigger initiating the occurrence of the phase transition.

It should be borne in mind, however, that a description of a stochastic system can be achieved not only by the determination of mean quantities, but also most probable quantities. In the field scheme the expression for the probability has an exponential form with an argument that reduces, apart from its sign, to the standard action.[3] Therefore, a description of the phase transition with the help of most probable values corresponds to using the principle of least action. We show that the indicated approach makes it possible to extend the self-consistent field method to a description of fluctuating quantities. Such a scheme reveals an extremely nontrivial property: for some ratio of the inhomogeneity scales of the system, the most probable values tend with time not to minima of the free energy $F(\psi)$, where $\partial F/\partial\psi=0$, but to points at which $\partial^3 F/\partial\psi^3=0$.

To determine the spatiotemporal dependence of the amplitude of the hydrodynamic mode $\psi(\mathbf{r},t)$, we begin with the Langevin equation

$$\dot{\psi}(\mathbf{r},t)=-\gamma\frac{\delta\mathcal{F}}{\delta\psi(\mathbf{r},t)}+\zeta(\mathbf{r},t). \tag{1}$$

Here the dot above a symbol denotes differentiation with respect to t, $\mathbf{r}$ is the position vector, γ is the kinetic coefficient,

$$\mathcal{F}=\int\left[F(\psi)+\frac{\beta}{2}|\nabla\psi|^2\right]d\mathbf{r}, \tag{2}$$

$F(\psi)$ is the specific thermodynamic potential, $\beta>0$ is a constant, $\nabla\equiv\partial/\partial\mathbf{r}$, $\zeta(\mathbf{r},t)$ is a stochastic term representing white noise

$$\langle\zeta(\mathbf{r},t)\rangle=0,\quad \langle\zeta(\mathbf{r},t)\zeta(0,0)\rangle=T\delta(\mathbf{r})\delta(t), \tag{3}$$

the angular brackets denote averaging, and T is the temperature. In what follows it will be convenient to transform to dimensionless variables, scaling the spatial coordinates $\mathbf{r}$ by the interatomic distance a, time t by the time scale $a^3/T\gamma$, the quantity F by T/a^3, and the fluctuation ζ by $T\gamma/a^3$. Equation (1) then takes the canonical form

$$\dot{\psi}(\mathbf{r},t)=f(\mathbf{r},t)+\zeta(\mathbf{r},t),$$
$$f(\mathbf{r},t)\equiv-\partial F/\partial\psi+\nabla^2\psi(\mathbf{r},t), \tag{4}$$

where $f(\mathbf{r},t)$ is the force conjugate to the order parameter (its magnitude is determined by taking account of the spatial inhomogeneity). The region of applicability of the Ginzburg–Landau approximation (2) is determined by the condition that the distance scale a be much smaller than the correlation length $\xi=\beta^{1/2}|\partial^2F/\partial\psi^2|_{\psi=0}^{-1/2}$ (Ref. 4). Averaging expression (4) neglecting correlations, we obtain the Landau–Khalatnikov equation for the order parameter $\langle\psi(\mathbf{r},t)\rangle$.

The standard field scheme[3] is based on a study of the generating functional responsible for stochastic equation (4). This functional represents the functional Laplace transformation

$$Z\{u(\mathbf{r},t)\}=\int Z\{\psi(\mathbf{r},t)\}\exp\left(\int u\psi d\mathbf{r}dt\right)D\psi(\mathbf{r},t) \tag{5}$$

for the partition function

$$Z\{\psi(\mathbf{r},t)\}=\left\langle\prod_{(\mathbf{r},t)}\delta\{\dot{\psi}(\mathbf{r},t)-f(\mathbf{r},t)-\zeta(\mathbf{r},t)\}\det\left|\frac{\delta\zeta(\mathbf{r},t)}{\delta\psi(\mathbf{r},t)}\right|\right\rangle. \tag{6}$$

Here the argument of the δ function reduces to the Langevin equation (4), and the determinant, which transforms from a continuum integral over $\zeta(\mathbf{r},t)$ to a continuum integral over $\psi(\mathbf{r},t)$, is equal in the Ito calculus to unity.

In the standard approach[3] n-tuple variation of the functional (5) with respect to the auxiliary field $u(\mathbf{r},t)$ allows one to find the nth-order correlator for the amplitude of the

hydrodynamic mode $\psi(\mathbf{r},t)$ and to construct the perturbation theory. We, however, will start out from expression (6) for the conjugate functional $Z\{\psi(\mathbf{r},t)\}$, whose variation leads to the most probable realization of the stochastic field $\psi(\mathbf{r},t)$. Obviously, in the mean field approximation, the functional (6) reduces to the dependence $Z\{\langle\psi(\mathbf{r},t)\rangle\}$, which is responsible for the Landau free energy $F\{\langle\psi(\mathbf{r},t)\rangle\}=-T\ln Z\{\langle\psi(\mathbf{r},t)\rangle\}$ (Ref. 4).

Proceeding to a consideration of the functional (6), we represent the δ function in integral form

$$\delta\{x(\mathbf{r},t)\}=\int_{-i\infty}^{i\infty}\exp\left(-\int\phi x d\mathbf{r}dt\right)D\phi. \tag{7}$$

Then, averaging over the noise ζ with the help of the Gaussian distribution

$$P_0\{\zeta\}\propto\exp\left\{-\frac{1}{2}\int\zeta^2(\mathbf{r},t)d\mathbf{r}dt\right\}, \tag{8}$$

corresponding to conditions (3), with the help of Eq. (7) we reduce the functional (6) to standard form

$$Z\{\psi(\mathbf{r},t)\}=\int P\{\psi(\mathbf{r},t),\phi(r,t)\}D\phi,\quad P\equiv e^{-S}. \tag{9}$$

Here the probability distribution $P\{\psi,\phi\}$ is determined by the action $S=\int L d\mathbf{r}dt$, where the Lagrangian

$$L(\psi,\phi)=\phi(\dot{\psi}-f)-\phi^2/2. \tag{10}$$

Next we use the Euler equation

$$\frac{\partial L}{\partial x}-\frac{d}{dt}\frac{\partial L}{\partial\dot{x}}+\nabla^2\frac{\partial L}{\partial\nabla^2 x}=\frac{\partial R}{\partial\dot{x}},\quad x\equiv\{\psi,\phi\}, \tag{11}$$

where the dissipative function

$$R=\dot{\psi}^2/2. \tag{12}$$

As a result, the equations for the most probable realizations $\eta(\mathbf{r},t)$, $\varphi(\mathbf{r},t)$ of the stochastic fields $\varphi(\mathbf{r},t)$, $\varphi(\mathbf{r},t)$ take the form

$$\dot{\eta}=(\nabla^2\eta-\partial F/\partial\eta)+\varphi, \tag{13}$$

$$\dot{\varphi}=-\nabla^2\varphi-\varphi(1-\partial^2F/\partial\eta^2)-(\nabla^2\eta-\partial F/\partial\eta). \tag{14}$$

Comparison of Eq. (13) with stochastic equation (4), which coincides with it in form, shows that the fields $\eta(\mathbf{r},t)$, $\varphi(\mathbf{r},t)$ represent the most probable values of the amplitudes of the hydrodynamic mode and the fluctuations of the conjugate force. In what follows, for brevity we will refer to the quantities η and φ as the order parameter and the amplitude of fluctuations of the conjugate force.

It is noteworthy that the inhomogeneity of the order parameter $\eta(\mathbf{r},t)$ has the usual dissipative character whereas the inhomogeneity of the fluctuation field inters with opposite sign. Since we will be interested in what follows only in the nature of the time dependence, we will use the simplest approximation for the gradient terms

$$\nabla^2\eta\to\xi^{-2}\eta,\quad \nabla^2\varphi\to\lambda^{-2}\varphi, \tag{15}$$

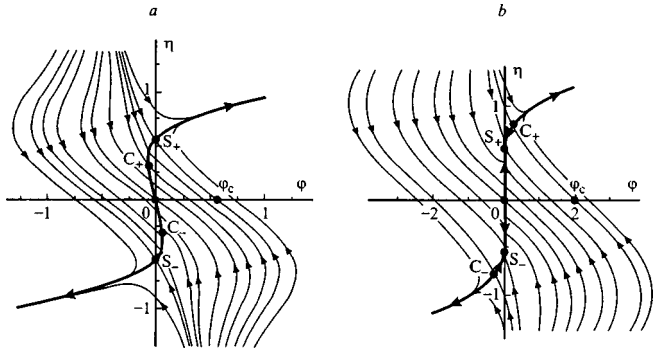

FIG. 1. Phase portrait for the η^4 model ($\varepsilon=-0.3$; $\xi=10^5$): $\lambda=10^5$ (a); $\lambda=0.8$ (b).

where the correlation length ξ and the parameter λ define the scales of the spatial inhomogeneities of the amplitudes of the hydrodynamic mode and the fluctuations of the force. As a result, Eqs. (13) and (14) take the form

$$\dot{\eta}=(\xi^{-2}\eta-\partial F/\partial\eta)+\varphi, \tag{16}$$

$$\dot{\varphi}=-\varphi[(1+\lambda^{-2})-\partial^2F/\partial\eta^2]-(\xi^{-2}\eta-\partial F/\partial\eta). \tag{17}$$

Let us first consider a second-order phase transition, for which the thermodynamic potential is represented by the η^4 model

$$F(\eta)=\frac{\varepsilon}{2}\eta^2+\frac{1}{4}\eta^4,\quad \epsilon\equiv\frac{T-T_c}{T_c}. \tag{18}$$

Substituting expression (18) into Eqs. (16) and (17), we obtain the system of equations

$$\dot{\eta}=\varphi+\eta[(\xi^{-2}-\varepsilon)-\eta^2], \tag{19}$$

$$\dot{\varphi}=\varphi\{-[(1+\lambda^{-2})-\varepsilon]+3\eta^2\}-\eta[(\xi^{-2}-\varepsilon)-\eta^2], \tag{20}$$

where analysis of this system of equations requires that we use the method of the phase plane.[5] Under conditions in which the Ginzburg–Landau approximation (2) is applicable, the correlation length $\xi\gg1$, and the magnitude of the gradient terms containing the order parameter has no effect on the form of the phase portrait (Fig. 1). The latter is characterized by the presence of singular points

$$O(0;0),\quad S_\pm(0;\pm(\xi^{-2}-\varepsilon)^{1/2}),$$
$$C_\pm(\pm3^{-3/2}(\lambda^{-2}-\varepsilon)^{1/2}[(\lambda^{-2}-3\xi^{-2})+2\varepsilon];$$
$$\pm3^{-1/2}(\lambda^{-2}-\varepsilon)^{1/2}). \tag{21}$$

For large λ the points O and $S_\pm$ are saddle points, and the points $C_\pm$ are stable nodes (Fig. 1a). Decreasing the parameter λ leads to a shift of the nodes $C_\pm$ toward the saddle points $S_\pm$ and for λ equal to its critical value $\lambda_c=(3\xi^{-2}-2\varepsilon)^{-1/2}$ they coalesce. With further decrease of the parameter λ, the nodes $C_\pm$ become saddle points, and the saddle points $S_\pm$ become nodes (Fig. 1b).

A characteristics peculiarity of these phase portraits is that the evolution of the system takes place in a region bounded by the critical value φ_c of the amplitude of the fluctuations corresponding to $\eta=0$ (outside of this region η

and φ grow without bound in the limit $t\to\infty$, which according to Eqs. (9) and (10) leads to the probability $P\to 0$). With increasing distance from the critical temperature the quantity φ_c increases monotonically. Growth of the inhomogeneity parameter in the region $\lambda<\lambda_c$ leads to a decrease in the critical fluctuations φ_c, and for values of $\lambda>\lambda_c$ the size of the fluctuation region does not change.

If we use the η^6 model

$$F=\frac{\varepsilon}{2}\eta^2-\frac{1}{4}\eta^4+\frac{1}{6}\eta^6 \tag{22}$$

for the first-order phase transition, Eqs. (16) and (17) take the form

$$\dot{\eta}=\varphi-\eta[-(\xi^{-2}-\varepsilon)-\eta^2+\eta^4], \tag{23}$$

$$\dot{\varphi}=\varphi\{-[(1+\lambda^{-2})-\varepsilon]-3\eta^2+5\eta^4\} + \eta[-(\xi^{-2}-\varepsilon)-\eta^2+\eta^4]. \tag{24}$$

The corresponding phase portrait is characterized by the singular points

$$O(0;0),\quad S_1^{\pm}(0;\pm\gamma_-),\quad S_2^{\pm}(0;\pm\gamma_+),$$

$$C_1^{\pm}(\pm 5^{-2}(5\lambda^{-2}-25\xi^{-2}-3(1-\beta)+20\varepsilon)\alpha_-;\pm\alpha_-),$$

$$C_2^{\pm}(\pm 5^{-2}(5\lambda^{-2}-25\xi^{-2}-3(1+\beta)+20\varepsilon)\alpha_+;\pm\alpha_+),$$

$$\alpha_{\pm}\equiv(3/10)^{1/2}(1\pm\beta)^{1/2},$$

$$\beta\equiv[1+(20/9)(\lambda^{-2}-\varepsilon)]^{1/2},$$

$$\gamma_{\pm}\equiv\{2^{-1}\pm[2^{-2}+(\xi^{-2}-\varepsilon)]^{1/2}\}^{1/2}. \tag{25}$$

In comparison with the corresponding set (21) for the second-order phase transition their number increases from 5 to 9. This is due to the appearance of a pair of centrosymmetric separatrices located between the separatrices belonging to the η^4 model passing through the points $(0;0)$, $(\pm\varphi c;0)$ in Fig. 1. Obviously, the appearance of additional separatrices reflects the presence of energy barriers in the region of intermediate values η of dependence (22).

As in the η^4 model, taking the inhomogeneity of the order parameter into account does not alter the form of the phase portrait whereas the inhomogeneity of the force fluctuations has a substantial effect. Indeed, with decrease of the parameter λ the nodes $C_1^{\pm}$ and saddle point O converge toward each other and finally coalesce in a single node at $\lambda_{c1}=\varepsilon^{-1/2}$. In turn, the nodes $C_2^{\pm}$ move along the separatrices toward the saddle points $S_2^{\pm}$, coalescing with them at $\lambda_{c2}=(\varepsilon-3\gamma_+^2+5\gamma_+^4)^{-1/2}$. With further decrease of the parameter λ the points $C_2^{\pm}$ become saddle points and continue their motion along the separatrices whereas the points $S_2^{\pm}$, transforming into stable nodes, remain as before on the η axis.

According to Eq. (9), the probability of obtaining the phase trajectory responsible for the initial conditions $(\varphi_0,0)$ is represented in the form

$$P\propto\exp\left\{-\int(\varphi^2/2)dt\right\}, \tag{26}$$

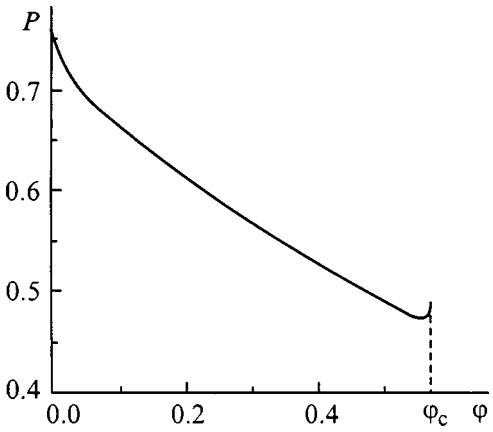

FIG. 2. Probability of obtaining phase trajectories with initial conditions $(\varphi_0,0)$ for the η^4 model ($\varepsilon=-0.3$; $\xi=\lambda=10^5$).

where expressions (10) and (13) have been taken into account. The corresponding dependence for a second-order transition is shown in Fig. 2, from which it is obvious that the probability (26) grows monotonically with approach to the origin. An insignificant increase is observed also near the point φ_c responsible for the separatrix. Outside the region bounded by the separatrix we have $P(\varphi)=0$ since here $\varphi(t)\to\pm\infty$ as $t\to\infty$. In the case of a first-order transition, the dependence plotted in Fig. 2 preserves its decreasing character with the difference that the indicated insignificant increase in the probability is observed near the critical value of φ responsible for the additional separatrix.

The indicated behavior of the probability $P(\varphi_0)$ is explained by the nature of the time dependence $\varphi(t)$ of the amplitude of the fluctuations during relaxation of the initial value φ_0. Far from the segment OCS (Fig. 1) the quantity φ changes its value rapidly, and with approach to this segment this variation of value slows down. This behavior is explained by the fact that the action $S\{\eta(\mathbf{r},t),\varphi(\mathbf{r},t)\}$ varies much more slowly near the indicated segment than far from it. This can be visualized by associating the segment OCS with the bed of a large river.[6]

The self-consistent behavior of the fluctuations of the conjugate force and of the hydrodynamic mode responsible for ordering allow us to represent the coordinates of the phase plane η and φ as components of a common vector in a super symmetric space.[7,8] As is well known,[9] the formal condition for such a representation, implying the presence of supersymmetry, consists in the requirement that the superpotential $\partial F/\partial\eta$ take opposite signs in the limits $\eta\to+\infty$ and $\eta\to-\infty$. Obviously, for the implemented models (18) and (22), this condition, which implies unbounded growth of the free energy $F(\eta)$ in the limit $\eta\to\pm\infty$, is fulfilled automatically. In contrast to the indicated condition, which has global character, the presence of a stationary state requires local supersymmetry. This means that, near points of the supersymmetric space responsible for the stationary state, there is no preferred direction (the presence of such symmetry leads to the fluctuation–dissipation theorem[3]). Within the framework of the developed scheme, local supersymmetry reduces to a trivial requirement: singular points should exist in the

phase portrait, near which the nature of the behavior of the trajectories does not depend on direction. Obviously, such points can be only centers or nodes (but not saddle points, near which local symmetry is violated). The presence of dissipation leads to a selection of attractive nodes while global supersymmetry limits their positions to finite values of the order parameter η. As a result, the stationary state of the system is responsible for the attractive nodes, at which, according to the equations of motion (16) and (17), the condition

$$\partial^2 F/\partial\eta^2=\lambda^{-2}, \quad \varphi=\partial F/\partial\eta-\xi^{-2}\eta\equiv -f. \tag{27}$$

is fulfilled. The first of these equations determines the susceptibility λ^2 on the scale λ, and according to the second the most probable value φ of the fluctuation of the self-consistent force is equal to it in magnitude but opposite in sign. As can be seen from Fig. 1, depending on the magnitude of the inhomogeneity parameter of the fluctuations, λ, two types of stationary states are possible. For a strongly inhomogeneous distribution of the fluctuations ($\lambda<\lambda_c$) an attractive node corresponds to the point *S* in Fig. 1b, where the amplitude of the fluctuations $\varphi=0$. According to Eq. (27), the equilibrium thermodynamic state $f=0$ is realized in this case. In the opposite case $\lambda>\lambda_c$, corresponding to the phase portrait in Fig. 1a, the system tends toward the point *C*, at which $\varphi,\eta\neq 0$, but $\partial^3 F/\partial\eta^3=0$.

We point out in conclusion the obvious analogy of the developed scheme to the Ginzburg–Landau theory of superconductors, the nature of whose behavior is determined by the ratio λ/ξ of scales of variation of the magnetic field (which corresponds here to the amplitude of the fluctuations) and the order parameter.[10] As is well known, for above-critical values of λ/ξ, a mixed state is realized which represents a stationary heterogeneous mixture of the normal and superconducting states. In our case, this corresponds to an alternation of regions with enhanced values of the order parameter or amplitude of the fluctuations. Since the size of regions of the first kind is determined by the correlation length ξ, and of regions of the second kind, by the scale λ, such a heterogeneous state does not reduce to a mixture of phases, but represents a unified thermodynamic state. According to this analysis, it is realized outside the region of the phase portrait bounded by the critical value φ_c of the initial fluctuation φ_0. Since unbounded growth of the amplitude of the fluctuations $\varphi(t)$ and the order parameter $\eta(t)$ takes place for $\varphi_0>\varphi_c$ (Fig. 1), this implies that the system is unstable with respect to heterogenization. However, according to Fig. 2, the probability of the occurrence of a process realizing such an instability is zero.

This work was carried out with the partial support of the Ukrainian Ministry of Science (Grant No. 2.4/4).

*)E-mail: Alexander@olem.sumy.ua
†)E-mail: valera@ssu.sumy.ua

[1] A. Z. Patashinskiĭ and V. L. Pokrovskiĭ, *Fluctuation Theory of Phase Transitions* [in Russian] (Nauka, Moscow, 1982), 381 pp.
[2] C. Domb, *The Critical Point* (Taylor and Francis, London, 1996), 376 pp.
[3] J. Zinn-Justin, *Quantum Field Theory and Critical Phenomena* (Clarendon Press, Oxford, 1994), 996 pp.
[4] L. D. Landau and E. M. Lifshitz, *Statistical Physics*, Parts 1 and 2, 3rd ed. (Pergamon Press, Oxford, 1980), 584 pp.
[5] A. A. Andronov, A. A. Vitt, and S. É. Khaĭkin, *Theory of Oscillations* [in Russian] (Nauka, Moscow, 1981), 568 pp.
[6] A. I. Olemskoĭ and A. V. Khomenko, Zh. Éksp. Teor. Fiz. **110**, 2144 (1996) [JETP **83**, 1180 (1996)].
[7] A. I. Olemskoi, I. V. Koplyk, and V. A. Brazhnyi, J. Phys. Stud. **1**, 324 (1997).
[8] A. I. Olemskoĭ and I. V. Koplyk, Usp. Fiz. Nauk **165**, 1105 (1995).
[9] L. É. Gendenshteĭn and I. V. Krive, Usp. Fiz. Nauk. **146**, 553 (1985) [Sov. Phys. Usp. **28**, 281 (1985)].
[10] E. M. Lifshitz and L. P. Pitaevskiĭ, *Statistical Physics*, Pt. 2 (Butterworth Heinemann, Oxford, 1995), 488 pp.

Translated by Paul F. Schippnick

LOW-DIMENSIONAL SYSTEMS AND SURFACE PHYSICS

Oscillations and quantization of resistance at the temperature critical points of PbS–PbTe–PbS three-layer films on (001) KCl

A. I. Fedorenko,*) V. V. Zorchenko, A. Yu. Sipatov, O. A. Mironov, S. V. Chistyakov, and O. N. Nashchekina

Khar'kov State Polytechnic University, 310002 Khar'kov, Ukraine
(Submitted October 20, 1998; accepted February 12, 1999)
Fiz. Tverd. Tela (St. Petersburg) **41**, 1693–1697 (September 1999)

Oscillations and a set of inflection points have been discovered in the temperature dependences of the resistance of single-crystal PbS–PbTe–PbS three-layer films on (001) KCl. Extrema and inflection points are observed at the temperatures $(m/n)T_0$ ($T_0=5.238$ K), and at these temperature critical points the resistance of the samples takes one of the values $(p/q)R_Q$, where $R_Q=25812.8\,\Omega$ is the resistance quantum; and m, n, p, and q are integers. © *1999 American Institute of Physics.* [S1063-7834(99)03409-7]

It was shown earlier that the temperature dependence of the resistance of metallic island films on an insulating substrate,[1] the two-layer films PbS/PbTe (111) and PbSe/PbTe (111) on mica,[2] and PbTe/Pbs (001) multilayers on KCl[3] have a set of inflection points at temperatures $T=nT_0$ (multiples of the temperature $T_0=5.238$ K), and at these critical points the resistance of the island films[1] and of tunnel contacts[4] with a dielectric buffer layer, inside of which an island metallic layer is sealed, turned out to be equal to $(p/q)R_Q$, where $R_Q=25812.8\,\Omega$ is the resistance quantum; n,p,q are integers. The present paper reports the observation of inflection points and oscillations in the temperature dependence of the resistance $R(T)$ and also on the quantization of $R(T)$ at the critical points of PbS–PbTe–PbS three-layer films on (001) KCl, which have the minimum number of layers of a structural unit manifesting superconducting properties.[3,5]

The samples were prepared in vacuum ($P\sim10^{-4}$–10^{-5} Pa) by successive thermal evaporation of lead chalcogenides onto a (001) KCl surface at 520–570 K.[3,5] The films were single-crystal layers with regular square grids of mismatch dislocations at the (001) interphase boundaries with distance between the dislocation grid-points equal to 5.2 nm. The layer thicknesses were monitored by a quartz resonator and were determined by x-ray diffraction techniques with an accuracy not worse than 0.1 nm (Ref. 5). The samples were condensed through the window of a mask having the shape of a double Hall cross. The dimensions of the samples were 10×1 mm^2. The resistance was measured by the constant-current four-probe technique with an error $\leqslant0.03\%$. The samples were mounted on a copper block which was placed in a metallic helium cryostat inside a superconducting solenoid. The temperature of the sample in the interval 4.2–300 K was controlled by the current through a resistance heater located inside the copper block. The temperature was stabilized with the help of an electronic feedback circuit which maintained the temperature at a prescribed level for an extended period of time with an accuracy not less than 0.05 K at $T\sim250$ K. When the temperature was lowered, the amplitude of the temperature oscillations of the sample rapidly decreased. The temperature interval 1.5–4.2 K was covered by outpumping liquid-helium vapors using a fore-vacuum pump (the temperature instability did not exceed 0.005 K). The resistance of the samples was determined during those time periods when their temperature remained unchanged. The temperature of the samples was monitored and measured by a platinum resistance thermometer (working interval 13–300 K) and two semiconductor resistive sensors with working intervals 2–30 K and 1.5–300 K. The temperature measurement error did not exceed 0.02 K at $T\sim250$ K and 0.002 K at $T\sim4$ K.

The current–voltage characteristics (CVC's) were recorded for each of the samples at $T=250$ K. The magnitude of the measuring current $(0.5-1)\times10^{-5}$ A was chosen so that this current corresponded to the linear ohmic segment of the CVC of the given sample and was roughly four times smaller than the currents at which deviations from linearity became noticeable. After cooling the sample and measuring $R(T)$, the CVC was measured a second time at a temperature slightly above the superconducting transition temperature of the sample. For all of the samples the initially chosen value of the measuring current was found to lie within the limits of the ohmic segment of the corresponding low-temperature CVC. Estimates showed that the heating of the films by the current did not exceed ~0.005 K over the entire range of temperatures in which the measurements were performed. During measurement of $R(T)$ the Earth's magnetic field and other possible external magnetic fields were compensated with the help of the superconducting solenoid.

Figures 1 and 2 display the temperature dependence of the resistance of three samples having different PbTe layer thicknesses (d_{PbTe}), whose general nature of behavior differ dramatically. For the sample with $d_{\mathrm{PbTe}}=5$ nm (Fig. 1) the resistance has a minimum at $T=209.53$ K and increases by

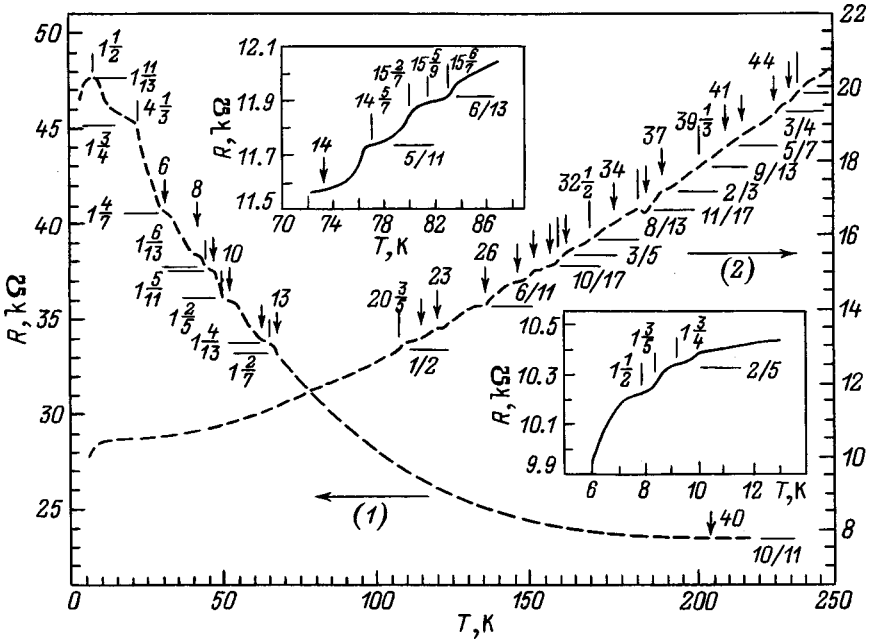

FIG. 1. Temperature dependence of the resistance of the three-layer films PbS (20 nm)–PbTe–PbS (20 nm) with PbTe layer thicknesses: $d_{\mathrm{PbTe}}=5$ nm (*1*) and $d_{\mathrm{PbTe}}=8$ nm (*2*). The insets show segments of curve (*2*) in magnified scale. The arrows and vertical lines segments here and in Fig. 2 indicate the position of temperature critical points of the form $T_{cr}=nT_0$ and $T_{cr}=(m/l)T_0$, and the figures above them show the values of n and m/l. The vertical dashes for which the values of m/l are not shown correspond to temperatures differing from nT_0 by $(1/2)T_0$. The horizontal dashes mark the resistance levels $(p/q)R_Q$, and the adjacent fractional values give the corresponding values of p/q. For curve (*2*) the upper horizontal level is $(10/13)R_Q$.

roughly twofold as the temperature is increased to 10 K. Note that an abrupt growth in the resistance as the temperature is lowered from 573 K to room temperature was observed earlier for two-layer films of lead chalcogenides having a hexagonal grid of mismatch dislocations on the interphase boundary,[2] although (111) PbTe single-layer films on mica exhibited the usual falloff in the resistance in the same temperature interval. This is evidence of a strong electron localization at the nuclei of the mismatch dislocations.[2] The resistance of the sample with $d_{\mathrm{PbTe}}=8$ nm (Fig. 1) decreased as the temperature was lowered while the sample with $d_{\mathrm{PbTe}}=16$ nm (Fig. 2) exhibited the usual behavior. Upon first cooling, its resistance behaved in a way similar to the resistance of the sample with $d_{\mathrm{PbTe}}=8$ nm (see the inset to Fig. 2) while on the second cooling the behavior of its resistance was radically different, manifesting oscillations with gigantic amplitude.

The temperature dependences $R(T)$ in Figs. 1 and 2 are characterized by the presence of a set of temperature critical points T_{cr}, which being inflection points and extrema of $R(T)$. The positions of these points were determined by numerical methods by interpolating the dependences $[R(T)]$ with trigonometric polynomials or a Lagrange interpolating polynomial with subsequent differentiation and then finding the extrema and zeros of dR/dT corresponding to the inflection points and extrema of $R(T)$. These interpolation methods delivered essentially identical results. Such a procedure gave values of the temperature critical points $R(T)$ and the

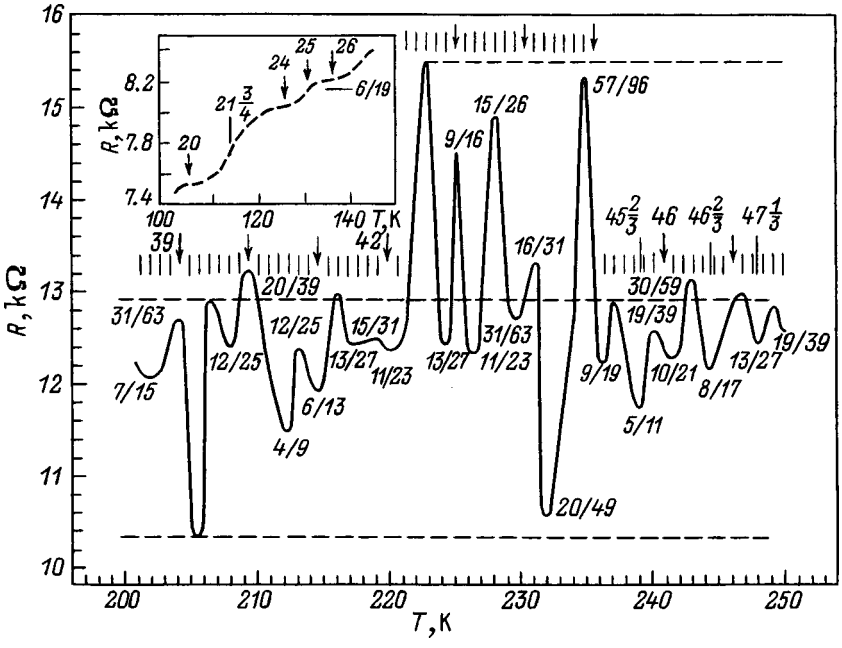

FIG. 2. Temperature dependence of the resistance of the PbS–PbTe–PbS three-layer films with layer thicknesses 16 nm upon being cooled a second time from room temperature. The inset shows the change in the resistance of the sample following the first cooling to 4.2 K. The short vertical dashes mark offsets from nT_0 by multiples of $T_0/7$. The figures alongside the extrema indicate the resistance of the sample at the given extrema in units of the resistance quantum $R_Q=25812.8\ \Omega$. The horizontal dashed lines mark the resistance levels (2/5), (1/2), and $(3/5)R_Q$.

magnitude of the resistance at them with roughly the same accuracy as was obtained for the temperature and resistance measurements.

It turned out that the critical temperatures T_{cr} take values from a discrete set $(m/n)T_0$ (m,n are integers). The positions of some of these points are shown in Figs. 1 and 2 by vertical arrows and dashes with the corresponding values of (m/n) indicated. For the sample with $d_{\mathrm{PbTe}}=16$ nm (Fig. 2), for which the temperature dependence was measured with a step of 0.2 K, extrema (and inflection points) were observed at $T_{cr}=(m/7)$ with the exception of three minima at (45 2/3), (46 2/3), and $(47\ 1/3)T_0$.

The values of (m/n) were determined as follows. For each critical point we calculated the ratio $\xi=T_{cr}/T_0$ and then compared ξ with all rational fractions of the form (m/n), where n are one- and two-digit integers. We chose those values of (m/n) that fell in the neighborhood of the ratio ξ: $\xi\pm(\Delta T/T_0)$, where ΔT is the measurement error of the temperature of the sample (including an estimate of heating of the film by the current). At temperatures T_{cr} below ~ 50 K only one value of (m/n) fell in the indicated interval. At higher temperatures, a unique choice of n was also maintained for T_{cr} with $n=1,2$ while for critical points T_{cr} with $n>2$ several values of (m/n) fell into this interval. For example, for the last minimum of $R(T)$ in Fig. 2, besides the value $(m/n)=47\ 1/3$ the alternate candidates 47 33/98 and 47 32/97 also presented themselves. In such cases of large n we gave preference to values of (m/n) for which n was a number with one digit ($n=3.7$).

Like for island films[1] and tunnel contacts,[4] it turned out that the resistance of the samples at least at some of the critical points takes one of the values $(p/q)R_Q$. The values (p/q) were determined using the same method as was used to find (m/n). Since the ratio $\Delta R/R_Q$ (ΔR is the measurement error of the resistance) is an order of magnitude smaller than the ratio $\Delta T/T_0$, the procedure gave the only possible value of (p/q) (with the exception of three cases, see below).

An analysis of the set of values (p/q) for Fig. 2 revealed that the resistance of the sample in the investigated temperature range undergoes oscillations lying in a band from (2/5) to $(3/5)R_Q$ centered at $(1/2)R_Q$. The experimental values of (p/q) for the extrema of $R(T)$ are numbers of the form $r/(2r+1)$ ($r=2$, 4–13, 15, 19, 31), $r/(2r-1)$ ($r=3$, 16, 20, 30), $3r/(5r+1)$ ($r=1$, 3, 5, 19), $2r/(5r-1)$ ($r=1, 2, 10$), while the fractions 2/5, 1/2, and 3/5 are limiting values of the numbers of this form in the limit $r\to\infty$. For the fifth and two last ($T>245$ K) maxima of $R(T)$ the corresponding values of p and q turn out to be very large, so that it was possible to choose them to have single-digit values within the limits of the measurement error. Note that for the sample with $d_{\mathrm{PbTe}}=8$ nm (Fig. 1) the values of the resistance (5/11), (6/13), (2/5), (1/2), and $(3/5)R_Q$ at the critical points coincide with the corresponding values for the sample with $d_{\mathrm{PbTe}}=16$ nm (Fig. 2). Note also that the superconducting transition temperature T_c of PbTe/PbS multilayers on KCl (Ref. 3) take one of the values $T_{cr}=(m/n)T_0$ if it is defined as the inflection point of the $R(T)$ curve in the region of the transition. For example, for the sample with $d_{\mathrm{PbTe}}=8$ nm we have $T_c=(5/7)T_0$ while the resistance of the sample at this temperature is equal to $(1/7)R_Q$.

We emphasize that, at temperatures differing from the temperature critical points by not more than 0.01–0.02 K, the measured resistance of the samples deviated from the quantized value by not more than 0.05%. For example, at the minimum of $R(T)$ at 217 K corresponding to $(41\ 3/7)T_0$ the experimental value $R=12430\ \Omega$ differs from the value $(13/27)R_Q=12428.38\ \Omega$ by only $\sim 0.013\%$. Possible inaccuracies in the extrapolation of the behavior of $R(T)$ between neighboring temperature points at which R was measured cannot noticeably influence the results. The data indicate that, within the limits of measurement error, the surface resistance of our samples $R_s=R/10$ is quantized at the temperature critical points since the deviations in the shape and size of the window of the mask from the prescribed values in its fabrication are of the same scale as the relative measurement error of the resistance.

The temperature dependence of the resistance of PbTe/PbS multilayers are characterized by the same peculiarities as the three-layer samples. However, we can still not draw a definite conclusion regarding the possibility of quantization of the resistance in the multilayer structures due to a lack of experimental data on the $R(T)$ dependences measured with a small enough temperature step.

Note that the $R(T)$ dependences measured by us on three-layer samples with intermediate thicknesses d_{PbTe} between 5 and 16 nm (7, 10, and 12 nm) look qualitatively similar to curve *2* in Fig. 1. Such pronounced oscillations of $R(T)$ as in Fig. 2 were not observed. The starting resistance and the temperature dependences $R(T)$ of samples with the same d_{PbTe} and d_{PbS} prepared during different condensation cycles differ from one another; this is probably due mainly to a small, uncontrollable difference in the stoichiometry of the films. For a specific film in the cooling–heating cycle in the temperature interval ~ 100 K, the forward and reverse legs of the $R(T)$ dependences usually essentially coincide although sometimes noticeable deviations of the $R(T)$ dependence were observed in a bounded temperature interval upon reheating. In the subsequent cycle of cooling and heating the $R(T)$ dependence deviated from its course in the previous cycle (an example of such a strong deviation is shown in Fig. 2). Such hysteretic behavior of the resistance is characteristic of lead chalcogenides, and also of structures in which the so-called systems of temperature critical points are manifested.[6] The peculiarities of $R(T)$ in our case can probably also be assigned to this class of phenomena (see, e.g., the paper by Balagurova *et al.* in Ref. 6, which shows peaks in $R(T)$ for samples of PbTe).

Note that PbTe/PbS superlattices (SL) on (001) KCl, in terms of their properties and to a certain extent in terms of their structure, are analogs of HTSC materials.[3,5] In this case, the role of the twinned CuO_2 planes in the unit cell, separated by their metal atoms (e.g., yttrium in $YBa_2Cu_3O_{7-\delta}$), is played by the square grids of mismatch dislocations at the boundary of PbTe with PbS, while the dislocation sites are analogs of the copper–oxygen tetrahedra with their base in the CuO_2 planes. From this point of view, PbS–PbTe–PbS sandwiches should be similar in their properties to

$YBa_2Cu_3O_{7-\delta}$ films which are one unit cell thick. Therefore, one can expect a qualitative similarity of the $R(T)$ temperature dependences for HTSC materials and PbTe/PbS multilayers. Indeed, in the $R(T)$ dependences presented in the literature, numerous steps and extrema are often visible (see, e.g., the data for La_2CuO_{4-y} (Ref. 7), $YBa_2Cu_3O_{7-\delta}$ (Ref. 8), and $Bi_2Sr_{2.2}Ca_{0.8}Cu_2O_8$ (Ref. 9) single crystals; however, one cannot determine the position of the critical points in $R(T)$ and the value of the surface resistance at these points from these dependences with sufficient accuracy. It is curious that for La_2CuO_{4-y} (Ref. 7) the $R(T)$ curve has a characteristic step between $12T_0$ and $13T_0$ which is very similar to the step in the same temperature interval for our sample with $d_{PbTe}=5$ nm (Fig. 1). Most suitable for comparison are superlattices fabricated from HTSC materials, and single HTSC layers sealed on both sides with insulating layers of a higher-resistance HTSC. We analyzed the data of Ref. 10 for a one-unit-cell thick $YBa_2Cu_3O_{7-\delta}$ film epitaxially grown on (100) $SrTiO_3$, covered on both sides by $PrBa_2Cu_3O_{7-\delta}$ films with a thickness of 6 and 11 unit cells, and also data for YBCO/PrBCO superlattices with one-unit-cell thick layers (10 periods). As far as can be determined from Figs. 2 and 3 of that paper, for a single YBCO layer and for a superlattice the superconducting transition temperature determined from the inflection point of the $R(T)$ curve is $(13\ 1/3)T_0$ and $13T_0$, and the resistance of samples with dimensions $10\times 1\ mm^2$ at these points are $1/3)R_Q$ and $(3/7)R_Q$ (calculated for one YBCO layer). Although these results support the hypothesis of qualitative similarity of the resistive properties of PbTe/PbS and HTSC multilayers, its confirmation would, of course, require special precision studies of these objects.

The observation of an ordered set of temperature critical points and quantization of the surface resistance of the samples at these points in such radically different objects as island metal films, layered structures of lead chalcogenides (and, apparently, HTSC's) points to the fundamental character of these phenomena, the reason for which is still unknown. All these structures are characterized by the presence of regions of electron localization—islands and dislocation grids, or CuO_2 planes in HTSC's. As was shown in Refs. 1 and 4, for tunnel contacts and island metallic films, the current–voltage characteristics have critical points in the form of current (or voltage) jumps for voltages on the samples that are multiples of $V_0=16.25$ mV, and the temperature $T_0=(1/36)eV_0$ (in energy units). The value of T_0 calculated from this equality, 5.238 K, gives a set of T_{cr} values in good agreement with the experimental data. Note that it is necessary to calculate T_0 out to three places beyond the decimal point since the calculated and experimental values of the temperature critical points can differ by tens of T_0 even for a relatively small error (~ 0.001 K) in the calculated value of T_0.

The potential difference V_0 can be represented in the form[4] $V_0=e/R_0$, where the length $R_0=88.607$ nm turns out to be a bit smaller (by 2.8%) than the inverse Rydberg constant $R_\infty^{-1}=91.127$ nm ($R_\infty=me^4/4\pi\hbar^3c$). Using the length R_0, it is possible formally to define a unit of the magnetic field $H_0=\phi_0/\pi R_0^2$, where $\phi_0=ch/2e$ is the magnetic flux quantum ($H_0=838.37$ Oe). It turns out that the magnetic-field dependence of the pinning force of PbTe/PbS superlattices on KCl and $YBa_2Cu_3O_{7-\delta}$ films, and also of the resistance of a Bi/Sb (111) superlattice on mica[11] exhibit oscillations with extrema which argue in favor of $H_{cr}=(p/q)H_0$. The closeness of R_0 and R_∞^{-1} is hardly random. This circumstance may show the way to an explanation of the described phenomena.

*)E-mail: fedor@kpi.kharkov.ua

[1] V. V. Zorchenko, V. P. Sapelkin, and A. A. Udovenko, Fiz. Tverd. Tela (Leningrad) **32**, 905 (1990) [Sov. Phys. Solid State **32**, 534 (1990)].
[2] S. N. Grigorov, V. V. Zorchenko, D. A. Litvinov, and V. P. Sapelkin, Ukr. Fiz. Zh. **35**, 708 (1990); Voprosy Atom. Nauki Tekh. Ser. Yaderno-Fiz. Issled. (Teor. Éksp.), No. 4(12), 88 (1990).
[3] O. A. Mironov, V. V. Zorchenko, A. Yu. Sipatov, A. I. Fedorenko, O. N. Nashchekina, and S. V. Chistyakov, Defect Diffus. Forum **103–105**, 473 (1993).
[4] V. V. Zorchenko, V. P. Sapelkin, and A. A. Udovenko, Fiz. Tverd. Tela (Leningrad) **30**, 2349 (1988) [Sov. Phys. Solid State **30**, 1354 (1988)].
[5] O. A. Mironov, B. A. Savitskiĭ, A. Yu. Sipatov, A. I. Fedorenko, A. N. Chirkin, and L. P. Shpakovskaya, JETP Lett. **48**, 106 (1988); N. L. Bobrov, L. F. Rybal'chenko, V. V. Fisun, I. K. Yanson, O. A. Mironov, S. V. Chistyakov, V. V. Zorchenko, A. Yu. Sipatov Fiz. Niz. Temp. **16**, 1531 (1990) [Sov. J. Low Temp. Phys. **16**, 862 (1990)].
[6] *Systems of Temperature Critical Points in Solids* [in Russian], edited by Yu. N. Venevtsev and V. I. Muromtsev (Nauka, Moscow, 1986).
[7] M. Ribault and J. Joffrin, Solid State Commun. **69**, 1031 (1989).
[8] L. I. Buravov, L. Ya. Vinnikov, G. A. Emel'chenko, P. A. Kononovich, V. N. Laukhin, Yu. A. Osip'yan, and I. F. Shchegolev, JETP Lett. **47**, 60 (1988).
[9] S. Martin, A. T. Fiory, R. M. Fleming, L. F. Schneemeyer, and J. V. Waszczak, Phys. Rev. Lett. **60**, 2194 (1988).
[10] Y. Matsuda, S. Komiyama, T. Terashima, K. Shimura, and Y. Bando, Phys. Rev. Lett. **69**, 3228 (1992).
[11] B. A. Aminov, S. Sh. Akhmedov, Do Tkhi Sham, V. V. Kondratenko, Ya. G. Ponomarev, A. B. Tennakun, and A. I. Fedorenko, Fiz. Niz. Temp. **16**, 939 (1990) [Sov. J. Low Temp. Phys. **16**, 548 (1990)].

Translated by Paul F. Schippnick

Transport and heating of electrons in semiconductors with a one-dimensional superlattice

Yu. A. Romanov and E. V. Demidov

Institute of the Physics of Microstructures, Russian Academy of Sciences, 603600 Nizhniĭ Novgorod, Russia
(Submitted February 23, 1999)
Fiz. Tverd. Tela (St. Petersburg) **41**, 1698–1706 (September 1999)

On the basis of the Boltzmann equation with a new model collision integral that takes into account the redistribution of energy and momentum of all degrees of freedom of the electron, we have constructed and investigated a three-dimensional model of electron transport in one-dimensional semiconductor superlattices (SL's). The current–voltage curves (CVC), mean energies, and effective temperatures of the electrons have been found for vertical and longitudinal transport. In contrast to one-dimensional models, the approach developed here allows one to take into account and describe not only longitudinal electron heating, but also electron heating transverse to the current. For vertical transport, transverse heating substantially alters the position, magnitude, and width of the current maximum. For longitudinal transport, electron heating that is non-quadratic in the field arises along the superlattice axis even in the approximation of a linear current–voltage characteristic. The possibility of describing electron transport in a superlattice using a mixed Fermi distribution with an isotropic temperature is analyzed. © *1999 American Institute of Physics.* [S1063-7834(99)03509-1]

The unique electrical properties of semiconducting superlattices (SL's) (negative differential conductivity (NDC),[1–3] absolute negative conductivity,[4,5] induced[5] and self-induced[4] transparency, etc.) are due to peculiarities in the dynamics of the electrons in narrow minibands (Bloch oscillations), and interminiband transitions and relaxation processes leading to heating of the electron gas. While the dynamics of an electron in the minibands both in a constant and in a harmonic electric field have been studied in sufficient detail, the relaxation processes of the electrons and their role in the properties of the superlattices have not been sufficiently examined. Ignoring them completely sometimes leads even to qualitatively invalid results. It was for this reason in particular that Holthaus[6] erroneously asserted that the effect of self-induced transparency is absent in a non-dissipative superlattice. Even very weak collisions qualitatively alter the spectrum of the plasmon vibrations,[7] the soliton dynamics,[8] etc.

The important role even of weak collisions in superlattices is tied to the possibility of the appearance of coherence of nonlinear Bloch oscillations both in a constant and in an alternating electric field, described by the collisionless dynamics of one electron. Collisions during a time $\Delta t \geqslant \tau$ (τ is the characteristic relaxation time of the electron distribution) destroys this coherence, and the corresponding coherence effects (e.g., oscillations of the current with the Bloch frequency) disappear. The effect of self-induced transparency contains within itself the effect of self-action and harmonic generation. It is well known[3] that completely ignoring collisions in a treatment of the self-action effect even in semiconductors with small nonparabolicity leads to a result that differs by a factor of three from the correct result obtained in the limit $\omega\tau \to \infty$ (ω is the frequency of the field). Mathematically, this means that the limit $\omega\tau \to \infty$ must be taken not at the beginning but at the end of the calculations since uncertainties arise in the intermediate equations reflecting the dependence of the result on the initial conditions and the time the field is switched on, i.e., on its initial phase.

Studies of the electrical properties of superlattices usually utilize the classical Boltzmann equation with one relaxation time τ in the collision integral (the so-called τ approximation). In this approximation, motion of the electrons along the superlattice axis and transverse to it (in the absence of a transverse magnetic field) are independent. Therefore, for example, in an electric field parallel to the superlattice axis (vertical transport) it gives zero transverse heating of the electron gas. Some merely quantitative refinement of the τ approximation is afforded by using a Boltzmann equation with two relaxation times, for the symmetric and antisymmetric parts of the one-dimensional distribution function[9] or the corresponding equations for the drift velocity and the mean longitudinal energy of the electron.[4] All of these are variants of the one-dimensional Cp model in which the collisions do not redistribute between the degrees of freedom of the electron the energy and momentum transferred to it by the electric field. However, real collisions alter and mix the states of the electron in all three dimensions. Therefore the energy and momentum get redistributed among the degrees of freedom of the electron. This, in particular, leads to heating of the electron gas not only in the direction of the electric current, but also transverse to it, which, of course, is reflected in the current–voltage characteristics of the superlattice.

It was with the aim of moving beyond the framework of one-dimensional models that Lei *et al.*[10,11] developed a model of balance equations based on a momentum-shifted three-dimensional Fermi electron distribution function with

an isotropic effective temperature T_e. This method is also unsatisfactory for describing transport and relaxation processes in superlattices. In particular, it gives continuous growth of T_e with growth of the electric field **E**, i.e., a greatly overestimated transverse heating, which contradicts the results of Monte Carlo calculations[12] and simple physical arguments. This is a direct consequence of incorrect substitution of the shifted Fermi distribution for the true electron distribution. Indeed, if $T_e \to \text{const}$ as $\mathbf{E} \to \infty$ (or more accurately, if the mean energy of the electron remains finite while the distribution function tends to some limiting function, which in fact is the case in a superlattice with narrow minibands for vertical transport due to fast Bloch oscillations and the random nature of the collisions), then the rate of transfer to the lattice of the energy delivered to the electrons by the field $\mathbf{jE} \to \text{const}$ (**j** is the current density). Consequently, $\mathbf{j} \to 0$ as $\mathbf{E} \to \infty$. For a shifted Fermi distribution function with isotropic temperature this is possible only in the limit $T_e \to \infty$ (we exclude an unreal shift to the boundary of the miniband). In this case the variant $\mathbf{j} \to \text{const}$, $T_e \to \infty$ as $\mathbf{E} \to \infty$ also exists. The assertion that electron–electron collisions undergird the validity of the shifted Fermi distribution in a superlattice is erroneous.[10] It is well known that, in crystals having narrow Brillouin bands and/or in the presence of a significant fraction of open isoenergy surfaces in them, as is the case in a superlattice, electron–electron collisions are accompanied, as a rule, by Peierls distortions. Such collisions lead to relaxation of the average momentum and drift velocity of the electrons (additional resistance of the sample) and, consequently, to the establishment of an ''isotropic'' (not momentum-shifted!) distribution function. This result is well known in the theory of metals with open Fermi surfaces.[13] With the aim of providing a solid basis for the results of Refs. 10 and 11, Lei in Refs. 14 analyzed the role of Peierls distortions in electron collisions with impurities and phonons. However, as his electron distribution function, he took the shifted Fermi function with isotropic temperature as in his previous work. Therefore, the refinements of Ref. 14 are only quantitative and the erroneous character of the description of heating remains as before.

Such a state of the theory hinders an interpretation and understanding of the experimental results on superlattices. For example, use of the one-dimensional model with two relaxation times—of the velocity (ν_p^{-1}) and the energy (ν_ε^{-1})—in the processing of the experimental current–voltage characteristics (CVC's) in the case $\nu_p/\nu_\varepsilon = 10$ gives a value for ν_ε that is four times too high.

The present work examines the CVC's and heating of the electrons in a semiconductor having a one-dimensional superlattice with all three degrees of freedom of the electron taken into account on the basis of the Boltzmann equation with the three-dimensional model collision integral proposed in Ref. 15. This integral allows for redistribution of the energy and momentum transferred from the field between all degrees of freedom of the electron and therefore describes both longitudinal and transverse (relative to the current) heating of the electron gas.

1. MAIN RELATIONS

We begin with the following three-stage physical picture of relaxation processes in the electron gas of a superlattice. In the first stage, after receiving additional energy and momentum from the electric field, the electrons, acted on by quasi-elastic collisions (scattering on impurities and phonons, elastic interelectron collisions, especially with Peierls distortions), distribute uniformly over the corresponding isoenergy surfaces. In the process, the directed momentum and drift velocity of the electron gas are lost, but the energy of each electron is conserved. Next (or simultaneously), via normal inelastic interelectron collisions and via inelastic interelectron collisions with Peierls distortions, the energy redistributes among the electrons and further relaxation of their total momentum takes place. As a result, the electron distribution function relaxes to the unshifted Fermi distribution with effective temperature T_e. Finally, in the third stage, via inelastic collisions (mainly with optical phonons) the electrons transfer energy to the lattice and their distribution relaxes to the equilibrium distribution, i.e., the Fermi function with the lattice temperature. According to the above-said, the Boltzmann equation with the model collision integral has the form

$$\frac{\partial f(\mathbf{k},t)}{\partial t} + \frac{e\mathbf{E}}{\hbar}\frac{\partial f(\mathbf{k},t)}{\partial \mathbf{k}} = -\left(\frac{\partial f}{\partial t}\right)_{col}, \tag{1}$$

$$\left(\frac{\partial f}{\partial t}\right)_{col} = \frac{f(\mathbf{k},t) - f_s(\varepsilon,t)}{\tau_1(\mathbf{k})} + \frac{f(\mathbf{k},t) - f_0(\varepsilon,T_e)}{\tau_{ee}(\mathbf{k})} + \frac{f(\mathbf{k},t) - f_0(\varepsilon,T_0)}{\tau_\varepsilon(\mathbf{k})}, \tag{2}$$

$$f_s(\varepsilon,t) = \int_{S_\varepsilon} f(\mathbf{k},t)\frac{dS}{|\nabla_{\mathbf{k}}\varepsilon|} \Big/ \int_{S_\varepsilon}\frac{dS}{|\nabla_{\mathbf{k}}\varepsilon|}, \tag{3}$$

$$\langle\varepsilon\rangle = \langle\varepsilon\rangle_s = \langle\varepsilon\rangle_e, \tag{4}$$

where **k** and ε are the wave vector and energy of the electron, t is time, $f(\mathbf{k},t)$, $f_s(\varepsilon,t)$, $f_0(\varepsilon,T_e)$, and $f_0(\varepsilon,T_0)$ are the field-perturbed Fermi electron distribution function, the Fermi electron distribution function averaged over the equipotential surfaces S_ε, and the equilibrium Fermi electron distribution function with effective temperature T_e and lattice temperature T_0, respectively; $\langle\rangle$, $\langle\rangle_s$, $\langle\rangle_e$, and $\langle\rangle_0$ denote the mean values over these distribution functions, $\tau_1(\mathbf{k})$ is the characteristic setup time of the uniform electron distribution on the isoenergy surfaces under the action of elastic collisions, $\tau_{ee}(\mathbf{k})$ is the inverse frequency of inelastic electron–electron collisions, $\tau_\varepsilon(\mathbf{k})$ is the relaxation time of the electron energy, e is the electron charge, **E** is the electric field, and $\hbar$ is Planck's constant. The temperature T_e is determined by condition (4), the equality of the mean energies of the electron weighted by the distributions $f(\mathbf{k},t)$ and $f_0(\varepsilon,T_e)$.

The collision integral (2) has two fundamental properties: the first and second terms describe redistribution of energy and momentum among the degrees of freedom of the electron, which is absent in one-dimensional models; and because of the above-noted important role of Peierls distor-

tions, the Fermi distribution function standing in the electron–electron collision integral, in contrast to Refs. 10 and 11, is not the momentum-shifted distribution function but the ordinary distribution function. It is important to note that $f_s(\varepsilon,t)$ is the ''isotropic,'' and not the symmetric part of the distribution function $f(\mathbf{k},t)$, i.e., $f_s(\varepsilon,t)\neq[f(\mathbf{k},t)+f(-\mathbf{k},t)]/2$. Such an identification implies the absence during the collisions of redistribution of the energy and momentum of the electron among its degrees of freedom and corresponds to the one-dimensional model of a superlattice.[4,9]

To investigate the electrical characteristics of a superlattice, instead of the kinetic equation it is sometimes convenient to use the balance equations—the equations for the current (or mean velocity) and the mean energy of the electron. We find these equations in the standard way from the kinetic equation (1).

The dispersion law of the electrons of a superlattice in the tight-binding approximation has the form

$$\varepsilon(k_3,\mathbf{k}_\perp)=\sum_{\alpha=1}^{3}\varepsilon_\alpha(k_\alpha)=\frac{\Delta}{2}[1-\cos(k_3d)]+\frac{\hbar^2\mathbf{k}_\perp^2}{2m},\quad \mathbf{k}_\perp(k_1,k_2), \tag{5}$$

where d is the period of the superlattice, $\hbar k_3$ and $\hbar\mathbf{k}_\perp$ are the components of the quasimomentum of the electron along and transverse to the superlattice axis, respectively, Δ is the width of the miniband, the x_3 axis is directed along the superlattice axis, the x_1 and x_2 axes are directed along the layers, and m is the effective transverse mass of the electron. For simplicity, we take τ_1, τ_{ee}, and τ_ε to be independent of the momentum of the electron. In this case, Eqs. (1)–(4) yield the following equations for the current and mean energies of the electron:

$$\frac{dj_\alpha}{dt}-ne^2\langle m_\alpha^{-1}(\varepsilon)\rangle E_\alpha=-\frac{j_\alpha}{\tau_p},\quad \alpha=1,2,3, \tag{6}$$

$$\frac{d}{dt}\langle\varepsilon_\alpha\rangle-\frac{1}{n}E_\alpha j_\alpha=-\frac{\langle\varepsilon_\alpha\rangle-\langle\varepsilon_\alpha\rangle_s}{\tau_1}-\frac{\langle\varepsilon_\alpha\rangle-\langle\varepsilon_\alpha\rangle_e}{\tau_{ee}}-\frac{\langle\varepsilon_\alpha\rangle-\langle\varepsilon_\alpha\rangle_0}{\tau_\varepsilon}, \tag{7}$$

$$\sum_{\alpha=1}^{3}\langle\varepsilon\rangle_s=\langle\varepsilon\rangle=\langle\varepsilon\rangle_e, \tag{8}$$

$$\frac{d}{dt}\langle\varepsilon\rangle-\frac{1}{n}(Ej)=-\frac{\langle\varepsilon\rangle-\langle\varepsilon\rangle_0}{\tau_\varepsilon}, \tag{9}$$

where

$$\langle m_3^{-1}\rangle=\left(\frac{\Delta}{2}-\langle\varepsilon_3\rangle\right)\frac{d^2}{\hbar^2}, \tag{10}$$

$m_1=m_2=m$, n is the electron concentration, $\tau_p^{-1}=\tau_1^{-1}+\tau_{ee}^{-1}+\tau_\varepsilon^{-1}$ is the inverse relaxation time of the velocity. The linear dependence of $\langle m_3^{-1}\rangle$ (10) on the mean longitudinal energy is a specific property of the dispersion law (5) and substantially simplifies solution of the problem. Equation (9) is an obvious consequence of Eqs. (7) and is presented for convenience.

It can be shown that, for the dispersion law (5), the longitudinal electron energy, averaged over the isoenergy surface, is given by

$$\overline{\varepsilon_3^s}(\varepsilon)=\frac{\Delta}{2}-\frac{\sqrt{\varepsilon(\Delta-\varepsilon)}}{\arccos(1-2\varepsilon/\Delta)}\theta(\Delta-\varepsilon)=\begin{cases}\varepsilon/3, & \varepsilon\ll\Delta\\ \Delta/2, & \varepsilon>\Delta.\end{cases} \tag{11}$$

Hence it follows that it is always true for any f_s that $\langle\varepsilon_3\rangle_s<\Delta/2$. This inequality, of course, is also valid for equilibrium distributions.

In contrast to integrodifferential equations (1)–(4), system of equations (6)–(10) is not closed. To close it, it is necessary either to write out an equation for the higher moments of the distribution function or prescribe the form of the ''isotropic'' distribution $f_s(\varepsilon,T)$. Let the electron concentration be such as to fulfill the following condition:

$$\tau_{ee}\ll\tau_\varepsilon. \tag{12}$$

In this case, the interelectron collisions almost completely form the electron energy distribution. Therefore, noting that by definition $f_s(\varepsilon,t)$ is the ''isotropic'' part of $f(\mathbf{k},t)$, we have

$$f_s(\varepsilon,t)\simeq f_0(\varepsilon,T_e). \tag{13}$$

For simplicity, we will use equality (13) for an arbitrary relation between the relaxation times. In this way, we unify the elastic and inelastic electron–electron collisions. This approximation, although not always valid, does not suffer from the fundamental drawback of the momentum-shifted Fermi distribution. In this approximation, for Maxwellian statistics

$$\langle\varepsilon_\perp\rangle_s=\langle\varepsilon_\perp\rangle_e=kT_e,\qquad \langle\varepsilon_3\rangle_s=\langle\varepsilon_3\rangle_e=\frac{\Delta}{2}\left[1-\frac{I_1(\Delta/2T_e)}{I_0(\Delta/2T_e)}\right], \tag{14}$$

where $I_n(x)$ is the Bessel function of imaginary argument. Now the system of equations (6)–(10), (14) is closed and also defines the effective temperature T_e. We may note that, in some situations (see below), quasi-elastic collisions and interelectron collisions with Peierls distortions are combined into one mechanism without the use of relation (13).

For a more accurate treatment of transport in a superlattice the relaxation time τ_p should be taken to be a tensor, and instead of τ_ε it is incumbent to introduce different relaxation times for each degree of freedom of the electron. Such an approach can be realized, but it is not advised because of the large number of parameters and the absence of detailed studies of the scattering mechanisms in a superlattice.

2. VERTICAL TRANSPORT

Let only one longitudinal field exist in the superlattice: $E_3=E$, $E_\perp=0$. In this case, according to Eqs. (6)–(10), (14), the current and mean energies and effective temperature of the electrons are given by

$$\frac{j}{j_0}=\frac{E/E_*}{1+(E/E_*)^2}\left[1+\frac{\delta\langle\varepsilon_\perp\rangle}{\Delta/2-\langle\varepsilon_3\rangle_0}\right], \tag{15}$$

$$\delta\langle\varepsilon_\perp\rangle\equiv\langle\varepsilon_\perp\rangle-\langle\varepsilon_\perp\rangle_0=\left(1-\frac{\nu_\varepsilon}{\nu_p}\right)\delta T, \tag{16}$$

$$\langle\varepsilon_3\rangle=\frac{\Delta}{2}-\frac{\Delta/2+\langle\varepsilon_\perp\rangle-\langle\varepsilon\rangle_0}{1+(E/E_*)^2}, \tag{17}$$

$$[1+(E/E_*)^2]\frac{I_1(x_e)}{I_0(x_e)}-\frac{I_1(x_0)}{I_0(x_0)}=\left[1+\frac{\nu_\varepsilon}{\varepsilon_p}\left(\frac{E}{E_*}\right)^2\right]\frac{2\,\delta T}{\Delta}, \tag{18}$$

where $j_0=\sigma_0 E_*\sim\sqrt{\nu_\varepsilon/\nu_p}$, $E_*=\sqrt{\nu_\varepsilon\nu_p}\hbar/ed$ is the effective field characterizing the nonlinearity of the CVC of the superlattice,

$$\sigma_0=\frac{ne^2d^2\tau_p}{\hbar^2}\left(\frac{\Delta}{2}-\langle\varepsilon_3\rangle_0\right) \tag{19}$$

is the linear conductivity of the superlattice, $\delta T\equiv T_e-T_0$, $\nu_{\varepsilon,p}=\tau_{\varepsilon,p}^{-1}$, and $x_{0,e}=\Delta/2T_{0,e}$.

In the absence of transverse heating (the one-dimensional model) $\delta\langle\varepsilon_\perp\rangle=0$ and the dimensionless current j/j_0 is a universal function of the dimensionless field E/E_* [the factor in front of the brackets in Eq. (15)] does not depend on ν_ε/ν_p or the form of the equilibrium distribution function. The second term inside the brackets in Eq. (15) is the correction to the result of the one-dimensional model[1,4] due to transverse heating of the electron gas. As numerical calculations show (see below), this correction can be large, and even exceed the ''main'' quantity. It leads to significant smoothing, growth, and shift of $j_{\max}$ toward larger fields in the CVC of the superlattice. At larger values of the ratio ν_p/ν_ε the transverse heating is large and can lead to the disappearance of the negative differential conductivity of the superlattice. In the limit $\nu_p/\nu_\varepsilon\to\infty$, it follows from Eqs. (15)–(18) that

$$\frac{j}{j_0}\simeq\frac{E/E_*}{1+(E/E_*)^2}\left[1+\frac{1}{\sqrt{2}(1-2\langle\varepsilon_3\rangle_0/\Delta)}\times\sqrt{\frac{1+(E/E_*)^2}{1+(\nu_\varepsilon/\nu_p)(E/E_*)^2}}\right]. \tag{20}$$

It is easy to show that for arbitrary fields

$$\langle\varepsilon_\perp\rangle<T_e,\quad \langle\varepsilon_3\rangle<\Delta/2,\quad \delta T<\frac{\Delta}{2\sqrt{2}}\sqrt{\frac{\nu_p}{\nu_\varepsilon}}. \tag{21}$$

For $E\to\infty$ and $\nu_p\gg\nu_\varepsilon$, Eq. (18) yields

$$T_e\simeq\frac{1}{2}(T_0+\sqrt{T_0^2+\Delta^2\nu_p/2\nu_\varepsilon}),\quad \langle\varepsilon_3\rangle=\frac{\Delta}{2}, \tag{22}$$

i.e., for $\nu_p/\nu_\varepsilon<10$ transverse heating cannot exceed the width of the miniband Δ, which differs from the results of Refs. 10, 11, and 14 which indicate unbounded growth of T_e with growth of the field. If we introduce a longitudinal ($T_\parallel$) and a transverse ($T_\perp$) electron temperature via the corresponding Fermi distributions, then we always have $T_\parallel>T_\perp$, and in strong fields $T_\parallel\gg T_\perp$, i.e., heating becomes substantially anisotropic. Transport in a superlattice can be described by a shifted Fermi distribution if desired, but with anisotropic temperature (see below).

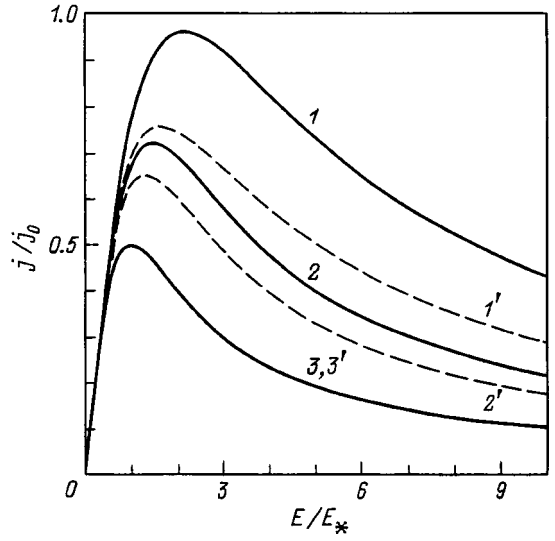

FIG. 1. Current–voltage characteristics of superlattices with different values of T_0 and ν_p/ν_ε. $2T_0/\Delta=1$ — solid lines, $2T_0/\Delta=0.1$ — dashed lines. ν_p/ν_ε: *1, 1′* — 10; *2, 2′* — 3; *3, 3′* — 1.

The dependences $j(E)$ and $T_e(E)$ are plotted in Figs. 1 and 2 for several values of ν_p/ν_ε and $2T_0/\Delta$. In the chosen variables, curves *3, 3′* correspond to the one-dimensional model of a superlattice for arbitrary ν_ε/ν_p, which does not take transverse heating of the electron gas into account. The difference (significant) between them and curves *1, 2* and *1′, 2′* is due entirely to transverse heating of the electrons. Figure 3 plots the changes in the position and magnitude of $j_{\max}$ versus ν_p/ν_ε due to transverse heating of the electrons (due to the difference between the expression in brackets in expression (15) and unity). These changes are significant and must be taken into account in the processing of the experimental results. As was already pointed out above, ignoring them can lead to a substantial error in the relaxation times of

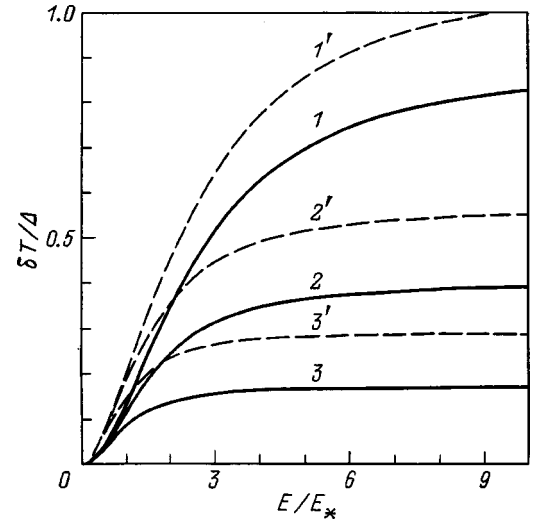

FIG. 2. Dependence of heating of the electron gas in a superlattice on the electric field. Notation the same as in Fig. 1.

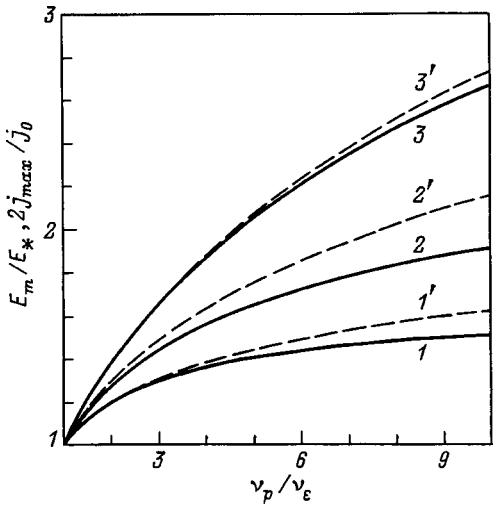

FIG. 3. Dependence of the position E_m/E_* (dashed lines) and current maximum $2j_{\max}/j_0$ (solid lines) in a superlattice on ν_p/ν_ε for different values of $2T_0/\Delta$. $2T_0/\Delta$: *1, 1′* — 0.1; *2, 2′* — 1; *3, 3′* — 3.

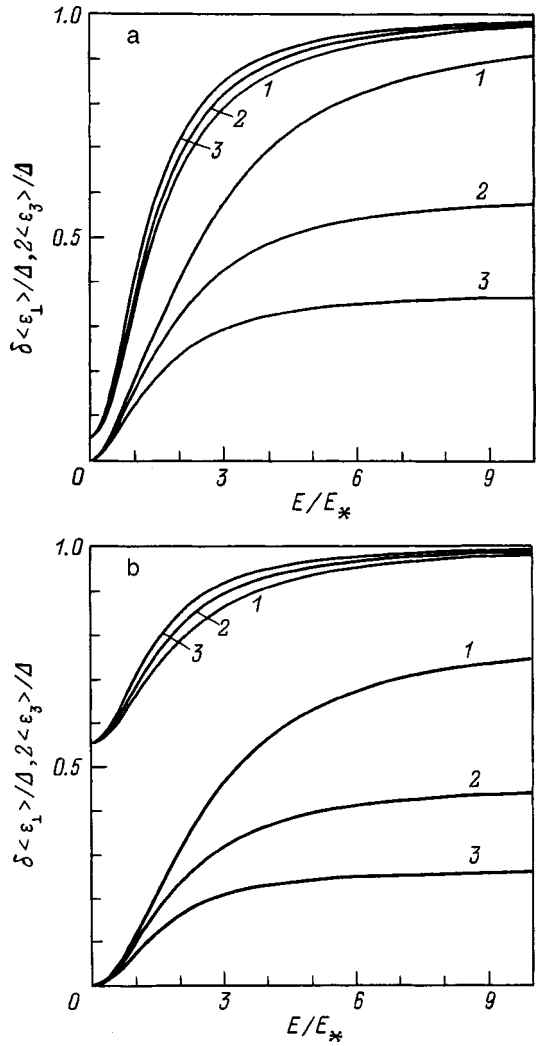

FIG. 4. Mean energies of the electron: $\langle\varepsilon_3\rangle/\Delta$ — upper, and $\delta\langle\varepsilon_\perp\rangle/\Delta$ — lower group of curves as functions of the field for different values of ν_p/ν_ε, $2T_0/\Delta=0.1$ (a), $2T_0/\Delta=1$ (b). Numbering of the curves is the same as in Fig. 1.

the electrons when determining them from the experimental CVC's. For example, the ratio of the energy relaxation times obtained from the experimental CVC's using the formulas of the three-dimensional and one-dimensional models $\tau_\varepsilon^{(3)}/\tau_\varepsilon^{(1)}=(E_m/E_*)^2$. In real situations this quantity (see Figs. 1 and 3) can reach as high as 10. Figure 4 plots the mean energies $\langle\varepsilon_3\rangle$ and $\langle\varepsilon_\perp\rangle$ as functions of the field. Figure 5 plots the electron temperature T_e for maximum current. Note that for $4T_0/\Delta<1$ the position and value of $j_{\max}$ (in dimensionless units) and $T_e(j_{\max})$ tend toward constant values with growth of ν_p/ν_ε. For $4T_0/\Delta>1$ these quantities (except for the current) tend to ∞. In both cases the dimensioned current $j_{\max}\to 0$.

We give here the solution of Eq. (1) for the distribution function in a static field

$$f(\mathbf{k})=\frac{2\pi\hbar^2 nd}{m}\sum_{\mu=-\infty}^{\infty}\left[\frac{\nu_\varepsilon I_\mu\left(\frac{\Delta}{2T_0}\right)}{T_0 I_0\left(\frac{\Delta}{2T_0}\right)}\exp\left(-\frac{\hbar^2k_\perp^2}{2mT_0}\right)+\frac{(\nu_p-\nu_\varepsilon)I_\mu\left(\frac{\Delta}{2T_e}\right)}{T_e I_0\left(\frac{\Delta}{2T_e}\right)}\exp\left(-\frac{\hbar^2k_\perp^2}{2mT_e}\right)\right]\times\frac{\nu_p\cos(\mu k_3 d)+\mu\Omega\sin(\mu k_3 d)}{\nu_p^2+(\mu\Omega)^2},\tag{23}$$

$$\langle k_3\rangle=\frac{2\Omega}{d}\sum_{\mu=1}^{\infty}\left[\nu_\varepsilon\frac{I_\mu\left(\frac{\Delta}{2T_0}\right)}{I_0\left(\frac{\Delta}{2T_0}\right)}+(\nu_p-\nu_\varepsilon)\frac{I_\mu\left(\frac{\Delta}{2T_e}\right)}{I_0\left(\frac{\Delta}{2T_e}\right)}\right]\times\frac{(-1)^{\mu+1}}{\nu_p^2+(\mu\Omega)^2},\quad \Omega=eEd/\hbar.\tag{24}$$

For simplicity, setting $f_0(k_3)=n\,\delta(k_3)$ and $\tau_p=\tau_\varepsilon=\tau$ in expression (23) we obtain

$$f(k_3)=\frac{2\pi\hbar n}{eE\tau}\exp\left(-\frac{\hbar k_3}{eE\tau}\right)\begin{cases}\left[1-\exp\left(-\frac{2\pi\hbar}{eEd\tau}\right)\right]^{-1}, & k>0\\ \left[\exp\left(\frac{2\pi\hbar}{eEd\tau}\right)-1\right]^{-1}, & k<0\end{cases}\qquad -\pi/d\leqslant k_3<\pi/d.\tag{25}$$

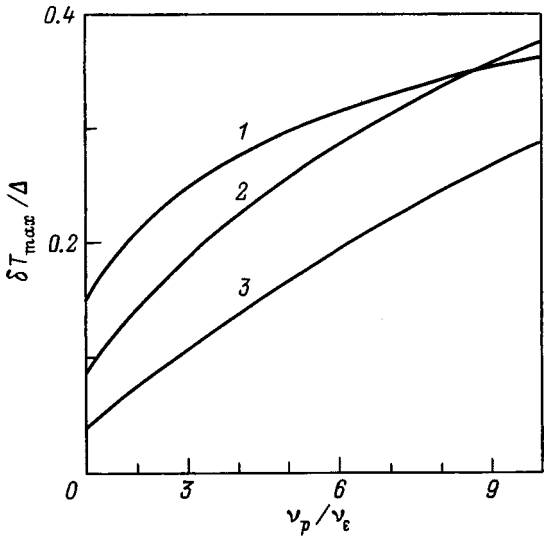

FIG. 5. Dependence of the effective electron temperature at maximum current as a function of ν_p/ν_ε. Numbering of the curves is the same as in Fig. 1.

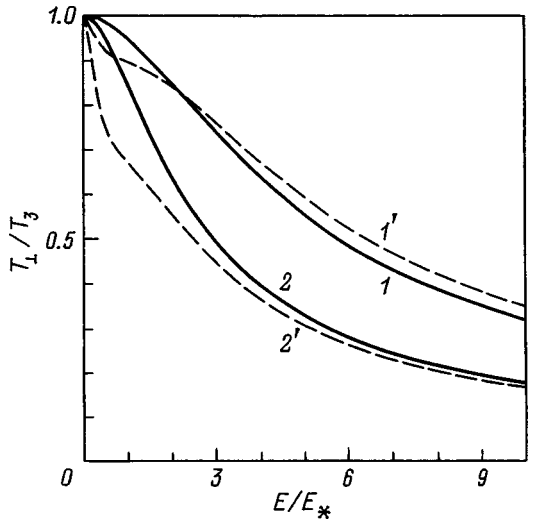

FIG. 6. Dependence of the ratio of electron temperatures $T_\perp/T_3$ on the field. Notation the same as in Fig. 1.

Function (25) is far from similar to the shifted Maxwellian for any field. Its maxima are always found at $k_3=0$ and π/d.

Let us attempt to approximate function (23) by a Maxwellian distribution with anisotropic temperature that has been momentum-shifted by $\hbar k_0$

$$f(\mathbf{k})=\frac{2\pi\hbar nd}{mT_\perp I_0(\Delta/2T_3)}\times\exp\left\{-\frac{\hbar^2k_\perp^2}{2mT_\perp}+\frac{\Delta}{2T_3}\cos[(k_3-k_0)d]\right\}, \quad (26)$$

where $T_{3,\perp}$ are the effective temperatures characterizing motion of the electrons along the axis and along the layers of the superlattice, respectively. Function (26) contains three parameters: k_0, T_3, and $T_\perp$, which are determined by the mean velocity (current), the mean longitudinal energy $\langle\varepsilon_3\rangle$, and the mean transverse energy of the electron $\langle\varepsilon_\perp\rangle$

$$\langle v_3\rangle=v_m\left(1-\frac{2\langle\varepsilon_3\rangle_{T_3}}{\Delta}\right)\sin(k_0d)=v_m\frac{I_1(\Delta/2T_3)}{I_0(\Delta/2T_3)}\sin(k_0d), \quad (27)$$

$$\langle\varepsilon_3\rangle=\langle\varepsilon_3\rangle_{T_3}\cos(k_0d)+\varepsilon_3(k_0)=\frac{\Delta}{2}\left[1-\frac{I_1(\Delta/2T_3)}{I_0(\Delta/2T_3)}\cos(k_0d)\right], \quad (28)$$

$$\langle\varepsilon_\perp\rangle=T_\perp, \quad v_m=\Delta d/2\hbar. \quad (29)$$

We can also find the mean quasimomentum of the electron (due to the Peierls distortions it is a poor characteristic of the system)

$$\overline{k_3}=\frac{2}{I_0(\Delta/2T_3)d}\sum_{n=1}^{\infty}\frac{(-1)^{n+1}\sin(nk_0d)}{n}I_n\left(\frac{\Delta}{2T_3}\right). \quad (30)$$

In contrast to the parabolic dispersion law

$$\overline{k_3}\neq k_0, \quad v_3(k_0)\neq\langle v_3\rangle\neq v_3(\overline{k_3}), \quad \langle\varepsilon_3\rangle\neq\langle\varepsilon_3\rangle_{T_3}+\varepsilon_3(k_0). \quad (31)$$

Only in weak fields ($k_0d\ll1$) and at low temperatures ($\Delta\gg T$) do we have $\overline{k_3}\simeq k_0$. In general, k_0 characterizes only the position of the maximum of the distribution function.

Comparing relations (27)–(29) with relations (13) and (14), we obtain relations determining the parameters k_0, T_3, and $T_\perp$ in terms of the field

$$\tan(k_0d)=\Omega\tau_p, \quad \Omega=eEd/\hbar, \quad k_0d<\pi/2, \quad (32)$$

$$T_\perp=T_0+\left(1-\frac{\nu_\varepsilon}{\nu_p}\right)(T_e-T_0), \quad (33)$$

$$\frac{I_1\left(\frac{\Delta}{2T_3}\right)}{I_0\left(\frac{\Delta}{2T_3}\right)}=\left[\frac{I_1\left(\frac{\Delta}{2T_0}\right)}{I_0\left(\frac{\Delta}{2T_0}\right)}+\left(1-\frac{\nu_\varepsilon}{\nu_p}\right)\frac{2(T_e-T_0)}{\Delta}\right]\times\frac{\sqrt{1+(\Omega\tau_p)^2}}{1+\Omega^2\tau_p\tau_\varepsilon}. \quad (34)$$

The temperature T_e is determined by Eq. (18). For Fermi statistics, it is necessary to make the substitution

$$\frac{I_1\left(\frac{\Delta}{2T_\alpha}\right)}{I_0\left(\frac{\Delta}{2T_\alpha}\right)}\to1-\frac{2\langle\varepsilon_3\rangle_{T_\alpha}}{\Delta}, \quad T_\alpha\to\langle\varepsilon_\perp\rangle_{T_\alpha}, \quad \alpha=0,e,\perp,3. \quad (35)$$

in Eqs. (33) and (34). It follows from Eqs. (32)–(35), (15) that as $E\to\infty$ $k_0d\to\pi/2$, $\langle\varepsilon_3\rangle\to\Delta/2$, $T_e\to$const, $T_\perp\to$const, and $T_3\to\infty$, which confirms the validity of the discussion of electron heating in the Introduction. Figure 6 plots the temperature ratio $T_\perp/T_3$ as a function of the field for

$2T_0/\Delta=0.1$, 1 and $\nu_p/\nu_\varepsilon=3,10$. In strong fields the temperature becomes substantially anisotropic, and for this reason transport in a superlattice cannot be described by a mixed Fermi distribution with isotropic temperature as was done in Refs. 10, 11, and 14.

3. LONGITUDINAL TRANSPORT

Let there by only a transverse field in the superlattice: $E_2=E$, $E_1=E_3=0$. In this case, the current, mean energy, and effective electron temperature are given, according to relations (6)–(10), (12), by

$$j=\sigma E, \quad \sigma=\frac{ne^2}{m\nu_p}, \tag{36}$$

$$\langle\varepsilon_1\rangle=\langle\varepsilon_1\rangle_0+\frac{1}{2}\left(1-\frac{\nu_\varepsilon}{\nu_p}\right)\delta T, \tag{37}$$

$$\langle\varepsilon_2\rangle=\langle\varepsilon_2\rangle_0+\frac{1}{2}\left(1-\frac{\nu_\varepsilon}{\nu_p}\right)\delta T+\frac{\nu_\varepsilon}{\nu_p}\delta\varepsilon, \tag{38}$$

$$\langle\varepsilon_3\rangle=\langle\varepsilon_3\rangle_0+\left(1-\frac{\nu_\varepsilon}{\nu_p}\right)(\delta\varepsilon-\delta T), \tag{39}$$

$$\frac{2\delta T}{\Delta}+\frac{I_1(\Delta/2T_0)}{I_0(\Delta/2T_0)}-\frac{I_1(\Delta/2T_e)}{I_0(\Delta/2T_e)}=\left(\frac{E}{E_0}\right)^2, \tag{40}$$

where

$$\delta\varepsilon\equiv\langle\varepsilon\rangle-\langle\varepsilon\rangle_0=\frac{e^2E^2}{m\nu_p\nu_\varepsilon}=\frac{\Delta}{2}\left(\frac{E}{E_0}\right)^2 \tag{41}$$

is the variation of the total electron energy in an electric field E, and $E_0=\sqrt{m\nu_p\nu_\varepsilon\Delta/2e^2}$ is the electric field in which the mean energy of the electron increases by $\Delta/2$. It is of the same order as the effective field E_* in the superlattice for vertical transport and is obtained from it by the substitution $m_3(k_3=0)\to m$.

The linearity of the CVC's of a superlattice in a longitudinal field [see Eq. (36)] is a result of the approximation $\tau_p=$const. The roughness of this approximation does not prevent a qualitatively correct description of heating of the electron gas in this case either or its redistribution over the degrees of freedom of the electron. If needed, $\nu_{\varepsilon,p}$ can be replaced by experimental dependences $\nu_{\varepsilon,p}(E)$ of the bulk material.

Figure 7 plots the function

$$F\left(\frac{T_0}{\Delta},\frac{E}{E_0}\right)\equiv\frac{\delta\langle\varepsilon\rangle-\delta T}{\Delta/2-\langle\varepsilon_3\rangle_0}=1-\frac{I_1\left(\frac{\Delta}{2T_e}\right)I_0\left(\frac{\Delta}{2T_0}\right)}{I_1\left(\frac{\Delta}{2T_0}\right)I_0\left(\frac{\Delta}{2T_e}\right)}, \tag{42}$$

which determines T_e and the mean electron energies

$$T_e=T_0+\frac{e^2E^2}{m\nu_\varepsilon\nu_p}-\left(\frac{\Delta}{2}-\langle\varepsilon_3\rangle_0\right)F(T_0,E), \tag{43}$$

$$\langle\varepsilon_3\rangle=\langle\varepsilon_3\rangle_0+\left(1-\frac{\nu_\varepsilon}{\nu_p}\right)\left(\frac{\Delta}{2}-\langle\varepsilon_3\rangle_0\right)F(T_0,E). \tag{44}$$

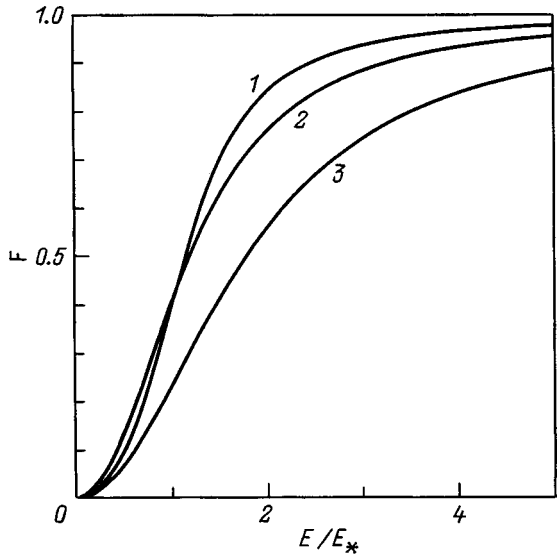

FIG. 7. Dependence of the function F on the electric field. Numbering of the curves as in Fig. 3.

The mean energies $\langle\varepsilon_{1,2}\rangle$ are determined by Eqs. (37), (38), (42)–(44). In the limit $E\to\infty$

$$\langle\varepsilon_3\rangle\to\frac{\nu_\varepsilon}{\nu_p}\langle\varepsilon_3\rangle_0+\left(1-\frac{\nu_\varepsilon}{\nu_p}\right)\frac{\Delta}{2}<\frac{\Delta}{2}, \tag{45}$$

$$\frac{\delta\langle\varepsilon_1\rangle}{\delta\langle\varepsilon_2\rangle}=\frac{\nu_p-\nu_\varepsilon}{\nu_p+\nu_\varepsilon}. \tag{46}$$

The plotted dependences show that, because of randomization of the direction of the momentum, significant heating of the electron gas transverse to the current also arises for longitudinal transport, i.e., in the given case along the superlattice axis. This can be used to to achieve parametric interaction of waves with orthogonal polarizations and to find the ratio ν_ε/ν_p.

Longitudinal transport can be described approximately by a shifted Fermi distribution with anisotropic temperature

$$T_1=T_e-\frac{\nu_\varepsilon}{\nu_p}(T_e-T_0), \quad T_2=T_1+\frac{e^2E^2}{m\nu_p^2}, \tag{47}$$

the temperature T_3 is determined by the equation

$$\frac{I_1(\Delta/2T_3)}{I_0(\Delta/2T_3)}=\frac{I_1(\Delta/2T_0)}{I_0(\Delta/2T_0)}\left[1-\left(1-\frac{\nu_\varepsilon}{\nu_p}\right)F(T_0,E)\right],$$

$$T_3<T_1. \tag{48}$$

As $E\to\infty$, $T_{1,2}\to\infty$ and $T_3\to$const since $\langle\varepsilon_3\rangle<\Delta/2$, i.e., the situation is analogous to vertical transport.

4. ELECTRON TRANSPORT IN μ-DIMENSIONAL SUPERLATTICES

To elucidate the role of the effect of transverse heating of an electron gas on the transport properties of one-dimensional superlattices in three-dimensional crystals, it is instructive to carry out a comparative analysis of transport in one-dimensional, two-dimensional, and three-dimensional crystals with dispersion law

$$\varepsilon(\mathbf{k})=\frac{\Delta}{2}\sum_{\alpha=1}^{\mu}[1-\cos(k_\alpha d)], \tag{49}$$

where μ is the dimensionality of the crystal. Such an analysis is important because it enables us to solve the problem without having to approximate the function $f_s(\varepsilon,t)$ and therewith have to estimate the accuracy of the approximations we have made. The case $\mu=1$ corresponds to the one-dimensional superlattice model, and the case $\mu=2$—to the two-dimensional superlattice model, investigated in detail in Ref. 15. The fundamental difference between relation (49) and the dispersion law (5) for a one-dimensional superlattice in a three-dimensional crystal is that the energies of the electron are bounded in all three dimensions. Therefore, in strong fields, for the dispersion law (49) we should expect weaker heating than for dispersion law (5). In these cases, by virtue of the symmetry of dispersion law (49) instead of Eqs. (3), (6), and (7) we have

$$\langle\varepsilon_\alpha\rangle_s=\langle\varepsilon_\alpha\rangle_e=\frac{1}{\mu}\langle\varepsilon\rangle, \tag{50}$$

$$\langle m_{\alpha\beta}^{-1}\rangle=\left(\frac{\Delta}{2}-\langle\varepsilon_\alpha\rangle\right)\frac{d^2}{\hbar^2}\delta_{\alpha\beta}. \tag{51}$$

Thanks to relation (50) system of equations (6)–(10), (50) becomes closed without any approximation of the function $f_s(\varepsilon,T)$, and the effective temperature T_e can be found at the end of the calculations from formulas (14) and (28). This is important since it provides us with a way to estimate the accuracy of approximation (13).

In a static field **E** for the current and the mean energies we have

$$j_\alpha=\sigma_0\frac{\Delta/2-\langle\varepsilon_\alpha\rangle}{\Delta/2-\langle\varepsilon_\alpha\rangle_0}E_\alpha, \tag{52}$$

$$\frac{\Delta/2-\langle\varepsilon_\alpha\rangle_0}{\Delta/2-\langle\varepsilon_\alpha\rangle}=\left[1+\left(\frac{E_\alpha}{E_0}\right)^2\right]\times\left[1+\frac{1}{\mu}\left(\frac{\tau_\varepsilon}{\tau_p}-1\right)\sum_{i=1}^{\mu}\frac{(E_i/E_0)^2}{1+(E_i/E_0)^2}\right], \tag{53}$$

where $E_0=\hbar/ed\tau_p$ and the linear conductivity σ_0, as before, is defined by relation (19).

If the electric field is directed along the crystallographic axis x ($E_x=E$), then the current and relative heating of the electrons are given by

$$j=\frac{\sigma_0 E}{1+(E/E_*^{(\mu)})^2}, \tag{54}$$

$$\frac{\delta\langle\varepsilon_i\rangle}{\delta\langle\varepsilon_x\rangle}=\frac{\tau_\varepsilon-\tau_p}{\tau_\varepsilon+(\mu-1)\tau_p},\quad i\neq x, \tag{55}$$

where $D_*^{(\mu)}=E_0/\sqrt{1+(\tau_{\varepsilon/\tau_p}-1)/\mu}$ is the effective field of a crystal of dimensionality μ at which the current is maximum. The lattice temperature enters only into σ_0 in explicit form. Because the energies of the electrons are bounded in all dimensions of the crystal in the same way, their transverse heating is always less than the longitudinal heating although still significant. The relation

$$\frac{E_*^{(\mu)}}{E_*^{(1)}}=\left[\frac{\tau_p}{\tau_\varepsilon}+\frac{1}{\mu}\left(1-\frac{\tau_p}{\tau_\varepsilon}\right)\right]^{-1/2} \tag{56}$$

describes the variation of the position and magnitude of $j_{\max}$ in the CVC of the crystal due to transverse heating of the electrons. These variations are quite large. For example, for $\mu=3$ and $\tau_p/\tau_\varepsilon=10$ transverse heating increases the effective field (in comparison with the one-dimensional model) by a factor of 1.6. The maximum current $j_{\max}$ is increased by the same factor, but its maximum becomes more washed out. These results are found to be in qualitative agreement with the results presented above for one-dimensional superlattices in three-dimensional crystals. This allows us to expect sufficient accuracy from approximation (13).

If the field is directed along the diagonal of the superlattice, then

$$\mathbf{j}=\frac{\sigma\mathbf{E}}{1+(\nu_p/\nu_{\varepsilon\mu})(\mathbf{E}/\mathbf{E}_0)^2}. \tag{57}$$

This current state is unstable with respect to transverse perturbations.[15]

In a recently appearing paper,[16] Wacker and Jauho presented a comparative analysis of various methods of describing electron transport in superlattices. Unfortunately, this analysis assumes that the electron temperature is independent of the field. Therefore, Ref. 16 does not provide an answer to the question considered in the present paper.

In summary, we may draw the following conclusions.

1) Transverse heating of an electron gas substantially alters the current–voltage characteristics of a superlattice.

2) The heating of electrons in a superlattice is significant and anisotropic. Therefore, electron transport in them cannot be described within the framework of one-dimensional models (even with two relaxation times), in which transverse heating is completely absent or by the usual shifted Fermi distribution, in which the heating is isotropic.

3) A momentum-shifted Fermi distribution with anisotropic effective temperature can be satisfactory and useful for numerical calculations.

This work was carried out with the support of the Russian Fund for Fundamental Research (Grant No. 96-02-19271) and INTAS–RFBR (Grant No. 96-615).

[1] L. Esaki and R. Tsu, IBM J. Res. Dev. **14**, 61 (1970).
[2] R. F. Kazarinov and R. A. Suris, Fiz. Tekh. Poluprovodn. **6**, 148 (1972) [Sov. Phys. Semicond. **7**, 120 (1972)]; **7**, 488 (1973) [Sov. Phys. Semicond. **7**, 347 (1973)].
[3] Yu. A. Romanov, Fiz. Tekh. Poluprovodn. **5**, 1434 (1971) [Sov. Phys. Semicond. **5**, 1256 (1971)]; Opt. Spektrosk. **33**, 917 (1972); *Multilayer Semiconductor Structures and Superlattices* [in Russian], edited by A. M. Belyantsev and Yu. A. Romanov (IPF AN SSSR, Gor'kiĭ, 1984).
[4] A. A. Ignatov and Yu. A. Romanov, Fiz. Tverd. Tela (Leningrad) **17**, 3388 (1975) [Sov. Phys. Solid State **17**, 2216 (1975)]; Phys. Status Solidi B **73**, 327 (1976); Izv. Vyssh. Uchebn. Zaved. Radiofiz. **21**, 132 (1978).
[5] Yu. A. Romanov and L. K. Orlov, Fiz. Tverd. Tela (Leningrad) **19**, 726 (1977) [Sov. Phys. Solid State **19**, 421 (1977)]; Fiz. Tekh. Poluprovodn. **12**, 1665 (1978) [Sov. Phys. Semicond. **12**, 987 (1978)].

[6] M. Holthaus, Phys. Rev. B **47**, 6499 (1993).
[7] Yu. A. Romanov, Fiz. Tverd. Tela (Leningrad) **21**, 877 (1979) [Sov. Phys. Solid State **21**, 513 (1979)].
[8] F. G. Bass, A. A. Bulgakov, and A. P. Tetervov, *High-Frequency Properties of Semiconductors and Superlattices* [in Russian] (Nauka, Moscow, 1989).
[9] S. A. Ktitorov, G. S. Simin, and V. Ya. Sindalovskiĭ, Fiz. Tverd. Tela (Leningrad) **13**, 2230 (1971) [Sov. Phys. Solid State **13**, 1872 (1971)].
[10] X. L. Lei, N. J. M. Horing, and H. L. Cui, Phys. Rev. Lett. **66**, 3277 (1991); J. Phys.: Condens. Matter **4**, 9375 (1992).
[11] X. L. Lei and X. F. Wang, J. Appl. Phys. **73**, 3867 (1973); X. L. Lei, N. J. M. Horing, H. L. Cui, K. K. Thomber, Phys. Rev. B **48**, 5366 (1993); Solid State Commun. **86**, 231 (1993); Appl. Phys. Lett. **65**, 2964 (1994).
[12] P. J. Price, IBM J. Res. Dev. **17**, 39 (1973).
[13] E. M. Lifshitz and L. P. Pitaevskiĭ, *Physical Kinetics* [in Russian] (Nauka, Moscow, 1997).
[14] X. L. Lei, Phys. Rev. B **51**, 5526 (1995); J. Appl. Phys. **79**, 3071 (1996).
[15] Yu. A. Romanov and E. V. Demidov, Fiz. Tekh. Poluprovodn. **31**, 308 (1997) [Semiconductors **31**, 252 (1997)].
[16] A. Wacker and A.-P. Jauho, Phys. Rev. Lett. **80**, 369 (1998).

Translated by Paul F. Schippnick

Heating of two-dimensional excitons by nonequilibrium acoustic phonons

A. V. Shcherbakov and A. V. Akimov

A. F. Ioffe Physicotechnical Institute, Russian Academy of Sciences, 194021 St. Petersburg, Russia
(Submitted October 22, 1998; resubmitted February 25, 1999)
Fiz. Tverd. Tela (St. Petersburg) **41**, 1707–1711 (September 1999)

The energy distribution functions of two-dimensional excitons in the presence of nonequilibrium acoustic phonons have been calculated for the geometry used in heat-pulse experiments. The results were obtained by solving numerically the kinetic equation for the case where the exciton gas equilibrates with phonons during its lifetime. The cases of the low and high exciton-gas density limits are considered. It is shown that at low exciton-gas densities the distribution does not follow the Boltzmann function and depends on the quantum-well width. A comparison with earlier experimental data is made. © *1999 American Institute of Physics.* [S1063-7834(99)03609-6]

Experimental studies of the effect of nonequilibrium acoustic phonons on exciton luminescence in semiconductor quantum wells (QW) have revealed clearly the distinctive features of the exciton-phonon interaction associated with the lowering of the exciton-gas dimension.[1] These experiments probed the effect of heating a two-dimensional exciton gas (2DExG) by nonequilibrium phonons in GaAs/AlGaAs QWs. The scheme of the experiment[1] is presented in Fig. 1. A 20-nm thick constantan film measuring $1.5\times 1\ \mathrm{mm}^2$, which served as a generator of nonequilibrium phonons, *h*, was deposited on the back side of a semi-insulating GaAs substrate. The film was heated by current pulses, which resulted in injection into the sample of thermal phonon pulses with a characteristic temperature $T_h \approx 12\ \mathrm{K}$. The phonons propagated through the substrate toward the opposite side of the sample and reached the QWs, where the 2DExG was created by a laser beam at a very short distance from *h*. One measured in the experiment the 2DExG effective temperature T_{eff}, and the method used to determine it depended on the QW width *d*. In thick QWs ($d>20\ \mathrm{nm}$), T_{eff} was derived from the intensity ratio of the heavy- (HH) and light-hole (LH) exciton luminescence lines. In the thin QW ($d=2.5\ \mathrm{nm}$), T_{eff} was found from thermal quenching of the exciton luminescence line. The main result obtained in the experiment[1] is the strong dependence of T_{eff} on the QW thickness and exciton-gas density n_{ex}. The authors[1] propose a qualitative interpretation of the experimental observations by analyzing the selection rules for exciton-phonon transitions.

In order to better understand the relations observed in the experiments of Ref. 1 and make quantitative estimates, one has to perform a theoretical analysis of the exciton distribution function $f(E)$. Such an analysis should show how $f(E)$ and, hence, 2DExG heating depend on the QW thickness, 2DExG density, and the spectrum of nonequilibrium phonons. An analysis of $f(E)$ is also of practical importance for the use of semiconductor nanostructures as phonon spectrometers.

This paper reports a calculation of $f(E)$ for the experimental geometry shown in Fig. 1. A theoretical method for such calculations has been recently developed by Golub.[2] The phonons in heater *h* are assumed to have a Planckian distribution with temperature T_h. Low-frequency phonons with $\omega \leqslant \omega_0$ reach 2DExG ballistically, whereas high-frequency ones with $\omega > \omega_0$ undergo strong elastic scattering in the substrate and practically do not reach 2DExG. The frequency cutoff ω_0 depends on the material of the substrate and its thickness. For GaAs substrates ~ 1 mm thick, $\hbar\omega_0$ is a few meV.[3] The existence of a cutoff ω_0 makes the phonon spectrum $N_{\mathbf{q},j}$ (here $\mathbf{q}$ is the phonon wave vector, $j=$ LA, TA is the phonon polarization) in the 2DExG region nonequilibrium, which becomes particularly noticeable for $k_B T_h > \hbar\omega_0$. The anisotropy of the phonon distribution in the 2DExG region also contributes to the nonequilibrium nature of the phonon spectrum. Indeed, because of the phonon generator being of a finite size, $N_{\mathbf{q}}$ in the 2DExG region is a function of the angle ϑ. The ballistic phonons propagating from *h* can have fairly large $N_{\mathbf{q}}$ only for $\vartheta < \vartheta^{\max}$ (see Fig. 1). For $\vartheta > \vartheta^{\max}$, $N_{\mathbf{q}}$ may be considered Planckian with $T=T_0$, where T_0 is the lattice temperature in the absence of nonequilibrium phonons. We are going to show that the anisotropy of $N_{\mathbf{q}}$ in the 2DExG region is essential for thick QWs, whereas the existence of the cutoff ω_0 affects strongly $f(E)$ in thin QWs.

The paper presents a theoretical analysis for GaAs/AlGaAs QWs, where one may assume the excitons to equilibrate during their lifetime $\tau_0 \sim 10^{-9}$ s with nonequilibrium phonons.[4] This is a valid assumption, because the mean exciton-phonon energy relaxation time for 2DExG in GaAs/AlGaAs QWs $\tau_{\mathrm{ph}} \sim 10^{-11}-10^{-10}$ s,[5,6] and, hence, $\tau_0 \gg \tau_{\mathrm{ph}}$.

Exciton-exciton and exciton-electron collisions should obviously affect $f(E)$ at high 2DExG densities. In the limit of high n_{ex}, where the collisional time $\tau_{\mathrm{col}} \ll \tau_{\mathrm{ph}}$, $f(E)$ may be considered a Boltzmann-type function with a temperature T_{eff}. This work presents also a T_{eff} calculation.

The paper is organized as follows. Section 1 presents matrix elements for the exciton-phonon deformation interaction and kinetic equations for low and high 2DExG densities, and Section 2 discusses the results of a numerical simulation

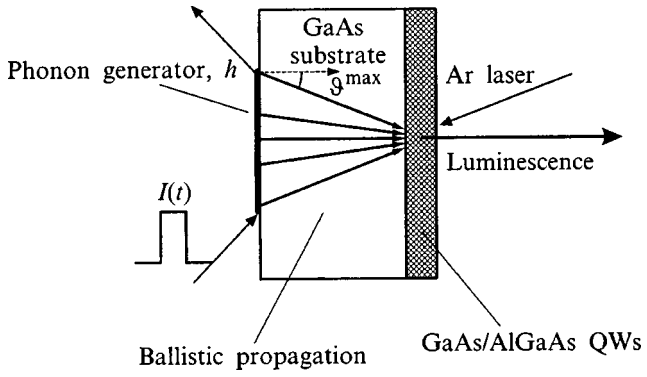

FIG. 1. Scheme of experiments with nonequilibrium phonons.

and compares them with experimental data,[1] to conclude with a short summing up.

1. THEORY

For $\tau_0 \gg \tau_{ex-ph}$, one may assume the 2DExG to be in equilibrium with nonequilibrium phonons, and neglect the creation and radiative recombination of excitons. In the case of low excitation densities one may also disregard the exciton-exciton interaction processes. In this case the kinetic equation for the exciton energy distribution $f(E_k)$ can be written

$$\sum_{\mathbf{k}'} [W_{\mathbf{k}'\to\mathbf{k}} f(E_{k'}) - W_{\mathbf{k}\to\mathbf{k}'} f(E_k)] = 0. \tag{1}$$

Here $\mathbf{k}$ is the exciton wave vector in the QW plane, and E_k is the exciton kinetic energy ($E_k = \hbar^2 k^2/2m$, and m is the in-plane exciton mass); the probability $W_{\mathbf{k}\to\mathbf{k}'}$ for the $\mathbf{k}\to\mathbf{k}'$ transition has the form

$$W_{\mathbf{k}\to\mathbf{k}'} = \frac{2\pi}{\hbar} \sum_{\mathbf{q},j} |M^{\mathbf{q},j}_{\mathbf{k}\to\mathbf{k}'}|^2 \left(N_{\mathbf{q},j} + \frac{1\pm 1}{2} \right) \times \delta(E_{k'} - E_k \pm \hbar\omega(\mathbf{q},j)), \tag{2}$$

where $M^{\mathbf{k},j}_{\mathbf{k}\to\mathbf{k}'}$ is the matrix element of the $\mathbf{k}\to\mathbf{k}'$ transition involving emission (+) or absorption (–) of an acoustic phonon with polarization j = LA, TA, wave vector $\mathbf{q}$, and frequency $\omega(q,j) = s_j q$ (s_j is the sound velocity).

The wave function of an exciton in a state with wave vector $\mathbf{k}$ can be written

$$\Psi^{ex}_{\mathbf{k}}(\mathbf{r}_e, \mathbf{r}_h) = e^{i\mathbf{k}\mathbf{R}_\parallel} F(\rho)\varphi_e(z_e)\varphi_h(z_h). \tag{3}$$

Here $\mathbf{r}_e$ and $\mathbf{r}_h$ are the position vectors of the electron and the hole, $\mathbf{R}$ is the position vector of the exciton center of mass, z is the direction normal to the well plane, the $\parallel$ index specifies an in-plane direction, $\varphi_{e(h)}(z)$ is the quantum confinement function of the first-level electron (hole), $F(\rho)$ is the function of relative motion of the electron and the hole, and $\rho = |\mathbf{r}_e - \mathbf{r}_h|$. In the first variational approximation

$$F(\rho) = \sqrt{\frac{2}{\pi a_0^2}} e^{-\rho/a_0}, \tag{4}$$

where a_0 is the in-plane effective radius.[7]

This work considers interaction of an exciton with an acoustic phonon only through the deformation potential and does not include the piezoacoustic mechanism. In this case the Hamiltonian for the generation (annihilation) of one acoustic phonon of mode j with a wave vector $\mathbf{q}$ has the form

$$H_{ex-ph} = H_{e-ph} + H_{h-ph} = \sqrt{\frac{\hbar}{2\rho_0 V s_j q}}\, iq(\Xi_e(\mathbf{q},j) e^{\mp i\mathbf{q}\mathbf{r}_e} + \Xi_h(\mathbf{q},j) e^{\mp i\mathbf{q}\mathbf{r}_h}). \tag{5}$$

Here Ξ_e and Ξ_h are the electron and hole deformation potentials, ρ_0 is the density of the material, and V is the total volume of the system. It is known that $\Xi_e = 0$ for TA phonons and is isotropic for LA phonons, and that the deformation potential for holes is anisotropic and depends on the angle between the wave vector $\mathbf{q}$ and the normal to the well plane. The expression for the hole deformation potential can be written[2,8]

$$\Xi_h(\mathbf{q}) = \begin{cases} a + \dfrac{b}{2} - \dfrac{3}{2} b \left(\dfrac{q_z}{q} \right)^2 & \text{for LA,} \\ -\dfrac{3}{2} b \left(\dfrac{q_z q_\parallel}{q^2} \right) & \text{for TA,} \end{cases} \tag{6}$$

where $q_z = q\cos\vartheta$, $q_\parallel = q\sin\vartheta$, ϑ is the angle between $\mathbf{q}$ and the z axis, and a and b are the deformation-potential constants.

Having calculated the matrix elements

$$M^{\mathbf{q},j}_{\mathbf{k}\to\mathbf{k}'} = \langle \Psi_{\mathbf{k}} | H_{ex-ph} | \Psi_{\mathbf{k}'} \rangle$$

and inserted the result in Eq. (2), one obtains an expression for the transition probabilities

$$W_{\mathbf{k}\to\mathbf{k}'} = \frac{\Gamma^2(\mathbf{q},j)}{\hbar\rho_0 S_0 s_j^2} \left(N_{\mathbf{q},j} + \frac{1\pm 1}{2} \right) \frac{q^2}{q_z} \Theta(q - q_\parallel), \tag{7}$$

where S_0 is the sample area; as follows from the energy and momentum conservation laws for the exciton-phonon interaction, $q = (\hbar/2ms_j)|k^2 - k'^2|$; m is the exciton mass in the well plane, $\mathbf{q}_\parallel = \mathbf{k} - \mathbf{k}'$, and $\Theta(x)$ is the Heaviside step function

$$\Theta(x) = \begin{cases} 1, & x > 0, \\ 0, & x < 0. \end{cases}$$

For the effective exciton deformation-potential constant we have

$$\Gamma(\mathbf{q},j) = \frac{\Xi_e(j) Z_e(q_z)}{\left[1 + \left(\dfrac{m_h}{2m} q_\parallel a_0 \right)^2 \right]^{3/2}} + \frac{\Xi_h(\mathbf{q},j) Z_h(q_z)}{\left[1 + \left(\dfrac{m_e}{2m} q_\parallel a_0 \right)^2 \right]^{3/2}}, \tag{8}$$

where $Z_{e,h}(q_z)$ are the overlap integrals for the electrons and holes

$$Z_{e,h}(q_z) = \int_{-\infty}^{+\infty} dz\, \varphi^2_{e,h}(z) e^{iq_z z}, \tag{9}$$

and m_e and m_h are the electron and hole effective masses. In the infinite-barrier approximation

$$Z_e(q_z)=Z_h(q_h)=\frac{\sin(q_z d/2)}{(q_z d/2)[1-(q_z d/2\pi)^2]}, \tag{10}$$

where d is the QW thickness. The $Z_{e,h}(q_z)$ function is unity for $q_z=0$ and decreases rapidly for $q_z>\pi/d$. We shall consider in what follows the barriers infinitely high and use Eq. (10) for numerical calculations.

Consider now the case of high excitation densities. Now we can no longer neglect the exciton-exciton interaction processes, and the kinetic equation for $f(E_k)$ cannot be written in the form (1). However in the limit of high 2DExG densities, where the probability of exciton-exciton collisions is far in excess of that of the exciton-phonon relaxation ($\tau_{\rm col} \ll \tau_{\rm ph}$), we can consider $f(E_k)$ a Boltzmann-type function with effective temperature $T_{\rm eff}$

$$f(E_k)=\exp\left[-\frac{E_k}{k_B T_{\rm eff}}\right]. \tag{11}$$

Then the equation for $f(E_k)$ can be recast in the form

$$\sum_{k,q,j} f(E_k)\hbar s_j q\, W^{+}_{\mathbf{k}\to\mathbf{k}'}=\sum_{k,q,j} f(E_k)\hbar s_j q\, W^{-}_{\mathbf{k}\to\mathbf{k}'}. \tag{12}$$

This expression is the condition of equality of the powers absorbed (the left-hand part) and emitted (right-hand part) by 2DExG in interaction with nonequilibrium phonons. The solution of this equation reduces actually to finding the exciton-gas effective temperature $T_{\rm eff}$. The expressions for the probabilities $W^{\pm}_{\mathbf{k}\to\mathbf{k}'}$ in Eq. (12) are found in the way this was done in the case of low 2DExG densities [see Eq. (7)].

The parameters used in the numerical calculations of the exciton energy distribution and effective temperature $T_{\rm eff}$ are as follows: $m_e=0.067\,m_0$, $m_h=0.15\,m_0$ (m_0 is the free-electron mass), $a_0=100$ Å, $\Xi_e=-7.3$, $a=-6.7$, $b=-2$ eV, $s_{\rm LA}=5\times10^5$ cm/s, and $s_{\rm TA}=3\times10^5$ cm/s.

We carried out the calculations separately for the TA and LA phonon polarizations, prescribing a nonequilibrium phonon spectrum $N_{\mathbf{q},j}$ in accordance with the heat-pulse experiment scheme chosen (see Fig. 1) and taking into account also the phonon flux reflected specularly from the QW surface. Then

$$N_{\mathbf{q},j}=\left\{\exp\left[\frac{\hbar s_j q}{k_B T(\mathbf{q})}\right]-1\right\}^{-1}, \tag{13}$$

where $T(\mathbf{q})=T_h$ for $n\pi-\vartheta^{\max}<\vartheta<n\pi+\vartheta^{\max}$ ($n=0,1$) and $T(\mathbf{q})=T_0$ for all other values of ϑ (T_0 is the thermostat temperature).

We took also into account the high-energy cutoff $\hbar\omega_0$ in the $N_{\mathbf{q},j}$ phonon spectrum by setting in Eq. (13)

$$T(\mathbf{q})=\begin{cases} T_h, & \omega<\omega_0, \\ T_0, & \omega>\omega_0. \end{cases} \tag{14}$$

The calculations were performed for $T_h=12$ K, $T_0=4.5$ K, and $\vartheta^{\max}=45°$, which is close to the actual experimental parameters.[1]

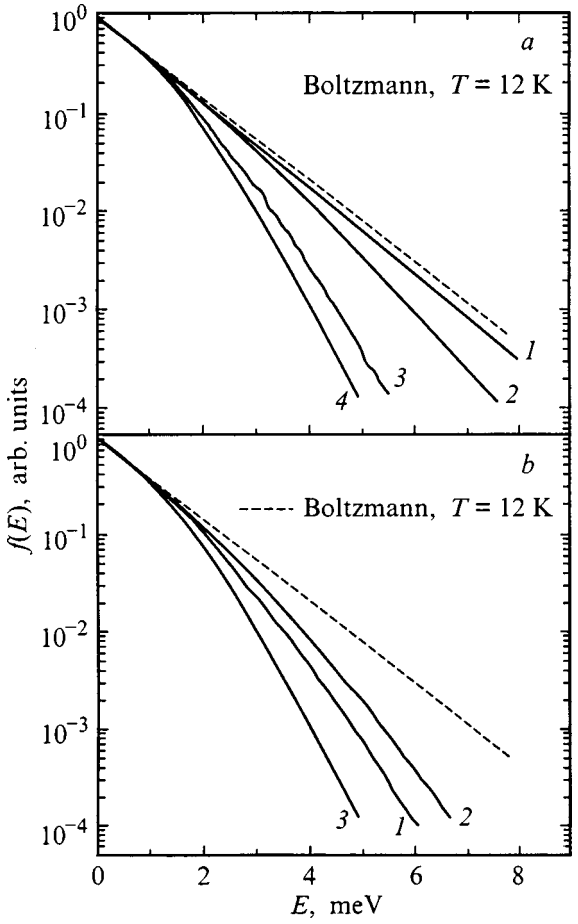

FIG. 2. The energy distribution of excitons interacting with LA phonons calculated for QWs of different thicknesses: (a) neglecting the high-energy cutoff, d (Å): *1*—25, *2*—100, *3*—200, *4*—300; (b) taking into account a high-energy cutoff $\hbar\omega_0=2$ meV; d(Å): *1*—25, *2*—100, *3*—300.

2. DISCUSSION OF THE RESULTS AND COMPARISON WITH EXPERIMENT

We shall first present and discuss the results obtained for low n_{ex}, where $f(E)$ calculated numerically using Eq. (1) can differ substantially from an equilibrium Boltzmann function. Figure 2 displays $f(E)$ functions for QWs of different thickness. Shown in Fig. 2a are $f(E)$ curves which were calculated taking into account only the angular dependence of $N_{\mathbf{q}}$ and disregarding the cutoff ω_0 in the phonon energy spectrum ($\hbar\omega_0 \gg k_B T_h$). From an experimental viewpoint, this corresponds to the case where phonons of all frequencies propagate from h to 2DExG ballistically, i.e., without scattering. The calculations show that $f(E)$ cannot be described by an equilibrium distribution. One readily sees that, as d decreases, $f(E)$ approaches ever closer the Boltzmann function, to become practically indistinguishable from an equilibrium distribution function with a temperature T_h for $d=2.5$ nm. This behavior is due to the angular dependence of the matrix element (7) of exciton-phonon interaction. The condition $q_\parallel<2k$ is satisfied in the 2DExG plane if one takes into account the energy and momentum conservation laws. A constraint on q_z is imposed by the overlap integral (10) in the direction perpendicular to the 2DExG plane, and it can be shown that 2DExG interacts primarily with $q_z \leqslant \pi/d$

phonons. For thin QWs, $2k \ll \pi/d$, and the matrix element of interaction, similarly to the electron-phonon deformation interaction, is strongly anisotropic.[9,10] As a result, $f(E)$ is dominated by the absorption and emission of phonons close in direction $\mathbf{q}$ to the normal to the 2DExG plane, so that in the geometry under study (Fig. 1) 2DExG will not practically feel the absence of phonons from h with $\vartheta > \vartheta^{\max}$. Hence in thin QWs one should expect the same heating of the 2DExG as if the latter was located directly at h, and, hence, $f(E)$ is close to the equilibrium function with $T = t_h$, the result confirmed by the numerical calculations. For thick QWs, $2k \sim \pi/d$, and the transition probability (7) has a smoother angular dependence (at least for LA phonons) than that for thin QWs. This means that 2DExG interacts practically in the same way with phonons propagating at different (arbitrary) angles (with the exception of $\vartheta = 0$). The transitions involving phonon absorption are significant only for $-\vartheta^{\max} \leqslant \vartheta \leqslant \vartheta^{\max}$ and $\pi - \vartheta^{\max} \leqslant \vartheta \leqslant \pi + \vartheta^{\max}$ [see Eq. (13)], whereas the emission of phonons occurs within a broader ϑ range. Hence 2DExG cannot be heated in thick QWs to temperatures close to T_h.

Figure 2b presents the results of the calculations made taking into account the high-energy cutoff $\hbar\omega_0 = 2$ meV in the $N_{\mathbf{q}}$ phonon spectrum in the 2DExG region. For thick QWs, taking the cutoff into account does not affect $f(E)$ (compare curve *4* in Fig. 2a with curve *3* in Fig. 2b). The presence of the cutoff becomes a significant factor as d decreases. This result can be qualitatively explained by the dependence of the overlap integral (10) on d. Indeed, as pointed out before, $q_z \leqslant \pi/d$ and, hence, phonons with $\omega > s\pi/d$ practically do not participate in exciton-phonon transitions. If $\omega_0 > s\pi/d$ (the case of thick QWs), the 2DExG is heated as if there were no high-energy cutoff in the spectrum of nonequilibrium phonons, and $f(E)$ does not feel the presence of the cutoff. As for thin QWs, transitions with phonon emission occur up to frequencies $\omega \sim s_j\pi/d$, whereas those involving phonon absorption from h occur only up to $\omega = \omega_0 < s_j\pi/d$, because of the cutoff. As a result, for $E > \hbar\omega_0$, the heating of 2DExG is suppressed compared to the thick-QW case. This effect is pronounced, particularly clearly for an isotropic $N_{\mathbf{q}}$ distribution (Ref. 2).

2DExG heating depends on phonon polarization. In all the cases under study here, heating in the geometry of Fig. 1 by TA phonons is stronger than that by LA phonons (Fig. 3). This can be explained on a qualitative level as due to two factors, which are essential separately for each of the two limiting cases of thick and thin QWs. In thick QWs, the most significant factor accounting for the difference between the TA and LA phonons is the anisotropy of Ξ_h^{TA} (6), which imposes a constraint on the directions $\mathbf{q}$ of the absorbed and emitted phonons. For instance, phonons with $\mathbf{q}$ lying in the 2DExG plane do not interact with excitons and, hence, their absence in the nonequilibrium spectrum $N_{\mathbf{q}}$ does not affect in any way $f(E)$. For thin QWs, the difference in the sonic velocities s_j between the LA phonons ($s_{\mathrm{LA}} = 5 \times 10^{-5}$ cm/s) and TA phonons ($s_{\mathrm{TA}} = 3 \times 10^{-5}$ cm/s) is essential. The $\omega_0 > s_j\pi/d$ condition, which is essential for a substantial heating of $f(E)$, may be satisfied for the TA while not met for the LA phonons.

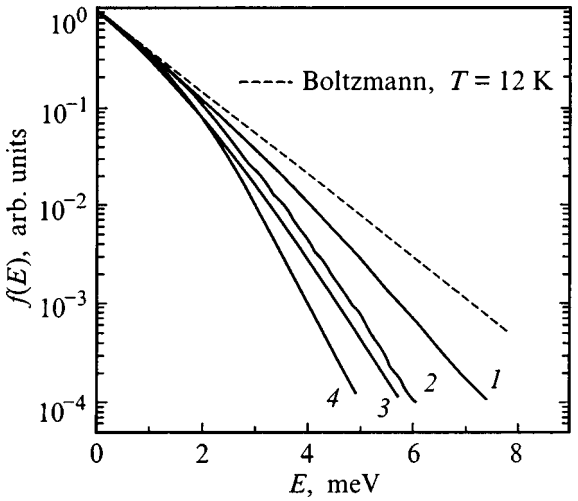

FIG. 3. The energy distribution of excitons interacting separately with LA or TA phonons calculated for QWs 25- and 300-Å thick taking into account a high-energy cutoff $\hbar\omega_0 = 2$ meV; *1*—interaction with TA phonons, $d = 25$ Å, *2*—LA, $d = 25$ Å, *3*—TA, $d = 300$ Å, *4*—LA, $d = 300$ Å.

We have presented results for a particular experimental geometry, dimensions of h, and the high-frequency cutoff ω_0. As the dimensions of h decrease, $\vartheta^{\max}$ decreases too (Fig. 1), and a difference from an equilibrium $f(E)$ with T_h will be seen clearly for thin QWs as well, without taking into account the cutoff ω_0. As the distance between h and 2DExG increases, ω_0 decreases, so that the effect of the cutoff ω_0 on $f(E)$ will become substantial for thick QWs as well.

The results of calculations made for a high density n_{ex} are given in Table I. One readily sees that the calculated T_{eff} increases with decreasing d. A qualitative explanation of this effect is similar to that proposed for the case of low n_{ex} and is related to the dependence of the matrix element of exciton-phonon interaction on the ϑ angle. The results of a numerical calculation are in a good agreement with experimental data[1] (see Table I). For high n_{ex} one observes a complete qualitative agreement, with T_{eff} increasing with decreasing d. The absolute experimental values of T_{eff} lie closer to the calculations made for TA phonons. For low n_{ex}, it was found that $f(E)$ cannot be described by a single temperature, and a comparison of calculated with experimental data should be made taking into account the method employed to determine the T_{eff} in experiment. For thick QWs, T_{eff} is derived from a comparison of the luminescence intensity ratio for the LH and HH excitons.[1] In this case the LH luminescence intensity

TABLE I. Calculated and experimental T_{eff}(K) for QWs of different thickness, obtained in the limit of high and low n_{ex}.

d, nm (E_{LH}, meV)		29.7 (1.9)	19.5 (4.1)	2.5
High n_{ex}	LA	7.3	8.6	9.0
$\tau_{\mathrm{col}} \ll \tau_{\mathrm{ph}}$	TA	9.1	10.1	10.3
	exp.	9.5	10.5	12.5
Low n_{ex}	LA	8.2	7.7	
$\tau_{\mathrm{col}} \gg \tau_{\mathrm{ph}}$	TA	9.4	9.5	
	exp.	9.5	9.5	<6

reflects the $f(E)$ distribution of HH excitons for $E=E_{\mathrm{LH}}$ (E_{LH}, the energy gap between the LH and HH exciton lines, is given in Table I for thick QWs). T_{eff} can be calculated from the expression

$$T_{\mathrm{eff}}=-\frac{E_{\mathrm{LH}}}{k_B \ln\left(\frac{f(E_{\mathrm{LH}})}{f(0)}\right)}. \tag{15}$$

The existence of an LH exciton band, which is necessary to make T_{eff} determination possible, can certainly affect $f(E)$. However the good agreement (within the experimental accuracy of Ref. 1) between the experiment and calculations (see Table I) permits a suggestion that the effect of LHs on $f(E)$, at least in the geometry under consideration, is insignificant.

The fact that one could not detect[1] noticeable heating of 2DExG in QWs with $d=2.5$ nm at low n_{ex} appears an interesting experimental finding. A quantitative comparison of the calculations performed for this case with experiment meets with difficulties. A qualitative analysis shows that, if excitons with $E\gg\hbar\omega_0$ are responsible for nonradiative processes, then for low n_{ex} $f(E)$ should be strongly suppressed for thin QWs in the region of high E, which is supported by calculations (Fig. 2b). A more precise analysis of $f(E)$ in thin QWs should apparently take into account exciton localization effects and the corresponding discrete exciton spectrum.

Thus we have calculated energy distribution functions of two-dimensional excitons in the presence of nonequilibrium phonons for the geometry employed in heat-pulse experiments. It is shown that the distribution function for low exciton-gas densities is not Boltzmannian and depends on the quantum-well thickness. For thick QWs, the distribution function of two-dimensional excitons is determined primarily by the angular distribution of the ballistic phonons reaching the 2D exciton gas. For thin QWs, the nonequilibrium character of the phonon frequency distribution is essential. The results of the calculations agree well with the experimental data obtained earlier.

The authors owe their thanks to A. A. Kaplyanskiĭ, E. S. Moskalenko, and L. E. Golub for discussions and fruitful comments.

Support of the Russian Fund for Fundamental Research (Grant 96-02-16952a) is gratefully acknowledged.

[1] E. S. Moskalenko, A. V. Akimov, A. L. Zhmodikov, A. A. Kaplyanskiĭ, T. Cheng, O. Hughes, and L. J. Chalis, Fiz. Tverd. Tela (St. Petersburg) **36**, 3140 (1994) [Phys. Solid State **36**, 1668 (1994)].
[2] L. E. Golub, A. V. Shcherbakov, and A. V. Akimov, J. Phys.: Condens. Matter **8**, 2163 (1996).
[3] S. Tamura, J. A. Shields, M. T. Rambsey, and J. P. Wolf, in *Phonon Scattering in Condensed Matter VII*, edited by M. Meissner and R. O. Pohl (Springer, Berlin, 1993), p. 79.
[4] J. Martinez-Pastor, A. Vinattieri, L. Carraresi, M. Collocci, Ph. Roussignol, and G. Weimann, Phys. Rev. B **47**, 10456 (1992).
[5] T. C. Damen, J. Shah, D. Y. Oberly, D. S. Chemla, J. E. Cunningham, and J. M. Kuo, Phys. Rev. B **42**, 7434 (1990).
[6] D. Oberhauser, K.-H. Pantke, J. M. Hvam, G. Weimann, and C. Klingshirn, Phys. Rev. B **47**, 6827 (1993).
[7] A. V. Kavokin, A. I. Nesvizhskiĭ, and R. P. Seysyan, Fiz. Tekh. Poluprovodn. **27**, 997 (1993) [Sov. Phys. Semicond. **27**, 540 (1993)].
[8] G. L. Bir and G. E. Pikus, *Symmetry and Strain-Induced Effects in Semiconductors* (Wiley, New York, 1974; Russian original, Nauka, Moscow, 1972).
[9] V. Karpus, Fiz. Tekh. Poluprovodn. **20**, 12 (1986) [Sov. Phys. Semicond. **20**, 6 (1986)].
[10] L. J. Chalis, G. A. Toombs, and F. W. Sheard, in *Physics of Phonons*, edited by T. Paszkiewicz, *Lecture Notes in Physics*, Vol. 285 (Springer, Berlin, 1987), p. 348.

Translated by G. Skrebtsov

Anneal kinetics of a deposited layer in the presence of thermal desorption and particle diffusion into the substrate

N. D. Potekhina

A. F. Ioffe Physicotechnical Institute, Russian Academy of Sciences, 194021 St. Petersburg, Russia
(Submitted November 3, 1998)
Fiz. Tverd. Tela (St. Petersburg) **41**, 1712–1719 (September 1999)

The dependences of the Auger signal and adsorbate desorption flux on the anneal time and rate constants of the near-surface reactions and diffusion into the bulk have been obtained from the theory of heat conductivity. It is shown that the decay of the Auger signal with time t is a linear function of $\sqrt{t}$ only under surface-limited diffusion of adatoms into the bulk, exactly what was observed in the annealing of Si/Ta. It is shown also that the initial adatom distribution in the bulk obtained during heating the adlayers of different thickness to the anneal temperature practically does not affect the dependence of the measured signals on time, while becoming manifest in their dependence on the anneal temperature. The relation between the dissolution time of an adlayer during heating and its thickness has been found.
 [S1063-7834(99)03709-0]

Penetration of adsorbed atoms into the substrate complicates greatly the analysis of temperature-programmed desorption (TPD) spectra. Obtaining information on the kinetic parameters of penetration into the bulk, emergence from the bulk, diffusion, and desorption becomes possible only by numerical simulation.[1,2] The large number of parameters contained in a model calculation (the prefactors k_i^0 and activation energies E_i^0 of all the four processes) complicate determination of the required set of rate constants. One has to invoke additional experimental data, which can be derived from annealing of an adsorbed film at a constant temperature. The variation of the Auger signal due to adsorbate atoms near the surface and of the desorption flux are determined by the same kinetic parameters as the TPD spectra. However, in the absence of analytic expressions relating experimental data with the kinetic parameters, these data were treated approximately at a qualitative or semiquantitative level,[3–8] despite the availability of a calculation[3] of the anneal process by some model. The results of this calculation were presented only in the form of integrals, which complicated their use. Our work was aimed at deriving analytic expressions needed for the treatment of experimental data on annealing of adsorbed films. The constancy of temperature during annealing permits one to use for this purpose methods of the theory of heat and mass transport.[9,10]

1. FORMULATION OF THE PROBLEM

An adlayer is deposited on the surface at a low temperature, at which neither diffusion of adatoms into the bulk of the substrate nor their desorption is possible. The sample is heated. The adatoms start to penetrate into the bulk at a temperature T_0. The annealing is performed at a temperature $T>T_0$, where adatom desorption becomes noticeable ($T=\text{const}$).

To describe this process, introduce the rate constants for desorption (k_d), for transfer from the adlayer into the first near-surface substrate layer (k_1), and for transfer from this layer onto the surface (k_2) or into the bulk (k_m). The diffusion coefficient is related to the jump probability between sites in the bulk through $D=a_0^2 k_m$, where a_0 is the substrate lattice constant. We assume the adlayer to be also at a distance a_0 from the near-surface layer, and that the volume coordinate x is reckoned from the near-surface layer.

One has to find the particle concentration in the adlayer $N(t)$ and in the bulk $n(x,t)$ as functions of the rate constants of all the above processes. The calculation will be carried out for two cases, (I) and (II).

(I) In the first case we use the continuum approximation, with no adsorbing plane isolated, where the rate constants are assumed to be in the following relation

$$k_1=k_2=k_m>k_d. \tag{I}$$

In this case the surface ($x=0$) layer of thickness a_0 and with a concentration $N(t)=a_0 n(0,t)$ plays the part of an adplane. Here diffusion and desorption proceed directly from the surface of the continuum, and one solves only one diffusion equation for $n(x,t)$.

(II) In the case where diffusion into the bulk is limited by near-surface processes, the inequality

$$k_m>k_2>k_1>k_d \tag{II}$$

is met, because only with the rate constants related in this way can the desorption kinetics depend both on diffusion into the bulk and on near-surface processes. Indeed, for $k_m<k_2$ diffusion into the bulk is impeded and does not play any role, and for $k_d>k_1$ the adlayer evolves from the surface before the onset of diffusion into the bulk has started. For $k_2<k_1$, the particles become stuck in the bulk to fill it nearly uniformly. Thus inequality (II) reflects the most complex case, where all the above-mentioned processes are equally significant. Then the $N(t)$ and $n(x,t)$ functions can be determined from two coupled equations.

2. SOLUTION OF THE PROBLEM IN A CONTINUUM APPROXIMATION

2.1. Effect of heating on diffusion into the bulk

The adsorbate film deposited on the surface at a low temperature is a source supplying particles into the bulk during the heating of the system from T_0 to T. The distribution of particles in the bulk for a constant diffusion coefficient $D=$ const is given by the equation

$$\frac{\partial n(x,t)}{\partial t}=D\frac{\partial^2 n(x,t)}{\partial x^2}, \tag{1}$$

as well as by the boundary and initial conditions.

If a thin layer has been formed on the surface prior to diffusion

$$f_a(x)=N_a^0\delta(x)\ \ (\mathrm{cm}^{-2}), \tag{2}$$

then at time t its spreadout in the bulk is described by the function[9,10]

$$f_b(x,t)=\frac{N_a^0}{\sqrt{\pi Dt}}\exp\left(-\frac{x^2}{4Dt}\right), \tag{3}$$

and for a constant particle concentration on the surface, $n(0,t)=n_1$, by the function

$$f_1(x,t)=n_1\Phi^*\left(\frac{x}{2\sqrt{Dt}}\right), \tag{4}$$

where $\Phi^*(y)=1-\Phi(y)$, and $\Phi(y)=(2/\sqrt{\pi})\int_0^y\exp(-u^2)\,du$ is the probability integral.

However during the heating of the system the diffusion coefficient will depend also on time in accordance with the Arrhenius law

$$D(T)=D_0\exp[-E_m/kT(t)], \tag{5}$$

where E_m is the activation energy of impurity migration (diffusion) in the bulk. It is known[10,11] that the distribution of diffusing particles is also given in this case by Eq. (1) if the time is replaced in it by a variable τ

$$\tau=\int_0^t\frac{D(t')}{D_0}\,dt'=\int_0^t\exp\left[-\frac{E_m}{kT(t')}\right]dt'. \tag{6}$$

Indeed, on replacing $\partial/\partial t=[D(T)/D_0]\partial/\partial\tau$ one obtains the diffusion equation in the form

$$\frac{\partial n(x,\tau)}{\partial\tau}=D_0\frac{\partial^2 n(x,\tau)}{\partial x^2}. \tag{7}$$

If the initial and boundary conditions are both time independent, the solutions by the time $\tau=\tau(t)$ can be written, as before, in the form of (4) and (3), but with t being replaced by $\tau(t)$, and D by D_0, i.e. with substitution of $D_0\tau$ for Dt.

In the case of a linear growth of the temperature with time

$$T=T_0(1+\beta t), \tag{8}$$

one can obtain an approximate explicit dependence of τ on t from Eq. (6). By replacing t' with a variable $y=(1+\beta t')^{-1}$ and introducing the notation $\epsilon=E_m/(kT_0)$, one recasts Eq. (6) to the form[11,12]

$$\tau=-\frac{1}{\beta}\int_1^y e^{-\epsilon y}\frac{dy}{y^2}$$
$$=\frac{e^{-\epsilon y}}{\epsilon\beta y^2}\left[1-\frac{2}{\epsilon y}+\frac{6}{\epsilon^2y^2}-\cdots\right]_1^{(1+\beta t)^{-1}}. \tag{9}$$

Taking into account that $\epsilon\gg1$, we retain only the leading term in this expansion

$$\tau=\tau(t)\approx\tau_0\exp\left(-\frac{E_m}{kT}\right),\quad \text{where } \tau_0=\frac{kT_0}{E_m\beta}\left(\frac{T}{T_0}\right)^2. \tag{10}$$

Using (5), one derives from Eq. (10)

$$D_0\tau=D(T)\tau_0\equiv D\tau_0, \tag{11}$$

where τ_0 also depends on T, but weaker than exponentially. Then the particle distribution in the bulk at the start of annealing (taking into account the heating from T_0 to T) can be written, as before, in the form of (1) and (3), but with $D(T)\tau_0$ being substituted for Dt.

Up to now, we have been disregarding the possibility that the particle concentration at the adsorbent surface at $x=0$ can also depend on temperature and, hence, on the heating time, if it is determined by the limiting solubility n_c of the adsorbate, $n_c(x,t)|_{x=0}=n_c(T)$, which, as a rule, grows with T. If the $n_c(T)$ relation can be presented in the form

$$n_c(T)=n_c^0\exp(-W/kT), \tag{12}$$

where W is the heat of dissolution, then one can readily write it as a function of τ during the heating. To do this, we insert the τ/τ_0 ratio from Eq. (10) into (12) in place of the exponential

$$n(T)=n_c^0(\tau/\tau_0)^{W/E_m}=\phi(\tau). \tag{13}$$

The function of reduced time $\phi(\tau)$ found in this way is then substituted into Duhamel's expression[9,10] describing the bulk concentration for a given $\phi(\tau)$

$$f(x,\tau)=\frac{2}{\sqrt{\pi}}\int_{\mu_0}^{\infty}\phi\left(\tau-\frac{x^2}{4D_0\mu^2}\right)e^{-\mu^2}\,d\mu, \tag{14}$$

where $\mu_0=x/(2\sqrt{D\tau_0})$. According to Eq. (13), in our case

$$\phi\left(\tau-\frac{x^2}{4D_0\mu^2}\right)\approx n_c^0\left[\left(\tau-\frac{x^2}{4D_0\mu^2}\right)\Big/\,\tau_0\right]^{W/E_m}, \tag{15}$$

where the weak dependence of τ_0 on T and, hence, on τ will be neglected.

Substituting (15) into (14), factoring τ out, and taking into account Eq. (13), we obtain

$$f_c(x,\tau_0)\approx n_c(T)\frac{2}{\sqrt{\pi}}\int_{\mu_0}^{\infty}\left(1-\frac{\mu_0^2}{\mu^2}\right)^m e^{-\mu^2}\,d\mu, \tag{16}$$

where $m=W/E_m>1$, and $D_0\tau$ was replaced by $D\tau_0$, in accordance with (11). By expanding the binomial into a series and integrating it, one can show that for $x\to 0$ ($\mu_0<1$), function (16) is close to the function

$$f_c^0(x,\tau_0)=n_c(T)\Phi^*[x/(2\sqrt{D\tau_0})], \tag{17}$$

describing the bulk distribution in the hypothetical case of a constant density at the boundary equal to the limiting concentration at a finite temperature T, $n(0)=n_c(T)=\text{const}$. Far from the surface ($\mu_0>1$), the $f_c(x,\tau_0)$ function falls off as $\exp(-\mu_0^2)/(\mu_0^3\sqrt{\pi})$, i.e. μ_0^2 times faster than $\Phi^*(\mu_0)$ (Ref. 12) does.

Thus taking into account the exponential growth of the density at the boundary with increasing temperature results in a more compressed distribution in the bulk than this would follow from Eq. (17). The amount of the adsorbate dissolved from a thick film during the heating from T_0 to T is determined for the boundary concentration in Appendix with due account of Eq. (12)

$$Q(T,m)=\frac{2}{\sqrt{\pi}}n_c(T)\sqrt{D\tau_0}\,\gamma(m), \tag{18}$$

where $\gamma(m)<1$ is given by Eq. (A5), and $\tau_0=\tau_0(T)$. Appendix presents also a relation (A7) between the film thickness and the temperature T_s at which the film dissolves in the substrate under heating, which is obtained from Eq. (18) using the expression (12) for $n_c(T)$.

2.2. Description of the annealing process at $T=\text{const}$

We denote the time required to heat the system up to the annealing temperature T by t_1, and reckon the annealing time t from the moment of reaching $T=\text{const}$. The solution of the diffusion equation is determined now by the initial condition $n(x,t)_{t=0}=f(x,\tau_0)$ and the boundary conditions

$$n(\infty,t)=0, \quad D\left.\frac{\partial n(x,t)}{\partial x}\right|_{x=0}=k_d a_0 n(0,t), \tag{19}$$

or $\partial n/\partial x|_{x=0}=hn(0,t)$, where $h=k_d a_0/D$ is the emissivity in the theory of heat conductivity. The solution has the form[9,10]

$$n(x,t)=\int_0^\infty \frac{f(x',\tau_0)}{2\sqrt{\pi Dt}}\left[\exp\left(-\frac{(x-x')^2}{4Dt}\right)+\exp\left(-\frac{(x+x')^2}{4Dt}\right)\right]dx'-h\exp(h^2Dt+hx)\int_0^\infty f(x',\tau_0)\Phi^*\left(\frac{x+x'}{2\sqrt{Dt}}+h\sqrt{Dt}\right)dx', \tag{20}$$

and it can describe particle distribution in a plate only if particles do not reach the second boundary of the plate and the latter does not affect their distribution near $x=0$, the conditions met frequently in the annealing.

The flux of the particles emitted from the surface is given by the expression

$$J(t)=k_d a_0 n(x,t)_{x=0}=hDn(0,t), \tag{21}$$

where, according to Eq. (20),

$$n(0,t)=\frac{1}{\sqrt{\pi Dt}}\int_0^\infty f(x,\tau_0)\exp\left(-\frac{x^2}{4Dt}\right)dx-h\exp(h^2Dt)\int_0^\infty f(x,\tau_0)e^{hx}\Phi^*\left(h\sqrt{Dt}+\frac{x}{2\sqrt{Dt}}\right)dx. \tag{22}$$

For long times, $h\sqrt{Dt}>1$, Eq. (22) allows simplification; indeed, using in the second term the asymptotic behavior[12]

$$\Phi^*(y)=e^{-y^2}\frac{1}{y\sqrt{\pi}}\left(1-\frac{1}{2y^2}\right), \quad \text{for } y>1 \tag{23}$$

and expanding $[h\sqrt{Dt}+x/(2\sqrt{Dt})]^{-1}$ in $x/(2\sqrt{Dt})<1$, one obtains in a first approximation in place of (21)

$$J(t)|_{h\sqrt{Dt}>1}\approx\frac{1}{2t\sqrt{\pi Dt}}\int_0^\infty f(x,\tau_0)\times\exp(-x^2/4Dt)(h^{-1}+x)\,dx. \tag{24}$$

Let us consider three different approximations (A, B, and C) for the $f(x,t_1)\equiv f(x,\tau_0)$ function.

Approximation A. The simplest is approximation (2), by which the monolayer is assumed to remain unchanged under heating up to the anneal temperature T. By this approximation, both the diffusion into the bulk and desorption are considered to start simultaneously during the annealing, $t_1=\tau_0=0$, and the particle distribution in the bulk is described by the function obtained by inserting (2) into Eq. (20):

$$n_a(x,t)=N_a^0\left[\exp\left(-\frac{x_2}{4Dt}\right)\Big/\sqrt{\pi Dt}-he^{h^2Dt+hx}\Phi^*\left(\frac{x}{2\sqrt{Dt}}+h\sqrt{Dt}\right)\right], \tag{25}$$

whose variation for different anneal times is presented graphically in Fig. 1 against $\xi=x/\lambda_1$ and $\tilde{t}$ for the parameter $h_0=h\lambda_1=0.2$, where λ_1 is the diffusion path length traversed in 1 s, and $\tilde{t}=t/1\ \text{s}$ is a dimensionless variable representing the time in seconds passed after the start of annealing.

Expansion of (25) in $x/(2\sqrt{Dt})<1$ yields, to within $h^2x^2/2$, a linear growth of the impurity density at the surface

$$n(x,t)\approx n(0,t)(1+hx) \quad \text{for } x<x_h, \tag{26}$$

which is seen from Fig. 1 and is in accord with the boundary condition (19). The region of linear growth of x_h is limited by the conditions $hx\ll 1$, $x/(2\sqrt{Dt})\ll 1$, and is determined by the smallest of the quantities $x_h=\min(\lambda_1/h_0, 2\lambda_1\sqrt{\tilde{t}})$. As seen from Fig. 1, it expands for small $\tilde{t}<(2h_0)^{-2}$ with increasing t.

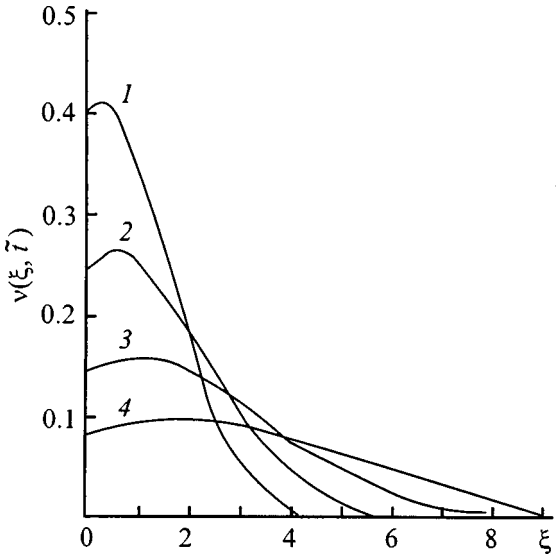

FIG. 1. Distribution of reduced density $\nu(\xi,\tilde{t})=n(x,t)\lambda_1/N_a^0$ in the bulk for various anneal times plotted in dimensionless variables $\xi=x/\lambda_1$ and $\tilde{t}=t/1$ s, where $\lambda_1=\sqrt{D\cdot 1\text{s}}$. $\tilde{t}$: *1* — 1, *2* — 2, *3* — 4, *4* — 8.

Approximation B. Taking into account monolayer spreading during the heating from T_0 to T with a diffusion coefficient $D(T)$, the initial distribution, according to Eqs. (3) and (11), will be presented by the function

$$f_b(x,\tau_0)=\frac{N_a^0}{\sqrt{\pi D\tau_0}}\exp\left(-\frac{x^2}{4D\tau_0}\right), \tag{27}$$

and its variation in the course of annealing, as well as the $n(0,t)$ relationship, can be found by substituting Eq. (27) in (20) and (22), respectively

$$n_b(0,t)=\frac{N_a^0}{\sqrt{\pi D(t+\tau_0)}}-h\exp(h^2Dt)\frac{N_a^0}{\sqrt{\pi D\tau_0}}\times\int_0^\infty\exp\left(-\frac{x'^2}{4D\tau_0}+hx'\right)\Phi^*\left(\frac{x'}{2\sqrt{Dt}}+h\sqrt{Dt}\right)dx'. \tag{28}$$

The $n(x,t)$ distribution is similar to the one shown in Fig. 1 but with the values of t displaced by τ_0. Within the region of linear growth, the bulk concentration is given by Eq. (26), as before.

Approximation C. When annealing a thick adsorbate film, the initial distribution reached under heating to T is described by the (16) function, which near the surface is close to the (17) function but falls off steeper thereafter. This results in a smaller contribution of the tail to the integrand in the (22) and (24) integrals. However in their calculation we use an approximate function (17) in place of Eq. (16), which yields only an upper estimate for these integrals.

As shown by an analysis of the exact $n_c(x,t)$ distribution, it exhibits a broader and smoother maximum for $x\geqslant x_h$ than the curve in Fig. 1, while retaining a linear growth of the adsorbate density near the surface with distance, in full accordance with Eq. (26).

Compare now the expressions for desorption fluxes for different initial distributions $f(x,\tau_0)$, namely, (2), (27), and (17), for the approximations A, B, and C, respectively.

For $h\sqrt{Dt}<1$, the second term in Eq. (22) is a correction, and therefore it will be calculated approximately using the expansion of the $\Phi^*(B+z)$ function for $z<1$, as well as the integral 6.282 from Ref. 12, to compute $n_b(0,t)$. We finally obtain the following relationships for the reduced fluxes $\tilde{J}_{a,b}(t)=J_{a,b}(t)/[a_0k_dN_a^0]$ (in cm^{-1}):

$$\tilde{J}_a(t)=1/\sqrt{\pi Dt}-h(1-2h\sqrt{Dt/\pi}\ ); \tag{29}$$

$$\tilde{J}_b(t)\approx 1/\sqrt{\pi D(t+\tau_0)}-(2h/\sqrt{\pi})\arctan\sqrt{\frac{t}{\tau_0}}, \tag{30}$$

or

$$\tilde{J}_b(t)\approx\begin{cases}(\sqrt{\pi D\tau_0})^{-1}(1-2h\sqrt{Dt/\pi}\ ), & t<\tau_0;\\ (\sqrt{\pi Dt})^{-1}(1-\pi h\sqrt{Dt}\ ), & t_h>t>\tau_0.\end{cases} \tag{31}$$

For approximation C,

$$J_c(t)\approx h\sqrt{D}2n_c(T)/\pi[\arctan\sqrt{\tau_0/t}-h\sqrt{\pi D}(\sqrt{t}+\sqrt{\tau_0}-\sqrt{t+\tau_0})]$$

or

$$\frac{J_c(t)}{k_da_0n_c(T)}\leqslant\begin{cases}[1-(2/\pi)\sqrt{t/\tau_0}-2h\sqrt{Dt/\pi}], & t<\tau_0;\\ 2/\pi\sqrt{\tau_0/t}(1-h\sqrt{\pi D\tau_0}-\tau_0/3), & t_h>t>\tau_0.\end{cases} \tag{32}$$

For $h\sqrt{Dt}>1$ $[t>t_h=(h^2D)^{-1}]$, we substitute Eqs. (2), (27), and (17) into the (23) integral for the approximations A, B, and C, respectively

$$J_a(t)\approx N_a^0/[2ht\sqrt{\pi Dt}], \tag{33}$$

$$J_b(t)\approx N_a^0(1+2h\sqrt{D\tau_0/\pi}\ )/[2ht\sqrt{Dt}], \tag{34}$$

$$J_c(t)\leqslant Q(T)(1+h\sqrt{\pi D\tau_0}/2\ )/[2ht\sqrt{\pi Dt}], \tag{35}$$

where $Q(T)=n_c(T)2\sqrt{D\tau_0/\pi}$ is the total amount of the adsorbate dissolved during the time t_1 the rod with the (17) bulk distribution was heated. For a real distribution (16), this amount should be multiplied, in accordance with (18), by a coefficient $\gamma(m)<1$. However if all of the adlayer had dissolved in the bulk during the heating before the annealing, $Q(T)$ in Eq. (35) should be replaced with the quantity $Q=n_1\bar{l}$, where $\bar{l}$ is the effective film thickness taking into account adatom evaporation during the heating [see (A8)].

These results show that the actual form of the initial distribution does not practically affect the pattern of the $J(t)$ distribution; indeed, for $t<\tau_0$ the flux decays linearly with $\sqrt{t}$, for $t_h>t>\tau_0$ it falls off proportional to $1/\sqrt{t}$, and for $t>t_h$ it varies as $(2ht\sqrt{Dt})^{-1}$, where $h=a_0k_d/D$.

Let us estimate the quantities τ_0 and t_h. For high anneal temperatures, i.e., for $T>T_0$, and for $E_m/(kT_0)>1$, Eq. (10) shows that τ_0 is less than the heating time t_1 which, as a rule, is shorter than the anneal time, $t>t_1>\tau_0$. On the other hand,

for $k_m > k_d$ the quantity $t_h = (h^2 D)^{-1} = k_m / k_d^2$ turns out to be about equal to the time required for the adsorbate to leave completely the substrate ($t_{\text{des}} \approx k_d^{-1}$). Therefore, at the beginning of annealing, the dependence of the flux on time in the continuum approximation always corresponds to the $t_h > t > \tau_0$ case.

The Auger signal of bulk atoms decays exponentially with increasing x, $I_A(x) \approx \exp(-px)$, and is determined by the $\lambda_A = 1/p$ layer, whose thickness is less than x_h (p is the Auger signal decay coefficient). Therefore, when calculating the Auger signal from the dissolved adsorbate

$$I_A(t) = I_A^0 \int_0^\infty n(x,t) e^{-px}\, dx, \tag{36}$$

one should use in all the above cases for $n(x,t)$ during the annealing the (26) relationship, which, after its substitution in (36), reduces to

$$I_A(t) \approx \ [I_A^0 n(0,t)/p](1 + h/p). \tag{37}$$

A comparison with the integral (36) calculated exactly for the (25) distribution in approximation *A* supports the validity of the latter. Thus the dependence of the Auger signal on time is determined in the continuum approximation by the density variation $n(0,t)$, which in all the cases of initial particle distribution in the bulk considered by us varies as $1/\sqrt{t}$ for typical measurement times. At the same time in the Si/Ta experiment[8] one observed a linear Auger-signal decay against $\sqrt{t}$. Therefore we shall now to consider the problem of an adlayer, where the probabilities of various processes obey inequality (II).

3. SOLUTION OF THE PROBLEM IN THE CASE OF SURFACE-LIMITED REACTIONS

In this section, we shall restrict ourselves to the adsorption of a monolayer, so that it will be appropriate to deal with concentrations reduced to one surface cell. In place of $N_a(t)$ we shall use surface coverage $\theta(t) = a_0^2 N_a(t)$, and in place of the bulk concentration $n_a(x,t)$ in cm^{-3}, the quantity $n(x,t) = n_b(x,t) a_0^2$ (in cm^{-1}). Then $a_0 n(0,t)$ is the coverage of the near-surface substrate layer. We have to solve the coupled equations

$$\partial\theta/\partial t = -(k_d + k_1)\theta + k_2 a_0 n(0,t); \quad \frac{\partial n}{\partial t} = D\frac{\partial^2 n(x,t)}{\partial x^2}; \tag{38}$$

subject to the conditions $n(\infty,t) = 0, n(x,0) = 0$, and $\theta|_{t=0} = 1$.

In writing the condition for the $x = 0$ boundary we take into account that if inequality (II) is met, particles leave the first bulk layer faster than enter it from the adlayer. Therefore one can use for the $x = 0$ boundary the flux continuity condition, or absence of particle buildup in this plane with time. In this way we neglect the time of onset of quasistationary concentration in the $x = 0$ plane and have the following equation for $n(0,t)$

$$a_0 \frac{\partial n(0,t)}{\partial t} = k_1\theta - k_2 a_0 n(0,t) + D\left.\frac{\partial n}{\partial x}\right|_{x=o} = 0. \tag{39}$$

By applying the Laplace transform to Eqs. (38) and (39)

$$\tilde{f}(x,s) = \int_0^\infty f(x,t) e^{-st}\, dt,$$

and solving coupled algebraic equations for the Laplace-transformed functions $\tilde{\theta}(s)$ and $\tilde{n}(x,s)$, we obtain the following solution to the system[3]

$$\tilde{\theta}(s) = \theta_0 \Big/ \left[S + k_1 \frac{\sqrt{sD}}{\sqrt{sD} + a_0 k_2} + k_d \right]; \tag{40}$$

$$\tilde{n}(x,s) = \frac{\theta_0 k_1 \exp(-x\sqrt{s/D})}{(s + k_1)\sqrt{sD} + a_0 k_2 s + k_d(\sqrt{sD} + a_0 k_2)}. \tag{41}$$

Because the available tables of inverse transforms[13,14] do not contain such functions, and the exact solution for the originals can be written only in the form of nonintegrable integrals[3], we shall construct approximations based on Eqs. (40) and (41). First, we assume that the terms with k_d in the denominator are smaller than the others, and that they can be taken into account by expanding the fraction in the ratio of k_d to the other terms in the denominator. Second, we take into account that annealing lasts from a few seconds to a few minutes, i.e. for $t > 1$ s. This means that the major contribution to the inversion integrals containing the factor $\exp(-st)$ or $\exp(-\rho t)$, where $\rho = \text{Re}(s)$, is due to regions with small $\rho \sim 1/t < 1$.

The dependence of the coverage θ on time is dominated by the relative magnitude of the quantities $a_0 k_2$ and $\sqrt{sD}$ in Eq. (40). If $a_0 k_2 \ll \sqrt{sD}$, then the transform (40) can be identified with the original $\theta(t) \approx \theta_0 \exp[-(k_1 + k_d)t]$, which means neglect of the reverse particle flux from the bulk into the adlayer. Such a regime is possible, however, only in the very beginning of the penetration, when the bulk is empty and $t < t^* = D/(a_0 k_2)^2$. This time interval is substantially shorter than 1 s and decreases with increasing T. For instance, for the parameters used in Ref. 3 for the O/Ta case, we obtain $t^* \approx 10^{-9}$ s. Because the times of interest in the annealing $t > 1$ s, it is the reverse inequality, $a_0 k_2 \gg \sqrt{sD}$, or $t > t^*$, that is most likely met. Then in the absence of desorption ($k_d \approx 0$) to the transform $\tilde{\theta}(s) \approx \theta_0/[\sqrt{s}(s + b)]$ corresponds the solution[13]

$$\theta_1(t) \approx \theta_0 e^{b^2 t} \Phi^*(b\sqrt{t}), \quad \text{where} \quad b = k_1\sqrt{D}/(a_0 k_2). \tag{42}$$

Expanding (40) in the ratio $k_d/(s + b\sqrt{s})$, we use tables[13,14] to take into account desorption in the first approximation. Next one can show that for $b\sqrt{t} < 1$ the $\theta(t)$ relationship is expressed by the relation

$$\theta(t) \approx \theta_0 \left[1 - \frac{2b}{\sqrt{\pi}}\sqrt{t} + (b^2 - k_d)t - \frac{4b^3 t^{3/2}}{3\sqrt{\pi}}\left(1 - \frac{2k_d}{b^2}\right)\right], \tag{43}$$

which is valid in the initial stages of annealing, but for $t \geqslant 1$ s. Neglecting the term $\sqrt{sD}$ compared to $a_0 k_d$ in Eq. (41), we use $\tilde{n}(x,s) \approx \exp(-x\sqrt{s/D})/(s + b\sqrt{s})$ to obtain the solution for the filling of the bulk[15]

$$n(x,t)\approx\frac{\theta_0 k_1}{a_0 k_2}\exp(b^2t+bx/\sqrt{D})\Phi^*\left(b\sqrt{t}+\frac{x}{2\sqrt{Dt}}\right). \quad (44)$$

In the theory of heat or mass transport,[9,10] Eq. (44) describes distribution in the bulk if the function

$$a_0 n(0,t)\approx\frac{k_1}{k_2}\theta_1(t)=\theta_0\frac{k_1}{k_2}e^{b^2t}\Phi^*(b\sqrt{t}) \quad (45)$$

is specified at the boundary.

Equation (45) is compatible with the accepted boundary condition (39) provided the particle fluxes between the adlayer and the bulk exceed by far the diffusion flux, $k_1\theta \approx k_2 a_0 n(0,t)\gg -D(\partial n/\partial x)|_{x=0}$. This regime can be realized if the bulk is already partially filled and the distribution gradient for $x\approx 0$ is very small, i.e. for $t>t^*$.

In case (II) under study here, the Auger signal from the adsorbate atoms has the form

$$I_A(t)=I_A^0 N_0\left[\theta(t)+e^{-p(a_0+a_1)}\int_0^\infty e^{-px}n(x,t)\,dx\right], \quad (46)$$

with a separate equation written for $\theta(t)$, where N_0 is the adatom density in the monolayer, $N_a(t)=N_0\theta(t)$, and a_1 is the adatom diameter. The factor in front of the integral takes into account the impurity screening in the near-surface layer $x=0$ by the substrate and adsorbate atoms. Substituting (44) in (46), we use integral 1.5.2.3 from Ref. 15 to obtain

$$\int_0^\infty e^{-px}n(x,t)\,dx=\frac{\theta_0 k_1}{a_0 k_2(p-b/\sqrt{D})}[e^{b^2t}\Phi^*(b\sqrt{t}) - e^{p^2Dt-b^2t}\Phi^*(p\sqrt{Dt})]. \quad (47)$$

Because the diffusion path length during the annealing time is substantially larger than the Auger signal penetration depth and $p\sqrt{Dt}\gg 1$, the contribution of the bulk to the Auger signal is dominated by the first term and is proportional to $\theta_1(t)$ from Eq. (42). In a first approximation, we obtain from Eqs. (42), (46), and (47) for the first moments of annealing

$$I_A(t)\approx I_A^0 N_0\theta_0\left[1-\frac{2b\sqrt{t}}{\sqrt{\pi}}+(b^2-k_d)t+\cdots\right] \times\left(1+\frac{k_1\exp[-p(a_0+a_1)]}{pa_0k_2}\right), \quad (48)$$

where $p\gg b/\sqrt{D}=k_1/(a_0k_2)$. As follows from Eq. (48), the Auger signal decreases linearly with $\sqrt{t}$. It is this relation that was found to hold when annealing a Si monolayer on Ta in Ref. 8. This means that penetration of Si into Ta is a process which is rate limited at the boundary, with the reaction rate constants related through inequality (II).

The number of particles desorbed by the time $t<1/b^2$ can be found from Eq. (43)

$$M_{\rm des}(t)=k_d\theta_0 N_0\left[t-\frac{4bt^{3/2}}{3\sqrt{\pi}}+\frac{(b^2-k_d)t^2}{2}+\cdots\right]. \quad (49)$$

4. DISCUSSION AND COMPARISON WITH EXPERIMENT

We have compared the behavior with time of the Auger signal and of the desorption flux calculated in the continuum approximation, where the properties of the diffusion medium remain unchanged up to the surface (case I), and in the approximation of surface-limited reactions, where the probabilities of adatom exchange with the bulk are less than those of hopping in the bulk (case II).

It was shown that the adatom concentration on the surface decreases in the beginning of annealing proportional to $1/\sqrt{t}$ in the first case, and linearly with $\sqrt{t}$, in the second. The dependence of the Auger signal on time in the beginning of annealing is given by $n(0,t)$ or $\theta(t)$ for $t<(h^2D)^{-1}$ and $t<1/b^2$ $[b=k_1\sqrt{D}/(a_0k_2)]$ for cases (I) and (II), respectively.

Si/Ta experiments[8] revealed an $I_A(t)$ dependence characteristic of case (II). A comparison of the slopes of graphs *5* for $I_A(\sqrt{t})$ in Ref. 8 with Eq. (48) yielded for this system

$$E_1-E_2+E_m/2\approx 1.9\ \text{eV};$$

$$b^0=k_1^0\sqrt{k_m^0}/k_2^0\approx 6\times 10^{-4}\ \text{s}^{-1/2},$$

or

$$E_1-E_2\approx(1.9\ \text{eV}-E_m/2)>0,$$

which is in agreement with inequality (II). This supports our approximation $t<b^{-2}$ accepted in Eqs. (43)–(49) for the early stage of annealing, because $b^{-2}(T)\approx 10^3-10^2$ s for $T\approx 1500-1700$ K.

In late stages of annealing, the desorption flux is determined by particles emerging from the bulk, and therefore Eqs. (24), (34), and (33) obtained in the continuum approximation are valid in case II as well. Note that $J(t)\sim\overline{Q}/(t\sqrt{Dt})$, where $\overline{Q}$ is the number of particles which have entered the bulk from 1 cm^2 of the surface during the heating to the anneal temperature. Thus we have shown that isolation of the adsorbed layer and solving the coupled equations (38) and (39) affect qualitatively the dependence of the Auger signal on time only in the early stages, where desorption is small.

Equations have been derived for the time required to dissolve an adsorbed layer and for the onset of the initial particle distribution in the bulk taking into account the dependence of the limiting concentration on temperature during the heating. It has been found what relations between the kinetic parameters of a system can be obtained from comparison with experiment.

I am indebted to V. N. Ageev for interest in the work and fruitful criticisms and to A. Yu. Potekhin for general assistance.

Support of the Program ''Surface Atomic Structures'' (Grant 95-2.12) is gratefully acknowledged.

APPENDIX A

Let us find the total amount of the adsorbate $Q(T)$ (in cm^{-2}) dissolved under heating by the time the temperature

reached T. The adsorbate distribution in the bulk during the heating is given by Eq. (16), and $Q(t)$ is determined by integration over x

$$Q(I,m)=\int_0^\infty f_c(x,I)\,dx=n_c(T)\,\frac{4\sqrt{D\tau_0}}{\sqrt{\pi}}\int_0^\infty d\mu_0 \times\int_{\mu_0}^\infty\left(1-\frac{\mu_0^2}{\mu^2}\right)^m e^{-\mu^2}\,d\mu. \quad \text{(A1)}$$

Changing the order of integration in (A1) and replacing the μ_0 variable with $z=\mu_0/\mu$, we come to

$$I=\int_0^\infty \mu e^{-\mu^2}\,d\mu\int_0^1(1-z^2)^m\,dz. \quad \text{(A2)}$$

The integral over z reduces to the B-function[12]

$$B(1/2,m+1)=2\int_0^1(1-z^2)^m\,dz=\frac{\sqrt{\pi}\Gamma(m+1)}{\Gamma(m+3/2)}. \quad \text{(A3)}$$

Thus (A1) can be recast

$$Q(T,m)=\frac{2\sqrt{D\tau_0}}{\sqrt{\pi}}n_c(T)\gamma(m), \quad \text{(A4)}$$

where the following notation has been introduced

$$\gamma(m)=\frac{\sqrt{\pi}\Gamma(m+1)}{2\Gamma(m+3/2)} \quad \text{(A5)}$$

and τ_0 is related to $T(t)$ by Eq. (10). The coefficient $\gamma(m)=1$ for $m=0$, i.e., for $W=0$, and decreases with increasing W from 2/3 for $m=1$ to 0.4 for $4<m<5$. Substituting (12), (5), and (8) for $n_c(T)$,$D(T)$, and $T(t)$ in Eqs. (A4) and (10), one can obtain the dissolution time t_s for a film of density $Q=n_1 l$ (where n_1 is the adsorbate concentration and l is the film thickness)

$$1+\beta t_s=(E_m+2W)/[kT_0\ln[4n_c^0D_0\tau_0/(\pi Q^2)]], \quad \text{(A6)}$$

and the expression relating the film thickness to the temperature at which it dissolves in the substrate

$$\frac{E_m+2W}{2}\left(\frac{1}{kT_{2s}}-\frac{1}{kT_{1s}}\right)=\ln\frac{T_{2s}l_1}{T_{1s}l_2}. \quad \text{(A7)}$$

As follows from Eq. (A6), the film dissolution time increases with increasing activation energies E_m and W and with decreasing T_0 and β, which is physically reasonable. The film dissolution comes to an end when the remaining surface coverage $\theta_c=a_0^3n_c(T)$ is considerably less than unity, $\theta_c\ll 1$, because $n_c(T)\ll a_0^{-3}$. Under these conditions, the Auger signal from the adsorbate is small and constitutes a fraction θ_c of that corresponding to a monolayer. Using Eq. (A6) in practical work may be complicated by the lack of data on $n_c(T)$.

The number of particles desorbed from a thick film under its heating from T_1 to T_2 can be obtained by analogy to the derivation of Eq. (10)

$$\Delta Q_{\text{des}}=k_d(T_2)n_1a_0\tau_2\left[1-\frac{T_1^2}{T_2^2}\exp\left(-\frac{E_d(T_2-T_1)}{kT_1T_2}\right)\right], \quad \text{(A8)}$$

where $\tau_2=kT_2^2/(\beta E_dT_0)$. Then the effective thickness of the dissolved film will decrease, $n_1\bar{l}=n_1l-\Delta Q_{\text{des}}$.

[1] V. N. Ageev, A. Yu. Potekhin, and N. D. Potekhina, Poverkhnost' No. 1, 31 (1987).
[2] V. N. Ageev, A. Yu. Potekhin, and N. D. Potekhina, Poverkhnost' No. 1, 5 (1991).
[3] A. I. Gubanov, Fiz. Tverd. Tela (Leningrad) **15**, 740 (1973) [Sov. Phys. Solid State **15**, 400 (1973)].
[4] V. N. Ageev, E. Yu. Afanas'eva, N. R. Gall', E. V. Rut'kov, and A. Ya. Tontegode, Poverkhnost' No. 5, 7 (1987).
[5] V. N. Ageev and E. Yu. Afanas'eva, Pis'ma Zh. Tekh. Fiz. **12**, 565 (1986) [Sov. Tech. Phys. Lett. **12**, 231 (1986)].
[6] V. N. Ageev, E. Yu. Afanas'eva, S. M. Solov'ev, and A. K. Grigor'ev, Fiz. Tverd. Tela (St. Petersburg) **35**, 481 (1993) [Phys. Solid State **35**, 248 (1993)].
[7] E. Yu. Afanas'eva, N. D. Potekhina, and S. M. Solov'ev, Fiz. Tverd. Tela (St. Petersburg) **37**, 463 (1995) [Phys. Solid State **37**, 251 (1995)].
[8] N. R. Gall, E. V. Rut'kov, A. Ya. Tontegode, and M. M. Usufov, Phys. Low-Dimens. Semicond. Struct. **4/5**, 75 (1996).
[9] H. S. Carslaw and J. C. Jaeger, *Conduction of Heat in Solids* (Clarendon Press, Oxford, 1958; Nauka, Moscow, 1964, 487 pp.).
[10] A. I. Raĭchenko, *Mathematical Theory of Diffusion in Applications* [in Russian] (Naukova Dumka, Kiev, 1981), 396 pp.
[11] P. A. Redhead, Vacuum **12**, 203 (1962).
[12] *Tables of Integrals, Series, and Products*, edited by I. S. Gradshteĭn and I. M. Ryzhik (Academic, New York, 1980; Russian original, Nauka, Moscow, 1971).
[13] G. Doetsch, *Theorie und Anwendungen der Laplace-Transformation* (Springer, Berlin, 1937; GIFML, Moscow, 1958).
[14] H. Bateman and A. Erdélyi, *Tables of Integral Transforms* (McGraw-Hill, New York, 1954; Nauka, Moscvow, 1969), Vol. 1.
[15] A. P. Prudnikov, Yu. A. Brychkov, and O. I. Marichev, *Integrals and Series* [in Russian] (Nauka, Moscow, 1981), 796 pp.

Translated by G. Skrebtsov